REPORT DOCUMENTATION PAGE

Form Approved OMB NO. 0704-0188

The public reporting burden for this collection of information is estimated to average 1 hour per response, including the time for reviewing instructions, searching existing data sources, gathering and maintaining the data needed, and completing and reviewing the collection of information. Send comments regarding this burden estimate or any other aspect of this collection of information, including suggesstions for reducing this burden, to Washington Headquarters Services, Directorate for Information Operations and Reports, 1215 Jefferson Davis Highway, Suite 1204, Arlington VA, 22202-4302. Respondents should be aware that notwithstanding any other provision of law, no person shall be subject to any oenalty for failing to comply with a collection of information if it does not display a currently valid OMB control number.
PLEASE DO NOT RETURN YOUR FORM TO THE ABOVE ADDRESS.

1. REPORT DATE (DD-MM-YYYY)	2. REPORT TYPE	3. DATES COVERED (From - To)
23-09-2022	Thesis or Dissertation	-

4. TITLE AND SUBTITLE
Graphene-based nanodevices in the superconducting and strongly correlated regimes

5a. CONTRACT NUMBER
W911NF-18-1-0116

5b. GRANT NUMBER

5c. PROGRAM ELEMENT NUMBER

6. AUTHORS
Daniel Rodan Legrain

5d. PROJECT NUMBER

5e. TASK NUMBER

5f. WORK UNIT NUMBER

7. PERFORMING ORGANIZATION NAMES AND ADDRESSES
Massachusetts Institute of Technology (MIT
77 Massachusetts Avenue
NE18-901
Cambridge, MA 02139 -4307

8. PERFORMING ORGANIZATION REPORT NUMBER

9. SPONSORING/MONITORING AGENCY NAME(S) AND ADDRESS (ES)
U.S. Army Research Office
P.O. Box 12211
Research Triangle Park, NC 27709-2211

10. SPONSOR/MONITOR'S ACRONYM(S)
ARO

11. SPONSOR/MONITOR'S REPORT NUMBER(S)
71720-PE-OC.11

12. DISTRIBUTION AVAILIBILITY STATEMENT
Approved for public release; distribution is unlimited

13. SUPPLEMENTARY NOTES
The views, opinions and/or findings contained in this report are those of the author(s) and should not contrued as an official Department of the Army position, policy or decision, unless so designated by other documentation.

14. ABSTRACT

15. SUBJECT TERMS

16. SECURITY CLASSIFICATION OF:			17. LIMITATION OF ABSTRACT	15. NUMBER OF PAGES	19a. NAME OF RESPONSIBLE PERSON
a. REPORT	b. ABSTRACT	c. THIS PAGE			William Oliver
UU	UU	UU	UU		19b. TELEPHONE NUMBER 617-258-6018

REPORT DOCUMENTATION PAGE (SF298)
(Continuation Sheet)

Continuation for Block 13

Proposal/Report Number: 71720.11-PE-QC

Report Title: Graphene-based nanodevices in the superconducting and strongly correlated regimes
Report Type: Ph.D. Dissertation

Publication Type: Thesis or Dissertation
Institution: Dept. of Physics, MIT
Date Received: 23-Sep-2022 Completion Date: 5/13/22 4:00PM
Title: Graphene-based nanodevices in the superconducting and strongly correlated regimes
Authors: Daniel Rodan Legrain
Acknowledged Federal Support: **N**

Graphene-based nanodevices in the superconducting and strongly correlated regimes

by

Daniel Rodan-Legrain

B.A., Polytechnic University of Catalonia (2016)

Submitted to the Department of Physics
in partial fulfillment of the requirements for the degree of

Doctor of Philosophy in Physics

at the

MASSACHUSETTS INSTITUTE OF TECHNOLOGY

May 2022

© Massachusetts Institute of Technology 2022. All rights reserved.

Author . . . . . .
Department of Physics
May 13, 2022

Certified by . . . . . .
Pablo Jarillo-Herrero
Cecil and Ida Green Professor of Physics
Thesis Supervisor

Accepted by . . . . . .
Deepto Chakrabarty
Associate Head of Physics

A mis padres, Linda y Alex,
mis hermanos, Emmy y Miky,
y mi (muy pronto) futura esposa, Teresa.

Graphene-based nanodevices in the superconducting and strongly correlated regimes

by

Daniel Rodan-Legrain

Submitted to the Department of Physics
on May 13, 2022, in partial fulfillment of the
requirements for the degree of
Doctor of Philosophy in Physics

Abstract

The ability to isolate and manipulate high-quality few-atoms-thick materials represents a major advance in condensed matter physics. Assembling these ultra-thin materials into van der Waals heterostructures, i.e., artificial meta-materials with atomically sharp interfaces, markedly increases the rich variety of physical properties accessible in 2D systems.

Graphene, a carbon-based 2D hexagonal lattice, possesses exceptional properties that since its discovery in 2004 have attracted wide attention from the scientific and engineering communities. In this work, I present a series of experiments via two different approaches, i.e., proximity effect and twist angle design, to induce superconductivity and strong correlations in graphene-based systems—two phenomena that do not intrinsically occur in this material.

In the first part of this thesis, graphene is flanked by two superconductors and inherits their superconducting properties by proximity effect. Initially, the underlying microscopic mechanism of this phenomenon is investigated using planar tunneling spectroscopy. Then, a superconductor-graphene-superconductor junction is coupled to a superconducting circuit to create and manipulate the first graphene-based transmon qubit.

In the second part of this dissertation, the electronic properties of graphene-based systems are engineered by controlling the relative twist angle between the atomic planes. In particular, when two graphene sheets are stacked on top of each other near the "magic angle," $\theta \approx 1.1^\circ$, nearly flat bands develop, featuring superconductivity and correlated insulating states. I begin by showing that local electrostatic control over the different electronic phases of magic-angle twisted bilayer graphene (MATBG) enables the creation of versatile hyper-tunable quantum devices. I also present low-temperature transport experiments to demonstrate the emergence of two exotic electronic phases in MATBG previously observed in other strongly correlated systems: nematicity and strange metal behavior. Next, I discuss local electronic compressibility measurements, evidencing that the low-temperature correlated phases originate from a high-energy state with an unusual band population sequence. Then, I describe nano-optics studies, probing plasmonic collective excitations in MATBG. Last, the study of a novel 2D moiré system beyond MATBG, i.e., twisted bilayer-bilayer graphene, is discussed.

The contributions of this thesis to the field pertain to graphene-based superconducting devices and the MATBG rich phase diagram and may find applications in next-generation superconducting electronics.

Thesis Supervisor: Pablo Jarillo-Herrero
Title: Cecil and Ida Green Professor of Physics

Acknowledgments

When I started this adventure six years ago, I was undoubtedly a very different person. These last few years would not have been the same without all the fantastic people that have accompanied me along this (*highly non-linear*) path and made me who I am now, and to whom I will be grateful the rest of my life.

First, I would like to thank Prof. Pablo Jarillo-Herrero, my PhD advisor, who invited me to join his group as a visiting student originally in 2015, and then offered me the opportunity to pursue my PhD surrounded by this very talented group of people. The doors of Pablo's office have always been opened for whatever needed to be discussed, no matter the time or the topic. He has always provided me with valuable advice in all aspects of life, including science, career and personal. Pablo has been a great support throughout all these years, both when things were running smoothly and in the most challenging times. I feel honored to have seen Pablo become a world-leading physicist in the field of twistronics and to some extent, been indirectly part of these achievements while I keep learning from him every day. Few people have such a long-term vision as he does, and his versatility to communicate science at all levels and make it accessible to everyone is a constant inspiration for me. It has been a true pleasure to have such a brilliant advisor!

On a more personal note, I am extremely grateful to the person I will walk hand-in-hand in life together, and a pillar of support throughout these years: my very soon-to-be future wife. My life has unimaginably improved since I met you, and I can't wait to build a life together for the years to come, wherever destiny takes us. I enjoy our conversations, little jokes and trips together as if they were the first! We probably met during one of the most challenging times of my PhD, right before my qualification exams and while working on a highly competitive research project. Yet, we bonded immediately and quickly realized that we were meant to be despite coming from opposite sides of the globe. Teresa, my PhD time (and my life!) would not have been the same without you. Never forget it: "I love you more!" I truly feel blessed we met, and extremely fortunate to be calling you my fiancée, and wife in a few weeks. To the best quarantine buddy I could have ever asked for, to my light in the darkest moments, and to my joy every single morning, this thesis is also yours,

Teresita!

A very special mention goes to my family. For always being there, the education they gifted me with, and the care they took of me. For always supporting me to achieve my goals, providing me with continuous encouragements, and teaching me to never surrender. Words cannot express all the sacrifices they have made on my behalf. None of this would have been possible without them, and this thesis goes to all of them. To my mum, Linda, for devoting her life to her family and children. Her strength, conviction for her ideas, and devotion are a constant inspiration. To my dad, Alex, for introducing me to science, teaching me the importance of being organized and disciplined in life from early ages, the value of logical thinking, and most importantly, his unconditional love and support. To my sister, Emmy, who constantly overcomes her goals with admirable perseverance. I am convinced she will soon become a phenomenal Doctor and keep achieving her life dreams. And last but not least, to my brother, my "best man" not only on the wedding day, but also in life! Thank you for reminding me tirelessly of the importance of these little details in life that make the difference. Thank you for taking me out of my comfort zone, challenging me, balancing my ways, and altogether making me a better person day after day. I feel grateful to have grown up close to you all! Family, there is only one, and I will always love you!

I want to express my acknowledgment to the whole research group that since the first day I arrived, they welcomed me, helped me, and cheered me on when things were not working as expected. I really want to thank all of them for the stimulating discussions, the sleepless nights we were working at the lab, and also all the fun we have had together!

In particular, I am immensely thankful to my mentors and colleagues with whom I have had the pleasure to work closely with these last few years.

In particular, I would like to acknowledge my first PhD mentor, colleague, collaborator, and friend, Joel Wang, now a research scientist in the group of Will Oliver. Joel taught me the value of being disciplined and rigorous in science and nano-fabrication. Joel never surrenders, and he taught me the importance of being persistent in this field when things do not work out until the tendency ultimately reverts. He has always been a model to follow, and I feel honored to say I am following his steps and will join the same group for my

Postdoc where he is currently working.

I am indebted to my undergrad thesis mentor Efren Navarro, currently a Professor in Valencia. Efren introduced me into the world of condensed matter physics research and taught me with limitless patience and motivation new things every day, ranging from physics, chemistry, nanofabrication techniques, to life lessons. His guidance helped during my visiting student stay and provided me with priceless support I will never forget when I started real-world research.

During my first PhD project, I feel privileged to have worked with Landry Bretheau, now a Professor at École Polytechnique. Landry has remarkable knowledge of mesoscopic physics and an enviable capacity to communicate it on a blackboard, patiently replying to all my questions one after the other. Landry taught me the importance of carefully thinking about an experiment's design before attempting to build anything, and that the evil (and interesting physics!) lies in the details. His meticulous and organized scientific approach has been a model to follow in my scientific career since that very first project with him.

Some of the projects that later on worked out and constituted part of the core of my PhD thesis were originally started with Mueed, now at IBM. Together, we developed several recipes that turned out to be of key importance in the fabrication of dual-gated twisted graphene devices, among other crucial developments. His enthusiasm and great sense of humor made me remember that period working together as one of my happiest moments in the PhD, despite the initial difficulties we encountered in the emerging field of twisted bilayer graphene.

All the magic-angle twisted graphene results presented throughout this PhD thesis were produced hand-in-hand with Yuan Cao, now a Junior Fellow at Harvard, and one of the brightest physicists I have ever encountered. I feel very grateful to all Yuan has taught me, which is now part of my scientific backpack. His scientific intuition, excellent physics knowledge, and electronics skills are admirable!

In the last few years of my PhD, I have had the delight to work closely with two fantastic physicists and amazing people, Mallika Randeria and Sergio de la Barrera. Mallika, formerly a Pappalardo Fellow and currently at Lincoln Lab, has infinite patience, and I have enjoyed every single scientific discussion with her. Her rigor is admirable; she always

has the right questions to ask and is always willing to offer her help. Sergio is currently a postdoc in Pablo and Ray's lab. I am convinced he will soon become a wonderful PI. He has all the qualities one could ask for: he has an excellent scientific intuition, he is an outstanding communicator, he has a deep knowledge of lab instrumentation, and he gets along and collaborates with everyone. They have both been a great support in some of the toughest moments I have encountered in my life, cheering me up tirelessly and converting every day together into a blessing. The quarantine would not have been the same without you and our never-ending scientific (and non-scientific) discussions! I feel very grateful to have in our team also Aviram Uri, the latest incorporation, a Pappalardo Fellow at MIT with a deep physics knowledge who I am convinced will do a tremendous job in our group in the years to come!

I also feel fortunate to have closely worked and mentored very bright and talented undergraduate and junior grad students. Oriol Rubies-Bigordà, now at Harvard, did a fantastic job and helped us with a wide variety of projects and collaborations during one of the most intense times in the lab. Jane Park has now flourished as a researcher with pioneering results in multilayered twisted graphene structures. Thao Dihn, now at Harvard, is one of the hardest-working and dedicated undergraduate students I have ever encountered. Last but not least, Ghadah Alshalan, now a Rhodes Fellow at Oxford, pioneered some of the tunneling experiments in twisted graphene devices currently under study.

I can't imagine my PhD without all the wonderful labmates with whom I have shared and enjoyed the everyday research life. Antonio Benítez, my very dear office mate in the last year and running buddy: I will surely miss our daily conversations and meals together. Dahlia Klein, we have grown together as scientists throughout these last few years sharing the good and less often bad days together. Your departure has left a vacancy in the lab that will surely be hard to fill. I am certain you will make great contributions throughout your Postdoc and become a fantastic PI as you have always wanted! Valla Fatemi, now at Cornell, I will always be indebted for your great mentoring in my first few years even though we never worked directly together, and for your availability to discuss at any time physics, general ideas, and any topic that might arise during random conversations and seminars! And thank you also for teaching me how to play a sport that would then change

my life: squash! Denis Bandurin, I am convinced you will do an excellent job in Singapour. Qiong Ma and Suyang Xu, I am happy you both found good positions in Boston, and I look forward to following your research at the frontier of science and seeing how you keep pushing the limits of human knowledge. Luiz Gustavo Pimientas, my very first officemate and very dear friend, Clément Collignon, David Macneill, Eric Soriano, Märta Tschudin, Kenji Yasuda, Yafang Yang, Yaqing Bie, Liqiao Xia, Xirui Wang, Isaac Zheng, Isabelle Phinney, Sanfeng Wu, Javier Sanchez-Yamagishi, Yonglong Xie, Xueqiao Wang, Jason Luo, Melis Tekant, Francisco Machado: to all of you, I will surely keep you in my heart, and I look forward to keeping in touch! And last but not least, I feel very lucky to have had such friendly and helpful assistants in our team, Monica Wolf and Gerry Miller!

I have been immensely privileged to collaborate with some of the most gifted people that helped me shape my PhD. Will Oliver, also a member of my thesis committee, is a role model for me to follow in the future. He is one of the most dedicated, talented, and nicest professors I have had the pleasure to interact with, and his Superconducting Qubits class awoke my interest and passion for the field of quantum computing. I feel honored to be able to call him my future postdoc advisor. I also enjoyed collaborating with several very talented and sharp physicists in Israel. Shahal Ilani and his students Asaf Rozen and Uri Zondiner have a state-of-the-art scanning SET tool that helped us discover several surprising phenomena in twisted bilayer graphene. Also in Israel at the Weizmann Institute, the group of Eli Zeldov, with his students Sameer Grover and Aviram Uri, has a complementary and equally impressive scanning-squid tool that *gifted* the field of condensed matter with astonishing scans, with nanometric resolution, of magic angle samples. In Spain, I have had the immense pleasure to work with Frank Koppens' group and his very talented and disciplined student Niels Hesp, performing optical near-field s-SNOM experiments in MATBG. On a theoretical front, our interactions with some of the best physicists in our field have been of invaluable scientific worth, some of which have resulted in publications together. I am thankful to Debanjan Chowdhury, Senthil Todadri, Noah F.Q. Yuan, Liang Fu, Z. Dong, Leonid Levitov, Shiang Fang, Stephen Carr, Efthimios Kaxiras, and Brian Skinner.

I would also like to acknowledge Marin Soljacic, together with Pablo and Will, for

being part of my PhD thesis Committee. Their sharp and to-the-point questions have undoubtedly helped me improve this thesis and provided valuable guidance along this path.

Ray has been an ideal academic advisor. He has provided me helpful advice academic-wise, science-wise, and career-wise throughout these years. Thank you, Ray!

To all the great friends I made along the way, many of which I'm sure will be friends for life: my years at MIT would not have been the same without you! I would not like to forget anyone, and will not cite them all here, but you surely know who you are! Thank you all and each of you for making this experience at MIT even more incredible and memorable!

I will always keep in my heart my former roommates, my *second* family in the USA: Ferran, Maria, Alex, Helena, Xavi, and the extended "Harvard St family"!

I am indebted to the La Caixa Fellowship, not only for supporting me during the first two years of my PhD, but also for giving me the opportunity to access a great network of people, many of which are now among my closest friends who we meet regularly in Boston, and yearly in Barcelona and for Thanksgiving! A special call out to our "quarantine buddies" and glamping mates, Alex and Pilar, who have become one of our inseparable friends here in Boston!

The student association Spain@MIT, which I have been part of the board for several years, has been a great resource to meet with the Spanish community and encounter interesting new people. It has offered me the opportunity to gather and play soccer and basketball with them, and compete in the MIT intramurals against other departments or students associations. I am also grateful to Catalans@MIT for the same reasons, and the Hellenic association HSA for accepting me as *one more greek* from the first day of my PhD to the very last one in your basketball team and share your victories and defeats surrounded by such a friendly team!

I would certainly be much less healthy now if I hadn't had such amazing gym and running buddies, who kept me sane and active all those years while motivating each other despite the weather, time, or tiredness: Francesco, Ari, Juanjo, Marc, Ximo, Antonio, and all the *Tomorrow runners*... thank you!

Last, I would like to express my gratitude to the Jewish associations on campus, Hillel, and Chabad, for always making me feel welcome and allowing me to attend the main

celebrations as if I was surrounded by my family, despite being on the other side of the Atlantic ocean! Thank you also for giving me the opportunity to meet wonderful people and make many new friends!

I would also like to express my special thanks to the Interdisciplinary Higher Education Center (CFIS), and its director and co-advisor of my undergraduate thesis, Prof. Miguel Angel Barja, for providing me with invaluable opportunities in my life through a high-quality education and an always personable treatment.

These lines would not be complete without remembering all my teachers and professors from Engineering Physics, Mathematics, and the Lycée Français de Barcelone. Their insight, expertise, and enthusiasm made a strong impression on me and enforced my will to pursue scientific studies.

Contents

1 Introduction **29**

1.1 Motivation 29

1.2 Overview and outline of this thesis 35

1.3 List of publications derived from this thesis 39

1.4 Talks and presentations derived from this thesis 41

2 Basic theoretical concepts and device fabrication **45**

2.1 2D Materials and van der Waals heterostructures 45

2.2 Electronic properties of graphene 49

2.2.1 Monolayer graphene 50

2.2.2 Bilayer graphene 55

2.3 Superconductivity 57

2.3.1 Introduction to superconductivity 57

2.3.2 BCS theory 58

2.3.3 High-T_c superconductors 59

2.3.4 Transport signatures of superconductivity 60

2.3.5 Density of states and tunneling 61

2.4 Proximity effect and Josephson effects 61

2.4.1 Proximity effect 61

2.4.2 DC Josephson effect 62

2.4.3 AC Josephson effect 63

2.4.4 Josephson junctions in a magnetic field 63

2.4.5 Summary of the Josephson effect 66

2.5 Circuit QED and superconducting qubits 67
2.5.1 Introduction to circuit QED 67
2.5.2 Quantum information via superconducting qubits: realization and manipulation 70
2.6 Moiré patterns 75
2.7 Commensurability 76
2.8 Twisted Bilayer Graphene 77
2.8.1 Motivation 77
2.8.2 Band structure 78
2.8.3 Localization 85
2.8.4 Correlated insulating states in MATBG 85
2.8.5 Superconductivity in MATBG 86
2.8.6 Phase diagram 87
2.8.7 Electronic behavior (two-probe measurements) 88
2.8.8 Transport characterization of superconductivity 89
2.8.9 Statistics 91
2.8.10 Twist-angle inhomogeneity 93
2.8.11 Magnetism and topology 94
2.8.12 Twisted bilayer-bilayer graphene and electric field tunability 96
2.9 Device fabrication 97
2.9.1 Boron nitride 98
2.9.2 Micromechanical exfoliation of flakes 101
2.9.3 Heat Cleaning 105
2.9.4 Flakehunting 106
2.9.5 Ultra-thin layers of hBN 107
2.9.6 Transfer setup, polymer-based dry transfer technique, tear-and-stack, and cut-and-stack 109
2.9.7 AFM Microscopy 121
2.9.8 Electron beam lithography 121
2.9.9 Reactive ion etching 124

2.9.10 Thermal evaporation and 1D contacts . . . 128
2.9.11 Additional cleaning of samples: AFM brooming . . . 130
2.9.12 Fabrication of an archetypal device combining the previous techniques . . . 131
2.10 Device measurement . . . 134
2.10.1 Low temperature transport measurements of the MATBG devices . 134
2.10.2 Twist angle extraction . . . 135
2.11 Scanning techniques . . . 138
2.11.1 Scanning SET . . . 140
2.11.2 Scanning near-field optical microscopy (s-SNOM) . . . 143

3 Tunneling spectroscopy of graphene nanodevices coupled to large gap superconductors 147
3.1 Motivation and introduction . . . 148
3.2 Device structure and fabrication . . . 149
3.3 Proximitized graphene: density of states . . . 151
3.4 Microscopic quantum dots weakly coupled to proximitized graphene . . . 153
3.5 Conclusion . . . 155

4 Coherent control of a hybrid superconducting circuit made with graphene-based van der Waals heterostructures 157
4.1 Introduction . . . 158
4.2 Experimental setup . . . 158
4.2.1 van der Waals materials and quantum information . . . 158
4.2.2 Experimental setup: hybrid superconducting circuit . . . 160
4.2.3 Sample fabrication and measurement setup . . . 160
4.3 Results and discussion . . . 161
4.3.1 Frequency-resolved spectroscopy of the graphene transmon qubit . 162
4.3.2 Temporal quantum coherence and control of the graphene transmon qubit . . . 165
4.3.3 Additional discussion on back gate dependence . . . 168

4.4 Summary and conclusion . . . 168
4.5 Outlook . . . 169

5 Highly tunable junctions and non-local Josephson effect in magic-angle graphene tunnelling devices 171

5.1 Introduction . . . 172
5.2 Highly Tunable Josephson Junctions . . . 173
5.3 Nonlocal Josephson Effect . . . 176
5.4 Tunneling spectroscopy in the superconducting regime . . . 178
5.5 Single-Electron transistor regime . . . 182
5.6 Summary and outlook . . . 185
5.7 Comparison of our work with a related experiment, published in the same issue of Nature Nanotechnology . . . 185
5.8 Extended data and supplementary information . . . 187
5.8.1 Additional Fraunhofer patterns for device A . . . 187
5.8.2 Anomalous pattern in device A . . . 187
5.8.3 Transport characterization of device B . . . 189
5.8.4 Evidence of superconducting gap and single-electron transistor behavior in device A . . . 190
5.8.5 SET oscillation frequency . . . 194
5.8.6 Transport characterization of device C . . . 195
5.8.7 Simulation of Bulk and Planar Josephson junctions in the presence of an external magnetic field . . . 195
5.8.8 Simulation of the charge distribution and the appearance of insulating barriers for the tunneling and the single-electron transistor . . . 198
5.8.9 Further analysis of the tunneling spectra in devices B and C . . . 200
5.8.10 Fits to the tunneling data . . . 200

6 Nematicity and Competing Orders in Superconducting Magic-Angle Graphene 207

6.1 Introduction . . . 208

6.2 Results . . . 209
6.2.1 Characterization of magic-angle graphene . . . 209
6.2.2 Anisotropic behavior in the normal phase . . . 211
6.2.3 Nematic superconducting state . . . 215
6.2.4 Anisotropic response of the superconducting gap . . . 218
6.3 Discussion . . . 221
6.4 Conclusion . . . 225
6.5 Extended data and supplementary information . . . 225
6.5.1 Sample fabrication . . . 225
6.5.2 Measurement setup and data analysis . . . 225
6.5.3 Landau fan diagram . . . 226
6.5.4 Normal-state anisotropy measured through transverse voltage . . . 226
6.5.5 Compensation for device tilt in in-plane magnetic field measurements 228
6.5.6 Statistics of superconducting devices . . . 230
6.5.7 Perpendicular critical magnetic field of devices A and B . . . 231
6.5.8 Nematicity versus current flow direction . . . 231
6.5.9 Nematicity vs. temperature and perpendicular field . . . 234
6.5.10 In-plane field response at the wedge-like feature . . . 235
6.5.11 Continuum modeling of TBG in an in-plane magnetic field . . . 236
6.5.12 Additional anisotropy data . . . 238
6.5.13 Phenomenological analysis of the nematicity . . . 239

7 Strange metal in magic-angle graphene with near Planckian dissipation 247
7.1 Introduction . . . 247
7.1.1 Planckian dissipation . . . 247
7.1.2 Magic-angle twisted bilayer graphene . . . 248
7.2 Transport characterization . . . 250
7.3 T-linear resistivity near $\nu = \pm 2 \pm \delta$ . . . 250
7.4 T-linear resistivity at other fillings . . . 253
7.5 Strange metal behaviour in the cuprates . . . 254

7.6 Planckian scattering in MATBG . . . 254
7.7 Comparison to other correlated materials and monolayer graphene . . . 257
7.8 Discussion: possible mechanisms responsible for the observed transport phenomenology . . . 257
7.9 Outlook . . . 260
7.10 Extended data and supplementary information . . . 261
7.10.1 Estimate of T_{coh} . . . 261
7.10.2 Theoretical estimate of the resistivity slope . . . 262
7.10.3 Phase stiffness . . . 262

8 Cascade of phase transitions and Dirac revivals in magic-angle graphene 267
8.1 Introduction . . . 268
8.2 Transport characterization . . . 269
8.3 Inverse compressibility and chemical potential . . . 270
8.4 Twist angle characterization . . . 270
8.5 Asymmetric sawtooth features in inverse compressibility . . . 272
8.6 Parallel magnetic field dependence of the asymmetric sawtooth features . . . 274
8.7 Temperature dependence of the asymmetric sawtooth features . . . 276
8.8 Discussion: phase transitions and Dirac revivals model . . . 277
8.9 Conclusion . . . 279
8.10 Entropic evidence for a Pomeranchuk effect in magic-angle graphene . . . 280

9 Observation of interband collective excitations in twisted bilayer graphene 283
9.1 Introduction . . . 284
9.2 Motivation . . . 284
9.3 Optical properties of TBG . . . 285
9.4 Near-field experiments on TBG . . . 287
9.4.1 Sample fabrication and pre-characterization . . . 287
9.4.2 Experimental setup: s-SNOM measurements . . . 287
9.4.3 Observation of collective excitations . . . 288
9.4.4 Analysis of the propagating collective modes . . . 290

9.4.5 Carrier-density dependence of the collective excitation wavelength . 292
9.5 Extraction of the optical conductivity. 292
9.6 Theory of interband transitions in TBG 293
9.6.1 Chirally-symmetric continuum model 295
9.6.2 Calculated properties of the relevant interband transition as functions of the tunnelling amplitude in the AA regions 296
9.6.3 AA tunneling amplitude reduction: discussion 297
9.7 Summary and outlook 298

10 Tunable correlated states and spin-polarized phases in twisted bilayer–bilayer graphene 299

10.1 Introduction and motivation 300
10.2 Transport characterization 301
10.3 Displacement field tunable correlated insulator states 303
10.4 Magnetic field response of the displacement-field-tunable correlated insulator states 306
10.5 Correlated insulator states in small twist angle bilayer-bilayer graphene, a multi-flat-band system 309
10.6 Summary 311
10.7 Extended data and supplementary information 311
10.7.1 Fabrication 311
10.7.2 List of measured TBBG devices 312
10.7.3 Sample quality and Landau fans 313
10.7.4 Linear R-T behaviour 315
10.7.5 Theoretical methods 317
10.7.6 Additional magnetic field response data 318
10.7.7 I-V curves 318

11 Summary and Outlook 321

11.1 Twisted bilayer graphene: summary, big questions, and follow-up experiments 322

11.1.1 MATBG 322
11.1.2 MATBG: a proxy for understanding strongly correlated systems . . 322
11.1.3 MATBG: an attractive material in its own right, a platform for the study of strongly correlated physics 323
11.1.4 Big questions 324
11.1.5 Additional open questions and possible follow up experiments to elucidate MATBG's biggest mysteries 324
11.2 Exotic physics in 2D systems with flat bands beyond MATBG 326
11.3 Technical challenges 328
11.4 Technological Interest 329
11.5 2D Materials and cQED 331

List of Figures

2-1 The family of 2-dimensional materials 47
2-2 Van der Waals heterostructures and Lego bricks 49
2-3 Graphene structure 52
2-4 Optical micrograph of a graphene flake 53
2-5 Graphene band structure 54
2-6 Bilayer graphene 56
2-7 Electrically tunable bandgap in bilayer graphene 56
2-8 Josephson junctions and SQUIDS 64
2-9 Basic architecture of cQED. 68
2-10 Superconducting qubits characterization. 72
2-11 Evolution of the lifetime of superconducting qubits 73
2-12 Examples of moiré patterns 76
2-13 α parameter 79
2-14 TBG reciprocal space and localization 81
2-15 TBG band structure (cartoon) 83
2-16 TBG band structure (calculation) 84
2-17 Simplified schematic of the MATBG phase diagram 88
2-18 Comparison of the two-probe conductivity of a large-angle TBG device, an intermediate-angle TBG device, and a magic-angle TBG device 90
2-19 Four-probe resistance R_{xx} versus temperature and filling for a prototypical device. 91
2-20 MATBG “statistics” (Figure 1/3) 92
2-21 MATBG “statistics” (Figure 2/3) 93

2-22 MATBG “"statistics”" (Figure 3/3) 94
2-23 Twist angle disorder 95
2-24 Electric-field dependence of the superconducting state? 96
2-25 Device structure of a finalized dual-gated device 97
2-26 Hexagonal Boron Nitride 99
2-27 Micromechanical cleavage of flakes: Scotch-tape technique 103
2-28 Ultra-thin hBN crystals (1-3L) 108
2-29 Picture of a transfer setup 110
2-30 Schematic of a PC slide 111
2-31 Preparation of PC slides 113
2-32 Polymer-assisted dry pickup and transfer technique 115
2-33 Tear-and-stack technique 118
2-34 Cut-and-stack technique 120
2-35 1D contacts 129
2-36 Fabrication steps of a prototypical device. 133
2-37 Predicted landau fan degeneracies and polarities from the Dirac revival model. 137
2-38 Landau fan diagrams of three prototypical devices 139
2-39 Illustration of the scanning SET experiment 141
2-40 Illustration of the s-SNOM experiment 144
2-41 Principle of operation of an s-SNOM system 145

3-1 Experimental setup 149
3-2 Phase and gate dependence of the graphene proximitized DOS. 152
3-3 Coulomb diamonds. 153

4-1 Fabrication of graphene transmon qubits. 159
4-2 Spectroscopy of a graphene transmon qubit. 163
4-3 Rabi oscillation and energy relaxation of a graphene qubit. 166
4-4 Qubit dephasing and Ramsey measurement. 167

5-1 Device ’A’ structure and transport characterization. 174

5-2 Comparison of planar 2D and bulk Josephson junctions. 179
5-3 Nonlocality and tunability of MATBG Josephson junctions. 180
5-4 Edge tunneling spectroscopy of the superconducting gap in MATBG. 183
5-5 Electrostatically defined single-electron transistor and Coulomb blockade in MATBG. 184
5-6 Supplementary Fraunhofer patterns for device A 188
5-7 Anomalous Fraunhofer pattern in device A 189
5-8 Transport characterization of device B. 191
5-9 Evidence of superconducting gap and single-electron transistor behavior in device A. 193
5-10 Characterization of device C. 196
5-11 Simulation of the potential for the tunneling and SET configurations. 198
5-12 Tunneling spectra across the different states in MATBG. 201
5-13 Normalized spectra of the superconducting gap in MATBG from Fig. 5-4. . 202
5-14 Fitting procedure for tunneling data from device C 202
5-15 Temperature evolution of the superconducting gap for device C. 206

6-1 Characterization and statistics of magic-angle twisted bilayer graphene devices. 210
6-2 Competing phases near the superconducting domes of magic-angle TBG. . 212
6-3 Normal-state anisotropy in magic-angle TBG device A. 213
6-4 Evidence for nematic superconductivity in magic-angle TBG. 216
6-5 Anisotropic response of the superconducting critical current. 219
6-6 Summary of various competing phases we identified in this chapter. 222
6-7 Landau fan diagram of device A, measured at the base temperature $T = 70\,\mathrm{mK}$. 226
6-8 Normal-state anisotropy via transverse voltage measurements in device A. . 229
6-9 Calibration of the offset in perpendicular magnetic field 230
6-10 Resistance-temperature curves for the magic-angle TBG devices listed in Table 6.1. 232

6-11 Resistivity ρ_{xx} for device A and B as a function of the carrier density n and the perpendicular magnetic field $B_\perp$ . . . 233
6-12 Change in two probe conductance of device B when it is sourced from the x direction and the y direction. . . . 233
6-13 Nematicity as a function of temperature and perpendicular magnetic field in device B. . . . 234
6-14 Nematicity temperature $T_{\rm nem}$ overlaid on the superconducting dome. . . . 236
6-15 In-plane field response in the wedge-like feature in device B. . . . 237
6-16 Anisotropy in device C with a twist angle of 1.07° . . . 239
6-17 Nematic superconductivity in devices M7 (device A), M12, M1, M2 . . . 240
6-18 Superconducting nematic director θ_s as function of the normalized strain parameter $\frac{\lambda\varepsilon}{|\gamma|\Phi_0^2}$ for the cases $\gamma < 0$ and $\gamma > 0$. . . . 243

7-1 Transport in MATBG . . . 249
7-2 $T-$linear resistivity near $\nu = \pm 2$ in MATBG . . . 252
7-3 Planckian scattering in magic-angle bilayer graphene . . . 255
7-4 $T_{\rm coh}$ versus carrier density in sample MA1 and MA4. . . . 261
7-5 Fermi temperature versus carrier density. . . . 264

8-1 Measurement setup and device characterization. . . . 271
8-2 Asymmetric sawtooth features in inverse compressibility. . . . 273
8-3 Dependence of the asymmetric sawtooth features at $\theta = 1.05°$ on parallel magnetic field and temperature. . . . 275
8-4 Phase transitions and Dirac revivals model. . . . 278
8-5 Measurement of large magnetic entropy above $\nu = 1$. . . . 282

9-1 Collective excitations in twisted bilayer graphene. . . . 286
9-2 Controlling the wavelength of interband plasmons. . . . 289
9-3 Extracting the optical conductivity from the plasmon dispersion. . . . 291
9-4 Electronic band structure and optical conductivity of twisted bilayer graphene with $\theta = 1.35°$. . . . 294

9-5 Calculated properties of the relevant interband transition as functions of the tunnelling amplitude in the AA regions. 295

10-1 Structure and transport characterization of twisted bilayer-bilayer graphene 302
10-2 Displacement field tunable correlated insulator states in TBBG. 305
10-3 Magnetic field response of the displacement-field-tunable correlated insulator states in TBBG. 307
10-4 Correlated insulator states in a multi flat band system. 310
10-5 V_{tg}-V_{bg} resistance maps of various TBBG devices. 313
10-6 Landau fan diagrams and Hall mobilities of the TBBG devices. 314
10-7 Linear resistance vs temperature behaviour in TBBG. 316
10-8 Additional magnetic field response of TBBG devices. 319
10-9 I-V curves in $\theta = 1.23^\circ$ TBBG device at different carrier densities. 320

List of Tables

6.1 List of superconducting magic-angle TBG devices. 231

7.1 Materials exhibiting Planckian scattering rates (Γ), where $\Gamma = Ck_BT/\hbar$. . 258

10.1 List of TBBG devices 312

Chapter 1

Introduction

1.1 Motivation

The ability to obtain single-atom- or few-atoms-thick materials of high quality, such as graphene, transition-metal dichalcogenides, and hexagonal boron nitride has caused a revolution in science and nanotechnology over the last 18 years. When thinned down to a sub-nanometric thickness, such layered van der Waals (vdW) materials can exhibit a dramatic evolution in terms of their most basic properties and display very different behavior and physics in comparison with those of their more bulky counterparts. In this atomically thin limit, even multilayers of the same material but varying thickness truly represent distinct electronic systems. The ability to isolate them, stack them on top of each other, and electrostatically tune them has converted atomically thin materials into a major field of interest at the intersection of condensed matter physics, engineering, chemistry, and materials science. Further, the bidimensional (2D) materials family is continuing to increase. Today, 2D materials can reproduce most of the well-known condensed matter electronic behaviors, which encompass metals, insulators, semiconductors, superconductors, topological insulators, and magnets.

The first 2D material to be discovered, graphene has exceptional properties: flexible, transparent, strong, it is also one of the best thermal and electrical conductors available. It should also be noted that the density of its charge carriers can easily be manipulated via electrostatic gating, placing this material at the heart of both technological applications and

electronic studies. However, one of the most attractive (and intriguing) states of matter, superconductivity, is not among the intrinsic properties of graphene. For this reason, my initial questions as I began the research reported herein centered on superconductivity and the potential for achieving it: **How can we make graphene a superconductor? How can we use its unique opportunities in the context of superconducting applications?**

Most of the research detailed in this thesis focuses on inducing and studying the properties of graphene-based heterostructures in superconducting and strongly correlated states and creating devices with potential applications at the frontier of physics and technology. Two main approaches to turning graphene into a superconductor are investigated: (1) by taking advantage of the proximity effect and (2) by creating magic-angle twisted bilayer graphene (MATBG) structures. This thesis is divided into two main parts accordingly.

In the first part of the thesis, graphene is sandwiched between two superconductors. At sufficiently low temperatures, the graphene itself becomes superconducting due to the proximity effect. **How does this *contagion* occur in graphene?** With the first project described, the purpose is to study this effect and its underlying microscopic mechanism in the energy domain using planar tunneling spectroscopy. This sandwich, known as a Josephson junction, constitutes the basic block of any superconducting qubit. The superconductor-graphene-superconductor junction can thus be coupled to a superconducting circuit to create a graphene-based transmon qubit. **Why are we interested in combining these two fields—2D materials and quantum information—which until now have been quite distinct from and independent of one another?**

In the field of superconducting circuits, 2D materials have immense potential, although it has remained largely unexplored to date. In particular, despite the success of state-of-the-art S-I-S superconducting qubits, major obstacles to scaling this technology into a *table-top* quantum computer remain. First, noise sources intrinsic to the qubit and Josephson junctions reduce the qubit's coherence and increase the resources required to make a fault-tolerant quantum computer. For instance, two-level defects naturally present in the amorphous oxide junction barrier and at the surfaces and interfaces result in dominant loss mechanisms that limit the performance of the qubits. Second, in conventional transmon qubits with superconductor-insulator-superconductor tunnel junctions, qubit frequency tunability

is achieved using a DC current to induce a magnetic field in a superconducting quantum interference device-type configuration. The current used to flux bias a qubit causes static power to dissipate, which contributes to the need for extensive resources and concurrently places an increasing heat load on the system. Third, the currents used to bias the qubits and flux lines generate stray magnetic fields and cross-talk between the different qubits, further complicating efforts to realize multi-qubit operations with high fidelity.

A graphene Josephson junction–based transmon could help mitigate some of these key challenges, potentially improving the qubit coherence and contributing to the extensibility of quantum technologies. Effectively, a van der Waals–based quantum bit retains the crystallographic structure and epitaxial cleanliness of the component layers, potentially diminishing the number of defects present. For instance, thanks to its atomically pristine nature, this kind of bit would reduce two-level noise sources intrinsic to the amorphous weak link, which is typically made of aluminum oxide. Additionally, in a superconductor-graphene-superconductor device, the value of the qubit frequency could be tuned via a gate voltage, thereby eliminating the need for a loop, which would, in turn, eradicate the qubit sensitivity to 1/f flux noise. In addition, this step would eliminate the need for a DC current to flux-bias the qubit, thus suppressing its continuous power static dissipation. Last but not least, the elimination of magnetic field biasing using DC currents would reduce cross-talk between the qubits. Overall, a graphene-based superconducting qubit compatible with future wafer-scale fabrication is highly desirable. The demonstration of such a prototype, introduced herein, opens the door to additional studies in this emerging interdisciplinary field at the intersection of condensed matter physics, materials science, and superconducting circuits—and at the core of both this dissertation and my postdoctoral research proposal.

It is also worth mentioning that the 2D nature of atomically thin materials combined with the planar geometry inherent to the superconducting quantum circuits makes a hybrid microwave circuit with van der Waals materials a promising platform for studying the electronic properties of these materials.

For several years, physicists have been puzzled by this *seemingly* simple question: **Can we make graphene superconducting *by itself* without proximitizing it to other super-**

conductors? The answer is far from obvious ...

In 2018, a pioneering discovery revealed that the twist angle between two atomically thin layers is an extremely powerful degree of freedom. At twist angles close to 1.1 degrees, "magic-angle" twisted bilayer graphene (TBG) displays nearly flat bands owing to strong interlayer coupling and leading to strong Coulomb interactions between the charge carriers. This system exhibits superconductivity and correlated insulating states when the temperature is low enough. This discovery constituted the inflection point of a new field of physics: *twistronics*. It is also the starting point of the second part of this dissertation.

From a more general perspective, strongly correlated systems are ubiquitous in nature and can give rise to spectacular phenomena, from high-temperature superconductivity to novel states of matter with long-range entanglement. In physics, we have several platforms from which to study correlated electron systems. One is the quantum materials themselves, such as cuprates and other high-T_c superconductors, which have been studied for several decades (with a lattice constant on the order of a few angstroms). Another possible approach to investigating correlated phenomena is to build cold atom lattices (with lattice scales on the order of a few microns), which compared with studying the materials themselves offer a greater degree of control in terms of the investigative approach. MATBG has emerged as a new arena for studying strongly correlated physics and superconductivity, with high tunability and accessible critical temperature T_c. The length scale of the superlattice in MATBG lies between the scale for quantum materials and that for cold atom lattices, as does MATBG's typical energy scale, on the order of the Kelvin. MATBG, thus, offers a complementary new approach to studying strongly correlated electronic systems.

The phase diagram of magic-angle twisted bilayer graphene displays several similarities with the phase diagram of high-temperature superconductors such as cuprates and pnictides. This resemblance between the two kinds of phase diagrams has generated a lot of research interest, with the hope that the former could serve as a *Rosetta Stone* to further the field's understanding of the latter. It is in this vein that I have pursued my doctoral studies, dedicating significant research effort to exploring the novel and exotic phases of MATBG. In the present day, several experimental groups are engaged in researching MATBG and other 2D moiré systems. However, in early 2018, Yuan Cao — the student who led the

work demonstrating superconductivity and correlated insulating states in MATBG — and I were probably the only two people in the world with the technical knowledge to fabricate such samples in a consistent way and to devote our time to this system. Our original motivation for studying this system was simple enough, and could be summarized as the following questions: **Why does MATBG feature superconducting and correlated insulating phases? Can this platform be used to explore exotic correlated quantum phenomena?** However, finding answers to key questions such as these is a complicated and iterative process. Our work, therefore, has been highly exploratory, and through these years, we have discovered that MATBG has several interesting and unexpected properties, as identified and discussed throughout this dissertation.

In particular, in certain strongly correlated materials, those referred to as *strange metals,* the resistivity scales linearly with the temperature down to very low temperatures, a behavior not exhibited by most metals. However, as demonstrated by an experiment presented in this work, in MATBG, for certain correlated fillings, a similar "strange metal" phase emerges. Traditional models of electron conduction fail to explain this *strange metallicity.* **Will MATBG help us elucidate this longstanding mystery in physics?**

Although there may be significant work ahead before we find a satisfactory answer to this question, it is worth mentioning that MATBG is, in certain aspects, more accessible to study than, for example, cuprate materials. Effectively, MATBG is purely carbon based, (relatively) easily reproducible, and highly tunable electrostatically. That is, as the density of the charge carriers in MATBG can be accessed experimentally, in situ, over the entire flat band, there is no need to grow thousands of samples, one for each doping, to recover the temperature-doping phase diagram. This accessibility makes MATBG a privileged platform for investigating strange metallicity and, more generally, strongly correlated phenomena and superconductivity in two dimensions.

Another characteristic feature of correlated materials, appearing in many families of quantum materials, including pnictides, cuprates, and heavily doped topological insulators, is nematicity. By definition, nematic order renders the crystal directions in the plane non-equivalent, thus breaking the discrete lattice rotational symmetry. **Is MATBG nematic?** Surprisingly, in MATGB, my colleagues and I have also observed, as demonstrated in ex-

periments presented in this thesis, anisotropies both in the superconducting state and in the normal state. These anisotropies suggest that the C_3 rotational symmetry is spontaneously broken in MATBG, indicating further similarities between this system and other exotic high-T_c compounds.

From the beginning of my research, even though I found MATBG's main features to be reproducible overall, it seemed clear that every device was unique. Thus, a question naturally arose: **Can we quantify local twist angle disorder? Can we correlate the disorder at the nanometer scale with the global device properties observed in transport experiments?** Two collaborative projects using state-of-the-art scanning techniques on high-quality MATBG devices addressed this question (one project was with Shahal Ilani's research group and the other with the research group led by Eli Zeldov, both of them at the Weizmann Institute of Science). In partnership with Shahal Ilani's group, an additional unanticipated property of MATBG was observed: the bands fill in a very particular way in this novel material and provoke a cascade of phase transitions and Dirac revivals. These results, presented in this dissertation, advanced our understanding of the high-temperature parent state from which the low-temperature many-body ground states in MATBG emanate.

What can be said about the optical properties of MATBG? In order to study the behaviour of this novel quantum material in the optical regime, we paired up with a world-leading group in nano-optics led by Frank Koppens at ICFO to investigate collective excitations in MATBG at infrared frequencies. The results, which are introduced later in this work, were, once again, surprising. That is, they demonstrate the presence of interband collective excitations in TBG, with larger-than-expected group velocity and thus a larger spectral weight of the infrared optical transitions.

In addition to its significant scientific interest, the wide range of phases appearing in MATBG, such as the metal, insulator, and superconductor states, unlocks great potential for creating highly tunable tunneling junctions and versatile devices. **Why do we even want such devices?** This question is actually at the intersection between physics and technology. First, they are ideal for studying 2D physics and interfaces, for example, in Josephson junctions. Second, from a technological point of view, tunneling devices are ubiquitous in modern electronics. In superconducting qubits, state-of-the-art Josephson

junctions typically utilize oxide tunnel barriers, which, however, suffer from disorder and are not electrostatically tunable. If tunability is wanted, we need junctions with several different materials. Yet, arrangements of this kind are likely to come with non-ideal interfaces and fabrication challenges. Now, we can go a step beyond the previously described Josephson junction in the graphene transmon qubit. With MATBG and local electrostatic gates, we can independently tune the electrodes and the weak link into different phases in a superconducting junction made of a single clean material to create a *hyper-tunable* Josephson junction, thereby enabling an exponentially larger number of possible configurations. We can even use these configurations to make gate-defined circuits with MATBG in future 2D integrated electronics! And, many more possible technological applications may become available, including electromagnetic sensing, low-power consumption devices, and high-precision electrometry. Some prototypes of these highly tunable versatile devices are presented in this thesis. In fact, this work has already attracted media interest: According to the journal Science, these devices "could power a new generation of superconducting electronics"!

The last question I address in this thesis is critical to defining research directions in this field in both the immediate and long-term future: **Is the physics phenomenology described specific to two twisted monolayers of graphene, or can it be extended to other 2D systems?** The last experiment described in this thesis investigates bilayer-bilayer graphene, a novel 2D moiré flat band system beyond MATBG. This novel meta-material is a fascinating new system in its own right, and several other studies involving other twisted 2D materials have followed this work in the last few years.

1.2 Overview and outline of this thesis

The organization of this thesis mostly follows the chronological evolution of my doctoral studies. As stated in the previous section, this dissertation is divided into two main parts. In the first, I present two experiments with graphene-based Josephson junctions, where the graphene—sandwiched between two conventional superconductors—becomes superconducting via the proximity effect. In the second, I discuss what happens when the twist

angle between two graphene lattices is set close to the *magic angle*. I show that this novel strongly correlated material displays several new phases, which I then discuss in detail.

In Chapter 2, I introduce the basic theoretical concepts to establish a foundation for the subsequent chapters. In particular, I introduce graphene and van der Waals heterostructures, superconductivity and the proximity effect, superconducting qubits, and twisted bilayer graphene. I also present device nanofabrication and the measurement techniques used to perform the experiments described.

Chapters 3 - 10 reproduce published studies, with the appropriate modifications made to the text and figures to adapt them to the structure of this dissertation.

Chapter 3 presents a fundamental study of the Josephson effect in proximitized graphene coupled to niobium/niobium-nitride superconducting electrodes. Spectroscopic measurements are used to investigate the behavior of the quasiparticles responsible for the superconducting properties of graphene when sandwiched between two superconductors: the Andreev states. The tunneling current is measured between a graphite probe and the graphene in the superconducting regime. Due to the proximity effect, the graphene density of states depends on the phase difference between the superconductors and exhibits a hard induced gap at zero phase, consistent with a continuum of Andreev bound states. These results are published in ref. [1].

Josephson junctions are the building blocks of superconducting quantum bits. And, as we know, for example, from the previous experiment, how to make high-quality graphene-based Josephson junctions, we can create a voltage-tunable graphene-based superconducting qubit. Chapter 4, based on ref. [2], extends the previous chapter by incorporating a similar graphene-based Josephson junction into the circuit quantum electrodynamics (cQED) architecture. Further, a platform is presented that enables both frequency-resolved spectroscopy and coherent quantum control of the graphene-based qubit using cQED techniques. This work was performed in close collaboration with Will Oliver's research group at MIT, a leading team in the field of superconducting qubits.

From a materials point of view, the system of interest in the first two chapters is a single (monolayer) graphene sheet contacted by superconducting electrodes. In the following chapters, two graphene sheets are stacked on top of each other at a small angle ($\theta \approx 1^\circ$).

Close to the magic angle, twisted bilayer graphene offers a highly tunable two-dimensional material platform exhibiting a wide range of phases, such as metal, insulator, and superconductor states (without the need for superconducting electrodes). In Chapter 5, the design of a set of metallic gates used to achieve local electrostatic control over such phases is described. This enables the creation of versatile quantum tunneling devices previously unachievable in other single-material platforms. One of the main findings in this chapter is the demonstration of a highly tunable and purely two-dimensional MATBG Josephson junction. I also provide an account of edge tunneling spectroscopy performed within the same MATBG devices and the measurement of the energy spectrum of MATBG in the superconducting phase. Additionally, these multi-purpose devices can also be operated as a single-electron transistor, which is also described. The results presented in this chapter are published in ref. [3].

The following chapters present a series of fundamental studies in which the rich physical phenomena that take place in MATBG are explored via multiple measurement techniques: electronic transport at cryogenic temperatures, a scanning nanotube-based single-electron transistor, and scattering-type scanning near-field optical microscopy (s-SNOM).

Chapter 6 reports on the observation of nematicity in MATBG. Nematicity is observed in many other correlated materials and is characterized by electrons spontaneously breaking the lattice rotational symmetry. The superconducting state is shown to exhibit an anisotropic response to a direction-dependent in-plane magnetic field, revealing nematic ordering across the entire superconducting dome. Additionally, a strongly anisotropic phase is found located in a "wedge" above the underdoped region of the superconducting dome. These results are published in ref. [4] .

The focus of chapter 7 is magic-angle twisted bilayer graphene studied over a wide range of temperatures. MATBG is shown to exhibit another hallmark of strongly correlated systems: a broad regime of T-linear resistivity down to very low temperatures for a range of fillings near the correlated insulator. This behavior is reminiscent of behavior in other strongly correlated systems, often denoted as *strange metals.* These results, reported in [5], establish MATBG as an alternative platform for investigating strange metal behavior, an ubiquitous yet still mysterious phase of correlated matter. Together with the

findings presented in the previous chapter, these observations constitute some of the earliest contributions to the complex phase diagram of MATBG in this rapidly evolving field.

Chapter 8 focuses on measurements of local electronic compressibility in MATBG samples. These experiments were performed in collaboration with Shahal Ilani's research group using its state-of-the-art scanning nanotube-based single-electron transistor system. We determine that the low-temperature correlated phases, such as superconductivity and insulating states, originate from a high-energy state with an unusual band population sequence. As carriers are added to the system, rather than filling all four spin and valley flavors equally, the population is found to occur through a sequence of sharp phase transitions, which appear as strong asymmetric jumps of the electronic compressibility near the integer fillings of the moiré lattice. At each transition, a single spin/valley flavor takes all the carriers from its partially filled peers, "resetting" them back to the vicinity of the charge neutrality point. Similar to other correlated electron systems, these results establish that strong correlations are present at temperatures higher than those for which superconducting or correlated insulating states are observed and indicate that electron-electron interactions play a key role in the physics of this system even at finite temperatures.

In chapter 9, I report on using mid-infrared near-field optical microscopy to probe collective excitations of TBG with 20 nanometer spatial resolution. Through this research undertaken with Frank Koppens's group, a propagating plasmon mode in charge-neutral TBG with $\theta = 1.1 - 1.7^\circ$ was found and interpreted as an interband plasmon associated with the optical transitions between minibands originating from the moiré superlattice. The details of this plasmon dispersion are directly related to the motion of electrons in the moiré superlattice and offer insight into the physical properties of TBG.

In chapter 10, it is shown for the first time that this "twistronics" machinery can naturally be extended to other 2D systems. An AB bilayer graphene sheet is stacked on top of another AB bilayer graphene sheet at the magic angle. The twisted bilayer-bilayer graphene exhibits a rich phase diagram similar to yet very different from that of MATBG, with tunable correlated insulator states that are highly sensitive to the twist angle, external magnetic fields, and electric displacement fields. This work sets a path towards the search for and study of moiré twisted structures in van der Waals materials other than monolayer graphene.

Finally, some concluding remarks and a perspective on future research directions are offered.

1.3 List of publications derived from this thesis

1. **Daniel Rodan-Legrain***†, Yuan Cao*†, Jeong Min Park*, Sergio C. de la Barrera, Mallika T. Randeria, Kenji Watanabe, Takashi Taniguchi, Pablo Jarillo-Herrero†. *"Highly Tunable Junctions and Nonlocal Josephson Effect in Magic Angle Graphene Tunneling Devices"*
   ***Nature Nanotechnology* 16**, 769-775 (2021)
   ∗: Equal contributing authors. †: Corresponding authors.

2. Yuan Cao†, **Daniel Rodan-Legrain**, Jeong Min Park, Fanqi Noah Yuan, Kenji Watanabe, Takashi Taniguchi, Rafael M. Fernandes, Liang Fu, Pablo Jarillo-Herrero†. *"Nematicity and competing orders in superconducting magic-angle graphene"*
   ***Science* 372**, 264-271 (2021)

3. Asaf Rozen*, Jeong Min Park*, Uri Zondiner*, Yuan Cao*, **Daniel Rodan-Legrain**, Takashi Taniguchi, Kenji Watanabe, Yuval Oreg, Ady Stern, Erez Berg†, Pablo Jarillo-Herrero†, Shahal Ilani†. *"Entropic evidence for a Pomeranchuk effect in magic angle graphene"*
   ***Nature* 592**, 214-219 (2021)

4. Niels C.H. Hesp*, Iacopo Torre*, **Daniel Rodan-Legrain***, Pietro Novelli*, Yuan Cao, Stephen Carr, Shiang Fang, Petr Stepanov, David Barcons-Ruiz, Hanan Herzig-Sheinfux, Kenji Watanabe, Takashi Taniguchi, Dmitri K. Efetov, Efthimios Kaxiras, Pablo Jarillo-Herrero†, Marco Polini†, Frank H.L. Koppens†. *"Observation of inter-band collective excitations in twisted bilayer graphene"*
   ***Nature Physics* 17**, 1162–1168 (2021)

5. Bingnan Han, Yuxuan Lin†, Yafang Yang, Nannan Mao, Wenyue Li, Haozhe Wang, Valla Fatemi, Lin Zhou, Joel I-Jan Wang, Qiong Ma, Yuan Cao, **Daniel Rodan-Legrain**, Ya-Qing Bie, Efrén Navarro-Moratalla, Dahlia Klein, David MacNeill, Sanfeng Wu, Wei Sun Leong, Hikari Kitadai, Xi Ling, Pablo Jarillo-Herrero†, Jing Kong†, Jihao Yin†, Tomás Palacios†. *" Deep-Learning-Enabled Fast Optical Identification and Characterization of 2D Materials"*
Advanced Materials **2000953** (2020)

6. Uri Zondiner*, Asaf Rozen*, **Daniel Rodan-Legrain***, Yuan Cao, Raquel Queiroz, Takashi Taniguchi, Kenji Watanabe, Yuval Oreg, Felix von Oppen, Ady Stern, Erez Berg, Pablo Jarillo-Herrero†, and Shahal Ilani†. *"Cascade of Phase Transitions and Dirac Revivals in Magic Angle Graphene"*
Nature **582**, 203-208 (2020)

7. Yuan Cao†, **Daniel Rodan-Legrain**, Oriol Rubies-Bigordà, Jeong Min Park, Kenji Watanabe, Takashi Taniguchi, Pablo Jarillo-Herrero†. *"Tunable correlated states and spin-polarized phases in twisted bilayer–bilayer graphene"*
Nature **583**, 215-220 (2020)

8. Aviram Uri*, Sameer Grover*, Yuan Cao*, J. A. Crosse, Kousik Bagani, **Daniel Rodan-Legrain**, Yuri Myasoedov, Kenji Watanabe, Takashi Taniguchi, Pilkyung Moon, Mikito Koshino, Pablo Jarillo-Herrero†, Eli Zeldov†. *"Mapping the twist angle and unconventional Landau levels in magic angle graphene"*
Nature **581**, 47 (2020)

9. Yuan Cao*, Debanjan Chowdhury*, **Daniel Rodan-Legrain**, Oriol Rubies-Bigordà, Kenji Watanabe, Takashi Taniguchi, T. Senthil†, Pablo Jarillo-Herrero†. *"Strange metal in magic-angle graphene with near Planckian dissipation"*
Phys. Rev. Lett. **124**, 076801 (2020)

10. Joel I-Jan Wang*†, **Daniel Rodan-Legrain***, Landry Bretheau, Daniel L. Campbell,

Bharath Kannan, David Kim, Morten Kjaergaard, Philip Krantz, Gabriel O. Samach, Fei Yan, Jonilyn L. Yoder, Kenji Watanabe, Takashi Taniguchi, Terry P. Orlando, Simon Gustavsson, Pablo Jarillo-Herrero† and William D. Oliver†. *"Coherent control of a hybrid superconducting circuit made with graphene-based van der Waals heterostructures "*
***Nature Nanotechnology* 14**, 120–125 (2019)

11. Siyuan Dai†, Wenjing Fang, Nicholas Rivera, Yijing Stehle, Bor-Yuan Jiang, Jialiang Shen, Roland Yingjie Tay, Christopher J. Ciccarino, Qiong Ma, **Daniel Rodan-Legrain**, Pablo Jarillo-Herrero, Edwin Hang Tong Teo, Michael M. Fogler, Prineha Narang, Jing Kong, and Dimitri N. Basov†. *"Phonon Polaritons in Monolayers of Hexagonal Boron Nitride"*
***Adv. Mater.* 31**, 1806603 (2019)

12. Joel I-Jan Wang, Landry Bretheau†, **Daniel Rodan-Legrain**, Riccardo Pisoni, Kenji Watanabe, Takashi Taniguchi, and Pablo Jarillo-Herrero. *"Tunneling spectroscopy of graphene nanodevices coupled to large-gap superconductors"*
***Phys. Rev. B* 98**, 121411 (2018)

1.4 Talks and presentations derived from this thesis

- **Nonlocal Josephson Effect in Magic Angle Graphene Devices**
  Contributed talk, APS March meeting, March 2021.

- **Highly Tunable Junctions in Magic-Angle Twisted Bilayer Graphene Tunneling Devices**
  Invited talk, Virtual Conference Series, India, Jan 2021.

- **Highly Tunable Junctions in Magic-Angle Twisted Bilayer Graphene Tunneling Devices**

Invited talk, Nano Explorations Seminar, MIT.nano, Cambridge MA, Nov 2020.

- **Magic-Angle Graphene Superlattices: a New Platform for Strongly Correlated Physics**
  Contributed talk, First ECUSA Boston Symposium, Cambridge MA, Oct 2019.
  3rd Best Presentation Award

- **Magic-Angle Graphene Superlattices: Electron Correlations, Superconductivity and Beyond**
  Invited talk, Quantum Designer Physics International Workshop, San Sebastian, Spain, July 2019.

- **Magic-Angle Graphene Superlattices: Electron Correlations, Superconductivity and Beyond**
  Invited talk, Quantum Designer Physics International Workshop, San Sebastian, Spain, July 2019.

- **Magic-Angle Graphene Superlattices: Electron Correlations, Superconductivity and Beyond**
  Invited talk, NANOSMAT-Mediterrane International Conference, Rabat, Marocco, May 2019.

- **Magic-Angle Graphene Superlattices: Electron Correlations, Superconductivity and Beyond**
  Invited talk, CNS Seminar, Harvard Universty, April 2019.

- **Magic-Angle Graphene - a New Platform for Strongly Correlated Physics.**
  Contributed Poster, MIT Physics Open House, Cambridge MA, April 2019.
  Best Poster Award.

- **Twisted Graphene Superlattices: Electron Correlations, Superconductivity and Beyond**

Invited talk (on the behalf of Y. Cao), APS March meeting, Boston, March 2019.

- **Systematic Analysis of Superconductivity in Magic-Angle Twisted Bilayer Graphene Nanodevices**

  Contributed talk, APS March meeting, Boston, March 2019.

- **Tunneling spectroscopy of graphene nanodevices coupled to large gap superconductors**

  Contributed Poster, Correlated Electron Systems Gordon Research Conference, South Hadley, MA, June 2018.

Chapter 2

Basic theoretical concepts and device fabrication

2.1 2D Materials and van der Waals heterostructures

God made the bulk; surfaces were invented by the devil.

Often quoted in the condensed matter community, Wolfgang Pauli's famous words highlight one of the main properties of 2D materials: they are the thinnest materials in the world. Monolayers represent an extreme case in surface science, as they possess two surfaces and no bulk. Given that all their atoms are exposed at the surface, it is possible to transform their properties without modifying their chemical composition.

In a groundbreaking discovery by Andre Geim and Konstantin Novoselov (2004) [6], graphene became the first 2D material to be isolated. The original method used to obtain graphene—the micromechanical cleavage technique (also called the "Scotch tape method")—is probably the simplest and most effective way of producing relatively large high-quality isolated graphene samples. The working principle is straightforward yet creative: a graphite bulk crystal (from a pencil lead, for example) is composed of individual graphene layers of carbon with strong in-plane covalent bonds held together by much weaker van der Waals (vdW) forces. Separate atomic planes can be *peeled off* (exfoliated) by using sticky tape to exceed the vdW interactions between the individual layers. There are hundreds of van der Waals layered materials that can be cleaved in a similar way as

graphite, and the same technique can be used to isolate their atomic planes. Since 2004, the field of 2D materials has grown exponentially and the family of 2D materials has expanded significantly, both in terms of quantity and variety (Fig. 2-1). The 2D materials family includes metals and semi-metals such as monolayer or few-layer graphene, insulators such as hexagonal boron nitride (hBN), semiconductors such as MoS_2 and other transition metal dichalcogenides (TMDs), superconductors such as $NbSe_2$, and ferromagnets such as CrI_3, [7, 8, 9, 10]. Many of these materials are stable in ambient conditions, and it is it is possible to manipulate those for which this is not the case in a controlled argon or nitrogen atmosphere inside a glovebox [11, 7]. Of all the 2D materials, graphene is the undisputed champion, exhibiting high stability, high mechanical strength, and high crystal quality [8]. It is undoubtedly the most studied 2D material to date. It has met with significant interest from the applied physics and engineering communities for its potential in materials science and its possible technological applications, although these remain modest to date. Its greatest significance lies in its potential to both replace silicon in next-generation electronics and offer long-term continuity for Moore's law.

Another family of 2D materials that has attracted a high level of research attention is TMDs, with the formula MX_2, where M is a transition metal and X a chalcogen. TMDs consist of layered structures, where a monolayer consists of three stacked layers (X-M-X), with the X atoms in two hexagonal planes separated by a plane of M atoms [13]. It is not coincidental that some of these structures are used in a range of applications that rely on thermal and chemical stability, including lubrication, catalysis, supercapacitors, and rechargeable battery systems [8]. Furthermore, the bandgap in some of these materials depends on the number of layers. In various semiconducting TMDs, for instance, there is a transition from an indirect bandgap in the bulk parent state to a direct gap in the monolayer form [14]. In particular, for MoS_2, the 1.3 eV bulk indirect bandgap becomes a 1.8 eV direct bandgap when this material is thinned down to its monolayer form. Further interest in single-layer MoS_2 and other monolayer TMDs focuses on the broken inversion symmetry, which allows efficient spin and valley polarization by optical pumping (a phenomenon not seen in bilayer MoS_2, for example) [8, 13, 15, 16]. In contrast to graphene, TMDs have strong spin-orbit coupling (particularly robust in the W compounds such as WSe_2)

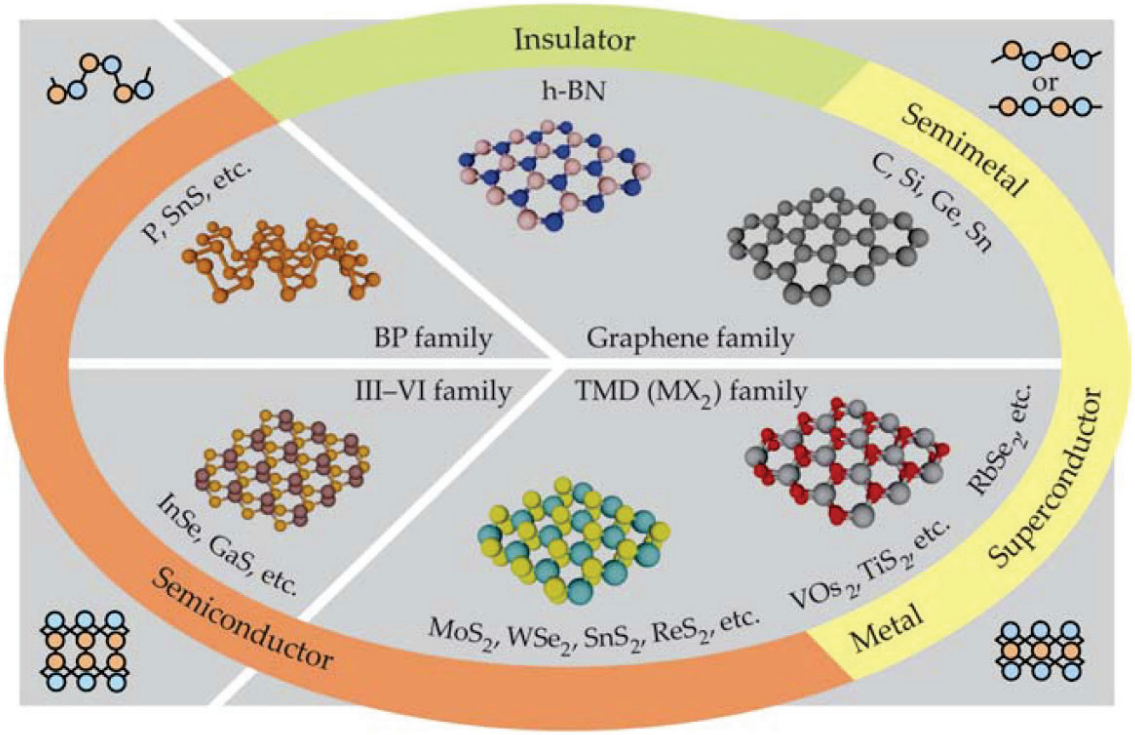

Figure 2-1: The (continuously expanding) family of 2-dimensional materials. Figure reproduced from ref. [12].

originating from the d orbitals of the metallic atoms.

Interestingly, these isolated atomic planes can be assembled into vdW heterostructures by stacking the different 2D materials on top of each other to engineer new artificial materials. The process has often been compared with building Lego sets (see Fig. 2-2), with single- or few-layer crystals used instead of blocks. The stack is kept together thanks to the vdW forces between the layers, the same interactions that bind bulk graphite and other layered crystals together [8]. This affinity between 2D crystals is typically stronger than that between the crystals and contaminants. Therefore, it is energetically favorable for two crystals to have an extensive common interface, which allows scientists to study micrometer-sized pristine and clean samples. As observed in transmission electron microscopy studies, this "self-cleansing" mechanism ensures that interfaces remain atomically sharp and flat, as contaminants are pushed away from their original positions and squeezed into *bubbles* [17, 7].

Even for materials comprising identical atomic layers, it is possible to create several

stable stacking configurations, further expanding the high degree of versatility and the landscape of possibilities these heterostructures offer. For example, vdW heterostructures have great potential in bandgap engineering because they can be used to control the relative crystallographic alignment between two neighboring sheets. Further, proximity effects between different kinds of 2D crystals can be used to generate exotic phenomena in a number of ways, including by inducing spin-orbit coupling and superconductivity [8, 7]. Overall, vdW heterostructures give us experimental access to new physics regimes with great tunability. Not without reason, they are now studied by thousands of physicists worldwide. The number of available combinations achievable with vdW materials is much greater than with any traditional growth method. Only our imagination limits the artificial meta-materials that can be engineered!

How long until 2D materials are part of our daily lives? In addition to the Scotch-tape exfoliation method, there are multiple physical and chemical bottom-up and top-down techniques through which these 2D materials can be produced, such as CVD, chemical exfoliation, surface segregation, van der Waals epitaxy, high-shear mixing, ultrasonication, electrochemical exfoliation, and wet chemistry synthesis [18, 8, 7, 19, 20]. However, a cheap way to generate continuous single- and few-layer prototypes of these 2D materials is still unavailable at a large industrial scale. Similarly, a scalable approach to van der Waals assembly has yet to be implemented. At the current time, many fascinating discoveries have been made in the vdW materials field, but the prospects for large-scale technological applications and mass production remain uncertain [18, 8, 7, 19, 20].

There is great hype worldwide about graphene and 2D materials, accompanied by significant investment focused on bridging this relatively young research field with real-world applications. In Europe, for instance, the Graphene Flagship is one of Europe's biggest ever research initiatives, with a budget of 1 billion euros. Additional information about graphene can be found on the initiative's official webpage (*graphene-flagship.eu*), including a general introduction to graphene for a broad audience, a timeline of the material's history, and videos about its potential to be applied in multiple industries and result in cutting-edge technologies to the market.

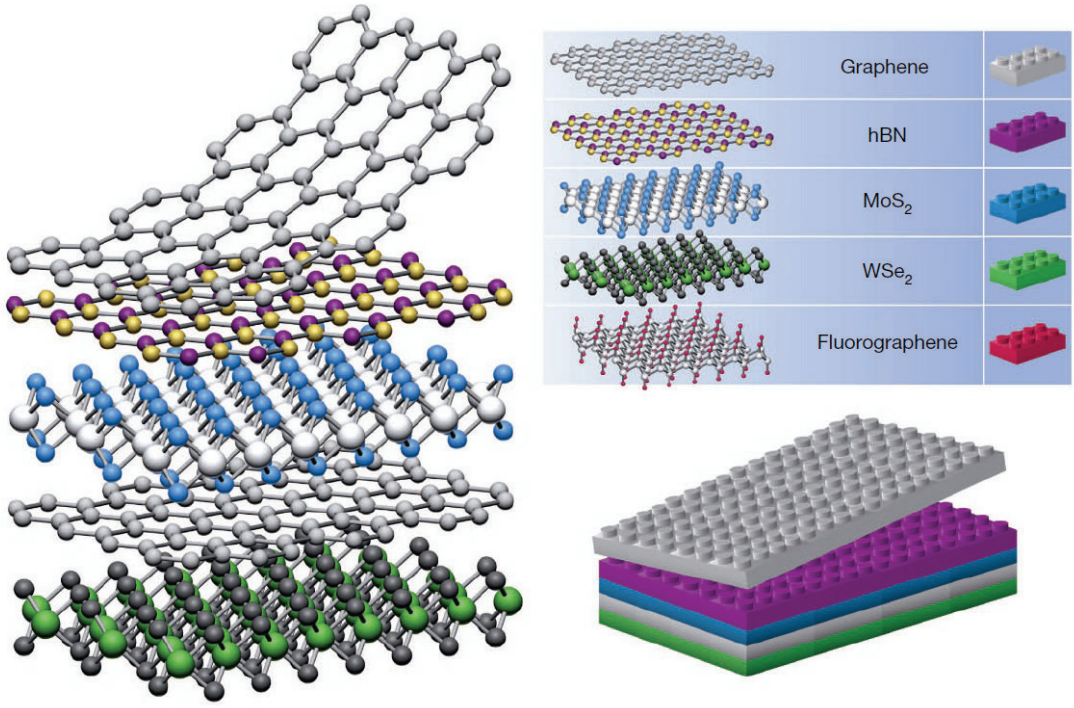

Figure 2-2: Van der Waals heterostructures and Lego bricks. Van der Waals heterostructures are built by stacking different 2D crystals on top of each other. The procedure is similar to building with Lego: First pick up, for example, a monolayer, then put it on top of another monolayer or few-layer crystal, after that add another 2D crystal to the structure, and so on until the stack is complete. The built stack corresponds to a new artificial material, possibly not present in nature. Contrary to other conventional techniques such as molecular beam epitaxy, 2D materials are highly compatible with one another. The resulting interfaces in a stack are atomically sharp and free from contamination up to a distance of several micrometers. Considering the number of 2D crystals currently available in the lab, the combinations of 2D materials that could be created are almost limitless! Throughout this thesis, we will see that the analogy between van der Waals heterostructures and Lego blocks is not entirely accurate, because the latter cannot be stacked on top of each other at an arbitrary angle. In contrast, for 2D materials, the twist angle plays a key role in the stacking configuration. Figure reproduced from ref. [8].

2.2 Electronic properties of graphene

Thanks to its unique properties, the atomically thin carbon allotrope graphene is considered the starting point for new innovative applications across a wide range of fields from sensors and electronics to energy storage and medicine. In 2010, six years after publishing their original results, Geim and Novoselov received the Nobel Prize in Physics "for groundbreaking experiments regarding the two-dimensional material graphene." Though approximately

a million times thinner than a human hair, graphene is flexible (which makes it appealing for potential applications in wearable devices and foldable electronics) and stronger than diamond. Further, it is light and transparent and an excellent conductor of heat and electricity. From an experimental point of view, graphene is a voltage-tunable conductor: it can be doped using electrostatic gates. By sweeping the gate voltage, these metallic gates allow graphene's charge carriers to be tuned continuously from hole-like to electron-like.

The basis of organic chemistry, carbon is integral to the essence of life. Thanks to the flexibility of carbon's bonding, carbon-based systems can be found in all kinds of structures with a range of physical properties in nature. Graphene can be seen as the building block of other allotropes. For example, graphite can be viewed as a stack of multiple graphene layers weakly coupled via vdW forces (Fig. 2-3c). When we write with a pencil, we are depositing graphene stacks on the paper. Even though graphite was invented in 1564, it took more than 400 years to isolate graphene in a lab! Carbon nanotubes, on the other hand, can also be seen as a cylinder of rolled-up graphene (Fig. 2-3b) [21].

Graphene was ultimately discovered through exploring a simple and yet extremely bright idea, requiring just three cheap basic ingredients: some Scotch tape, a graphite crystal, and a silicon dioxide substrate (see section 2.9.2 for the explanation of this idea). Before that, physicists were not even sure whether graphene could exist and remain stable in ambient conditions!

2.2.1 Monolayer graphene

Graphene is a 2-dimensional material made of carbon atoms arranged in a hexagonal structure (Fig. 2-3a). Carbon has six electrons in a two-shell structure, two in the inner shell and four in the outer shell. Of the four outer-shell valence electrons, three occupy sp^2 hybrid orbitals (formed by the 2s, $2p_x$ and $2p_y$ orbitals) and lead to tight σ-bonds with neighboring atoms in the plane. These orbitals have three major lobes at 120 degrees and ensure the hexagonal structure of graphene. Remaining available in the third dimension, the fourth electron is responsible for electron conduction in graphene. These highly mobile electrons (called π electrons) are in a p_z state (perpendicular to the graphene plane) [22]. The p_z

orbitals of different atoms combine to form the π-bonds. It is precisely these π orbitals that dictate the unusual electronic properties of graphene.

The graphene honeycomb structure can be thought of as a triangular lattice with two atoms per unit cell, and with lattice vectors [23, 21, 22]

$$\boldsymbol{a_1} = \frac{a}{2}(3, \sqrt{3})\,, \qquad \boldsymbol{a_2} = \frac{a}{2}(3, -\sqrt{3})\,,$$

where $a \approx 1.42$ Å is the carbon-carbon distance. The reciprocal lattice vectors are given by (Fig. 2-3a):

$$\boldsymbol{b_1} = \frac{2\pi}{3a}(1, \sqrt{3})\,, \qquad \boldsymbol{b_2} = \frac{2\pi}{3a}(1, -\sqrt{3})\,.$$

The inequivalent corners of the Brillouin zone are the Dirac cones, and are central to the understanding of graphene physics. Their positions in momentum space are given by [23, 21]:

$$\boldsymbol{K} = \left(\frac{2\pi}{3a}, \frac{2\pi}{3\sqrt{3}a}\right)\,, \qquad \boldsymbol{K'} = \left(\frac{2\pi}{3a}, -\frac{2\pi}{3\sqrt{3}a}\right)\,.$$

The band structure of graphene was first calculated by Wallace in 1946 [22], which showed the unusual semimetallic properties of this material. Back then, graphene had not been conceived, and these theoretical calculations were used to study the parent compound, graphite, used in nuclear reactors in the mid-twentieth century [21]. It is a standard textbook problem to calculate the electronic band dispersion of graphene using the tight-binding model. The three nearest neighbors vectors are given by:

$$\boldsymbol{\delta_1} = \frac{a}{2}(1, \sqrt{3}) \qquad \boldsymbol{\delta_2} = \frac{a}{2}(1, -\sqrt{3}) \qquad \boldsymbol{\delta_3} = -a(1, 0)$$

and the six second-nearest neighbors are: $\boldsymbol{\delta}'_1 = \pm\boldsymbol{a}_1, \boldsymbol{\delta}'_2 = \pm\boldsymbol{a}_2, \boldsymbol{\delta}'_3 = \pm(\boldsymbol{a}_2 - \boldsymbol{a}_1)$.

Keeping up to second-nearest neighbours in the calculation, the following approximate analytic expressions for the conduction and valence bands are obtained [23, 21] (see Fig. 2-5a):

$$E_{\pm}(q) \approx 3t' \pm \hbar v_0 |\boldsymbol{q}| - \left(\frac{9t'a^2}{4} \pm \frac{3ta^2}{8}\sin(3\theta_q)\right)|\boldsymbol{q}|^2,$$

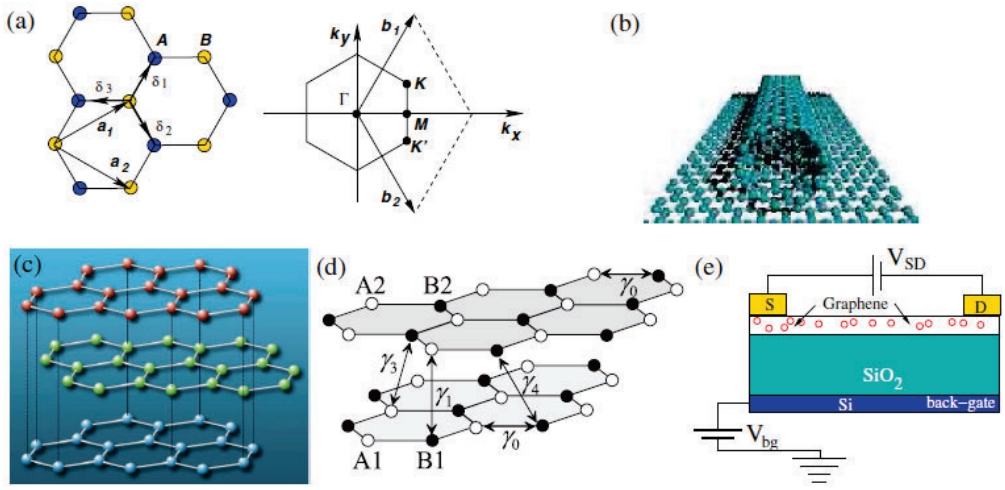

Figure 2-3: Graphene structure. (a) Graphene honeycomb lattice (left). Blue and yellow colors show the two triangular sublattices. Vectors $\boldsymbol{a}_1$ and $\boldsymbol{a}_2$ are the lattice unit vectors, and $\boldsymbol{\delta}_i$ denote the nearest neighbor vectors. Right: Graphene Brillouin zone in momentum space. (b) A rolled-up graphene flake in the plane becomes a carbon nanotube. (c) Graphite can be seen as several graphene layers stacked on top of each other, with weak interlayer tunneling. (d) Lattice structure of bilayer graphene. γ_0 (=t in the main text) is the intralayer hopping parameter, and γ_1 (=$t_\perp$ in the main text, see section 2.2.2) is the interlayer hopping parameter between atoms A1-B2 and A2-B1. In this figure, the graphite nomenclature for the hopping parameters has been used. γ_3 and γ_4 (interlayer hoppings) are typically neglected. (e) Schematic representation of a graphene (most basic) transport device, directly lying on a silicon dioxide substrate and without encapsulation. Figure reproduced from ref. [23].

where $\theta_q = \arctan^{-1}[q_x/q_y]$, $\boldsymbol{q}$ is the momentum measured relatively to the Dirac points, and $v_0 = 3ta/2$ is the Fermi velocity. The hopping amplitudes are denoted by t, t' for the nearest-neighbor (inter-sublattice, A-B) and next-nearest-neighbor (intra-sublattice, A-A or B-B), respectively, and $t(\approx 2.5\ \mathrm{eV}) \gg t'(\approx 0.1\ \mathrm{eV})$. Taking $t \approx 2.5\ \mathrm{eV}$ and $a = 0.14\ \mathrm{nm}$ gives $v_0 \approx 10^8\ \mathrm{cm/s}$ for the empty graphene band [23, 21].

The almost universally used graphene band dispersion at long wavelength puts $t' = 0$, and results in electron-hole symmetry [23]. By expanding the band structure close to the Dirac points, for small q relative to the Dirac point, we obtain (see Fig. 2-5b):

$$E_\pm(q) = \pm\hbar v_0 q + \mathcal{O}(q/k)^2.$$

In a prototypical example of a band dispersion in a solid-state textbook, one would have

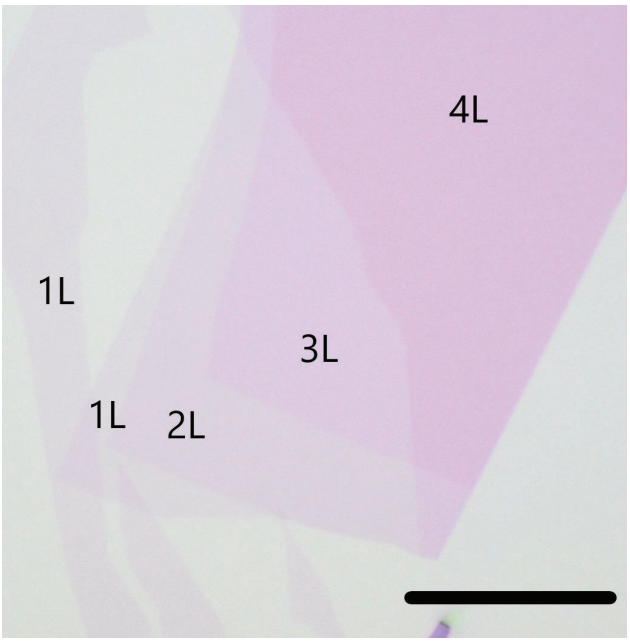

Figure 2-4: Optical micrograph of a graphene flake. Labels denote the number of layers of each part of the flake, from 1 layer (1L) to 4 layers (4L). The scale bar is 20 micrometers.

a quadratic energy dispersion, $\epsilon(\mathbf{q}) = q^2/(2m)$, with m the electron mass. The velocity is then given by $v = k/m = \sqrt{2E/m}$, i.e., the velocity changes with energy. However, graphene has a linear (instead of quadratic) long-wavelength energy dispersion with the conduction and valence bands intersecting at $q = 0$ (see Fig. 2-5), and no energy gap (it is, therefore, a zero bandgap semiconductor) [23, 21]. Even though the Fermi energy of the charge carriers can be tuned by electrostatic doping, the absence of a gap makes graphene unsuitable for switching electronics, such as monolayer-graphene-based transistors.

Crucially, the Fermi velocity of graphene does not depend on energy or momentum, i.e., graphene's quasiparticles move at a constant speed v_0. Together with its purely 2D nature, the linear long-wavelength Dirac dispersion of graphene is probably the most distinguishing feature of graphene. The Fermi velocity is roughly $1/300$ of the corresponding velocity of light, which means that the graphene Dirac fermions move with speed 300 times lower than the speed of light. The particular dispersion of graphene hence mimics the physics of quantum electrodynamics for massless fermions, but at smaller speeds [23, 21, 24]. This opens to door to study relativistic effects in tabletop experiments.

The existence of two Dirac points at K and K' where the Dirac cones for electrons

and holes touch in momentum space gives rise to a valley degeneracy of 2. We note that the spin degeneracy is also 2 (at low magnetic fields), altogether producing a four-fold band degeneracy [23, 21]. Since the Dirac points separate the valence and conduction bands, the Fermi surface is just these two points at charge neutrality. The band crossings at the Dirac points are protected by C_{2z} (in-plane inversion), T_r (time-reversal), and C_3 (three-fold rotation) symmetries, which prevent a gap from opening in graphene's energy spectrum unless one of these three discrete symmetries is broken [25].

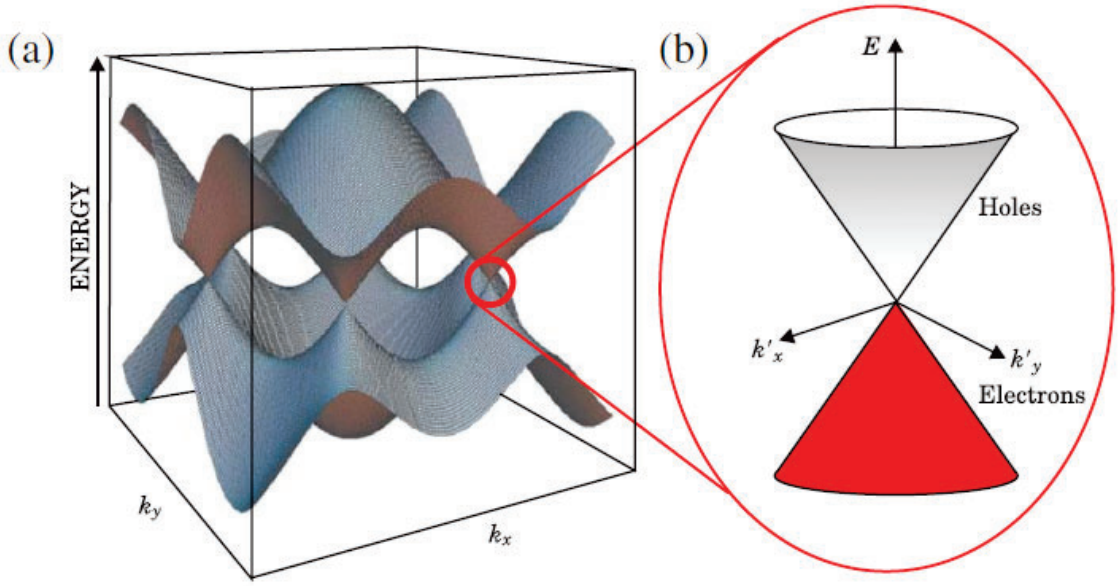

Figure 2-5: Graphene band structure. (a) Energy spectrum of graphene. (b) Energy bands near the K and K' points where the valence and the conduction band touch (also called Dirac points), showing the Dirac cones. In non-doped graphene, the chemical potential crosses exactly the Dirac point. Figure adapted from ref. [23].

We note that the previously mentioned easiness to control the chemical potential of monolayer graphene via electrostatic doping is directly related to its density of states, which is linear in energy E (at low energies), and vanishes at the Dirac point [25]:

$$\rho(E) \approx \frac{2|E|}{\pi(\hbar v_0)^2}.$$

If contacted by superconducting leads, supercurrent can flow through graphene [26, 27, 1]. In Chapter 3 we will explore this topic in more depth, and show the spectroscopic observation of Andreev bound states, the microscopic electron-hole states responsible of this

proximity effect [28, 29, 30, 31], in graphene. The prominent superconducting proximity effect in graphene further confirms the robust electronic coherence in this 2D material [21].

The physics of monolayer graphene beyond the features presented above is extremely rich and fascinating, although it falls out of the scope of this thesis to review it in detail. There are several great reviews and general articles an interested reader could refer to [23, 21, 32, 24, 33, 34, 35, 36].

2.2.2 Bilayer graphene

In addition to monolayer graphene, it is also interesting to consider the case of bilayer graphene, two graphene monolayers weakly coupled by interlayer carbon hopping (Fig. 2-3d) with a 0.34 nm separation. However, it would be an oversimplification to reduce bilayer graphene to two graphene monolayers, and bilayer graphene is a different material in its own right. As Novoselov would state in his Nobel Lecture, "this is one of those cases where one plus one is greater than two" [32]. Stacking can change the electronic properties of the system, and as we will see in this section, some phenomena appearing in bilayer graphene do not occur in simple graphene monolayers [37, 38, 39, 40, 41, 42, 43].

Bilayer graphene can be seen as an intermediate structure between monolayer graphene and graphite (see Fig. 2-3). Bilayer graphene is also the starting block of the experiment presented in Chapter 10.

In the following, we will focus on bilayer graphene's most usual form, AB-stacked bilayer graphene (also called Bernal-stacked form), shown in Figs. 2-3d and 2-6. This Bernal stacking is also the most common one in stacks with more than one layer of graphene (and in particular in bulk graphite).

We use the tight-binding model to study the electronic structure of bilayer graphene. The low energy, long-wavelength electronic structure of bilayer graphene is given by the following energy dispersion relation [23]:

$$\begin{aligned} E_{\pm}(q) &= \Big[V^2 + \hbar^2 v_0^2 q^2 + t_\perp^2/2 \\ &\quad \pm \left(4V^2\hbar^2 v_0^2 q^2 + t_\perp^2 \hbar^2 v_0^2 q^2 + t_\perp^4/4\right)^{1/2}\Big]^{1/2}, \end{aligned}$$

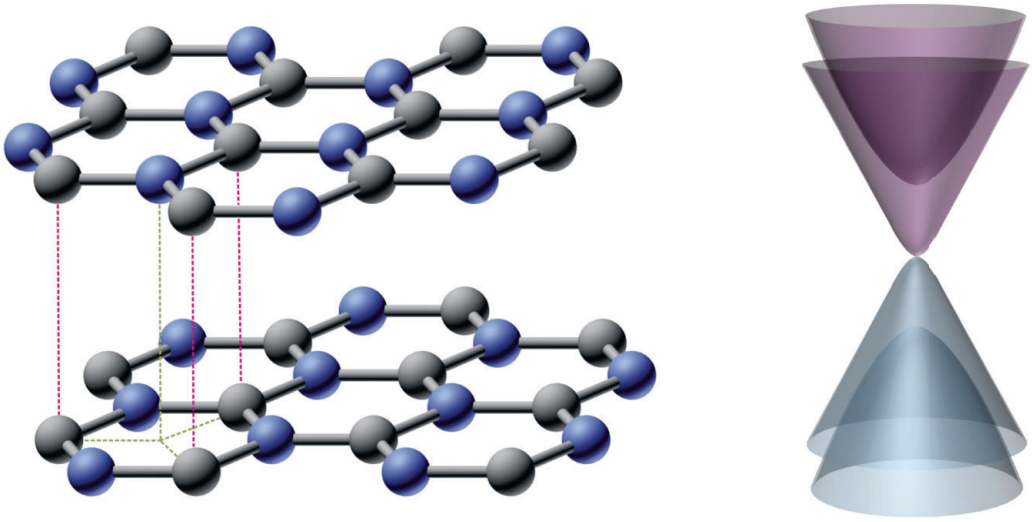

Figure 2-6: Bilayer graphene. Left: Crystal structure of Bernal-stacked bilayer graphene. In this arrangement (the most stable and common one), the two graphene layers do not lie exactly on top of each other. Only half of the carbon atoms have a neighbor in the other layer; the other half are projected into the middle of the hexagon of the other layer. Right: band structure of bilayer graphene near the K point. The low-energy bands cross at zero energy (in the absence of an electric field), but contrary to those in monolayer graphene, here they are parabolic. Figure adapted from ref. [32].

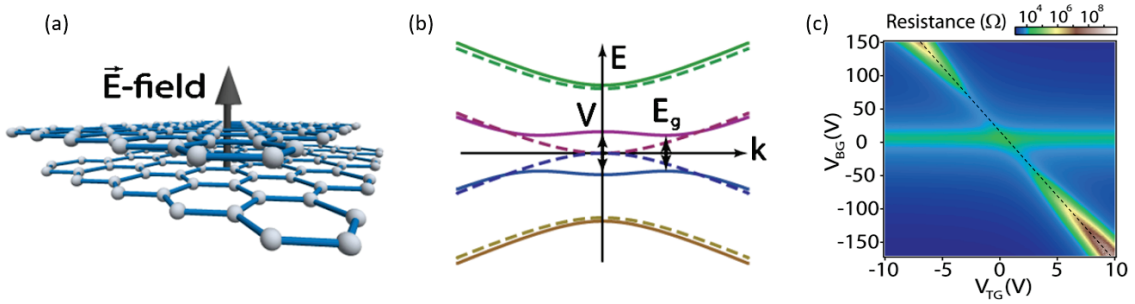

Figure 2-7: Electrically tunable bandgap in bilayer graphene. (a) A perpendicular electric field creates a potential difference across the bilayer graphene and breaks the symmetry between the top and bottom layers. (b) Band structure of bilayer graphene with $V = 0$ (dashed lines, gapless) and subject to an electric field (solid lines), showing a gap opening in the latter case. (c) Resistance as a function of top and bottom gates. A band gap develops near charge neutrality (black dashed line) and changes as the electric field is varied along this line. Figure adapted from ref. [44].

where $t_\perp$ is the effective interlayer hopping energy, t is the intra-layer hopping energy for monolayer graphene and v_0 is the Fermi velocity for monolayer graphene. The term V has dimensions of energy and breaks inversion symmetry, i.e., the equivalence between the two

graphene layers. For small momenta, and assuming $V \ll t$, the energy dispersion relation can be expanded to leading order :

$$E_{\pm}(q) = \pm[V - 2\hbar^2 v_0^2 V q^2/t_\perp^2 + \hbar^4 v_0^4 q^4/(2t_\perp^2 V)]. \tag{2.1}$$

One of the most interesting properties of bilayer graphene is the ability to experimentally modify the band structure and open a gap, which can easily be larger than 200 meV. Effectively, by applying an external electric field perpendicular to the layers, a tunable bandgap near the Dirac point can thus be generated [37, 38, 39, 40, 41, 42, 43, 44]. Figure 2-7 illustrates this phenomenon in a dual-gated transport device [44]. Alternatively, by chemically doping the bilayer graphene from only one side, inversion symmetry can be broken, and a gap also opens in the spectrum [32].

Below, we will show that the system changes if a twist close to the so-called "first magic angle" is generated between the two graphene layers. A-B stacked bilayer graphene is metamorphosed from a weakly correlated Fermi liquid to a strongly-correlated 2D system purely made out of carbon, which displays a plethora of novel exotic phases, including gate-tunable insulating and superconducting states.

2.3 Superconductivity

A detailed review of the theory of superconductivity falls out of the scope of this thesis, and an interested reader can find additional information in most solid-state physics textbooks [45, 46]. The purpose of this section is to motivate the study of this phenomenon in new materials, and to introduce the main definitions and concepts to guide the discussions in subsequent chapters, without a strict mathematical rigor. We will not explicitly state all the assumptions at stake.

2.3.1 Introduction to superconductivity

Superconductivity is probably one of the most intriguing physical phenomena discovered to date. What defines superconductivity unambiguously is the combination of zero electrical

resistance and the perfect expulsion of weak magnetic fields (Meissner effect). It occurs in certain materials when cooled down below a characteristic temperature, called the critical temperature (T_c). If a current is started in a closed loop made of a superconductor with no power source, the current can be maintained for years without a noticeable decay. Further, the magnetic flux through the ring is quantized due to the Meissner effect.

The milestone work by Onnes in 1911 on the electrical resistivity of mercury opened a new era in science and technology, and the interest in superconducting materials is still one of the most active areas of research. Superconductivity finds numerous applications in real life. For instance, superconductivity is of outermost importance in powerful superconducting magnets, which are used in various fields, from healthcare to energy. Those include MRI machines, mass spectrometers, and plasma confining magnets in tokamaks. Another famous example of superconductivity is Maglev trains in Japan (from "magnetic levitating"), which use superconducting magnets to be suspended and reduce friction. Several Nobel prizes directly related to superconductivity have been awarded over the last century (1913, 1962, 1972, 1973, 1978, 1987, 1996, and 2003). However, some of its mysteries are still far from being understood.

Despite intensive research, superconductivity eluded a complete understanding for four decades since Onnes's original discovery in 1911. Two different approaches then provided an explanation of this phenomenon: the phenomenological theory of Ginzburg and Landau, and the posterior microscopic theory developed by Bardeen, Cooper, and Schrieffer (BCS) in 1957 [47, 48]. Later, Gor'kov demonstrated that the Ginzburg-Landau theory is a limit of the BCS theory and can be deduced from the latter [49]. Superconductivity, like ferromagnetism, is a phenomenon that can only be explained within a quantum mechanics framework.

2.3.2 BCS theory

Microscopically, superconductivity is linked to an effective attractive interaction between electrons at sufficiently low temperatures. This attraction results in highly correlated pairs of electrons, the Cooper pairs. It is well accepted that phonons mediate this small attractive

interaction between electrons near the Fermi surface for conventional superconductors. The cartoon picture can be explained as follows: to start with, consider electrons near the Fermi energy in an energy shell given by the Debye phonon energy. A first electron interacts with the lattice and polarizes it; then, a second electron interacts with the polarized lattice, resulting in an effective attraction between the two electrons.

Cooper pairs obey Bose-Einstein statistics, and condense into a stable ground state with phase coherence. Each Cooper pair is composed of two electrons with opposite spins and momenta, with average distance in real space equal to the *coherence length* $\xi_0 = (1/\pi)\frac{\hbar v_F}{\Delta_0}$ (proportional to the Fermi velocity v_F and inversely proportional to the binding energy of a Cooper pair $2\Delta_0$). All the fascinating properties of superconductivity follow from this unusual pairing, and can be derived within the BCS theory: perfect conductivity with no resistance, perfect diamagnetism, magnetic flux quantization, coherent tunneling, anomalous specific heat and thermodynamics, an opening of an energy gap in the quasiparticle spectrum, and many other phenomena. For the so-called high-T_c superconductors (see below), such as cuprates and pnictides, and for moiré superconducting lattices, the precise microscopic pairing mechanism remains an open question at the moment of the writing of this thesis.

2.3.3 High-T_c superconductors

In 1986, Bednorz and Müller discovered high-T_c superconductivity in cuprates. Ever since, new superconductors with higher critical temperatures are occasionally discovered, now consistently overcoming the 77 K barrier (boiling point of nitrogen). At the moment of the writing of this thesis, the highest critical temperature superconductor reported, to the best of our knowledge, has a T_c = 135 K at atmospheric pressure [50], in a cuprate compound. The ultimate goal of this field is to achieve a superconductor at room temperature (and atmospheric pressure). Such a ground-breaking discovery would likely trigger a technological revolution with immediate applications. For example, a superconductor with no losses might relieve some of the world's energy problems. New and faster computers might also be created, among many other fascinating applications.

However, high-T_c superconductors cannot be fully explained by conventional BCS theory. The BCS model relies on the Fermi liquid theory, which assumes electrons are non-interacting ballistic particles. To explain the behavior of certain unconventional superconductors, however, Coulomb interactions between the charge carriers cannot be ignored (see, for example, Chapter 7 for additional information about *strange metals*).

The absence of a unified microscopic theory that explains the properties of high-T_c superconductors limits our understanding of these materials and hinders possible future developments. Part of the difficulty lies in the complex interaction of electrons with other electrons, phonons, magnetic fluctuations, and impurities. Those are experimentally very hard to disentangle, yet it is a crucial task to understand the phenomenology and establish new accurate theories [50]. One of the big hopes of magic-angle twisted bilayer graphene (MATBG), and other moiré systems in general, is to serve as a proxy to help elucidate some of the long-standing mysteries of high-T_c superconductors.

2.3.4 Transport signatures of superconductivity

This thesis will mainly focus on the electronic signatures of superconductivity accessible via transport experiments. In ordinary metals, the resistivity typically decreases when the temperature is lowered. However, this decrease is limited by impurities and defects, and saturates when the electrons mean-free path and the lattice constant become comparable. Even at zero temperature, ordinary metals would still show some resistance.

In superconductors, on the other hand, the resistance drops to zero abruptly when cooled below their critical temperature (see for example Fig. 2-20). However, the current flow in the quantum Hall regime, and other high-mobility ballistic systems, might also display zero resistance, so this is not unique to superconductors.

Additionally, superconductors can maintain a current with no voltage drop (as seen from their characteristic I-V curves, see for example Fig. 5-8c). For a fixed temperature below T_c, superconductors stop displaying zero resistance in the presence of a magnetic field greater than the critical field B_c (for MATBG, the critical magnetic field in the perpendicular direction is around a few tens of mT). For 2D systems, since the Meissner effect

is too weak, superconductivity can be undoubtedly confirmed via an alternative method: the Josephson effect (see next section).

2.3.5 Density of states and tunneling

The BCS theory predicts that an energy gap opens in the quasiparticle spectra of superconductors at low enough temperatures. As the temperature is raised, the gap decreases and eventually disappears at the critical temperature, marking the transition to the normal state.

The density of quasiparticles in an s-wave superconductor satisfies:

$$D_s(E) = \frac{|E - E_F|}{\sqrt{(E - E_F)^2 - \Delta_0^2}} \text{ for } |E - E_F| > \Delta_0,$$

and is equal to zero otherwise. This density of quasiparticle states presents a singularity at energies $E = E_F \pm \Delta_0$. Here, E_F is the Fermi energy and Δ_0 is the gap function at zero temperature; $2\Delta_0$ can be interpreted as the energy cost to break up a Cooper pair.

2.4 Proximity effect and Josephson effects

The following section aims at introducing Josephson junctions from a general perspective, to guide the subsequent discussion in Chapters 3 and 4. A detailed description of Josephson junctions - including the RCSJ model to describe resistively and capacitively shunted junctions, or thermal activation effects - falls out of the scope of this thesis, and can easily be found in many textbooks [45, 46].

2.4.1 Proximity effect

When two superconductors *sandwich* a narrow non-superconducting material (Fig. 2-8a), Cooper pairs can coherently tunnel through the barrier separating the two superconductors, and supercurrent can flow in this system [51]. The center layer, which can be made of a normal metal, an insulator, a ferromagnet, or any other material, and which can be of any dimension, thus acquires superconducting properties at low enough temperatures. In particular, for graphene flanked by two superconductors, supercurrent can flow through it

[26, 27, 1]. Chapter 3 explores, via tunneling spectroscopy, the underlying microscopic mechanism of this proximity effect.

2.4.2 DC Josephson effect

When the two superconductors are close enough, their quantum-mechanical wavefunctions coherently extend through the thin barrier separating them. Their exponentially decaying tails can thus interact with one another, resulting in a finite probability of Cooper pairs tunneling between the two superconductors. The supercurrent through this junction is not driven by a voltage difference (like in metals); instead, the supercurrent is driven by the phase difference between the order parameter of the two superconductors. This phenomenon is also known as the DC Josephson effect.

There are several ways to derive the DC Josephson effect, and each textbook has its own. One of my favorite derivations comes from the famous Feymann physics lectures [52], because it only requires the superconducting Ginzburg–Landau quantum mechanical wavefunctions on each side of the weak link, $\Psi(\mathbf{r},t) = \sqrt{n^*}e^{i\theta(\mathbf{r},t)}$ (where n^* is the super-electron density, and θ is the phase of the wavefunction), and two Schrodinger-like differential equations coupling them. I will not reproduce the details here; I will simply mention that trivial algebra directly leads to the famous Josephson relations:

$$J_s = J_c \sin(\theta_2 - \theta_1) \qquad \text{(current-phase relation)},$$

and

$$\frac{d\delta}{dt} = \frac{2\pi}{\Phi_0} V \qquad \text{(voltage-phase relation)},$$

where $\delta = \theta_2 - \theta_1$ is the phase difference between the two superconductors, $\Phi_0 = h/2e$ is the flux quantum, and J_c is the maximum zero-voltage current density that can pass through the junction. J_c depends on the physical properties of the weak link and the geometry of

the junction, and can be computed from the superconducting gap of the junction electrodes and their normal-state resistance via the Ambegaokar-Baratoff formula.

2.4.3 AC Josephson effect

The DC Josephson effect can be straightforwardly rederived from the previous two equations. The AC Josephson effect also follows from the previous expressions, and occurs when a constant voltage V_0 is applied across the junction. Integrating the second equation, and inserting it into the first one, yields to the following conclusion: the phase difference linearly changes with time, resulting in an AC current developing across the junction of the form $J_c \sin\left(\delta_0 + \frac{V_0 2\pi t}{\Phi_0}\right)$ with frequency $f_J = \frac{V_0}{\Phi_0} = \frac{2e}{h} V_0 = 483.6 \times 10^{12}\ V_0$ (Hz) (called the Josephson frequency). We note that f_J plays a special role in metrology, as it directly relates the second to the volt through fundamental constants.

2.4.4 Josephson junctions in a magnetic field

In the presence of a magnetic field, the phase difference $\delta = \theta_2 - \theta_1$ is not an invariant quantity; hence it cannot determine the current I_s which is a well-defined gauge-invariant quantity. This can be cured by replacing the phase by the gauge-invariant phase difference [45]:

$$\varphi(\vec{r}, t) = \theta_2(\vec{r}, t) - \theta_1(\vec{r}, t) - \frac{2\pi}{\Phi_0} \int_1^2 \vec{A}(\vec{r}, t) \cdot d\vec{l}.$$

In the presence of an external magnetic field, the phase difference between the two superconductors is affected following the previous expression. In particular, two very fascinating phenomena involving Josephson junctions occur in the presence of an external magnetic flux: Fraunhofer patterns and SQUID patterns.

Fraunhofer patterns

Let us first place a conventional Josephson junction in an external magnetic flux. The Fraunhofer pattern describes the oscillation of the maximum critical current of the Josephson junction in a magnetic field. It exhibits zeros at fluxes equal to multiple integers of

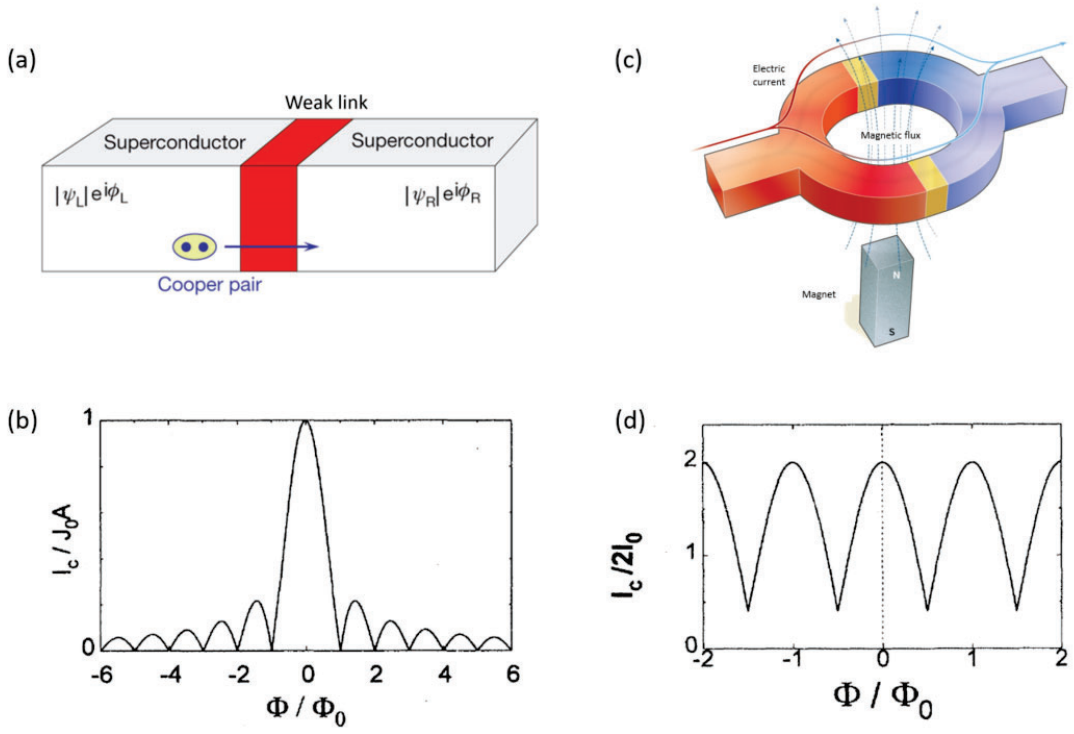

Figure 2-8: (a) Schematic of a Josephson junction. (b) Fraunhofern pattern of a Josephson junction in the presence of an external magnetic field. (c) Schematic of a superconducting quantum interference device (SQUID). (d) Modulation of the SQUID response as a function of an applied magnetic flux. Panel (a) has been reproduced from ref. [53], panel (b) adapted from ref. [54], and panels (c-d) from ref. [55].

the flux quantum and displays a characteristic $|\mathrm{sinc}(x)|$ shape. I will skip the details of the mathematical derivation, which can be found in any standard textbook, although I have decided to summarize its main ideas below. One of the simplest derivations I know [46] involves taking a rectangular closed-loop contour with infinitesimal width and length perpendicular to the junction weak link (as seen from above). Requiring the line integral of the phase gradient to be single-valued, and after some algebra, one can obtain the spatial variation of the gauge-invariant phase difference along the junction. Then, by substituting that phase difference into the Josephson current-phase relation, we obtain the local value of the supercurrent. Surprisingly, the supercurrent oscillates sinusoidally in space, along the direction of the weak link.

Last, by integrating the value of the local supercurrent along the spatial extension of the junction, the well-known Fraunhofer pattern can be obtained. It describes the value of the

maximum supercurrent in a Josephson junction in the presence of a magnetic flux Φ (Fig. 2-8b):

$$I_c(B_z) = I_c \left| \frac{\sin \frac{\pi\Phi}{\Phi_0}}{\frac{\pi\Phi}{\Phi_0}} \right| \qquad \text{(Fraunhofer pattern).}$$

This expression is analogous to the one obtained for the optical intensity (diffraction pattern) of coherent light interfering with itself after passing through a single slit. The interference of the local supercurrents makes the total supercurrent go to zero for certain magnetic fields. We further explore this topic in Chapter 5.

SQUIDs

Another exciting configuration is a SQUID (superconducting quantum interference device), with two superconducting Josephson junctions combined in parallel (Fig. 2-8c). In a SQUID, the maximum supercurrent shows interference effects as a function of an external magnetic field. This interference pattern is caused by the difference in the phase of the merging currents through the two different paths, modulated by the external B-field [52].

The details of the derivation will be, once again, skipped here and we refer to the numerous textbooks with a dedicated chapter on superconductivity for the interested readers [46, 45]. However, the general idea is easy. Let us assume that both junctions are identical, the magnetic flux threading the junctions is negligible, and the thickness of the superconductors is much larger than the penetration depth: We first apply Kirchoff's laws and the current-phase relation to each of the two junctions. The gauge-invariant phase differences between the two junctions can be found by considering a line integral along the contour through the SQUID loop, and imposing that the total phase change along the closed contour is a multiple of 2π. Then, the maximum supercurrent of the combination is given by

(Fig. 2-8d):

$$I_s^m = 2I_c \left| \cos\left(\pi \frac{\Phi}{\Phi_0}\right) \right| \qquad \text{(SQUID pattern).}$$

I_c is the maximum current that can flow in the SQUID without dissipation and no voltage drop across it. This formula is also analogous to another optics experiment: the interference of coherent light passing through two different slits.

The maximum supercurrent in a SQUID is periodic with the magnetic flux and changes from maxima to minima for fluxes as small as $\Phi_0/2$. This fundamental characteristic of SQUIDs makes them ideal for detecting tiny magnetic fields. Compared to Josephson junctions, SQUIDs typically enclose a larger area, and hence are particularly sensitive to probing small changes in magnetic fields.

Real-world clinical applications of SQUIDs include magneto-encephalography and mangeto-cardiography to detect the small signals in our brain or heart activities. The experiment of ref. [56], mentioned multiple times along this thesis (but without a dedicated chapter), is based on a nano-sQUID scanning tool capable of detecting extremely small magnetic fields with a nanometric spatial resolution.

2.4.5 Summary of the Josephson effect

In summary, the device described in this section, a Josephson junction, is as simple as two superconductors coupled by a weak link. Josephson junctions are elemental superconducting electronic devices. They are fundamental to superconducting quantum computing (see next section), for superconducting tunnel junction detectors, and even in metrology to define the Volt [45]. Of particular relevance for this thesis, a graphene-based Josephson junction is first studied in Chapter 3 in the energy domain. Then, in Chapter 4, a similar junction is incorporated into a superconducting circuit to make a graphene-based qubit. Chapter 5 reports on the realization of purely 2-dimensional MATBG-based Josephson junctions.

2.5 Circuit QED and superconducting qubits

This section aims at introducing circuit quantum electrodynamics from a general perspective. The techniques introduced here are central to the experiments described in Chapter 4.

2.5.1 Introduction to circuit QED

Bridging techniques from condensed matter physics and AMO, circuit quantum electrodynamics (cQED) introduces well-established concepts of cavity QED to superconducting qubits [57]. It is nowadays one of the leading architectures for quantum computation. It simultaneously offers a complementary platform to explore quantum optics physics on a chip, allowing access to nonlinear regimes at the level of single microwave photons.

Basic theory of circuit QED

The physics and tools longly used to study cavity QED can be naturally exported to circuits, by strongly coupling superconducting quantum circuits to electromagnetic fields confined in inductors and capacitors. The fundamental ingredients of cQED are shown in Fig. 2-9, and consist of a superconducting qubit (playing the role of an atom in cavity QED) coupled to a microwave oscillator, such as a 1D transmission-line resonator (the cavity) [58, 59].

Resonators can be on the order of a centimeter-long. They have a fundamental frequency between 5-15 GHz, suitable for microwave operations, while being high enough to minimize thermal photon population at the typical temperatures at which these experiments are performed (few tens of mK). Close to one of its normal mode frequencies, the resonator can be modeled as a parallel LC oscillator such that $\omega_R = 1/\sqrt{LC}$. The corresponding quantum mechanical Hamiltonian is that of a simple harmonic oscillator, given by

$$H_{LC} = \hbar\omega_R \hat{a}^\dagger \hat{a}. \tag{2.2}$$

The creation and annihilation photon operators $a^\dagger$ and a for the LC circuit are defined in terms of two conjugated variables, the flux threading the inductor and the charge on the

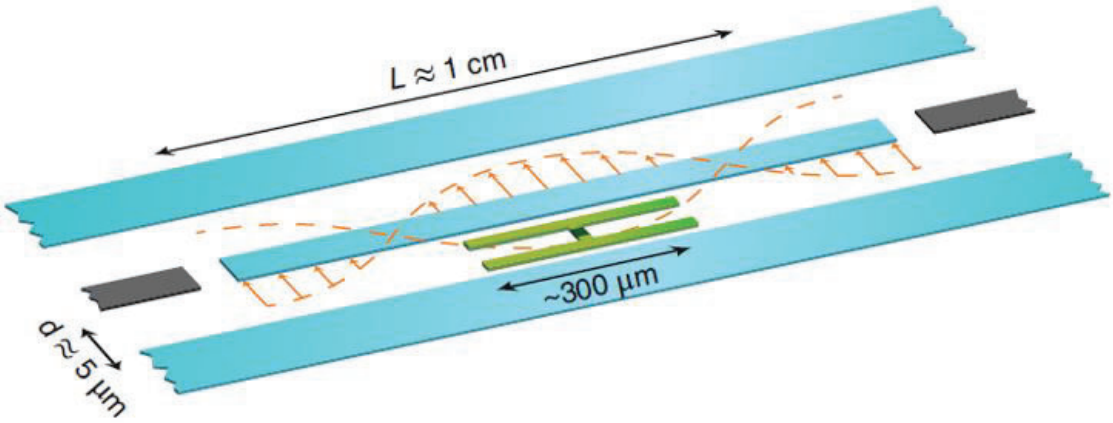

Figure 2-9: Basic architecture of cQED. Schematic representation of a superconducting qubit (here, a transmon, shown in green) coupled to a transmission-line resonator (in blue) consisting of a signal carrying centerline surrounded by two grounded planes. The electric field distribution for the second mode of the resonator is shown with orange arrows. In grey, the input and output ports of the resonator. Figure reproduced from ref. [58].

capacitor. The average photon number is given by $n = \langle \hat{a}^\dagger \hat{a} \rangle = \langle \hat{n} \rangle$ [58, 59].

While the average voltage across the LC resonator vanishes in the vacuum state, its rms value is given by $V_{zpf} = \langle 0|\hat{V}^2|0\rangle^{1/2} = \sqrt{\hbar\omega_R/2C}$, typically on the order of 1 μV. Assuming a typical separation between the center conductor and the ground plane (Fig. 2-9) of $d \sim 5$ μm, the resulting zero-point electric field $E_{zpf} = V_{zpf}/d \sim 0.2$ V m^{-1} is remarkably large [59, 58]. These large vacuum fluctuations of the electric field arise from the small volume mode of the resonator, and cause light-matter couplings in cQED to be potentially much larger than in cavity QED.

The qubit is placed in proximity to the center conductor of the transmission-line resonator, close to the antinodal positions, where the voltage of the standing wave is maximum for a strong electric dipole interaction. The input and output port signals are coupled to the resonator via the capacitive gaps in the center line (Fig. 2-9). These points where the current vanishes also serve to define discrete normal modes inside the center conductor. Measurements of the amplitude and phase of the cavity transmission are performed via transmission lines, which allow the introduction of dc and rf pulses to manipulate the state of the qubit [59].

The qubit can be reduced to an effective 2-level system, with excited state $|e\rangle$ and

ground state $|g\rangle$. Transitions between the two quantum states are driven by sending pulses at the resonant transition frequency ω_{eg} via the capacitively coupled microwave source. In this two-level approximation, the Hamiltonian describing the qubit is given by

$$H_q = \frac{\hbar\omega_{eg}}{2}\hat{\sigma}_z. \tag{2.3}$$

These circuits are typically made out of Aluminum ($T_c = 1$ K), *the silicon of superconductiviy* [60], to minimize dissipation. They benefit from semiconductor fabrication methods, including lithographic extensibility and manufacturability on silicon chips, which makes them potentially scalable. Furthermore, this approach allows placing multiple qubits at different antinodes of the standing wave, thus allowing to generate entanglement across centimeter-distances and two-bit quantum gates [59, 58, 61].

Quantum light-matter interaction in a circuit

So far, we have discussed the qubit and the resonator independently. The coupling Hamiltonian can be written as

$$H_{coupling} = \hbar g(\hat{a}^\dagger\hat{\sigma}_- + \hat{a}\hat{\sigma}_+), \tag{2.4}$$

where $\hat{\sigma}_-$ and $\hat{\sigma}_+$ are the Pauli lowering and raising operators describing the process of de-exciting and exciting the qubit. We have dropped rapidly oscillating terms (rotating wave approximation), which lead to negligible frequency shifts for the usual parameter range in cQED. The final Hamiltonian of the combined system [58, 62, 59, 61] is the well-known Jaynes-Cummings Hamiltonian

$$\begin{aligned} H_{JC} &= H_{LC} + H_q + H_{coupling} \\ &= \hbar\omega_R\hat{a}^\dagger\hat{a} + \frac{\hbar\omega_{eg}}{2}\hat{\sigma}_z + \hbar g(\hat{a}^\dagger\hat{\sigma}_- + \hat{a}\hat{\sigma}_+), \end{aligned} \tag{2.5}$$

which models the interaction between the two-level system and a single microwave photon from the LC oscillator. The exchanges of energy between the resonator and the artificial qubit are stimulated by the zero-point voltage fluctuations V_{zpf} of the capacitively coupled oscillator. The coupling constant g packages all the prefactors. It is given by the product of

the electric dipole moment of the qubit and the zero-point electric field of the mode. In the strong coupling regime $g > \kappa, \gamma$, where κ denotes the rate at which photons are lost in the resonator and γ is the decoherence rate of the qubit.

2.5.2 Quantum information via superconducting qubits: realization and manipulation

The cQED architecture combining 1D transmission line resonators and qubits is attractive both for quantum optics studies on a chip [57, 63] and in quantum computing and control. In order to have long coherence times, it is fundamental for qubits to be well isolated and decoupled from sources of noise and non-controllable degrees of freedom (such as electromagnetic noise, dielectric losses, broken Cooper pairs,...), while being strongly coupled to the external control electronics realizing the logical operations and readout. As already predicted in the original theoretical work that introduced cQED [59], this architecture provides an advantageous platform for the coherent control, entanglement, and readout of qubits. It achieves strong inhibition of radiative decay, allows quantum non-demolition studies to determine the state of multiple qubits while minimally disrupting their state, and offers a platform to entangle several qubits separated by centimeter distances. In contrast to other platforms, such as electron spins in atoms, trapped ions, ultracold atoms, nitrogen vacancies in diamond,... superconducting qubits are macroscopic in size and lithographically designed [61, 58]. They are one of the most popular artificial quantum bits at present.

Back in 1985, a pioneering experiment by Martinis, Devoret, and Clarke demonstrated the possibility of building artificial atoms that could be controlled and connected by electrical wires [60]. These artificial atoms have enabled a wide variety of superconducting qubits (including the Cooper pair box, transmon, flux qubit, phase qubit, quantronium, fluxonium), which have in turn symbiotically enabled cQED.

The dynamics of a superconducting qubit can be understood by replacing the inductor in a quantum LC resonant circuit (i.e., a quantum harmonic oscillator) by a Josephson Junction (two superconductors separated by a thin insulator [45, 46] as introduced in the previous section), behaving as a nonlinear inductor (see Fig. 2-10a). The inductive energy

for the junction is not quadratic, but a cosine function of the generalized flux through it (which sets the phase difference between the order parameter of the two superconductors ϕ [45]). This crucial difference has significant consequences for the spectrum and leads to anharmonicity (non-equal separation between the different energy levels), allowing access to the subspace of only the two lowest energy levels [61, 64].

Qubit readout

In the dispersive limit, out of resonance when $|\Delta| = |\omega_{eg} - \omega_R| \gg g$, it is possible to perform a quantum non-demolition measurement of the state of the qubit. In this situation, the resonator acts as a band-pass filter, protecting the qubit from noise at its natural frequency, possibly causing unwanted transitions. Furthermore, in the limit of low photon number, and using second-order perturbation theory in terms of g/Δ [59, 65], the Jaynes-Cummings Hamiltonian is well approximated by the simpler model

$$H_{disp} = \hbar(\omega_R + \chi\hat{\sigma_z})\hat{a}^\dagger\hat{a} + \frac{\hbar\omega_{eg}}{2}\hat{\sigma}_z, \tag{2.6}$$

where $\chi = g^2/\Delta$ is known as the dispersive shift [58, 59, 57, 61]. From the first term, one can see that the oscillator's frequency depends on the state of the qubit $\omega_R \pm \chi$. By measuring the transmission of the resonator to a probe rf tone, the qubit's state can thus be inferred with high fidelity, without directly interacting with the qubit itself in the measurement process. Conversely, the transition frequency of the qubit is also shifted by the dispersive coupling (as can be seen by collecting the $\hat{\sigma_z}$ terms). Two terms can be identified: a Lamb term induced by the vacuum fluctuations in the resonator, χ, and an ac Stark shift, $2\chi\hat{a}^\dagger\hat{a}$, shifting the transition frequency of the qubit by an amount proportional to the number of photons in the cavity [57, 59, 66, 61, 58].

Relaxation times characterization

We briefly present now a paradigmatic example from ref. [61] on standard coherence measurements in superconducting qubits. The techniques presented here are aligned with those employed in chapter 4, where we demonstrate temporal coherence and control of a voltage-

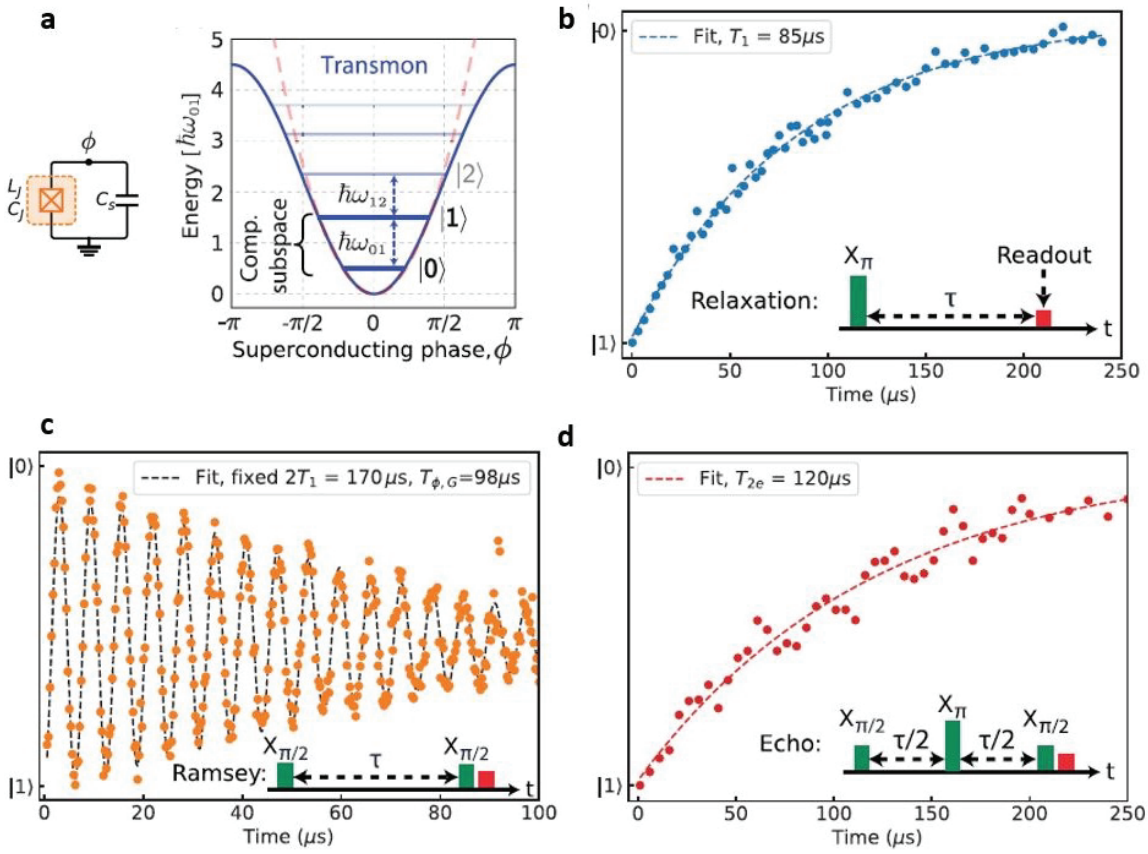

Figure 2-10: Superconducting qubits characterization. (a) Left: Circuit of a parallel LC oscillator, where the nonlinear inductance L_J, shunted by a capacitance C_J (Josephson Junction), replaces the inductor. Right: The resulting energy potential is reshaped into the blue dashed line compared to the LC quantum harmonic oscillator, yielding non-equidistant energy levels. The system can be reduced to an effective 2-level artificial atom if one applies the proper frequency between these quantum states (usually the two lowest energy levels). However, higher excited states can potentially be accessed. (b) Characterization of T_1 longitudinal relaxation time in a transmon qubit. (c) Determination of T_2^* via Ramsey interferometry. (d) Transverse relaxation measurement via a Hahn echo experiment. Figure assembled from subfigures from ref. [61].

tunable graphene-based transmon qubit. In the remaining of this thesis, we will mainly focus on transmon qubits (an abbreviation of "transmission line shunted plasma oscillation qubits"). Transmons are a type of capacitively shunted superconducting charge qubits. They are probably the most widely used superconducting qubit at the moment. Transmons are designed to have reduced sensitivity to charge noise by shunting the Josephson junction with a large capacitor. The ratio of the Josephson energy E_J to the charging energy E_c is in the so-called transmon regime, $E_J/E_c \sim 10 - 100$. This suppresses exponentially the

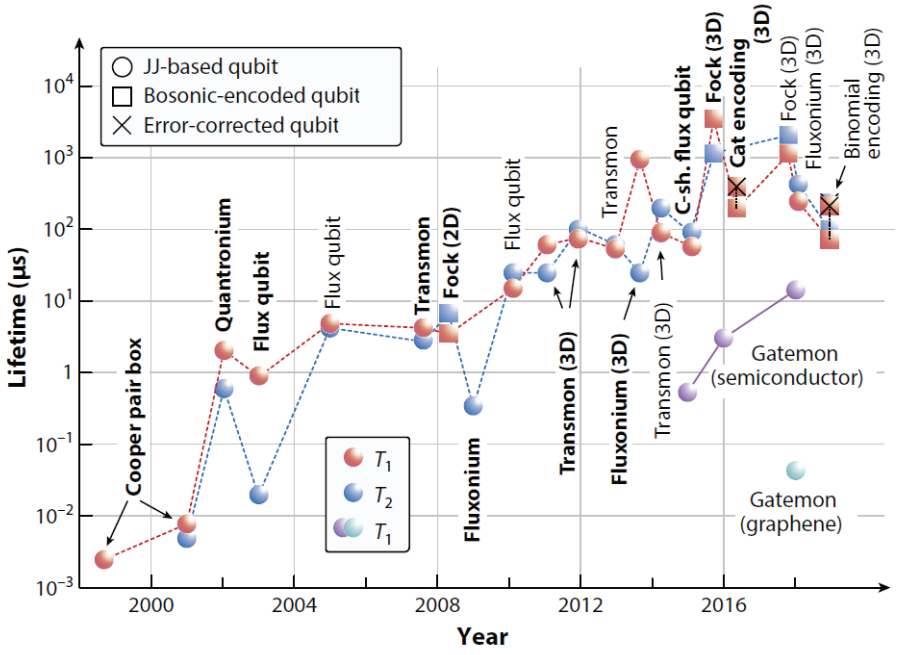

Figure 2-11: Evolution of the lifetime of superconducting qubits, and comparison with the lifetime of our graphene gatemon presented in Chapter 4. Over the last two decades, the coherence of superconducting qubits has improved by more than five orders of magnitude. The graphene gatemon should be regarded as a proof of concept at this stage. While it already performs better than the original Cooper Pair Box qubit, its coherence time is far from that of state-of-the-art transmons. Addressing and mitigating the sources of decoherence may substantially improve the coherence time of the graphene-based qubit. Figure reproduced from reference [70].

sensitivity to charge fluctuations, at the cost of a reduction in the anharmonicity due to the increased capacitance [67, 68, 69, 70, 71].

Based on the Bloch model, we can define the longitudinal relaxation rate $\Gamma_1 = 1/T_1$ (characteristic time scale over which the qubit population relaxes to its steady-state value) and the transverse relaxation rate $\Gamma_2 = 1/T_2$ (loss of coherence of a superposition state) [61].

T_1 measurement is performed using the Rabi method. A pi pulse sets the qubit in its excited state, and is then left to spontaneously decay to its ground state for a time τ. After $t = \tau$, the qubit state is measured by projecting it into its ground or excited state (see Fig. 2-10b).

The transverse relaxation T_2 can be measured using Ramsey interferometry (Fig. 2-10c). A $\pi/2$ pulse first sets the Bloch vector on the equator. After a time τ, a second

$\pi/2$ pulse projects the Bloch vector onto the z-axis of the Bloch sphere, in one of the two-qubit states [61]. From the exponential decay of the oscillations, one can extract T_2^*. A Hahn echo, insensitive to inhomogeneous broadening, can also be performed by placing a π pulse at the center of the Ramsey experiment, leading to a usually higher estimation T_{2E} as shown in Fig. 2-10d.

Summary: cQED and superconducting circuits

In summary, since its theoretical prediction [59] and first experimental demonstration [57] in 2004, the cQED architecture and superconducting qubits have both experienced and enabled numerous experimental and theoretical advances (Fig. 2-11). It is already possible to execute specific quantum algorithms, including quantum simulations of small molecular systems, chemical physics processes, quantum many-body problems, and recently Google's demonstration of quantum supremacy [72, 58, 60]. Even though cQED has emerged as a promising platform to build quantum computers, many challenges still need to be faced before they become a practical reality [58, 64]. For instance, quantum processors have to be made from high-coherence materials while using reproducible and scalable fabrication processes. They must also be able to be read and controlled with high fidelity, which becomes more challenging as the number of qubits increases. The processor will need to be able to sustain a large number of control and readout signals. In addition, each qubit and resonator frequency will require individual calibration to be appropriately manipulated and readout. And all the setup must furthermore be thermalized at millikelvin temperatures. There are just a few among the challenges the cQED still needs to face to transition from a scientific curiosity to a technical real application [73].

Two different approaches can be taken to face those challenges. In the short term, the brute-force era, where qubits are individually wired and calibrated for manipulation and readout. This currently allows qubit processors with up to tens of qubits [73], although this approach does not become viable when reaching four-digit qubits. The second approach, in the longer-term (the scaling era), will need to introduce integrated methods to control more qubits with fewer wires, possibly at the expense of increased complexity and additional heating challenges to be addressed [73].

In Chapter 4, we address some of these challenges by combining 2D materials with the cQED architecture to create a voltage-tunable graphene superconducting qubit (see also Chapter 1 for a general motivation on voltage-tunable graphene-based superconducting qubits).

In addition to providing an excellent platform to perform foundations of quantum engineering, cQED has arisen as a fertile arena for studying light-matter fundamental science on a chip, as we have illustrated across this section.

2.6 Moiré patterns

A moiré pattern is a large-scale interference pattern that appears when a periodic structure is overlaid on another periodic structure. This pattern, which consists of alternating bright and dark areas, is not observed in the individual original structures [74]. Moiré patterns can be found everywhere, from mathematics, to art, to textiles (from which the word originates, "moire" meaning "watered fabric" in French). For a moiré pattern to appear, the constituting 2D meshes must be displaced, rotated, or have a slightly different scaling factor (in the case of 2D materials, the latter would correspond to a different lattice constant). A few examples of moiré patterns are shown in Fig. 2-12. In particular, two monolayers of vdW crystals can produce a moiré pattern.

As described in the introductory chapter, in 2004, a revolution took place in condensed matter with the isolation of 2D materials, which gave rise to the much broader field of van der Waals heterostructures. One of the most famous ways in which vdW materials has been described is through making a comparison with Lego; that is, like Lego pieces, vdW materials can be stacked on top of each other, in any way one can think of. For 2D heterostructures, all the elements of the stack stick together thanks to the van der Waals forces. This analogy emphasizes one unique property of 2D materials. However, the analogy breaks down on an important point: For Lego pieces to stick together in a stack, they must be perfectly aligned. On the other hand, 2D materials can be stacked on top of each other at any desired angle. Crucially, the properties of the system change dramatically depending on the twist angle, a degree of freedom unique to vdW heterostructures. This

angle control cannot be achieved in lab-grown bulk crystals or heterostructures grown by molecular beam epitaxy.

In particular, when two graphene layers are placed on top of each other and slightly twisted, a moiré pattern appears (see Fig. 2-12e). The moiré wavelength, i.e., the distance between the centers of the hexagon-like features in Fig. 2-12e, is given by $\lambda_m = a/(2\sin(\theta/2))$ (see section 2.10.2), where a is the lattice constant of graphene. A long-range modulation of the stacking order, consisting of alternating AA- and AB-stacked regions, emerges in the system. The first experimental observation according to which the twist angle can control the electronic properties of two twisted graphene layers is attributed to Eva Andrei's research group in 2010 [75].

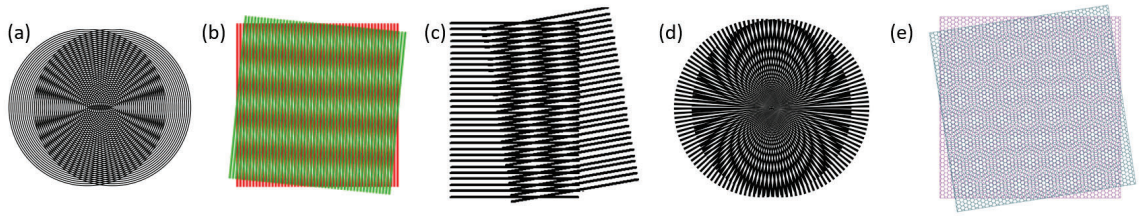

Figure 2-12: Examples of moiré patterns. Panels (a) - (d) adapted from ref. [76]. (e) Moiré pattern created by twisting two hexagonal lattices.

2.7 Commensurability

Strictly speaking, from a mathematical point of view, the lattice is perfectly periodic only for a discrete set of twist angles (denoted *commensurate structures*). For example, if the second layer is rotated with respect to the first layer around, let us say, a A_1B_2 position, a commensurate structure is obtained only when an A_1B_2 stacking configuration occurs elsewhere after rotation, and the lattice possesses translation symmetry [77, 78]. For interested readers, a mathematical derivation of the precise conditions needed for the superlattice to be periodic and several studies on commensurate structures can be found in the literature [79, 80, 81, 77, 78, 74].

This issue goes far beyond mere scientific curiosity: For incommensurate twist angles, Bloch's theorem does not apply, and band structure calculations may thus seem impossi-

ble [81, 82]. However, in realistic experimental realizations, incommensurate angles are not only feasible, but highly likely. It is, therefore, necessary to describe the electronic structure in a meaningful way both for commensurate and non-commensurate twist angles. For small-twist-angle devices close to the magic angle (where the superlattice periodicity is much larger than that of the underlying lattices), the band structure can be seen as semi-continuous, and is well approximated by a continuum model [83, 81, 78, 84, 85]. Under this approximation, infinitesimal changes in the twist angle do not significantly affect the band structure of MATBG, and commensuration effects are smoothed out. In McDonald's implementation of this model, for instance, hopping is local and periodic such that Bloch's theorem can be applied to any arbitrary small twist angle [81]. In addition, minimal structures (those with one moiré spot per unit cell) are suitable for representing all nearby commensurate structures [83, 81, 78, 86].

2.8 Twisted Bilayer Graphene

2.8.1 Motivation

One of the reasons MATBG has attracted significant attention in the scientific community is its ability to become a new and complementary two-dimensional platform for investigating strongly correlated physics and superconductivity. This ability of MATBG is developed in this section with reference to it as a clean, accessible, and purely carbon-based material—and one that is precisely tunable. For instance, when compared to high-temperature superconductors such as cuprates and pnictides, the phase diagrams and phenomenology of these materials and MATBG show certain resemblances, including superconducting domes flanking correlated insulating phases (Fig. 2-17), strong coupling manifested by a high T_c/T_F [83], a strange metal phase (see Chapter 7), anisotropic phases both in the normal and superconducting states evidencing nematic order, a reduction in the superconducting dome due to competing orders (see Chapter 6), and a pseudogap state opening at the Fermi energy at temperatures above the superconducting transition observed in STM experiments [87, 88, 89, 90, 25]. However, unconventional superconductors are very challenging to

study both experimentally and theoretically for several reasons. First, it is typically necessary to individually grow multiple samples with different chemical dopants to recreate their phase diagrams. Those samples tend to have specimen-dependent disorders, making the comparison between different samples even more challenging. Second, the theoretical models generally used to describe these materials cannot be solved exactly [83]. Third, multiple phenomena may manifest simultaneously and coexist in high-T_c superconductors. For all these reasons, establishing tractable theoretical models to identify and describe key phenomenology is a complicated and arduous endeavor [91].

For MATBG, it is possible to access the superconducting and insulating phases (and other exotic phases reported later in this thesis) within a single device, by continuously tuning, in situ, the charge carrier density, the in-plane magnetic field, the perpendicular magnetic field, the electric field, and the temperature. Investigations drawing on all these experimental aspects may lead to further clarity in understanding and differentiating between the mechanisms driving competing phenomenology.

The unprecedented gate tunability of MATBG enables access to its phase diagram over the full range of flat bands and beyond. Further, its gate tunability may provide a basis for identifying and understanding universal behaviors without the added uncertainty of sample-dependent specific effects. From a theoretical point of view, this purely carbon-based crystal is potentially easier to treat than its high-T_c *cousins*, and substantial progress has already been made in describing this system on this front in the last few years.

2.8.2 Band structure

α parameter

When two graphene lattices are rotated in real space, the reciprocal space is also rotated by a twist angle θ, leading to a separation in momentum space between the two Dirac cones. This separation is proportional to the sine of half the twist angle (Fig. 2-15), $k_\theta = 2k_D \sin(\theta/2)$ (where k_D is the magnitude of the Dirac wave vector, i.e., the wave vector for the monolayer graphene at the corner of the Brillouin zone). It has been shown that the physics of TBG, which is sensitive to, even depends on, the twist angle, can be described

in terms of two small parameters: the moiré wavevector k_θ, and w, the latter of which determines the coupling strength between the two incommensurate layers [81, 92, 83, 25, 91] (see Fig. 2-15). In particular, their ratio, $\alpha = w/v_0 k_\theta$ (where v_0 is the Dirac velocity of graphene), quantifies the hybridization between the bands of the two graphene layers.

This parameter α controls the band structure of MATBG, and encompasses the two competing quantities that determine the flatness of the bands (see Fig. 2-15). For small α values, corresponding to large twist angles, the Dirac cones of the two layers are far apart, and the low-energy spectrum is barely affected by the presence of the second graphene layer (Fig. 2-15a). As α is increased (or the twist angle decreased), the Fermi energy is renormalized, resulting in a Fermi velocity lower than that of monolayer graphene, $v^*/v_0 = \frac{1-3\alpha^2}{1+6\alpha^2}$ (v^* is the band velocity at the Dirac point for TBG) [81]. At certain discrete values of α, corresponding to what are referred to as "magic angles," the exact values of α beyond the one for first magic angle are sensitive to the model used [92, 81, 93], see Fig. 2-13), and flat bands occur with zero Fermi velocity. Throughout this thesis, only the "first" magic angle $\theta \approx 1.1°$ [81, 91, 25, 92], is investigated.

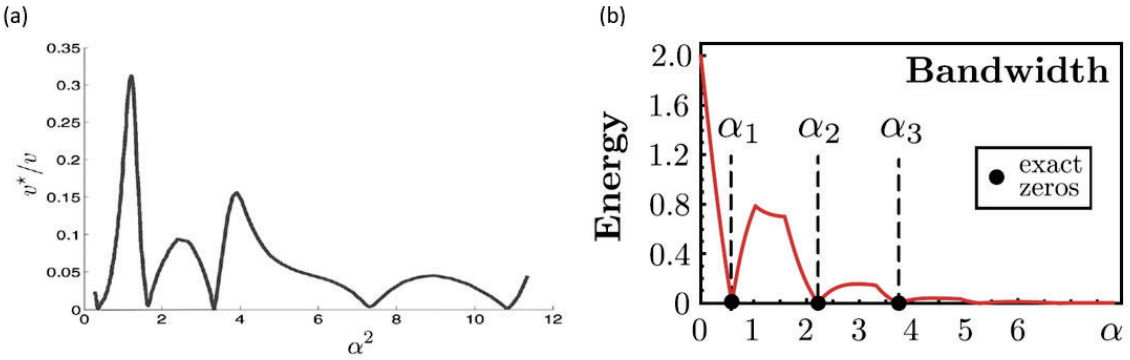

Figure 2-13: (a) In ref. [81], the magic angles are defineD as the twists for which the Fermi velocity vanishes at the Dirac point. The predicted sequence of magic angles is $\theta \approx$ 1.05°, 0.5°, 0.35°, 0.24°, and 0.2°. (b). In ref. [92], the magic angle is defined as the twist for which the bandwidth is minimized. The first magic angle is given by $\alpha = 0.58$, corresponding to $\theta \approx 1.09°$. This value is very close to the one obtained in the model developed by Bistritzer *et al.*, and also to the value reported in the experiments described in this thesis. Higher-order angles predicted by the Bistritzer (panel (a)) and Tarnopolsky (panel (b)) models differ. Figure adapted from ref. [81] (panel (a)) and ref. [92] (panel (b)).

Typically, $k_\theta a_0 \ll 1$ and $w/t \ll 1$ (where a_0 is the distance between atoms and t

the strength of the intra-layer hopping). Based on these conditions, the continuum model described above can be applied [77, 78, 81, 91].

Two possible visualizations of the band structure of MATBG are now presented: first, a *hand wavy* explanation based on intuitive schematics, and second, the models used to compute the band structure.

Band structure: cartoon picture

It has been well known for more than a decade that at *large* twist angles (small α), an effective decoupling between the layers takes place, giving rise to the linear Dirac spectrum of a single graphene layer with a modified Fermi velocity [77, 21]. The large-twist-angle case is approximately equivalent to the situation with no interlayer tunneling (Fig. 2-15a): the band structure of twisted bilayer graphene can be seen as four independent Dirac cones intersecting at two energies with separation $\Delta E = \hbar v_0 k_\theta$ [77, 21].

Thus, for a large angle ($\theta > 3°$), the two Dirac cones can be seen as separated in momentum space with minimal interaction, where the hybridization only occurs at high energies, similar to that shown in Fig. 2-15a. At finite yet small tunneling, an avoided crossing opens at these intersections, resulting in saddle points in the band structure (giving rise to peaks in the density of the states referred to as "van Hove singularities").

For smaller twist angles, such as $\theta = 1.8°$, hybridization occurs at much smaller energies, leading to dramatic changes in the band structure. In particular, competition between the kinetic energy and the interlayer hybridization starts to take place. In this case, an energy gap opens at the intersection of the two Dirac cones such that the system cannot be described as two weakly coupled graphene layers [94]. Additionally, the Fermi velocity at the Dirac point decreases even further from its typical monolayer graphene value.

When the hybridization energy $2w$ is comparable to the energy at which the Dirac cones cross $\hbar v_0 k_\theta/2$ (Fig. 2-15c), the lowest hybridized state is pushed towards lower energies [79]. This happens precisely at the magic angle [81, 75, 95], and the band structure near zero Fermi energy becomes flat due to strong interlayer coupling. The Fermi velocity is renormalized to zero at the Dirac point. Large effective masses have also been experimentally reported, as a consequence of the flatness of the bands [79].

Band structure: theoretical models

For moiré superlattices, the superlattice potential folds the band structure into the mini Brillouin zone [83, 25, 91]. Owing to a large moiré wavelength in real space (on the order of 13 nm for MATBG, much larger than the graphene lattice constant), the superlattice Brillouin zone in reciprocal space is small (Fig. 2-14a) [79, 94]. This Brillouin zone, corresponding to that of the superlattice unit cell, is constructed by joining the corners of the two graphene reciprocal hexagonal lattices (see Fig. 2-14a). The states in the K and K' mini Brillouin zones (upper and lower small black hexagons in Fig. 2-14a) have opposite chirality. Each superlattice Brillouin zone has two Dirac cones, one from each layer, which are protected by $C_{2z}T$ symmetry (similar to monolayer graphene). Spectral gaps can be opened by breaking this symmetry, either by applying an external magnetic field or by aligning the MATBG with an hBN substrate [25, 96, 97].

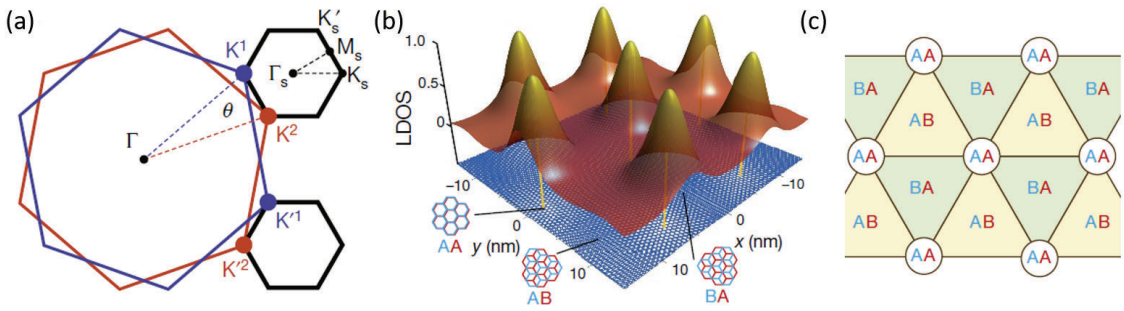

Figure 2-14: TBG reciprocal space and localization. (a) In reciprocal space, the Brillouin zone of the second graphene layer is rotated by a twist angle θ with respect to the Γ point. The mini Brillouin zone (small black hexagon) is constructed from the K points of the two graphene layers. $k_\theta \approx 2k_D \sin(\theta/2)$ (defined in the main text) corresponds to the displacement of the two Dirac cones K^1 and K^2. (b) Local density of states, showing that the electrons are strongly localized in the AA regions. (c) Simplified schematic of the stacking order, showing the resulting triangular lattice. Adapted from ref. [79].

The low-energy Hamiltonian for the K mini Brillouin zone is given by [25, 77, 98, 81, 92, 99]:

$$H_K = \begin{pmatrix} v_F \boldsymbol{\sigma} \cdot \boldsymbol{p}_1 & T_m(\boldsymbol{r}) \\ T_m^+(\boldsymbol{r}) & v_F \boldsymbol{\sigma} \cdot \boldsymbol{p}_2 \end{pmatrix}$$

where $\boldsymbol{p}_1 = \hbar(\boldsymbol{k} - \boldsymbol{K}_i)$, and $i = 1, 2$ is the layer index. The Hamiltonian for the K' mini Brillouin zone is its time-reversal partner. $T_m(\boldsymbol{r})$ is the moiré potential coupling the

two layers. This Hamiltonian can be seen as two single-layer Hamiltonians for each of the graphene layers and a tunneling term that describes the hopping between the two layers [81].

The evolution of the electronic bands with twist angle was proposed more than a decade ago based on tight-binding calculations [95]. These band structures have since been refined by the Kaxiras group using fully self-consistent ab-initio DFT calculations, and more recently with the effects of strain included [100, 101, 102, 103]. However, ab initio calculations typically involve a large number of carbon atoms per unit cell ($\sim$ 13000), which calls for alternative approaches to describing this system [25, 93]. Another option is the continuum model [81, 77], which can be run on a personal computer in a matter of minutes. Unlike the tight-binding model, for which $\sim 10^4$ large matrices must be diagonalized (as it builds upon atomic bases), in the continuum model, the eigenstates are plane waves propagating in each layer (coupled by interlayer hybridization). All atomic details are, therefore, lost [86, 77, 98, 92, 81, 84]. For a more in-depth discussion of the tight-binding model and the continuum model used to obtain the single-particle band structure of TBG and a detailed comparison of the models, interested readers can consult Yuan Cao's PhD thesis [86].

Relaxation

In the tight-binding and continuum models referred to above, the carbon atoms are assumed to be rigid; i.e., the distance between the atoms and the interlayer distance is constant. However, the AA stacking regions have higher potential energy than do the AB stacking regions. Nothing prevents the atoms from moving around their *assigned fixed* positions in the plane to minimize their energy (distortions) or the out-of-plane interlayer distance from modulating (corrugations) [104, 86, 105, 93]. Especially at small angles $\theta < 2°$, the *relaxed* lattice reduces the size of the AA regions and simultaneously increases the size of the low-stacking-energy AB and BA regions [93, 104], thereby favoring the formation of triangular domains. Below a critical twist angle close to $\theta \approx 1°$, the local atomic structure near the AA and AB regions becomes independent of the twist angle. This results in AA stacking regions that are small and circular and surrounded by large triangular AB and BA stacking

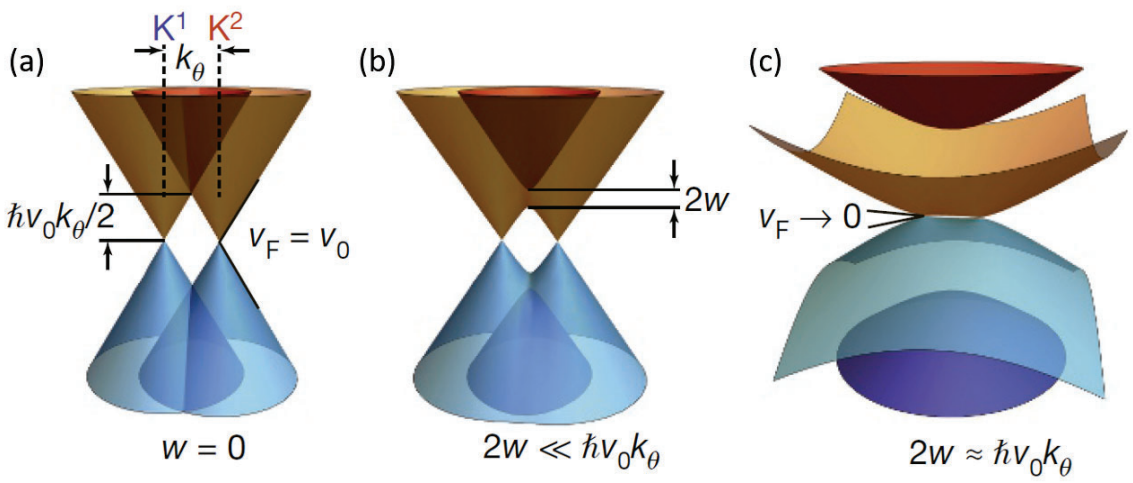

Figure 2-15: TBG band structure (cartoon). When 2 graphene layers are twisted, the Dirac cones from each layer are separated in momentum space by k_θ. (a) Schematic of the band structure when no interlayer interaction is included (hybridization energy $w = 0$), i.e., if the tunneling between the two bands is ignored. This is, approximately, the case for large-angle TBG, $\theta > 3°$. (b) When electrons can tunnel, a gap opens due to band repulsion. This situation occurs, for example, in a device with a twist angle $\theta = 1.8°$. Only hybridization between adjacent Dirac cones is shown here, i.e., between cones within each valley (such as K^1 and K^2 in Fig. 2-14). Intervalley interactions are strongly suppressed. (c) If the twist angle is further decreased ($\theta \approx 1.1°$), the interlayer interaction becomes the same order as the energy at which the crossing happens. In the *magic-angle* case, the two saddle points merge, leading to nearly flat bands near charge neutrality with zero Fermi velocity [81, 75, 95]. Adapted from ref. [79].

regions, with all regions separated from each other by intermediate stacking domain walls [93, 106, 104, 101]. The interlayer distance is also smaller in the AA stacked regions than in either the AB or the BA stacked regions. Equilibrium is reached as a compromise between the stacking energy and the strain energy, both induced in the domain formation process, often referred to as a spontaneous *relaxation* process [104, 86, 93].

Relaxation effects have a significant impact on the electronic band structure of MATBG, as they both modify the moiré pattern and add strain. These effects must be taken into account in any attempt to go beyond mere qualitative observations to accurately calculate single-particle band structures. The relaxation effects can be accounted for in the tight-binding model and in the continuum approximation.

Reference [93] additionally reports that the inclusion of relaxation effects eliminates the appearance of magic angles where the Fermi velocity vanishes beyond the first magic

angle.

Band structure calculation

The band structure calculations using the continuum model [81, 86] (including relaxation effects) of "large-angle" TBG and "intermediate-angle" TBG and MATBG are shown in Fig. 2-5.

At the magic angle, regardless of the model, the bands are nearly flat, although the calculated band structure is sensitive to the approximations used [25, 82, 107]. Gaps separate the low-energy flat bands from the next higher-energy dispersive bands.

Each electronic band has a 4-fold degeneracy (spin and valley), which is inherited from the constituent graphene monolayers. The massless Dirac dispersion near zero energy is preserved, akin to monolayer graphene. A reduction of the Fermi velocity is accompanied by sharp peaks in the density of states, the van Hove singularities.

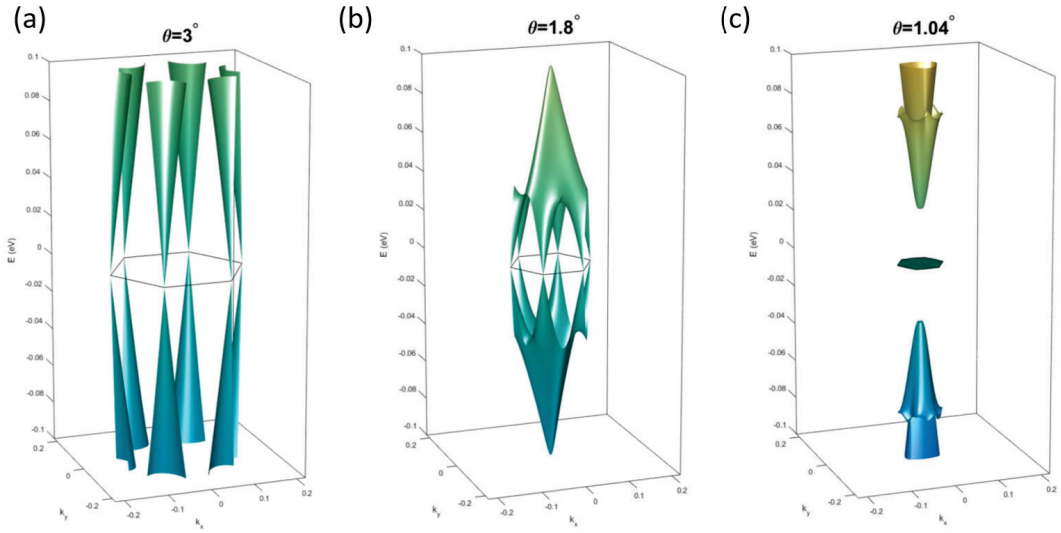

Figure 2-16: Calculation of the TBG band structure for three different twist angles (includes lattice relaxation). (a) For larger angles, such as 3 degrees, the band structure is similar to that of monolayer graphene. As the twist angle is reduced, the superlattice Brillouin zone (hexagon in the center) decreases in size. (b) At $\theta = 1.8°$, the two lowest energy bands are separated by bandgaps from the next highly dispersive bands. (c) Close to the magic angle, a flat band is observed. Adapted with permission from an animation created by Yuan Cao in collaboration with the Kaxiras group.

Flat bands and strong correlations

Flat bands are of particular interest in condensed matter physics: electrons move slowly and densely occupy the available energy levels (high density of states), where the energy of the electrons is almost independent of their momenta. Flat bands thus amplify the effects of the interactions and may lead to exotic quantum phenomena [108, 91].

In MATBG, the kinetic energy of the electrons is set by the bandwidth W, which is on the order of 10 meV [79, 83, 89, 87, 88, 90]. As the bands are almost flat, when the chemical potential of the electrons lies within the low-energy bands, the Coulomb energy U between the charge carriers can substantially exceed the kinetic energy of the charge carriers ($U \gg W$) [109, 83]. This defines, precisely, MATBG as a strongly correlated system. Electron-electron interactions, therefore, become dominant and so determine the physics of MATBG.

2.8.3 Localization

Flat bands in momentum space translate into highly localized charge carriers in real space, which, in turn, favor strong interactions between the localized electrons. In MATBG, the electronic states in the flat bands are strongly localized in the AA stacked regions of the superlattice, where locally the carbon atoms from the two layers are *one on top of the other*, as shown in Fig. 2-14b. On the other hand, the density of states in the interconnecting AB and BA regions (Bernal-stacked) is low. A top view of the normalized local charge density is shown in Fig. 6-1.

2.8.4 Correlated insulating states in MATBG

The first groundbreaking observation in MATBG [79] was the experimental demonstration of insulating states with a density approaching half that of the superlattice density (see Fig. 2-17). These insulating states—referred to as correlated insulators—are not expected in the absence of interactions, but are a consequence of the narrow bandwidth W. Before addressing the MATBG case, let us start by addressing a general physics question: What is a correlated insulator?

According to single-particle band theory, if a bandgap separates two bands and the lower band is filled whereas the next upper band is empty, then the system behaves as an insulator. On the other hand, if one of the bands is partially occupied, then the material can conduct electricity and is, therefore, a metal. In principle and with just single-particle physics accounted for, these are the only two options—given that a semiconductor is analogous to an insulator with a smaller bandgap. However, it is possible for the Fermi level to lie in the middle of the band (hence, the material should be classified as a metal), but due to strong interactions between the electrons, the system is insulating. This phenomenon is attributed to interactions between electrons that open a *correlated gap*. The appearance of insulating states at integer fillings, where single-particle band theory predicts a metal, has been observed in other quantum materials, such as transition metal oxides, where they are typically denoted as Mott insulators [91, 79]. The electronic signatures of the correlated insulating states are considered in more detail in section 2.8.7.

2.8.5 Superconductivity in MATBG

The second groundbreaking discovery, which also took place in 2018 [83], is the experimental demonstration of superconductivity in this purely carbon-based system (Figs. 2-20 - 2-22).

Originally, superconductivity was reported only around the correlated insulator for holes. We now know, however, that twisted bilayer graphene at the magic angle superconducts when holes are used to dope the system, and also when electrons are used for this purpose (see Figs. 2-19 and 2-22).

It should be well noted that MATBG does not require either ionic liquid gating or chemical doping to achieve superconductivity, which can be achieved instead by electrostatic gating [83]. Further, the density at which MATBG superconducts is an order of magnitude lower than that of any other known superconductor.

Moreover, the critical temperature of MATBG as compared with its very low Fermi temperature is exceptionally high. In particular, MATBG is among the superconductors with the strongest pairing strength between electrons, comparable to other high-

temperature unconventional superconductors [83].

Presented next is a general discussion on the electronic phase diagram of MATBG followed by a brief consideration of the transport evidence of correlated insulators and superconductivity in this system.

2.8.6 Phase diagram

A simplified schematic of the TBG phase diagram near the magic angle is shown in Fig. 2-17. The details are angle-dependent and vary from one device to another. In this diagram, and throughout this thesis, filling ν is defined from 0 at charge neutrality (where half the bands are filled) to -4 (i.e., four holes per moiré unit cell), or +4 electrons per unit cell, accounting for spin and valley degeneracies. We equivalently denote the density required to fill the mini Brillouin zone as $n = \pm n_s$. At full filling of the superlattice density $\nu = \pm 4$ ($n = \pm n_s$), band insulators (commonly denoted as *superlattice gaps*) are observed, with a thermally activated measured gap on the order of 30-60 meV [79, 83, 94]. Correlated insulators emerge around two holes and two electrons per unit cell ($\nu = \pm 2$), at near half the superlattice density, with up to two pronounced superconducting domes flanking each insulator. The superconducting state is explored further in section 2.8.8. Thermal activation measurements suggest that these correlated insulating gaps are around two orders of magnitude smaller than the superlattice gaps [79].

Above a few Kelvins, the system behaves as a metal, with decreasing resistance as the temperature is lowered. Fig. 7-1 shows the temperature-dependence of the system across a broad range of temperatures for two devices. At zero magnetic field, a metal-insulator transition occurs at any doping that corresponds to the correlated insulating state, and a metal-superconductor transition (with a possible intermediate region where the system is insulating) can be seen for each nearby doping.

With input from several groups, this phase diagram has evolved very fast since it was first proposed [83]. As shown throughout this thesis, the diagram now has greater complexity, including the observation of a strange metal phase (Chapter 7), anisotropic and nematic phases spontaneously breaking the C_3 lattice rotational symmetry (Chapter 6), and

a higher-energy parent state with a broken electronic flavor symmetry (Chapter 8).

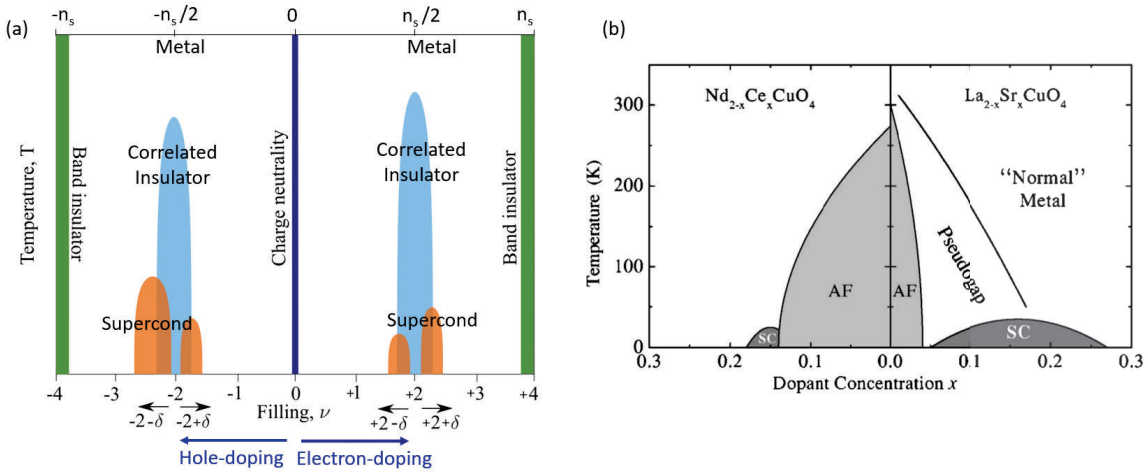

Figure 2-17: (a) Simplified schematic of the MATBG temperature-density phase diagram. This phase diagram has some similarities with the one for high-T_c superconductors (b), which has generated a high level of interest in the scientific community. The greatest hope is that MATBG will provide a basis for answering some important questions pertaining to these unconventional superconductors. Subfigure reproduced from ref. [110].

2.8.7 Electronic behavior (two-probe measurements)

Next, the electronic behavior of TBG is considered in terms of different twist angles and related to their band structures (Fig. 2-16). Figure 2-18 shows the two-probe conductivity of a few TBG devices that differ in regard to twist angle at low temperatures (qualitative comparison).

- For a "large-angle" TBG device ($\theta > 3°$), whose band structure at low energies is similar to that of monolayer graphene (Fig. 2-16a), the conductance shows typical ambipolar behavior, with a characteristic V-shape at the charge neutrality point (orange trace in Fig. 2-18). This minimum in the conductivity corresponds to the Dirac points in both layers.

- For a device with a smaller twist angle, such as 1.8 degrees, this V-shaped conductivity minimum originating from the renormalized Dirac cones is also observed around charge neutrality. However, at fillings $\nu = \pm 4$, and symmetrically around $\nu = 0$,

when the low energy bands are fully filled or fully emptied (in Fig. 2-16b), gaps are reached (green trace in Fig. 2-18). Two insulating states with poor conductivity are thus observed at $n = \pm n_s$. At similar densities, monolayer graphene is highly conductive ... but two twisted graphene layers at $\theta = 1.8°$ are insulating! These insulating states can be understood in a single-particle picture, because they correspond to completely filling an isolated band (see Fig. 2-16b).

- For a prototypical device close to the magic angle, near full filling, single-particle (*trivial*) insulating states are also observed (blue trace in Fig. 2-18). However, at fillings $\nu = \pm 2$ (equivalently, densities $n = \pm n_s/2$), where the system *should* according to single-particle physics behave as a metal (as the band is only half-filled), an insulating behavior emerges. As explained previously, in the absence of electron-electron correlations, these insulating states at half-filling of the superlattice density are not expected and correspond to a correlated insulator.

2.8.8 Transport characterization of superconductivity

Two-probe measurements are suitable for measuring resistive states. However, they are a far from ideal way to measure highly conductive or superconducting states, as they also account for the contact and cable resistance in the measured value. A 4-probe contact setup (see, for instance, the hall bar in Fig. 2-25), is better suited to these cases. Since 2018, we have fabricated several superconducting devices following this procedure.

The first evidence for superconductivity is that the resistance vs. temperature curve moves towards a zero resistance state, as shown in Fig. 2-20. As the density can be tuned continuously from electrons to holes by changing the gate voltage with our parallel plate capacitor-like electrostatic gates, the resistance-temperature-density map can be obtained in a matter of hours. The phase diagram displays up to four tunable zero-resistance dome-shaped regions around fillings $\nu = \pm 2$ (Fig. 2-19). However, as zero resistance can accrue for many reasons (see section 2.3.4), the presence of these zero-resistance dome-shaped regions is not sufficient to prove superconductivity [91].

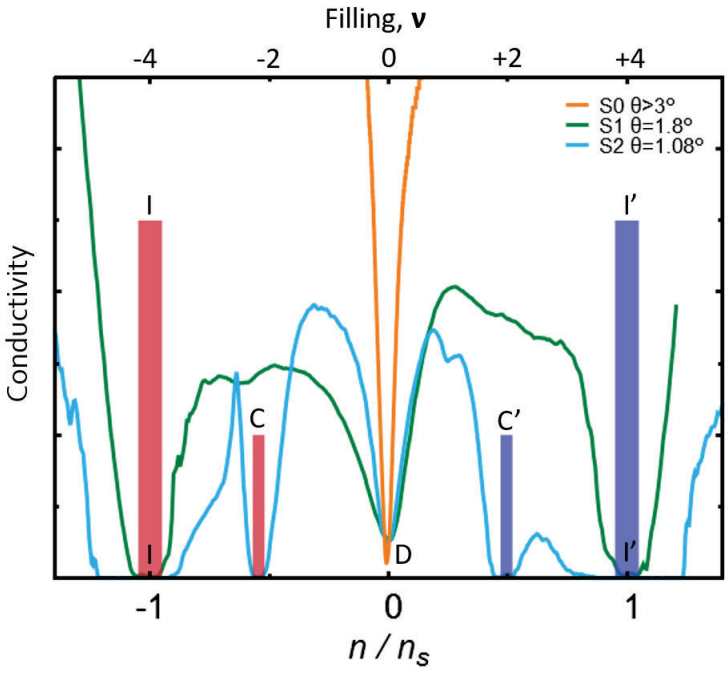

Figure 2-18: Qualitative comparison of the conductivity of a large-angle TBG device, an intermediate-angle TBG device, and a magic-angle TBG device. The absolute density is normalized with respect to n_s for a direct comparison between the different traces. Orange trace: conductance vs. density for a large-twist-angle device, showing similar behavior to monolayer graphene (note: here, n_S is defined as the full-filling density for the 1.8° twist-angle device, and conductivity is scaled by a constant factor; see [94] for the non-normalized density trace). Green trace: conductivity for a 1.8° twist-angle device. Blue trace: conductivity for a TBG device close to the magic angle. The following notations are used, as introduced in Chapter 5: I, full-filling band-insulating state; S, superconducting; C, correlated insulator at half-filling; and D, Dirac (charge-neutral) point. Primes denote positive fillings (that is, electron doping with $E_F > 0$). Adapted from refs. [79] and [94] by Yuan Cao. Reproduced with permission.

The second indication of superconductivity is nonlinear IV curves, which display a finite current bias and a zero voltage drop (see, for example, inset of Fig. 5-1c). As the temperature increases, the curves become progressively linear (ohmic).

In a bulk 3D superconductor, in order to confirm that a state is truly superconducting, the Meisner effect should also be considered (see Chapter 2.3). For 2D systems, for reasons that will become clear in Chapter 5, the Meissner effect is too weak to be observed with current state-of-the-art magnetic sensors. In the case of 2D systems, an unambiguous test for superconductivity is to demonstrate the Josephson effect. In Chapter 5, it is shown that the Josephson effect can be induced and also tuned and controlled in MATBG.

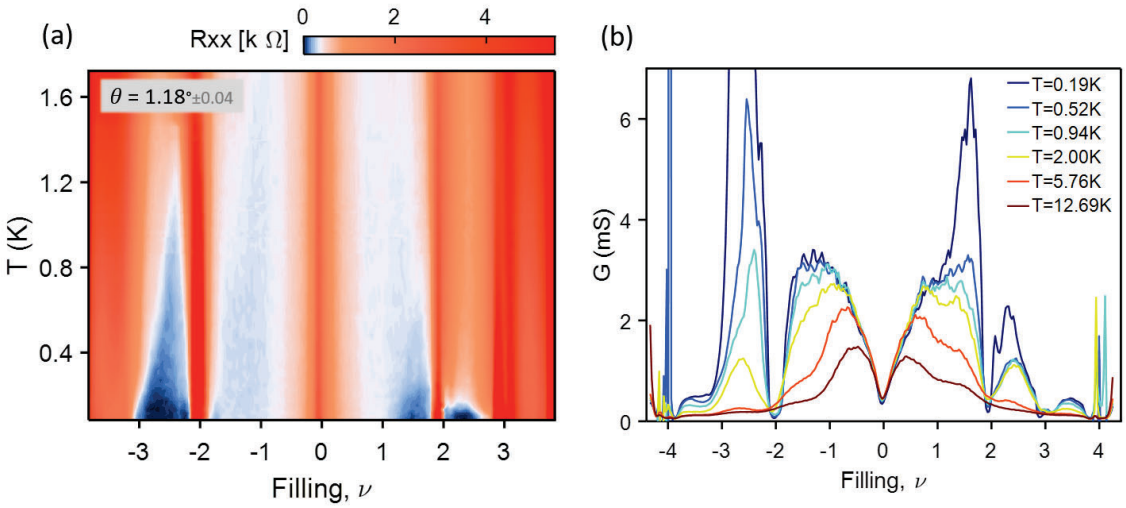

Figure 2-19: (a) Four-probe resistance R_{xx} versus temperature and filling for a prototypical device close to the magic angle. Up to four superconducting domes with zero resistance can be observed, two on each side of the half-filling correlated insulating state for electrons and two around the correlated insulating state for holes (see schematic in Fig. 2-17). (b) Line traces at selected temperatures.

It should be noted here that phase-coherent transport through arrays of Josephson junctions is demonstrated in the original MATBG paper [83]. These junctions are attributed to spatial variations in the moiré pattern or charge disorder; i.e., they cannot be precisely controlled.

2.8.9 Statistics

During my doctoral studies, my colleagues and I fabricated and measured many superconducting MATBG samples. We obtained temperature-carrier density-resistance maps for multiple devices, some of which are plotted in Fig. 2-21 for angles ranging from 0.98 to 1.16 deg. The shape of the superconducting domes varies substantially from one device to another, and so does the critical temperature. Two devices have yet to exhibit the same precise superconducting response, to the best of our knowledge. We conclude, therefore, that each device is unique and also of interest in its own right. However, this uniqueness also calls for new fabrication techniques that can ensure consistency and reproducibility among the different samples. Accurate control over twist-angle heterogeneity, inhomogeneous stain effects, charge disorder, and other related uncontrolled parameters that lead to spatial variations in the moiré pattern are highly desirable.

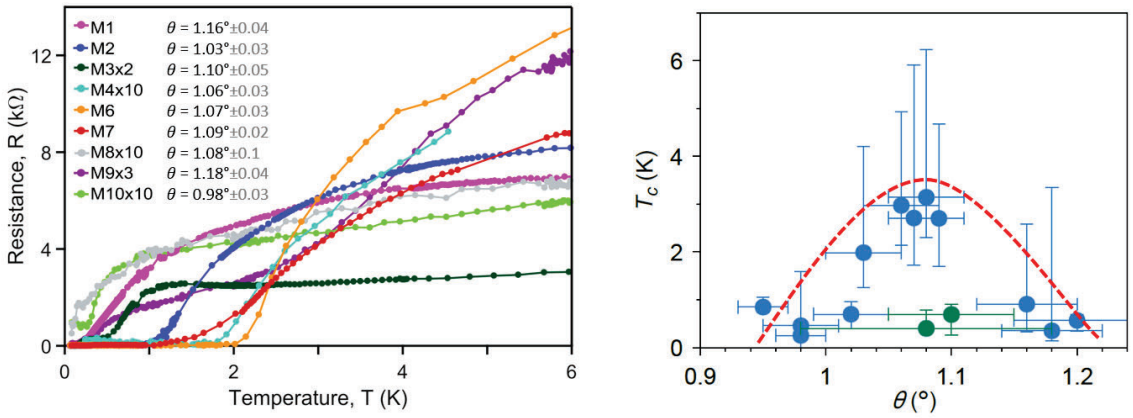

Figure 2-20: MATBG "statistics" (Figure 1/3). Left: R-T superconducting curves for a few superconducting samples at optimal filling $\nu = -2 - \delta$, with varying twist angles (see also Fig. 6-10 for a complete list of devices). Right: Critical temperature as a function of the twist angle for our MATBG devices. The critical temperature is estimated from 50% of the normal-state resistance. The optimal T_c follows a dome shape as a function of of the twist angle θ. The red curve is included as a visual guide. The phase diagrams of three of the devices with a high T_c are studied further near $-n_s/2$ in Chapter 6. Green dots indicate two highly disordered samples (hence, the large error bars in the x-axis), resulting in a significantly lower T_c as compared to other devices with similar twist angle. Table 6.1 includes additional information about the performance of the devices.

With all the devices we measured, we started to collect some *statistics*. In Fig. 2-20 (left panel), the RT curves of a few devices are plotted at optimal doping on the hole doping side of the $n = -n_s/2$ state, where the superconducting critical temperature is consistently the highest. Our superconducting devices span a range of twist angles $\gtrsim 0.2°$.

Based on mapping out the critical temperature as a function of the twist angle at optimal doping at filling $\nu = -2 - \delta$ (here, δ represents a small deviation from filling $\nu = -2$), a strong dependence on the critical temperature as a function of the twist angle is observed (Fig. 2-20, right panel). In particular, the highest T_c — on the order of 3 K as estimated from 50% of the normal-state resistance — occurs for a twist angle close to 1.06-1.09 degrees. Superconductivity is observed in only a narrow range of twist angles around $\theta \approx 1.1°$. It should be noted that the twist angle cannot, in principle, be changed in situ. Every data point in the right panel of Fig. 2-20, therefore, requires fabricating and measuring a different superconducting device—tasks that typically take a few weeks to a few months of dedicated work to complete.

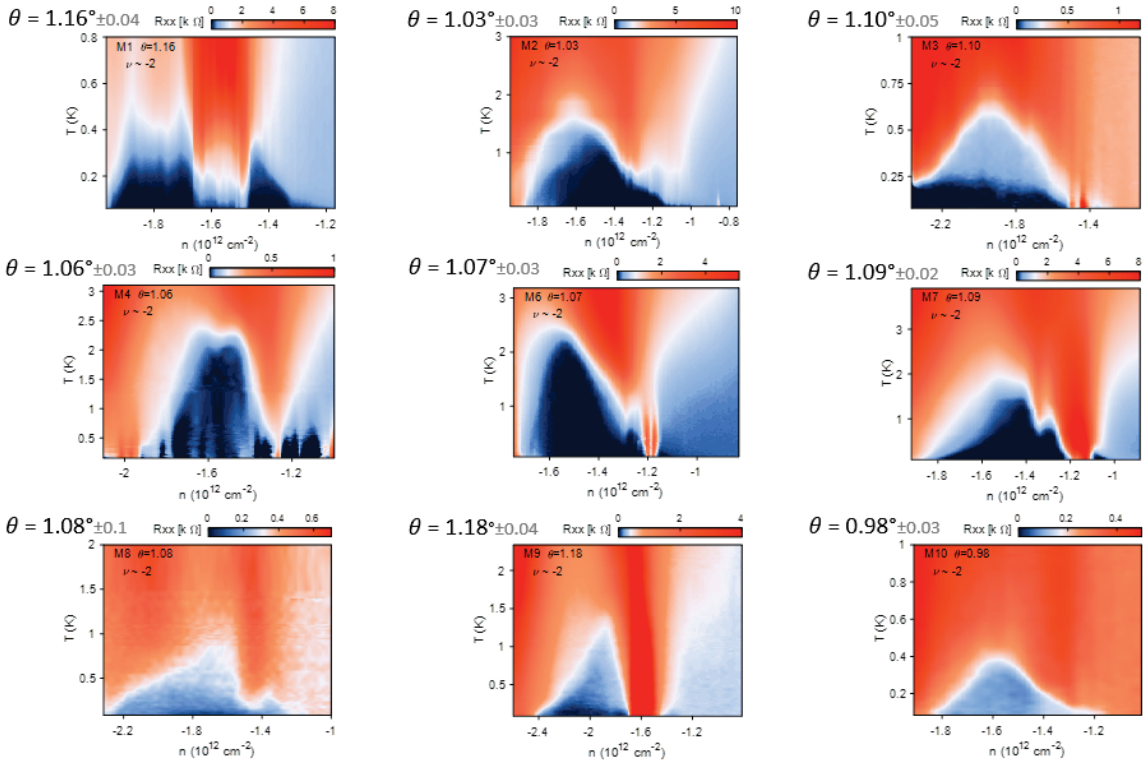

Figure 2-21: MATBG "statistics" (Figure 2/3). Density-temperature-resistance diagrams for fillings around $\nu = -2 - \delta$ for nine selected MATBG samples with angles ranging from $0.98°$ to $1.16°$. The shape of the superconducting domes varies significantly from one device to another.

2.8.10 Twist-angle inhomogeneity

By now, we know that the twist angle is not homogeneous within a single device. These inhomogeneities are believed to be introduced during the fabrication process, possibly by local strain, bubbles, or substrate imperfections, among others. One can, therefore, rightfully ask the question: What is the extracted twist angle previously mentioned, then? For all the devices discussed above, the twist angle is extracted via transport measurements, using the Landau fan in a magnetic field, as explained later in this chapter. The extracted twist angle typically correlates with the *dominating* twist angle in the region located between the contacts used to extract R_{xx}.

In two different collaborations with the Weizmann Institute (Fig. 2-23), we characterize the twist angle disorder for a few devices using high-resolution scanning techniques. These experiments made it evident that every device has a sizeable twist angle heterogeneity, up to

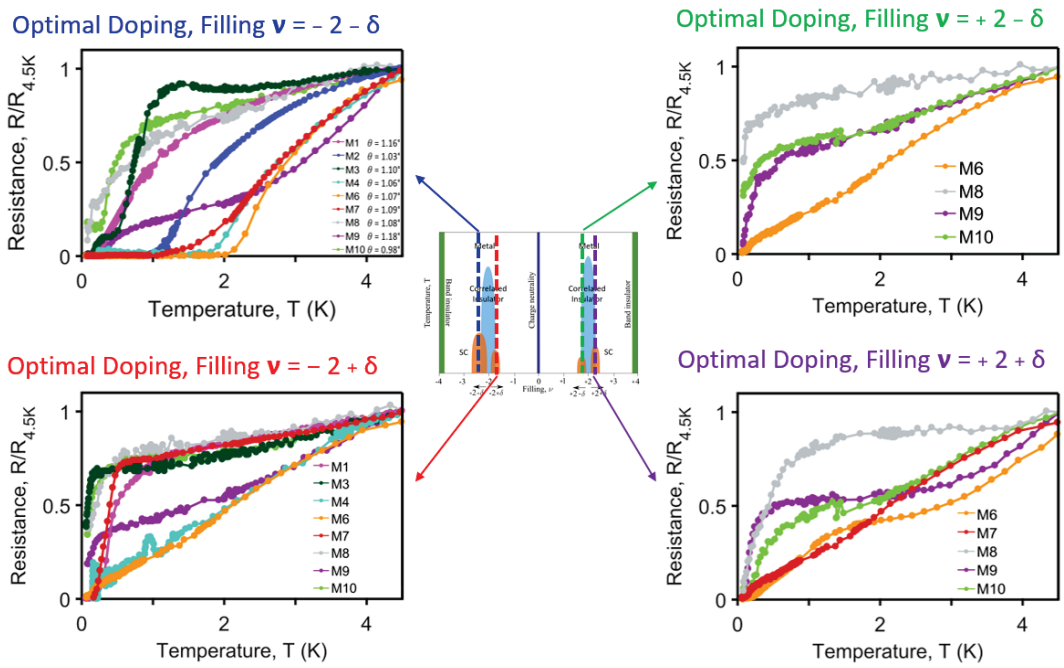

Figure 2-22: MATBG “"statistics”" (Figure 3/3). R-T curves for a few selected devices at fillings $\nu = -2 - \delta$, $\nu = -2 + \delta$, $\nu = +2 - \delta$, and $\nu = +2 + \delta$. SThe superconductivity is typically most robust around $\nu = -2 - \delta$. N; not all samples display all four superconducting domes.

a tenth of a degree, corresponding to 10% of the magic angle. Twist-angle inhomogeneities act as a strong source of disorder and lead to substantial spatial variations of the electronic properties, especially at larger fillings. CVD-grown MATBG might help mitigate this issue and could help scaling the fabrication of these samples [25].

2.8.11 Magnetism and topology

While magnetism and topology are not directly studied in this thesis, this introduction to MATBG would not be complete without mentioning a few words about them.

Ferromagnetism is not expected in a carbon-based system: graphene contains no magnetic atoms, and has very weak spin-orbit coupling. Effectively, in bulk materials, the magnetization has two known origins: the intrinsic spins degrees of freedom (alignment of the magnetic atoms), and the orbital motion of the electrons (usually generated by spin-orbit coupling and causing current loops at the atomic scale) [108, 25, 112].

MATBG appears to be the first example of purely orbital magnetism, which, together

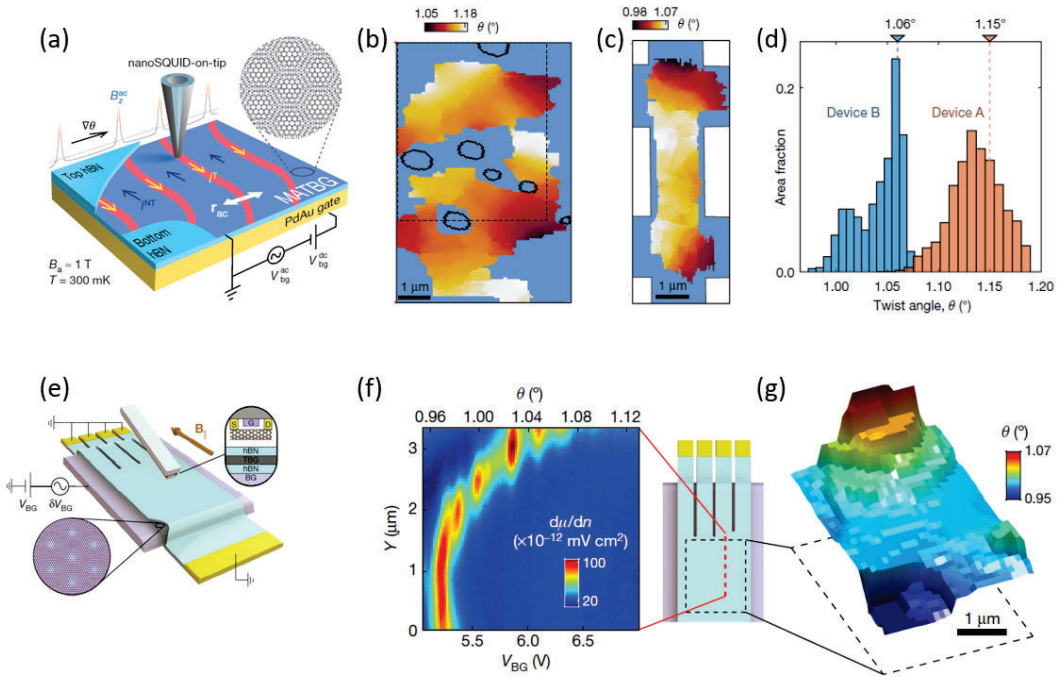

Figure 2-23: (a-d) Twist angle disorder in two samples, measured in collaboration with Eli Zeldov using a nanoscale on-tip scanning superconducting quantum interference device to map the local twist angle variations with a relative precision better than 0.002 degrees and a spatial resolution of a few moiré periods. (e-g) A scanning nanotube-based single-electron transistor is used to map the local inverse compressibility of a different MATBG sample, in collaboration with Shahal Ilani. This technique, discussed in detail later in this chapter, allows extracting the local relative twist angle with a high precision, which even appears to climb in steps in certain parts of this particular device. These results are published in references [56] and [111] -see also Chapter 8-, respectively.

with superconductivity and correlated insulating states, became one of the biggest surprises in the community [96, 113]. Microscopically, orbital magnetism is associated with real-space current loop patterns on a scale of the moiré wavelength [112, 108].

The first observed signatures of this phase are a (quantized) anomalous Hall effect, present in the absence of a magnetic field, and a hysteretic Hall signal persisting when the field is turned off. Both of these effects were originally observed near filling $\nu = 3$ in samples where the TBG was aligned with the hBN substrate [96, 113].

These experiments signaled the presence of a Chern insulator at $\nu = 3$, and were shortly followed by a panoply of experiments revealing the topological character of the moiré bands [114, 115, 116, 117, 118, 119, 120, 121, 112, 99].

We refer the interested reader to ref. [112] for a comprehensive review on orbital magnetism in moiré graphene systems.

2.8.12 Twisted bilayer-bilayer graphene and electric field tunability

If instead of two monolayers of graphene twisted at the magic angle, we take two twisted Bernal-stacked AB bilayer graphene sheets, the system dramatically changes and becomes a totally new system interesting on its own. We extend the *twistronics* techniques to the study of magic-angle twisted bilayer-bilayer graphene (TBBG) in Chapter 10. TBBG exhibits a rich phase diagram, as can be seen, for instance, in Fig. 10-2. It possesses tunable correlated insulator states that are highly sensitive to both the twist angle and to the application of magnetic fields and electric displacement fields. In particular, the gaps at $\nu = 0, 1, 2$ are highly tunable by an electric field. In contrast, in MATBG the electric field has minimal effect on the correlated phases [122], except for one particular outlying device, shown in Fig. 2-24.

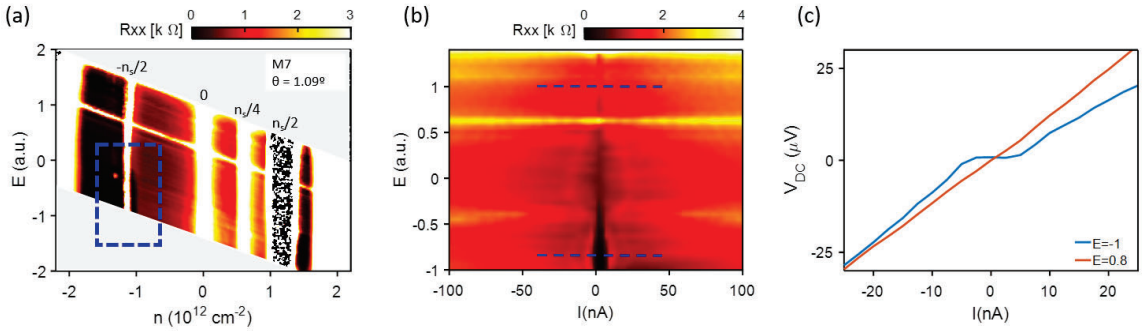

Figure 2-24: In the devices with both a top and a bottom gate, one can simultaneously control the charge carrier density and the electric field across the layers (panel a). As predicted from flat-band models [81, 123], and as also previously noted experimentally [122], MATBG is not expected to have a strong electric-field dependence due to the strong interlayer hybridization. However, in one single device (and only one), the superconducting state around the correlated insulator state in the hole-doped region ($E_F < 0$) seems to disappear at around 0 electric field (panel b). We confirm this by applying a current bias to the sample along the dashed lines in panel b: the I-V curves are ohmic for positive E and nonlinear for negative E (panel c). We do not understand this behavior at the moment of the writing of this thesis. The goal of this figure is not to confuse an inexperienced reader (for which the message should simply be that MATBG does not experience E-field dependence in principle), but to share these outlying (unpublished) data with the community.

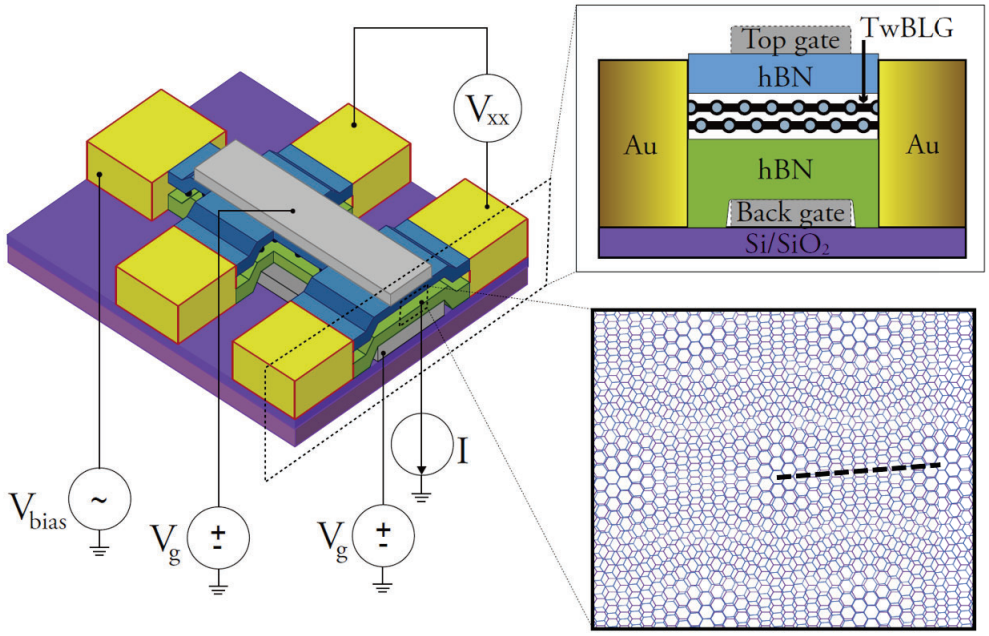

Figure 2-25: Left: Schematic of a typical dual-gated device, and standard four-probe measurement configuration for transport studies. Top right: side view of the device structure. HBN flakes on both sides sandwich the two twisted monolayers of graphene. The metallic gates at the top and the bottom of the graphene flakes tune the carrier density and the transverse electric field. Bottom right: schematic of the MATBG moiré pattern (angle enhanced for visual purposes compared to the "magic" angle, $\theta = 1.1°$). The distance between two *soccer-ball-like* features corresponds to the moiré wavelength (black line), $\lambda_m = a/(2\sin(\theta/2))$, where a is the graphene lattice constant and θ the twist angle. The magic-angle TBG superlattice periodicity is around 13 nm.

2.9 Device fabrication

This section aims to introduce the main techniques involved in the nanofabrication of a MATBG (or, similarly, a TBBG) device. Other devices beyond TBG presented in this thesis require similar fabrication techniques, with possibly some minor differences carefully described in the corresponding chapters. None of the proposed methods is by itself particularly challenging or exclusive to our expertise. It is the combination of the mastery of all of them that guarantees a successful device. Nanofabrication requires patience, perseverance, (some) skills, and most importantly, good nanofabrication facilities. During all these years in Pablo's lab, I have spent countless hours, days, and certainly months fabricating such devices. Several of the techniques I will present in this section have been directly taught to me by former students and are well-established in the field of 2D materials, while some

others have been discovered or fine-tuned during the years of my PhD either by me or by other students in the lab. As Newton once said, I have doubtlessly *stood on the shoulders of giants* throughout the times of my PhD. The goal of this section is to gather this expertise to share it with future generations of experimental scientists looking to nanofabricate similar devices.

The fabrication of any device presented in this thesis can be divided into three main parts:

1. exfoliation of the 2D materials,
2. stacking of the previously isolated flakes, and
3. design of the device and clean room processing (lithographies, etchings, evaporations).

For each batch of MATBG fabrication, we typically make between 5 and 7 stacks, which result in 10 to 15 different hall bar devices at the end of this few-weeks-long process. One can safely store these devices under ambient conditions for several months before measuring them.

I will first describe the materials, precursors, and techniques separately, and then explain the fabrication of an archetypal device (a dual-gated magic-angle twisted bilayer graphene nanodevice). The techniques described below can be easily generalized to any other device presented in this thesis beyond MATBG and TBBG.

2.9.1 Boron nitride

Let us start by introducing hexagonal boron nitride, a thin insulator used in every single device presented in this thesis, and one of the most commonly used 2D vdW materials.

Boron nitride (BN) is a group III–V compound with boron and nitrogen atoms. Its hexagonal form (hBN) is the most stable of the BN polymorphs. Hexagonal boron nitride is a wide bandgap semiconductor (hence, it is usually considered insulating), with a reported indirect bandgap of 5.955 eV (UV range) measured via optical spectroscopy [124]. It can sustain large electric fields, on the order of 0.5V per layer and above [7]. In addition to

its importance in condensed matter research, boron nitride is put to use as a lubricant and additive in the cosmetics industry.

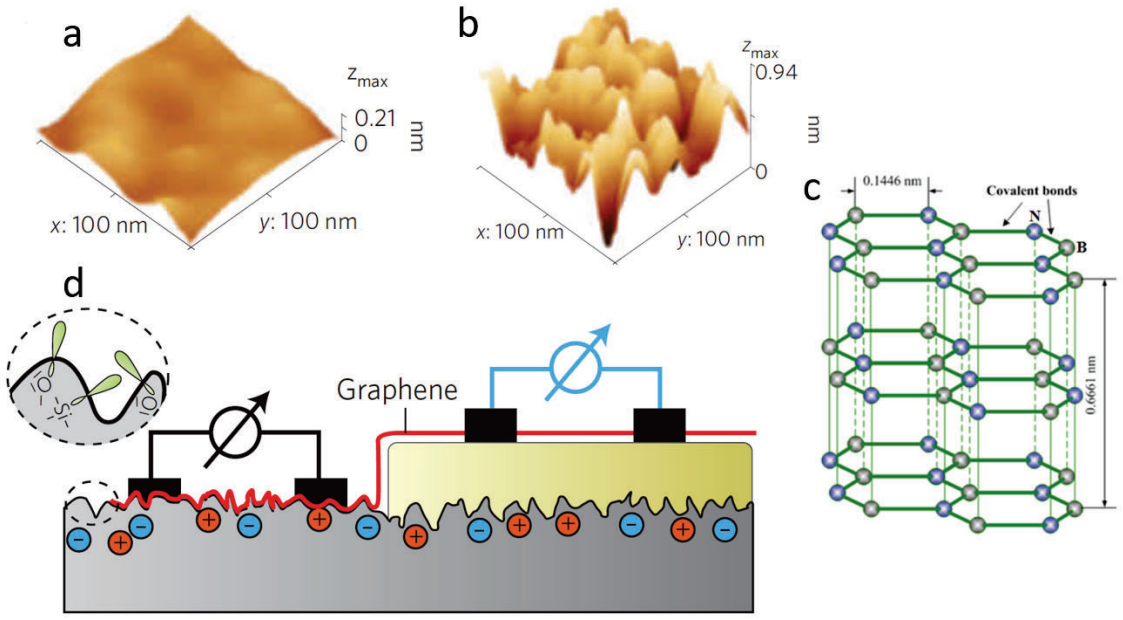

Figure 2-26: Hexagonal Boron Nitride. (a) STM topographic image of graphene on hBN and (b) image of graphene on SiO_2, showing increased corrugations. (c) Crystal structure of hBN. (d) Representation of a monolayer graphene on a silicon dioxide substrate (left) and an hBN flake (right). The corrugations, dangling bonds (dashed circle), and charge traps that are inherent to the silicon dioxide reduce the mobility of graphene. Figure adapted from references [125] (panels a-b), [18] (panel c), and [126] (panel d).

The structure of hexagonal boron nitride is similar to that of graphene, with boron and nitrogen atoms instead of carbon atoms. Sheets of hBN are composed of alternating boron and nitrogen atoms in a honeycomb structure in an sp^2-bonded network (Fig. 2-26c). The lattice constant of hBN is only 1.8 % larger than that of graphene [7].

Hexagonal boron nitride has not always been an essential ingredient in condensed matter physicists' recipes. It only became so after a pioneering experiment in which Corey Dean and colleagues established hBN as a high-quality substrate for graphene. Dean *et al.* showed that the mobility of hBN-encapsulated graphene devices is comparable to that of suspended graphene samples. Many other substrates had already been tried for use with graphene without success. Before this revolutionary discovery, the usual purpose of state-of-the-art graphene-based devices was to reduce disorder by suspending graphene, which

made certain experiments, such as local spectroscopic measurements, particularly difficult if not impossible [125].

Dean's observation is attributed to the use of charged impurity-free hBN surfaces [127], which—unlike the nanometric intrinsic roughness of typical SiO_2 substrates—were also ultra flat, as shown in Fig. 2-26. As a consequence, in graphene devices built on hBN crystals, charge fluctuations are diminished by two orders of magnitude when compared to graphene devices directly made on silicon oxide [125]. Crucially, hBN substrates leave the graphene band in the vicinity of the Dirac point essentially unperturbed (under the assumption that the crystallographic axes of graphene and hBN are not aligned) [7].

In addition to offering a suitable substrate for building stacks of vdW materials, hexagonal boron nitride is also ideal for the encapsulation of graphene and other 2D materials. In a fully-encapsulated device, the material under study is protected from external contamination by two hBN crystals, one on either side. Chemically stable, thermally stable, and mechanically robust, hBN has consistently enabled the fabrication of high-quality devices that do not deteriorate under ambient conditions. Now a preferred substrate among physicists and engineers, hBN has enabled technical developments that have proved to be key in the field of van der Waals heterostructures. All the graphene-based devices presented in this thesis are double-encapsulated with hBN.

All the hBN crystals used during the course of this thesis are provided by Watanabe and Taniguchi, from NIMS. High-purity boron nitride single crystals are synthesized using the temperature-gradient method under high-pressure (4.5 GPa) and high-temperature (1500 C) conditions with barium boron nitride used as a solvent [128, 129].

In summary, high-quality hexagonal boron nitride layers like the ones grown by Watanabe and Taniguchi, with minimal pinholes and defects, and displaying a high breakdown field, play a crucial role in all the experiments presented herein. Overall, hBN plays multiple roles: It serves as a dielectric for electrostatic gating, acts as an excellent substrate for building the different vdW heterostructures given that it is flat and inert, serves as an encapsulation layer, and enables the tear-and-stack technique used to make twisted superlattice structures. It has also been used successfully as a high-quality insulating ultrathin barrier in tunneling spectroscopy experiments in graphene-based systems, as shown in Chapter 3.

2.9.2 Micromechanical exfoliation of flakes

Si/SiO_2 chip

Any micromechanical exfoliation starts with a Si/SiO_2 clean chip ($\simeq$ 2 cm x 2 cm) diced from a wafer. A 6-inch p-doped (conductivity: 0.001-0.005 ohm-cm) Si wafer (NOVA electronics, item # FP02-61160-AS) is typically employed for standard exfoliations.

At earlier stages of my PhD, several techniques — typically sonication in solvents and aggressive oxygen plasma, or piranha/HF cleaning — were used to remove the residues on the surface of the chips. These contaminants came from the cutting process or other organic residues deposited due to air exposition. However, we then decided that there is probably no need to further clean the chips after dicing them if the original wafers came straight from the manufacturer's box and already appeared clean under bright field and dark field optical microscopy. Indeed, we now believe that the original cleaning performed at the factory might be better than any further cleaning one might attempt in the lab! Therefore, no cleaning of the wafer is typically performed before exfoliation.

However, for certain specific cases, namely, if a pre-processing involving lithographic resists has been performed on the chip before the exfoliation, cleaning the chip is highly recommended. This situation is encountered when a subsequent lithography with a precise alignment is required immediately after the exfoliation. In that case, Cr/Au markers, or Cr/PdAu gates (which also include markers), are generally written and evaporated prior to the exfoliation to provide the chip with an array of absolute spatial coordinates. An oxygen plasma or a heat cleaning are two preferred cleaning methods for that purpose.

Heat cleaning is explained in the next section. The procedure to clean the chip with markers using oxygen plasma can be described as follows:

- First, the chip is soaked in acetone and sonicated for 5 minutes at maximum power.
- After blow-drying with a nitrogen gun, the same process is repeated with isopropanol (IPA).
- The chip is then transported to the Organic and Nanostructured Electronics Lab (Prof. Bulovic's lab) or CMSE laboratories, both of them equipped with an oxygen plasma

tool.

Plasma cleaning removes impurities and contaminants from surfaces via an energetic plasma in the presence of oxygen gas. The high energy breaks most organic bonds of surface high molecular weight contaminants. In the presence of the oxygen plasma, organic contaminants form water, carbon dioxide and carbon monoxide, and other hydrocarbons with low molecular weight. These compounds are removed from the chamber during the process [130]. Oxygen plasma is an effective, economical, and more environmentally safe method for cleaning chips in comparison to the HF/piranha cleaning method presented in [131].

Micromechanical exfoliation of flakes: scotch-tape technique

Micromechanical exfoliation, also known as the scotch tape technique, is a top-down method used to peel atomically thin layers from a vdW material (such as graphene, hBN, or MoS_2) using adhesive tape. This simple and inexpensive technique was originally developed by Geim and Novoselov, which allowed them to perform the "groundbreaking experiments regarding the two-dimensional material graphene" for which they obtained the Nobel prize [6]. Surprisingly, it is still used up to date in the experimental condensed matter community as one of the most reliable ways to obtain high-quality thin flakes. A crystal of the precursor bulk material (such as graphite for graphene) is first placed on a sticky tape. By folding and peeling the tape several times, one can create successively thinner layers of the material via exfoliation.

After the sticky tape is dense enough and no thick crystals remain on the tape, it is placed on a clean Si/SiO_2 chip (Fig. 2-27). Sometimes, it may be helpful to use soft tweezers to gently press the sticky tape with the exfoliated crystals against the chip. This enables the reduction of bubbles and improves the adhesion to the substrate. After waiting for a few minutes, the tape is gently removed from the Si/SiO_2 chip. This process results in the deposition of several vdW crystals with a range of thicknesses on the silicon-based substrate. Selecting the right flake, or *flakehunting*, is typically performed by scanning the chip manually under an optical microscope, a simple and non-invasive approach described

in section 2.9.4. Collignon *et al.*, from our group, are currently developing a procedure to automatize this process [unpublished].

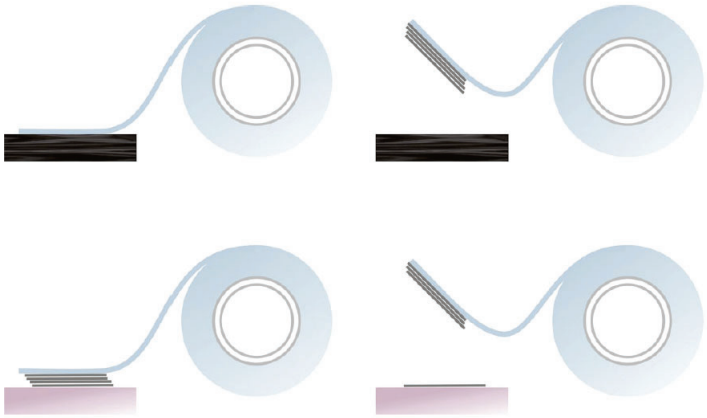

Figure 2-27: Micromechanical cleavage of flakes: Scotch-tape technique. The top few layers of a layered bulk crystal are cleaved with sticky tape. The tape with flakes is then pressed against the host substrate. After the tape is removed, some flakes stick to the silicon dioxide host substrate. We note that the 2D crystals from tape are usually not integrally transferred to the substrate. In most cases, only part of the crystal is deposited on the chip due to the competition between the chip stickiness and the tape. As a result, the topmost layer generally remains clean and doesn't have glue from the tape. Figure reproduced from reference [32].

In our group, contrary to many other groups, we do not use ordinary scotch tape (except for transition metal dichalcogenide thin layers). Instead, we use blue wafer dicing tape (Ultron Systems, 1007R-6.0). We find that it is cleaner and easier to remove, as it leaves less glue residue than other adhesive tapes.

The original exfoliation method, established in 2004, provides relatively small flakes (typically a few to several hundreds of square microns at most), with moderate yield. However, this procedure is typically enough for our research purposes, provided a few minor additional considerations are taken into account when exfoliating. Since 2004, many attempts have been made to increase the yield of thin flake crystals by adapting the previous technique. According to our experience, the essential points to obtain a good exfoliation are a *nice, big and shiny* initial crystal and a dense exfoliating tape. In addition to that, every researcher has different *tricks* to achieve, from their personal experiences, better exfoliations.

In my experience, for a decent graphene exfoliation with an acceptable yield of large monolayers, the Si/SiO_2 clean chip is pre-heated with a hot plate for a few minutes at 220 C. After removing the chip from the hot plate, the sticky tape with graphite is immediately placed on top of the hot chip [86].

For hBN exfoliations, the Si/SiO_2 chip can be optionally pre-heated to around 110 C. This may help eliminating the water molecules' adsorbates from the substrate and potentially enhances the adhesion between the sticky tape and the silicon-based chip. The tape with hBN crystals is then placed on the (hot) SiO_2 chip. After it has cooled down, the chip (with the tape stuck to it) is heated again at the same temperature for around 15-20 seconds, for a higher yield of deposition of hBN flakes [132].

From what I have noticed, high-yield exfoliations are typically achieved when the SiO_2 chip is *a little bit* sticky. Brand new wafers are sometimes not sticky enough, so I prefer using slightly older clean wafers. Alternatively, one can perform a mild O_2 plasma cleaning or UV ozone exposition to the chip immediately before the exfoliation. Another method to enhance the yield of certain delicate materials, such as ultrathin hBN, requires peeling the tape as slowly as possible. Further details about ultrathin hBNs are provided below in section 2.9.5.

To sum up, mechanical cleavage produces single-crystal flakes of high purity and cleanliness, suitable for fundamental characterization, in a matter of minutes. Following this procedure, one can obtain the hBN, graphene, thin graphite, and transition metal dichalcogenides flakes used in this thesis. It allows, for example, obtaining monolayer graphene and hBN flakes larger than 100 microns regularly, provided enough chips are patiently exfoliated. Micromechanical exfoliation will likely remain the preferred technique to obtain individual 2D materials in labs like ours for the years to come. However, scotch-tape exfoliation is not a scalable technique, and does not allow to systematically control the dimensions and thickness of a flake [13]. Other more scalable exfoliation and bottom-up growth techniques to achieve wafer-scale 2D materials have received wide attention over the last few years. Some of these techniques include liquid exfoliation, chemical exfoliation, co-vapor tube CVD, MOCVD, MBE, ALD, PLD, sputtering, and thermal evaporation [133, 134, 19].

2.9.3 Heat Cleaning

Flakes may contain residues on their top surface, either from previous nanofabrication processes (such as a pickup and transfer) or glue from the exfoliation. In such cases, annealing them at high temperatures in the presence of argon/hydrogen (known as forming gas) or in vacuum is usually helpful. Annealing the flakes is a possible solution to clean them, flatten the hBN, and in the case of vdW heterostructures, for smoothing the whole stack, rearranging the bubbles, and removing other impurities.

We note, however, that small-angle twisted graphene stacks cannot be annealed. The magic angle is not a globally stable configuration and tends to relax at high temperatures towards other twist angles, such as 0 degrees (Bernal stacked AB bilayer graphene). We also note that large monolayer graphene flakes often detach from the substrate and roll up during the annealing process, and hence they are typically not heat cleaned. An optical inspection (both using bright-field micrographs and dark-field images at high exposure), and an AFM scan, are used to decide if an atomically thin flake is clean (and hence good to use), or whether it must be discarded. Further details are provided in sections 2.9.4 and 2.9.7.

During the annealing, organic residues are vaporized or decomposed in the presence of heat (and in the presence of a low pressure for a vacuum annealing), and the flow of forming gas (or vacuum pump) removes them from the environment.

The chip with the flakes is first placed on a quartz boat and inserted into a quartz tube. After closing both ends of the quartz tube, one end of the tube is connected to the flow regulators of argon and hydrogen (alternatively, to a turbo pump), and the other end is connected to a safe exhaust pipe. For the work presented in this thesis, the annealing is generally performed under atmospheric pressure (no vacuum), with a flow of ~ 40 sccm for each of the two gases. The temperature is then ramped from room temperature up to 300 - 350C (may vary in the range 300C - 500C as various different protocols were attempted during this work) in less than 30 minutes. Annealing is performed at a fixed temperature for several hours for at least for 3 hours, and typically for 12 hours.

As we mentioned in the previous section, heat cleaning can also be used to clean a pre-

patterned chip before transferring 2D materials. In particular, the Cr/PdAu bottom gates are also annealed, usually at 300 C for 4 hours, before building a stack on top of them.

In the fabrication procedure of a typical MATBG device, three annealings are therefore performed:

1. right after the hBN exfoliation,

2. to clean the bottom gates, and

3. after the bottom hBN is transferred to the bottom Cr/PdAu back gate (but before the rest of the stack is transferred on top of it).

2.9.4 Flakehunting

Finding the right hBN flake or graphene monolayer (known as *flakehunting* in our lab's jargon) is not rocket science, although it is not always straightforward either. In short, the chips with the freshly exfoliated flakes are manually scanned under an optical microscope. For graphene, the color and contrast of thin crystals are typically enough for a trained eye to distinguish monolayers, bilayers, and other thicker flakes (see Fig. 2-4). However, if uncertain, one can also perform Raman spectroscopy to confirm the number of layers.

The flakes must have the appropriate size (we typically search for hBN thin crystals that are large enough, on the order of several tens of microns in each direction), without cracks or observable steps. Similarly, we look for graphene monolayers as large as possible to maximize the chances of success in the tear-and-stack (or cut-and-stack) procedure, preferably around or larger than 100 μm.

For hBN flakes used as dielectric layers for back and top gating (excluding ultra-thin hBN layers used for tunneling devices), we aim at flakes with thicknesses on the order of 10-80 nm (typical colors of the flakes when observed with a standard optical microscope are blue, green, or yellow). Candidate flakes are first identified by optical microscopy, and selected using contrast-tuned optical micrographs and high-exposure dark field images.

After selecting a few candidate flakes, the bests ones are optionally imaged via atomic force microscopy (AFM). The goal for this AFM measurement is double: to determine if

the flake is flat and clean, i.e., to certify that it does not contain steps, impurities, cracks, or folds potentially invisible under optical microscopy, and to measure its exact thickness. Graphene flakes can also be scanned under an AFM to certify they do not have cracks or organic residues on their surface. If any flake has any apparent defect that could compromise the final device, it is immediately discarded.

2.9.5 Ultra-thin layers of hBN

Ultra-thin hBN flakes (1-4 layers) deserve an independent section in this thesis. While these materials are not present in a standard twisted bilayer graphene nano-device, they are used in Chapter 3 as ideal tunneling insulating barriers with optimal tunneling resistance. Such devices allow us to access the density of states of graphene-based systems in planar tunneling spectroscopy experiments.

Ultra-thin hBN flakes are ideal tunneling barriers thanks to their crystalline structure, the low number of impurity states within the barrier, largeband gap (~ 6 eV) in the electronic spectrum, and atomically flatness. In the case of hBN, like graphene, mono-, bi- and few-layer 2D crystals are first identified by their optical contrast. However, their contrast to light is much lower than that of most of the other 2D materials: ultra-thin hBN does not absorb visible light and gives only rise to optical contrast due to deviations in the optical path. If exfoliated on standard 300 nm- thick SiO_2 wafers, hBN monolayers have a white-light contrast of less than 1.5%, which makes them nearly undetectable by our eye [135]. Furthermore, hBN flakes have a much lower yield from deposition than does graphene, and the resulting flakes are much smaller.

In order to enhance the optical contrast of few-layer hBN flakes, we exfoliate the hBN crystal on 90nm SiO_2 substrates (Nova Electronic Materials p-doped 90nm SiO_2 wafers, part number HS39626-OX), which offer a contrast of around 2.5% for hBN monolayers (four times less than that for graphene monolayers), just enough to render them visible under optical microscopy [135].

We found, empirically, that a few considerations can be taken into account to improve the yield of ultra-thin hBN flakes during the exfoliation process (see also ref. [131]):

1. Use a dense hBN tape, with minimally-fractured crystals

2. Heat the substrate to 110 C before deposition. Heat again to 110 C after deposition, with the tape on the substrate, for around 20 seconds.

3. Peel the tape from the chip very slowly (take at least 30 min to peel the tape from the chip). For that, we typically use a homemade (by Valla Fatemi *et al.*) exfoliation stage with a micro stepper actuator.

The poor optical contrast of hBN even on 90nm SiO_2 substrates makes their flakehunting tedious and time-consuming: the chips need to be scanned manually and carefully at 50x magnification. Recently, Clément Collignon developed a procedure to automatize this step, which will surely help future generations of students in our group.

After exfoliation, and before flakehunting, an annealing of the sample is performed as described in section 2.9.3. This is particularly useful here, since tape residues have a similar color to the hBN monolayers and can further hinder their search.

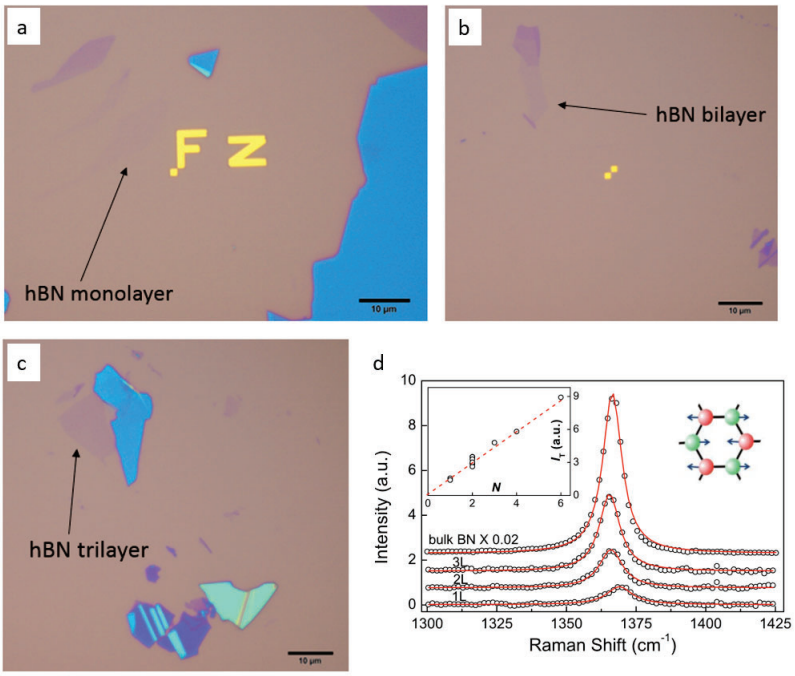

Figure 2-28: Ultra-thin hBN crystals (1-3L). (a - c) Optical micrographs of a monolayer, a bilayer and a trilayer hBN. Scale bars are 10 μm. (d) Raman spectra of ultra-thin hBN flakes, showing that the integrated intensity is proportional to the number of layers. Panel (d) is reproduced from ref. [135].

For a more systematic and consistent characterization of the number of hBN layers, one can perform Raman spectroscopy on selected hBN flakes [135]. I refer to my undergraduate thesis [136] for the experimental details on this procedure.

Last but not least, if an hBN ultrathin flake is part of the dry polymer-based pick-up and transfer process described below, the alignment becomes challenging. Effectively, hBN monolayers are optically invisible when lying on a PC slide. Therefore, one can only *guess* their position using the relative position of nearby thicker flakes, and having a previously taken high-contrast picture at hand to use as a reference.

2.9.6 Transfer setup, polymer-based dry transfer technique, tear-and-stack, and cut-and-stack

A crucial step for the field of van der Waals heterostructures is marked by the development of techniques allowing for stacking 2D materials on top of each other with micrometer accuracy. The technique employed in this thesis is the polymer-based dry transfer method, described below. It offers high throughput, and allows to customize the layer sequence.

Transfer setup

In the early ages of this field, the standard stacking procedure required isolating micrometer-sized 2D crystals on top of a thin transparent film and placing them, one by one, with the face down, onto a chosen target. This fabrication process could take various days, since the supporting film had to be dissolved, every time, between different steps. If the desired stack had multiple layers, then the removal of the film had to be repeated after every layer until the full stack was assembled. [8].

With the current state-of-the-art techniques, we can now pick up various flakes sequentially with the same polymer (PC). For example, there is no need anymore to deposit a 2D crystal, e.g., hBN, directly on top of another thin crystal, such as WSe_2 or graphene, and repeat this sequence at every step. Instead, we can use the hBN to pick up the graphene or WSe_2 from the substrate. This can be done thanks to the combination of the van-der-Waals force between two adjacent materials and the stickiness of the polymer.

Crucially, the interface between two consecutive crystals is not contaminated by any polymer with this method. Altogether, the different 2D materials composing the stack remain much cleaner, and the stack can also be fabricated faster.

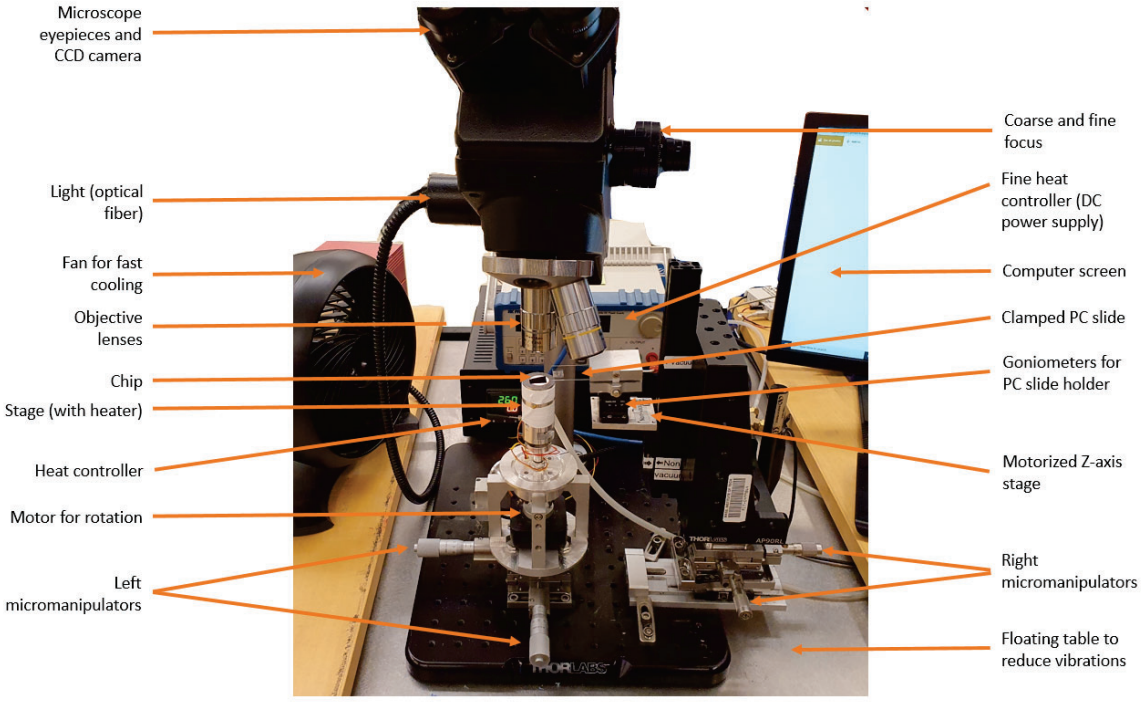

Figure 2-29: Picture of a transfer setup. The sample (chip) is vacuum-mounted on a heated stage. The position of the sample and the *PC slide* (polymer stack on a glass slide) can be independently controlled via micro-manipulators. Flakes are picked up by slowly engaging the polymer to the substrate.

However, the process is far from being trivial, and requires a high precision transfer setup (home-made) tool. The chip is placed under a microscope, and precisely positioned via micromanipulators (as shown in Fig. 2-29).

The whole transfer setup is installed on a vibration isolation floating table. The chip with the sample is mounted on a metallic block and kept fixed in position (for instance, thanks to a generated low-pressure region under the chip with a vacuum pump preventing the sample from moving). The aluminum block may be heated up to around 180 C in a controlled way, using either a (fast but rough) temperature controller or a much finer DC power supply (see Fig. 2-29).

Then, a glass slide with a PC polymer film (see below for the preparation procedure)

is mounted on a 3-axis micromanipulator stage, with the PC film facing down. The flakes already picked up by the poly-carbonate film can thus be aligned to the flakes on the chip (fixed in position by the vacuum) with a micrometric precision. A CCD camera attached to a long working distance microscope allows to visualize the process both on the eyepieces of the microscope and on a computer screen, the latter being ultimately preferred to minimize vibrations caused by manual manipulation of the hardware. A fan or cooling liquid can be employed for a faster cooldown of the aluminum block.

Our lab currently has four different transfer setups: The original and first transfer setup was built by Javier Sanchez-Tamaguichi (presently a Professor at UC Irvine) during his PhD in Prof. Jarillo-Herrero's group. In 2015, Valla Fatemi *et al.* built an automatized transfer setup for the glovebox. This tool allows us to work with air-sensitive materials. The other two transfer setups were built by Yuan Cao *et al.* and allowed a better accuracy than the original one. The working principle of all of them is similar, although the designs slightly differ from one another. Fig. 2-29 shows the optical picture of one of the high-precision transfer setups used during my PhD.

Polycarbonate (PC) slides

The fabrication of any van der Waals heterostructure starts with the preparation of a *PC slide*, a glass slide containing a stack of transparent polymers used to pick up sequentially the 2D crystals. From top to bottom, an upside-down *PC slide* is composed of a glass slide, a layer of double-sided adhesive tape, a cube of a soft viscoelastic polymer (PDMS), and a very sticky polymer layer (PC) (Fig. 2-30).

Figure 2-30: Side view of a PC slide

To make a PC slide, we first prepare a solution of poly(bisphenol A carbonate) (PC, Fluka Analytical, 6% in weight dissolved in chloroform). We then deposit a few droplets

of this PC solution on a glass slide. PC solution does not easily spin coat; therefore, in order to make a thin film of PC solution, we take a second glass slide, place it on top of the one with the PC solution, and slightly press the two slides against each other. Then, we separate the two glass slides by sliding them against each other quickly, fully spreading the PC. This process results in a thin and relatively uniform PC film, which is then left to dry and solidify in the air for a few minutes [137, 131]. Only the glass slide with the PC layer on its topmost face is kept; the uppermost glass slide is discarded since the PC layer might have come into contact with the table (Fig. 2-31). Rainy and humid days are typically recommended to prepare high-quality PC films with optimal stickiness. Humid conditions can be reinforced by performing the previous and subsequent steps on a wet fab wipe.

To follow, we rinse a new glass slide with isopropanol, and place a small pre-cut $\sim$2x2x1.5 mm cube of polydimethylsiloxane (PDMS) near one of its ends. PDMS is inert, optically clear, non-flammable, and non-toxic. PDMS is also viscoelastic, i.e., it is both viscous and elastic when deformed, and hence can be used as a *soft cushion* to ensure the PC film contacts the chip smoothly (see Fig. 2-30). After ensuring the PDMS surface does not contain bubbles or any visible residues, we place a double-sided tape with a pierced hole around the PDMS block.

Finally, the PC thin layer is removed from the glass slide using another double-sided adhesive tape with a pierced hole, and is then deposited across the PDMS. If prepared in dry conditions, the PC may wrinkle (especially during the winter, since the humidity is lower and the PC is more difficult to peel from the slide).

If any of the finalized PC slides appears to have any dust or visible impurities under a microscope inspection, it is discarded. Otherwise, the newly made PC-slide is ready to be used to build a vdW stack (Figs. 2-30 and 2-31). I typically let the PC slide age for a few days, ideally weeks, before using it for optimal results.

We note that, after the vdW stack is transferred on its final substrate, the order of the layers from top to bottom corresponds to the order of the different pickups (the first flake being picked up is the topmost layer of the resulting stack).

We also note that, several years ago, PC was not the default transfer polymer used in our lab. In fact, many labs still use other sticky polymers to build their heterostructures, such

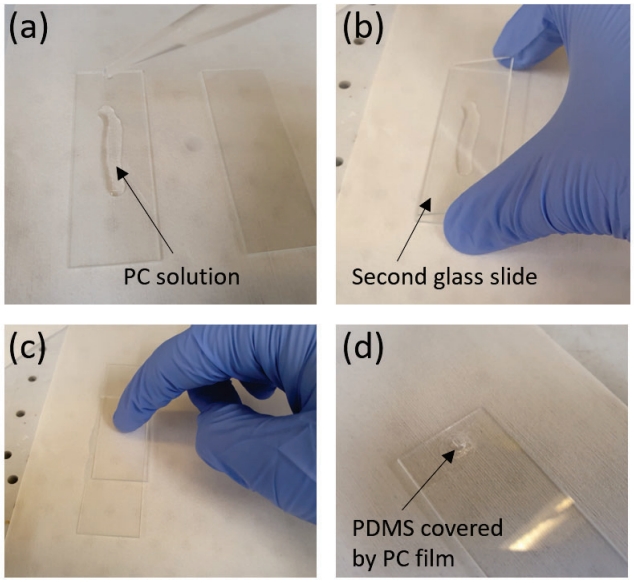

Figure 2-31: Preparation of PC slides. (a) Deposit PC solution on a clean glass slide. (b) Smear the liquid with another glass slide, ensuring no bubbles are formed. (c) Slide the two slides against each other (this can be done either along the long side of the glass slide or the short side), resulting in a thin PC film. Keep only the bottom slide. (d) Final PC slide.

as PPC. However, attempts to pick up atomically thin hBN with polymers such as PMMA, MMA and PPC have negligible success rates, based on the group's previous experience. After trying various polymers, our group found, eight years ago, that a PC film is much more effective than all those previously attempted polymers for picking up hBN monolayers. Our group also realized that PC slides are suited to pick up graphene flakes from SiO_2 substrates, thanks to the strong adhesion between the polymer and the graphene crystals upon heating the PC film. Ever since, our whole group has converged towards using PC for the vast majority of our devices. Crucially, PC film is so robust, that we can now reliably pick up thick and big flakes with a high success rate. Furthermore, it allows to execute several successive pick-up and transfer iterations without breaking apart (see Fig. 2-32). This is of extreme importance to realize complex multi-layer heterostructures [131, 137].

Polymer-assisted dry pickup and transfer technique

The PC slide is first mounted, with the PC film facing down, on the right arm of the transfer setup. The substrate with the target flake is placed on the other micromanipulator-controlled

stage, and held fixed by vacuum (Fig. 2-29).

Pickup process

The pickup process is closely monitored via the eyepiece of the optical microscope or the computer screen connected to the CCD camera. A pickup, for example, of an hBN flake, can be performed by slowly bringing close together the PC and the desired hBN crystal, until the PC and the hBN are entirely in touch (the color of the image changes from orange to green-ish as the PC and the substrate come into contact). The hBN flake is picked-up by heating the substrate to around 110 C, as the temperature increases the stickiness of the PC (Fig. 2-32a-c).

After the PC has fully retracted, the hBN flake now lies on the PC film. The PC film is robust and should remain intact on the PDMS after this procedure. This pick-up process can be repeated multiple times to build the desired vdW heterostructure, as shown in Fig. 2-32d-f [137, 131]. For certain 2D vdW materials, the van der Waals forces between them may be strong enough to stick the two crystals together during the pick-up process (*pick-and-lift* technique), without requiring additional heat. For example, hBN can be used to pick up a graphene monolayer at room temperature.

During the stacking process, we use a program that turns the foreground window semi-transparent in Windows. In particular, we can use this software to make *Inkscape* semi-transparent, to keep track of the position and orientation of all the picked-up layers. For that, the flakes of interest are traced, together with some of the relevant surrounding flakes, using the live image observed on the computer screen of the transfer setup or a contrast-tuned optical picture previously taken. This is useful for many reasons:

1. It enables to accurately control the alignment between the different flakes that are being picked up with micrometer-precision, as flakes can appear blurry during the pick-up process. Additionally, flakes already picked up may be hard to see when lying on the PC slide.

2. It is crucial to record each flake's relative position and orientation. Saving the position and orientation of the flakes is especially relevant for the design step, when the position of the hall bar, the contacts, the top gate, etc. are defined using a CAD

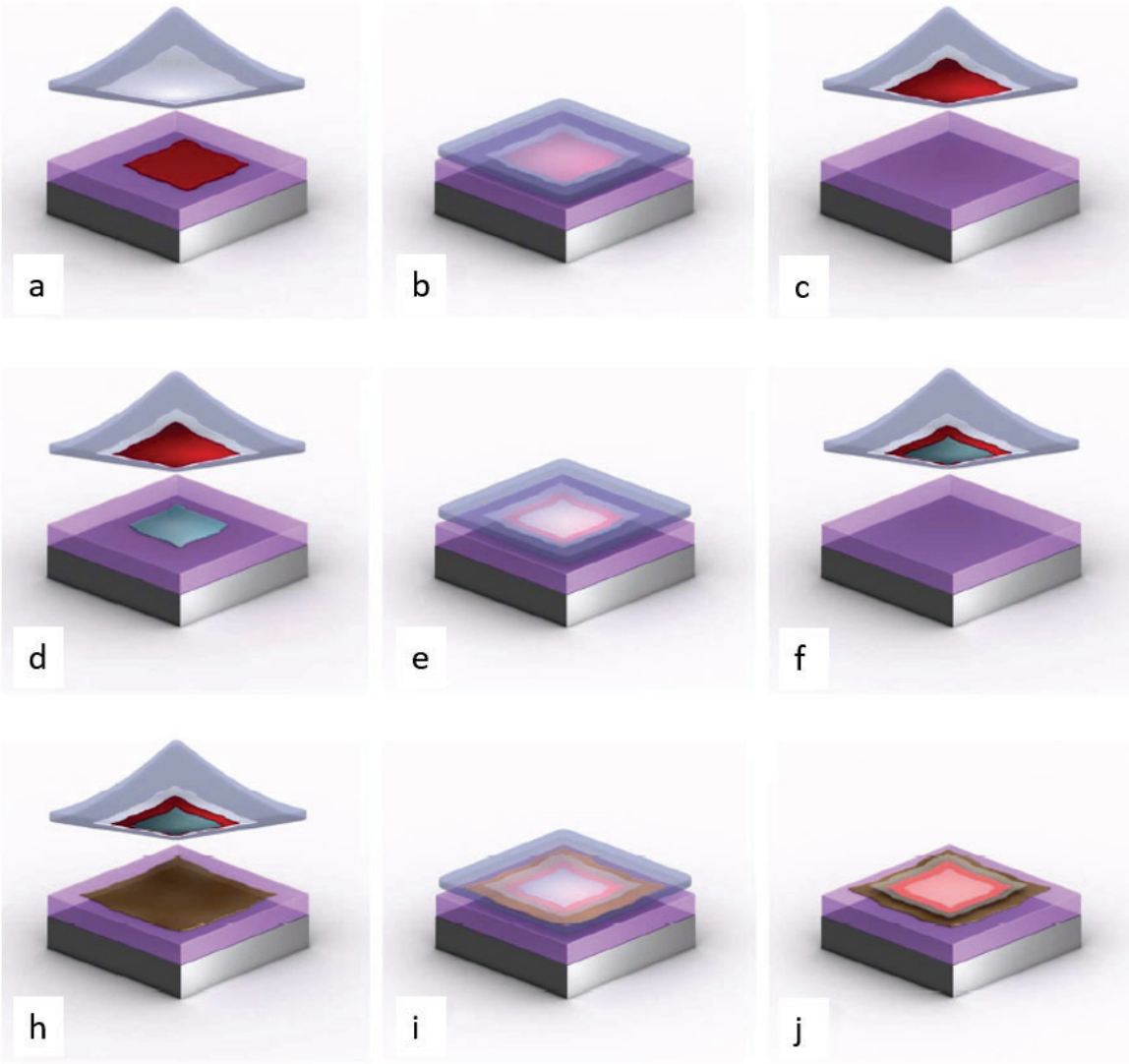

Figure 2-32: Polymer-assisted dry pickup and transfer technique: Building LEGOs with 2D materials. (a-c) The first micrometer-sized 2D crystal is picked up (see text). (d-f) The substrate with the second flake is positioned in the transfer setup, and the flake on the PC slide is aligned to the new target flake. Then, the second flake is picked up. This sequence can be repeated for as many additional flakes as desired. (h) The stack is finally softly deposited on a host substrate by melting (i) and dissolving the membrane (j). Figure adapted from ref. [7].

software. Individual flakes cannot always be traced back once the stack is finalized without having this file at hand. Together with the AFM and optical images, it is one of the must-have pieces of information for designing good devices.

Release of the stack

To release the multilayer vdW stack onto a substrate containing the host structure (usually a back gate, another flake, or a grid of markers), the same procedure as the pickup process applies until the disengagement step. To be precise, we bring the recently built vdW stack on the PC slide close to the target surface of the substrate, align them using the microscope, and engage them slowly. While the PC film and the host substrate are still in contact, we heat up the substrate to around 170 C to melt the PC. Next, the PC slide is slowly disengaged from the hot substrate. The melted PC detaches from the PDMS, and leaves the desired stack on the host substrate (Fig. 2-32i) [131, 137]. During this process, the PC film is also transferred to the substrate and must be subsequently dissolved.

Alternatively, for a final stack with fewer bubbles on average, the substrate can be first heated above the melting temperature of the PC (around 165 C) and then engaged at moderate speed [138, 139]. This is a more challenging option, since the PC cannot be detached from the substrate to correct its position in case of misalignment.

As we mentioned in Chapter 2.1, trapped hydrocarbons are typically pushed and squeezed into *bubbles*, resulting in clean interfaces between the different layers [8, 7, 17]. In my experience, releasing the stack at room temperature and then heating the chip to 170 C allows achieving few-μm-scale devices that are free from bubbles and contamination, whereas hot transfer released stacks result in much larger bubble-free samples (tens of μm-scale devices).

PC removal

The PC membrane on top of the vdW stack is removed by immersing the chip in chloroform for 5 to 45 mins, and rinsing it with isopropanol. Optionally, one can also immerse the chip in acetone for 3 minutes before the isopropanol rinse. The stack is then characterized both optically and with an AFM microscope. We show some pictures of a prototypical

stack in figure 2-36.

Additional cleaning

The dry polymer-based technique allows the surfaces of the 2D materials to be preserved in a pristine state and minimize contamination. No liquid or any wet polymer comes into contact with the cleaved surfaces during this process (see Fig. 2-32). However, the first flake picked up is unavoidably in contact with the PC. Thermal annealing in an inert atmosphere (not suitable for twisted graphene structures), or an AFM "tip clean" (see section 2.9.11), may be performed to clean the stack a posteriori.

Tear-and-stack and cut-and-stack techniques

Twisted graphene structures, such as magic-angle twisted bilayer graphene (or magic-angle twisted bilayer-bilayer graphene) stacks, need one more "twist" to be reliable: how can one control the twist angle between two graphene layers with an accuracy better than a tenth of a degree?

A rough way to "control" the angle between any two flakes is to align straight edges, which typically correspond to crystallographic axes. However, such an optical alignment can hardly be performed with an accuracy better than a few degrees. Furthermore, for graphene, one has an added uncertainty between the armchair and zig-zag edges.

The solution proposed by our group and Tutuc's group, independently, to control the twist angle between two graphene sheets is elegant and relatively simple [94, 140, 123]: start from a large graphene flake and cut it into two halves. Even though its absolute crystallographic axes are unknown, under the assumption that the original monolayer is a single crystal, the *relative* twist angle of the half monolayers can be accurately controlled with a motor rotation stage.

The procedure can be described as follows (see Fig. 2-33):

1. Pick up the top hBN (10-60nm thick approx.) following the abovementioned process. This flake needs to have a natural straight edge, which for simplicity is placed vertically as seen on the screen, and facing towards the right side of the screen (assuming the PC engages from left to right on the screen, with a vertical wavefront).

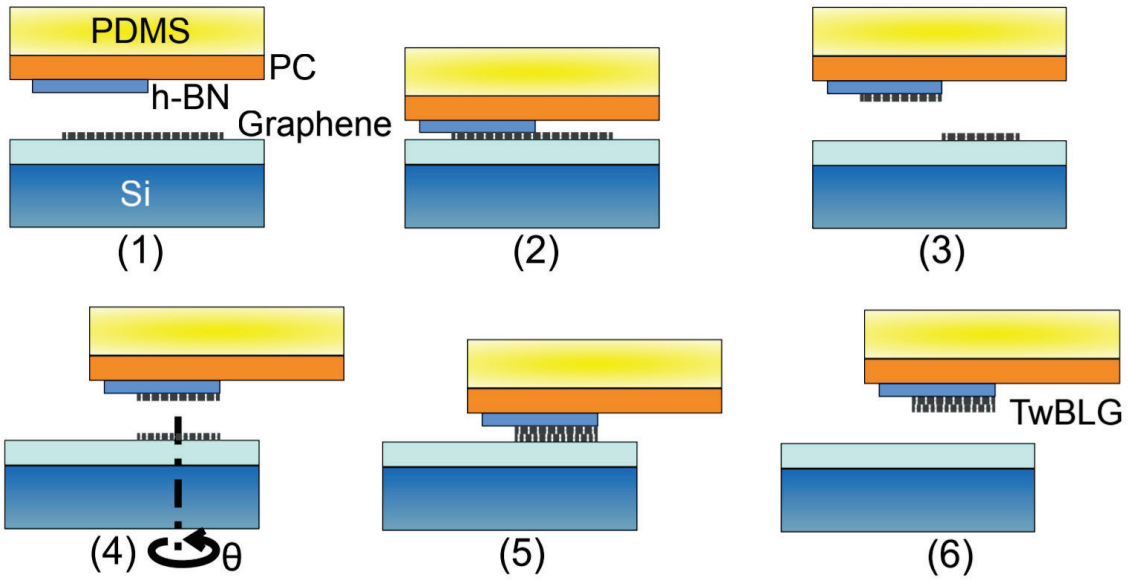

Figure 2-33: Tear-and-stack technique. (0) Not shown in the illustration: an hBN flake with a straight edge is first picked up. (1) The hBN and graphene flakes are brought into contact, aligning the straight edge of the hBN with an imaginary line dividing the graphene into two pieces of similar dimensions. (2) Only half of the graphene is contacted by the hBN; the PC wavefront is stopped at the hBN straight edge. (3) The graphene is torn apart and picked up by the hBN, at room temperature. (4) The second piece of graphene is rotated by a small twist angle close to 1.1°. (5-6) The second piece of graphene is picked up. This process results in a twisted graphene stack. Figure reproduced from reference [94].

2. Place the monolayer graphene under the microscope of the transfer setup. The line along which the graphene will be cut in two halves must be aligned with the wavefront of the PC when engaging the substrate.

3. Place the hBN halfway on top of the graphene sheet, aligning the straight edge of the hBN, which will act as a *blade*, with the imaginary (future) cut in the graphene.

4. Engage the hBN and the graphene flakes very slowly. A small electrical current that increases by a few mA per minute and heats the substrate by only a few tens of a degree every few minutes can be used for a finer control.

5. When the wavefront reaches precisely the right straight edge of the hBN, turn off the electrical current. Do not let the PC go beyond the hBN edge to keep the graphene's second half clean from polymeric residue. Disengage at the lowest possible speed

(using a motorized micromanipulator in the up-down direction).

6. During the disengagement, the left half of the graphene will adhere to the hBN, whereas the right half of the graphene will stay stuck to the substrate. The adhesion to the hBN occurs because the van der Waals forces between the hBN and the graphene are stronger than the adhesion forces between the graphene and the SiO_2 substrate [137]. This process, however, is not guaranteed to work. Only in around 50-75% of the cases, the graphene is torn apart nicely along the straight edge of the top hBN. This process can fail for many reasons: the graphene may roll up after tearing apart, it may not get fully picked up, it may break after tearing apart, the PC may not stop at the straight edge of the hBN and contaminate the second half of the graphene, etc.

7. Once the PC and the substrate are fully disengaged, rotate the substrate chip (containing the second half of the graphene) by 1.1° approximately using a precise motorized rotating stage. In the early stages of this project, we used a stepper-motor-driven rotation stage with a minimal resolution of 0.1°. Given that such motors suffer from backslash, a systematic backslash clearing had to be realized before picking up the first half of the graphene by making sure the rotator would not change the rotating direction at any point during this process. This procedure gave acceptable results, although Yuan Cao replaced it recently with a brushless DC rotating stage motor with no backslash, enabling finer control of the twist angle [86].

8. Align the hBN/graphene stack on the PC slide with the remaining half of the graphene, and engage very slowly (lowest possible speed available in the motorized z-arm) for a smooth engagement with minimal bubbles.

9. Pick up the second graphene, either by heating the substrate a few degrees above room temperature, or taking advantage of the vdW forces between the two graphene flakes.

10. Transfer the hBN/twisted bilayer graphene stack to a pre-made and cleaned back gate with hBN, following the aforementioned transfer procedure. Note: do not pick up the bottom hBN crystal after picking up the TBG. This may cause additional strain on

the graphene layers, and may result in relaxation of the stack to another configuration with a twist away from the magic angle.

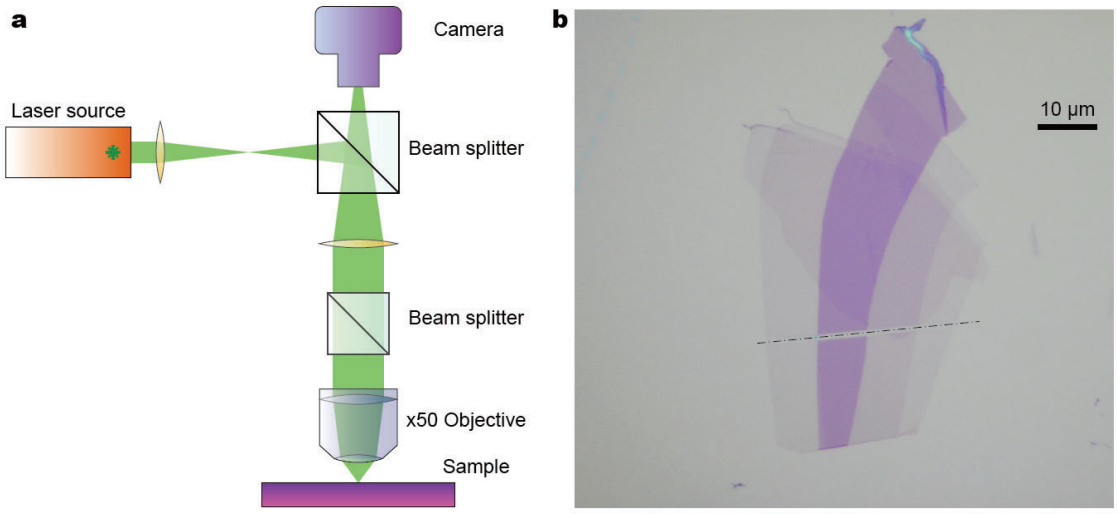

Figure 2-34: Cut-and-stack technique. (a) Setup to laser-cut the graphene, integrated in the dry-transfer setup. (b) Example of a graphene/graphite flake cut by the laser. Figure reproduced from reference [121].

The cut-and-stack technique is similar in essence to the tear-and-stack, except that the graphene is previously cut in two halves with a laser. The laser beam has a Gaussian profile with a $\sim 1\mu$m spot size and is integrated in the transfer setup (for details, see refs. [86, 121]). The laser produces a micrometer-sized sharp cut, leaves little residue on the graphene surface, and does not compromise the quality of the devices. This procedure increases the success rate compared to the tear-and-stack technique, since the graphene does not need to be torn apart to be picked up, often leading to cracks and the graphene rolling up near the torn edge. Additionally, it eases the fabrication of multiple twisted graphene layer stacks, such as twisted trilayer graphene [141, 142]. Last, it may also reduce the mechanical strain on the graphene, lattice deformations, and thus twist angle disorder that could appear during the tear-and-stack process (Fig. 2-34).

2.9.7 AFM Microscopy

Atomic Force Microscopy (AFM) is a versatile technique that helps us *see* what cannot be seen optically. While one would ideally like to have an AFM image of the device at every step, due to time limitations, and for practicality, an AFM picture is only taken after the most crucial stages of the fabrication process. AFM images are typically taken: after exfoliation to make sure a flake is clean and flat (and to determine its thickness), after the preparation of metallic back gates to certify those are of acceptable quality, after placing the bottom hBN onto the back gate (for MATBG samples), and after the vdW stack is built, to select the cleanest bubble-free regions in order to design the device in that precise area.

AFMs operate by measuring the force between a probe and the sample, and valuable information is extracted from the height, phase and amplitude. In tapping mode, which is the one used for imaging (contact mode is used for AFM brooming; see section 2.9.11), the cantilever is driven to oscillate up and down near its resonance frequency and the tip contacts the sample surface intermittently. Normally, the probe is a sharp tip that can detect vertical irregularities up to 0.1nm. Both Jing Kong's lab AFM and CMSE's AFM were used for this purpose indistinctly.

2.9.8 Electron beam lithography

Electron-beam lithography is a well-established technique in all nanofabrication facilities. It consists of scanning a focused beam of electrons in a high vacuum chamber, to pattern the surface of a chip covered with an electron-sensitive resist with a nanometric precision. The electron beam breaks the long chains of the electrosensitive resist and changes its solubility in the presence of a particular solvent, enabling the removal of only the exposed regions of the resist (for the case of a positive resist); this step is called the *development*.

E-beam lithography is a versatile technique that is used to write any type of pattern: contacts, gates, markers, etch masks, etc. Although with some nuances, the procedure is very similar for all of these cases.

For the projects presented in this thesis from Chapters 5 and onward (the previous two chapters use similar but slightly different recipes), we can distinguish two main recipes:

EBL writing for an etch mask

1. Set the hotplate to 180 C.
2. Spin Poly(methyl methacrylate) 950A5 (PMMA 950A5 from Microchem) at 500 rpm for 5 s followed by 3000 rpm for 60 s. The speed of rotation, together with the density and viscosity of the resist, determine its final thickness.
3. Bake at 180 C for 3 min.
4. Blow dry with a nitrogen gun.
5. Expose in Elionix (EBL tool, MTL/RLE/MIT.nano) with a current of 2-50 nA, depending on the dimensions of the finest feature of the pattern (dose: 1700 μC/cm^2).
6. Prepare a solution of water/isopropanol (1:3 in weight) at T = 0 C.
7. Thermalize and maintain the beaker with the IPA/water solution at 0 C (thermal bath with coexistence of water and ice).
8. Immerse the exposed chip in the cold IPA/Water solution for 30 s to develop the exposed PMMA.
9. Rinse with IPA (but not with acetone, since acetone lifts off the resist).

EBL writing for gates, markers, and contacts

1. Set the hotplate to 180 C.
2. Spin PMMA 495A5 at 500 rpm for 5 s (to spread out the resist) followed by 3000 rpm for 60 s.
3. Bake at 180 C for 3 min. Wait a few mins to cool down.
4. Blow dry with a nitrogen gun.
5. Spin PMMA 950A2 at 500 rpm for 5 s followed by 3000 rpm for 60 s. The double-layer resist layer enables an easier lift-off.

6. Bake at 180 C for 3 min.

7. Blow dry with a nitrogen gun.

8. Expose in Elionix (EBL tool, MTL/RLE/MIT.nano) with a current of 2-50nA depending on the dimensions of the finest feature of the pattern (dose: 1700 μC/cm^2).

9. Prepare a solution of water/isopropanol (1:3 in weight) at 0 C.

10. Thermalize and maintain the beaker with the IPA/water solution at 0 C.

11. Immerse in the cold IPA/water solution for 2 mins to develop the PMMA (or 2:30 mins for back gates writings to remove all exposed resist fully).

12. Rinse with IPA.

Often, the writing of the design must be performed at a precise location. This spatial constriction requires the presence of a reference coordinate system pre-printed on the substrate. For this purpose, pre-fabricated e-beam markers can be used as a reference, i.e., a grid of markers covering selected chip regions to establish labeled reference points. These are used to determine, with a sub micrometric precision, the exact position where the patterns must be written.

Clean room processing

After the lithographic writing and development, the sample is taken to the reactive ion etcher (for 1D contacts and general etchings), or an evaporator chamber (for metallic gates and other markers).

In summary, I here list the electron beam lithography writings required in a prototypical MATBG sample fabrication process:

1. Back gate and markers (followed by a Cr/PdAu evaporation)

2. Broad etching mask (followed by an etching to minimize relaxation of the MATBG during subsequent steps)

3. Contacts (followed by an etching and a Cr/Au evaporation)

4. Top gate (followed by a Cr/Au evaporation)

5. Final etching (followed by an etching to define the final shape of the device, generally a hall bar)

Lift-off

Finally, a lift-off in solvent removes the unexposed resist and excess material on top of it, leaving only the desired structures on the device. For that, the sample is left in a covered beaker with acetone for several hours, and then rinsed with IPA and blow-dried with nitrogen.

For the lift-off of small features concentrated around the same area, such as contacts, it is recommended to check under the microscope that all the unwanted metallic residues have been removed before drying up the chip.

The primary advantage of electron-beam lithography compared to photolithography is that it can pattern custom designs with a sub-10 nm resolution, whereas the resolution of photolithography is limited by the wavelength of light. Only e-beam lithography has been used in the projects presented in this thesis.

2.9.9 Reactive ion etching

Reactive ion etching (RIE) is a directional and high-resolution etching process, heavily used during the nanofabrication of the devices presented in this thesis to: (1) etch single 2D materials, (2) etch stacks of different vdW materials, and (3) to make electrical contacts to encapsulated graphene. All the recipes presented below have been tested at the Center for Nanoscale Systems (Harvard) for the tool *RIE-8*.

During the RIE process, the substrate is exposed to reactive gas discharges to remove a specific deposited material. The gases required to etch a particular structure, and the etching rates, are material-dependent.

As I described in the previous section, before the samples are taken to RIE-8 at Harvard, they are first masked with PMMA resist, exposed to electron-beam lithography to define the pattern to be etched, and developed in a cold solution of IPA/water.

Reactive ion etching recipe for hBN

1. Pre-clean the chamber for 20 mins with aggressive O_2 plasma.
2. Pre-condition the chamber by running the recipe described below for 3 mins without the substrate.
3. Load the sample in the vacuum chamber.
4. Expose to a mixture of Ar (10 sccm), CHF_3 (10 sccm), and O_2 (5 sccm) for 20-60 seconds (repeat for longer times if needed). The etching rate is non-linear and varies substantially from one day to another. On a normal day, a 30-seconds etching time typically removes between 10 nm and 40nm of hBN.

Reactive ion etching recipe for graphite

1. Pre-clean the chamber for 20 mins with aggressive O_2 plasma.
2. Load the sample in the vacuum chamber.
3. Expose to reactive oxygen plasma for 40 seconds. Repeat for another 40 seconds if needed. This is typically enough to etch $\sim$10 nm-thick graphite flakes.

Reactive ion etching recipe for hBN/graphene/hBN stacks (includes MATBG and TBBG stacks)

This recipe combines the previous two reactive ion etching recipes for hBN and graphite.

1. Pre-clean the chamber for 20 mins with aggressive O_2 plasma.
2. Pre-condition the chamber by running the recipe described below for 3 mins without the substrate.
3. Load the sample in the vacuum chamber.
4. Expose to a mixture of Ar (10 sccm), CHF_3 (10 sccm), and O_2 (5 sccm) for 100 seconds. This recipe mostly etches the hBN, although it also etches the thin graphene

at a much lower rate. Check under the optical microscope that the stack is fully etched. Repeat, if needed, in intervals of 30 seconds.

5. Expose to reactive oxygen plasma for 30-45 seconds to etch graphene/graphite residues that might short the contacts (for example, from graphene that rolled up during the tear-and-stack process, or other nearby graphite flakes that might have been deposited).

Reactive ion etching recipe for 1D contacts

1. Pre-clean the chamber for 20 mins with aggressive O_2 plasma.

2. Pre-condition the chamber by running the recipe described below for 3 mins without the substrate.

3. Load the sample in the vacuum chamber.

4. Expose to a mixture of Ar (10 sccm), CHF_3 (10 sccm), and O_2 (5 sccm) for 100 seconds. Check under the optical microscope that the contacts are fully etched. Load the sample in the evaporator chamber immediately.

In most of our twisted bilayer devices (see, for example, upper left panel in Fig. 2-35), the contact electrodes are located outside of the metallic back gate to avoid a possible short between the contacts and the gate. This creates a $\sim 1\mu$m-long region where the electrical connection from the gold contacts to the core of the hall bar is ensured by ungated MATBG. This region becomes insulating at high magnetic fields, and may affect the transport data in such regimes. While this is typically acceptable in most of the experiments presented in this thesis, there are several techniques that can be used to work around it if needed:

- Use p-doped silicon substrates instead of high-resist SiO_2 when evaporating the metallic back gate electrodes. The SiO_2 can then be used as a global gate to dope that $\sim 1\mu$m-region. Bonding needs to be performed carefully to not punch through the SiO_2.

- If the gold contacts MUST be located on top of the metallic back gate (see for example Chapter 4), the previous recipe for 1D contacts can be adapted to etch partially through the stack carefully. For that, one needs to etch carefully beyond the top hBN and the graphene, but minimally etch the bottom hBN to not short the contacts to the gate:

    1. Use a very thick bottom hBN. If the resulting hBN thickness after etching is not large enough, leakage issues may arise.
    2. Measure, before stacking, the exact thickness of the top and the bottom hBN dielectric layers.
    3. Perform a calibration test with the same exact etching conditions (to be performed on the same day as the sample etching): (a) Prepare a calibration sample for hBN etching. For that, take a chip with exfoliated hBN crystals and pre-write with e-beam lithography a grid of few-μm-wide stripes separated by a few tens of μm from each other. (b) Etch this calibration hBN sample for around 30-45 seconds. (c) Lift-off in acetone. (d) Measure under AFM the amount of etched hBN (for example, a thick flake will have a stripe of partially etched hBN). (e) Repeat until the etching time needed to fully etch the top hBN (without over-etching the bottom hBN) is accurately determined. (f) Etch the actual sample following the recipe described above for 1D contacts.

- Denis Bandurin developed a recipe to make selective planar "quasi-2D" contacts for fully encapsulated graphene samples. The recipe is detailed in the section below.

Reactive ion etching recipe for planar contacts

Denis Bandurin, now a Professor in Singapore, developed a technique to only etch the top hBN flake and selectively stop the etching at the graphene in an hBN-TBG-hBN stack. The graphene is contacted via a "quasi-2D contact" in a subsequent evaporation. Note: not everyone in our group has had successful results using this recipe.

1. Pre-clean the chamber for 20 mins with aggressive O_2 plasma.

2. Load the sample in the vacuum chamber.

3. Expose to a "gentle" O_2 plasma (lower flow than the O_2 plasma recipe used for the pre-cleaning of the chamber) for 20 seconds to remove PMMA residues that may alter the subsequent selective etching.

4. Expose to a mixture of CHF_3 (20 sccm) and O_2 (10 sccm) for 10-13 seconds. This should be enough time to etch the top hBN flake but not the graphene layers. Check with optical microscopy that the top hBN is fully etched. Proceed to evaporation. Note: It is recommended to pattern, during the same lithography process as the contacts exposure, a polygon enclosing a region with only top hBN. This is used to ensure that the top hBN is fully etched after the etching process.

2.9.10 Thermal evaporation and 1D contacts

Thermal evaporation is used to evaporate contacts, the back gate, and the top gate, after the corresponding e-beam writings. In the remaining of this section, we will focus on the evaporation of 1D edge contacts (any other thermal evaporation requires only a subset of the steps described below).

The transfer method described in Fig. 2-32 has a nuance worth noticing: if the inner layer is fully encapsulated, making contacts to it becomes, to some extent, a challenge. In order to contact the MATBG, gold contacts are evaporated with a pioneering technique established by Cory Dean and coworkers in 2013 [143]. This procedure permits contacting the MATBG from the side, while the material under study remains encapsulated and protected against exposure to solvents and contaminants during the whole fabrication process.

To achieve such contacts, a reactive ion etching (see recipe in the previous section) is followed by a thermal evaporation at the Center for Nanoscale Systems (Harvard). By performing a reactive plasma etching, the graphene edges become exposed and can be contacted via metallic evaporation using a rotating stage at a tilted angle. This procedure typically ensures a high success rate of good contacts with a contact resistance of a few tenths or hundreds of Ohms per micron.

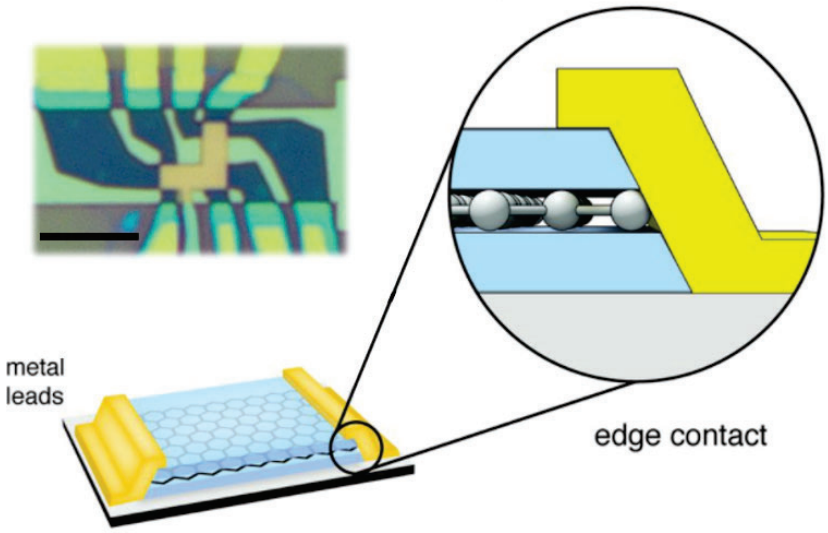

Figure 2-35: 1D edge contacts to graphene and twisted graphene stacks. Bottom and Right: Schematic of a 1D Cr/Au contact to a monolayer graphene. Upper left: Optical picture of a MATBG device (same sample as described in Fig. 2-36 and in Fig. 6-3). The yellow leads are the gold contacts to the MATBG. The scale bar is 5 microns. Figure adapted from reference [143].

The working principle of a thermal evaporator is straightforward: gold precursor pellets are thermally melted via the application of large currents. A high vacuum atmosphere allows the metallic particles to travel directly to the target object (the substrate), where they condense back to a solid state, forming a thin layer on top of our sample. The substrate is continuously rotated with a $\sim$15-degree tilt during the evaporation process to ensure a uniform contact between the exposed graphene edges and the Cr/Au metal (or Ti/Al for the samples presented in Chapter 4).

A general recipe to make reliable 1D contacts can be summarized as follows (optimized for tools *TE-3* and *TE-4* at the Harvard Center for Nanoscale Systems):

1. Perform a CHF_3/Ar/O_2 reactive ion etching to expose the graphene edges (see recipe in previous section).

2. Immediately load the substrate in the evaporator chamber and pump down until the pressure is in the 10^{-7} torr range. Use a rotating holder.

3. Manually rotate the sample; keep doing so during the whole evaporation process.

4. Evaporate 2 nanometers of chromium at 0.1 - 0.2 angstrom per second (sticking layer).

5. Evaporate between 20 and 90 nanometers of gold at 0.5 angstrom per second. The gold layer should be at least a few nanometers thicker than the thickness of the bottom hBN. Note: In Chapter 4, Ti/Al is used instead of Cr/Au to make the 1D contacts.

6. Bring the sample back to MIT. Lift-off using acetone at room temperature for several hours. Do not dry the sample until all the spurious pieces of metal in the device's proximity have been removed. Check under an optical microscope, with the sample in liquid, to ensure this is the case. If any metallic piece remains and shorts to the contacts, it is much harder to remove after the chip has been dried.

The evaporation of the top gates follows the same procedure, except that a rotating evaporation is not required. For the back gates, we typically use an alloy of Pd/Au (60/40). We note that highly doped silicon (the easiest and less reliable option from a fabrication point of view) and graphite flakes (believed to produce the highest quality devices) could also be used as electrostatic gating materials. We used 5-8 μm-wide Pd/Au metallic back gates as a compromise between fabrication easiness and device quality, as they offer clean and flat metallic gates and have consistently enabled us to fabricate high-quality twisted graphene devices. These metallic gates also help with the screening of the charged impurities present in the SiO_2 substrate, as explained in Chapter 2.9.1.

2.9.11 Additional cleaning of samples: AFM brooming

Post fabrication treatment is typically required to remove the polymeric residue left by the e-beam resist, especially during the markers and back gate evaporations. For markers and gates, standard cleanings are a three minutes oxygen plasma exposure and a heat cleaning, respectively (as explained in sections 2.9.2 and 2.9.3).

If these cleaning techniques fail, or for more delicate structures that cannot undergo the previous processes such as finalized stacks, an *AFM brooming* to mechanically sweep the residues off the surface of the device [144, 145] can be performed. For that, a contact-mode AFM tip is scanned over the sample (typically at least two or more times), exerting

a constant force on the tip. This process is slow and tedious, but it is usually effective if the sample has a few contaminants that cannot be removed using a thermal annealing or an oxygen plasma exposure.

2.9.12 Fabrication of an archetypal device combining the previous techniques

To illustrate how the previous techniques come together, we describe the fabrication steps for our devices in Chapter 5.

Description of the devices

Our devices comprise a 4-layer van der Waals heterostructure placed in between two metallic gates, as illustrated in Fig. 5-1a and Fig. 5-4a. From bottom to top, they all have a gold/palladium (60/40) back gate, a bottom hexagonal boron nitride substrate (hBN), MATBG, a top hBN, and a gold top gate. Device A: bottom hBN 28 nm, top hBN 25 nm. Device B: bottom hBN 55 nm, top hBN 26 nm. Device C: bottom hBN 50 nm, top hBN 50 nm. Device A has a narrow top gate, while devices B and C have two top gates separated by a narrow gap.

Exfoliation and stacking

All the two-dimensional materials are obtained via mechanical exfoliation on a SiO_2/Si chip, and high-quality flakes are carefully selected using optical microscopy and atomic force microscopy. First, $\sim$30 nm-thick back gates are patterned with e-beam lithography and thermal evaporation of Cr and Pd/Au. Heat annealing in forming gas (H_2/Ar) is employed to clean the gates. All gates are first inspected optically and then via AFM to confirm their thickness, guarantee they do not show traces of organic residues, and check they are flat without visible inhomogeneities. After that, a bottom hBN flake is placed on top of each local metallic gate, and heat annealed again to remove possible residues from the removal of polymer. An AFM "tip cleaning" [144, 145] can be optionally performed to "broom" the remaining polymer residues off the hBN.

The vdW heterostructure is assembled via a modified polymer-based dry pick up and transfer technique. A poly(bisphenol A carbonate) (PC) thin film (Fluka Analytical, part number 181641) covering a polydimethylsiloxane (PDMS) 2 mm x 2 mm piece, lying on a glass slide and mounted on a custom-made micropositioning stage, is used to successively pick up the topmost hBN and the graphene sheets with high success rates. The hBN flake is picked up by heating the substrate in contact with the PC film up to 110°C. Graphene is torn in half at room temperature by the vdW forces between the hBN and the region of the graphene flake in contact with the hBN. The remaining half of the graphene is rotated to an angle close to 1.1° and then picked up. The full stack is then released onto the previously prepared bottom hBN on a metallic back gate, by melting the PC at 170°C. Finally, the PC film is dissolved in a chloroform bath for 5 minutes.

Design of the device geometry

The device geometry is designed using a CAD software, based on the optical and AFM micrographs of the stack (Fig. 2-36c), keeping only the cleanest and bubble-free parts of the twisted bilayer region.

Clean room processing

The first step of fabrication is an etching step in order to minimize relaxation of the graphene layers during subsequent steps. The etch mask is electron-beam lithographically defined via Poly(methyl methacrylate) (PMMA 950A5 from Microchem). The geometry of this etch mask is larger than the actual final device, but must lie (at least partially) on the inner part of the two graphene layers, while leaving a path for the top gate.

Then the device is again patterned by electron-beam lithography (double-layer resist PMMA 495A5/ PMMA 950A2) to define the edge contacts. Following another reactive ion etching, the device is mounted on a tilted rotating stage and edge-contacted by thermally evaporated chromium/gold (2 nm and around 65 nm$\sim$90 nm, respectively)[143]. Liftoff is performed in acetone for several hours at room temperature (Fig. 2-36e). To define the narrow top gate (for device A showed in Chapter 5) ($\sim$160 nm wide and 25 nm thick), or two top gates (for devices B and C), one more electron beam lithography, thermal evapo-

ration, and liftoff steps are needed (Fig. 2-36f). Finally, the device geometry is defined via reactive ion etching with PMMA etch mask similar to the one described above, followed by an oxygen plasma etching to remove possible graphene or graphite residues shorting the contacts. We illustrate in Fig. 2-36 the fabrication sequence for device A as a paradigmatic example of one of our top gated devices.

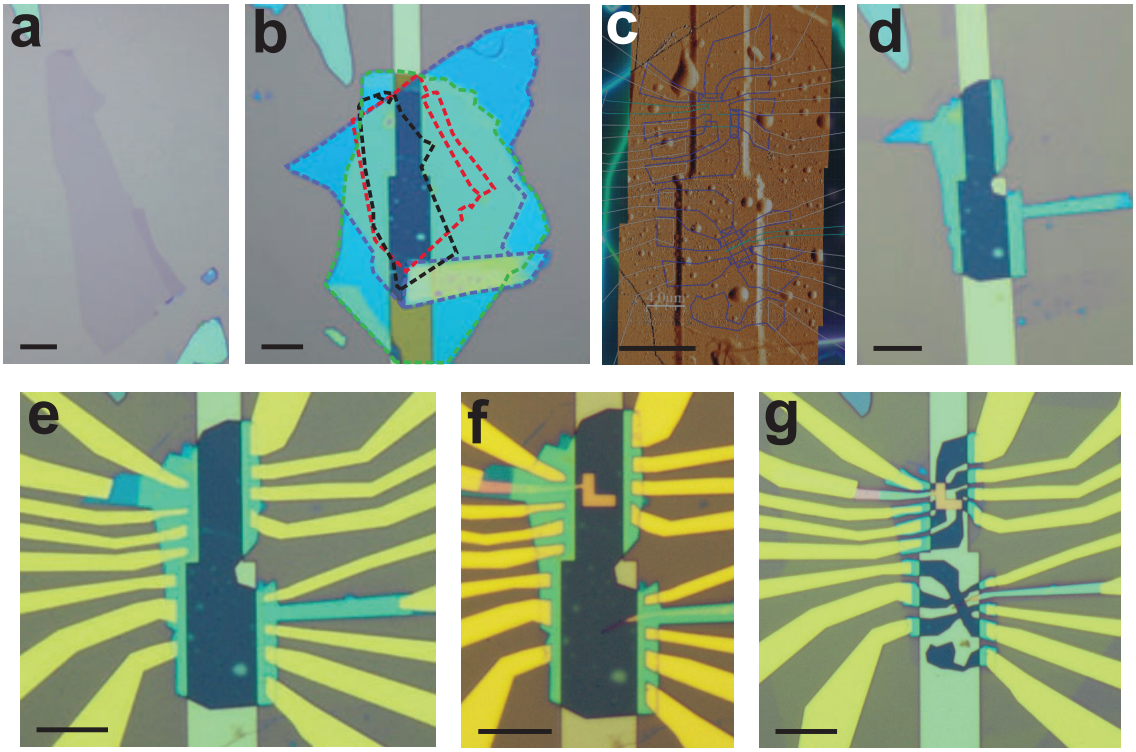

Figure 2-36: Fabrication steps of a prototypical device (device A, measured in Chapter 5). (a) Optical image of the graphene flake. (b) Resulting stack (blue line indicates the top hBN, green line the bottom hBN, red line the original graphene (but after tearing apart) and black line the second piece of graphene). (c) Design of the stack, based on optical images and AFM amplitude images. (d) Stack after the first broad etching. (e) Optical image after evaporation of the contacts. (f) Optical micrograph after evaporation of the top gate. The finalized image is shown in panel (g). Device A is the lower hall-bar device. The upper device has an L-shaped top gate, and is reported in Chapter 6. All scale bars are 8 microns.

2.10 Device measurement

2.10.1 Low temperature transport measurements of the MATBG devices

After mounting a finalized device on a chip carrier and wire-bonding it, the transport device is measured in vacuum, in one of our cryogenic setups (*triple-axis dilution refrigerator*, *cryo-free dilution refrigerator*, *He^3 fridge* or *4K He^4 fridge*), with base temperatures ranging between 70 mK to 4 K. Most of the transport studies presented in this thesis have been performed in the triple-axis *vector magnet* dilution refrigerator or the cryo-free dilution refrigerator. Both of them are ^{3}He/^{4}He dilution refrigerators, which utilize the unique properties of ^{3}He/^{4}He mixtures to achieve cooling down to a few tens of millikelvins [146].

Both the cryo-free dilution refrigerator and the triple-axis dilution refrigerator have low-pass RC filters installed to reduce the high-frequency thermal noise carried by the sample wires.This filtering is crucial to thermalize the sample at milli-kelvin temperatures effectively, and of outermost importance to measure some of the phenomena presented in this thesis (see refs. [131, 86] for the details on the filtering in each of the systems).

All transport data are acquired using standard low-frequency lock-in techniques. Both the current flowing through the sample and the four-probe voltages (see Fig. 2-25) are amplified during measurements using a current pre-amplifier and a voltage pre-amplifier, respectively, and then measured using different SR-830 lock-in amplifiers that are all synchronized to a frequency of 1 Hz $\sim$ 20 Hz. The sample resistance is obtained by dividing the four-probe voltage V_{xx} by the current flowing through the sample I (excitation current $I_{ac} \approx 1$ nA).

Around 50% of the measured devices fabricated following this procedure displayed correlated insulating states at half-filling and superconductivity. For the other devices that *failed*, several causes may be attributed to a non-magic behavior: the twist angle deviated from the *magic-angle* ($\theta \approx 1.1^\circ$) and displayed transport signatures characteristic of lower or larger twist angle devices, the gates leaked at low voltage, or the edge contacts had a too-large contact resistance.

2.10.2 Twist angle extraction

Superlattice density, unit cell area, and moiré wavelength

An accurate determination of the twist angle is crucial to studying MATBG physics. Slight variations in twist angle may lead to dramatic consequences in the electronic and optics behavior of the system. The first step is to determine the superlattice density, or the unit-cell area, both of them directly related to the twist angle.

In particular, from the deduced density of the full-filling states $n = \pm n_s$, the unit cell area $A = 4/n$ can be deduced. The unit cell area is related to the moiré wavelenght via the expression $A = (\sqrt{3}/2)\lambda_m^2$, and the moiré pediod is related to the twist angle by $\lambda_m = a/(2\sin(\theta/2))$, where $a = 0.246$ nm is the lattice constant of graphene [94] (see refs. [74, 86] for a derivation of this expression). For small twist angles close to the magic angle, Taylor-expanding to first order, the following expression applies:

$$n_s = 4/A \approx 8\theta^2/(\sqrt{3}a^2).$$

Therefore, the twist angle is deduced either from estimating the superlattice densities $\pm n_s$ associated with the single-particle band gaps (in transport), or by directly measuring the unit cell area (STM experiments).

Method 1: Twist angle determination at zero magnetic field

The first method to determine the twist angle, and probably the less precise one, is to convert the gate voltage to a density via a parallel-plate capacitor expression without an externally applied magnetic field. We use the expression $n = CV_{gate}/e$, with the capacitance given by $C = \epsilon\epsilon_0/t$ (where t is the thickness of the bottom hBN, ϵ the dielectric constant, e the electron charge, C the gate capacitance per unit area, and V_{gate} the gate voltage), and take n_s to be the value at the center of the insulating state at zero magnetic field. In some cases, $n_s/2$ might be more accurately determined, from which n_s can be inferred. Uncertainties in the thickness of the hBN crystal, the dielectric constant, and an inaccurate determination of the *center* of the insulating state may all lead to significant errors up to a

few tenths of a degree.

Method 2: Twist angle determination using magnetotransport data

The previous method is not very accurate, and can be complemented with the transport data in a perpendicular magnetic field to refine the twist angle determination. This second method relies on the fact that the charge neutrality point, and the band edges of the single-particle superlattice bands (and also the correlated states) have their own Landau fans.

By applying a magnetic field, the value of n_s and sub-multiples of n_s can be more accurately established by determining the precise density from which the Landau fans emanate (extrapolating the Landau levels to zero magnetic field). Effectively, the slope of the Landau levels is given by the Wannier diagram, $n = \nu' B/\phi_0$ ($\phi_0 = h/e$ is the non-superconducting magnetic flux quantum and ν' should not be confused with the filling factor $\nu \in [-4, 4]$ proportional to the MATBG density), with filling factor $\nu' = \pm 4, 8, 12, ...$ at the charge neutrality point (the four-fold degeneracy is due to spin and valley), $\nu' = \pm 4, 8, 12, ...$ for the fan resulting from electron- or hole-like quasiparticles at $n = \pm n_s$, and $\nu' = \pm 2, 4, 6, ...$ at $n = \pm n_s/2$ [83]. We refer to Chapter 8 and Fig. 2-37 for the predicted Landau fan sequence from the Dirac revivals model.

In addition, since the capacitance value is used to convert from gate voltages to carrier densities, the scaling factor of the whole Landau fan crucially depends on the capacitance. Thus, by fitting the slope of the Landau fans to the expressions above, the capacitance can be precisely extracted. Contrary to the first method, in this second method, only the ratio of the dielectric constant to the hBN thickness becomes relevant, irrespective of their independent values; the slope of the Landau fans directly gives this ratio.

Using this method, the steps to determine the twist angle are:

1. Correct for the shift in gate voltage at charge neutrality from which the main Landau fan emanates.

2. Extract the capacitance by fitting the Landau level slopes at the charge neutrality.

3. Determine the value of n_s from which the satellite Landau levels emanate ($n_s/2$ states can also be used).

4. Fine-tune the capacitance value by adjusting the Landau levels away from the charge neutrality.

5. Iterate until the fits match the data. Then, n_s can be accurately extracted, from which the twist angle is deduced.

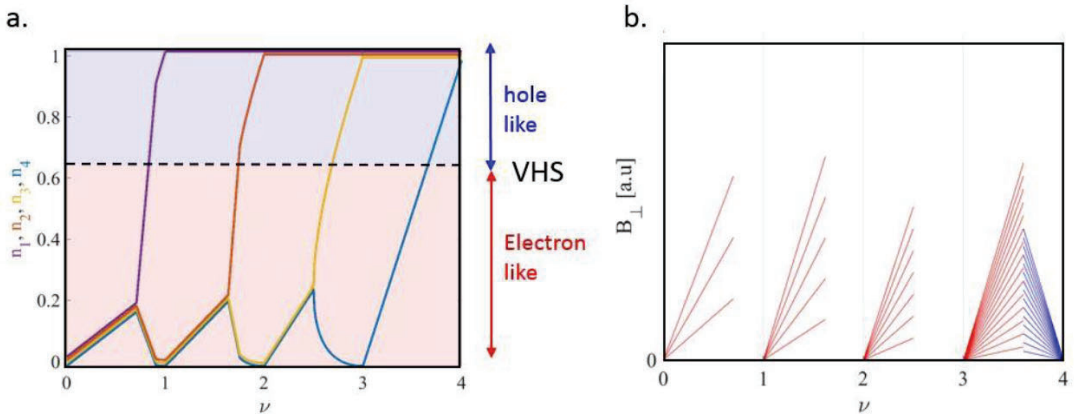

Figure 2-37: Predicted landau fan degeneracies and polarities from the Dirac revival model. (a) Partial flavor occupation of the bands as a function of filling factor, from the model of Dirac revivals. As $\nu = 1$ is approached, one band takes all the carriers resetting the other three bands back to near the charge neutrality point (CNP). Consequently, just after $\nu = 1$, the flavor degeneracy reduces to 3-fold. The process repeats at $\nu = 2$ and 3, leading to 2-fold and 1-fold degeneracies just after these filling factors. (b) Landau fans predicted from the Dirac revivals model, with a 4,3,2,1-fold degeneracy after $\nu = 0, 1, 2, 3$. The directionality of the Landau fans depend on the polarity of the carriers. The Dirac revivals model suggests that after every integer ν, the bands start refilling from the bottom of the conduction band (the CNP), but never make it to the van Hove singularity (VHS), because they are always reset back before reaching the VHS. Thus, the carriers always retain an electronic character (red lines), explaining why the Landau fans always point away from the CNP for $\nu = 0 - 3$. In contrast, the last band to fill, between $\nu = 3$ to 4, continuously fills from its bottom to its top and therefore has to cross the VHS at a certain point. Thus it starts with an electron character and ends with a hole character. Consequently, the Landau fans emerging from $\nu = 3$ will point away from the CNP, whereas those emerging from $\nu = 4$ should point toward the CNP. Analogously for the valence band, with a mirror-symmetric behavior around the CNP. We note that this model does not accurately predict the degeneracy of the fan emanating from $\nu = 4$ [94, 79, 83]. This model predicts that the hole-like Landau fan emerging from $\nu = 4$ should have 1- fold degeneracy, although experiments see a 4-fold hole-like fan. This discrepancy highlights that close to full filling of the flat bands, the flavor symmetry breaking should disappear. For additional details, see Chapter 8 and the SI section of reference [111].

In summary, fitting the Landau levels to the Wannier diagram makes it possible to

accurately determine the twist angle up to a few hundredths of a degree.

Method 3: Brown-Zak oscillations

A complementary method, which also involves applying a large magnetic field, can be used to cross-check the extracted twist angle. Since in the Wannier model, Landau levels intersect when $1/B = qA/\phi_0$ [79, 147], where q is another integer, Landau level crossings are seen with a 1/B periodicity (Brown-Zak oscillations). From this periodicity, the unit cell area can be extracted [79, 147].

Hall density

Last, we note that the value of the density extracted using the previous methods can be cross-checked with the hall density $n_{Hall} = B/(-eR_{xy})$ (as performed for example in the SI of reference [148]).

Landau fan diagrams of three different devices

We use the magnetotransport data to determine the twist angle of three archetypal twisted graphene devices. Without loss of generality, we show the Landau fans of devices A, B, and C measured in Chapter 5 (Fig. 2-38). The errors in the angle can be estimated by visually inspecting how well the Landau levels at the Dirac point, $\pm n_s/2$, and $\pm n_s$ fit to the expected Landau fans of a given twist angle (fits to the Wannier diagram are not shown here for clarity). From the analysis of the magnetotransport data following the procedure described previously, we conclude that device A has an estimated twist angle of 0.95° ± 0.02, device B has a twist angle 1.2° ± 0.05, and device C has a twist angle 0.98° ± 0.02. Additional examples of twist angle determinations following the procedures here described abound in the literature [79, 83, 94, 148, 122].

2.11 Scanning techniques

Our research group's expertise lies in transport measurements of nanodevices. Transport characterization is a versatile and relatively fast technique to gain direct access to a material's electronic properties. However, transport studies only probe the physical properties

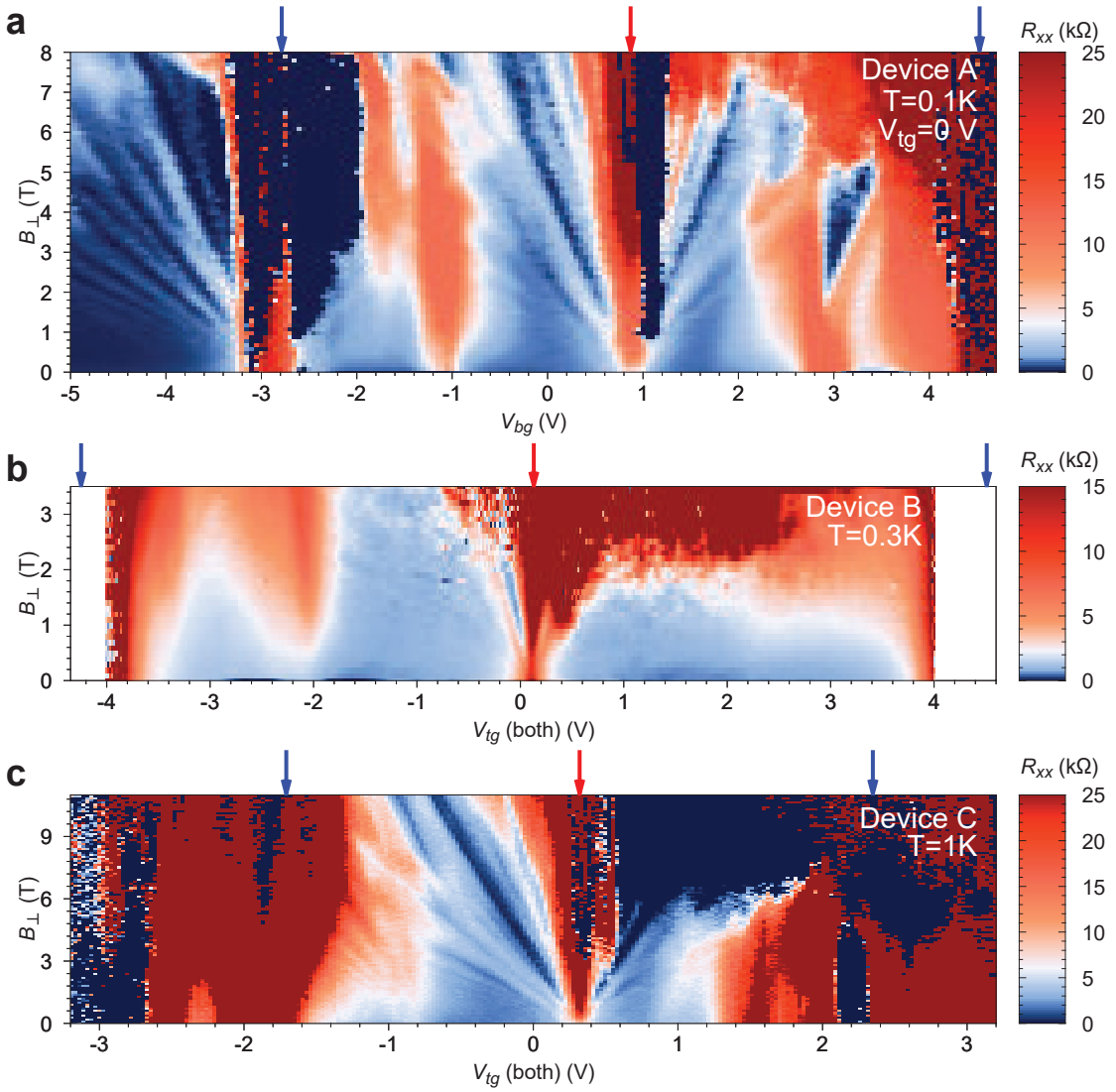

Figure 2-38: Landau fan diagrams of three prototypical samples: devices A, B and C (measured in Chapter 5). (a) Resistance vs. back gate voltage and perpendicular magnetic field with no top gate voltage applied, at base temperature for device A. (b) Resistance vs. top gates voltages (both connected together) and perpendicular magnetic field at 0.3 K, for device B. The back gate voltage is swept simultaneously to the top gates from –4 V to 5 V for each line. (c) Resistance vs. top gates voltages (both connected together) for device C, with top gates both swept from –3.2 V to 3.2 V and simultaneously back gate swept from –8.8 V to 8.1 V at 1 K. Red arrows denote the position of the charge neutrality point for each device, and the blue arrows denote the extracted position of $n = \pm n_s$.

at a global scale, and potentially miss some of the details at sub-micrometric scales.

For instance, a sample only shows superconductivity in transport measurements if a superconducting percolating path exists between the two R_{xx} electrodes. Otherwise, if magic

angle regions do not form a continuous path between the electrodes, superconductivity cannot be measured. Similarly, the magnitude of the correlated gaps is likely reduced and smeared out in transport measurements.

As we discussed in section 2.8.10, the twist angle in TBG structures is not homogeneous, and can display considerable local variations of up to 0.1 degrees. Transport measurements, on the contrary, only probe spatially-averaged twist angles, missing the local twist angle inhomogeneities and relaxations that arise in such devices. Scanning tools, such as STM, scanning-squid, scanning SET, s-SNOM, etc., are thus complementary tools to study the physics of these devices in non-disordered regions at scales comparable to the moiré wavelength, which are not accessible in transport experiments.

During my PhD, I have had the opportunity to collaborate with several research groups that mapped out our MATBG devices with state-of-the-art scanning tools. Together, we studied the physical properties of TBG at the nanometric scale, and *visualized* what cannot be seen using transport measurements. In particular, I collaborated with the group of Eli Zeldov (ref. [56]), who has a home-built nanoscale on-tip scanning superconducting quantum interference device, the group of Shahal Ilani (see Chapter 8), and the group of Frank Koppens (see Chapter 9). Below, I review the experimental techniques presented in Chapters 8 and 9.

2.11.1 Scanning SET

In Chapter 8, in collaboration with the group of Shahal Ilani, we image the local inverse compressibility of TBG with a nanotube-based scanning single electron transistor (SET) [111]. This unconventional and unique scanning tool is capable of imaging electrostatic signals with an unprecedented energy resolution, and a nanometric spatial resolution [149]. The scanning SET is a non-invasive and non-contact local detector, that does not involve charge transfer (compared, for example, to STM).

A semiconducting carbon nanotube is suspended over a gate electrode, and connected at the end of a scanning probe cantilever to source and drain electrodes separated by 800 nm (see Fig. 2-39). When cooled down to cryogenic temperatures, it is possible to form

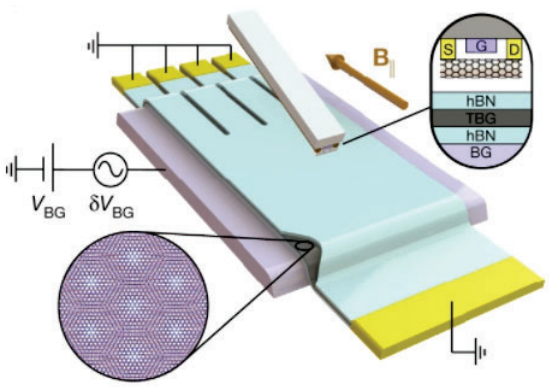

Figure 2-39: Illustration of the scanning SET experiment presented in Chapter 8 [111].

a quantum dot in the suspended segment of the nanotube using the local gate. The quantum dot is separated by two p–n junction barriers from the hole-doped segments near the contacts.

The system exhibits Coulomb Blockage oscillations in a SET-like fashion (similar to Fig. 5-5) as a function of the induced charge. The SET current, governed by the Coulomb blockade effect, thus sensitively depends on the electric field that the dot experiences from the sample's surface under study. By measuring this current, it is possible to resolve tiny fractions of the electron charge. The local electrostatic potential landscape of the sample under study can therefore be obtained by scanning the SET along the surface while monitoring the SET current [150, 149]. In particular, in the experiment presented in Chapter 8, we are interested in the inverse compressibility (and chemical potential) of twisted bilayer graphene. The explanation below closely follows reference [111].

To measure the inverse compressibility of the TBG, two AC excitations at different acoustic frequencies are applied to the back gate (BG) (δV_{BG}) and to the TBG (δV_{TBG}). The inverse compressibility is then obtained from the ratio of the measured SET current response at these corresponding frequencies, as explained below.

In our experiment presented in Chapter 8, keeping the TBG grounded, the SET monitors the local electrostatic potential modulation above the TBG in response to a back-gate voltage modulation δn, produced by an a.c. voltage on the back-gate, $\delta V_{BG} = 25$ mV, at an acoustic tone f_{BG} (in the range 80 - 1000 Hz), while parking the SET at a fixed location above the TBG. This yields the local inverse compressibility, $d\mu/dn$, where μ is the

chemical potential of the carriers in the TBG and n is their density.

We measure the modulations of the source-drain current through the SET δI_{SET}, at frequency f_{BG}. The back gate excitation modulates the density of the TBG via $\delta n_{TBG} = \delta V_{BG} C_{BG-TBG}/e$, where C_{BG-TBG} is the capacitance between the back gate and the TBG, and e is the electronic charge. Consequently, the chemical potential of the TBG also changes as $\delta\mu_{TBG} = (d\mu/dn)\delta n_{TBG}$. The TBG's electrochemical potential (V_{TBG}), electrostatic potential (ϕ_{TBG}), and chemical potential (μ_{TBG}) are tied together via the identity $V_{TBG} - \phi_{TBG} = \mu_{TBG}$.

Since we keep the TBG grounded at the relevant frequency, $\delta V_{TBG} = 0$, then the change of the TBG's chemical potential translates directly to a change of its electrostatic potential: $\delta\phi_{TBG} = -\delta\mu_{TBG}$. This electrostatic potential gates the SET, modifying the average charge of its central *island*, which is formed in the suspended part of the nanotube between two p-n junctions. The modification to the SET charge is $\delta n_{SET} = \delta\phi_{TBG} C_{TBG-SET}/e$, where $C_{TBG-SET}$ is the capacitance between the area under study in the TBG and the SET's island. Owing to the Coulomb blockade phenomenon, a small change in δn_{SET} causes a sharp change in the current through the SET, δI_{SET}, allowing us to detect small changes in the TBG's chemical potential. To experimentally normalize out the gain of the SET and its capacitance to the TBG, we apply simultaneously a second AC excitation on the contacts of the TBG, $\delta V_{TBG} = 1 - 5$ mV, at a different frequency f_{TBG}. At this frequency, the chemical potential of the TBG remains constant, $\delta\mu_{TBG} = 0$ (the gating due to the small excitation is negligible) so the electrochemical modulation that we impose translates directly to an electrostatic modulation, $\delta\phi_{TBG} = -\delta V_{TBG}$, which is similarly sensed by the SET. The ratio of the detected current modulations in response to these two excitations gives us directly:

$$\frac{\delta\mu_{TBG}}{\delta V_{BG}} = \left(\frac{\delta I_{SET}}{\delta V_{BG}}\right) / \left(\frac{\delta I_{SET}}{\delta V_{TBG}}\right)$$

The inverse compressibility of the TBG then follows from:

$$\left(\frac{d\mu}{dn}\right)_{TBG} = e\frac{\delta\mu_{TBG}}{\delta V_{BG}}/C_{BG-TBG}$$

The only parameter in this relation is the geometrical capacitance between the back gate and the TBG, which is known to $\pm 10\%$ in our experiment. It appears as a normalization factor in the relation above, and not as a large additive term as in capacitance measurements. Thus, in contrast to capacitance measurements, where few percent error in the value of the geometrical capacitance can lead to hundreds of percent error in the extracted compressibility, here it translates only to a few percent error in the determined compressibility, making this measurement scheme quantitatively reliable [111].

2.11.2 Scanning near-field optical microscopy (s-SNOM)

In Chapter 9 of this thesis, in collaboration with the group of Frank Koppens and Marco Polini, we apply near-field microscopy techniques to study the optical properties of MATBG when it interacts with light at nanometer-size scales. Here, we describe the experimental technique used in this experiment. The explanation below closely follows reference [148].

The large degree of band nesting (the phenomenon of two bands being parallel in the energy-wavevector space, in this case, the flat and remote bands) leads to a resonance in the absorption spectrum and makes MATBG an exciting candidate for optical studies. In particular, the distance between the bands is on the order of 100 meV between the M and K points, corresponding to infrared frequencies [151, 148].

Given that the infrared wavelength is comparable to typical device dimensions, which makes far-field experiments on these systems challenging due to diffraction-limit, most optical experiments performed on TBG or hBN aligned with graphene are performed using near-field techniques [151]. We here use near-field microscopy to probe the optical properties of TBG near the magic angle [85], via the interaction between light and the near-field electromagnetic fields existing near the surface of the material under study.

Specifically, scattering-type scanning near-field optical microscope (s-SNOM) allows probing the response to perturbations carrying a well-defined in-plane wavevector and angular frequency. It is thus a particularly suited technique to study collective excitations in TBG, where electron-electron interactions play a key role in the physics of the system

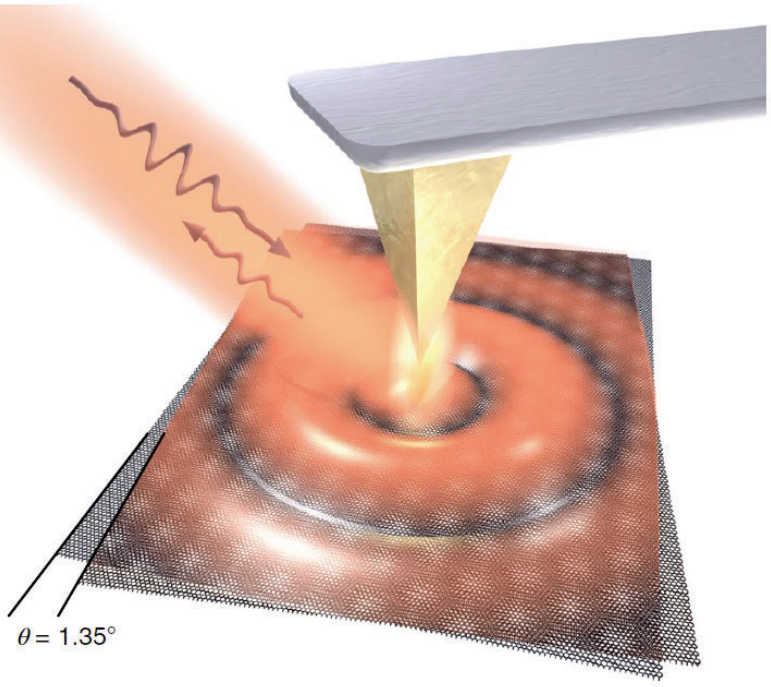

Figure 2-40: Illustration of the s-SNOM experiment presented in Chapter 9 [148].

[151, 85].

In the s-SNOM experiment presented in Chapter 9, a sharp AFM metallic tip is illuminated by infrared light (see Fig. 2-40), where a sharp hotspot of light forms at the apex of the tip. The tip interacts with the sample via the evanescent waves forming at the hotspot of light, and provides sufficient momentum to launch a collective excitation in TBG. The plasmon can then (for example, by reflection from an edge or interface) scatter into light at the tip. This scattered light is detected by a photodetector (Fig. 2-41). For a more detailed description of the principle of operation of s-sNOM, and a review of s-SNOM experiments used in the detection of propagating plasmons in graphene, we refer the interested reader to reference [151].

The sharpness of the tip defines the spatial resolution, and hence can bypass the far-field diffraction limit [151]. In the experiment presented in Chapter 9, we study collective light-matter phenomena on the nanoscale, while we simultaneously resolve spatial variations of the sample's properties with a resolution of around 20 nm.

The near-field measurements presented in Chapter 9 [148] are carried out with a commercial scattering-type scanning near-field optical microscope (Neaspec). A tuneable

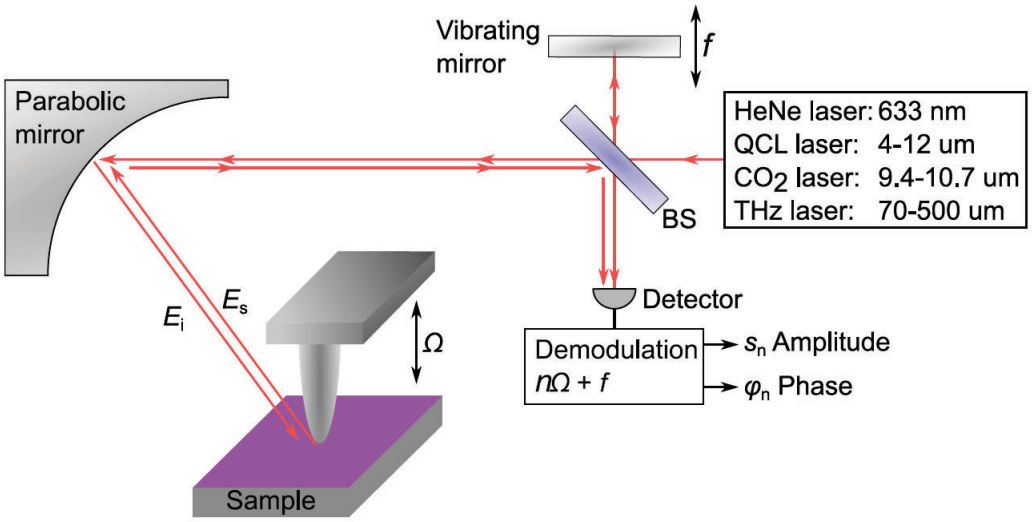

Figure 2-41: Principle of operation of the s-SNOM system. The light source is first attenuated, then passes through a beamsplitter and impinges on the parabolic mirror that focuses the (vertically-polarized) light onto the apex of the tip, which is maintained fixed at the focal point of the parabolic mirror. The light hotspot at the tip apex interacts with the charge carriers of the material underneath, and can produce collective excitations. After interacting with the sample (for example, the launched plasmon can reflect from an edge or interface and return to the tip), the plasmon is then scattered into light at the tip, which is directed to a photodetector. This scheme allows interferometric detection using a reference arm to measure both the amplitude and phase difference of the impinging and scattered out light at the AFM tip apex. Oscillations in the near-field signal can thus be recorded, as shown in Chapter 9 [148]. Figure reproduced from reference [151].

quantum cascade laser (Daylight Solutions) and a CO_2 gas laser (Access Laser) are used as mid-infrared light sources with a typical power of 5 - 10 mW, and the light is focussed on the metal-coated AFM tip (Nanoworld). The AFM tip oscillates at a frequency ≈ 250 kHz with a tapping amplitude of 80 - 100 nm, and modulates the scattered optical signal that is measured with a fast cryogenic HgCdTe detector (Kolmar Technologies). The near-field contribution to the optical signal is strongly dependent on the tip-sample distance, and therefore we can filter out the far-field contributions by locking to the 3rd harmonic [148].

We operate the s-SNOM in a non-interferometric detection scheme to obtain the optical signal $S_{opt}(x)$, as presented in Chapter 9. This offers a higher signal-to noise-ratio compared to pseudoheterodyne detection, and allows us to vary the excitation wavelength while scanning. This non-interferometric scheme can cause small far-field contributions to

the measured signal, which we have verified to be insignificant for our conclusions. We performed a small planar correction to the data to correct for signal loss during the scans [148].

To ensure clean and flat surfaces for the s-SNOM measurements, we perform AFM-brooming after the low-temperature transport characterization. Repeatedly scanning in contact-mode over the sample removes from the sample surface residues originating from the fabrication process (as explained in Chapter 2.9.11) [144, 145]. These residues mask the fine optical and topographic features studied in Chapter 9, and form therefore a hurdle for s-SNOM measurements. Additionally, this AFM-brooming procedure helps to minimize the residues picked up by the apex of the AFM tip, and therefore reduces the loss of near-field signal during s-SNOM measurements. For this cleaning procedure, we use a standard AFM (Veeco) equipped with soft tips (Veeco OTR8-35, stiffness 0.15 N/m, and Nanoworld Arrow CONT, stiffness 0.2 N/m) and scan over the surface with a typical force 20 - 40 nN (corresponding to a pressure of 20 - 40 MPa) and speed 2 - 4 μm/s for several hours [148]. After this procedure, the root-mean-square roughness is 120 - 200 pm, which is similar to that of a pristine hBN flake [127].

Chapter 3

Tunneling spectroscopy of graphene nanodevices coupled to large gap superconductors

In this chapter, we present results on tunneling spectroscopy measurements of graphene coupled to niobium/niobium-nitride superconducting electrodes, using graphite probes and hexagonal boron nitride tunneling barriers. Due to the proximity effect, the graphene density of states depends on the phase difference between the superconductors and exhibits a hard induced gap at zero phase. The energy spectra are measured at different carrier density and are consistent with a continuum of Andreev bound states, microscopic electron-hole states at the origin of the Josephson effect. The corresponding critical supercurrent is independently measured and display Fabry-Pérot oscillations, demonstrating ballistic transport in the graphene nanodevices. At energies larger than the superconducting gap, we observed phase-dependent energy levels displaying the Coulomb blockade effect. These features are interpreted as spurious quantum dots, presumably embedded in the heterostructures, and coupled to proximitized graphene. This Chapter is based on the work published in reference [1].

This Chapter is the first of the results presented in this thesis where graphene is turned superconducting via the proximity effect. This is achieved by sandwiching the graphene between two large-gap superconductors (see Chapter 2.4 for a more in-depth introduction

to the proximity effect). This fundamental study of a graphene-based Josephson Junction sets the grounds for some of the subsequent chapters of this thesis, including graphene-based superconducting qubits (Chapter 4), and highly tunable magic-angle twisted bilayer graphene tunneling junctions (Chapter 5).

3.1 Motivation and introduction

The superconducting proximity effect in graphene has attracted considerable experimental interest this last decade, either via supercurrent measurements of graphene-based Josephson junctions [26, 152, 153, 154, 155, 156, 157, 158], via tunneling spectroscopy studies of proximitized graphene [159, 160, 27] or via phase transition measurements of tin-decorated graphene [161, 162]. Graphene's extended two-dimensional nature makes it a promising platform to explore the interplay of superconductivity with the quantum Hall effect, which could lead to the detection of exotic quasiparticles with non-trivial braiding statistics [163, 164, 165, 166]. To do so, it is necessary to strongly couple low-disorder graphene to large critical field superconductors, such as niobium, molybdenum-rhenium or niobium-nitride (NbN). Along this line, improvement in nanofabrication lead recently to the demonstration of high-field Josephson effect in ballistic graphene coupled to niobium, evidenced by Fabry-Perot oscillations of the supercurrent and anomalous Fraunhofer patterns [155]. Even more recently, it was shown that the Josephson effect could persist in the quantum Hall regime by coupling a graphene sheet to molybdenum-rhenium [158]. Further studies are however needed to elucidate the origin of these phenomena. Phase-controlled tunneling spectroscopy seems promising as it enables to probe Josephson physics in the energy domain [27].

Microscopically, the Josephson effect arises from the formation in the normal conductor of entangled electron-hole states called Andreev bound states (ABS) [28, 29, 30, 31]. These fermionic states have energies inside the superconducting gap $[-\Delta, \Delta]$ that depend on the phase difference φ between the two superconductors sandwiching the central conductor. Although phase-dependent spectroscopy of ABS have been performed in few systems [167, 168, 169, 170, 171, 172, 27], the way ABS form in graphene coupled to large

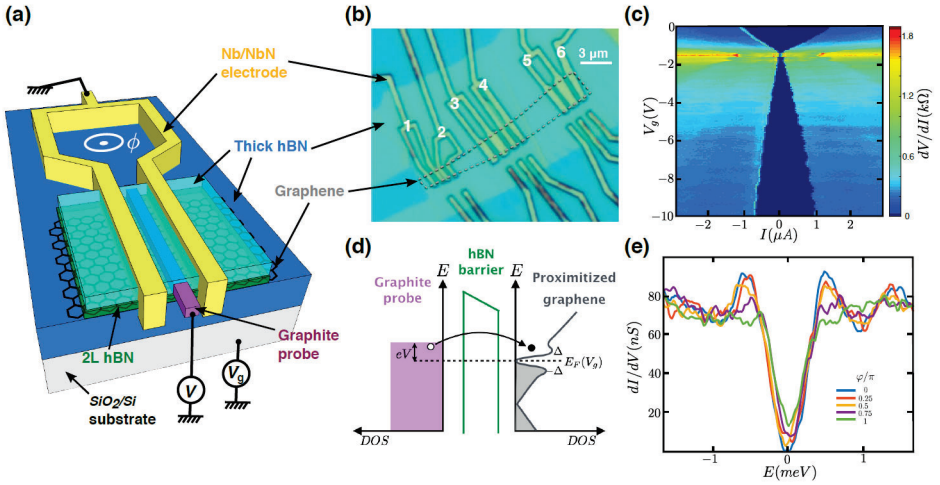

Figure 3-1: (a) Device structure. An encapsulated graphene flake is connected to two Nb/NbN superconducting electrodes. Magnetic flux ϕ threading the loop imposes a phase difference $\varphi = \phi/\phi_0$ across graphene. (b) Optical micrograph of the sample showing several S-G-S devices, built on a same graphene flake. (c) Color-coded differential resistance, dV/dI, between junction #5 and #6 as a function of current bias I and gate voltage V_g. The critical current exhibits Fabry-Perot oscillations for hole doping. (d) Schematics of the tunneling spectroscopy process. The normal probe is a graphite electrode and the tunneling barrier a bilayer hBN crystal. (e) Differential conductance of junction #4, dI/dV, as a function of energy, $E = eV$, for different phases, φ, and at a gate voltage $V_g = 40\ V$. The DOS exhibits a hard induced gap at zero phase.

critical field superconductors and subject to high magnetic field remains unclear. For this purpose, we have performed tuneling spectroscopy measurements of graphene proximitized by niobium/niobium-nitride (Nb/NbN) electrodes. The measured energy spectra reveal a strong proximity effect in graphene and the presence of a continuum of ABS, which varies with the graphene carrier density. We also observe phase-dependent out-of-gap energy features associated with microscopic quantum dots.

3.2 Device structure and fabrication

The experiment is performed using a complex van der Waals heterostructure, schematized in Fig. 3-1a, which is assembled with a polymer-based dry pick up and transfer technique (see Chapter 2.9.6). It consists of (from top to bottom) a hexagonal boron nitride (hBN) encapsulation layer, a micro-fabricated graphite probe, a bilayer-hBN tunneling barrier, a

monolayer graphene sheet and a bottom hBN substrate. The use of graphite as a probe reduces doping in graphene owing to their small work function mismatch while the top and bottom hBN flakes fully isolate graphene from contamination during the fabrication process. This strategy enables us to access the low carrier density regime of a pristine graphene sheet, whose Fermi energy is controlled electrostatically by the gate voltage V_g. The encapsulated graphene (G) is connected at both ends via 1-D edge contacts to two superconducting (S) electrodes made out of Nb/NbN, thus forming an S-G-S Josephson junction. The superconducting contacts are deposited onto the exposed graphene edges using e-beam evaporation of titanium as a sticking layer (5 nm) and *in situ* reactive sputtering of Nb (15 nm) and NbN (50 nm). The superconductor prepared this way has a critical temperature $T_c \sim 9$ K and remains superconducting at a magnetic field $B = 9$ T (characterized separately), well above the onset of integer quantum Hall effect in a high quality graphene device. To control the superconducting phase difference $\varphi = \phi/\phi_0$ across the S-G-S Josephson junction, we apply a magnetic flux ϕ through the superconducting leads patterned in a loop, where $\phi_0 = \hbar/2e$ is the reduced flux quantum.

The full device actually consists of five superconducting loops built on a same monolayer graphene sheet (see Fig. 3-1b). In each loop, the lead-to-lead distance L of the graphene weak link is 440 nm, and the width W ranges from 1.3 μm to 3.4 μm. The tunneling measurements presented in this chapter are obtained from tunnel junction #1 ($W = 1.3$ μm) and tunnel junction #4 ($W = 2.7$ μm). Such a geometry allows for both spectroscopic and transport measurements in the same graphene flake. Indeed, by measuring at low temperature ($\sim$20 mK) the current between two neighboring loops, one can extract the Josephson critical current through graphene. Such a measurement is shown in Fig. 3-1c, as a function of the gate voltage V_g. The Fabry-Perot oscillations in the critical current observed in the hole p-dope region ($V_g < -1.8$ V) demonstrate that transport is ballistic in graphene [155, 156, 157].

3.3 Proximitized graphene: density of states

The density of states (DOS) of graphene can be extracted by measuring (at 20 mK) the differential conductance dI/dV between the graphite probe and the superconducting lead (Fig. 3-1d). Fig. 3-1e shows such a measurement for junction #4 at $V_g = 40$ V, with dI/dV plotted as a function of bias voltage V (converted into energy $E = eV$) for different values of the magnetic flux ϕ (converted into phase φ). Due to the proximity effect, the extracted graphene DOS displays an induced gap $\Delta \sim 0.6$ meV. It's 40% smaller than the gap size of NbN, which might be related to the anti-proximity effect associated with the intermediate layers of Nb ($T_c \sim 7$ K) and Ti ($T_c \sim 0.4$ K). At $\varphi = 0$, the DOS exhibits a hard induced gap (zero DOS at low energy), which demonstrates the strength of the proximity effect and the high transparency of the SG interfaces. The DOS oscillates when varying the phase, which reveals the presence of a continuum of ABS in graphene, as expected from a 2-D quantum conductor that accommodates a large number of conduction channels and associated ABS [28, 29, 30, 31].

To investigate further how proximity effect develops in graphene, we now tune the Fermi energy by varying the gate voltage V_g. The measured energy spectra, plotted in Fig. 3-2 as a function of both energy and phase for junction #1, strongly depend on the carrier density, which is tuned from hole type (Fig. 3-2a), through the charge neutrality point (CNP) (Fig. 3-2b-d) to electron type (Fig. 3-2e-f). The phase modulation of the DOS is weaker when the graphene is hole-doped, in good agreement with transport measurements from Fig. 3-1c that shows a big asymmetry in supercurrent between electron and hole-doped regions. This is due to the presence of p-n junctions at the SG interfaces (owing to the electron n-doping of graphene by the Nb/NbN contacts), which reduce the contacts' transparency and weaken the phase-modulation of the ABS. Strikingly, the phase modulation remains well-pronounced at the CNP, which demonstrates the low-disorder of our graphene nanodevice. This observation and the one of the hard gap are in clear contrast with measurements obtained in a former work using aluminum as a superconductor [27]. Such improvements, combined with the use of large critical field superconductors, are very promising for projects that require quantum coherence in ultra-clean hybrid superconduct-

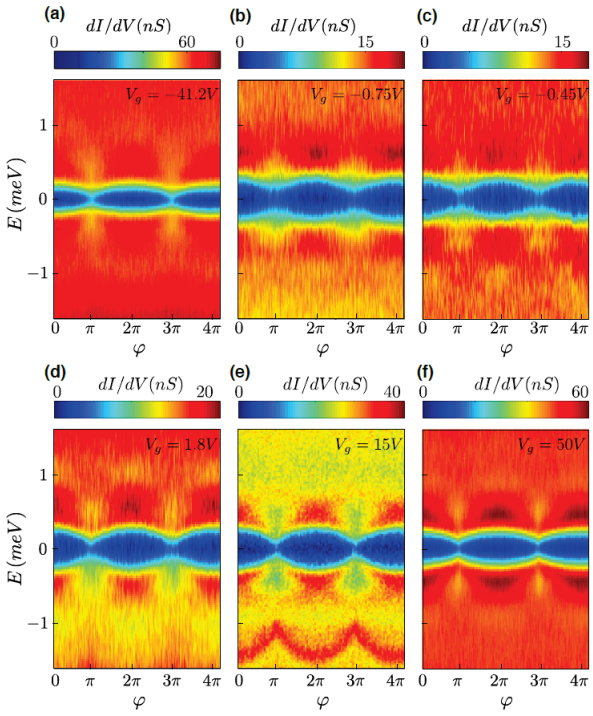

Figure 3-2: Phase and gate dependence of the graphene proximitized DOS. (a-f) Differential conductance of junction #1, dI/dV, as a function of both energy $E = eV$ and superconducting phase difference φ, for different gate voltages V_g (indicated in each panel). The oscillating spectrum is evidence for a continuum of ABS.

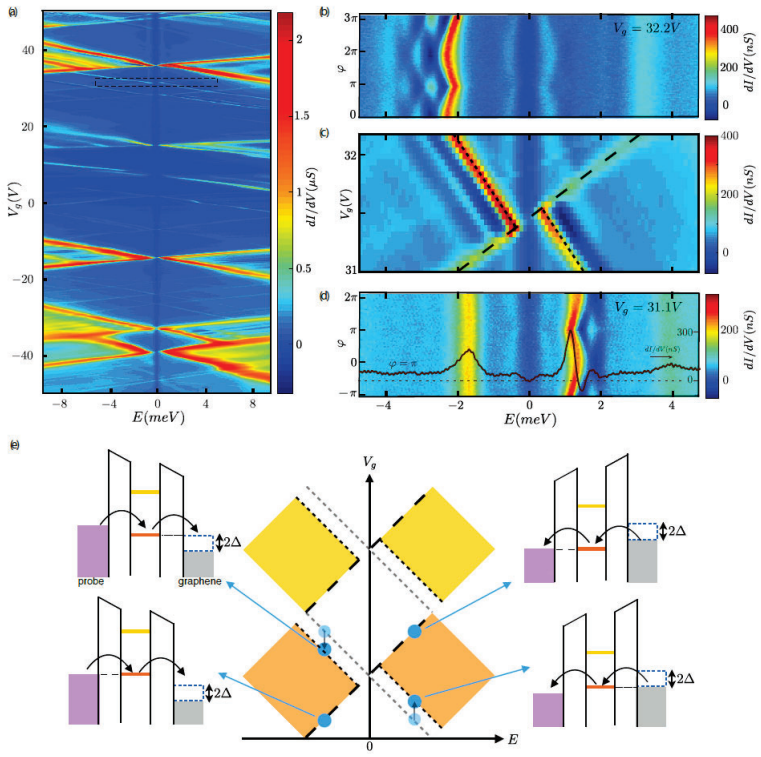

Figure 3-3: Coulomb diamonds. (a) Differential conductance of junction #4, dI/dV, as a function of both energy $E = eV$ and gate voltage V_g. (c) Zoom-in at the crossing of one Coulomb Diamond, highlighted by a dashed rectangle in (a). The dashed lines highlight the splitting of the negative slope diamond peaks (nsdp), while the positive slope diamond peaks (psdb) remain aligned across the induced gap. (b) and (d) Phase-dependence of nsdp at $V_g = 32.2$ V and 31.1 V, respectively. The dI/dV linecut at $\varphi = \pi$ in (d) shows the change of sign, which is associated with the graphene proximitized DOS. (e) Middle: schematics of the Coulomb diamonds with gap opening. Around: schematics of transport through a quantum dot connected to a normal and a superconducting electrode.

ing Dirac materials [163, 164, 165, 166].

3.4 Microscopic quantum dots weakly coupled to proximitized graphene

This set of measurements establishes that a continuum of supercurrent-carrying ABS form in graphene, with energies $|E| < \Delta$. At some specific gate voltages, however (see e.g., the oscillating red feature for $E < 1$ meV in Fig. 3-2e), we observe resonant out-of-gap energy features that depend on the phase difference. To understand their origin, we measure the

differential conductance as a function of both energy and gate voltage, at a constant phase and over a large energy range. As represented in Fig. 3-3a, on top of the induced gap that appears at low energy, one can see sharp resonances that disperse in the manner of Coulomb diamonds. A detailed analysis suggests that they correspond to 5-20 nm size quantum dots (QD) with typical addition energy of $\sim$ 5-60 meV. These quantum dots might be related either to spurious defects embedded in the van der Waals heterostructure or to charge puddles in graphene around charged impurities [173]. Another somehow more fundamental explanation could be scattering centers at the graphene edge, which were recently evidenced as being located every 2-20 nm using scanning nano-SQUID thermometry [174].

Fig. 3-3c shows a zoom-in on a given diamond at low energy. Strikingly, the diamond peaks in dI/dV that disperse in (eV, V_g) with a negative slop (hereafter called nsdp) split around zero energy, while the positive slope diamond peaks (psdp) are aligned. Moreover, the nsdp are accompanied with dI/dV peaks of opposite sign (see inset in Fig. 3-3d). Similar effects were already observed in S-QD-S hybrid systems, using metallic nanoparticles [175, 176], carbon nanotubes [177], semiconductor nanowires [178] or fullerene molecules [179]. However, the configuration here is asymmetric with a QD weakly coupled on one side to the graphite probe and on the other side to the proximitized graphene. The nsdp (respectively psdp) thus correspond to the alignment of the resonant dot level with the peak at the edge of the induced superconducting gap in the graphene DOS (resp. with the Fermi level of the graphite probe), as schematized in Fig. 3-3e. Further, when the phase difference is varied, the graphene DOS modulates and the nsdp oscillate in energy. This phenomenon can therefore happen at positive or negative energy, depending on the gate voltage (Fig. 3-3b,d).

In this experiment, the quantum dots behave as energy filters in the tunneling process from graphite to graphene, with a rate that depends on both energy and gate voltage. Out of resonance, the tunneling rate is weak, it hardly depends on energy and one directly probes the graphene DOS by measuring the differential conductance. At resonance, the differential conductance is greatly increased and the tunneling rate strongly depends on energy. In the simple case of a very weakly coupled QD, the tunneling rate can be modeled as a Dirac delta function. The dI/dV signal is then proportional to the derivative of the graphene

DOS, which explains the observed positive-followed-by-negative dI/dV values.

3.5 Conclusion

In conclusion, using tunneling spectroscopy in a full van der Waals heterostructure, we demonstrated that graphene coupled to Nb/NbN superconductors can develop a strong proximity effect, with a DOS displaying a hard induced gap and a pronounced phase modulation at the Dirac point. These results open the way to exploring exotic Andreev physics at large magnetic field, using ultra-clean Dirac materials coupled to large critical field superconductors [163, 164, 165, 166]. Further measurements at large energies and their gate dependence reveal the presence of microscopic quantum dots weakly coupled to proximitized graphene, that behave as energy filters in the tunneling process. To elucidate their origin, which could be intrinsic and associated to graphene finiteness, one could combine tunneling spectroscopy and nano-SQUID thermotry measurements in order to locate their position.

Chapter 4

Coherent control of a hybrid superconducting circuit made with graphene-based van der Waals heterostructures

As we introduced in Chapter 2, quantum coherence and control is foundational to the science and engineering of quantum systems [180, 64]. In van der Waals materials, the collective coherent behaviour of carriers has been probed successfully by transport measurements [26, 156, 155, 27]. However, temporal coherence and control, as exemplified by manipulating a single quantum degree of freedom, remained to be verified before this work. In this chapter, based on reference [2], we demonstrate such coherence and control of a superconducting circuit incorporating graphene-based Josephson junctions similar to the ones presented in Chapter 3. Furthermore, we show that our device can be operated as a voltage-tunable transmon qubit [181, 182, 183], whose spectrum reflects the electronic properties of massless Dirac fermions travelling ballistically [156, 155]. In addition to the potential for advancing extensible quantum computing technology, these results represent a new approach to studying van der Waals materials using microwave photons in coherent quantum circuits. This work has been performed in close collaboration with Joel Wang and

the group of William D. Oliver.

4.1 Introduction

Since the first observation of quantum oscillations in a single-Cooper-pair box [180], superconducting qubit technology has evolved to become a leading modality for quantum computation [184], with a six orders of magnitude increase in coherence times (see Fig. 2-11) resulting from the development of new circuit design concepts [67, 185], improved material quality and refined fabrication techniques (for a review, see ref. [69]). Hybrid superconducting circuits also provide a platform for hosting other materials or devices with alternative electronic or mechanical degrees of freedom to access their coherent characteristics and properties via interactions with artificial atoms (qubits) or microwave photons [186, 187] (see Chapter 2.5). Given this relevance of hybrid superconducting circuits to both quantum computing technologies and the fundamental sciences, it is essential to expand the scope of the field by introducing new materials and experimental approaches.

4.2 Experimental setup

4.2.1 van der Waals materials and quantum information

One highly anticipated development is the application of van der Waals (vdW) materials (see Chapter 2.1 in the context of quantum information science [188, 189, 190]. While vdW heterostructures have been studied intensively using d.c. transport measurements, only a few very recent experimental studies on vdW materials integrated into circuit quantum electrodynamics (cQED) systems have been reported so far [191, 192]. More importantly, the literature does not include any accounts of temporal quantum coherence or quantum control with these material systems, and both are prerequisites for quantum information science and technology applications.

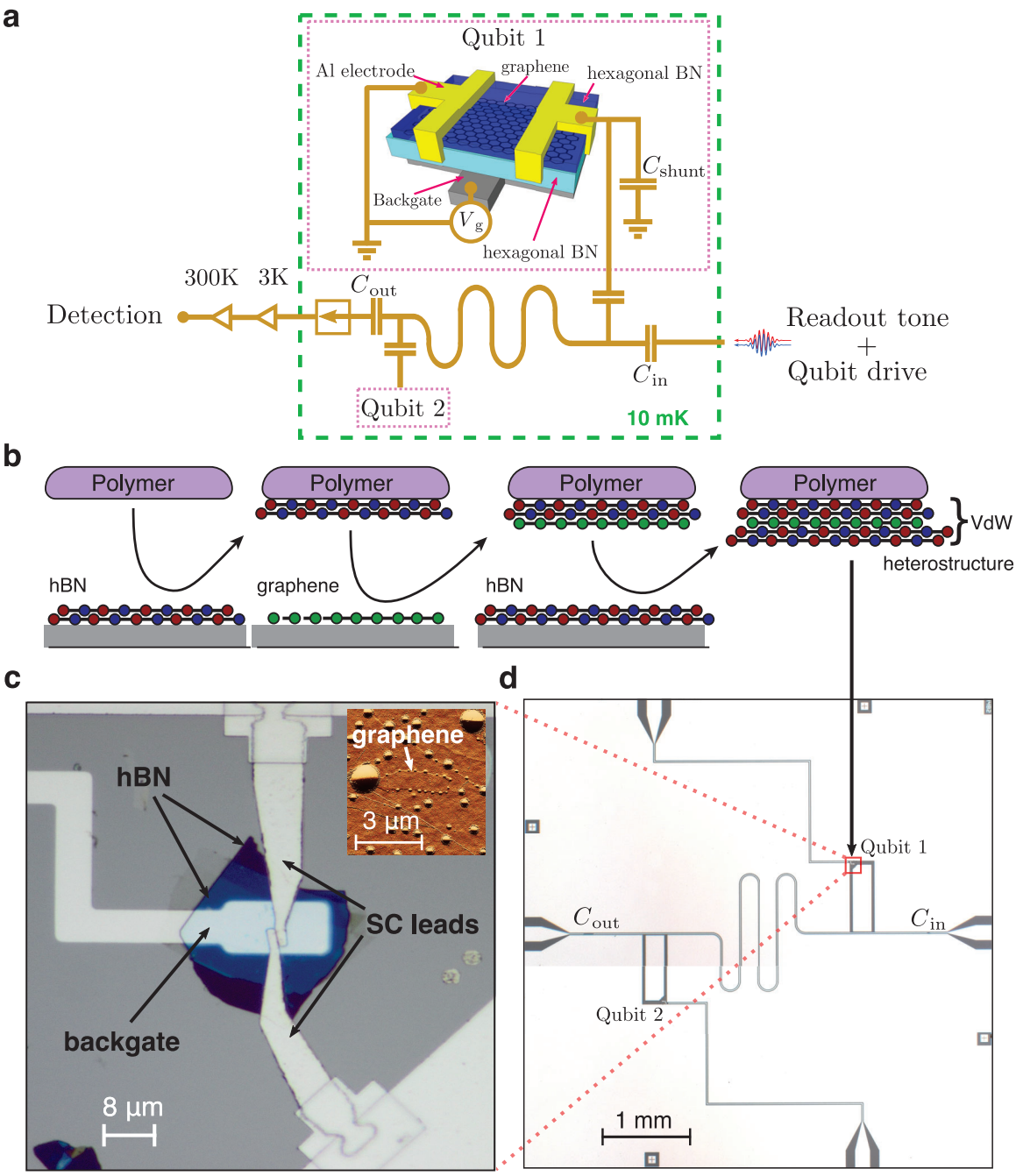

Figure 4-1: Fabrication of graphene transmon qubits. (a) Schematic of the hBN-encapsulated S–G–S junctions embedded in a cQED system. (b) Assembly of vdW heterostructures using a dry polymer-based pick-up and transfer technique. (c) Optical micrograph of the graphene transmon qubit. SC, superconducting. Inset, atomic force microscopy image of the encapsulated graphene before making electrical contact to the superconducting electrodes. (d) Qubit chip made of high-quality aluminium. Each shunting capacitor is cut out at the corner (red box; see c) to host the assembled vdW stack. Bonding pads on the top and bottom of the chip are used for backgate control.

4.2.2 Experimental setup: hybrid superconducting circuit

Figure 4-1a presents a schematic of a hybrid superconducting circuit made with graphene-based vdW heterostructures. Graphene, an atomic layer of carbon atoms in a hexagonal lattice [193], can inherit superconductivity through the proximity effect [26, 27] (see Chapter 2.4). When encapsulated in hexagonal boron nitride (hBN), the superconductor–graphene–superconductor (S–G–S) junction supports a voltage-tunable, bipolar Josephson current in the ballistic regime [156, 155, 194]. In our experiment, the S–G–S junctions are built into a voltage-controlled transmon circuit that enables us to perform both frequency-resolved spectroscopy and coherent quantum control using cQED techniques (Fig. 4-1a), as introduced in Chapter 2.5.

The voltage-controlled transmon, also known as a gatemon, employs superconductor–normal-conductor–superconductor junctions as the nonlinear element in a superconducting circuit. Voltage-controlled transmons have been realized with a semiconductor nanowire [181, 182] and a two-dimensional (2D) electron gas [183] proximitized by epitaxially grown superconductors, and, over time, have achieved temporal coherence comparable to that of typical transmon qubits in the cQED architecture based on superconductor–insulator–superconductor junctions [182, 183]. While the graphene-based gatemon shares the same voltage tunability as its semiconductor-based counterparts, it may also offer complementary benefits to existing schemes, owing to its unique electronic properties and extensibility to complex heterostructures in high-quality-factor (low dissipation) superconducting circuits. In addition to its relevance for extensible quantum computing [181, 195], this particular qubit configuration enables simultaneous access to time- and energy-domain information pertaining to the underlying quantum conductor, the electronic properties of which can be largely tuned by the gate voltage.

4.2.3 Sample fabrication and measurement setup

The vdW heterostructures were made using a dry-polymer based process (Fig. 4-1b) [27, 143] followed by annealing at $\sim$ 350 degrees Celsius in vacuum or forming gas [27, 1] to remove excessive hydrocarbon compounds within the heterostructures (see sec-

tions 2.9.6 and 2.9.3). From bottom to top, they consist of a thick hBN substrate, a monolayer graphene sheet and a top hBN layer. The bottom hBN layer serves as an atomically flat, pristine gate dielectric [8], which allows access to a wide carrier density range through electrostatic gating as explained in Chapter 2.9.1. The top hBN layer encapsulates the graphene, thereby protecting it from becoming contaminated in subsequent steps. The assembled vdW stack is then transferred onto an aluminium backgate on the qubit substrate, a high-resistivity silicon chip coated with high-quality aluminium, and patterned into a coplanar wave guide, shunting capacitors, d.c. bias lines and the ground plane (Fig. 4-1d). After transferring the stack onto the qubit chip, superconducting leads were defined by standard electron-beam lithography and reactive ion etching (RIE), which facilitated the 1D edge contact [27, 143, 1], to thermally evaporated titanium (7 nm) and aluminium (120 nm) (see Chapter 2.9.10). The aluminium superconducting electrodes of the S–G–S junctions thus couple to the encapsulated graphene flakes via the aforementioned 1D edge channels, and make transparent connections to the ground plane and capacitors. A second lithography step was then applied to define areas for in situ ion milling and electron-beam evaporation of 250 nm of aluminium to bridge the electrodes to the ground plane and shunting capacitors.

The devices were measured in a dilution refrigerator with a base temperature of ~ 10 mK. Dispersive readout and qubit control were implemented using microwave pulses applied to a half-wavelength coplanar waveguide resonator, which capacitively coupled to two qubits at opposite ends of the waveguide resonator in a standard circuit-based cQED set-up (Fig. 4-1a–d). The backgate voltage was applied through low-pass-filtered d.c.-bias lines and used to tune the Fermi energy in the graphene.

4.3 Results and discussion

Without loss of generality, we centre our discussion on the device shown in Fig. 4-1c (qubit 1 in Fig. 4-1a), on which all measurements discussed in this chapter were taken, while the backgate of the other qubit on the same chip was fixed at 5 V (measurements from additional devices are not included in this thesis, but can be found in the Supplementary materi-

als of reference [2]). The charging energy E_C of this device is given by $E_C/h = 100$ MHz (where h is Planck's constant), as determined based on an electromagnetic simulation of the shunting capacitor.

4.3.1 Frequency-resolved spectroscopy of the graphene transmon qubit

First, we measure how the transmission of the resonator responds to a varying gate voltage V_g by scanning the readout frequency f_{ro} around the bare-resonator frequency $f_{R,bare} = 7.34$ GHz. In Fig. 4-2a, the resonator spectrum is plotted as a function of f_{ro} and V_g. We observe a splitting of the cavity resonance frequency f_R at $V_g \approx -2.2$ and -2.8 V, indicating hybridization between the resonator and the qubit in the strong coupling regime.

The cQED approach (see section 2.5) enables qubit readout by monitoring the qubit-state-dependent transmission through the resonator. In addition to the readout tone, another driving pulse f_{dr} is applied to induce state transitions in the qubit. Figure 4-2b (main panel) shows such a qubit spectrum plotted against the driving frequency f_{dr} and V_g. The distinct peak position indicates the qubit frequency f_{qb}, which corresponds to the transition energy $E_{01} = hf_{qb}$ at any given gate voltage. We now discuss major features of this spectrum.

The qubit frequency f_{qb} exhibits a large tunability range from 6 GHz to 12 GHz. In transmon qubits, the qubit frequency is generally given by $f_{qb} = E_{01}/h \sim \sqrt{8E_C E_J(V_g)}/h - E_c/h$ (ref. [67]), where E_{01} is the energy corresponding to the transition from ground state to the first excited state, E_C is the charging energy of the junction, E_J is the Josephson coupling energy of the junction [45] and h is Plank's constant. With $E_C/h = 100$ MHz used for this circuit, the critical Josephson current I_c of the S–G–S junction is estimated to be $\sim$ 90–360 nA, consistent with results reported in previous d.c. transport studies [26]. In contrast to superconductor–insulator–superconductor tunnel junctions, where E_J is generally modified using a current to induce a magnetic field in a superconducting quantum interference device-type configuration, in superconductor–normal conductor–superconductor devices the value of E_J can be tuned with V_g due to two effects: (1) V_g changes the Fermi energy and thereby directly modifies the density of states,

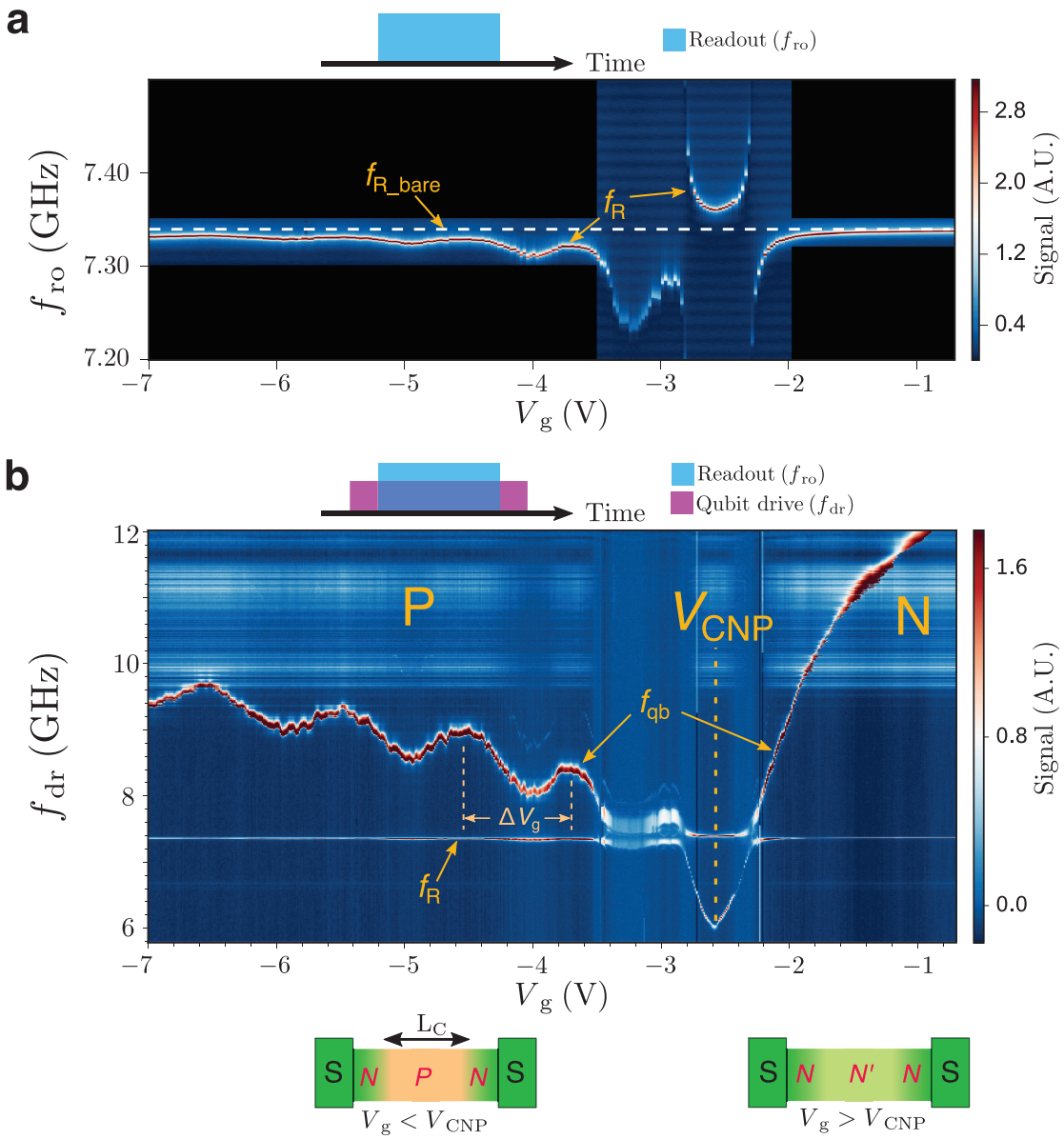

Figure 4-2: Spectroscopy of a graphene transmon qubit. (a) Resonator spectrum as a function of readout frequency f_{ro} and gate voltage V_g. Resonance frequency f_R exhibits a splitting at $V_g \approx -2.2$ and -2.8 V. The bare resonance frequency $f_{R,bare}$ of the resonator is marked at 7.34 GHz by the white dashed line. (b) Qubit spectrum as a function of drive frequency f_{dr} and V_g. Qubit frequency f_{qb} is asymmetric with respect to the charge neutrality point ($V_{CNP} \approx -2.5$ V). The Fabry–Pérot oscillation and an aperiodic fluctuation of f_{qb} appear in the p-doped region. Bottom, schematics of the graphene potential profiles in p (left) and n (right) regions. The cavity length L_C extracted from ΔV_g is ∼110 nm. Note that the backgate of the other qubit on the same chip is fixed at 5 V throughout the measurements presented in this chapter.

and therefore the total number of transmission channels [27, 193, 1], and (2) V_g modifies the transmission probability for a number of high-transmission conduction channels [181, 182, 196]. Overall this results in electrostatic control of the Andreev spectrum in graphene [27] and the corresponding Josephson coupling energy E_J (ref. [45]). The qubit spectrum has a minimum at $V_g = -2.52$ V, where the Fermi level reaches the point with minimum density of states (minimum E_J) and is identified as the charge neutrality point (V_{CNP}) of the graphene qubit. As a gapless semi-metal, graphene supports the Josephson effect in the n-doped ($V_g > V_{CNP}$) region with electron-like charge carriers and in the p-doped ($V_g < V_{CNP}$) region with hole-like carriers.

The qubit spectrum shows clear asymmetry in f_{qb} with respect to V_{CNP}, manifested as a lower f_{qb} value in the p-doped region for a given gate voltage (as compared to its equal-carrier-density (same $|V_g - V_{CNP}|$) counterpart in the n-doped region), and pronounced f_{qb} oscillations observed in the p-doped region. This asymmetry arises from the n-type doping provided by the Ti/Al electrodes [197], as evidenced by the negative V_{CNP} value of our device. In the vicinity of the electrode, doping from electrodes outweighs the effect of negative V_g and yields an n–p–n potential profile within the graphene (Fig. 4-2b, bottom panel), resulting in two semi-transparent interfaces (p–n junctions) for charge carriers. In addition to suppressing the magnitude of f_{qb} (see Chapter 3), the doping—and the resulting interfaces—create an electronic equivalence of a Fabry–Pérot cavity with an effective cavity length L_C inside the S–G–S junction. Furthermore, as a function of V_g, the Fermi wavevector $k_F \propto \sqrt{V_g}$ of the carriers inside this cavity varies. This variation is manifested in the local maxima (minima) of f_{qb}, where the resonant transmission (reflection) condition for adjacent peaks $\Delta k_F L_c = n\pi$ for integer n is satisfied. From the peak-to-peak separation in the gate voltage (ΔV_g in Fig. 4-2b), we extract the L_C for our device as $\sim$110 nm, accounting for $\sim$200 nm in total for the regions doped by the metallic electrodes [156, 155]. In addition to observing the Fabry–Pérot oscillations, we note an aperiodic fluctuation of f_{qb} with an amplitude of $\sim$100 MHz in the p-doped region. This reproducible (over weeks of measurement) fluctuation might be associated with a universal conductance fluctuation in mesoscopic Josephson weak links [198].

4.3.2 Temporal quantum coherence and control of the graphene transmon qubit

Next, we demonstrate that the device can be operated as an artificial atom by performing qubit operations in the time domain (see Chapter 2.5). Figure 4-3a shows measurements of the qubit state while varying the drive frequency and the pulse duration τ_{Rabi} for four different powers, measured at a fixed $V_g = -4.38$ V. When $f_{dr} = f_{qb}$ (8.811 GHz), the pulse induces Rabi oscillations of the qubit. In the Bloch sphere representation, this oscillation corresponds to rotations about the x axis and the qubit continuously alternates between $|0\rangle$ and $|1\rangle$ states. The Rabi oscillations are also used to calibrate the R_X^{π} and $R_X^{\pi/2}$ pulses, which rotate the Bloch vector about the x axis by π and $\pi/2$, respectively. We apply a R_X^{π} pulse followed by a delayed readout pulse, yielding an exponential decay trace with an energy relaxation time of $T_1 \approx 36$ ns (Fig. 4-3b). Figure 4-3c plots the T_1 measurement repeated at different bias points with values that range from 12 to 36 ns.

We studied the dephasing of our graphene qubit using Ramsey interferometry techniques. In the rotating frame, the application of two slightly detuned $R_X^{\pi/2}$ pulses separated by a delay time τ_{Ramsey} flips the qubit to the $x-y$ plane and allows the qubit to rotate about the z axis by $\Delta f \times \tau_{Ramsey}$, where $\Delta f = f_{dr} - f_{qb}$ is the detuning. Figure 4-4a (main panel) shows Ramsey oscillations as a function of detuning and time delay at a given gate voltage. Fringes at finite detuning indicate coherent precession around the z axis of the qubit. Figure 4-4b plots the discrete-time Fourier transform of the Ramsey fringes (calculated using the fast Fourier transform algorithm) and reveals at least three frequency components in addition to the main qubit frequency. The additional frequency components may be associated with coupling to spurious two-level systems embedded in the heterostructures (similar to the ones described in the previous chapter) [182] or unintentional population of higher-excited qubit states due to the relatively low qubit anharmoncity. Finally, fitting the decay envelope of the pattern at finite detuning yields T_2^* of ~ 55 ns (Fig. 4-4a, middle panel). This value is close to twice T_1 at the same gate voltage, suggesting that our qubit coherence is currently limited by energy relaxation.

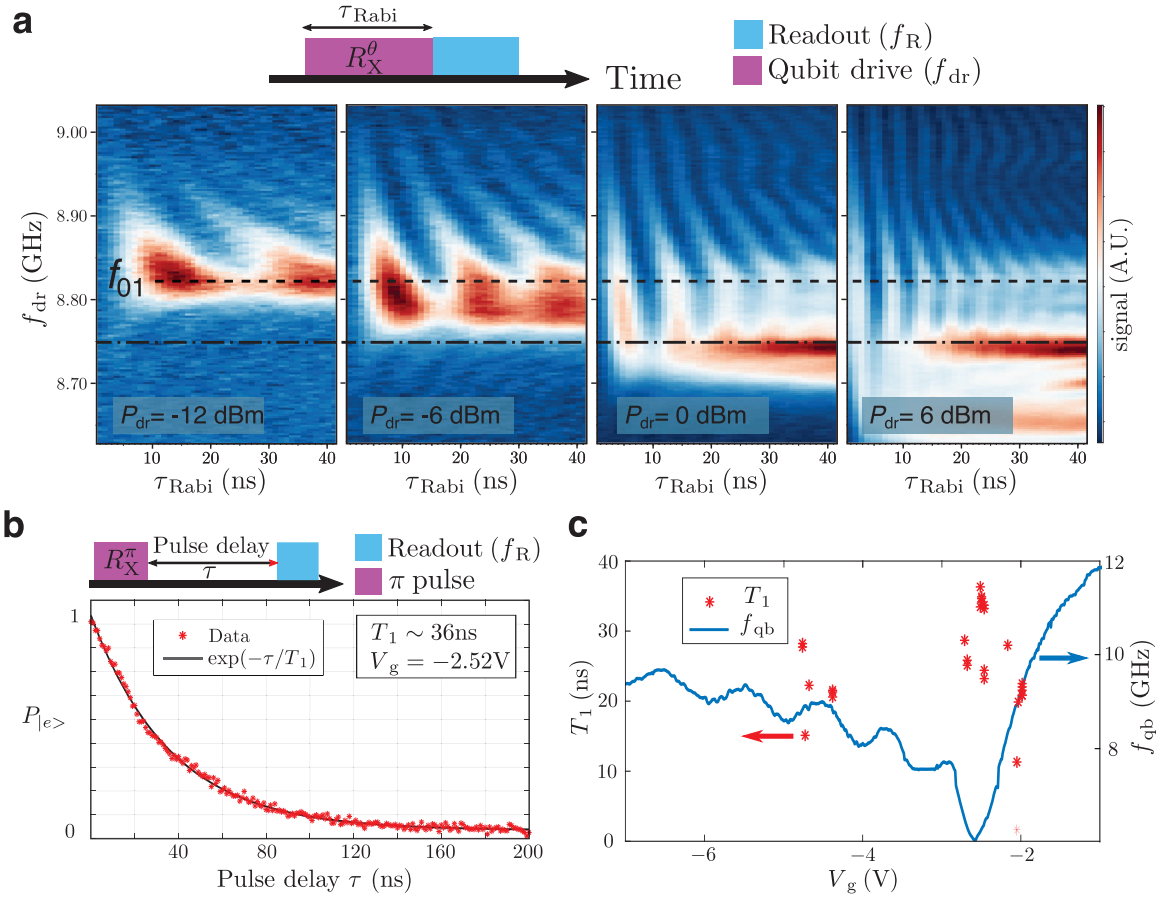

Figure 4-3: Rabi oscillation and energy relaxation of a graphene qubit. (a) Rabi oscillation, associated with the f_{01} qubit transition, as a function of drive frequency f_{dr} and pulse duration τ_{Rabi} measured with different qubit drive power values at $V_g = -4.38$ V. The qubit f_{12} and/or two-photon $f_{02}/2$ transition is induced at high driving power ($P_{dr} = 0$ and 6 dBm), as indicated by the pronounced signal below the Rabi oscillation (dot-dashed line). (b) Energy relaxation time T_1 measurement taken at $V_g = -2.52$ V using a π-pulse calibrated from the Rabi oscillation. The fitting of the qubit population to an exponential decay yields $T_1 \approx 36$ ns. (c) T_1 measured at different voltage bias points.

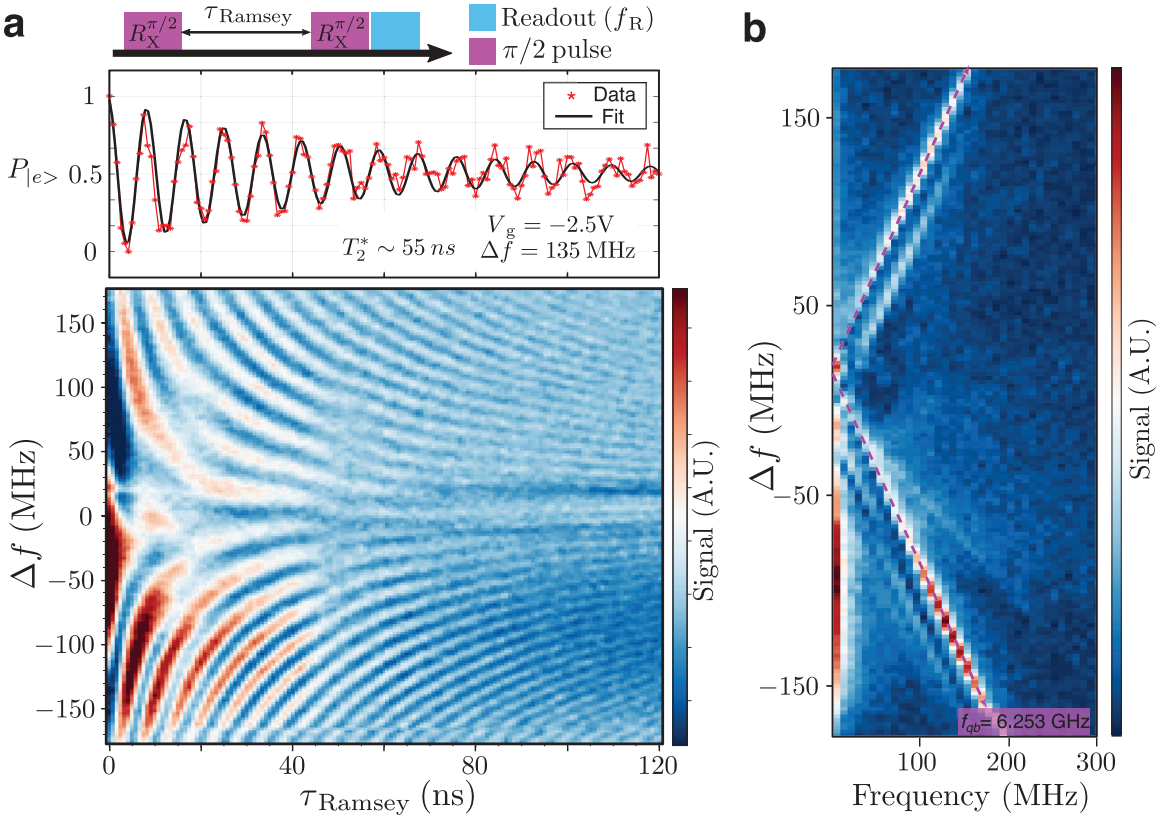

Figure 4-4: Qubit dephasing and Ramsey measurement. (a) Bottom, Ramsey fringes as a function of detuning and time delay τ_{Ramsey} measured at $V_g = -2.5$ V. A repeated beating pattern appears around $|\Delta f| < 75$ MHz, separated by $\sim$ 30 ns. Middle, line cut in the Ramsey fringes with finite detuning. The dephasing time T_2^* of $\sim$ 55 ns is obtained by fitting to the function $\exp(-\tau_{Ramsey}/T_2^*) \times cos(2\pi\Delta f \times \tau_{Ramsey})$. (b) Discrete time Fourier transform of the Ramsey measurement. The condition $\Delta f = |f_{dr} - f_{qb}|$ is represented by the dashed purple line. Extra frequency components presented in this plot might be associated with coupling to a spurious two-level system or excitation of a two-photon transition in the heterostructures.

4.3.3 Additional discussion on back gate dependence

It has been shown that the supercurrent transport characteristics in proximitized graphene vary with the Fermi energy [155, 27, 194, 199, 200]. In this work, however, we do not observe a strong V_g dependence of the coherence (Fig. 4-3c) to the extent recently observed in nanowire gatemons [182]. This strongly indicates that the coherence in our device is not limited by the graphene junction. Rather, we attribute the lack of a strong V_g dependence to the relatively short relaxation times T_1 in the present measurement, due to other decay channels in parallel with the intrinsic loss of the graphene junction. For example, it is clear that one major contribution to the relaxation in the current generation of our devices is photon loss due to geometric capacitive coupling between the qubit shunting capacitor and the backgate. This will be improved in a straightforward manner in future devices by redesigning the capacitor geometry and introducing on-chip low-pass filters [201].

4.4 Summary and conclusion

In summary, we have successfully demonstrated temporal quantum coherence and control of a superconducting circuit based on vdW heterostructures. Our demonstration used a transmon qubit comprising S–G–S junctions. The spectrum of the qubit exhibits the characteristic electronic properties of the underlying ballistic S–G–S junction, such as voltage tunability over more than 6 GHz, and Fabry–Pérot oscillations in the p-doped region. Our results show that there is an opportunity to engineer a qubit spectrum in order to optimize charge stability and coherence. For example, a device can be designed with multiple voltage sweet spots given by the Fabry–Pérot oscillations where the dephasing is minimized [182]. With the assistance of local electrostatic gating or a superlattice band structure given by vdW heterostructures [8], it is possible to further engineer the spectrum in order to achieve different functionality. The existing rich context of graphene physics, such as the topologically protected Josephson effect [157, 200, 158] and the gate-dependent current–phase relation [194], also provide the opportunity to sense and investigate the effects of microscopic transport processes via a single quantum degree of freedom—that is, the temporal coherence of a qubit—supporting both fundamental discovery and new qubit de-

sign concepts. These results suggest that the graphene-based superconducting qubit has great potential for extensible superconducting quantum computing and could be a key element of topological quantum computing architectures [192, 195].

4.5 Outlook

Finally, we emphasize that the experiments presented in this study can be adapted for other vdW materials and for more complex heterostructures, the planar geometry of which is highly integrable to the cQED architecture. The extraordinary and versatile electronic properties of these heterostructures, in combination with their epitaxial precision, make vdW-based devices a promising alternative for constructing key elements of novel solid-state quantum computing platforms. A hybrid superconducting circuit with vdW materials also provides a fertile arena for studying the light–matter interaction in such materials, as well as probing the electronic degrees of freedom using a non-invasive approach with high precision. Of particular interest are systems showing intrinsic superconductivity with a topological phase [202] or many-body phases [83], which can be readily incorporated into a superconducting quantum circuit similar to the one presented herein.

Chapter 5

Highly tunable junctions and non-local Josephson effect in magic-angle graphene tunnelling devices

As was introduced in Chapter 2.8, magic-angle twisted bilayer graphene (MATBG) is a highly tunable two-dimensional (2D) material platform that can exhibit a wide range of phases, such as metal, insulator, and superconductor states. Local electrostatic control over these phases may enable the creation of versatile quantum devices that were previously not achievable in other single material platforms. In this chapter, we engineer Josephson junctions and tunneling transistors in MATBG, defined solely by electrostatic gates. Our multi-gated device geometry offers independent control of the weak link, barriers, and tunneling electrodes. These purely 2D MATBG Josephson junctions exhibit nonlocal electrodynamics in a magnetic field, in agreement with the Pearl theory for ultrathin superconductors. Utilizing the intrinsic bandgaps of MATBG, we also demonstrate monolithic edge tunneling spectroscopy within the same MATBG devices and measure the energy spectrum of MATBG in the superconducting phase. Furthermore, by inducing a double barrier geometry, the devices can be operated as a single-electron transistor, exhibiting Coulomb blockade. With versatile functionality encompassed within a single material, these MATBG tunneling devices may find applications in graphene-based tunable superconducting qubits, on-chip superconducting circuits, and electromagnetic sensing. These

results have been published in reference [3].

5.1 Introduction

Tunneling devices are ubiquitous in modern electronics, with applications ranging from tunneling diodes to magnetic tunnel junctions and superconducting Josephson Junctions (JJ). These devices typically involve heterojunctions of different materials to achieve conducting electrodes in series with a weak link or insulating barrier [45, 203]. In superconducting circuits, state-of-the-art JJs utilizing oxide tunnel barriers often suffer from disorder and localized states in the noncrystalline barriers [69]. Semiconductor-based JJs necessarily involve heterojunctions, and thus potentially non-ideal interfaces, but offer some advantages for integrated electronics, such as partial tunability of the semiconducting weak link [181, 2]. While this offers a number of different operation regimes, the ability to independently tune the electrodes into different phases would enable an exponentially larger number of tunable configurations, qualitatively changing the nature of the device *in situ*. A superconducting junction made of a single clean material, which simultaneously offers a high degree of tunability both in the weak link and in the superconducting electrodes themselves, is therefore highly desirable, but has not been realized to date.

The recent discovery of correlated insulators and superconductivity in MATBG (see Chapter 2.8) accessible via electrostatic doping [79, 83, 122, 116] makes this possible, introducing MATBG as an unexplored material platform for superconducting electronics. Using electrostatic gating, a plethora of possible regimes, including p-n junctions, superconducting regions, metallic leads, and insulating islands, among others, become accessible in a single device, making this system attractive both for scientific and technological applications. We exploit this unprecedented tunability to create an all-in-one device that can be used both for superconducting electronics and normal-state operations, bridging the fields of tunable van der Waals materials and superconducting circuits. This could open the door towards fully integrated superconducting electronics, where entire circuits are made out of a single material with local gates and customizable coupling within and between each of the electronic components.

In this chapter, we demonstrate the versatility of multiply-gated MATBG devices. We report on fully tunable lateral JJs, where both the superconducting electrodes and the weak link can be locally controlled. Such JJs additionally provide definitive evidence of superconducting phase coherence in MATBG. Independent control of the weak link is performed via applying a top gate voltage, achieving a junction that can be continuously switched from insulating, metallic, to superconducting regimes, generating a tunable critical supercurrent. In the same multi-gated devices we obtain spectroscopic evidence of the superconducting gap in MATBG by utilizing its intrinsic bandgaps to create lateral tunneling barriers. Finally, inducing barriers on either side of a narrow MATBG strip allows us to transform the device into a single-electron transistor displaying periodic Coulomb diamonds.

5.2 Highly Tunable Josephson Junctions

To demonstrate these effects, we have measured three superconducting devices labeled A, B, and C. All devices were fabricated using the tear-and-stack dry-transfer technique [140, 94, 79] (see Chapter 2.9 for a detailed description of sample fabrication). Here, we focus on device A with a twist angle $0.95^\circ \pm 0.02^\circ$ (see Chapter 2.10.2 for the twist angle extraction). The entire device is gated by the back gate, while the top gate is patterned into a narrow strip ($\sim 160\,\text{nm}$) at the center of the device to enable independent control of the region underneath it (Figure 5-1a). Fig. 1b shows the temperature dependence of the resistance of device A at the optimal doping with $V_{tg} = 0\,\text{V}$, and back gate $V_{bg} = -1.4\,\text{V}$ (corresponding to the blue square in Fig. 5-1c), displaying a superconducting transition at $T_c \sim 0.85\,\text{K}$, as estimated from 50% of the normal state resistance. The non-linear I-V curves captured near optimal doping (Fig. 5-1c inset) display zero resistance up to a critical current $I_c \approx 35\,\text{nA}$.

To map out the complex electrostatic response of these devices, we now explore the complete dual-gate parameter space available, which exhibits a number of different insulating, metallic, and superconducting states. Using the back gate and narrow top gate together, we can define three separate regions within the same device with independent phases in series. In each region of the MATBG, when the four-fold valley and spin-degenerate bands

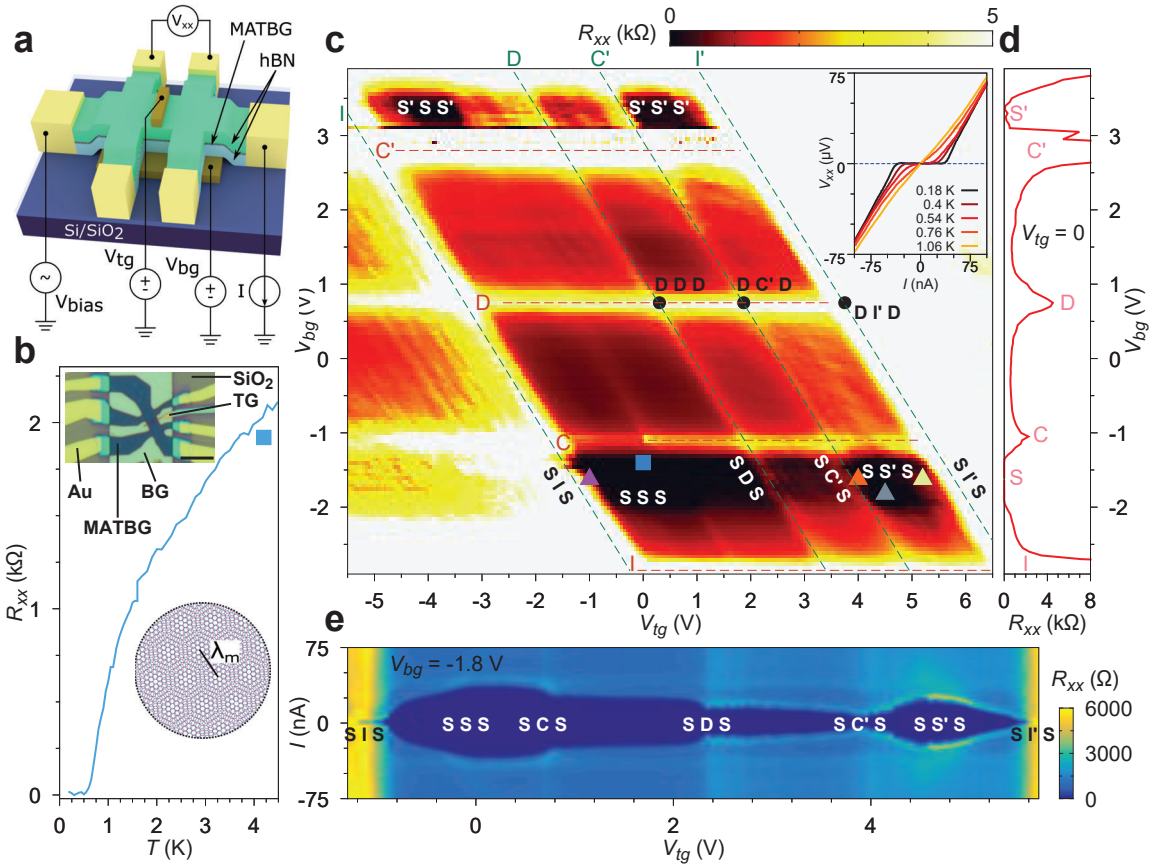

Figure 5-1: Device 'A' structure and transport characterization. (a) Schematic illustration: A narrow top gate (~ 160 nm wide) controls the electronic state of the region underneath. (b) Resistance vs. temperature curve measured at the blue square in panel (c). Upper left inset: optical image of the final device. A back gate (BG) tunes the electron density in the overlapping region of the MATBG. The narrow top gate (TG) controlling the electronic state of the weak link can be seen at the center of the device. A bias voltage V_{bias} is applied between the drain and source electrodes, and the 4-probe resistance $R_{xx} = V_{xx}/I$ is measured. The scale bar corresponds to 4 μm. Lower right inset: moiré pattern in twisted bilayer graphene. The displayed twist angle is enlarged for clarity with respect to the first magic angle $\theta \approx 1.1°$. The moiré wavelength is given by $\lambda_m = a/[2\sin(\theta/2)]$, where $a = 0.246$ nm is the lattice constant of monolayer graphene, and θ is the twist angle (see Chapter 2.6). (c) Resistance as a function of the back gate and the top gate. The dark regions correspond to the superconducting states. Color-coded triangles indicate the points at which Fraunhofer patterns are taken in Fig. 5-2. Inset: Current-Voltage curves measured at $V_{bg} = -1.6$ V, $V_{tg} = 0$ V at different temperatures. (d) Line-cut in panel (c) along $V_{tg} = 0$. I = Full filling band insulating state, S = Superconducting, C = Correlated Insulator at Half Filling, D = Dirac (charge neutrality) point. Primes denote positive fillings (i.e., electron doping). (e) Resistance as a function of current bias and top gate voltage, for $V_{bg} = -1.8$ V in the superconducting state.

are fully filled or fully depleted at densities $n = \pm n_s$, where $n_s = 4/A$ and A is the area of the moiré unit cell, the system behaves as a band insulator [94, 123, 104]. In the following, we denote the insulator at $-n_s$ as I, and the insulator at n_s as I'. Correlated insulator states are observed at $n = \pm n_s/2$, and we denote them as C ($-n_s/2$) and C' ($n_s/2$), respectively. Similarly, S and S' denote the superconducting states near $\mp n_s/2$, respectively. Let us also denote D as the charge neutrality (Dirac) point, and n (n') the normal metallic states at fillings $n < -n_s$ ($n > n_s$), when the higher energy dispersive bands become populated by holes (electrons). Metallic states are also observed throughout the flat bands, away from charge neutrality and the correlated fillings, denoted as N. Fig. 5-1d shows a vertical line cut of the resistance map at $V_{tg} = 0\,\mathrm{V}$. The transition between the different series combinations of the central and outside regions are readily seen from the horizontal and diagonal features of the V_{tg}-V_{bg} resistance map (Fig. 5-1c). We interpret the diagonal features (dependent on both V_{tg} and V_{bg}) as stemming from the dual-gated region beneath the top gate, and the horizontal features (independent of V_{tg}) as coming from the regions outside the top-gated area. The intersection between a few horizontal (red) and diagonal (green) lines are labeled with black circles in Fig. 5-1c. For example, DDD denotes the coincidence of the Dirac points in all three regions, whereas DC'D occurs when the central region enters the C' correlated insulator state and the outside regions are at charge neutrality, and similarly for other intersections of the dashed lines. More interesting device behavior is obtained by doping away from the horizontal lines in the dual-gate map. For instance, supercurrent through a variable Josephson junction is observed across the device if we use V_{bg} to globally tune the MATBG into S and use V_{tg} to form a weak link with the central region in an insulating state (diagonal labels in Fig. 5-1c) such as C', or close to the resistance maxima of states I and I' (before the sample becomes fully insulating). White labels of the form *SXS* or *S'XS'* indicate that at these points the source and drain are in S or S' state while the top-gated region is in the X=I', C', D, S, S', C, or I state. Figure 5-1e illustrates the wide region of supercurrent observed (dark blue), whereas the ability to continuously vary the barrier strength with V_{tg} is indicated by the evolution of the critical current (where the differential resistance becomes finite). We can turn off the supercurrent completely by gating the central region deep into the insulating state (beyond full filling).

In this regime the superconducting coherence across the junction is lost, and a dissipative junction is obtained.

5.3 Nonlocal Josephson Effect

Next we address the expected behavior for 2D JJs in the presence of magnetic flux. 2D superconductors screen external magnetic fields in a fundamentally different way from their bulk (3D) counterparts (see Chapter 2.3). In ultra-thin superconductors where the film thickness is less than the London penetration depth λ, the characteristic length that governs the spatial magnetic field distribution is given by the Pearl length [204] $\Lambda = 2\lambda^2/d \gg \lambda$, where d is the film thickness. In the case of MATBG, the thickness is less than 1 nm and the Pearl length can reach macroscopic dimensions, exceeding the dimensions of the device itself. Under such conditions, the screening currents cannot effectively expel the external magnetic field (illustrated in Fig. 5-2a), in striking contrast with bulk samples (Fig. 5-2b). The origin of this effect can be understood by recognizing that the self-field of the screening current in a thin-film superconductor scales as $\frac{w}{\Lambda}B$, where w is the lateral dimension of the sample and B is the external magnetic field [205]. When $w \ll \Lambda$, the self-field is therefore negligible compared to the external field, allowing finite field penetration.

The distribution of Josephson current and magnetic flux in a JJ is altered in the 2D limit as well. In a bulk JJ, the magnetic field only penetrates a distance $\sim \lambda$ into the superconductor and is therefore mostly confined within the junction barrier. The phase difference across the junction is a simple function that only depends on λ and B (see Chapter 2 for additional information on bulk Josephson junctions). On the other hand, for edge-type Josephson junctions in ultra-thin films, the magnetic field distribution is not confined to the tunneling barrier (Fig. 5-2c). An additional distinction between bulk and edge-type 2D JJs is that the Josephson electrodynamics are nonlocal in the 2D case, that is, the magnetic flux in the junction results from a non-negligible superconducting phase gradient in both 2D superconducting regions[206, 207, 45, 208].

In Fig. 5-2c-d, we simulate the magnetic field and the screening currents in a bulk JJ and a 2D JJ with similar dimensions as device A, placed in an external magnetic field $\mathbf{B} =$

$B_0\hat{z}$[209, 210, 205]. From the magnetic field distribution, we can obtain the distribution of the phase difference across the junction which gives rise to the Fraunhofer interference pattern (section 5.8.7). Our calculated field dependence of the maximum supercurrent in the 2D JJ, in agreement with previous analytical and numerical predictions [209, 210, 205, 211], differs noticeably from the typical Fraunhofer pattern of bulk junctions in two ways (Fig. 5-2e). First, the high-field periodicity $\sim 1.8\Phi_0/w^2$ depends solely on the geometry of the sample and is usually much smaller than the bulk periodicity $\Phi_0/w(a+2\lambda)$, where a is the length of the weak link itself. Second, unlike the bulk case, the zeros of $I_c(B)$ for edge-type thin-film junctions are not equidistant at low-fields.

We now present measurements to test these predictions experimentally. Based on the analytical expression $1.8\Phi_0/w^2$, we expect an interference period ~ 1.7 mT in device A ($w \approx 1.5$ μm). We first gate the device into the SIS regime, pushing the middle region as far as possible into the insulating region while maintaining superconducting coherence across the junction (Fig. 5-3a). We observe field-induced oscillations in the critical current with a periodicity of $\sim$ 1–1.5 mT for the finest oscillations. An approximation of the bulk formula Φ_0/wl using $l \approx a$ gives a periodicity of 8.5 mT, significantly larger than the measured oscillation period. However, our measured periodicity of $\sim$ 1–1.5 mT is clearly in agreement with the simulations (Fig. 5-2e) and consistent with the Pearl regime governing the ultrathin superconducting electrodes. This anomalous periodicity is further corroborated by devices B and C (Figs. 5-8 and 5-10). Critical current oscillations with similar periodicity are also observed close to the SC'S (Fig. 5-3b) and SI'S (Fig. 5-3c) configurations. Slight deviations from ideal Fraunhofer behavior and differences between each pattern may be attributed to inhomogeneities and asymmetries across each junction. Josephson oscillations with correlated insulator barriers are weaker in comparison to the SIS and SI'S configurations, possibly due to smaller bandgaps in C, C' compared to I, I', as determined by thermal activation [79]. Overall, a weak link between superconducting regions is achievable in this geometry using different insulating phases. Alternatively, if we bring the weak link into the SS'S regime, the oscillations in the critical current disappear (Fig. 5-3d). Another piece of evidence for the nonlocal Josephson effect [207] is the resistance as a function of the magnetic field and temperature of the junction close to the SIS

regime (Fig. 5-3f). The oscillation period does not change as the temperature approaches T_c. This is in contrast to the expected behavior in the local regime where, since $\lambda(T)$ diverges as $T \to T_c$, one expects the oscillation period, which is inversely proportional to λ, to be progressively suppressed with temperature [212].

In the SnS regime, we find oscillatory behavior of the critical current with respect to V_{tg} (Fig. 5-3e). We attribute this to a Fabry-Pérot-like resonance from the interfaces between the dual-gated region and the singly gated regions, which occurs in high-quality devices close to the ballistic transport regime [156, 155]. In a JJ, I_c and the normal state resistance R_N typically scale inversely with each other (the Ambegaokar-Baratoff relationship [45]). When the Fabry-Pérot resonance of the electron wave becomes prominent, R_N and I_c are periodically modulated by $\sqrt{n + n_s}$. We observe the resonance only in the SnS regime, likely due to the low effective mass and high mobility in the dispersive band at $n < -n_s$.

5.4 Tunneling spectroscopy in the superconducting regime

We now turn our attention to devices B and C with the structure shown in Fig. 5-4a. Instead of the narrow top gate in device A, here we pattern two isolated top gates separated by a narrow gap, allowing us to realize a p-n junction. In Fig. 5-4b, we show the simulated charge carrier density distribution across a gate-defined p-n junction (relative to $-n_s$) in a scenario similar to device B (section 5.8.8). The density evolves continuously and crosses the value $n = -n_s$ at a position between the left gated and right gated regions. Due to quantum capacitance effects in MATBG, a narrow region is kept inside the bandgap at $-n_s$ and acts as a tunneling barrier. If we put one side of the junction in the S state, we then realize an nIS configuration, enabling edge tunneling spectroscopy into the S state, where the tunneling current flows between the 1D edge along the n-I boundary and the 1D edge along the I-S boundary. Using this configuration, in Fig. 5-4c-f we show tunneling spectra of MATBG in the superconducting regime.

The data show clear spectroscopic evidence of a superconducting gap, including well-

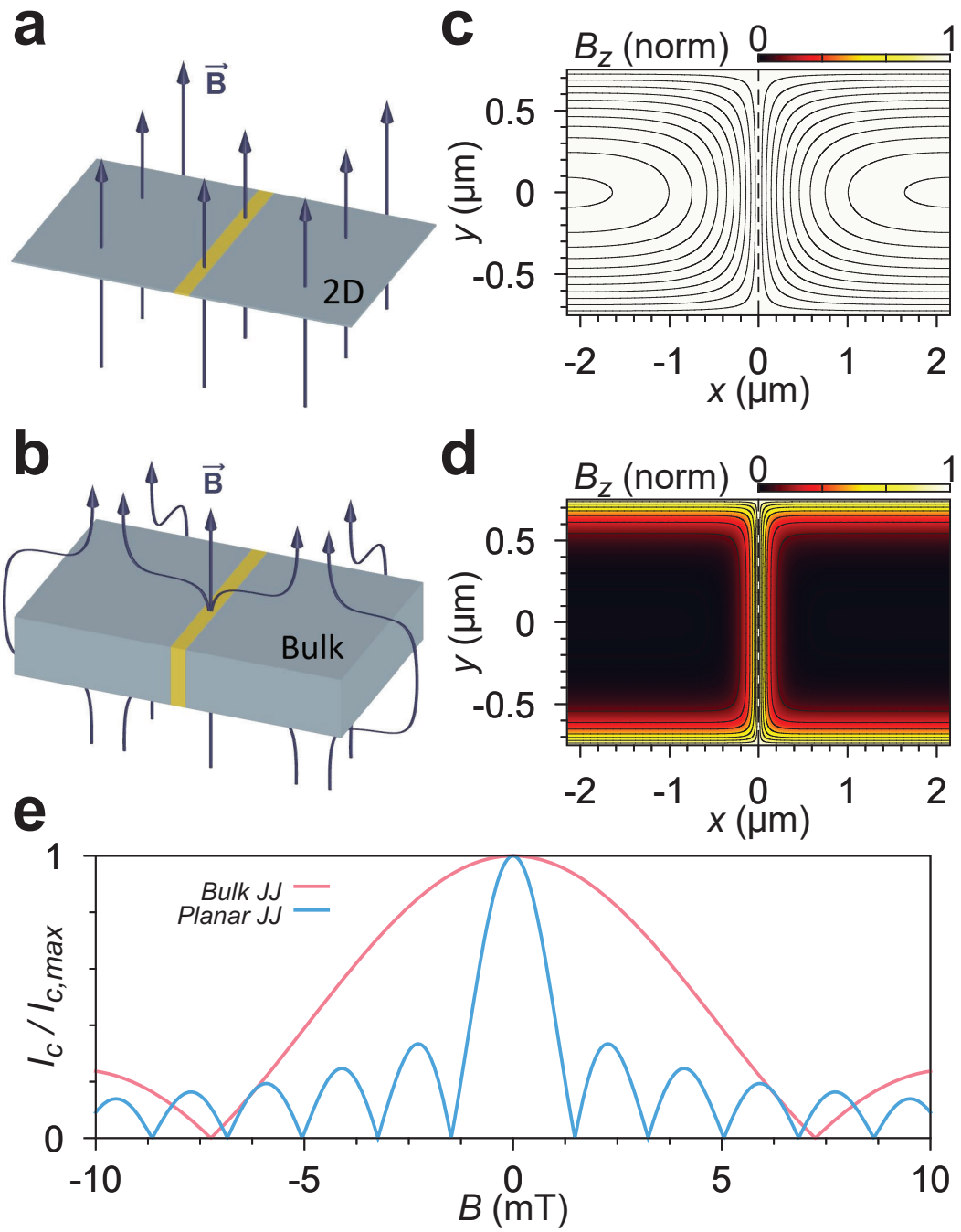

Figure 5-2: Comparison of planar 2D and bulk Josephson junctions. (a-b) Schematic representation of (a) a planar 2D Josephson junction and (b) a bulk Josephson junction in an external magnetic field. (c-d) Simulated distribution of the normalized magnetic field B_z in a Josephson junction located at $x = 0$ in the case of (c) planar and (d) bulk superconductor (see section 5.8.7). While in bulk superconductors (d), the magnetic field decays exponentially at the edges within a distance λ, in the 2D case (c), it is essentially unaltered across the entire sample area. The streamlines denote the flow of screening currents in the superconductor. The bulk case assumes a penetration depth of $\lambda = 100\,\text{nm}$. (e) Calculated critical current (normalized) as a function of the magnetic field for bulk and planar Josephson junctions.

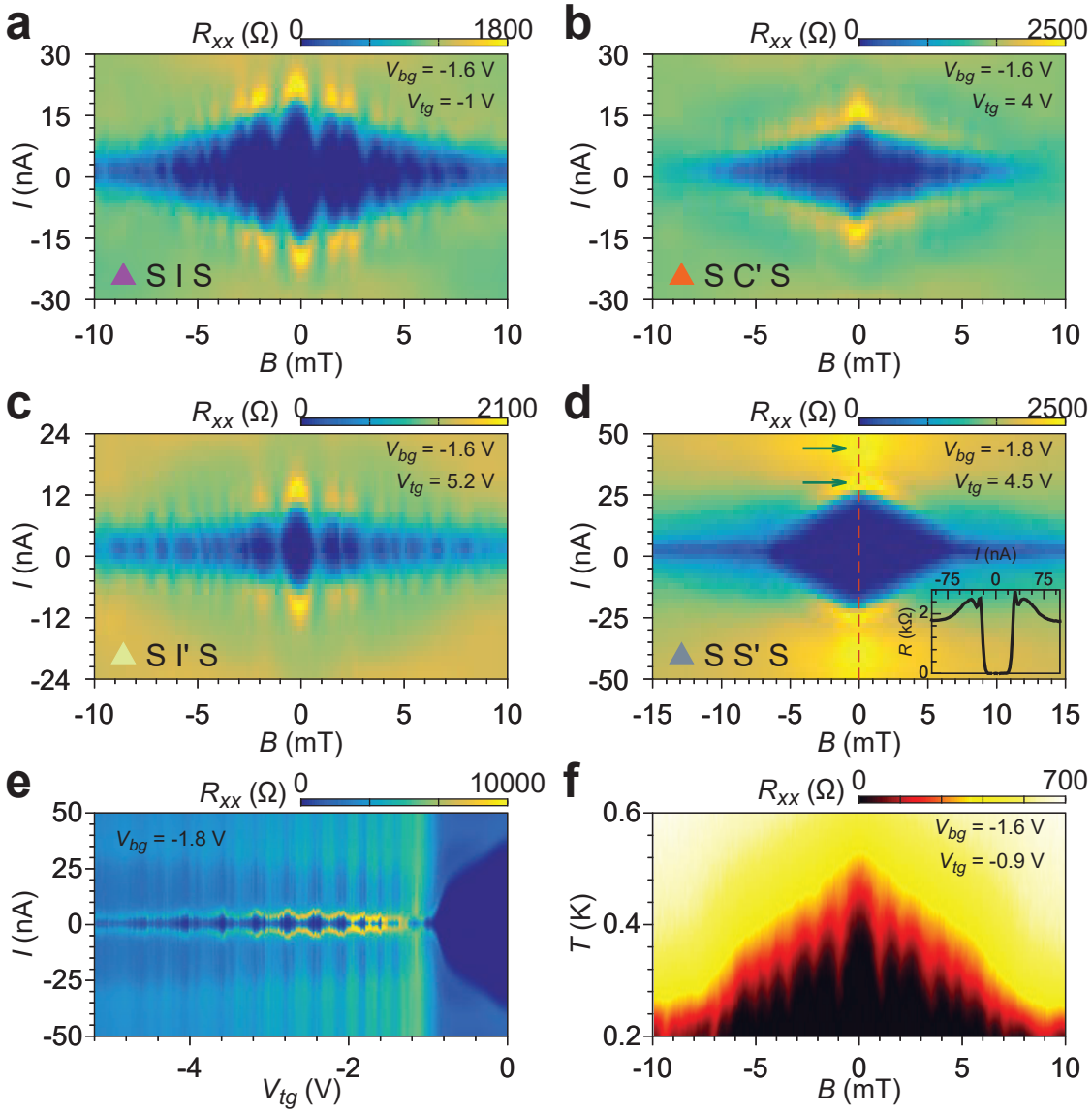

Figure 5-3: Nonlocality and tunability of MATBG Josephson junctions. (a-d) Measured Fraunhofer pattern in device A (a) close to SIS regime, (b) SC'S regime, (c) SI'S regime, and (d) SS'S regime. Color-coded triangles correspond to those in Fig. 5-1c. Inset in (d) shows a linecut across the red dashed line at $B = 0$ T. The two pairs of peaks in the curve correspond to the critical currents of the S and S' states, respectively (green arrows in main panel). (e) Fabry-Pérot-like oscillations in the critical current. (f) Resistance as a function of magnetic field and temperature of the junction close to the SIS regime.

defined coherence peaks and a minimum at zero bias. We fit the spectral lineshape to a model for the quasiparticle density of states in an nIS junction to obtain a quantitative measure of the gap. Choosing the simplest such model, that of a conventional isotropic s-wave order parameter [45], we incorporate the effects of thermal and lifetime broadening, and extract a gap of $\Delta_{\text{fit}} = 44\,\mu\text{eV}$ at $T = 95\,\text{mK}$ for device B, and $\Delta_{\text{fit}} = 51\,\mu\text{eV}$ at $T = 100\,\text{mK}$ for device C (see section5.8.10). The tunneling conductance minimum and coherence peaks are well captured by this fit, including the absence of a hard gap due to thermal broadening at the lowest experimental temperature. We note that, microscopically, the density distribution is more intricate than the ideal nIS profile due to the nature of the edge tunneling scheme (Fig. 5-4b). The energy spectra may include a contribution from proximitized normal regions $\tilde{\text{N}}$ between the superconductor and the insulating state (resulting in an nI$\tilde{\text{N}}$S distribution), in addition to other weaker superconducting states, thus leading to an underestimation of the superconducting gap. Taking the $\Delta_{\text{fit}} = 51\,\mu\text{eV}$ for device C as a lower bound for the superconducting gap at zero temperature ($\Delta_{\text{fit}} \lesssim \Delta_0$), we can estimate an associated transition temperature from the BCS approximation $T_c \gtrsim \Delta_{\text{fit}}/(1.764k_B) \approx 340\,\text{mK}$. This value is reasonable considering the transition temperature extracted from 50% of the normal-state resistance at a nearby doping value, $\sim 400\,\text{mK}$ (see Fig. 5-10). However, we emphasize that such a fitting procedure cannot distinguish the symmetry of the superconducting order parameter in our data, as there is significant spectral broadening due to temperature, disorder, and the lateral junction geometry. In fact, we have found equally good quality fits using other non s-wave order parameters. Direct measurements of the pairing symmetry in MATBG remain a fundamental yet unresolved question in the field, and these device structures may be adapted to shed light on this topic.

As the temperature is increased above $\sim 300\,\text{mK}$ (for both devices B and C), the coherence peaks are significantly broadened due to thermal excitations. As the temperature is further increased, the dip at $V_{\text{bias}} = 0$ is suppressed and eventually disappears, indicating that the system is no longer superconducting. Similarly, by applying a perpendicular magnetic field at base temperature, the coherence peaks are also suppressed at $B \approx 50\,\text{mT}$ for device B ($B \approx 100\,\text{mT}$ for device C), comparable to the upper critical field observed in transport in magic-angle devices with similar T_c [83]. The closing of the gap and sup-

pression of the coherence peaks with temperature and magnetic field further support a superconducting origin for the observed gap. A portion of the tunneling minimum at zero bias persists to much larger magnetic fields, however, a similar tunneling minimum is observed above the critical field for a wide range of densities outside of the superconducting dome, without associated coherence peaks at zero field (Fig. 5-12), and thus arises from a distinct mechanism. Such a suppression in the tunneling spectra may be related to the Efros-Shklovskii-type Coulomb gap that arises at the Fermi level due to localization in disordered semiconducting thin films [213, 214], or alternatively, it may result from electronic interactions during the tunneling process [215, 216, 217]. Although we consistently observe a suppression in the tunneling conductance at zero bias for all three measured devices, further detailed studies are required to determine the precise origin of this spectral feature.

5.5 Single-Electron transistor regime

Further exploiting the flexibility of the split-gate geometry, we can create a single-electron transistor (SET) within the same multipurpose devices. To achieve this, we tune the left and right top gates to bring the two sides of the device into metallic states with densities $n < -n_s$. The central narrow region, being singly gated, is brought into the density range $-n_s < n < -n_s/2$. With similar arguments as those mentioned above, two insulating plateaus with $n = -n_s$ form around the central region of the sample, resulting in an isolated island in the middle. Fig. 5-5a illustrates such an nINIn configuration, as seen from above, and the calculated charge carrier density distribution. At low temperatures ($k_B T \ll e^2/C_\Sigma$, where C_Σ is the total capacitance of the island) and with large tunneling resistance ($R_{\text{tunnel}} \gg h/e^2$), electron tunneling is allowed only if there are available discrete energy levels between the Fermi energies of the source and the drain (Fig. 5-5b), whereas the Coulomb blockade effect prohibits tunneling otherwise (Fig. 5-5c) [45, 218].

In Fig. 5-5d, we measure the tunneling conductance of the gate-defined single-electron transistor as the back gate voltage is varied, keeping the source and drain densities fixed. The signal displays fine, reproducible oscillations as a function of the back gate voltage. A

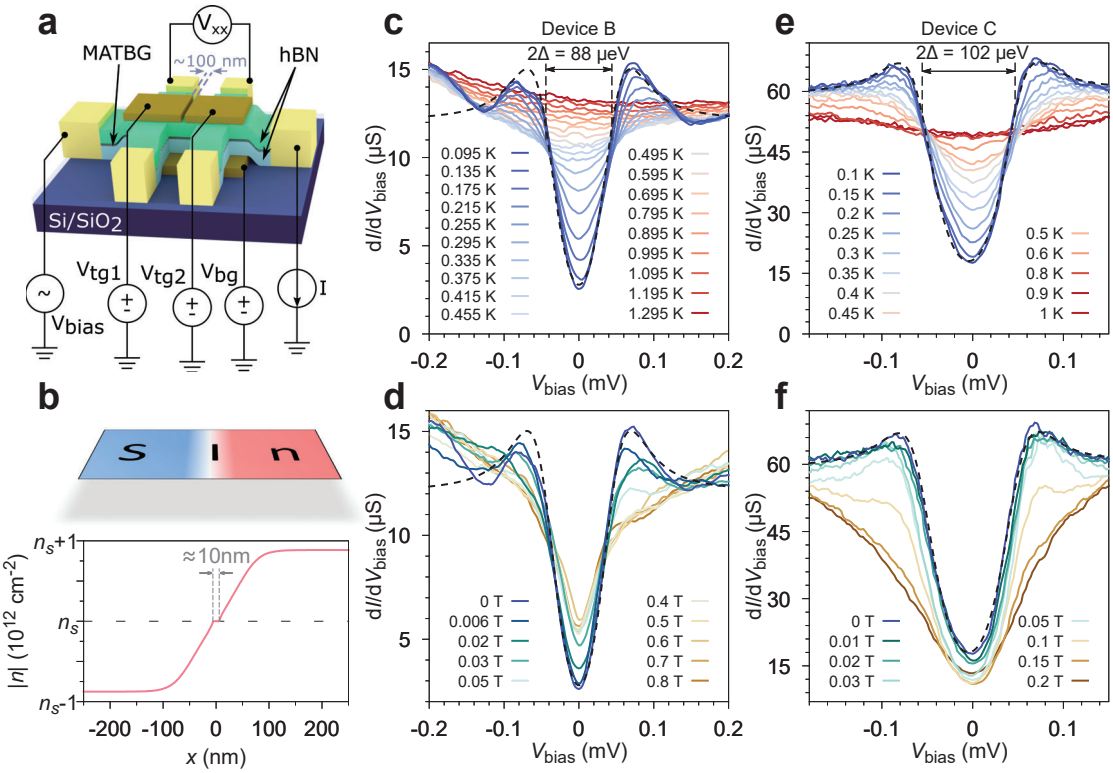

Figure 5-4: Edge tunneling spectroscopy of the superconducting gap in MATBG. (a) Structure of devices B and C with two top gates separated by a narrow gap. (b) Numerical calculated charge carrier density distribution in the p-n junction regime performed for device B (device C analogous). The left half is brought into the superconducting state S at $n \approx -0.6n_s$, while the right half is brought into a normal metallic regime with density $n \approx -1.4n_s$ (all densities are for hole doping and thus are all negative). In the central region of the device, the density passes through the band insulator I ($n = -n_s$), thus creating a tunneling barrier. (c) Raw tunneling spectra as a function of temperature, from 0.095 K to 1.295 K for device B. The black dashed line is a theoretical fit to the quasiparticle density of states (section 5.8.10), yielding an extracted gap $\Delta_{\text{fit}} = 44\,\mu\text{eV}$ (with negligible broadening). (d) Magnetic field dependence of the edge tunneling spectra, from 0 T to 0.8 T for device B. (e) Similarly, tunneling spectra as a function of temperature and (f) perpendicular magnetic field for device C, with the left half of the device in the superconducting state S at $n \approx -0.775n_s$, and the right half at a density $n \approx -1.2n_s$. The dashed line is the theoretical fit giving an extracted corresponding gap $\Delta_{\text{fit}} = 51\,\mu\text{eV}$ (with Dynes broadening $15\,\mu\text{eV}$).

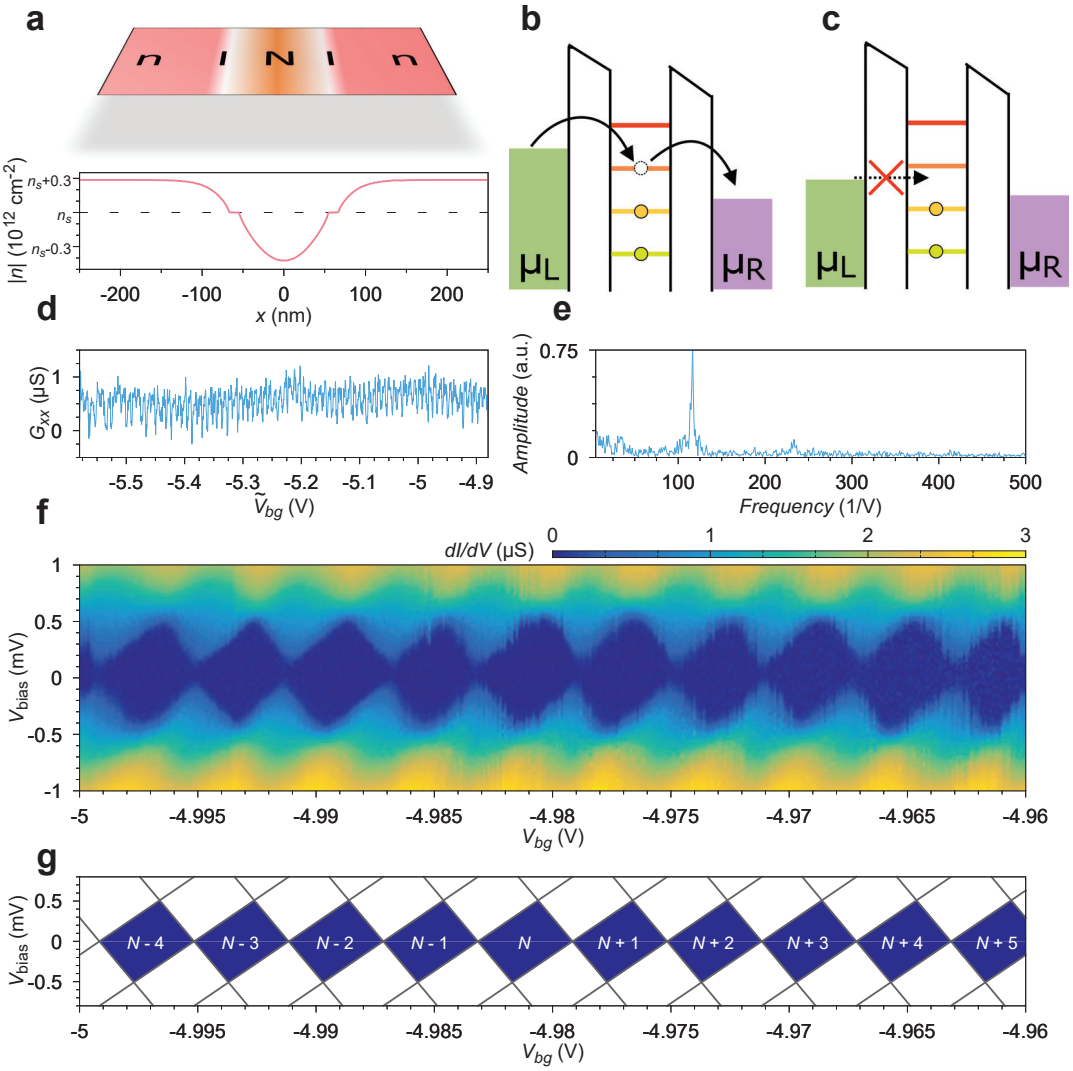

Figure 5-5: Electrostatically defined single-electron transistor and Coulomb blockade in MATBG. (a) Gating scheme of the device and simulation of the charge density across the sample. Two effective insulating barriers emerge, and the central island can be operated as a single-electron transistor. (b-c) Schematic space-energy diagram of a single-electron transistor in the (b) conducting and (c) Coulomb blockade regimes. μ_L and μ_R are the chemical potentials of the source and drain electrodes, respectively. (d) Conductance versus back gate voltage V_{bg}, while the two top gates keep the densities on the source and drain at $n \approx -1.1 n_s$. (e) Fourier transform of the two-probe tunneling current, showing a single peak at $116\,\mathrm{V}^{-1}$. (f) Differential conductance as a function of back gate voltage and source-drain bias voltage. Pronounced Coulomb diamonds, corresponding to the absence of tunneling current, are observed. In this scan, only the back gate is swept while both top gates are fixed. (g) Schematic of the Coulomb diamonds (see text for the details). N denotes the number of electrons in the central island. The mismatch of the periodicities in panels (d-e) and panels (f-g) is attributed to cross-coupling of the top gates and is discussed in section 5.8.5 (we have added a tilde in the x-axis label of panel (d) to avoid possible confusion). All the data in this figure correspond to device B.

Fourier transform of the measured tunneling current reveals a single periodicity (Fig. 5-5e). Figure 5-5f shows the differential conductance in a narrower range of back gate voltages, as a function of the source-drain bias voltage. We observe well-developed Coulomb diamonds with zero conductance in the blockaded regime. These observations are in agreement with a single-electron transistor with capacitances $C_g = 40\,\text{aF}$, $C_1 \approx C_2 = 110\,\text{aF}$, $C_\Sigma = 310\,\text{aF}$ (see section 5.8.5 for definitions), as shown in Fig. 5-5g. Thus we find that the band insulator in MATBG provides a suitable barrier for SET physics in graphene with appropriate local gating, adding to the broad tunability of these MATBG devices.

5.6 Summary and outlook

The unprecedented tunability of MATBG together with local electrostatic gating in this work enables complete control of the weak link and junction electrodes, independently. With this versatile platform, we demonstrate multiple Josephson junctions with differing barrier strength and character, edge-tunneling spectroscopy of the superconducting state, and robust SET physics in a double-barrier configuration. While multiple devices are presented here, critically, all three aforementioned experiments are achievable in a single device geometry. Gate-defined tunnel junctions present a significant advance toward probing the superconducting order parameter in MATBG, and will inspire further advances for exploring physics within the expanding class of moiré systems. Furthermore, these multipurpose devices establish a clear path toward gate-defined circuits with MATBG in future 2D integrated electronics, with potential applications in low-temperature circuits, quantum computing, and electromagnetic sensing.

5.7 Comparison of our work with a related experiment, published in the same issue of Nature Nanotechnology

These results were originally published alongside an independent but related work on gate-defined Josephson junctions in MATBG [219]. In reference [219], the authors electrostatically define the superconducting and insulating regions of a Josephson junction and observe

tunable d.c. and a.c. Josephson effects. The device of de Vries *et al.* is similar to the one reported in Fig. 5-5. However, their configuration allows them to define Josephson junctions with different lengths by using combinations of the L (left), R (right), and C (central) gates. The central gate C, in particular, is obtained by evaporating another gate on top of the two left and right top gates, separated by a thin layer of AlO_x, which tunes the center of the junction away from the SC state. For the observation of the a.c. Josephson effect, they applied a radiofrequency voltage excitation to the central gate C, leading to the observation of Shapiro steps that are proportional to the frequency and the superconducting flux quantum $h/2e$.

In contrast to our work, they do not report tunneling spectroscopy or single electron transistor behaviour in their devices. On the other hand, they report the observation of the a.c. Josephson effect and Shapiro steps. Also, contrary to our work, their device is 2-terminal, whereas ours are all 4-terminal. They, therefore, do not measure 0-resistance in the superconducting state, due to contributions from the contact and lead resistances.

Finally, they also observe a Fraunhofer pattern in the presence of a small perpendicular magnetic field compatible with the theoretical prediction for purely 2-dimensional Josephson Junctions. As predicted, the maxima of the critical current in their device scale proportionally to the inverse square root of the magnetic field. However, the periodicity observed by de Vries *et al.* does not seem to follow the expression $1.8\Phi_0/w^2$. This deviation might be caused by the appearance of unintentional junctions due to twist angle inhomogeneity, similar to the ones reported in ref. [83].

Our results and the related work from ETH received good press in the media. The journal Science was the first one to feature these reports [220], as soon as we posted them in the Arxiv around the same time. Nature Nanotechnology dedicated a News and Views article [221] in the same issue, and immediately after publication, several media reported our results, including MIT News, La Vanguardia, and Phys.org.

5.8 Extended data and supplementary information

5.8.1 Additional Fraunhofer patterns for device A

Figure 5-6a shows the magnetic field dependence of a horizontal line cut in Fig. 5-1c for $V_{bg} = -1.6\,\mathrm{V}$, which gates the source/drain regions into the superconducting state. The vertical red lines label the electronic state of the region under the narrow top gate. By fixing the density at one of those top gates or close-by values, and the back gate such that the rest of the junction is in the superconducting state, our devices can realize a tunable Josephson junction. Figure 5-6b displays the resistance as a function of top gate and current bias for the back gate in the superconducting state.

Here, we show additional Josephson effect measurements, specifically in the SSS and S'SS' regimes, in addition to the ones shown above in Fig. 5-3. In particular, in principle if we switch the top gate voltage to 0 V, the entire device becomes superconducting. In this SSS case (see Fig. 5-6c), we do not observe a clear Fraunhofer-like pattern. The small oscillations in the critical current may arise from inhomogeneity in the device. It is also possible to realize a junction with the superconducting electrodes on the electron doping (S') by putting $V_{bg} = 3.2\,\mathrm{V}$, and use the top gate to bring the narrow region into S state, *i.e.* an S'SS' junction (similar to Fig. 5-3d, but swapping the S and S' states). Measurement in this regime is shown in Fig. 5-6d.

We note that no in-gap features, such as multiple Andreev reflections in the SNS regime (which would appear as local minima within the superconducting gap in dV_{bias}/dI versus V_{bias} at fractions of the superconducting gap 2Δ [222]) have been observed in our samples. This might be due to the fact the gap is small compared to the spectral resolution of our measurement.

5.8.2 Anomalous pattern in device A

We have argued previously that the oscillation period goes as $\sim \Phi_0/w^2$ for Josephson junctions in ultrathin films. However, we find that at one particular top and back gate voltage, the periodicity is anomalously larger than the above value by $\sim$6 times. This may

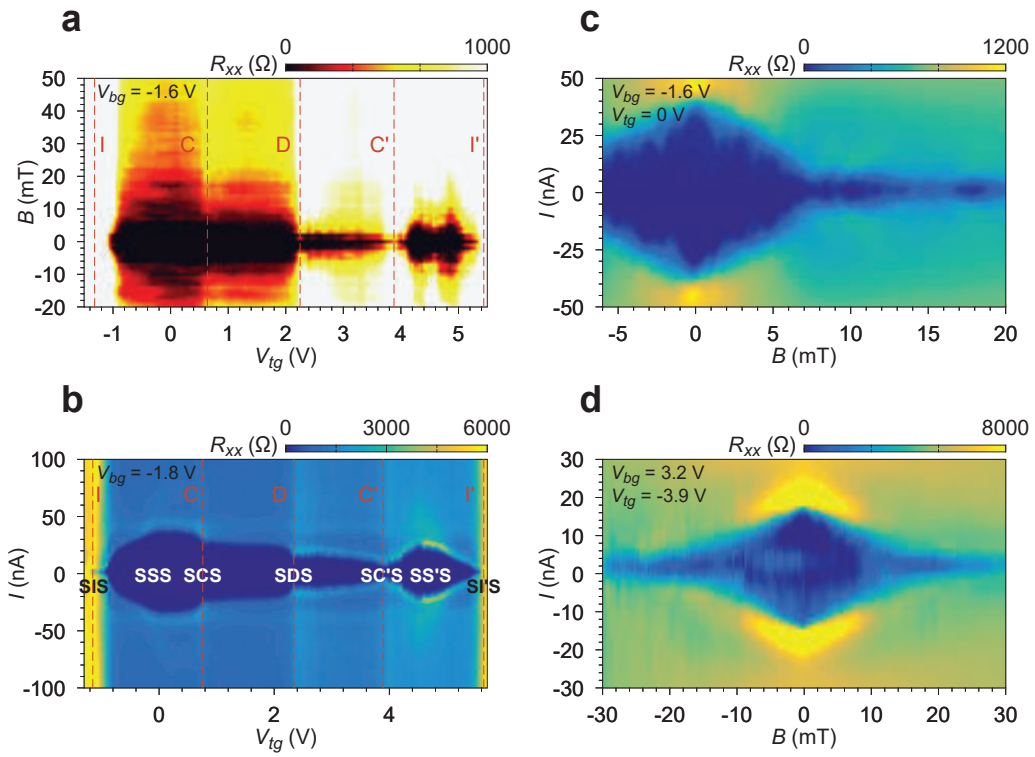

Figure 5-6: Supplementary Fraunhofer patterns for device A. (a) Magnetic field dependence of a horizontal linecut in Fig. 5-1c. The back gate is fixed at $V_{bg} = -1.6$ V, corresponding to the back gated region in the superconducting state. The states I, S, C, S', I' and D are labeled. (b) Resistance as a function of current bias and top gate voltage, for $V_{bg} = -1.8$ V in the superconducting state. The barrier strength of the junction is continuously tuned by the top gate voltage. Figure reproduced from Fig. 5-1e. (c) Interference pattern of the junction when the narrow top gated region is in the S state and the rest of the device in the superconducting state (SSS configuration), corresponding to $V_{tg} = 0$ V. (d) A similar experiment can be realized for the device in the superconducting state in the electron side, in an S'SS' junction.

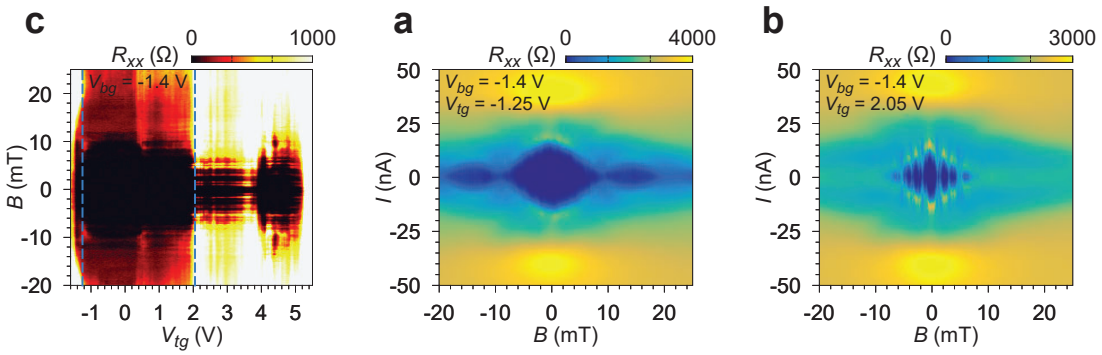

Figure 5-7: Anomalous Fraunhofer pattern in device A. (a) Magnetic field dependence of a horizontal linecut in Fig. 5-1c with the back gate fixed at $V_{bg} = -1.4$ V. (b) Interference pattern showing a periodicity ~ 10 mT ($\gg 1.5$ mT reported in the other interference patterns), resembling the Fraunhofer pattern of classical bulk Josephson junctions. We attribute this anomalously large periodicity to disorder at that particular voltages, and the close proximity of this scan to the insulating state as seen in panel (a). (c) Interference pattern at the same back gate voltage, and with a top gated region close to the Dirac point, displaying a periodicity of a few mT.

be attributed to an inhomogeneous distribution of current across the junction due to twist angle disorder, so that the effective junction width is much smaller than the width of the sample. Fig. 5-7b shows the R_{xx} data at this gate configuration.

For comparison, we also include a Fraunhofer pattern with the same back gate voltage but a different top gate voltage (close to the charge neutrality point), displaying an interference pattern with a similar oscillation period compared with the ones in Fig. 5-3a-c.

5.8.3 Transport characterization of device B

Device B shows a similar Josephson effect as device A, despite the different device structure (shown in Fig. 5-4a). Fig. 5-8a shows the 4-probe R_{xx} resistance as a function of V_{bg} and V_{tg} (the two top gates are connected together). The $V_{tg} - V_{bg}$ map for device B is fundamentally different compared the one for device A (see Fig. 5-1c). The top gate of device B covers most of the device except a narrow region of a few tens of nm at the center of the device (designed to be ~ 135 nm), in contrast to device A where the top gate only covers a narrow region at the center of the device. The horizontal features correspond to the sole effect of the back gate in the gapped region between the two top gates. Tilted features with a negative slope are associated with a constant density in the dual gated regions. The dark

region indicates the superconducting phase. It corresponds to a density range spanning around the half-filling state for holes, $n = -n_s/2 \pm \delta$ (following the notation introduced in Chapter 2.8).

Figure 5-8b displays the R-T curve in the superconducting state of device B, which shows a transition at 0.55 K, as estimated from 50% of the normal-state resistance value. Fitting the data to the Halperin-Nelson formula $R \propto \exp\left[-b/(T - T_{\mathrm{BKT}})^{1/2}\right]$, we extract $T_{BKT} = 0.3$ K [223]. The I-V curves are shown in Fig. 5-8c, for $V_{tg} = -2.7$ V, $V_{bg} = -2.18$ V. The critical current is ~ 20 nA.

Figure 5-8d shows the Fraunhofer pattern measured in device B in the SCS regime. The periodicity is approximately 3 mT, consistent with the estimate from theory of ultrathin Josephson junctions [205] ($w \approx 1.1$ μm in device B, the expected periodicity is around $1.8\Phi_0/w^2 \approx 3$ mT). Noticeably, the tunability of the barrier strength of the weak link in the configuration with two top gates is intrinsically much weaker than for the narrow top gate configuration, due to the edge capacitance effects from the top gates. We attribute this effect to the cross-doping of the weak link caused by the stray field from the top gates (even though the top gates are not placed directly above the weak link). We note that in this device, we did not find any double periodicity as observed in device A. In addition, the field dependence of the critical currents do not reach zero, which we attribute to the nonuniform Josephson coupling across the interface [224].

Similar to Fig. 5-3f for device A, in Fig. 5-8e we show the resistance as a function of temperature and magnetic field for device B, for the same configuration as in Fig. 5-8d. Consistent with device A, the oscillation period is invariant with temperature, which is consistent with the nonlocal electrostatic regime governing our samples [207].

5.8.4 Evidence of superconducting gap and single-electron transistor behavior in device A

Fig. 5-9 shows the possible coexistence of single-electron transistor (SET) behavior and superconducting tunneling in device A. At low bias voltages, we find Coulomb diamonds, while at larger bias voltages we find features consistent with tunneling spectra into the

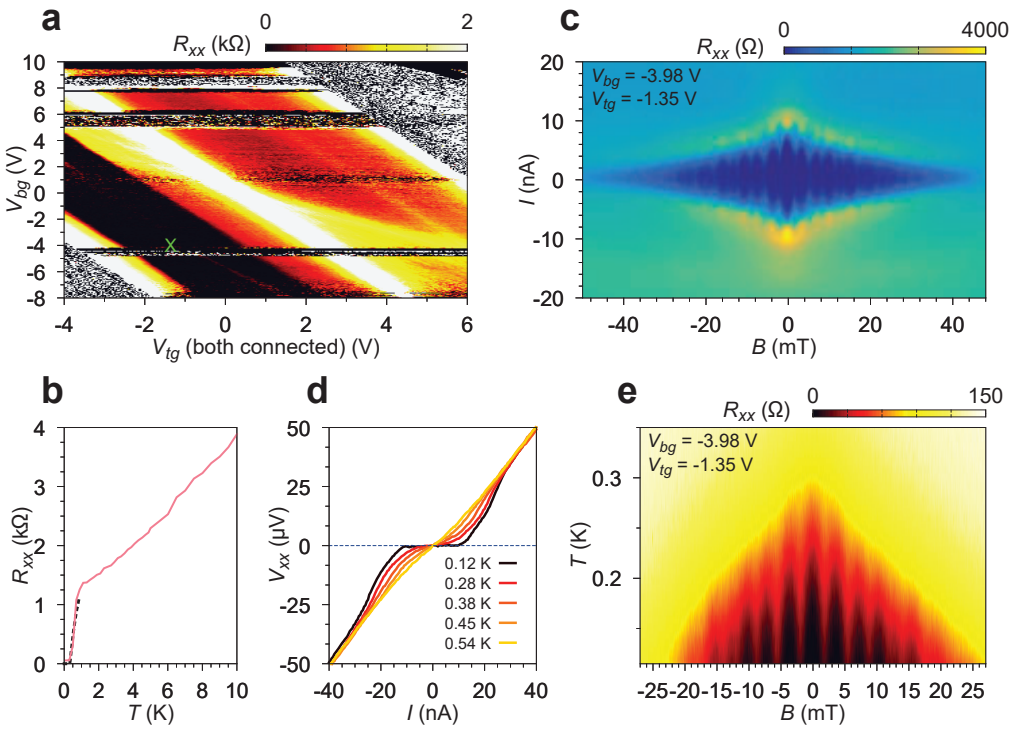

Figure 5-8: Transport characterization of device B. (a) Resistance as a function of top gates (both connected in parallel) and back gate. (b) Resistance vs. temperature trace. Device B shows a $T_c \sim 0.55\,\mathrm{K}$ ($V_{tg,both} = -2.58\,\mathrm{V}, V_{bg} = -2.4\,\mathrm{V}$). Black dotted lines show the fit to Halperin-Nelson formula $R \propto \exp\left[-b/(T - T_{\mathrm{BKT}})^{1/2}\right]$, giving $T_{BKT} = 0.3\,\mathrm{K}$ [223]. (c) Current–voltage ($V_{xx} - I$) curves in the superconducting region ($V_{bg} = -2.18\,\mathrm{V}$, $V_{tg,both} = -2.7\,\mathrm{V}$). (d) Characteristic interference pattern of device B for a region close to the SCS configuration, taken at the position of the green cross in panel (a). (e) Resistance as a function of magnetic field and temperature of the junction close to the SCS regime, for the same densities as the interference pattern shown in panel (d) ($V_{tg} = -1.35\,\mathrm{V}$, $V_{bg} = -3.98\,\mathrm{V}$).

superconducting gap. We attribute this unusual coexistence to the relatively low tunneling resistance of the insulating barriers $R \lesssim h/e^2$.

For small drain-source voltage biases, device A can be brought close to an SET regime by setting the back gate electrode to a density beyond the superlattice density for holes, and then tuning the top gate such that the central 'island' is in a superconducting state near $n = -n_s/2$. Because of the continuity of the charge density, two insulating regions in the superlattice gap $n = -n_s$ appear and provide a tunneling barrier connecting the electrodes to the central 'island' (in a similar fashion as in Fig. 5-5), thus creating a junction of the form nISIn.

Figure 5-9a shows the four-probe differential resistance as a function of the top gate voltage for a fixed back gate and bias voltage ($V_{bg} = -4$ V, $V_{bias,applied} = 40\,\mu$V). We perform the Fourier transform of these oscillations (see inset Fig. 5-9a) and find a prominent peak at a frequency of around 600 V^{-1}, corresponding to a periodicity of $1/600 = 1.7$ mV. If we sweep the bias voltage between the electrodes, we indeed observe Coulomb diamonds with periodicity ~ 1.7 mV (Fig. 5-9b). We note that the quality of the diamonds are not as good as in device A, which might be due to the low resistance of the insulating barriers.

On the other hand, at higher biases we find the tunneling spectra to be qualitatively similar to the edge tunneling spectra we found in devices B and C. In device A, we cannot achieve an NIS configuration since the left and right parts of the junction cannot be independently controlled (see Fig. 5-1a for a scheme of device A). However, in the same nISIn configuration as the SET regime above ($V_{tg} = 2.8$ V, $V_{bg} = -4.5$ V), we find two prominent coherent peaks at higher bias voltages. The behavior of the tunneling spectra of device A as a function of temperature and magnetic field (Fig. 5-9c-d) are similar to the ones reported above for devices B and C in Fig. 5-4. The tunneling peaks are progressively suppressed when the temperature is increased, and become almost flat above 1.5 K. However, quantitative analysis of the gap size is unreliable since the alignment of the chemical potential of the N, S, and N regions is unknown. In a perpendicular magnetic field, the coherence peaks are suppressed, while the zero-bias anomaly persists, as discussed previously for devices B and C and shown in Fig. 5-4.

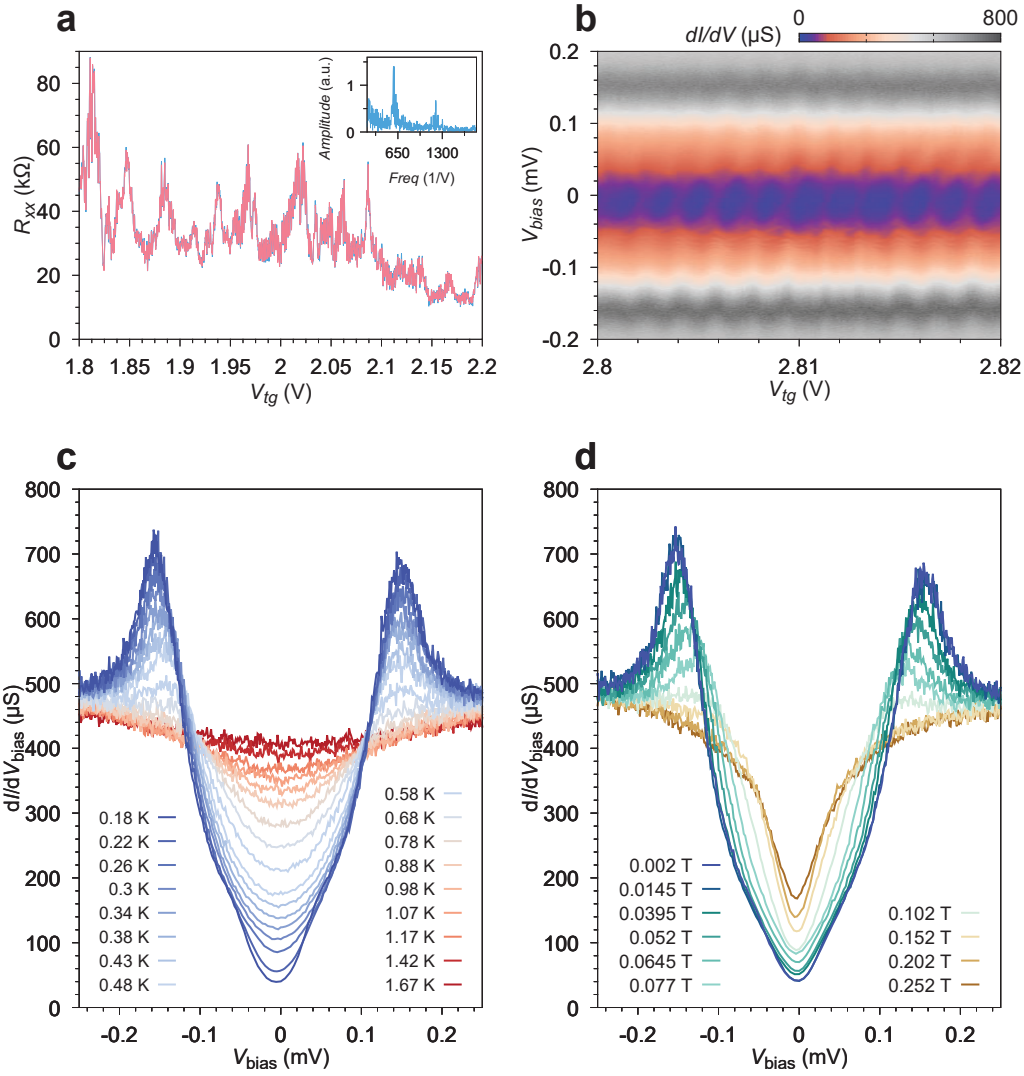

Figure 5-9: Evidence of superconducting gap and single-electron transistor behavior in device A. (a) Differential conductance as a function of top gate voltage, for two different R_{xx} pairs of contacts in blue and red ($V_{tg} \sim 2\,\mathrm{V}$, $V_{bg} = -4\,\mathrm{V}$). The signal is periodic across most of the range, with frequency $f \approx 600\,\mathrm{V}^{-1}$. The inset shows the Fourier transform of the previous signal, for the region $1.9544\,\mathrm{V} < V_{tg} < 2.09\,\mathrm{V}$ (region selected from the local Fourier transform to display the sharpest peak for easy read-out of the frequency, without loss of generality). (b) Coulomb diamonds at small V_{bias} ($V_{bg} = -4.5\,\mathrm{V}$). (c) Differential resistance as a function of bias voltage and temperature ($V_{tg} = 2.8\,\mathrm{V}$, $V_{bg} = -4.5\,\mathrm{V}$). (d) Differential resistance as a function of bias voltage and perpendicular magnetic field ($V_{tg} = 2.8\,\mathrm{V}$, $V_{bg} = -4.5\,\mathrm{V}$).

5.8.5 SET oscillation frequency

We note that the periodicity reported in Fig. 5-5d,e and the periodicity of the Coulomb diamonds in Fig. 5-5f ($\sim 4\,\mathrm{mV}$) are not equal. While none of the qualitative observations we have made are affected, quantitatively, we attribute such a mismatch to the influence of the top gates in the central 'island' of the SET (meaning that the two top gates have significant coupling to the 'island'). In particular, Fig. 5-5d is taken by sweeping the back gate and correcting the top gate voltage on the right and left parts of the device to keep the densities constant, while Fig. 5-5f has been obtained with fixed top gates (over a much narrower range of back gate voltages than Fig. 5-5d). To avoid possible confusion, we have labeled the x-axis of Fig. 5-5f with a tilde, where the top gates are compensating at each point for the back gate voltage to keep the density constant in the left and right parts of the device.

With one electron per period, one expects the periodicity in the back gate voltage to be given by $\Delta V_{bg} = e/C_{bg}$, with e the elementary charge and C_{bg} the back gate capacitance. One can approximate, in a first approach, $C_{bg} \approx \dfrac{\epsilon_r \epsilon_0 w L}{d}$, with $\epsilon_r \approx 2.7$ (found to be the value that best fits from our Landau fans), $w \approx 0.9\,\mu m$ (total width of device at the constriction), $L \approx 135\,\mathrm{nm}$ (width of the 'island' as designed by electron beam lithography, corresponding to the gap between the two top gates), and $d \approx 55\,\mathrm{nm}$ (hBN thickness). Using these values, we obtain $\Delta V_{bg} \approx 3\,\mathrm{mV}$, which matches relatively well with the value extracted from the Coulomb blockade diamonds ($\approx 4\,\mathrm{mV}$), given that the exact geometry of the "island" is not known a priori.

Our observations can be faithfully simulated (Fig. 5-5g) with an ideal single-electron transistor with capacitances $C_g = 40\,\mathrm{aF}$, $C_1 = 110\,\mathrm{aF}$, $C_\Sigma = 310\,\mathrm{aF}$, where C_g is the gate capacitance, $C_\Sigma = C_1 + C_2 + C_g + C_0$, C_0 is the stray capacitance, and C_1, C_2 are the drain and source capacitances [225]. Such values are in qualitative agreement with electrostatic simulations of capacitors with similar geometry. The displayed lines correspond to the discrete energy levels at the island being aligned with one of the chemical potentials of the electrodes. For a given discrete energy level at the constriction, the range of back gate voltages for which the current can flow increases linearly with increasing bias voltage

[218], resulting in the characteristic Coulomb diamonds. Their slope is associated with the capacitances (negative slope = $-0.35 = -C_g/C_1$, positive slope = $0.2 = C_g/(C_\Sigma - C_1)$, and the x-axis separation between two consecutive diamonds is $\Delta V_{\text{bias}} = 4\,\text{mV} = e/C_g$). In the extreme case where $C_0 = 0$, we get $C_2 = 160\,\text{aF}$, $C_1 = 110\,\text{aF}$. In the symmetric case where $C_2 = C_1 = 110\,\text{aF}$, we get $C_0 = 50\,\text{aF}$. Within the diamonds shaded in blue (and corresponding to the situation in Fig. 5-5c), no electron can tunnel through the island between the electrodes.

5.8.6 Transport characterization of device C

Figure 5-10 shows the characterization of device C. The device structure of this sample is similar to that of device B (see Fig. 5-4a), with a 120 nm gap between the top gates. All features reported in the previous sections are qualitatively reproduced in this device. The R-T curve is shown in Fig. 5-10d, with a superconducting transition around $T_c \sim 0.4\,\text{K}$ as extracted from 50% of the normal-state resistance value, and $T_{BKT} = 0.19\,\text{K}$. The Fraunhofer patterns have a periodicity of $\sim 3\,\text{mT}$. The envelope of the oscillaton has a substantially different morphology than for devices A and B, which we attribute to a different microscopic current distribution. The measurement of Coulomb diamonds in the SET regime shows a nonuniform periodicity, which might be explained by the presence of two quantum dots due to inhomogeneity in the sample [218, 226].

5.8.7 Simulation of Bulk and Planar Josephson junctions in the presence of an external magnetic field

We simulate the behavior of magnetic fields inside bulk and a 2D Josephson Junctions [209, 210, 205, 211], placed in an external magnetic field $\mathbf{B} = B_0\hat{z}$, to evaluate the field dependence of the maximum supercurrent both in bulk junctions and in planar 2D edge-type Josephson Junctions, given the geometry of our device A (simulation performed using $w = 1.5\,\mu\text{m}$ (width of junction in y), and $L = 2.15\,\mu\text{m}$ (half-length in x)). For a bulk superconductor, the magnetic field B_z satisfies the screened Poisson equation $\nabla^2 B_z - \frac{1}{\lambda^2} B_z = 0$ where λ is the penetration depth. The solution in a general case is an exponential decay

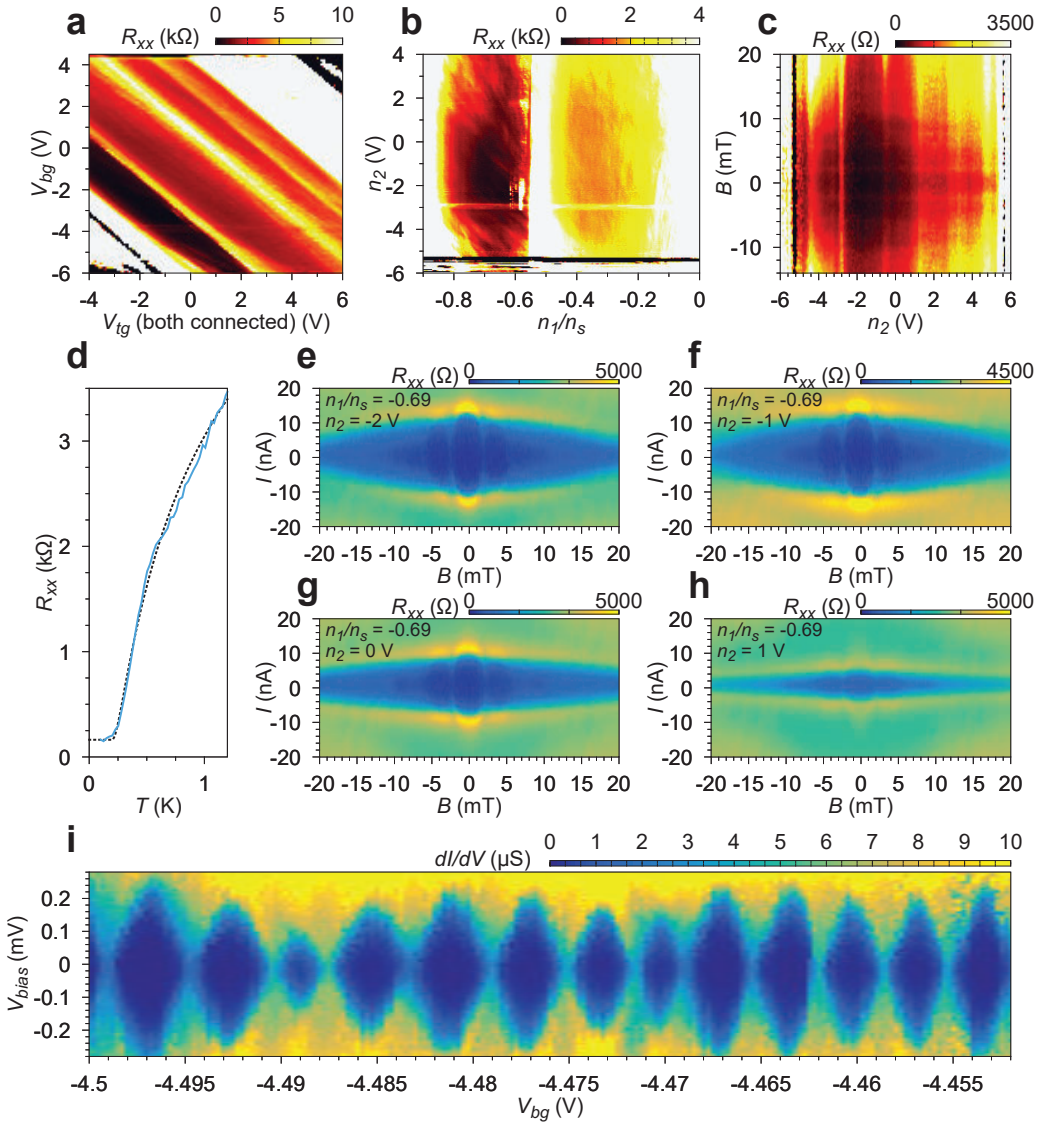

Figure 5-10: Characterization of device C. (a) V_{tg}-V_{bg} map of the resistance. The two top gates are connected together. (b) Zoom-in and rotated scan of the lower quadrant under the negative diagonal of the previous map. The x-axis denotes the density of the top gated parts (in units of the filling factor n/n_s), and the vertical axis is directly related to the back gate (with a shift to account for intrinsic doping), therefore proportional to the density in the narrow central region (transformation given by $V_{tg,left} = 8n_1/n_s - n_2 + 1.8$, $V_{tg,right} = 8n_3/n_s - n_2 + 1.8$ $V_{bg} = n_2 - 0.9$; note here both top gates are connected together and thus $n_1/n_s = n_3/n_s$). (c) n_2 vs B sweep at optimal doping $n_1/n_s = -0.69$. The periodicity as a function of the magnetic field is constant throughout n_2, as also shown in several interference patterns in Fig. (e)-(h). (d) R vs T curve for n_2 = –0.8 V and $n_1/n_s = -0.699$. Black dotted lines show the fit to Halperin-Nelson formula $R \propto \exp\left[-b/(T - T_{\mathrm{BKT}})^{1/2}\right]$, giving $T_{BKT} = 0.19$ K [223]. (i) Coulomb diamonds for device C ($V_{tg,both} = -4.8V$). The alternation of diamonds of different sizes could be an indication of two quantum dots in parallel.

with characteristic scale λ, and therefore in a bulk JJ the magnetic flux only penetrates in a region within 2λ centered around the junction. On the other hand, the characteristic length in a 2D superconductor is the Pearl length $\Lambda = 2\lambda^2/d$, where d is the film thickness. In a perpendicular magnetic field, the thin slab is no longer capable of expelling the magnetic field at the center and the magnetic field will penetrate the sample almost uniformly through vortices. In particular, when the length scales are much smaller than the Pearl length, $w, L \ll \dfrac{\lambda^2}{d}$, the second term of the equation can be dropped and the Poisson equation dominates the magnetic field distribution in ultrathin films $\nabla^2 B_z = 0$ [209].

In our simulation, we numerically solve for the z direction magnetic field $H(x, y)$ in the two extreme cases of an infinitely thick bulk junction and an ultrathin junction. H satisfies $\nabla^2 H - \frac{1}{\lambda^2} H = 0$ in the bulk case and $\nabla^2 H = 0$ in the 2D case. At the upper and lower boundaries $y = \pm W/2$ and at the junction $x = 0$, we set Dirichlet boundary conditions $H = H_0$ (H_0 is the externally applied field). On the left and right boundaries $x = \pm L$, we set Neumann boundary conditions $\partial_x H = 0$. In the bulk case, we use a penetration depth of $\lambda = 100$ nm. In Fig. 5-2c and 5-2d, we show the result of the simulation of the magnetic field distribution for a Josephson Junction with the junction at $x = 0$. The color scale represents the relative amplitude of $B_z = \mu_0 H_z$ inside the superconducting electrodes, i.e., the amount of magnetic field penetrating the sample. The solution is of the form $B_z \sim e^{-y/\lambda}$ with an exponential dropping of the field for the bulk Josephson junction. On the other hand, for the 2D superconductor, the solution is essentially uniform, which indicates that the magnetic field is not screened by the 2D superconductor. From the Maxwell equation, current density is $\boldsymbol{j} = \nabla \times \boldsymbol{H}$, which translates to $(j_x, j_y) = (\partial_y H_z, -\partial_x H_z)$. Therefore, the contour lines of H_z are parallel to the screening current flow. Once again we see that in the bulk sample the screening currents are mostly confined at a distance λ from the edges, whereas they spread across most of the sample in the ultrathin case.

This discrepancy in magnetic field screening has an important impact on the Josephson relationship of the junction. In a wide junction, the total critical current can be computed by integrating $I_c = \int_{-w/2}^{w/2} i_c(y) \cos\gamma(y) dy$, where $i_c(y)$ is the Josephson current density and $\gamma(y)$ is the phase difference across the junction. For the bulk case, the phase $\gamma(y)$ winds as $\gamma(y) = \gamma_0 + \dfrac{2\pi}{\phi_0} 2B\lambda \cdot y$ (we assume the length of the junction in x is negligible), which

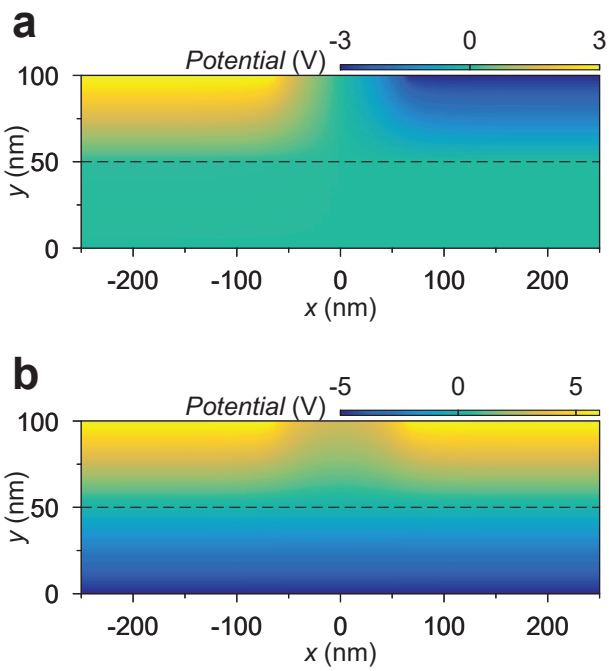

Figure 5-11: Simulation of the potential for the Tunneling (a) and SET (b) configurations. Two top gates are added at y=100 nm for positive and negative x axis, and a back gate at y=0, setting the boundary conditions V_{g1}, V_{g2} and V_{g0}. The dashed line at $y = 50\,\text{nm}$ denotes the MATBG.

gives the well-known Fraunhofer pattern with a periodicity $\Delta B = \dfrac{\phi_0}{2w\lambda}$. These formulae reflect that the magnetic field penetrates only in a distance of 2λ near the junction. For the 2D case, on the other hand, since the magnetic field is no longer localized at the junction, in general the phase difference $\gamma(y)$ cannot be analytically written down. Instead, we obtain $\gamma(y)$ by numerically integrating the relationship $\partial_y \gamma(y) = -\frac{4\pi\mu_0\lambda^2}{\phi_0} j_y(0^+, y)$ (take $\lambda \to \infty$ in 2D limit) [209]. The periodicity ΔB is no longer constant in this case, but can be approximated at larger fields as $\Delta B' \sim \dfrac{1.8\phi_0}{w^2}$ [227, 205].

5.8.8 Simulation of the charge distribution and the appearance of insulating barriers for the tunneling and the single-electron transistor

At the magic angle, the band structure of TBG exhibits bandgaps on the order of $\sim 30\,\text{meV}$ at densities $n = \pm n_s$ (see Chapter 2.8) [79]. In this work, we exploit these superlattice

gaps as in-situ tunneling barriers for tunneling spectroscopy of the superconducting gap and the single-electron transistor.

In the case of the tunneling spectroscopy configuration, as shown in Fig. 5-4, one side of the sample is set to a density larger than the superlattice gap, and the other side to a density lower than the superlattice gap. Therefore we expect to have at least one point in space at which the density equals the superlattice density and thus is insulating. If quantum capacitance effects are taken into account, the density will in fact have a plateau at the superlattice density. In order to simulate this phenomenon, we self-consistently solve the electrostatic model governed by a Poisson equation with a nonlinear boundary condition. In the dielectric, electrostatic potential satisfies $\nabla^2 V = 0$. The boundary conditions are taken to be $V = V_{g1}$ at the left top gate, $V = V_{g2}$ at the right top gate, $V = V_{g0}$ at the back gate. Side boundaries are set to Neumann conditions $\partial_x V = 0$.

Since the MATBG is grounded, it has zero *electrochemical* potential at any point on it $\mu(n(x)) - V(x) = 0$, where $n(x) = [E_y^+(x) - E_y^-(x)]/e$ is the electron charge density, and $\mu(n)$ is the chemical potential of MATBG. The boundary condition at the MATBG is therefore $V_{\mathrm{TBG}}(x) = \mu\left(\frac{1}{e}(\partial_y V^+ - \partial_y V^-)\right)$ [228]. Here, $E^\pm$ and $V^\pm$ are the electric field and electric potential above and below TBG respectively. To capture the fundamental features with minimal complexity, we assume a band gap of 30 meV and parabolic bands with effective masses $m_1 = 0.4 m_e$ for $n > -n_s$ and $m_2 = 0.05 m_e$ for $n < -n_s$. The problem is solved with an iterative method. In each iteration, V_{TBG}^n is calculated from $V_{\mathrm{TBG}}^n = \mu\left(\frac{1}{e}(\partial_y V^{n-1,+} - \partial_y V^{n-1,-})\right)$, and the Poisson equation $\nabla^2 V = 0$ is solved using boundary condition V_{TBG}^n to obtain V^n.

For the tunneling spectroscopy configuration (displayed in Fig. 5-4), we use the values $V_{g1} = 3$ V, $V_{g2} = -3$ V, and $V_{g0} = 0$ V (see Fig. 5-11a). This results in the density induced in the twisted bilayer graphene displayed in Fig. 5-4b, and a barrier width on the order of 10 nm. An analogous procedure is performed for the SET configuration (Fig. 5-11b) with $V_{g1} = 6$ V, $V_{g2} = 6$ V, and $V_{g0} = -5$ V. The resulting density is displayed in Fig 5-5a.

5.8.9 Further analysis of the tunneling spectra in devices B and C

Fig. 5-12 shows the tunneling spectra for device C at a fixed back gate ($V_{bg} = -1.2\,\mathrm{V}$) and fixed top right gate voltage ($V_{tg,right} = -7.5\,\mathrm{V}$), while varying the top left gate voltage. In this configuration, we observe tunneling from a region in the normal state with density $n_3/n_s \approx -1.2n_s$ into different regions on the left side of the device (I, S, C, metallic region with hole doping in between D and C, D, and C'), via the insulating barrier I (in a similar fashion as shown in Fig 5-4b). Spectra are plotted for zero magnetic field (solid lines) and in a perpendicular magnetic field of 0.2 T (dashed lines). Tunneling peaks fitting the phenomenology of superconducting coherence peaks (represented in black, with a thicker trace) are only observed at densities near the superconducting state ($V_{tg,left} = -4.1\,\mathrm{V}$, corresponding to the configuration SIn where the left part of the device is at a density $n_1/n_s \approx -0.775n_s$). The coherence peaks disappear in the presence of a perpendicular magnetic field (denoted by the double-headed arrows in Fig. 5-12), as explained previously in section 5.4.

For both devices B and C, four different pieces of evidence support the conclusion that the tunneling spectra shown in Fig. 5-4 indeed correspond to the superconducting gap of MATBG. First, the 4-terminal transport obtained at the same densities display zero or close to zero resistance. Second, the shape of the coherence peaks surrounding the spectroscopic gap fits well to our model for the superconducting quasiparticle density of states. Third, the coherence peaks disappear with temperature in the appropriate range. Finally, the coherence peaks disappear in a magnetic field (although there is an unrelated conductance minimum surviving at much higher fields, attributed to a separate mechanism). We also reiterate, from Fig. 5-12, that the only densities at which coherence peaks are observed coincide with densities at which the superconducting state is observed in transport.

5.8.10 Fits to the tunneling data

Theoretical fits to the tunneling data shown in Fig. 5-4 were performed using a simple model for the tunneling conductance between a metal and a superconductor [45]. This model involves the product of the quasiparticle density of states in the superconductor and

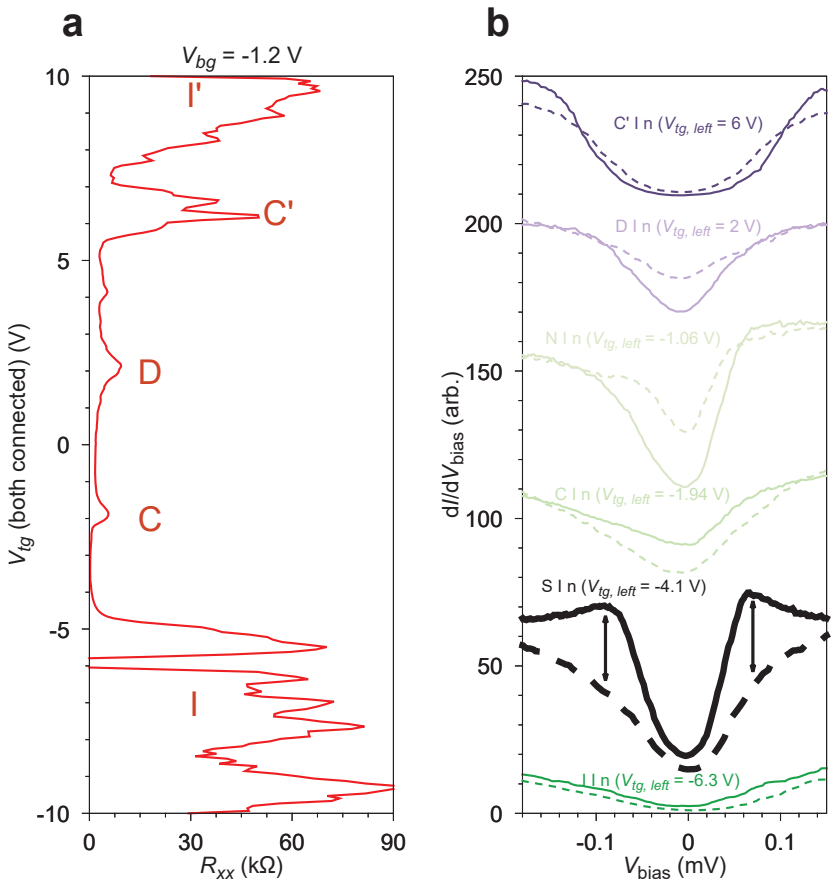

Figure 5-12: Tunneling spectra across the different states in MATBG. (a) Linecut in the back gate-top gate map for device C at $V_{bg} = -1.2$ V. Labels in red denote features induced by the top gate gates. (b) Tunneling spectra for device C. The back gate ($V_{bg} = -1.2$ V) and top right gate ($V_{tg,right} = -7.5$ V) voltages are fixed, and the top left gate voltage is varied. This allows tunneling from the right region in the normal state n with density $n_3/n_s \approx -1.2n_s$ into different regions on the left side of the device (I, S, C, N, D, and C'), via the insulating barrier I. Spectra are shown in zero magnetic field (solid lines) and in a perpendicular magnetic field of 0.2 T (dashed traces).

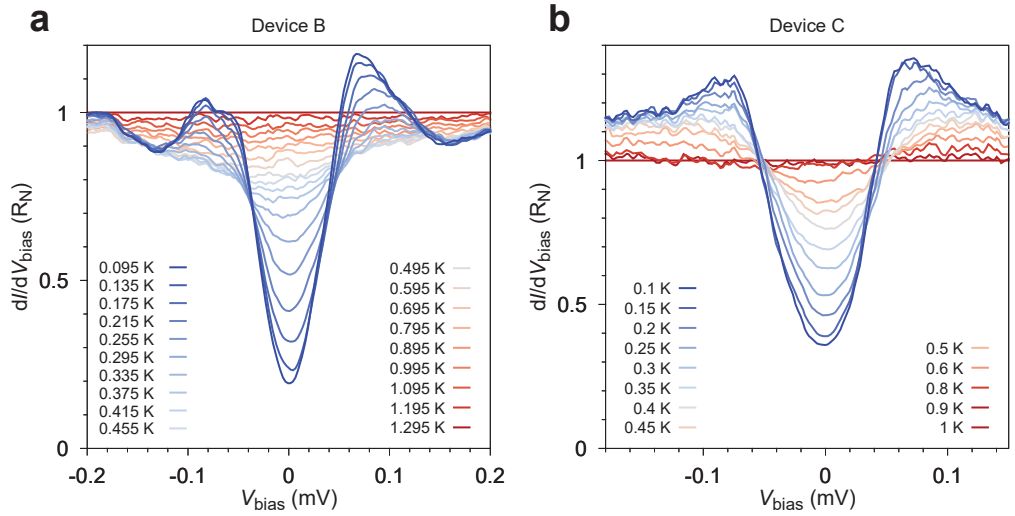

Figure 5-13: Normalized spectra of the superconducting gap in MATBG from Fig. 5-4. (a) Normalized tunneling spectra with respect to the spectrum at 1.295 K as a function of temperature for device B. (b) Similarly, normalized tunneling spectra with respect to the spectrum at 1 K as a function of temperature for device C.

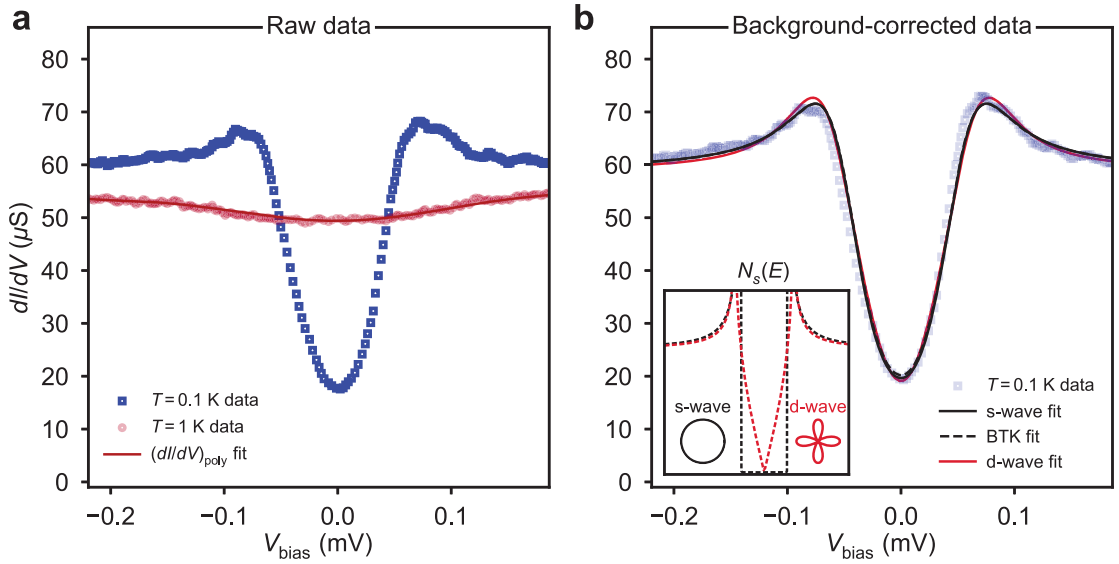

Figure 5-14: Fitting procedure for tunneling data from device C. (a) Raw tunneling data and (b) background-corrected data with s-wave and BTK fits superimposed. Best-fit parameters are $\Delta = 51\,\mu\text{eV}$, $T = 113\,\text{mK}$, and $\Gamma = 14\,\mu\text{eV}$ in both cases, with all values of $Z \geq 1.1$ fitting equally well in the BTK case. An anisotropic d-wave fit, using $\Delta_{\mathbf{k}} = \Delta\cos(2\theta)$, also produces a high-quality fit with amplitude $\Delta = 64\,\mu\text{eV}$, $T = 152\,\text{mK}$ and $\Gamma \approx 0$. Although the underlying quasiparticle densities of states $N_s(E)$ differ substantially (inset, shown with same axis limits as (a)-(b)), the two fits are indistinguishable at the finite temperatures of the experiment.

a constant density of states with the derivative of the Fermi occupation function,

$$\frac{dI}{dV} \propto \int_{-\infty}^{\infty} dE\, N_s(E) \frac{df}{dV}, \tag{5.1}$$

for $f(E) = \left[\exp\left(\frac{E-eV}{k_B T}\right) + 1\right]^{-1}$ at temperature T and bias voltage $V = V_{\text{bias}}$ (the constant density of states in the normal metal is a constant prefactor and is ignored here). The quasiparticle density of states at zero temperature is given by [229],

$$N_s(E) = N_0\, \text{Re}\, \frac{E}{\sqrt{E^2 - \Delta_{\mathbf{k}}^2}}, \tag{5.2}$$

with $\Delta_{\mathbf{k}} = \Delta$ for an isotropic (s-wave) gap Δ, and with the substitution $E \rightarrow E + i\Gamma$ incorporating a phenomenological quasiparticle lifetime broadening, Γ (Dynes broadening). At temperatures well above the superconducting transition, the tunneling spectra in devices B and C exhibit background curvature attributable to details of the normal metal density of states and the tunneling barrier. To isolate the superconducting part of the tunneling data, we perform a background correction before fitting the data to Eq. 5.1. This is carried out by first fitting a polynomial function, $(dI/dV)_{\text{poly}}$, to a tunneling spectrum acquired at a sufficiently high temperature for each device (where the changes in spectroscopic behavior begin to saturate with increasing temperature), and then dividing away this smooth background function $(dI/dV)_{\text{sub}} = (dI/dV)_{\text{raw}}/(dI/dV)_{\text{poly}}$ such that the background-corrected data $(dI/dV)_{\text{sub}}$ do not contain the curvature observed at high temperatures (see Fig. 5-14a). The differential conductance in Eq. 5.1 is then fit to the background-corrected tunneling data taken at the lowest temperature with Δ and Γ as free parameters, along with T, to account for a potentially elevated electron temperature, and an overall scale factor. The data shown in Fig. 5-4 are raw data, without any background correction. To show the correspondence between the fits to the superconducting (SC) part of tunneling spectrum and the raw data, we include the polynomial background in the plotted fits by multiplying each fit by the polynomial part extracted from the data at high temperature, $(dI/dV)_{\text{fit}} = (dI/dV)_{\text{SC}} \times (dI/dV)_{\text{poly}}$. Employing a similar fitting procedure using the standard Blonder-Tinkham-Klapwijk (BTK) relation [230] (with $E \rightarrow E + i\Gamma$) rather than

Eq. 5.2 also fits the data nicely (see BTK fit in Fig. 5-14b). Using the BTK formula, we find similar Δ and Γ values and a dimensionless barrier strength value $Z > 1$, indicating a low-transparency barrier between the normal metal and superconducting regions. The value $Z > 1$ supports our conclusion that the barrier region is indeed in the tunnel coupling limit, enabling our spectroscopic analysis of the superconducting gap.

Though the fits described here employ an isotropic assumption for the order parameter, we must emphasize that the quality of these fits do not preclude order parameters with other symmetries. For instance, we find that a modification of Eq. 5.2 using the substitution $\Delta_{\mathbf{k}} = \Delta\cos(2\theta)$ and integrating over the polar angle $N_s(E) = (1/\pi)\int d\theta N_s(E,\theta)$, a model for a nodal order parameter with $d_{x^2-y^2}$ symmetry (d-wave), fits our tunneling data equally well (Fig. 5-14b). An order parameter with d_{xy} symmetry ($\Delta_{\mathbf{k}} = \Delta\sin(2\theta)$) produces an identical tunneling spectrum. While both the isotropic and d-wave fits appear to match the data, note that the implied quasiparticle densities of states $N_s(E)$ differ substantially in the two cases (see inset of Fig. 5-14b). However, these differences are obscured in our experiment by thermal and lifetime broadening, preventing us from determining the symmetry of the underlying order parameter.

One might also wonder whether the temperature dependence of these curves could provide additional information about the symmetry of the superconducting order parameter. Although we do expect differences in both the shape of the spectrum and in the temperature dependence of the magnitude of the order parameter as a function of temperature Δ(T), there are at least three reasons that this analysis fails in practice: (1) The shape of the expected dI/dV curves at higher temperatures are nearly indistinguishable due to thermal broadening. (2) We do not have an independent measure of the electronic temperature in the MATBG, and therefore an accurate measure of (T) is not possible (e.g. to compare the shape of these curves). (3) The edge-tunneling process may include tunneling into a thin, proximitized metal region between the insulator and superconductor that produces an underestimation of the true bulk value of the gap in the superconductor. To support this, we have performed further calculations to investigate whether it would be possible to distinguish between s-wave and d-wave order parameters from the temperature dependence of the spectral curves from device C. In Figure 5-15, we show (a) our background corrected

data, (b) a model for the temperature dependence of an s-wave spectrum including thermal broadening and (c) a similar model for a d-wave gap. The two models are based on the tunneling current expressions given in Eqs. 5.1 and 5.2, using the approximate formula [231],

$$\Delta(T) = \Delta(0)\tanh\left(\pi k_b T_c/\Delta(0)\sqrt{a(T/T_c - 1)}\right), \tag{5.3}$$

with $\Delta(0) = 51\,\mu\text{eV}$ and $T_c = 0.85\,\text{K}$ (in reasonable agreement with our transport data given the broadness of the superconducting transition and the uncertainty in the determination of the exact electronic temperature of the system) to determine the evolution of the gap with temperature, using a matching set of temperatures to those measured in the experiment. Thermal broadening is included via the Fermi occupation function in Eq. 5.1 and quasiparticle lifetime broadening is set to $\Gamma = 14\,\mu\text{eV}$ for the s-wave model and $\Gamma \approx 0$ for the d-wave model, as in the best fits from Fig. 5-14 at 100 mK. Using these parameters we find the best agreement with our experimental curves over the full temperature range and conclude that, based on this model, thermal broadening prevents distinguishing the spectral curves within the range of temperatures available in our system. Moreover, a possible mismatch between the measured temperature of our Cernox thermometer and the electronic temperature in the MATBG further complicates this analysis. For instance, while the s-wave and d-wave models shown for $T = 0.1\,\text{K}$ in panels (b) and (c) of Fig. 5-15 differ slightly, a more accurate best-fit analysis (as shown in Fig. 5-15) shows that the d-wave model is nearly indistinguishable from the s-wave model even if the electronic temperature is elevated only slightly (e.g. $\sim 150\,\text{mK}$ in the best fit analysis). It would therefore be difficult to draw a conclusion distinguishing between these two superconducting (or other) order parameters based on our present measurements. Nevertheless, future spectroscopic measurements from tunneling in similar devices may uncover additional details of the superconductivity in MATBG.

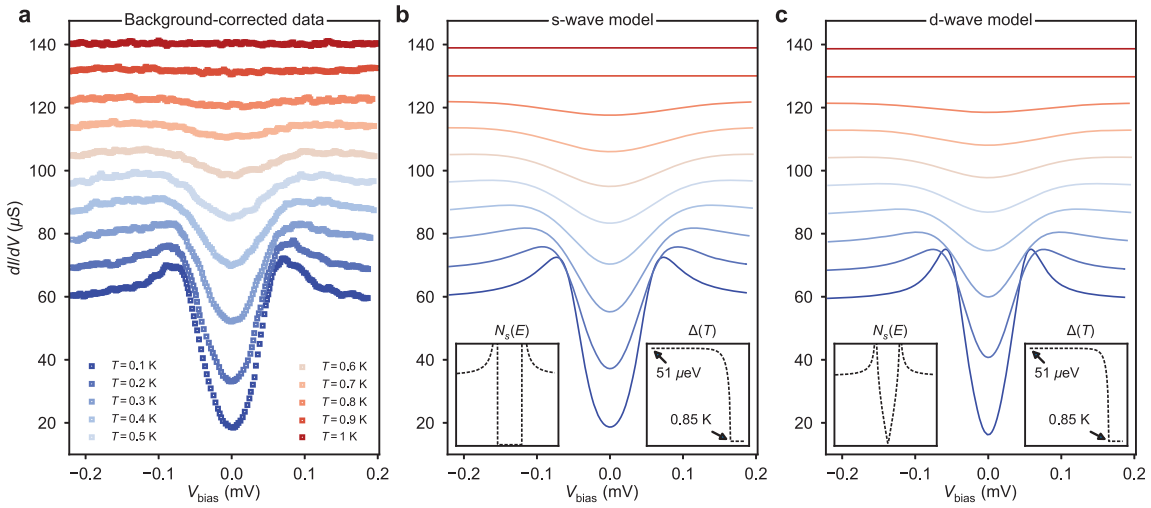

Figure 5-15: Temperature evolution of the superconducting gap for device C. (a) Background corrected data, (b) a model for the temperature dependence of an s-wave tunneling spectrum including thermal broadening and (c) a similar model for a d-wave gap. The details of the models and the background subtraction are explained in the text.

Chapter 6

Nematicity and Competing Orders in Superconducting Magic-Angle Graphene

Strongly interacting electrons in solid-state systems often display tendency towards multiple broken symmetries in the ground state. The complex interplay between different order parameters can give rise to a rich phase diagram. In this chapter, we report on the identification of intertwined phases with broken rotational symmetry in magic-angle twisted bilayer graphene (TBG). Using transverse resistance measurements, we find a strongly anisotropic phase located in a 'wedge' above the underdoped region of the superconducting dome. Upon its crossing with the superconducting dome, a reduction of the critical temperature is observed. Furthermore, the superconducting state exhibits an anisotropic response to a direction-dependent in-plane magnetic field, revealing a nematic pairing state across the entire superconducting dome. These results indicate that nematic fluctuations might play an important role in the low-temperature phases of magic-angle TBG, and pave the way for using highly-tunable moiré superlattices to investigate intertwined phases in quantum materials. The results presented in this chapter have been published in reference [4].

6.1 Introduction

Spontaneous symmetry breaking is a ubiquitous process that occurs at all length scales in nature [232], from the endowment of mass to elementary particles through the Higgs mechanism, the emergence of ferromagnetism and superconductivity in mesoscopic and macroscopic systems, all the way to the creation of stars and galaxies in the early universe. In a solid-state system, besides time-reversal and gauge symmetries, there are certain discrete symmetries imposed by the underlying crystal lattice. However, these symmetries can be spontaneously broken when many-body electron-electron interactions in the system are significant. Studying these broken-symmetry states is fundamental to elucidate the various phases in these many-body systems [233, 234]. One example is an electronic nematic phase, where the discrete rotational symmetry of the lattice is spontaneously broken due to electron correlations, while lattice translational and time-reversal symmetries are preserved [235, 236]. The resulting anisotropy of the system is in turn manifested in the spin, charge, and lattice degrees of freedom, and can be measured via scattering, transport and scanning probe experiments [237, 238, 239, 240, 241, 242].

When a correlated system has multiple broken-symmetry phases, their relationship often goes beyond mere competition, giving rise to a complex phase diagram of intertwined phases [243, 244, 245]. For example, in the underdoped region of the phase diagram of certain cuprate superconductors, a depletion in the critical temperature T_c is found near $p \approx 1/8$, where p is the hole doping concentration [246]. This observation is typically attributed to the competition between superconductivity and a stripe phase that has spin and/or charge ordering [246, 234, 247]. Charge order and superconductivity may also intertwine to form a pair density-wave state [244, 248]. Another example of intertwined order is a nematic superconducting state, which simultaneously breaks lattice rotational and gauge symmetries. Nematic pairing states have been reported in certain iron pnictides and in doped Bi_2Se_3, as revealed by thermal, magnetic, and transport measurements [249, 250, 251, 252, 253, 254, 255], although their microscopic origin is still unclear.

The discovery of correlated insulator and superconducting behaviors (see Chapter 2.8) [79, 83] in two-dimensional (2D) graphene superlattices brings the possibility of studying

correlated superconducting materials with unprecedented tunability and richness. In this chapter, we study the interplay between the superconducting phase and other many-body phases in magic-angle TBG. Compared to conventional materials, a major advantage of magic-angle TBG is that the band filling can be continuously tuned by electrostatic gating instead of chemical doping, so that different phases can be accessed in a single device.

6.2 Results

In this chapter, we investigate the phase diagram of magic-angle TBG in detail, focusing particularly on anisotropic properties in the superconducting and normal phases. We uncover an anisotropic in-plane electrical transport in magic-angle TBG at low temperatures using longitudinal and transverse resistivity measurements. In addition, we reveal an anisotropic in-plane critical field and an anistropic response of the superconducting critical current to an in-plane magnetic field. Our results show that magic-angle TBG can spontaneously break lattice rotational symmetry in both the normal and superconducting phases, although the anisotropic properties of these two states are manifested in different observables, suggesting that the origins of these two anisotropic states might be different.

6.2.1 Characterization of magic-angle graphene

Using the previously developed 'tear and stack' dry-transfer technique (see Chapter 2.9) [94, 140], we fabricate high quality encapsulated TBG devices with twist angles around the first magic angle $\theta \approx 1.1°$ (see Fig. 6-7 for the Landau fan diagram). The main devices we report about are devices A and B (not to be confused with devices with similar names from other chapters), with twist angles of $\theta = 1.09°$ and $\theta = 1.08°$, respectively. We also have a third device C with $\theta = 1.07°$ shown in section 6.5, which exhibits very similar behavior as devices A and B.

The low-energy bands in TBG are four-fold degenerate (due to spin and valley degrees of freedom) and can sustain an electron density of $n_s = 4/A$, where A is the area of a moiré unit cell. This density corresponds to filling four electrons or holes per moiré unit cell, as explained in detail in Chapter 2.8. Near the first magic angle, correlated states can

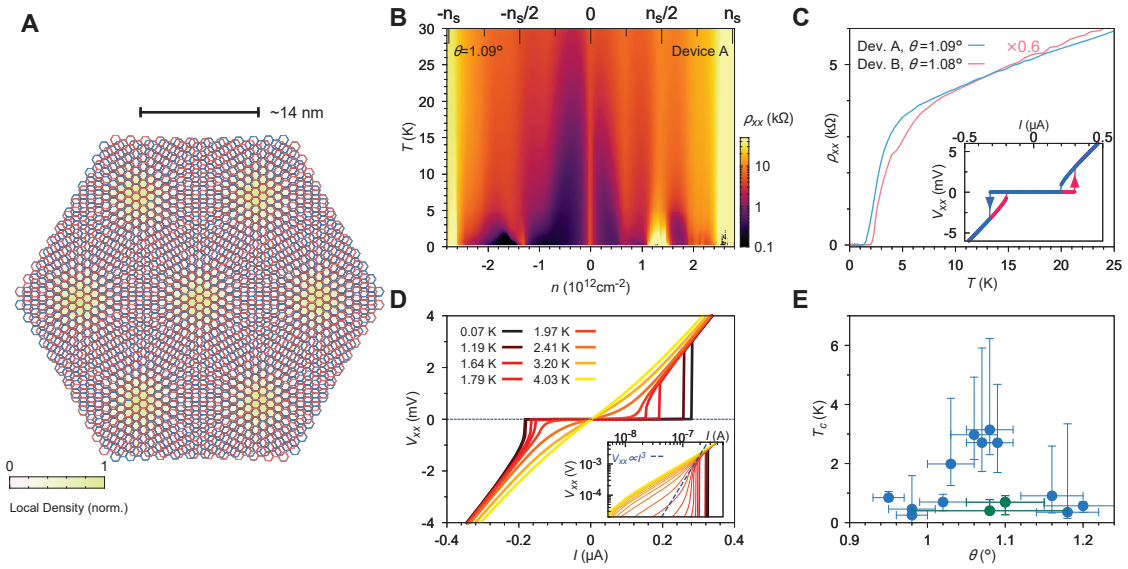

Figure 6-1: Characterization and statistics of magic-angle twisted bilayer graphene devices. (a) Illustration of the moiré pattern in twisted bilayer graphene. The color scale shows the normalized local density in the flat bands when the twist angle is close to magic angle. The twist angle of the displayed pattern is enlarged for clarity. (b) Resistivity of device A (twist angle $\theta = 1.09°$) versus gate induced carrier density and temperature, showing correlated features at all integer electron fillings of the superlattice. Superconductivity is found at hole-doping of the $-n_s/2$ insulator with critical temperature $\sim$2.5 K. (c) Resistivity versus temperature for devices A and B, with twist angles $\theta = 1.09°$ and $\theta = 1.08°$, respectively, at their optimal doping concentrations. Inset shows the forward and backward sweeps of the I-V_{xx} curves in device B which exhibit a significant hysteresis. (d) I-V_{xx} curves at different temperatures measured in device B. Inset shows the log-log plot of the $I > 0$ part of the data. The Berezinskii-Kosterlitz-Thouless transition temperature $T_{\mathrm{BKT}} \approx 2.2$ K is identified where the slope of the curve crosses $\mathrm{d}(\log V_{xx})/\mathrm{d}(\log I) = 3$ (equivalent to $V_{xx} \propto I^3$). (e) Statistics of optimal doping T_c in 14 of the magic-angle TBG devices we have measured. We find that the trend of T_c peaks around 1.1°, the theoretically predicted first magic-angle in TBG. The green data points are from devices exhibiting substantial disorder, hence the large error bars in the twist angle determination. This disorder may be responsible for the relatively low T_c.

form at integer electron fillings of the moiré superlattice, i.e. when $n = \pm\frac{n_s}{4}, \pm\frac{n_s}{2}, \pm\frac{3n_s}{4}$. This is believed to be a consequence of the fact that the electronic interactions become comparable to the bandwidth of the nearly-flat bands. In the resistivity measurements of device A shown in Fig. 6-1b, we indeed find an enhancement of the resistivity ρ_{xx} at all these integer fillings. A superconducting dome is recognizable upon hole-doping of the $-n_s/2$ insulating state, at temperatures below 2.5 K. Fig. 6-1c shows the $\rho_{xx}(T)$ curves of device A and device B at their optimal doping levels (highest T_c). Both devices exhibit a T_c in the range of 2.5–3 K (at 50 % normal resistance), which is among the highest in our MATBG devices (see. Fig. 6-1e). Figure 6-1d shows the evolution of the I-V curves with temperature. From the log-log plot shown in the inset, we can extract the Berezinskii-Kosterlitz-Thouless (BKT) transition temperature to be $T_{\mathrm{BKT}} \approx 2.2$ K. Devices A and B have in fact some of the highest transition temperatures among all reported magic-angle TBG devices so far (see Table 6.1 and Fig. 6-10), as evident from the T_c statistics shown in Fig. 6-1e (and Chapter 2.8.9), as well as devices reported in the literature [83, 122, 256].

6.2.2 Anisotropic behavior in the normal phase

Figs. 6-2a-b show the resistivity versus gate-induced density, n, and temperature, T, maps of devices A and B, respectively, in the vicinity of $-n_s/2$. We find that in both devices the $-n_s/2$ region of the phase diagram has a rather complicated structure. As can be seen in Figs. 6-2a-b, there are two resistive features in the normal state: one 'wedge'-like feature above the superconducting dome (near -1.5×10^{12} cm^{-2} for device A and -1.4×10^{12} cm^{-2} for device B) that bends at elevated temperatures, and one resistive feature on the right hand side of the dome (near -1.3×10^{12} cm^{-2} for both devices). While the latter feature corresponds to the $-n_s/2$ state similar to the correlated states previously reported in magic-angle TBG [79, 83, 122, 256], the wedge-like feature creates a noticeable 'kink' (i.e., decrease in T_c) where it intersects with the superconducting dome. To further probe the resistive wedge-like feature, we apply a small perpendicular magnetic field to fully suppress superconductivity, as shown in Figs. 6-2c-d. Line cuts of the resistivity versus temperature at the densities corresponding to the 'kinks' of T_c are compared in Figs. 6-2e-f for the two

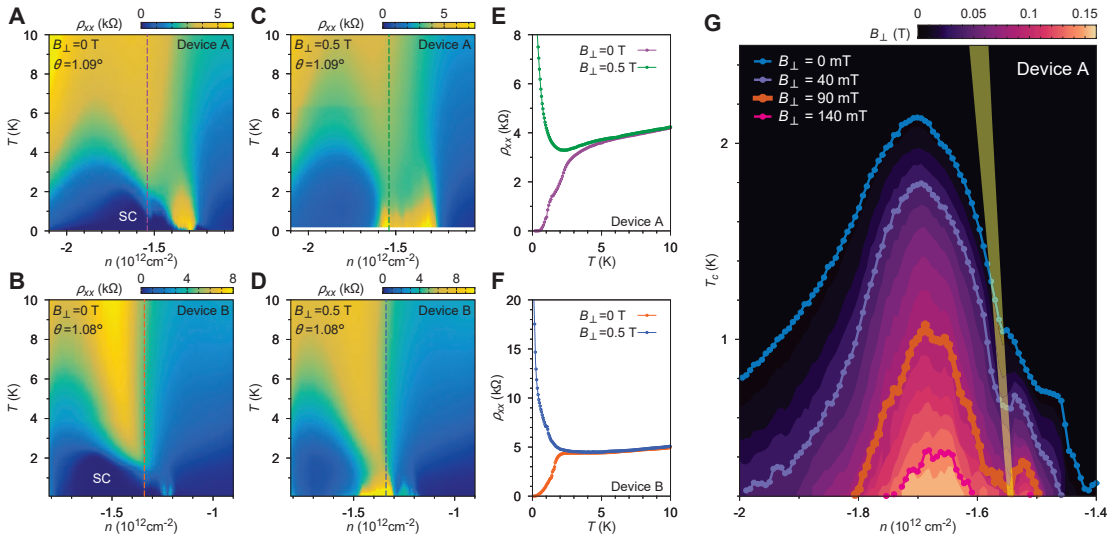

Figure 6-2: Competing phases near the superconducting domes of magic-angle TBG. (a-b) Resistivity versus gate-induced carrier density and temperature for device A and device B, respectively. (c-d) Same measurement but in a perpendicular magnetic field of 0.5 T. (e-f) Line cuts of resistivity versus temperature for devices A and B at 0 T and 0.5 T at the densities indicated by the dashed lines in (a-d), showing a superconductor-to-insulator transition induced by the magnetic field. In both devices, we find a wedge-like feature above the superconducting dome in addition to the $-n_s/2$ correlated state. This feature shifts noticeably towards negative relative densities at elevated temperatures. At zero magnetic field, the wedge-like feature disappears into the superconductiviting dome and creates a 'kink' on the $T_c(n)$ curve, while in 0.5 T it persists down to the lowest temperatures and turns into an insulator. The gray circles in (a-d) indicate the resistivity maxima associated with the wedge-like feature at different temperatures. (g) Evolution of T_c of device A in a perpendicular magnetic field up to 0.18 T. Each contour line is T_c (10 % normal resistance) versus carrier density at the magnetic field indicated by the color shading. The yellow band represents the approximate position of the wedge-like feature. At $B_\perp = 0.09$ T (orange curve), the T_c-kink touches zero at the same density where the wedge-like feature extrapolates to zero temperature. Above this field, the superconducting dome splits into two domes roughly centered at -1.52×10^{12} cm^{-2} and -1.67×10^{12} cm^{-2}, respectively.

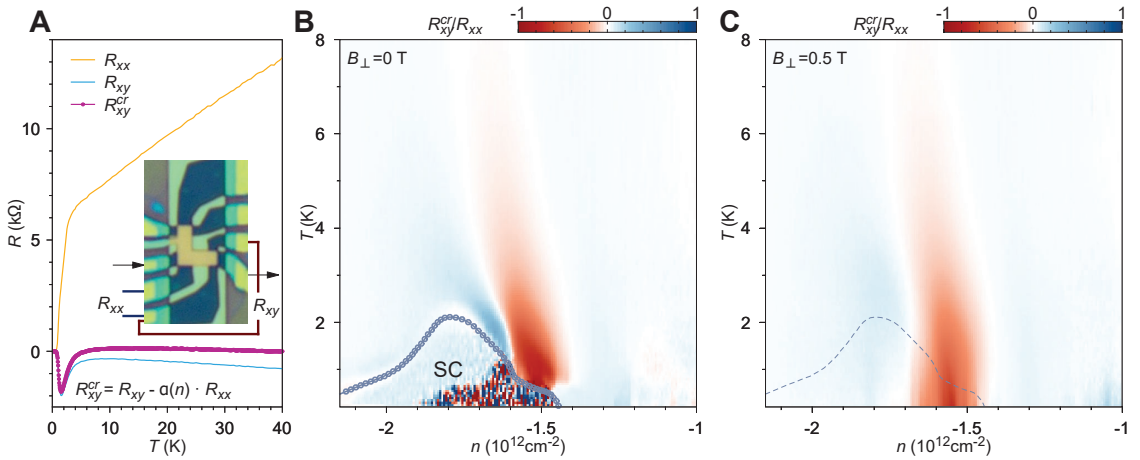

Figure 6-3: Normal-state anisotropy in magic-angle TBG device A. (a) Illustration of how we extract the resistivity anisotropy by measuring the transverse resistance. Inset shows the actual device configuration that we used to obtain the data, where black arrows indicate current source and drain. R_{xx}, R_{xy} label the leads on which longitudinal and transverse resistances are measured, respectively. The purple trace, R_{xy}^{cr}, is the transverse resistance corrected for leads misalignment (see section 6.5). $n = -1.53\times10^{12}\,\mathrm{cm}^{-2}$ in this measurement. (b-c) Anisotropy ratio versus carrier density and temperature at zero magnetic field and $B_\perp = 0.5\,\mathrm{T}$, respectively (see section 6.5). The circles in (b) and the dashed line in (c) outline the approximate shape of the superconducting dome (at zero field). We find the strongest anisotropy near the kink in T_c at $n = -1.54\times10^{12}\,\mathrm{cm}^{-2}$, coinciding with the resistive wedge-like feature we identified in Figs. 6-2a and 6-2g.

devices. It can be clearly seen that when superconductivity is suppressed, the resistive wedge-like feature turns insulating upon approaching zero temperature. A small magnetic field thus results in a superconductor-to-insulator transition at this density. In Fig. 6-2g, we show the gradual suppression of T_c by the perpendicular magnetic field from zero to 180 mT in device A. We find that above about 90 mT, the superconducting dome splits at $n \approx -1.54\times10^{12}\,\mathrm{cm}^{-2}$ into two domes. This density approximately coincides with the density where the wedge-like feature extrapolates to zero temperature. The separated domes are centered at around $-1.52\times10^{12}\,\mathrm{cm}^{-2}$ and $-1.67\times10^{12}\,\mathrm{cm}^{-2}$ respectively. The position of the splitting point corresponds to 15±5 % hole doping with respect to the correlated insulator state. These findings are reminiscent of the behavior in certain underdoped cuprates near $1/8$ doping [246, 234, 247, 257].

To gain more insight into the possible origin of the resistive wedge-like feature, we measure the transverse voltage across the sample at zero magnetic field, which gives us the

transverse resistance $R_{xy} = V_y/I_x$ [258, 259]. In an anisotropic conductor in two dimensions, the 2-by-2 resistivity tensor has two diagonal components $\hat{\rho} = \mathrm{diag}\{\rho_1, \rho_2\}$. If the major axis of the anisotropy (usually one of the crystal axis) is not aligned with the reference frame of the tensor, the off-diagonal terms of the resistivity tensor are proportional to $(\rho_1 - \rho_2)\sin(2\theta)$, where θ is the angle between the anisotropy axis and the reference x-axis (see section 6.5 for derivation). As a result, when an electrical current I_x flows in the x direction, a transverse voltage V_y appears across the edges perpendicular to the y axis, giving a nonvanishing $R_{xy} = V_y/I_x \propto (\rho_1 - \rho_2)\sin(2\theta)$ as long as $\sin(2\theta) \neq 0$ and $\rho_1 \neq \rho_2$. The first condition is assumed to be true in our experiment, since the lattice orientation is random with respect to the sample edge. Consequently, a non-vanishing transverse resistance in our experiment implies anisotropic resistivity, $\rho_1 \neq \rho_2$, and therefore the breaking of the six-fold rotational symmetry of TBG. Note that this transverse voltage is fundamentally different from the Hall effect since time-reversal symmetry is not broken. In order to quantitatively analyze the transverse voltage, we need to remove any residual longitudinal component that might appear in the transverse voltage due to imperfect alignment of the four-probe voltage contacts and/or sample inhomogeneity (see also section 6.5) [260]. Fig. 6-3a shows the raw R_{xx} and R_{xy} measured for device A near the wedge-like feature, as shown in Fig. 6-2a. At high temperatures (40 K), where the anisotropies associated with electron correlation effects are presumably overwhelmed by thermal fluctuations, both R_{xx} and R_{xy} are linear in T and proportional to each other: $R_{xy} \approx -0.05R_{xx}$ [258]. To correct for this background signal that is likely a result of the imperfect voltage probe alignment, we subtract this R_{xx} component from R_{xy} so that at the highest temperature of 40 K the net signal is zero. This corrected transverse voltage $R_{xy}^{\mathrm{cr}} = R_{xy} - \alpha(n)R_{xx}$, where $\alpha(n)$ is a density-dependent numerical factor typically within ± 0.1, constitutes an accurate measure of the resistivity anisotropy (purple curve in Fig. 6-3a). We note that, while no signal is present at higher temperatures, below 6 K there is a significant negative peak in R_{xy}^{cr}, which indicates the onset of anisotropy at this temperature.

The gate and temperature dependence of the anisotropy, shown in Figs. 6-3b-c for zero magnetic field and $B_\perp = 0.5$ T (see section 6.5), clearly reveals a prominent anisotropy 'wedge' as well. The transverse voltage measured at $B_\perp = 0.5$ T is symmetrized with data

measured at $B_\perp = -0.5\,\mathrm{T}$ to remove the contribution from the Hall voltage. Here we plot the normalized quantity $R_{xy}^{\mathrm{cr}}/R_{xx}$, which is approximately proportional to the anisotropy ratio $\frac{\rho_1-\rho_2}{\rho_1+\rho_2}$ (see section 6.5). We also mark out the superconducting dome in Fig. 6-3b-c. Immediately above the superconducting dome on the 'underdoped' side (lower $|n|$), we find a strong transverse voltage signal with a sign change at around $-1.59\times10^{12}\,\mathrm{cm}^{-2}$ (see Fig. 6-8 for the entire range of density). The position of the anisotropy wedge matches well with the resistive wedge-like feature that we observed in Fig. 6-2a. The sign change indicates that the anisotropy changes from $\rho_1 > \rho_2$ to $\rho_1 < \rho_2$ (or vice versa). In $B_\perp = 0.5\,\mathrm{T}$ (Fig. 6-3c), the anisotropy wedge with negative values of R_{xy}^{cr} persists to zero temperature, consistent with the behavior of the resistive wedge-like feature in Fig. 6-2b as well. On the other hand, we notice that the anisotropy with positive R_{xy}^{cr} near $-1.65\times10^{12}\,\mathrm{cm}^{-2}$ disappears as superconductivity is suppressed by the magnetic field, which might be explained by the vestigial order from the nematic superconductivity that will be discussed in the next section.

6.2.3 Nematic superconducting state

A natural question to ask is whether the superconducting phase exhibits any anisotropic properties as well. To investigate this, we measure the angle-dependent in-plane magnetic field response of the superconducting phase. In magic-angle TBG, the superconductivity is suppressed by an in-plane magnetic field of the same order of magnitude as the Pauli paramagnetic limit [83]. Using a vector magnet in a dilution refrigerator, we apply a magnetic field up to 1 T in an arbitrary direction within the sample plane (see Fig. 6-4a for illustration). We compensate for possible sample tilt by applying a small out-of-plane magnetic field, so that the magnetic field is parallel to the sample to within $|B_\perp| < 2\,\mathrm{mT}$ at $|B_\parallel| = 1\,\mathrm{T}$, which is much less than the perpendicular critical magnetic field of our devices (see section 6.5 and Fig. 6-9 for the detailed calibration procedure, and see Fig. 6-11 for the perpendicular critical magnetic fields of devices A and B). Figure 6-4b shows an example of the resistivity versus in-plane magnetic field magnitude and angle θ_B (with respect to the length of the Hall bar, see Fig. 6-4a). A two-fold anisotropic suppression of

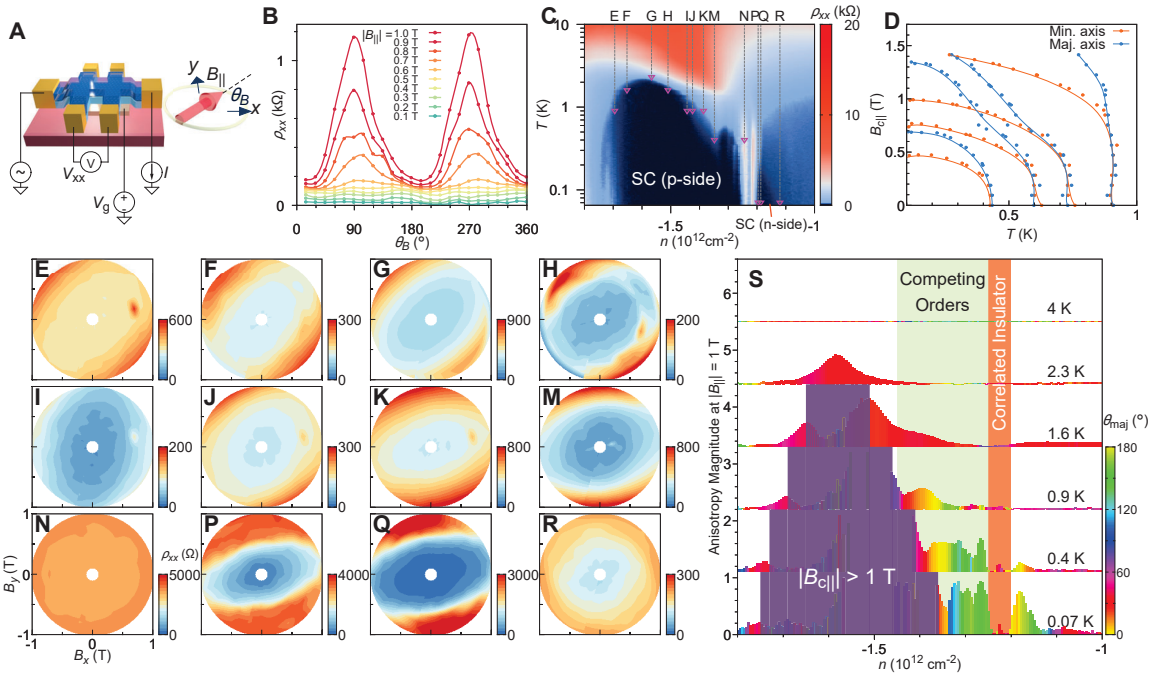

Figure 6-4: Evidence for nematic superconductivity in magic-angle TBG. (a) Definition of the in-plane field angle θ_B with respect to the device orientation. $\theta_B = 0$ (x-axis) is defined as the source-drain direction of the Hall bar device. (b) Resistivity as a function of θ_B for different magnitudes of the in-plane magnetic field, showing a clear two-fold anisotropy. Measurement is taken at $n = -1.18\times10^{12}\,\mathrm{cm}^{-2}$ and $T = 70\,\mathrm{mK}$. (c) Detailed view of the superconducting domes in device B, showing a large and a small superconducting dome on the p-side and n-side of the insulating state. (d) Critical in-plane magnetic field $B_{c\|}$ versus temperature along the major and minor axis of the two-fold anisotropy, measured in device A at carrier densities of $-1.44\times10^{12}\,\mathrm{cm}^{-2}$, $-1.42\times10^{12}\,\mathrm{cm}^{-2}$, $-1.40\times10^{12}\,\mathrm{cm}^{-2}$ and $-1.23\times10^{12}\,\mathrm{cm}^{-2}$ respectively (from right to left). (e-r) Polar maps of the anisotropic response of the resistivity across the superconducting domes. The carrier densities and temperatures at which (d-q) are measured correlate with the labels in (c). (s) For device B, we extracted the magnitude (represented by height) and the polar angle of the major axis θ_{maj} (represented by the color, see section 6.5 for details) of the nematicity at different densities and temperatures, with $|B_\|| = 1\,\mathrm{T}$. The data for different temperatures are shifted vertically for clarity. Inside the region shaded in purple, the critical in-plane magnetic field is larger than 1 T and cannot be measured in our setup. In the density range of -1.45×10^{12}–$-1.2\times10^{12}\,\mathrm{cm}^{-2}$, the anisotropy polar angle θ_{maj} rotates rapidly with the carrier density, possibly due to the competition with the wedge-like feature we identified in Fig. 6-2 and Fig. 6-3.

the superconductivity can be clearly seen. We have checked that the direction of the current flow is not correlated with the anisotropy direction, and therefore the anisotropic Lorentz force contribution can be excluded (see Fig. 6-12). The anisotropy is not aligned with the length or width of the Hall bar either (see Fig. 6-12).

The two-fold anisotropy of the in-plane magnetotransport response points towards nematicity that is intrinsic to the superconducting phase, since it breaks the six-fold rotational symmetry of the moiré superlattice. We have systematically studied this nematic behavior across the entire superconducting dome of device B. In Figs. 6-4e-r we show polar maps of the magneto-resistivity at different carrier densities and temperatures in the hole-doping and electron-doping superconducting domes as labeled in Fig. 6-4c. At all densities except those in Figs. 6-4n and 6-4r, we find elliptic contours that have major/minor axis ratio up to 3. Note that we chose to always measure near T_c, since deep inside the superconducting dome the in-plane critical field is usually larger than 1 T and cannot be measured in our setup. However, we have confirmed the nematicity in the $T \ll T_c$ region by simultaneously applying a small perpendicular field to partially suppress the superconducting state (see Fig. 6-13). At the densities corresponding to Figs. 6-4n and 6-4r, which are outside the superconducting regions, the anisotropy is essentially nonexistent. In general, the two-fold anisotropy occurs inside the broad transition from superconducting to normal state as a function of $B_{\parallel}$, suggesting that it is a property intrinsic of the superconducting fluctuations [261], since the normal state does not show any anisotropy in the in-plane magnetoresistance (see Fig. 6-15). In device A, we have also observed similar two-fold anisotropic in-plane critical field (Fig. 6-4d). The critical magnetic field $B_{c\parallel}$ along the major axis extrapolated to zero temperature exceeds that along the minor axis by 40–80 % in this device.

Fig. 6-4s shows the evolution of the magnitude and of the director of the nematic component of the superconducting state in device B as a function of carrier density and temperature. Our data shows that the nematic director, as measured by the angle of rotation of the ellipse's major axis, does not appear to be exactly locked to any particular spatial axis, but instead evolves continuously with carrier density and temperature. In particular, in the superconducting dome on the hole-doping side of $-n_s/2$,

the direction of the major axis varies slowly within −10–20° in the density range of -1.70×10^{12}–-1.45×10^{12} cm^{-2} (corresponding to the ellipses from Fig. 6-4e to 6-4h), while in the range of -1.45×10^{12}–-1.25×10^{12} cm^{-2} (from Fig. 6-4i-m) the major axis rotates quickly with the carrier density. From Fig. 6-4i to Fig. 6-4m, the major axis rotates by ∼90°. We note that the latter range of density again coincides with the resistive wedge-like feature for device B, as shown from Figs. 6-2b and 6-2d. The smaller superconducting dome on the electron-doping side near -1.20×10^{12} cm^{-2} exhibits significant nematicity as well (Fig. 6-4p and q), with a director pointing from 120° to 160°. As we explain below, the fact that the nematic director changes direction as a function of doping and temperature makes it unlikely that the superconducting anisotropy is simply a response to strain present in the sample. On the contrary, this observation is consistent with spontaneous rotational symmetry-breaking characteristic of an intrinsic nematic superconductor.

6.2.4 Anisotropic response of the superconducting gap

The observation of nematicity puts certain constraints on possible pairing symmetries of the superconducting order parameter [245, 262, 263]. One can obtain information about the superconducting gap by measuring the critical current I_c. Here, by measuring I_c of device B in the presence of in-plane magnetic fields, we demonstrate that the nematicity is not only manifested in the resistivity measurements, but also creates an anisotropic modulation of the superconducting gap. Figs. 6-5a-b show the waterfall plots of differential resistance $dV_{\mathrm{xx}}/dI_{\mathrm{bias}}$ versus dc bias current I_{bias} at two carrier densities, in an in-plane magnetic field $|B_{\parallel}| = 1$ T along different directions indicated by the colors. At the carrier density in Fig. 6-5b, the plot shows two critical currents at 110 nA and 210 nA respectively, which might be due to domains in the device with different twist angles or nematic directors. Interestingly, at both carrier densities the critical current shows significant two-fold modulation by the in-plane magnetic field direction θ_B. The θ_B dependence can be fit by a sinusoidal function $\cos 2(\theta_B - \theta_{B0})$ (Fig. 6-5c), where θ_{B0} is the direction of the major axis. The modulation amplitude as a function of the in-plane field magnitude is shown in the inset of Fig. 6-5c, and follows an approximately quadratic power law dependence.

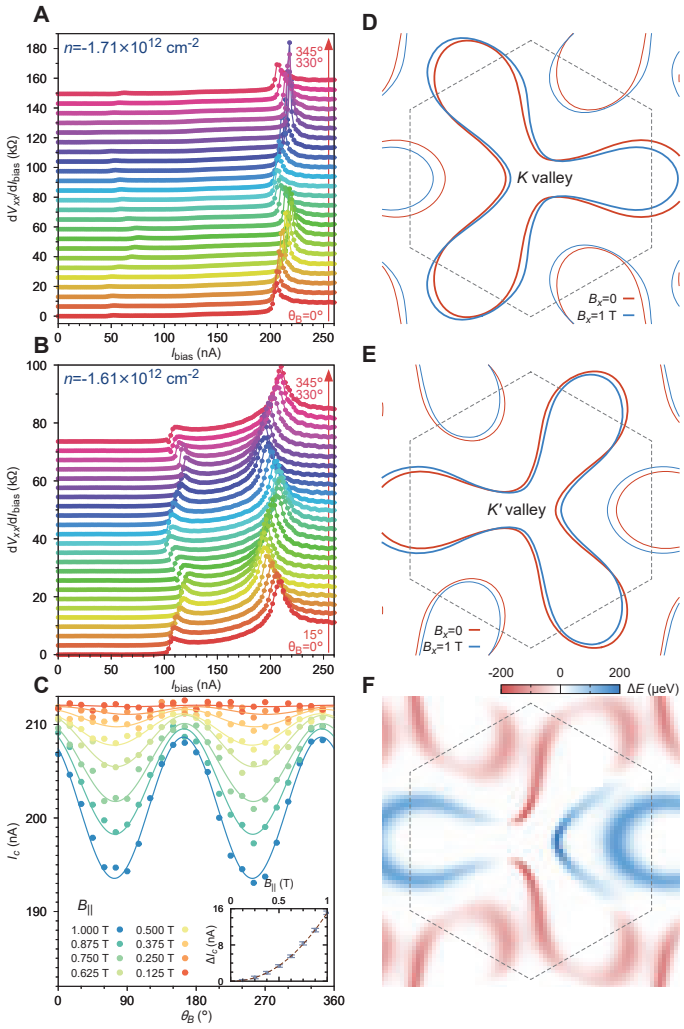

Figure 6-5: Anisotropic response of the superconducting critical current. (a-b) Differential resistance $dV_{\mathrm{xx}}/dI_{\mathrm{bias}}$ versus bias current I_{bias} as a function of the orientation of the in-plane magnetic field at two carrier densities. The orientation is indicated by the color, differing by 15° between adjacent curves, which are vertically shifted for clarity. (c) Modulation of the larger critical current in (b) by in-plane magnetic fields with different orientations and magnitudes. A sinusoidal function is used to fit the data (see text). The inset shows the modulation amplitude (peak-peak) as a function of the field magnitude, which can be fit by a power law $\Delta I_c \propto |B_\parallel|^\alpha$ with $\alpha \approx 2.1$. (d-e) Calculated Fermi contour of $\theta = 1.09°$ TBG at $B_x = 0$ and $B_x = 1\,\mathrm{T}$ around K and K' valleys respectively. (f) Energy splitting between states at opposite momentum and opposite valleys along the Fermi surface $\Delta E(\vec{k}) = E_{K'}(\vec{k}) - E_K(-\vec{k})$ at $B_x = 1\,\mathrm{T}$. For comparison, the Zeeman splitting $g\mu_B B$ at $B = 1\,\mathrm{T}$ for $g = 2$ is 115 μeV. The gray hexagons in (d-f) denote the moiré Brillouin zone.

An anisotropic response in the critical current may originate from (i) the superconducting gap Δ and/or (ii) anisotropic properties of the underlying normal state (R_n). Although we have shown that the normal state exhibits considerable resistivity anisotropy at densities near the wedge-like feature in Fig. 6-3, we argue here that the anisotropic response of the critical current is not a result of the anisotropy of R_n. First, Fig. 6-5a is measured at a density for which there is essentially no resistivity anisotropy in the normal state ($R_{xy}^{\mathrm{cr}}/R_{xx} = -0.007$ at the lowest T in Fig. 6-3c), while Fig. 6-5b is measured at one with significant anisotropy in the normal state ($R_{xy}^{\mathrm{cr}}/R_{xx} = -0.325$ at the lowest T in Fig. 6-3c). However, the modulation of the critical current at these two densities shows similar magnitudes. Second, an anisotropy in the resistivity tensor may not necessarily imply a large anisotropic response of the resistivity versus in-plane magnetic field. In fact, as we show in Fig. 6-15, inside the wedge-like feature in the normal state in device A, we could not measure significant anisotropic response to the in-plane field. Thus, these results suggest that the anisotropic response of the critical current might not be directly related to the resistivity anisotropy of the normal state and hence may originate from an anisotropic superconducting gap.

To discuss the mechanism by which the in-plane field couples to the superconducting gap, we note that if the former couples solely to the spin degree of freedom (and thus the gap is only suppressed by the Zeeman coupling), spin-orbit interaction must be introduced to explain the dependence of I_c on the direction of $B_{\parallel}$. However, the intrinsic spin-orbit coupling in graphene-based systems is known to be very weak. We might consider the following mechanism to reconcile these facts. As illustrated in Fig. 6-1a, the unit cell of magic-angle TBG has a length scale of $a \sim 14\,\mathrm{nm}$. Despite the separation between the graphene sheets in TBG being merely $\delta \sim 0.3\,\mathrm{nm}$, an in-plane magnetic field penetrating them induces a small but non-negligible magnetic flux in the cross-section of the unit cell with an area $S \sim a \cdot \delta$, which modifies the Fermi contours. To demonstrate this effect, we numerically calculated the Fermi contours at $-n_s/2$ for $B_{\parallel} = 0$ and $B_{\parallel} = 1\,\mathrm{T}$ along the x direction using the Bistritzer-MacDonald continuum model [81]. Figs. 6-5d and 5e show the original and modified Fermi contours for the K and K' valleys respectively. As can be seen from the contours, a noticeable shift is induced by the in-plane magnetic field. The

K/K' valley degeneracy is lifted by the momentum shift between the two layers introduced by the in-plane field, which is proportional to $e\delta B_{\parallel}$, a substantial shift given the small size of the Brillouin zone. If one assumes that only electrons with opposite momentum and valley are allowed to form Cooper pairs in the superconducting phase, the two states from opposite valleys would be at slightly different energies when an in-plane field is applied, which serves to suppress the superconductivity in a similar fashion as the paramagnetic (Zeeman) effect in the case of spins. To more intuitively demonstrate this, Fig. 6-5f shows the de-pairing energy along the Fermi contour $\Delta E(\vec{k}) = E_{K'}(\vec{k}) - E_K(-\vec{k})$. It is strongly directional dependent and has a similar order of magnitude as the Zeeman energy at $B_{\parallel} = 1\,\mathrm{T}$ ($g\mu_B B_{\parallel} \approx 115\,\mu\mathrm{eV}$ where $g = 2$, μ_B is the Bohr magneton). The de-pairing energy exhibits a six-fold variation with respect to the direction of the in-plane magnetic field, while the nematic component of the superconducting order can further spontanously break this symmetry down to the observed two-fold symmetry [261, 262, 264]. A small strain can further assist to pin down the nematic domain along a given direction.

6.3 Discussion

Our measurements reveal two distinct anisotropic states in the phase diagram of magic-angle TBG: a normal-state wedge-like feature above the superconducting dome and a nematic pairing state. As shown by the longitudinal resistivity and transverse voltage measurements presented in Fig. 6-2 and Fig. 6-3, the wedge-like feature is associated with a zero-temperature insulating phase that shows significant resistivity anisotropy, indicative of broken six-fold lattice rotational symmetry. Thus, this normal state phase might be either an electronic nematic state or an electronic smectic state – i.e. a charge or spin density-wave that, in addition to rotational symmetry, also breaks translational lattice symmetry. In either case, the rotational symmetry-breaking can be described by a two-component 3-state Potts nematic order parameter [265, 264]. Electronic correlations might be important for the formation of such a state. Twisted bilayer graphene is well-known to exhibit van Hove singularities (vHs), which in general do not occur exactly at half-filling [75, 266]. Near the vHs, it has been theoretically shown that the significant nesting between the K- and

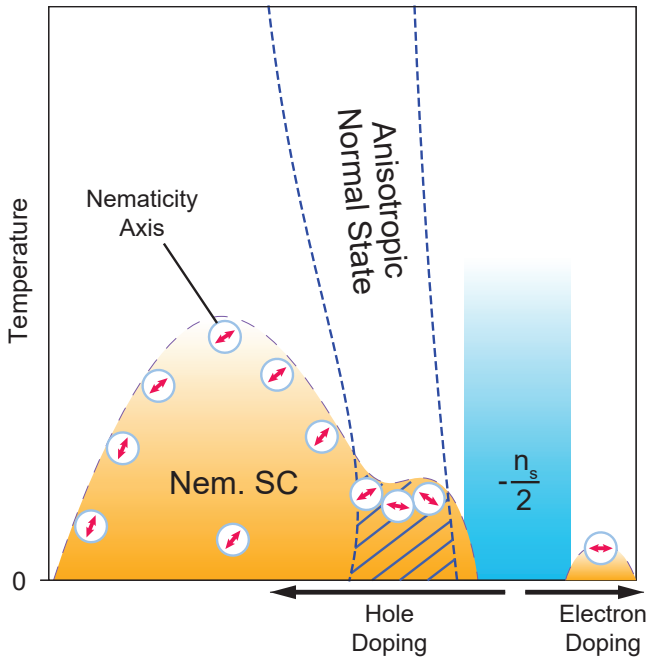

Figure 6-6: Summary of various competing phases we identified in this chapter. In the underdoped side of the superconducting dome, we find a normal state anisotropic phase that, at low temperatures, competes with superconductivity, creating a depression in the T_c curve. In the superconducting state we find nematicity, manifested in its response to in-plane magnetic fields. By comparing the extracted nematicity temperature $T_{\rm nem}$ to T_c we find that the entire superconducting dome exhibits nematicity, which suggests that the nematicity is intrinsic to the superconductivity and points towards a possible unconventional pairing symmetry. The dashed area denotes the competing region between the two states, where a reduction in T_c as well as a strong rotation of the nematicity axis are seen.

K'-valley Fermi contours might induce density wave ordering [263]. Remarkably, recent scanning tunneling experiments have identified prominent rotational-symmetry-broken features in the normal state local density of states [87, 88, 267]. Alternatively, strong-coupling models can also yield nematic and density-wave states [268, 269]. For the superconducting phase, it remains to be seen whether its nematic character, as revealed by the measured in-plane anisotropy of the critical field, can be reconciled with s-wave pairing. Alternatively, this behavior could be explained in terms of a two-component p-wave/d-wave gap, indicative of an unconventional pairing mechanism [270].

A crucial question is whether the anisotropies observed here have intrinsic or extrinsic origins. The fact that we do not observe multiple nematic domains within the same device implies that some degree of residual strain is present. The issue is whether this strain is the sole cause of the anisotropy (extrinsic origin), or whether it is mainly pinning one of the three underlying nematic domains (intrinsic origin). To address this, we note that such a residual strain should be a property of the device, and thus should be present at all temperatures and doping. In contrast, as shown in Fig. 6-3, the onset of the normal-state anisotropy is restricted to a narrow doping range and to temperatures below 10 K. Furthermore, the resistance anisotropy is on the order of one in the 'wedge'-like feature (see Fig. 6-3b). Such a large effect would be difficult to be explained by a reasonably sized residual strain.

While these quantitative arguments rely on the amplitude of the anisotropy, a more direct argument against an extrinsic origin can be made from the direction of the anisotropy. Our measurements in the superconducting state clearly show a rotation of the nematic director (Fig. 6-4e-r, s). In the 3-state Potts model, the three states correspond to the three nearest-neighbor directions in the moiré superlattice [264]. Here, strain acts as a conjugate field to the nematic order parameter, similarly to how a magnetic field acts on a ferromagnet. If the strain is "parallel" to one of the three anisotropy directions, the corresponding nematic director is favored over the other two. As a result, the nematic director is fixed at all temperatures. If the strain is "anti-parallel" to a direction, the other two directions become favored. Consequently, as the temperature is lowered towards the nematic state, the nematic director continuously rotates from the disfavored direction to one of the two

favored directions [264]. Importantly, this can only happen if nematic order is spontaneous, i.e., if it is an intrinsic instability of the system, as it is supported by a phenomenological calculation shown in section 6.5. Therefore, the continuous rotation of the nematic director in our observation indicates that the anisotropy of the superconducting state is more likely to be intrinsic, as an extrinsic origin would result in a fixed orientation.

Another possible source of anisotropy is twist angle variations across the device, which could create an inhomogeneous distribution of strain [56]. While further studies are needed, we note that such an inhomogeneous strain would act as a random field to the Potts-nematic order parameter, which might affect the nematic properties in 2D [271]. However, the fact that we do not see different nematic domains across our device seems to suggest that the global residual strain is probably dominating over the local strain caused by twist angle fluctuations.

The various phases discussed throughout this chapter are summarized in Fig. 6-6 (see section 6.5 and Fig. 6-14 for the extracted nematicity temperature T_{nem}). The fact that an anisotropic response to an in-plane magnetic field is seen only in the superconducting state, but not in the wedge-like feature, suggests that the origins of nematicity in the normal and superconducting states are likely different. This is also consistent with the fact that these two orders compete, as evident from the suppression of T_c when the wedge-like feature intersects with the superconducting dome. However, since both phases break the same six-fold lattice rotational symmetry, the order parameters of these two phases can interact beyond mere competition, which may be responsible for the rapid change of the ellipse direction in the coexisting region of the phase diagram (see section 6.5). Moreover, normal-state nematic fluctuations may play an important role in favoring a superconducting ground state that is also nematic. While the onset of nematicity and of superconductivity seem very close in our experiment (see section 6.5), it is possible that the nematic order in magic-angle TBG persists even above T_c, a phenomenon known as vestigial nematic order [243, 245, 265]. Interestingly, in Fig. 6-3b, there is a region just above the superconducting dome with positive transverse voltage signal at $n \approx -1.65{\times}10^{12}\,\mathrm{cm}^{-2}$ and $T \approx 2\,\mathrm{K}$. This not only has opposite sign than the anisotropy of the wedge-like state, but it also disappears when superconductivity is suppressed (Fig. 6-3c). Thus, this feature might be explained

by a vestigial nematic order that forms prior to the condensation of Cooper pairs [243, 245, 265]. Scanning probe experiments are encouraged in the future to confirm this nematic phase above the superconducting transition.

6.4 Conclusion

In summary, our experiments extend the already rich phase diagram of magic-angle TBG to include a nematic superconducting state and an anisotropic normal state above the 'underdoped' part of the superconducting dome. The competition between them results in a reduction of T_c and in a fast rotation of the nematic director of the superconducting state. Our results pioneer the study of competing/intertwined quantum phases in a highly tunable two-dimensional correlated platform, which in turn may shed more light onto the unconventional superconductivity in iron-based compounds, doped Bi_2Se_3 and other nematic superconductors.

6.5 Extended data and supplementary information

6.5.1 Sample fabrication

High quality magic-angle twisted bilayer graphene (TBG) devices are fabricated using the techniques described in Chapter 2.9.

6.5.2 Measurement setup and data analysis

Transport measurements are performed using the setup described in Chapter 2.10.1. The twist angles of the devices are determined using the procedure described in Chapter 2.10.2. The error bars in Fig. 6-1e are estimated by visually inspecting how well the Landau levels emanating from the Dirac point, $\pm n_s/2$ and $\pm n_s$ fit to the expected Landau fan of a given twist angle.

6.5.3 Landau fan diagram

To demonstrate the high quality and similarity in device A and device B that we discussed throughout this chapter, in Fig. 6-7 we show the Landau fan diagram of device A measured at low temperatures. The Landau fan diagram of device B can be found in Fig. 1 of Ref. [56], which is measured on the same device. Note that in Ref. [56], the twist angle is determined to be $\theta = 1.06°$, while in this work we assign a value of $\theta = 1.08 \pm 0.03°$. In both devices A and B, we observe 4-fold degenerate Landau levels at the charge neutrality, which break down to two-fold or one-fold at high fields. We also observe two-fold degenerate levels emanating from $\pm n_s/2$, consistent with the original report in magic-angle TBG [83].

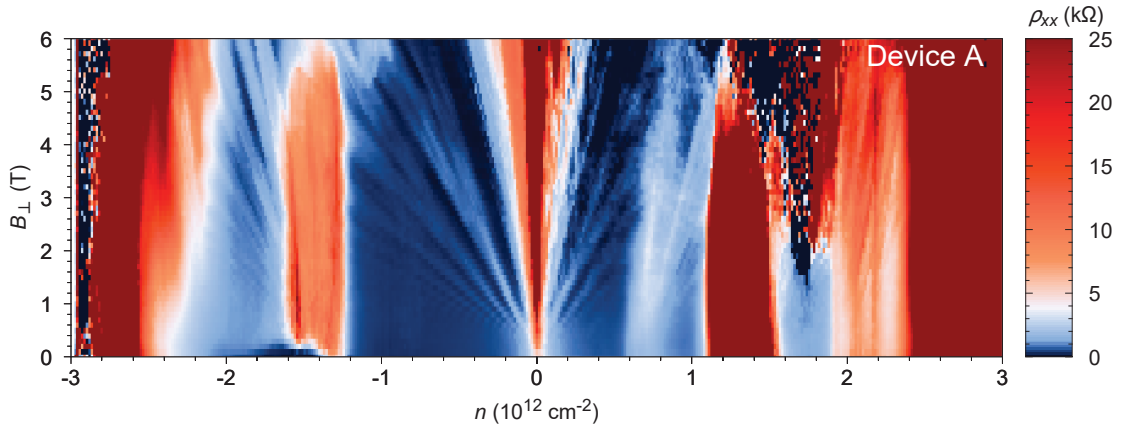

Figure 6-7: Landau fan diagram of device A, measured at the base temperature $T = 70\,\text{mK}$.

6.5.4 Normal-state anisotropy measured through transverse voltage

In Fig. 6-3 we use transverse voltage measurements to infer possible anisotropy in the resistivity tensor when $T > T_c$. Specifically, an anisotropic 2D conductor has different resistivity along its principle axis

$$\rho = \begin{pmatrix} \rho_1 & 0 \\ 0 & \rho_2 \end{pmatrix}, \tag{6.1}$$

where $\rho_1 \neq \rho_2$. In a reference frame that is rotated from the principle axis by θ, the resistivity tensor transforms as

$$\rho' = \begin{pmatrix} \frac{1}{2}(\rho_1+\rho_2) + \frac{1}{2}(\rho_1-\rho_2)\cos(2\theta) & \frac{1}{2}(\rho_1-\rho_2)\sin(2\theta) \\ \frac{1}{2}(\rho_1-\rho_2)\sin(2\theta) & \frac{1}{2}(\rho_1+\rho_2) - \frac{1}{2}(\rho_1-\rho_2)\cos(2\theta) \end{pmatrix} \tag{6.2}$$

Therefore, the off-diagonal term $\rho'_{12} = \rho'_{21}$ is proportional to the anisotropy in resistivity $\rho_1 - \rho_2$. This term can be experimentally observed in the transverse voltage configuration by measuring $R_{xy} = V_y/I_x$, similar to Hall effect measurement except that no external magnetic field is applied. In actual devices, however, R_{xy} is frequently measured to be non-zero even in isotropic materials due to R_{xx} mix-in. This can for example occur due to imperfect alignment of the transverse voltage probes, obscuring the anisotropic signal by introducing a large background [258]. The mix-in results in a component in R_{xy} that is proportional to R_{xx} at all temperatures. To account for this, we assume that the device is isotropic at high temperatures, so that ρ_{12} is zero, and then estimate the contribution from the R_{xx} mix-in by dividing the measured R_{xy} over R_{xx} at this temperature for each density n, obtaining the ratio $\alpha(n) = R_{xy}(T_{\max})/R_{xx}(T_{\max})$. Assuming the mix-in is temperature independent, we subtract the contribution proportional to R_{xx} at all temperatures. This corrected R_{xy} is denoted as $R^{\mathrm{cr}}_{xy}(n,T) = R_{xy}(n,T) - \alpha(n)R_{xx}(n,T)$, which by definition satisfies $R^{\mathrm{cr}}_{xy}(T = T_{\max}) = 0$. Finally, we normalize the corrected quantity by R_{xx}, which is approximately related to the anisotropy as

$$\frac{R^{\mathrm{cr}}_{xy}}{R_{xx}} \approx \frac{W}{L}\frac{\rho_1-\rho_2}{\rho_1+\rho_2}\sin(2\theta) \approx \frac{W}{L}\frac{\Delta\rho}{2\rho}\sin(2\theta), \tag{6.3}$$

provided that $\rho_1 - \rho_2 \ll \rho_1, \rho_2$. L and W are the length and width of the sample respectively. Unless the device is coincidentally aligned with the anisotropy axis such that $\theta = 0$, this normalized quantity is characteristic of the anisotropy ratio $\frac{\Delta\rho}{\rho}$. It should be noted that this measurement always tends to underestimate the anisotropy, since $|\sin(2\theta)| < 1$.

In a perpendicular magnetic field, the transverse voltage will attain an additional Hall component proportional to $B_\perp$. To probe the normal-state anisotropy in a small perpendicular magnetic field, we measure R_{xy} at both $B_\perp$ and $-B_\perp$ and take the average between

them. The R_{xy} signal symmetrized in this fashion would in principle contain no Hall voltage and is attributed only to the anisotropy.

In addition to the vicinity of the superconducting domes, we measured the transverse voltage in the entire flat-band densities $-n_s \leq n \leq n_s$, up to 40 K. As shown in Fig. 6-8, we find that there is considerable anisotropy near $+n_s/2$ and $+3n_s/4$ as well, which might be related to the same type of phase that is responsible for the anisotropy near $-n_s/2$. Noticeably, near the Dirac point ($n = 0$) there is a diffuse triangular region with weak anisotropy that changes direction as n crosses zero. This phenomena might be related to the recently proposed nematic topological semimetallic behavior near the charge neutrality point of TBG [272]. Recent scanning tunneling experiments also show evidence of C_3-symmetry breaking near the charge neutrality of magic-angle TBG [88].

6.5.5 Compensation for device tilt in in-plane magnetic field measurements

The in-plane field behavior of the TBG devices is measured in an American Magnetics Inc. 3-axis vector magnet with maximum x/y fields of 1 T. When loading samples into the cryostat, however, it is hardly possible to perfectly align the sample plane to the x-y field plane. Typically the sample is tilted by about 1–2° with respect to the field plane.

To calibrate and compensate for this tilt, we use the superconductivity of magic-angle TBG itself to act as a perpendicular magnetic field sensor. Near the edge of the superconducting dome (where superconductivity barely survives), the resistance of the device is highly sensitive to the variation in perpendicular magnetic field and therefore can be used as a reference to nullify the residual perpendicular magnetic field, accurate to 1–2 mT. Figure 6-9a shows examples of resistance versus $B_\perp$ curves at various (B_x, B_y). Sharp reductions of the resistance can be seen in each curve, the center of which we identify as the 'true' zero magnetic field at each (B_x, B_y) point.

We use a two-step procedure to calibrate the sample tilt:

1. Global rough calibration. We measure the perpendicular magnetic field $B_\perp$ at which the resistance is minimized, at a number of points (B_x, B_y), and fit the loci of the

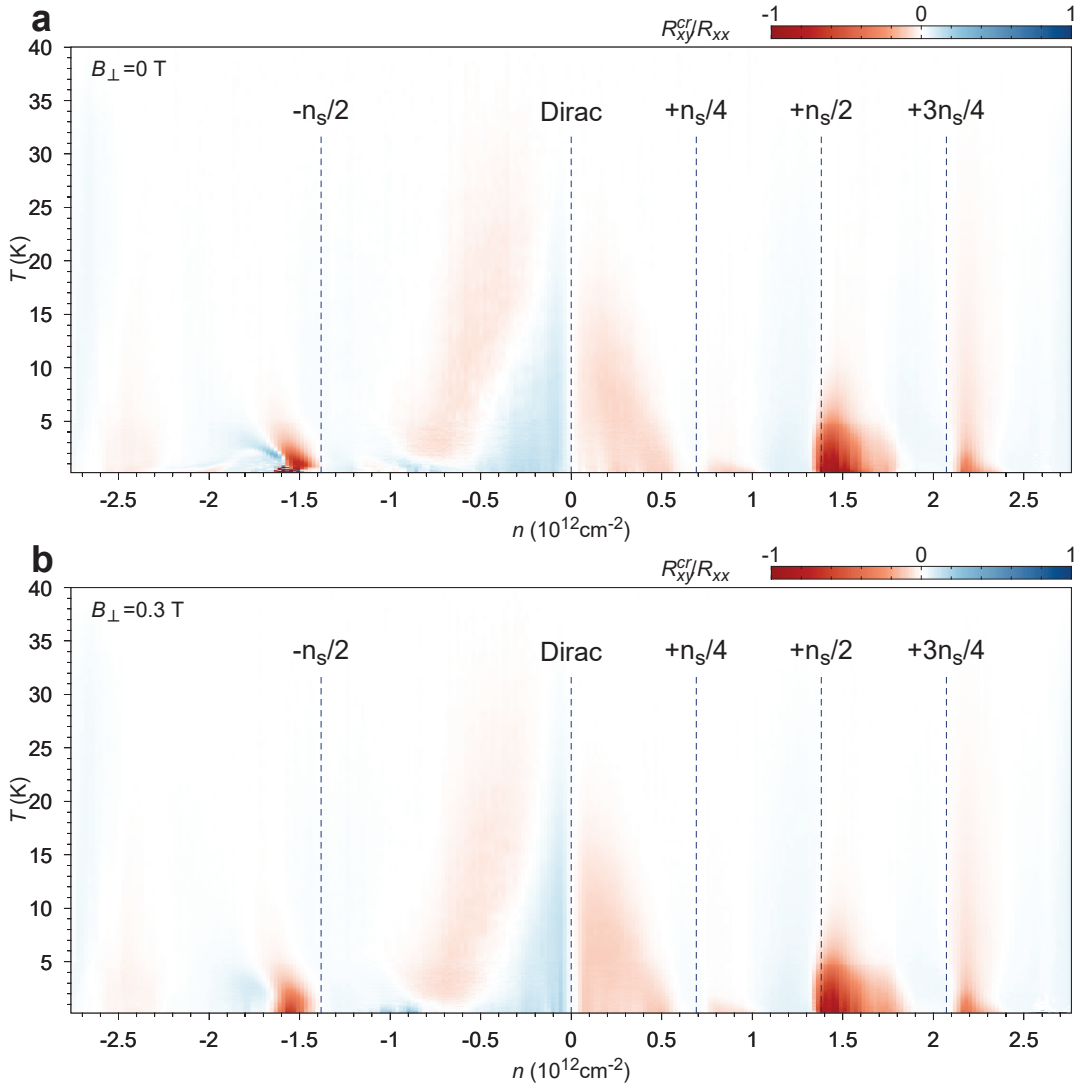

Figure 6-8: Normal-state anisotropy via transverse voltage measurements in device A. (a) $R_{xy}^{\mathrm{cr}}/R_{xx}$ ratio in device A across the entire density range $-n_s \leq n \leq n_s$ at zero magnetic field. (b) Same measurement, performed at $B_\perp = 0.3\,\mathrm{T}$.

minima to a function in the form of $B_\perp = aB_x + bB_y + c$, to obtain the tilted plane of the sample. Figure 6-9(b) shows an example of such a plane fit, with an adjusted R^2 of 0.9884 and maximal deviation of 6.6 mT from the data.

2. Fine calibration. Using the plane-fit value obtained from the global calibration, random deviations by more than 5 mT from the 'true' zero field value still occur, either due to a change in magnetization of the cryostat or tilting/tipping of the sample holder

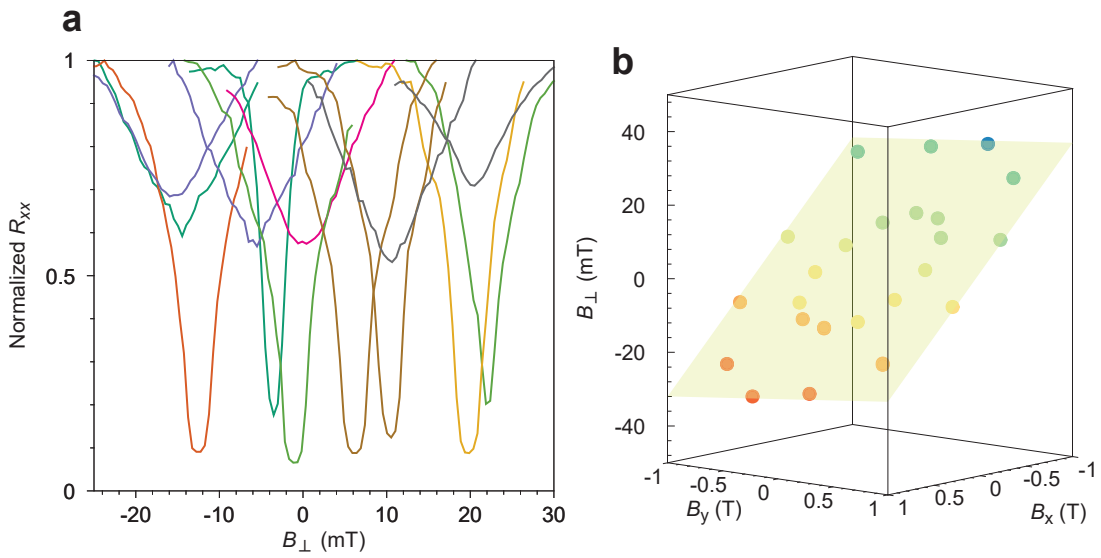

Figure 6-9: (a) Example curves of normalized R_{xx} used for calibrating offset in perpendicular magnetic field taken at various in-plane fields and temperatures. (b) Example of planar fitting that we use to globally correct for the sample tilt. In this example 24 points are taken in the $B_x - B_y$ plane, and for each point a calibration similar to those shown in (a) is performed and the minimum is plotted in the graph. The plane shown in the graph is a least-square fit of the minima to a plane, $aB_x + bB_y + c$. The coefficients are fit to be $a = -0.029\,99, b = 0.003\,625, c = 0.001\,658$ T, with an adjusted R^2 of 0.9884. These values correspond to a tilt angle of about 1.7° from the $B_x - B_y$ plane.

due to magnetic forces. Therefore we perform an additional fine correction around the plane-fit value, whenever B_x or B_y is changed. The principle is similar: we take a fine scan of $B_\perp$ around the plane-fit value and find the minimum in R_{xx}. This procedure greatly reduces the residual field to < 2 mT at the cost of increased measurement time. Any systematic error from the sample tilt is in principle eliminated in this step.

6.5.6 Statistics of superconducting devices

Table 6.1 lists the twist angle and T_c (50 % normal resistance) at optimal doping of all superconducting magic-angle TBG devices we have measured. We show the resistance-temperature (R_{xx}-T) curves for all these listed devices at their optimal doping in Fig. 6-10. T_c is obtained by first fitting the high temperature part of the R_{xx}-T curve to a straight line $AT + B$, then find the temperature where $R_{xx}(T) = 0.5(AT + B)$. In the last column

Device	Twist Angle	T_c (50 %)	Anisotropy/Comments
M1	1.16±0.04°	0.91 K	SC
M2	1.03±0.03°	1.99 K	SC
M3	1.10±0.05°	0.69 K	Disordered
M4	1.06±0.03°	2.98 K	
M6 (Device B)	1.08±0.03°	3.14 K	SC, Normal
M7 (Device A)	1.09±0.02°	2.70 K	SC, Normal
M8	1.08±0.10°	0.40 K	Disordered
M9	1.18±0.04°	0.35 K	
M10	0.98±0.03°	0.46 K	
M12	0.95±0.02°	0.85 K	SC
M13	1.20±0.05°	0.57 K	
M15	0.98±0.02°	0.26 K	
M16	1.02±0.03°	0.70 K	
M18 (Device C)	1.07±0.02°	2.71 K	SC, Normal

Table 6.1: List of superconducting magic-angle TBG devices.

in Table 6.1, we also list what type of anisotropy (SC and/or normal state) we measured in each device. The relevant anisotropy/nematicity data are presented in Section 6.5.12. Among these devices, M3 and M8 have relatively large twist angle disorder and relatively low T_c accordingly. These points are shown in green color in Fig. 6-1.

6.5.7 Perpendicular critical magnetic field of devices A and B

Figure 6-11 shows the resistivity ρ_{xx} in device A and B versus carrier density and perpendicular magnetic field $B_\perp$. The maximum critical perpendicular magnetic field of device A is ~ 0.2 T, and that of device B is ~ 0.3 T. Therefore, any residual perpendicular field < 2 mT that results from imperfect sample tilt correction is much smaller than the critical perpendicular magnetic field and is unlikely to be sufficient to account for the observed two-fold anisotropy.

6.5.8 Nematicity versus current flow direction

To rule out the possibility that the in-plane field anisotropy is related to the current flow direction (due to Lorentz force acting on the electron movement for example), we measure the anisotropy for two perpendicular current flow directions and find that the anisotropy

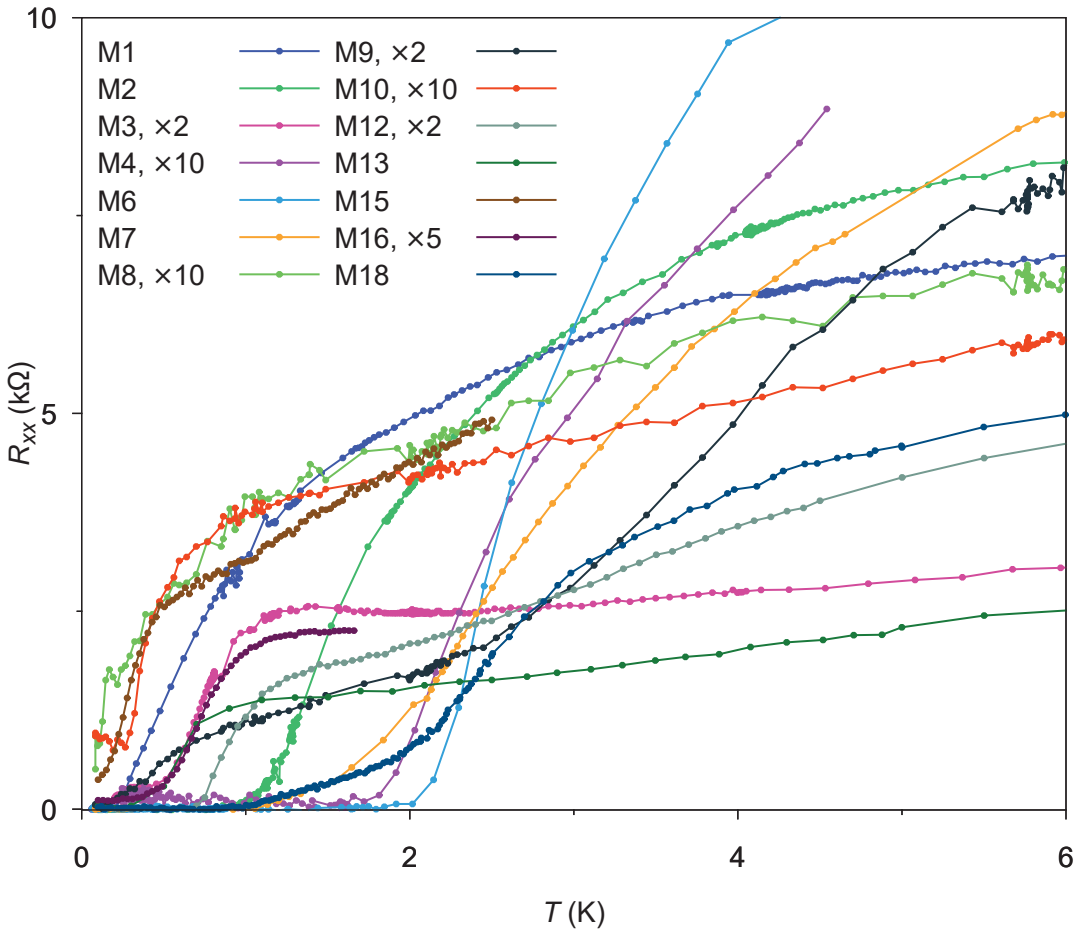

Figure 6-10: Resistance-temperature curves for the magic-angle TBG devices listed in Table 6.1.

axis is invariant, and not aligned to either of flow directions. We measure the two-probe conductance of the device along x and y directions as illustrated in Fig. 6-12a and b respectively. The in-plane field magnitude is fixed at $B_{\parallel} = 1$ T while its orientation is rotated. In both cases, we observe maximum conductance (major axis) along the direction $\theta_B \approx 135°$, which is neither along x (0°) nor y (90°) axis of the Hall bar. This experiment confirms that the spontaneous symmetry-breaking is intrinsic to TBG instead of being determined by the sample geometry or by the external current.

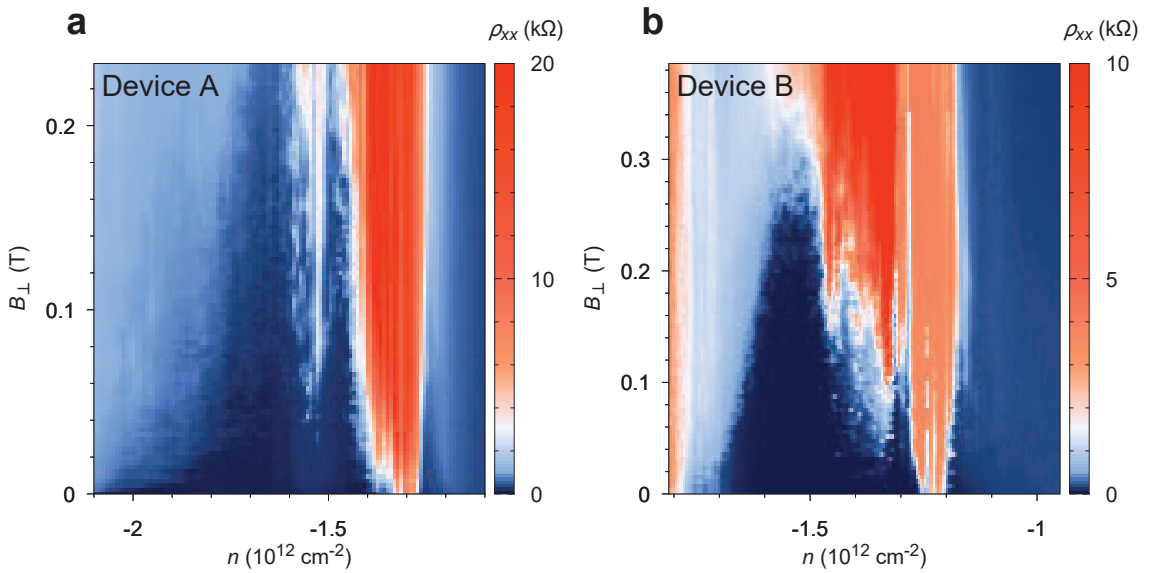

Figure 6-11: The resistivity ρ_{xx} for (a) device A and (b) device B as a function of the carrier density n and the perpendicular magnetic field $B_\perp$, respectively. Measurements are performed at $T = 70\,\text{mK}$.

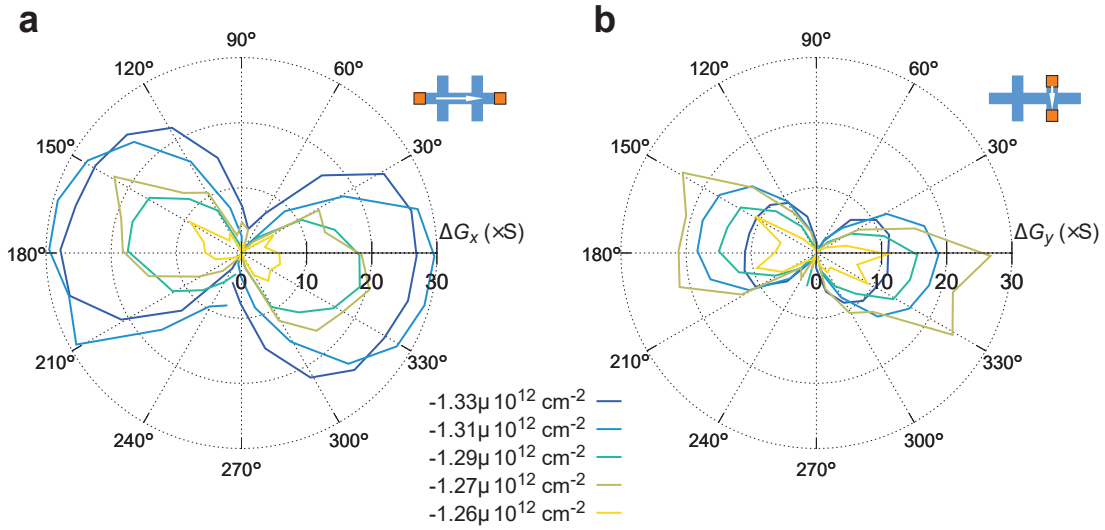

Figure 6-12: Change in two probe conductance of device B when it is sourced from (a) the x direction and (b) the y direction of the Hall-bar sample, in an in-plane magnetic field with the same magnitude of $|B_\parallel| = 1\,\text{T}$ but pointing to the direction indicated by the polar angle. The carrier density is taken at five different values in the underdoped region of the p-side superconducting dome (see Fig. 6-4c for reference of what those carrier densities correspond to in the phase diagram).

6.5.9 Nematicity vs. temperature and perpendicular field

To demonstrate the nematicity across the entire superconducting dome, we have measured the $B_{\parallel}$-θ_B maps of resistivity across the superconducting dome at six different temperatures, 0.07 K, 0.4 K, 0.9 K, 1.7 K, 2.3 K and 4 K respectively. As the temperature is raised, the magnitude of the nematicity in general decreases. We analyze the in-plane magneto-transport data by comparing the resistance measured at $|B_{\parallel}| = 1\,\mathrm{T}$ along different directions. We extract the anisotropy magnitude, defined as $A = (\rho_{\max} - \rho_{\min})/(\rho_{\max} + \rho_{\min})$, as well as the azimuthal angle of the major axis θ_{maj} along which the resistivity is lowest. These results are summarized in Fig. 6-4s, with the anisotropy magnitude and the major axis angle represented by the height and the color of the bars respectively, at each of the measured temperatures.

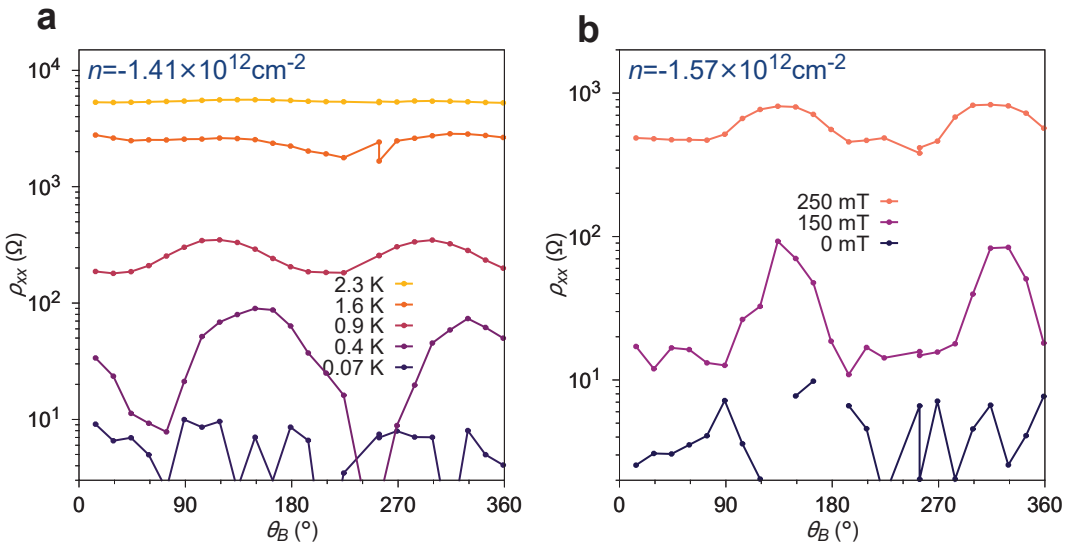

Figure 6-13: Nematicity as a function of temperature and perpendicular magnetic field in device B. The curves are the resistivity as a function of in-plane field direction θ_B, as (a) temperature is raised or (b) a small perpendicular field is applied. The in-plane field magnitude is fixed at at $|B_{\parallel}| = 1\,\mathrm{T}$. In (a), the perpendicular field is zero and in (b), the temperature is at the lowest temperature 70 mK.

In Fig. 6-4s, in a range of densities near the optimal doping density, $-1.6\times10^{-12}\,\mathrm{cm}^{-2}$, the nematicity cannot be measured because the critical magnetic field is higher than the maximum field we can apply (1 T in any in-plane direction). The resistivity is universally small up to $B_{\parallel} = 1\,\mathrm{T}$ and thus preventing us from extracting the magnitude and axis of

the anisotropy. However, the nematicity at these densities near optimal doping can still be demonstrated if we reduce the superconducting gap size by either raising the temperature or applying a small perpendicular field, so that we could reach the critical magnetic field within 1 T. Fig. 6-13 shows such experiments performed in device B. In both cases of Fig. 6-13a and b, when temperature is at base and no perpendicular field is applied (the lowest and darkest curve in each plot), the resistivity is very low (close to the instrumentation noise floor) and does not exhibit significant anisotropy with respect to θ_B. However if we raise the temperature (Fig. 6-13a) or apply a small perpendicular magnetic field (Fig. 6-13b) so that the superconductivity is partially suppressed, we can then observe the two-fold anisotropy versus θ_B.

In Fig. 6-14, we overlay the extracted nematicity temperature $T_{\rm nem}$ on top of the superconducting critical temperature T_c (at 10 % normal resistance). To obtain $T_{\rm nem}$ versus density, we set a threshold for the anisotropy magnitude of $A_{\rm th} = 0.1$ and find the carrier density that satisfies the condition $A = A_{\rm th}$ at each of the measured temperatures (no carrier density is found at 4 K satisfying this condition). The anisotropy in the ellipses would be barely visible if $A < A_{\rm th}$.

From this plot, it is evident that the nematicity essentially persists as long as the superconductivity still exists. At several points, $T_{\rm nem}$ is even higher than $T_c^{10\%}$, which we attribute to the broad superconducting transition at these densities. We find that varying the threshold $A_{\rm th}$ will slightly change the shape of the $T_{\rm nem}$ curve, but our conclusion that $T_{\rm nem}$ roughly follows T_c remains unchanged.

6.5.10 In-plane field response at the wedge-like feature

We previously discussed two types of broken rotational symmetry phases: anisotropic resistivity at the wedge-like feature above the superconducting dome, as well as the nematicity in the superconducting state. We argue that these two phases are distinct and might have different origins. To see this, we show the in-plane field nematicity measurements at two points inside the wedge-like feature in Fig. 6-15. At both points in the phase diagram, we cannot observe significant modulation of the resisitivity by the in-plane magnetic

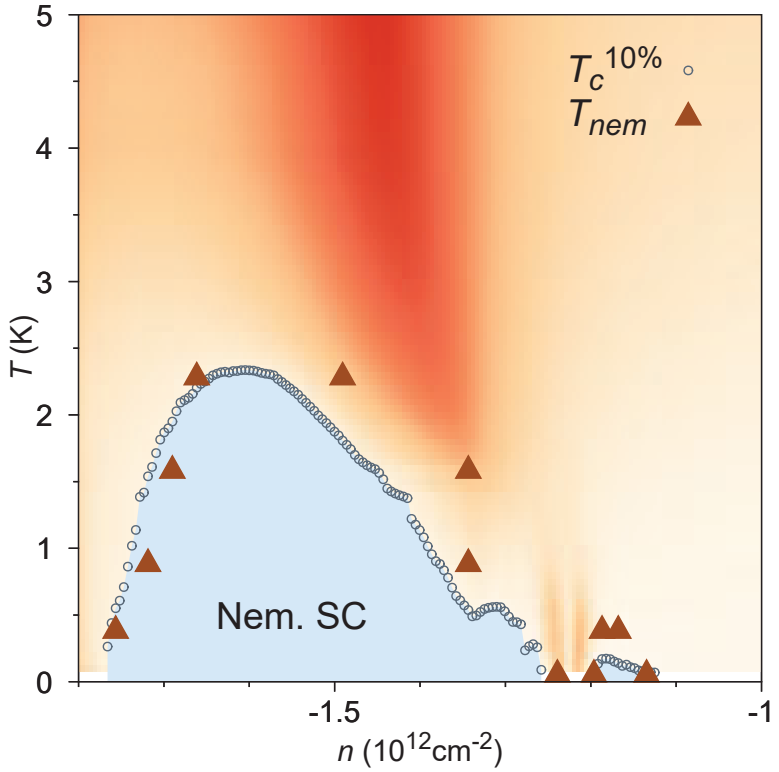

Figure 6-14: Nematicity temperature T_{nem} overlaid on the superconducting dome. The color map is the same data presented in Fig. 6-2b in the normal state for showing the position of the wedge-like feature and correlated insulator state.

field, albeit the resistivity tensor of the similar device A has been shown to exhibit siginificant anisotropy inside the wedge-like feature right above the superconducting transition. This result indicates that an anisotropic resistivity tensor does not necessarily give rise to anisotropic response to the in-plane field in the normal state. The vice versa case is also true from the measurements we have shown in Fig. 6-5a and 6-5b: anisotropic response to the in-plane field can occur at a point in the phase diagram that does not exhibit normal-state anisotropy.

6.5.11 Continuum modeling of TBG in an in-plane magnetic field

We calculated the Fermi surface of magic-angle TBG using the Bistritzer-MacDonald model [81]. Under in-plane magnetic field $\boldsymbol{B}_{\parallel}$, the continuum model Hamiltonian of twisted bilayer graphene (TBG) for valley $\tau = \pm$ is written on the basis of (A_1, B_1, A_2, B_2)

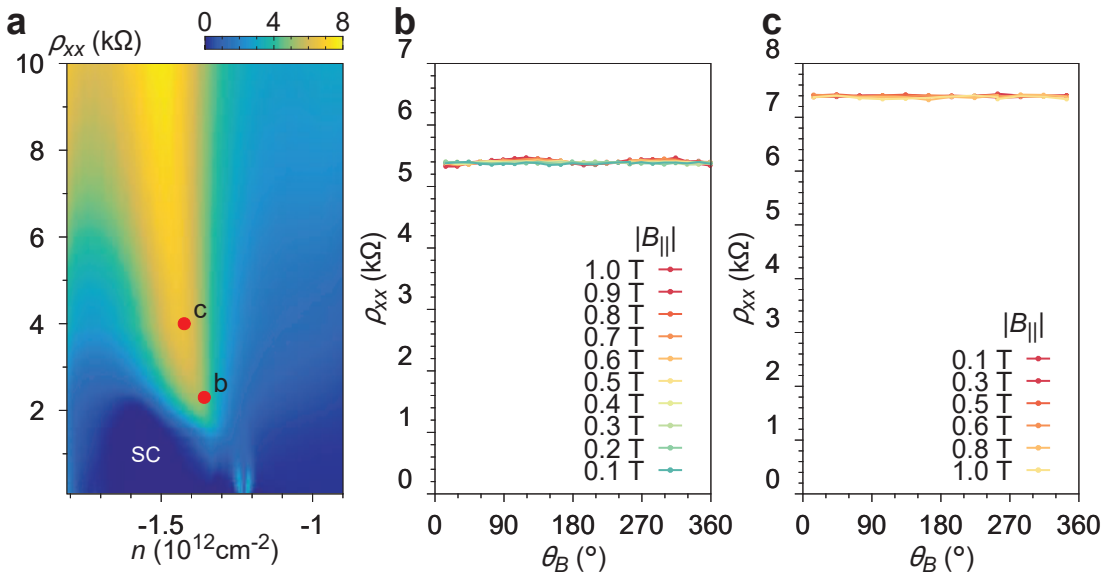

Figure 6-15: In-plane field response in the wedge-like feature in device B. Curves in (b) and (c) are the resisitivity versus in-plane field orientation and magnitude at two different points in the phase diagram, as indicated in (a). In both cases, we find no prominent two-fold symmetry in the in-plane field response.

as

$$H^{(\tau)} = \begin{pmatrix} H_1 & U^\dagger \\ U & H_2 \end{pmatrix}. \tag{6.4}$$

Here H_l is the intralayer Hamiltonian of layer $l = 1, 2$

$$H_l = -\hbar v \left[\boldsymbol{k} - \tau \boldsymbol{K}^{(l)} \pm \frac{ed}{2} \boldsymbol{B}_{\|} \times \hat{\boldsymbol{z}} \right] \cdot (\tau \sigma_x, \sigma_y), \tag{6.5}$$

where $\pm$ is for $l = 1$ and 2, respectively, $\boldsymbol{K}^{(1,2)} = 4\pi/(3a)(\cos\frac{\theta}{2}, \pm\sin\frac{\theta}{2})$, a is the lattice constant of monolayer graphene and d is the interlayer distance of TBG.

U is the effective interlayer coupling given by

$$U = \begin{pmatrix} U_{A_2A_1} & U_{A_2B_1} \\ U_{B_2A_1} & U_{B_2B_1} \end{pmatrix} = \begin{pmatrix} u & u' \\ u' & u \end{pmatrix} + \begin{pmatrix} u & u'\omega^\tau \\ u'\omega^{-\tau} & u \end{pmatrix} e^{i\tau \boldsymbol{G}_1^{\mathrm{M}} \cdot \boldsymbol{r}} + \begin{pmatrix} u & u'\omega^{-\tau} \\ u'\omega^{\tau} & u \end{pmatrix} e^{i\tau \boldsymbol{G}_2^{\mathrm{M}} \cdot \boldsymbol{r}}, \tag{6.6}$$

where $\omega = e^{2\pi i/3}$, u and u' denote interlayer couplings in AA and AB regions respec-

tively. The reciprocal vectors of moiré Brillouin zone are $\boldsymbol{G}^{\mathrm{M}}_{1,2} = G^{\mathrm{M}}(\pm\frac{1}{2}, \frac{\sqrt{3}}{2})$ with $G^{\mathrm{M}} = 4\pi/(3L_{\mathrm{M}})$, and $L_{\mathrm{M}} = a/(2\sin\frac{\theta}{2})$ is the superlattice constant. In the calculation, we use parameters $u = 0.0797\mathrm{eV}, u' = 0.0975\mathrm{eV}, d = 3.5$.

6.5.12 Additional anisotropy data

In this section, we present additional data that we measured in the normal state and superconducting anisotropy of MATBG. In particular, in device C with a twist angle of 1.07±0.02° (see Table 6.1), which is very close to device A and B shown above, we also find a similar 'wedge'-like feature on the underdoped side of the superconducting dome, as well as nematicity in the superconducting state. Fig. 6-16 shows the normal state anisotropy and nematic superconductivity in device C. Between -1.5×10^{12} cm^{-2} and -1.4×10^{12} cm^{-2}, we find the 'wedge'-like resistive state, which has a significant anisotropy as manifested in the transverse voltage measurement. Remarkably, this 'wedge' fully suppresses superconductivity in the small density range where it is present, compared to the partial suppression of T_c in devices A and B. In a small magnetic field, the 'wedge' feature turns into an insulator, similarly to the other devices. Devices A,B,C are the only devices in which we have found clear evidence for the 'wedge'-like feature, and they all lie within the narrow range of twist angles 1.07±0.03°. In addition, during the prepration of the paper where these results where originally reported, we became aware of Ref. [273], in which two of their MATBG devices (device 2 and device 3 at 1.04±0.02° and 1.09±0.02° respectively) with close-by twist angles also showed similar resistive wedge features in the n-T phase diagram. Therefore, we believe that the normal-state anisotropy in the 'wedge' region is a distinct feature of MATBG that occurs when the twist angle is in the range of about 1.07±0.03°.

On the other hand, the nematic superconductivity appears to be a more ubiquitous phenomena across the entire range of twist angles where superconductivity emerges. Fig. 6-17 shows the H_{c2} anisotropy, similar to Fig. 6-5e to 6-5r, measured at representative densities in devices M7 (device A), M12, M1, and M2, respectively. As can be seen, all these devices exhibit nematicity, albeit their twist angles span from 0.95° to 1.16°. By observing nematic superconductivity in total six devices across the wide range of twist angles,

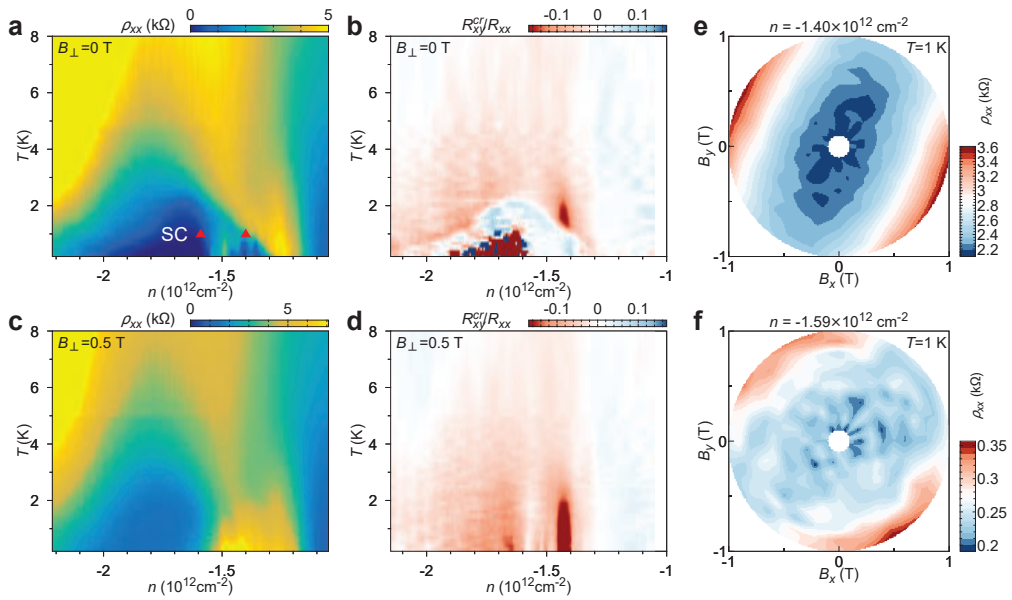

Figure 6-16: Anisotropy in device C with a twist angle of 1.07°. (a-b) ρ_{xx} and R_{xy}^{cr} measured in device C as a function of n and T. An anisotropic 'wedge'-like feature is observed between $-1.5{\times}10^{12}$ cm^{-2} and $-1.4{\times}10^{12}$ cm^{-2}, which fully suppresses the superconductivity in this density range. (c-d) Same measurements as in (a-b) but in $B_\perp = 0.5\,\mathrm{T}$. (e-f) Nematic superconductivity measured at the red triangles indicated in (a).

we conclude that the nematicity is more likely to be intrinsic to the superconductivity, as opposed to present for only a small range of twist angles. We believe that the nematic symmetry of the pairing state component should be taken into consideration for understanding the superconducting order parameter of MATBG in general.

6.5.13 Phenomenological analysis of the nematicity

The Ginzburg-Landau free-energy density for a superconducting order parameter $\boldsymbol{\Delta} = (\Delta_1, \Delta_2)$ that transforms as the E representation (i.e. d-wave/p-wave) of the D_3 space group is given by [274]:

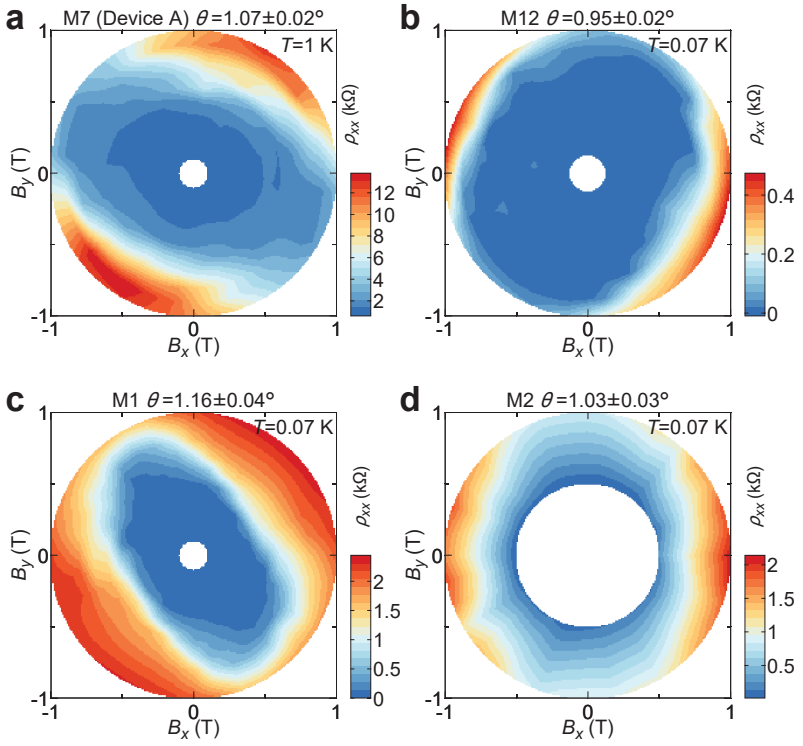

Figure 6-17: Nematic superconductivity in devices M7 (device A), M12, M1, M2. Each plot shows the resistivity versus in-plane magnetic field at a representative density in their respective superconducting domes.

$$
\begin{aligned}
f_{\mathrm{SC}} = {} & r\left(|\Delta_1|^2 + |\Delta_2|^2\right) + \frac{u}{2}\left(|\Delta_1|^2 + |\Delta_2|^2\right)^2 \\
& + K_1\left|\partial_x\Delta_1 + \partial_y\Delta_2\right|^2 + K_2\left|\partial_x\Delta_2 - \partial_y\Delta_1\right|^2 + \frac{K_3}{2}\left[\left|\partial_x\Delta_1 - \partial_y\Delta_2\right|^2 + \left|\partial_x\Delta_2 + \partial_y\Delta_1\right|^2\right] \\
& - \frac{g}{2}\left[\left(|\Delta_1|^2 - |\Delta_2|^2\right)^2 + \left(\Delta_1\Delta_2^* + \Delta_1^*\Delta_2\right)^2\right] + \frac{w}{3}\left[\left(\Delta_1 + i\Delta_2\right)^3\left(\Delta_1^* + i\Delta_2^*\right)^3 + \mathrm{h.c.}\right]
\end{aligned}
\tag{6.7}
$$

Here, $r \propto T - T_{c,0}$, where $T_{c,0}$ is the mean-field superconducting transition temperature; K_i is a superconducting stiffness; $g > 0$ ensures that the ground state is the nematic one, i.e. $\mathbf{\Delta} = \Delta\left(\cos\theta_s,\, \sin\theta_s\right)$; $u > g$ ensures that the functional is bounded; and the sixth-order term restricts θ_s to three values (modulo-π). The superconducting nematic order parameter $\mathbf{\Phi}_s = \left(\Phi_{1,s},\, \Phi_{2,s}\right)$ arises as a composite order parameter – for instance, by performing a

Hubbard-Stratonovich decoupling of the quartic term that has the coefficient g [265, 245]:

$$\begin{aligned}\Phi_{1,s} &= g\left(|\Delta_1|^2 - |\Delta_2|^2\right)\\ \Phi_{2,s} &= g\left(\Delta_1\Delta_2^* + \Delta_1^*\Delta_2\right)\end{aligned} \tag{6.8}$$

As discussed elsewhere [265, 245], $\mathbf{\Phi}_s$ can spontaneously order on its own and give rise to a vestigial nematic phase, i.e. a phase where $\langle\mathbf{\Phi}_s\rangle \neq 0$ but $\langle\Delta_i\rangle = 0$. In our case, since strain is assumed to be present, one expects $\mathbf{\Phi}_s$ to be non-zero above T_c. This not only selects $\mathbf{\Delta} = \Delta\left(\cos\theta_s, \sin\theta_s\right)$ as the ground state, but it also gives rise to the following term in the free energy:

$$f_{\text{coupl}} = -\Phi_s\Delta^2\cos\left(2\theta_s - 2\theta_s'\right) \tag{6.9}$$

where we parametrized $\mathbf{\Phi}_s = \Phi_s\left(\cos 2\theta_s', \sin 2\theta_s'\right)$. Minimization of this term gives $\theta_s = \theta_s'$, i.e. the relative amplitude of the two components of $\mathbf{\Delta}$ in the ground state is determined by the superconducting nematic director θ_s', which is set above T_c in the presence of strain.

By fixing the value of θ_s, one obtains an anisotropic superconducting susceptibility χ_s. The latter can be readily obtained from the quadratic terms in Eq. (6.7). Performing a Fourier transformation, we find:

$$\chi_s^{-1}\left(\mathbf{q}\right) = A\left[r + K_0q^2 + \bar{K}q^2\cos\left(2\theta_s - 2\varphi\right)\right] \tag{6.10}$$

where $K_0 \equiv \frac{K_1+K_2+K_3}{2}$, $\bar{K} \equiv \frac{K_1-K_2}{2}$, $A > 0$ is a constant, and $\tan\varphi = q_y/q_x$. Now, as argued previously, because orbital effects are expected to be significant even in the presence of an in-plane magnetic field, we assume that the anisotropy in H_c can be related to the anisotropy of the superconducting susceptibility. Since the contours of Eq. (6.10) give ellipses that make an angle θ_s with respect to the q_x axis, we therefore expect that measurements of the in-plane H_c will also produce ellipses oriented according to the angle θ_s. This reasoning is similar to that proposed in Ref. [261] to explain the observed critical field anisotropy in doped Bi_2Se_3 – note, however, that in that case the critical field is given

simply by H_{c2}.

We now discuss how θ_s is affected by uniaxial strain applied along an axis rotated α with respect to the x axis. We focus on the free energy of the composite order parameter $\mathbf{\Phi}_s = \Phi_s\,(\cos 2\theta_s', \sin 2\theta_s')$; since $\theta_s = \theta_s'$, we will drop the prime hereafter. Following the results of Ref. [264], the free energy of the nematic superconducting order parameter in the presence of strain ε is:

$$f_{\text{nem}} = \frac{a}{2}\,\Phi_s^2 + \frac{u}{4}\,\Phi_s^4 + \frac{\gamma}{3}\,\Phi_s^3 \cos 6\theta_s - \lambda\varepsilon\Phi_s \cos\left(2\theta_s - 2\alpha\right) \tag{6.11}$$

Here, a, u, γ, λ are phenomenological parameters. Note that γ selects three possible values for θ_s (modulo-π): $\gamma > 0$ chooses $\theta_s = \frac{\pi}{6}, \frac{\pi}{2}, \frac{5\pi}{6}$, whereas $\gamma < 0$ chooses $\theta_s = 0, \frac{\pi}{3}, \frac{2\pi}{3}$. Hence, $\mathbf{\Phi}_s$ is a 3-state Potts model order parameter.

The key point, as discussed in Ref. [264], is that if the system is in the nematic disordered state ($a > 0$), we can restrict the free-energy analysis to the quadratic level and minimize it with respect to θ_s and Φ_s, finding either $\theta_s = \alpha$ (if $\lambda\varepsilon > 0$) or $\theta_s = \frac{\pi}{2} + \alpha$ (if $\lambda\varepsilon < 0$). Thus, if the anisotropy in H_c seen in the experiment was caused solely by strain, we would expect it to be unchanged as function of doping, since $\lambda\varepsilon$ is a property of the device.

The situation changes if the nematic order parameter is not simply induced by the strain, but would spontaneously onset even in the absence of strain. In this case, as discussed in Ref. [264], one can approximate Φ_s by a constant Φ_0 and minimize the last two terms of the free energy (6.11) with respect to θ_s:

$$\sin 6\theta_s = \left(\frac{\lambda\varepsilon}{\gamma\Phi_0^2}\right) \sin\left(2\theta_s - 2\alpha\right) \tag{6.12}$$

The result is that, depending on the relative sign between γ and $\lambda\varepsilon$, the angle θ_s will change as the magnitude of the nematic order parameter Φ_0 changes. A changing Φ_0 is presumably what happens as the superconducting dome is traversed by varying the doping concentration.

For concreteness, let us consider the simpler case in which the strain is applied along one of the high-symmetry directions of the moiré superlattice, say $\alpha = 0$. Fig. 6-18 shows

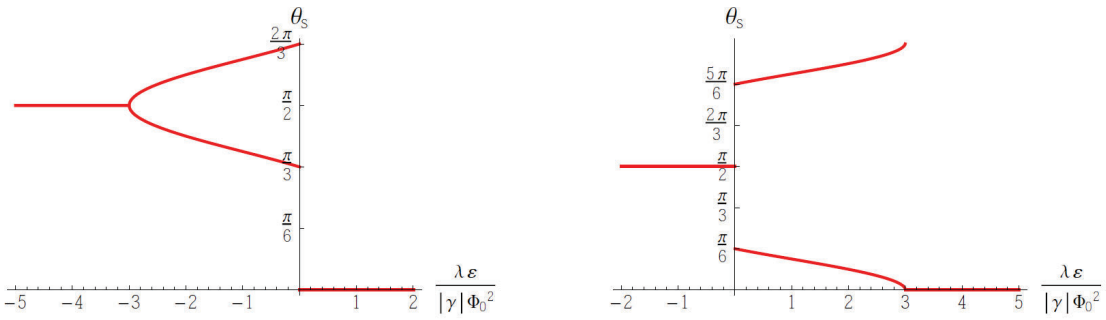

Figure 6-18: Superconducting nematic director θ_s as function of the normalized strain parameter $\frac{\lambda\varepsilon}{|\gamma|\Phi_0^2}$ for the cases $\gamma < 0$ (left panel) and $\gamma > 0$ (right panel). Here, $\alpha = 0$, i.e. strain is applied along the x axis.

the solution of Eq. (6.12) as function of the parameter $\frac{\lambda\varepsilon}{|\gamma|\Phi_0^2}$ for fixed $\gamma < 0$ (left panel) and fixed $\gamma > 0$ (right panel). In the left panel, we see that when $\lambda\varepsilon > 0$, θ_s is pinned at 0 for any value of Φ_0. However, when $\lambda\varepsilon < 0$, θ_s rotates from $\pi/2$ to either $\pi/3$ or $2\pi/3$ as Φ_0 increases. The right panel illustrates the corresponding behavior for $\gamma > 0$. Thus, the experimental observation that θ_s rotates as a function of doping provides strong evidence in favor of the scenario in which the superconducting nematic order would be present even in the absence of strain. In this regard, strain is selecting a nematic domain rather than being the driving force behind the anisotropy.

While a complete description of the experimental observations regarding the doping dependence of θ_s is beyond the scope of our phenomenological approach, it is interesting to further discuss what can cause the rapid rotation of θ_s in the doping range -1.45×10^{12}–-1.25×10^{12} cm^{-2}(Figs. 6-4I to 6-4M). This is the same region of the phase diagram where the wedge-like feature intercepts the superconducting dome. As explained in the main text, the wedge-like state has a nematic component $\mathbf{\Phi}_n = \Phi_n\,(\cos 2\theta_n,\, \sin 2\theta_n)$. This nematic component, which is presumably independent from the superconducting nematic order parameter $\mathbf{\Phi}_s$, couples to the latter in a similar way as strain does:

$$\tilde{f}_{\text{nem}} = -\tilde{\lambda}\Phi_n\Phi_s\cos\left(2\theta_s - 2\theta_n\right) \tag{6.13}$$

Now, if θ_n is alligned with the strain direction for all temperatures, then Φ_n com-

bines with ε to form an effective strain $\varepsilon_{\rm eff} = \varepsilon + \frac{\tilde{\lambda}}{\lambda}\Phi_n$. Thus, if $\tilde{\lambda}$ and λ have opposite signs, a finite Φ_n could cause a sign change in $\lambda\varepsilon_{\rm eff}$. This in turn would cause θ_s to jump from 0 to $\pi/3$ (or from π to $2\pi/3$), and then rotate continuously towards $\pi/2$, as shown in the left panel of Fig. 6-18 . Of course, if the strain is not precisely aligned with one the high-symmetry directions, the jump would be replaced by a smooth behavior. It is interesting that this sequence of rotations seems to be realized in the doping range –1.45×10^{12}––1.25×10^{12} cm^{-2}, where normal-state and superconducting nematicities coexist. As shown in Figs. 6-4I to 6-4M (see also Fig. 6-6), starting from the highest doping concentration and moving towards $-n_s/2$, the major axis of the H_c ellipse seems to rotate by $\pi/2$. It would be interesting to perform STM measurements to further map the orientation of the nematic director and correlate it with residual strains present in the device.

This analysis reveals how the nematic order parameter associated with the wedge-like feature, $\mathbf{\Phi}_n$, affects the director of the superconducting nematic ground state. More generally, $\mathbf{\Phi}_n = (\Phi_{n,1},\, \Phi_{n,2})$ couples to $\mathbf{\Delta} = (\Delta_1,\, \Delta_2)$ in two rather distinct ways. Symmetry considerations restrict the Landau free-energy expansion to:

$$f_{\rm SC-nem} = \alpha_1 \left(\Phi_{n,1}^2 + \Phi_{n,2}^2\right)\left(|\Delta_1|^2 + |\Delta_2|^2\right) + \alpha_2 \left[\Phi_{n,1}\left(|\Delta_1|^2 - |\Delta_2|^2\right) + \Phi_{n,2}\left(\Delta_1\Delta_2^* + \Delta_1^*\Delta_2\right)\right] \tag{6.14}$$

The first term is just the standard biquadratic coupling between ordered states that break different symmetries. The second term, which is essentially just a rewritten form of Eq. (6.13), is a linear-quadratic coupling that reflects the fact that the two ordered states share one similar broken symmetry, namely, three-fold rotations. The first term implies phase competition when $\alpha_1 > 0$, since nematic order would cause a suppression in the superconducting T_c. One of the effects of the second term is to correlate the nematic directors of the wedge-like feature and of the superconducting state, as discussed above. However, even when there is no long-range nematic order in the normal state – i.e. outside the wedge-like region in the phase diagram – this term can significantly impact the nature of the superconducting ground state. In this regime, one can integrate out the Gaussian normal-state nematic fluctuations and obtain the following contribution to the superconducting free en-

ergy:

$$\tilde{f}_{\rm SC} = -\frac{\alpha_2^2 \chi_{\rm nem}}{2}\left[\left(|\Delta_1|^2 - |\Delta_2|^2\right)^2 + \left(\Delta_1\Delta_2^* + \Delta_1^*\Delta_2\right)^2\right] \tag{6.15}$$

Here, $\chi_{\rm nem}$ is the nematic susceptibility associated with the wedge-like feature. Comparing to Eq. (6.7), we conclude that the normal-state nematic fluctuations favor the nematic ground state, as opposed to the time-reversal symmetry-breaking ground state ($p+ip$ or $d+id$) that would be favored if $g < 0$ in Eq. (6.7). A similar effect was identified in tetragonal systems with nearly-degenerate s-wave and d-wave superconducting instabilities in Ref. [275]. Similarly, Ref. [262] found that unidirectional charge-density wave fluctuations also favor a nematic superconducting ground state. Indeed, in the case where the wedge-like feature is associated with charge density-wave order, Φ_n can be expressed as a composite charge order parameter.

Chapter 7

Strange metal in magic-angle graphene with near Planckian dissipation

In this chapter, we show that magic-angle bilayer graphene exhibits another hallmark of strongly correlated systems — a broad regime of $T-$linear resistivity above a small, density-dependent, crossover temperature— for a range of fillings near the correlated insulator. We also extract a transport “scattering rate", which satisfies a near Planckian form that is universally related to the ratio of $(k_B T/\hbar)$. This work has been realized in close collaboration with the theory group of Senthil Todadri and Debanjan Chowdhury. The results presented in this chapter closely follow reference [5]. Our results establish magic-angle bilayer graphene as a highly tunable platform to investigate strange metal behavior, which could shed light on this mysterious ubiquitous phase of correlated matter.

7.1 Introduction

7.1.1 Planckian dissipation

A panoply of strongly correlated materials have metallic parent states that display properties at odds with the expectations in a conventional Fermi liquid and are marked by the absence of coherent quasiparticle excitations. Some well known families of materials, such as the ruthenates [276, 277], cobaltates [278, 279] and a subset of the iron-based

superconductors [280], show non-Fermi liquid (NFL) behavior over a broad intermediate range of temperatures, with a crossover to a conventional Fermi liquid below an emergent low-energy scale, $T_{\rm coh}$, at which coherent electronic quasiparticles emerge as well-defined excitations. Even more striking examples of NFL behavior are observed in the hole-doped cuprates [281, 282] and certain quantum critical heavy-fermion compounds [283] where the incoherent features appear to survive down to the lowest measurable temperatures, i.e. $T_{\rm coh} \to 0$, when superconductivity is suppressed externally. In the incoherent regime, all of these materials in spite of being microscopically distinct have a resistivity, $\rho(T) \sim T$, and exhibit a number of anomalous features [284, 285, 286, 283] clearly indicating the absence of sharp electronic quasiparticles. In strongly interacting non-quasiparticle systems, it has been conjectured [287] that transport "scattering rates" (Γ) satisfy a universal 'Planckian' bound $\Gamma \lesssim O(k_B T/\hbar)$ at a temperature T. It is however worth noting that in a NFL there is in general no clear definition for Γ; the scattering rates defined through different measurements, such as dc and optical conductivity, need not be identical [288]. A microscopic basis for Planckian limited scattering currently does not exist; see however Ref. [289, 290] for some attempts. One of the most surprising aspects of incoherent transport in these systems, in spite of these subtleties, is that Γ extracted from the dc resistivity (through a procedure specified in Ref. [291]) appears to satisfy a universal form $\Gamma = C k_B T/\hbar$ with C a number of order 1 [291, 292].

7.1.2 Magic-angle twisted bilayer graphene

As extensively discussed in Chapter 2.8, the theoretically estimated electronic bandwidth, W, is strongly renormalized near these small magic-angles [77, 95, 81]; then the strength of the typical Coulomb interactions, U, becomes at least comparable to (if not greater than) the bandwidth, $U \gtrsim W$.

Investigating the properties of MATBG as a function of temperature and carrier density with unprecedented tunability in a controlled setup can lead to new insights into the nature of electronic transport in other low-dimensional strongly correlated metallic systems.

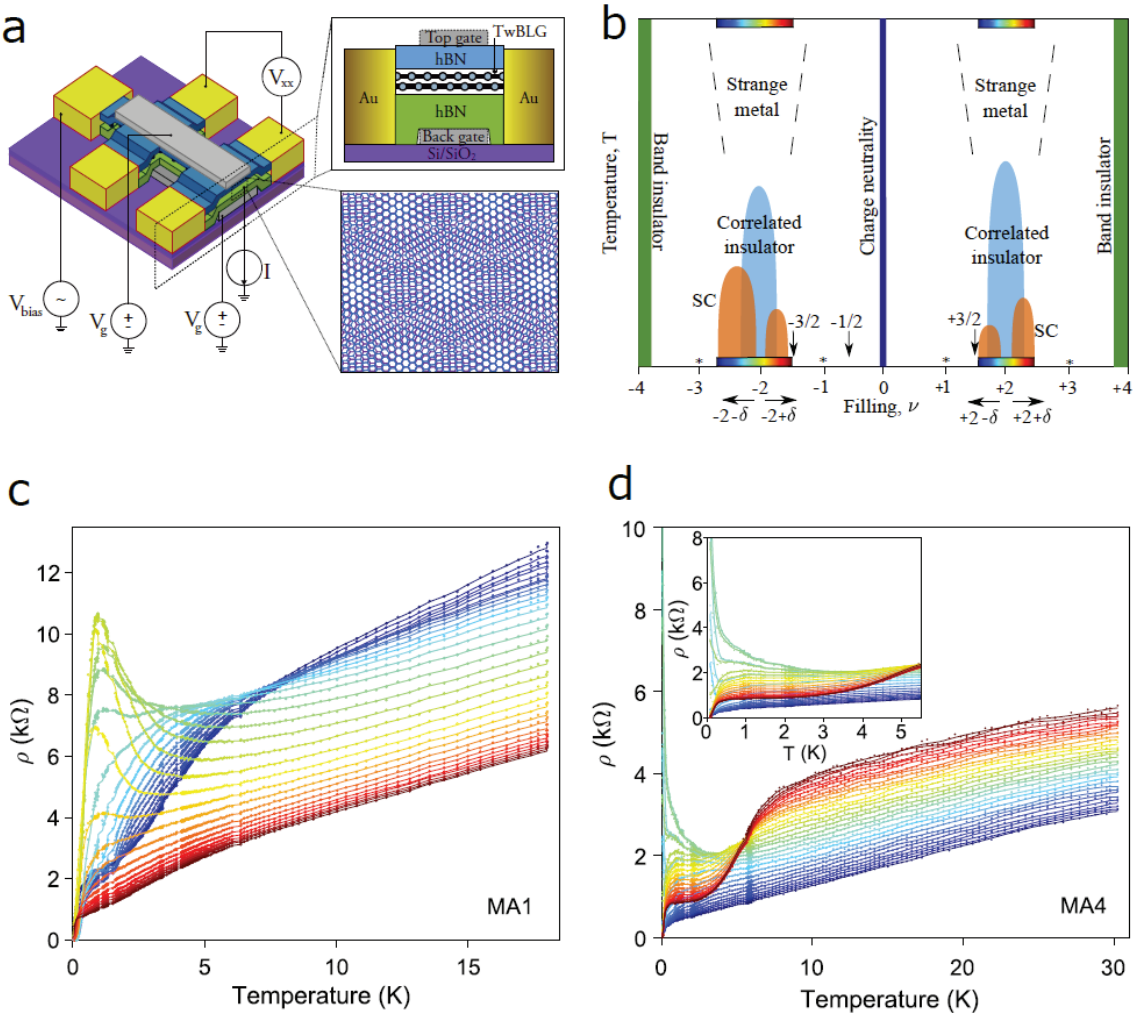

Figure 7-1: Transport in MATBG. (a) Device schematic and four-probe transport measurement configuration (left). Top-right: side-view of the device structure, consisting of bilayers of graphene twisted by θ relative to each other, sandwiched by hBN on the top and bottom. The carrier density is tuned using the metal gates at the top/bottom. Bottom-right: schematic MATBG moiré pattern. (b) A schematic phase diagram for MATBG as a function of temperature and filling, ν. The strange metal behavior with $T-$linear resistivity is primarily restricted to fillings near $\nu = \pm 2$. Orange regions denote superconductivity. Light blue regions denote the correlated insulator region. The color bars indicate the approximate filling ranges investigated and shown in fig. 1c,d. (c) Resistivity (ρ) as a function of temperature for device MA1 ($\theta = 1.16^0$) for gate-induced densities from -1.96×10^{12} cm^{-2} (blue) to -1.22×10^{12} cm^{-2} (red); see horizontal colorbar near $\nu = -2$ in Fig.7-1b. (d) $\rho(T)$ for device MA4 ($\theta = 1.18^0$) for gate-induced densities ranging from 1.23×10^{12} cm^{-2} (blue) to 1.89×10^{12} cm^{-2} (red); see horizontal colorbar near $\nu = +2$ in Fig.7-1b. The inset shows the traces for the same device at low temperatures. The solid smooth lines have been obtained by using a gaussian-weighted filter.

7.2 Transport characterization

For our experiments, we have fabricated multiple high-quality encapsulated MATBG devices (see Fig. 7-1a) using the 'tear and stack' technique described in Chapter 2.9 [123, 94]. As explained in Chapter 2.8 [94, 79], we obtain band-insulators with a large gap near $n \approx \pm n_s$, where n is the carrier density tuned externally by applying a gate voltage and n_s corresponds to four electrons per moiré unit cell. On the other hand, correlation driven insulators with much smaller gap-scales [79, 83, 122] appear near $n \approx \pm n_s/2$; we denote these fillings as $\nu = \pm 2$ from now on (the fully filled band corresponds to $\nu = +4$). Doping away from these correlated insulators by an additional amount, δ, with holes ($\nu = \pm 2 - \delta$) and electrons ($\nu = \pm 2 + \delta$) leads to superconductivity (SC) [83, 122]. The superconducting transition temperature (T_c) measured relative to the Fermi-energy (ε_F), as inferred from low temperature quantum oscillations measurements [83], is high, with the largest value of $(T_c/\varepsilon_F) \sim 0.07 - 0.08$, indicating strong coupling superconductivity [83]. A schematic $\nu - T$ phase diagram for MATBG, also introduced in Chapter 2.8, is reproduced in Fig.7-1b.

7.3 T-linear resistivity near $\nu = \pm 2 \pm \delta$

In this chapter, we investigate the transport phenomenology of the metallic states in MATBG as a function of increasing temperature over a large range of externally tuned fillings. We have analyzed the temperature dependence of the longitudinal DC resistivity, $\rho(T)$, for a number of devices (MA1 - MA6) over a wide range of fillings, the results of which appear to be qualitatively similar across devices. In order to highlight the universal aspects of the behavior, both within and across different samples, we show the temperature dependent traces of $\rho(T)$ for a range of different ν in two devices MA1 and MA4 in Fig.7-1c and Fig.7-1d respectively. The range of ν chosen for this purpose is shown as a color-bar in Fig.7-1b; see caption for details. As it is evident from these traces, at low temperatures the resistivity exhibits highly non-monotonic features as a function of ν, reflecting the complicated and distinct nature of the ground states [293] (see also inset of Fig. 7-1d). On the other hand, at higher temperatures, the traces for both devices look qualitatively similar and

show a clear monotonic trend as a function of the gate-tuned filling in spite of the underlying low-temperature differences. As ν is tuned externally starting from near the superlattice density, the number of carriers increases resulting in an enhanced conductivity. This simple picture is to be taken seriously only at high temperatures; at low temperatures the effective number of carriers changes non-monotonically across $\nu = -2$ [83]. We identify the characteristic temperature scale associated with the crossover between these distinct regimes, which depends on ν itself, as $T_{\rm coh}(\nu)$. For a wide range of fillings in the vicinity of $\nu = \pm 2$, we find that $\rho(T) \sim AT$ for $T \gtrsim T_{\rm coh}(\nu)$, where A denotes the slope of the resistivity in units of ohms/K (Ω/K). In a given device, A has a relatively weak dependence on ν, but there is a substantial variation in the value of A for fillings $\nu = \pm 2$ for a given device, as well as in between devices (which have invariably slightly different twist angles, θ). As we shall demonstrate below, the linearity of the resistivity is accompanied by a number of puzzling features due to which we refer to this regime as a "strange metal" [294].

Fig. 7-2a shows $\rho(T)$ for two separate MATBG devices, MA3 and MA4, at optimal hole doping, i.e. at fillings where the superconductivity is strongest on the hole-doped side of the correlated insulators at $\nu = -2 - \delta$ (MA3) and $\nu = 2 - \delta$ (MA4). From a linear fit to the regime $T > T_{\rm coh}$, we obtain $A \approx 335\ \Omega$/K for MA3 and $A \approx 95\ \Omega$/K for MA4. It is interesting to note that a naive estimate for the slope of the resistivity, assuming $\rho(T) \sim AT$ and accounting for the spin and valley degeneracies at high temperatures, would lead to a value of $A \sim (h/4e^2W)$, up to $O(1)$ prefactors (see section 7.10). For an estimated bandwidth of order $W \sim 10$ meV, this gives $A \approx 60\ \Omega$/K which is not far from the observed values.

We now compare and contrast the above results for MATBG with monolayer graphene (MLG), a chemically similar, but weakly correlated metallic system, that also displays $T-$linear resistivity extending over a much wider range of temperatures. In the inset of Fig. 7-2a, we show two representative examples of $\rho(T)$ for MLG on a SiO_2 [295] and hBN [296] substrate, respectively. The resistivity in MLG devices is approximately two orders of magnitude smaller than MATBG, making it a significantly more conducting metal compared to MATBG. Similarly, the slope of the resistivity for MLG on both substrates is $A \approx 0.1\ \Omega$/K and is nearly doping independent for a range of different densities near charge

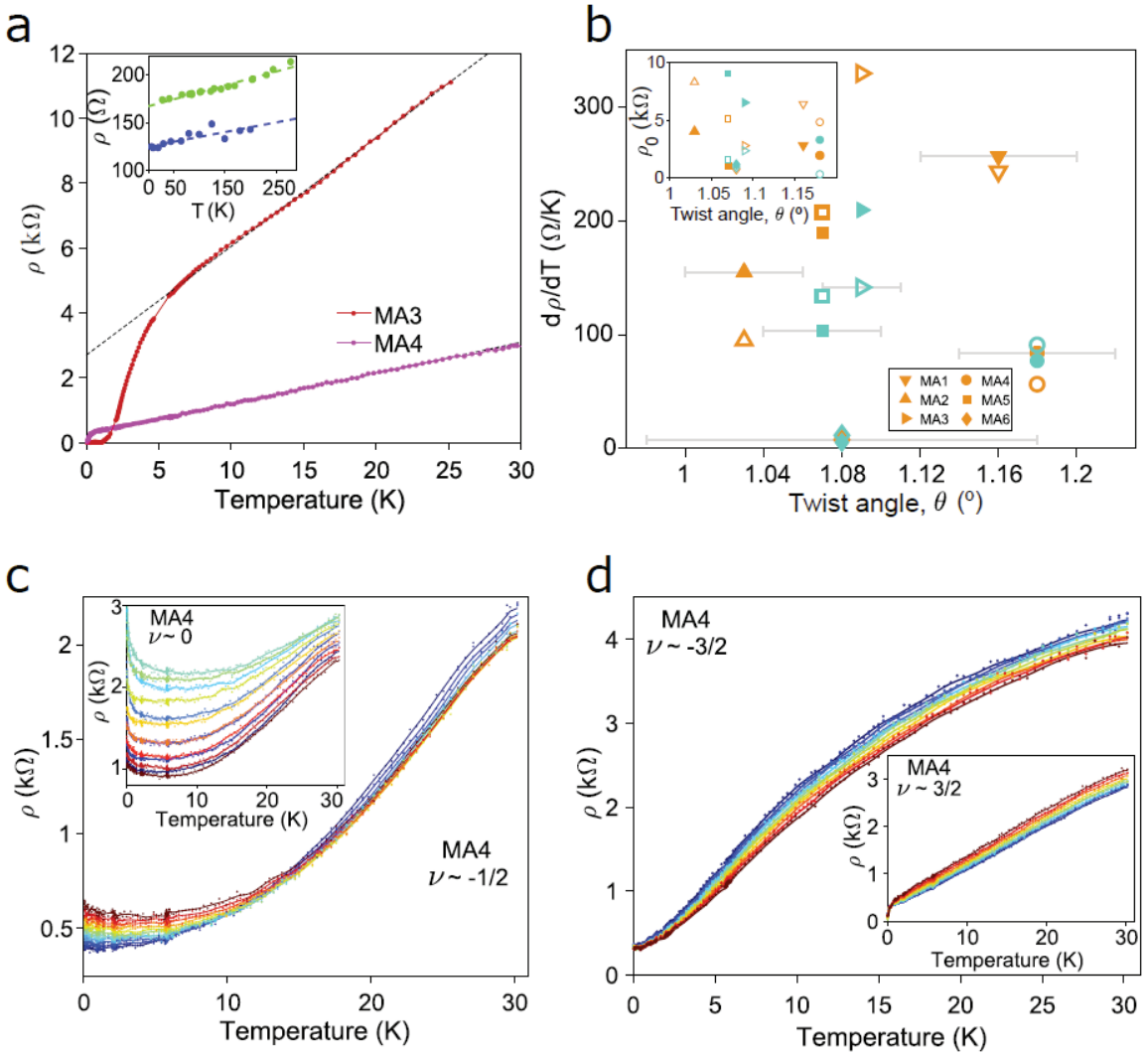

Figure 7-2: $T-$linear resistivity near $\nu = \pm 2$ in MATBG. (a) Resistivity (ρ) as a function of temperature for device MA3 ($\theta = 1.09^0$) and MA4 ($\theta = 1.18^0$) at a gate-tuned density of -1.46×10^{12} cm^{-2} ($\nu = -2 - \delta$) and 1.19×10^{12} cm^{-2} ($\nu = 2 - \delta$), respectively. The inset shows $\rho(T)$ in ohms for MLG on SiO_2 (green) and hBN (blue), respectively (data from [295, 296]). (b) The slopes $A = d\rho/dT$ obtained at the fillings near $\nu = \pm 2 \pm \delta$ with optimal superconducting T_c for six different devices (MA1 - MA6) as a function of respective twist-angles. Orange (cyan) markers denote fillings with $\nu > 0$ ($\nu < 0$), while solid (empty) symbols denote deviations, $\delta > 0$ ($\delta < 0$), away from the correlated insulators at $\nu = \pm 2$. The inset shows the extrapolated resistivity, ρ_0, for the same devices. (c) $\rho(T)$ for device MA4 near $\nu = -1/2$ for gate-induced densities -0.51 to -0.29×10^{12} cm^{-2}. The data look similar near $\nu = +1/2$. The inset shows $\rho(T)$ for the same device near $\nu = 0$ and densities between $\pm 0.13 \times 10^{12}$ cm^{-2}. (d) $\rho(T)$ for device MA4 near $\nu = -3/2$ for gate-induced densities -1.28 to -1.08×10^{12} cm^{-2}. The inset shows $\rho(T)$ for device MA4 near $\nu = +3/2$ over a symmetric range of densities.

neutrality. The slope in MLG is thus approximately three to four orders of magnitude smaller than the corresponding slope in MATBG.

Since there is some variation in the value of the slopes across different samples, we have studied the dependence of A on the twist angle, θ, as shown in Fig. 7-2b. The slopes are always evaluated for optimal doping, i.e. the filling at which T_c is the highest. Orange (cyan) markers denote fillings with $\nu > 0$ ($\nu < 0$), while solid (empty) symbols denote deviations, $\delta > 0$ ($\delta < 0$), away from the correlated insulators at $\nu = \pm 2$. As it is clear from the figure, the slopes at a given θ depend on the sign of ν. Experimentally, it is unclear at what value of θ the magic-angle condition is satisfied precisely. However, we find the highest superconducting T_c around $\theta \sim 1.07^0$, which might possibly indicate closest proximity to the magic-angle. While we do not have enough data-points to obtain a clear trend, the typical values of the slopes are large near $\theta = 1.07^0 - 1.09^0$ (MA5, MA3, respectively) and $\theta = 1.16^0$ (MA1). Fillings $\nu > 0$ also tend to have higher slopes than $\nu < 0$. We can also obtain the intercept, $\rho_0 = \rho(T \to 0)$, from an extrapolation of the data from high temperatures which gives us a rough estimate of the residual resistivity due to elastic scattering. The results are shown in the inset of Fig. 7-2b.

7.4 T-linear resistivity at other fillings

One of the most interesting aspects of the low-temperature ($T < 30\ K$) longitudinal transport data in MATBG is that the $T-$linear resistivity is primarily confined to fillings near the correlated insulators at $\nu = \pm 2 \pm \delta$ with $\delta \lesssim 1/2$. We note however that we do observe a number of correlated phenomena [79, 83, 122, 96, 116], and some unusual transport properties including $T-$linear resistivity, also near $\nu = \pm 1, \pm 3$ (marked by asterisks in Fig.7-1b) in some of our devices, results that will be reported elsewhere. Fig. 7-2c shows the traces of $\rho(T)$ in the vicinity of $\nu = -1/2$ (see corresponding arrow on the schematic phase diagram in Fig. 7-1b) for device MA4 ; the traces at $\nu = +1/2$ look qualitatively similar. The inset of Fig. 7-2c shows $\rho(T)$ near charge neutrality at $\nu = 0$. It is clear that $\rho(T)$ exhibits qualitatively distinct behavior near these fillings, without any clear indication of a broad regime of $T-$linear resistivity. In Fig.7-2d and its inset we plot $\rho(T)$ near $\nu = -3/2$ and

$\nu = +3/2$ for device MA4 (fillings marked by arrows in Fig.7-1b), respectively. While for fillings near $\nu = -3/2$ there is no apparent $T-$linear resistivity, there is some indication of such behavior near $\nu = 3/2$.

7.5 Strange metal behaviour in the cuprates

One of the most celebrated examples of strange metal behavior is observed in the hole-doped cuprates near optimal doping. It shows a number of remarkable features, including $\rho(T) \sim BT$ over hundreds of kelvin without any apparent signs of crossovers [281, 282, 291, 292], anomalous power-law dependent optical conductivities [285] and incoherent spectral functions in the presence of a sharp Fermi surface [284]. Focusing on the transport properties, the typical value of the in-plane sheet resistivity in LSCO (which depends on sample quality) at $T = 300$ K is approximately $\rho \sim 0.2 - 0.3$ $\mu\Omega$ cm [281, 282], which when normalized by the appropriate interplane distance ($d \sim 6.4$ angstroms) leads to a value of the resistivity, $\rho \sim 3.1 \times 10^3 - 4.7 \times 10^3$ Ω. These values are roughly comparable to the measured values of the resistivity in MATBG. On the other hand, the value of the slope in LSCO is approximately $B \sim 1.0 - 2.0$ $\mu\Omega$ cm/K [281, 282], which when normalized by d leads to $B \sim 15.6 - 31.2$ Ω/K. The slope is thus slightly smaller than the typical values in MATBG.

7.6 Planckian scattering in MATBG

Thus far we have compared the typical (non-universal) values of the resistivities and their slopes across different MATBG devices, as well as with other materials such as MLG and optimally doped cuprates. We now focus on a more detailed presentation and analysis of device MA2. We begin by showing the traces of $\rho(T)$ for MA2 in Fig.7-3a for a range of $\nu = -2 \pm \delta$, roughly corresponding to the color-bar in Fig.7-1b. As in the other devices, we observe that the resistivity at high temperatures is linear and it decreases monotonically as ν increases towards charge neutrality, presumably due to the increase in the number of carriers measured relative to the superlattice filling. We have evaluated the slope $A =$

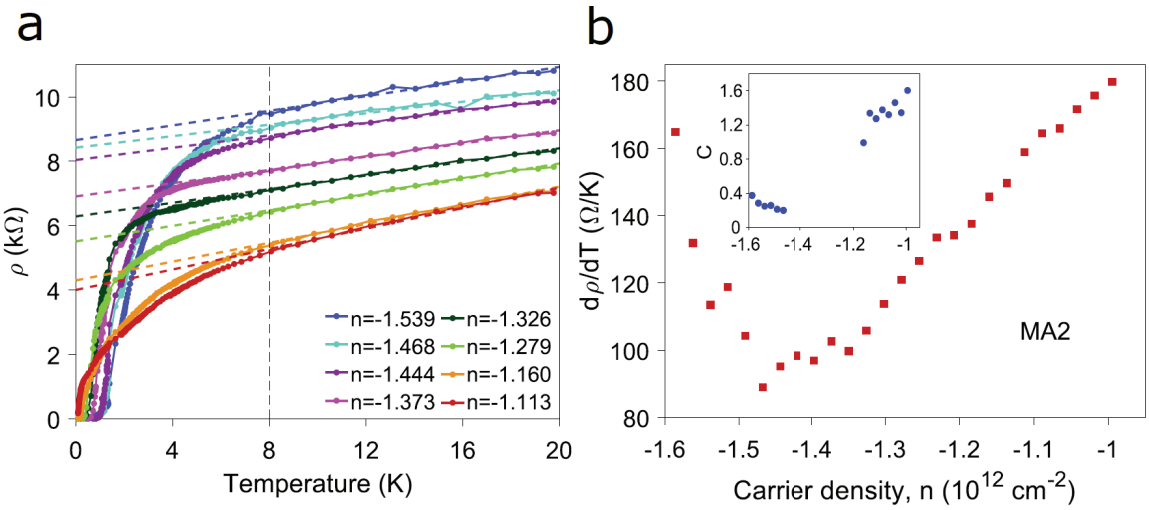

Figure 7-3: Planckian scattering in magic-angle bilayer graphene. (a) Resistivity as a function of temperature for device MA2 ($\theta = 1.03^0$) near $\nu = -2$ for gate-tuned densities -1.539×10^{12} cm^{-2} (blue) to -1.113×10^{12} cm^{-2} (red). The correlated insulator at $\nu = -2$ is approximately located near -1.3×10^{12} cm^{-2}. The solid smooth lines have been obtained by using a gaussian-weighted filter. (b) Slope of resistivity as a function of filling above 8 K for the same device evaluated using a linear fit. The inset shows the coefficient C of the scattering rate $\Gamma = Ck_BT/\hbar$ for the same fillings as in Fig. 7-3b, respectively.

$d\rho(T)/dT$ at high temperatures for the same range of ν considered in Fig.7-3a above. Fig.7-3b shows the values of A as a function of the gate-induced carrier density for fillings near $\nu = -2$. The slope here is obtained directly from a linear least-squares fit to the resistivity (see section 7.10) for $T > 8$ K. It is interesting to note that the slope varies non-monotonically with ν. On the other hand, it is possible that a transport "scattering rate" (Γ) exhibits more universal character. In order to define and obtain Γ from just transport data within the same device, we shall now adopt the procedure used in Ref.[291]. In the regime of $T-$linear resistivity, we write the scattering rate, $\Gamma = Ck_BT/\hbar$, and *define* the numerical prefactor C as a function of ν for device MA2 by assuming that the resistivity can be well described by a Drude-like expression [291, 292], such that

$$C = \frac{\hbar}{k_B}\frac{e^2\, n_c(0)}{m^*(0)}A, \tag{7.1}$$

where $n_c(0),\ m^*(0)$ are the measured density and effective mass values at low temperatures, $T \to 0$. This expression gives an operational definition of C, and hence of the scattering rate Γ. In device MA2, we have also been able to extract the *actual* low-T carrier density ($n_c(0)$) and effective mass ($m^*(0)$) from Shubnikov-de Haas (SdH) quantum oscillations measurements [83]. Note that $n_c(0)$, as inferred from SdH measurements, is not simply proportional to ν everywhere in the phase-diagram. Instead for $\nu = -2 - \delta$, $n_c(0)$ corresponds to the gate-induced density relative to the correlated insulator at $\nu = -2$[83]. On the other hand, for $\nu = -2 + \delta$, $n_c(0)$ corresponds to the gate-induced density relative to charge-neutrality at $\nu = 0$ [83], in agreement with low-temperature Hall measurements. From the SdH measurements, we can estimate the Fermi-temperature, $T_F = 2\pi\hbar^2 n_c(0)/(k_B g m^*(0))$, where g is the degeneracy factor. Interestingly, $\rho(T)$ does not exhibit any characteristic changes or crossovers as the temperature approaches T_F for fillings near $\nu = -2 - \delta$, where $T_F \lesssim 30$ K (see section 7.10). In all other examples of strange metals in solid-state systems, the range over which $T-$linear resistivity is observed is significantly below T_F. MATBG is thus unique in that the $T-$linear resistivity appears to persist to the electron degeneracy temperature, as inferred from the low-temperature measurements.

It is remarkable that $C \sim O(1)$ number for all ν studied near $\nu = -2$ (see inset of Fig. 7-3). Moreover, C is weakly dependent on the filling for $\nu = -2 - \delta$ and varies from $C \sim 0.2 - 0.4$. On the other hand, for $\nu = -2 + \delta$, the coefficient increases monotonically with increasing δ, with $C \sim 1.0 - 1.6$. It is interesting to note that the superconducting T_c is lower for the fillings where Γ is larger (see section 7.10). A similar analysis cannot be carried out asymptotically close to the insulating filling $\nu = -2$ because of the absence of low-temperature SdH measurements of m^* and n_c. However, since the slope in the metallic regime at high temperatures evolves smoothly as a function of δ near $\nu = -2$ and the value of n_c/m^* is almost independent of the filling, we may naively use the extrapolated value of this ratio for $\delta \to 0$ to infer that the high-temperature metal at $\nu = -2$ has a similar form of scattering rate.

7.7 Comparison to other correlated materials and monolayer graphene

A similar procedure when used to determine the scattering rates for other strongly correlated metals [291, 292], including ones that lead to unconventional superconductivity at low temperatures, also leads to $C \sim O(1)$ number. A major advantage of our analysis for MATBG is that all of our measurements are carried out on the same device (MA2) to extract C, as opposed to using data from multiple devices at different dopings. For various members of the cuprate family, the coefficient $C \sim 0.7-1.2$, both on the hole and electron-doped side of the phase-diagram [291, 292]. It is worth mentioning that $C \sim O(1)$ number even for metals like copper, aluminum and palladium above their respective Debye temperatures, where they exhibit a $T-$linear resistivity due to electron-phonon scattering [291]. In MLG, the $T-$linear resistivity is also likely due to electron-phonon scattering above a density-dependent temperature [297]. We can calculate the scattering rates for MLG on SiO_2 in the regime where they display $T-$linear resistivity. Let us express the resistivity (in units of h/e^2) as

$$\rho(T) = \frac{h}{e^2}\frac{\hbar\Gamma}{2\varepsilon_F(V)}, \tag{7.2}$$

where Γ is as defined earlier and $\varepsilon_F(V)$ is controlled by an external gate-voltage, V. This leads to an approximate estimate of $C \sim 0.009 - 0.022$ for the entire range of densities studied in Ref. [295], which is a few orders of magnitude smaller than the value in MATBG. In Table 7.1, we show a few representative examples of systems where the scattering rate has been calculated using the above procedure.

7.8 Discussion: possible mechanisms responsible for the observed transport phenomenology

We now critically examine some possible mechanisms that may be responsible for the unusual transport phenomenology in MATBG. Recently, different electron-phonon scattering

	Material	Slope of resistivity (A) 3D: $\mu\Omega$ cm / K 2D: Ω / K	C	Refs.
3D	$CeCoIn_5$	1.6	1	[291]
	$CeRu_2Si_2$	0.91	1.1	[291]
	$(TMTSF)_2PF_6$ (11.8 kbar)	0.38	0.9	[291]
	UPt_3	1.1	1.1	[291]
	Cu ($T > 100$ K)	7×10^{-3}	1.0	[291]
	Au ($T > 100$ K)	8.4×10^{-3}	0.96	[291]
(Quasi-)2D	Bi2212 ($p = 0.22$)	8.0	1.1	[292]
	LSCO ($p = 0.26$)	8.2	0.9	[292]
	PCCO ($x = 0.17$)	1.7	1.0	[292]
	MLG on SiO_2	0.1	$0.01 - 0.02$	[295], This chapter
	MATBG	$100 - 300$	$0.2 - 1.6$	This chapter

Table 7.1: Materials exhibiting Planckian scattering rates (Γ), where $\Gamma = Ck_BT/\hbar$.

models have been suggested trying to explain the origin of $T-$linear resistivity in twisted BLG near the magic-angle [298, 299, 300]. These theoretical models are applicable primarily in the vicinity of fillings $\nu = 0$, for angles close to (but not including) the magic angle, and the coefficient of the high temperature $\rho \sim T$ regime is then controlled by the strongly renormalized band-structure near charge-neutrality (Dirac-points). However, in our devices, clear evidence for $\rho \sim T$ and Planckian scattering rates can only be seen near the commensurate fillings of $\nu = \pm 2 \pm \delta$ with $\delta \lesssim 1/2$ for $T < 30\ K$, but not in the vicinity of charge neutrality $|\nu| \lesssim 1/2$. Similarly, a recent transport study of twisted BLG devices at angles $\theta \gtrsim 2^0$ [301] has reported a power-law behavior of the resistivity, $\rho(T) \sim \rho_0 + T^\beta$, with a non-monotonic value of $\beta \sim 0.9 - 1.7$ as a function of filling. As in our case, super-linear behavior (power law exponent substantially higher than 1) was observed near charge neutrality. A non-linear behavior of the resistivity has also been seen recently near charge neutrality for devices with angles between 1^0 and 2^0 [302]. Moreover, our data show that $T_{\rm coh}(\nu)$ can be as low as 0.5 K (e.g. for device MA4 near $\nu = -2$ in Fig.7-2a), which is an order of magnitude lower than the predicted crossover temperature above which linear behavior is expected[298]. The maximum value of the slope of the $T-$linear resistivity, which has a weak dependence on ν in a given device, is observed near the angle ($\theta \sim 1.07^0$) as well as at an angle of $\theta \sim 1.16^0$ (Fig.7-2b). However, refs.[298, 299, 300] predict a very

strong angle dependence of the slope, with the largest value near the magic-angle, and this dependence is tied to the strong renormalization of the Dirac velocity. Although we do not observe this trend, such a discrepancy could arise as a result of long-wavelength disorder and slow variations in the twist-angle across our devices. In addition, these models seem to underestimate the slope values and their angular dependence substantially, possibly indicating that phonons may not represent the full contribution to the observed T-linear behavior.

A more sophisticated future theory of electron-phonon scattering that incorporates: i) the underlying details of the electronic band structure of MATBG away from charge-neutrality, including the strongly non-linear energy momentum dispersion and presence of van-Hove singularities, as well as ii) a possible renormalization of the deformation potential due to electron-electron interactions, iii) a folding of the phonon dispersion due to the moiré brillouin-zone, as well as iv) the possible effects of density and twist-angle disorder, would be highly desirable for a detailed comparison to our experimental data. However, we also note that since the $T-$linear resistivity persists to scales $T \sim T_F$ without any signs of a crossover near $\nu = -2 - \delta$, while the electrons are no longer in the degenerate limit, electron-phonon scattering in the metallic state ($T > T_c$) might still be insufficient to explain the origin of these unusual results. In principle, $T-$linear resistivity can arise as a result of scattering off any electronic collective mode fluctuations (instead of phonons) for $T_M \lesssim T$, where T_M is a characteristic scale associated with the respective collective mode, but a crossover across $T \sim T_F$ is nevertheless expected. It is unclear at the moment if such electronic collective modes are present near $\nu = \pm 2$.

Under conditions of local equilibrium, the conductivity is given by $\sigma = \chi D_c$, where $\chi = \partial n / \partial \mu$ is the electronic compressibility and $D_c \sim v^2/\Gamma$ is the charge diffusivity ($v \equiv$ a characteristic velocity). Thus far, we have inherently assumed that the temperature dependence of the resistivity arises as a result of the temperature dependence of $\Gamma \sim k_B T/\hbar$. An alternative scenario that could, in principle, lead to $\rho \sim T$ at high temperatures arises solely from the temperature dependence of the compressibility, $\chi \sim 1/T$, in a system with a bounded kinetic energy. However, in some of our devices the $\rho \sim AT$ behavior persists from high temperatures down to temperatures as low as 0.5 K without any change

in the slope, A (e.g. device MA4 in Fig. 7-2a). Moreover, as emphasized earlier, ρ does not show any crossovers as the temperature is swept through the estimated ε_F for fillings near $\nu = -2 - \delta$. Thus while it is unlikely that the above mechanism is responsible for the observed temperature dependence of the resistivity, a systematic future study of the charge compressibility in MATBG as a function of increasing temperature is highly desirable. Instead of relying on the dc transport measurements to extract Γ, it will be interesting to measure and analyze the extent to which the optical scattering rates in MATBG satisfy a universal form in future experiments. Interestingly, recent measurements of diffusivity and compressibility in a cold-atoms based experiment [303] find $\rho \sim T$ from temperatures higher than the bandwidth down to lower temperatures without any signs of a crossover.

7.9 Outlook

In light of these results, any successful theory has to account for the following universal aspects of the phenomenology: (i) a $T-$linear resistivity with values $O(h/e^2)$ in the vicinity of commensurate fillings, $\nu = \pm 2$, with near Planckian ($C \sim O(1)$) "scattering rates", (ii) a weak dependence of the slope of the resistivity on ν, (iii) relative insensitivity of the resistivity to T_F and by extension, to the underlying details of the Fermi-surface at low temperatures, and (iv) the presence of a small $T_{\rm coh}$ above which the transport is unconventional. Since $T_{\rm coh}$ can be as low as 0.5 K in some of our devices, it will be interesting to see if future experiments find evidence of $T-$linear resistivity down to even lower temperatures (i.e. $T_{\rm coh} \to 0$). If so, it is possible that the NFL behavior in MATBG is controlled by a $T = 0$ quantum critical point or quantum critical phase; there is not enough conclusive experimental information available at present to elaborate on this aspect. On the other hand, if $T_{\rm coh}$ is non-zero, it is likely that the metallic regime of MATBG for fillings near $\nu = \pm 2$ realizes an intermediate-scale NFL. Assuming that the temperature remains smaller than the typical interaction strengths but large compared to $T_{\rm coh}$, the state is neither a classical liquid (or gas) nor a degenerate quantum liquid. The system can then be best described as a "semi-quantum" liquid, with no coherent quasiparticle excitations and no sharply defined Fermi surface. Describing such a regime in a theoretically controlled limit is challenging

but recent progress has been made in the study of some models [304, 288] which find evidence of such incoherent behavior. Guided by these studies and by the present experiments, further develop microscopic theories of transport in such a regime could be developed.

7.10 Extended data and supplementary information

7.10.1 Estimate of T_{coh}

In Fig. 7-4, we plot the density dependent T_{coh} for MA1 and MA4. The coherence temperature is obtained using the following procedure: 1) From high temperatures, we fit a prominently linear region of the ρ-T curve to a straight line. The error of the fitting is small since the data is extremely linear. 2) We extrapolate the fitted line to lower temperatures and compute the error between the extrapolated line and the data points. As we lower the temperature, the fitting error gradually increases due to non-linear behavior near T_{coh}. 3) The T_{coh} is identified as the temperature at which the fitting error exceeds a certain threshold, which is taken to be constant for all densities.

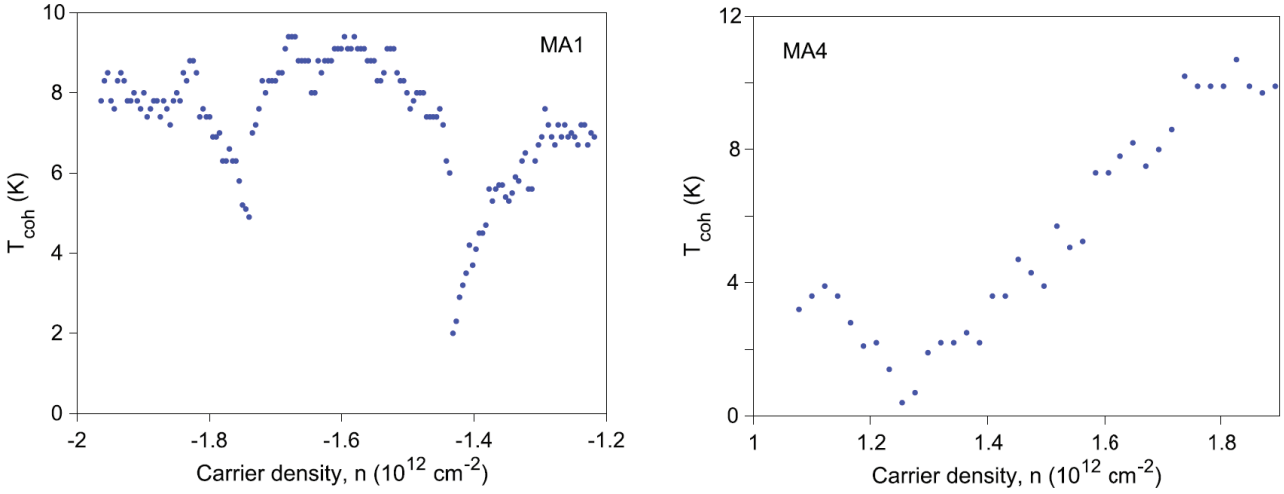

Figure 7-4: T_{coh} versus carrier density in sample MA1 and MA4. The extraction procedure for T_{coh} from the linear resistivity data is explained in section 7.10.1.

7.10.2 Theoretical estimate of the resistivity slope

Let us now estimate the slope of the resistivity, A, assuming that the $T-$linear resistivity arises as a result of electron-electron interactions. For MATBG, there are three relevant energy scales — the band width (W), the super-lattice gap to other higher-energy bands (E_0), and the interaction strength (U). Experimentally, it is known that E_0 is large [94, 79] and so we consider the limit $E_0 \gg W, U$ (we can formally consider the limit $E_0 \to \infty$). However, as emphasized earlier, U is comparable to W.

We now express the resistivity as $\rho = \rho_0 + AT$, where ρ_0 is affected by disorder in the sample, but where we assume that A is largely unaffected by disorder. In order to estimate A, it is clear from dimensional analysis that $[A] = [\text{quantum of resistance}]/[\text{energy}]$. In the high-temperature regime, taking into account the degeneracy from the spin and valley degrees of freedom ($g = 4$), we may write

$$A = \frac{h}{4e^2}\frac{1}{W}F\left(\frac{W}{U}, \nu, ...\right), \tag{7.3}$$

where $F(...)$ is a function of W/U, the filling ν and, in principle, other quantities including the twist-angle (which affects W).

However, when W is comparable to U and $F(\nu, ...)$ does not depend strongly on ν, we expect $F(\nu) \sim O(1)$ number. This leads to an estimated slope of $A \approx h/(4e^2W)$. For a realistic estimate of $W \sim 10$ meV, we get $A \approx 60\ \Omega/\text{K}$, which is similar to the measured values up to $O(1)$ factors. Interestingly, in the strange metal regime of optimally doped cuprates, a similar estimate with $g = 2$ leads to an expected slope of $A \sim h/(2e^2J)$, where J represents the strength of the antiferromagnetic exchange interaction, which is close to the measured value.

7.10.3 Phase stiffness

Based on the existing quantum oscillation data [83] at low temperatures, we may try to address several questions related to the superconductor that emerges out of the metallic state.

In particular, since we know the effective carrier concentration, n_c (from the frequencies measured in SdH oscillations) and the effective mass, m^*, we may immediately try to infer the behavior of the 'phase stiffness' (related to the zero temperature penetration depth by $D_S \propto \lambda_L^{-2}(0)$), $D_S \sim n_c/m^*$, of the superconducting state. The phase stiffness will determine how susceptible the superconductor is to thermal phase fluctuations. Naively, we expect that in superconductors that arise from doping a Mott insulator, the phase stiffness vanishes upon approaching the Mott insulator (since the number of carriers that may participate in pairing vanish in that limit). The onset of long-range phase coherence and T_c is then determined by the phase stiffness, which determines the scale at which the phase of the order parameter locks in over long distances. Indeed, in the hole-doped cuprates, the phase stiffness on the underdoped side of the phase diagram exhibits such behavior [305]. However, in MATBG, for $\nu = -2 - \delta$, the effective mass vanishes as $\delta \to 0$ (see Fig. 7-5), as does the carrier density. Therefore we are interested in the behavior of the ratio, D_S, especially in the vicinity of the correlated insulator.

Before attempting to infer the behavior of D_S, let us review a more general principle. While there is no optical conductivity data available on MATBG at present, it is useful to place these measurements in the context of D_S. When a metal undergoes a SC transition, the low energy optical weight for frequencies $\omega < 2\Delta$ has to be rearranged dramatically (Δ is the SC gap). It is natural for all of this weight to go into the delta-function at zero-frequencies (we are assuming that there is no appreciable spectral weight transfer to $\omega \gg \Delta$), which precisely measures the phase stiffness, i.e. the 'missing-area' is given by,

$$D_S \approx \frac{2\Gamma}{\pi} \int_0^{2\Delta/\Gamma} \sigma(z)\, dz, \tag{7.4}$$

where Γ is the appropriate scattering rate which includes the effects of disorder, and $z \equiv \omega/\Gamma$. When $\Delta/\Gamma \gg 1$, the above reduces to $D_S = D_N$, where D_N is the conductivity spectral weight (or the 'Drude-weight) in the normal state. On the other hand, when $\Delta/\Gamma \ll 1$, the above relation can be simplified to yield the relation $D_S \approx \sigma(0)\Delta$, with $\sigma(0)$ the extrapolated $T \to 0$ value of the conductivity from above $T > T_c$. A number of superconductors satisfy the above relationship [306]. In this regime, D_S can be sub-

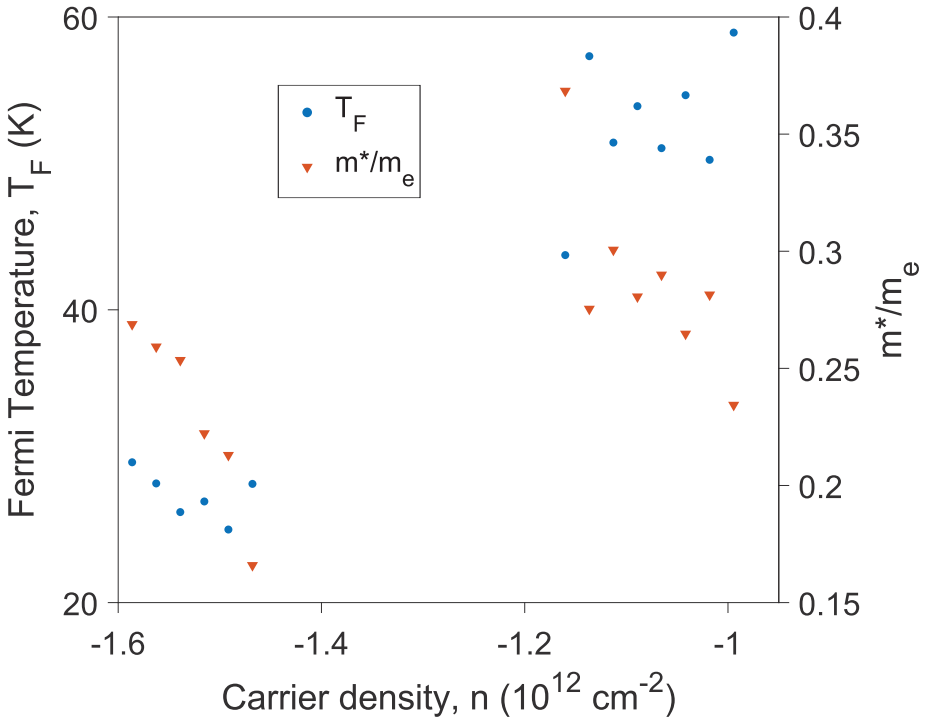

Figure 7-5: Fermi temperature versus carrier density. Left: The calculated T_F (blue circles), with an assumed degeneracy of $g = 2$ for $\nu = -2 - \delta$ and $g = 4$ for $\nu = -2 + \delta$, respectively. The correlated insulator at $\nu = -2$ is located in the vicinity of $n \approx -1.3 \times 10^{12}$ cm^{-2}. Right: The effective mass, m^*/m_e, obtained from SdH oscillations (orange inverted triangles) [83].

stantially smaller than D_N, meaning that only a tiny fraction of the normal state spectral weight, compared to the width of the conductivity ($\omega \leq 2\Delta \ll 2\Gamma$), condenses into the delta-function below T_c. Since we do not know Δ in the experiments on MATBG, it may be reasonable to use T_c/Γ as a proxy instead.

It is more useful to express the expected phase stiffness (i.e. n_c/m^*) in terms of an energy scale, which in two-dimensions is simply the Fermi-temperature, $T_F = (2\pi\hbar^2 n_c)/(k_B g m^*)$. In this expression, g is the degeneracy factor; based on the low-temperature SdH oscillations [83] for $\nu = -2 - \delta$ and $\nu = -2 + \delta$ we use $g = 2$ and $g = 4$, respectively. Note that the combination

$$\frac{\pi\hbar^2}{k_B}\frac{10^{12}\ \text{cm}^{-2}}{m_e} = 27.78\ \text{K}. \tag{7.5}$$

We plot the Fermi temperature in Fig.7-5. For fillings $\nu = -2 - \delta$, we find that T_F is roughly a constant independent of n. A naive extrapolation all the way to the correlated insulating filling ($n \approx -1.3\times10^{12}$ cm^{-2}) would seem to suggest that the superfluid stiffness remains finite, even as one approaches the insulator. This implies that superconductivity is lost not due to loss of phase-coherence, but due to destruction of the pairing amplitude. It is however worth pointing out that it is, in principle, possible for D_S to collapse dramatically as one approaches the insulator at $\nu = -2$. We also note that Ref. [307] has recently proposed an upper bound on the phase stiffness in superconducting MATBG, which is approximately a tenth of our estimated T_F.

Chapter 8

Cascade of phase transitions and Dirac revivals in magic-angle graphene

In Chapter 2.8, we showed that twisted bilayer graphene near the magic angle [81, 77, 79, 83] exhibits rich electron-correlation physics, displaying insulating [79, 83, 122, 116], magnetic [96, 97] and superconducting phases [83, 122, 116]. The electronic bands of this system were predicted [81, 78, 79] to narrow markedly [95, 308] near the magic angle, leading to a variety of possible symmetry-breaking ground states [309, 310, 272, 311, 312, 263, 313]. In this chapter, using measurements of the local electronic compressibility (see Chapter 2.11 for a description of the experimental technique) performed in close collaboration with the group of Shahal Ilani, we show that these correlated phases originate from a high-energy state with an unusual sequence of band population. As carriers are added to the system, the four electronic *flavours*, which correspond to the spin and valley degrees of freedom, are not filled equally. Rather, they are populated through a sequence of sharp phase transitions, which appear as strong asymmetric jumps of the electronic compressibility near integer fillings of the moiré lattice. At each transition, a single spin/valley flavour takes all the carriers from its partially filled peers, 'resetting' them to the vicinity of the charge neutrality point. As a result, the Dirac-like character observed near charge neutrality reappears after each integer filling. Measurement of the in-plane magnetic field dependence of the chemical potential near filling factor one reveals a large spontaneous magnetization, further substantiating this picture of a cascade of symmetry breaking. The

sequence of phase transitions and Dirac revivals is observed at temperatures well above the onset of the superconducting and correlated insulating states. This indicates that the state that we report here, with its strongly broken electronic flavour symmetry and revived Dirac-like electronic character, is important in the physics of magic-angle graphene, forming the parent state out of which the more fragile superconducting and correlated insulating ground states emerge. The results presented in this chapter are published in references [111, 314].

8.1 Introduction

When a system of interacting electrons is cooled to low temperatures, it gradually loses its high-energy degrees of freedom while developing correlations that give rise to new collective degrees of freedom. The result is a hierarchy of energy scales, where the effective degrees of freedom at each scale are built out of a subset of those of the preceding scale. Understanding the effective degrees of freedom and their correlations at higher energies is therefore foundational for understanding more fragile states that emerge at lower energies.

The discovery that twisted bilayer graphene (TBG) exhibits correlated insulating [79], superconducting [83, 122] and ferromagnetic [96, 97] phases has opened a playground for studying such strongly correlated states. For twist angles that approach a magic angle of about $1.1°$, the bands were predicted [81, 78, 79] to narrow down markedly [81, 95, 308], leading to a variety of possible symmetry-breaking ground states [309, 310, 272, 311, 312, 263, 313]. These bands, identified directly by spectroscopic [75, 315, 316] and capacitive measurements [317], were shown to broaden substantially owing to interactions [87, 90, 89], and to exhibit correlation-induced gaps at the Fermi energy [87, 90, 88] as well as lattice symmetry breaking [87, 90, 88]. Yet a key question remains: what is the nature of the correlated state at energy scales comparable to the band width that gives rise to the low-energy many-body ground states?

In this chapter, using scanning measurements of the local electronic compressibility, we show that the energy bands of magic-angle twisted bilayer graphene (MATBG) undergo a dramatic transformation near integer fillings. Starting at the charge neutrality point (CNP), the four spin/valley flavours exhibit a Dirac-like character. However, as integer fillings are

approached, sharp transitions occur in which a single flavour takes all the carriers from its partially filled peers, 'resetting' them to the vicinity of the CNP. This results in a Sisyphean band filling—the electrons attempt to fill all flavours symmetrically, yet repeatedly slip back to the Dirac point, reviving their Dirac-like character. Near these transitions, the compressibility reveals an asymmetry of the electronic state: the compressibility is high below any of the transitions, and drops precipitously above them. This behaviour is observed at temperatures well above the onset of the correlated insulator and superconducting states, demonstrating that the state we reveal here—with its strongly broken electronic flavour symmetry and revived Dirac-like electronic character—is the parent state of the superconducting and correlated insulating ground states at lower energies.

8.2 Transport characterization

The fabricated devices consist of hexagonal boron nitride (hBN)-encapsulated TBG [94, 140], placed over a local metallic back-gate [83, 79]. The main device studied in this chapter (sample A, Fig. 8-1a) features a large (5 μm $\times$ 5 μm) area for imaging compressibility and multiple contacts for transport characterization. The results are reproduced in a second sample (sample B). We note that samples A and B are distinct from those described in the previous chapters (despite having the same names). The local twist angles in these samples together span a range from below to above the magic angle (MA). Figure 8-1b shows the four-probe longitudinal resistance of sample A versus carrier density, n (controlled by the back-gate voltage, V_{BG}), and parallel magnetic field, $B_{//}$, at a temperature of $T = 50$ mK. These measurements are consistent with the electronic signatures described in Chapter 2.8. In particular, they exhibit insulating peaks when the flat bands are completely full or empty, namely when the filling fraction $\nu \equiv n/(n_s/4)$ equals ± 4 (n is the electron density, n_s corresponds to the density of four electrons per moiré unit cell), and at half-filling, $\nu = \pm 2$. Incipient superconductivity appears as resistance drops on the electron-doped side of $\nu = 2$ (up to $B_{//} \lessapprox 0.5$ T) and on the hole-doped side of $\nu = -2$ (up to $B_{//} \lessapprox 1$ T), similar to the observed phenomenology in magic angle samples (see Chapter 2.8.8) [83, 122]. Transport through various pairs of contacts shows spatial

variations of n_s across the device, reflecting approximately 10% (0.1°) modulations of the twist angle. This is confirmed more clearly by the local imaging measurements below.

8.3 Inverse compressibility and chemical potential

Inverse compressibility is imaged with a nanotube-based scanning single electron transistor [318, 149] (SET), described in more detail in Chapter 2.11. Keeping the TBG grounded, the SET monitors the local electrostatic potential modulation above the TBG in response to back-gate voltage modulation. This yields the local inverse compressibility, $d\mu/dn$ (here μ is the chemical potential). A typical trace of $d\mu/dn$ versus n, measured at $T = 4$ K and twist angle $\theta = 0.99^\circ$ (black, Fig. 8-1c) features sharp $d\mu/dn$ peaks at $\nu = \pm 4$, originating from the energy gaps between the flat bands and the higher-energy bands, as well as increased $d\mu/dn$ around the CNP corresponding to Dirac-like behaviour. Integrating this curve yields ν versus n (blue, Fig. 8-1c), which reveals the energy gaps as jumps in ν, and the Dirac-like behaviour as a $\sqrt{n}$-like dependence around the CNP.

8.4 Twist angle characterization

We characterize the varying twist angle across the sample [106, 56] by spatially tracking the back-gate voltage, $V_{BG}(\mathbf{r})$, which corresponds to the $d\mu/dn$ peak at ν = 4 ($\mathbf{r}$ is the spatial position). From this we deduce $n_s(\mathbf{r}) = \epsilon V_{BG}(\mathbf{r})/d$ and the local twist angle $\theta(\mathbf{r}) = a\sqrt{n_s(r)\sqrt{3}/8}$ (d is the atomic force microscope (AFM)-measured back-gate distance, $\epsilon = 3.3 \pm 0.5$ is the hBN dielectric constant, and $a = 0.246$ nm is the graphene lattice constant). Figure 8-1d shows $d\mu/dn$ measured versus the spatial coordinate, Y, along a line-cut across the sample (dashed red line), and versus V_{BG}. The $\nu = 4$ peak shifts from $V_{BG} = 5.4$ V at the sample centre to $V_{BG} = 6.5$ V near its top edge, corresponding to an approximately 10% change in θ (top axis). This variation occurs in discrete steps, reflecting domains with constant θ within the sample, consistent with recent observations [56]. Mapping θ across the entire accessible area (Fig. 8-1e) shows a terraced θ landscape, with constant-θ domains a few hundred nanometres in size. Since our measurements are local, the variation

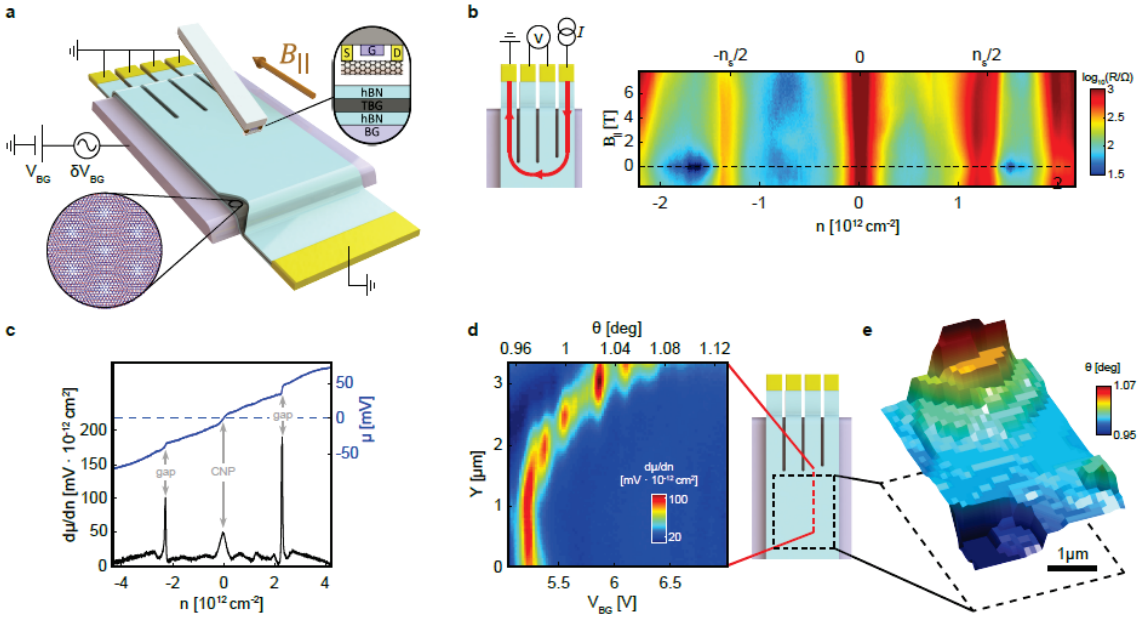

Figure 8-1: Measurement setup and device characterization. (a) Twisted bilayer graphene (TBG) encapsulated between top and bottom hBN (blue), placed on a metallic back-gate (purple) and contacted by side contacts (yellow). We image the inverse electronic compressibility, $d\mu/dn$, using a scanning nanotube-based single electron transistor (SET; inset). (Here μ is the chemical potential of the carriers in the TBG and n is their density.) The SET measures the local $\delta\mu$ in response to a density modulation, δn, produced by an a.c. voltage on the back-gate, δV_{BG} (see Chapter 2.11). In these measurements the TBG is kept grounded, and a d.c. back-gate voltage, V_{BG}, sets the overall n. Some measurements use a parallel magnetic field, $B_{//}$, whose orientation is indicated by the orange arrow. (b) Four-probe resistance, R, measured using the top four contacts (left inset) as a function of carrier density, n, and $B_{//}$, at $T = 50$ mK. The $\pm n_s/2$ labels on the top axis mark half-filled valence and conduction flat bands. (c) Characteristic $d\mu/dn$ (black trace) and μ (blue trace, obtained by integrating the former) measured as function of n, at $T = 4$ K. Arrows mark the charge neutrality point (CNP) and the gaps separating the flat bands from the higher-energy dispersive bands. (d) Measurement of $d\mu/dn$ as a function of a spatial coordinate, Y, along a line-cut across the sample (red dashed line, inset) and V_{BG} focusing on the peak of $d\mu/dn$ that corresponds to a full flat band ($n = n_s$). The local twist angle, θ, is obtained directly from the back-gate voltage at which this peak appears (see text), and is indicated in the top y axis. In the centre of the sample, θ is rather homogeneous and smaller than the magic angle. In the top part of the sample, θ climbs in steps (fixed- domains) towards the MA. (e) Spatial map of the twist angle, θ (covering the black dashed region in the inset), determined in a similar fashion to d but from a three-dimensional measurement of $d\mu/dn$ as a function of V_{BG}, X and Y. A terraced landscape with constant-θ domains is visible. All measurements shown in the figure were performed on sample A.

of θ across the sample enables a systematic study of the angle dependence of the physics.

8.5 Asymmetric sawtooth features in inverse compressibility

The electronic compressibility shows interesting features near integer moiré fillings, which emerge in a narrow twist angle range around the MA (Fig. 8-2). We first study the compressibility at finite $B_{//}$, where features at odd fillings (ν = 1, 3) are strengthened, and then proceed to $B_{//}$ = 0. Figure 8-2a plots a colour map of $d\mu/dn$, measured at $B_{//}$ = 12 T, as a function of ν and the spatial coordinate, Y, along the same line-cut as in Fig. 8-1d. Along this line-cut, θ gradually climbs towards the MA (right y axis). We define the ν axis by separately normalizing the density at each Y with respect to the local moiré band density, $\nu = n/(n_s(Y)/4)$. Figure 8-2b features selected curves from this spatial evolution with θ = 0.99°–1.07° (offset for clarity) together with curves from sample B with θ = 1.13°–1.31°, covering angles from below to above the MA. At θ = 0.99°, $d\mu/dn$ shows a sharp jump near ν = 2, and a symmetric peak above ν = 3. As θ increases towards θ = 1.13°, these features evolve into a cascade of asymmetric sawtooth features: approaching the integers ν = 1, 2, 3 from below, $d\mu/dn$ drops gradually (to high compressibility), jumps up sharply (to low compressibility) near each integer ν, and then decreases gradually again. These asymmetric sawtooth-like features are fundamentally different from the signature of a gap, which corresponds to a jump in the chemical potential, μ , and therefore to a narrow symmetric peak in $d\mu/dn$. A similar cascade of sawtooth features appears in both samples, demonstrating the robustness of the phenomena. When the angle reaches θ = 1.31° the sawtooth features completely disappear and the compressibility is rather featureless.

We note that all the observed sawtooth features point away from the CNP. Moreover, while showing an approximate mirror symmetry about the CNP, they are clearly asymmetric with respect to the centres of the conduction and valence flat bands (ν = 2, -2): $d\mu/dn$ at $|\nu| = 2 + x$ is radically different from $d\mu/dn$ at $|\nu| = 2 - x$. This emphasizes the unique role of the CNP, and strongly indicates that an asymmetry of the single-particle dis-

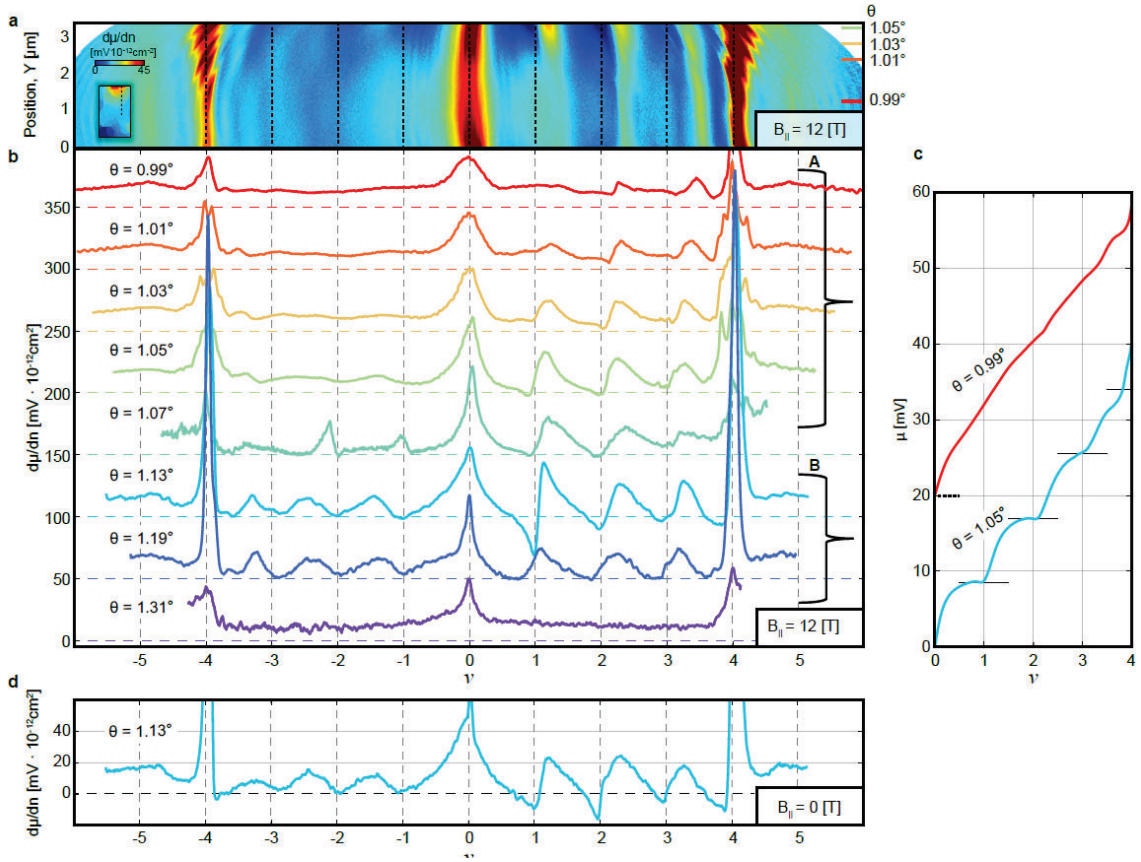

Figure 8-2: Asymmetric sawtooth features in inverse compressibility. (a) $d\mu/dn$ measured as a function of ν and spatial position Y in sample A (along the same line-cut as in Fig. 8-1d; dashed line in the inset) at $B_{//} = 12$ T and $T = 50$ mK. The local twist angle changes along this line-cut, as indicated on the right y axis. The filling factor ν is determined by the local $n_s(Y)$. (b) Selected $d\mu/dn$ traces from panel a (sample A, $T = 50$ mK) together with traces from sample B ($T = 4$ K), with their corresponding θ labelled (offset for clarity). An asymmetric cascade of sawtooth features is apparent, consistent between the two samples. This structure appears in a relatively narrow twist angle range around the MA. All curves are measured at $B_{//}$ = 12 T apart from that of $\theta = 1.07°$, which was measured at $B_{//} = 10$ T. (c) The chemical potential μ as function of ν, obtained by integrating the traces in b that correspond to $\theta = 0.99°$ and $1.05°$, offset for clarity. Near the CNP, in both curves μ increases in a $\sqrt{n}$-like fashion owing to the Dirac-like dispersion. In the larger-θ curve this $\sqrt{n}$-like dependence reappears at all integer ν, demonstrating the revival of Dirac-like behaviour at the Fermi level (overall slope uncertainty is discussed in the Supplementary Information section 3 of reference [111]). The horizontal black lines are equidistant in μ. (d) $d\mu/dn$ versus measured in sample B at $B_{//} = 0$ T, $T = 4$ K and $\theta = 1.13°$.

persion around the centres of the conduction and valence bands is essential for the observed asymmetry.

The high value of $d\mu/dn$ immediately after the jumps and its subsequent gradual decrease with n resemble the behaviour of $d\mu/dn$ around the CNP, suggesting a revival of Dirac-like electronic character after each integer filling. This is also apparent by comparing the $\mu(n)$ traces measured at $\theta = 0.99°$, $1.05°$ (Fig. 8-2c): at $\theta = 0.99°$, $\mu(n)$ features a $\sqrt{n}$-like dependence around the CNP, characteristic of a Dirac-like dispersion, but then climbs roughly linearly as the flat band is filled. In contrast, at $\theta = 1.05°$ a $\sqrt{n}$-like dependence re-emerges after every integer filling.

At $\nu = 2, 3$, sawtooth features appear at small θ, and as the MA is approached they increase in magnitude and move towards exact integer fillings. In contrast, the $\nu = 1, -1, -2$ sawtooth features emerge only at larger twist angles, suggesting that holes need larger θ than electrons to exhibit this behaviour.

Close to the MA the sawtooth features also appear at zero magnetic field. Figure 8-2d shows a $d\mu/dn$ trace measured at $\theta = 1.13°$ and $B_{//} = 0$, exhibiting asymmetric sawtooth features with sharp jumps of $d\mu/dn$. Moreover, $d\mu/dn$ becomes negative before all integer fillings of the conduction flat band [319], a clear signature of strong electronic interactions.

8.6 Parallel magnetic field dependence of the asymmetric sawtooth features

The systematic $B_{//}$ dependence of $d\mu/dn$ at $\theta = 1.05°$ is shown in Fig. 8-3a. $d\mu/dn$ hardly changes with $B_{//}$ around the CNP, but exhibits an even–odd dependence around integer fillings: at even fillings the sawtooth weakens ($\nu = -2$) or hardly changes ($\nu = 2$) with$B_{//}$, whereas at odd fillings ($\nu = 1, 3$) it strengthens with $B_{//}$. This reflects alternating spin polarizations as integer fillings are crossed, consistent with previous transport observations [79, 83, 122, 116].

The prominent magnetic-field dependence of the sawtooth feature around $\nu = 1$ allows us to study its energetics more closely. Figure 8-3b shows μ as a function of ν for

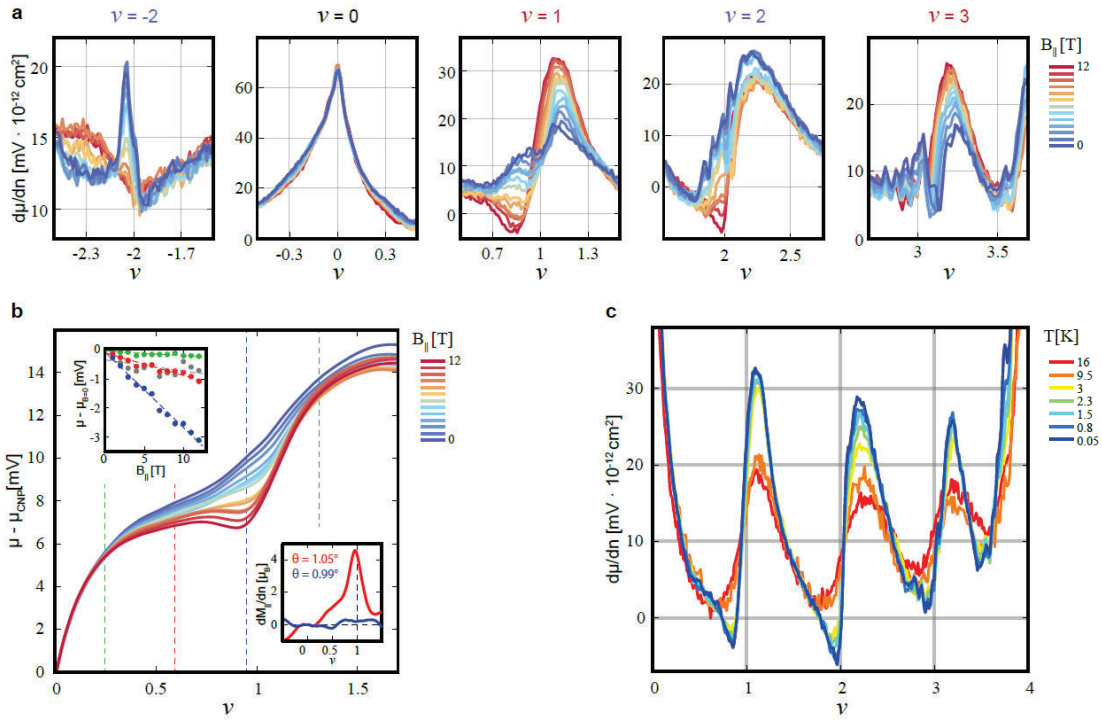

Figure 8-3: Dependence of the asymmetric sawtooth features at $\theta = 1.05°$ on parallel magnetic field and temperature. (a) Parallel field dependence: shown is $d\mu/dn$ measured in sample A as a function of filling factor around $\nu = -2, 0, 1, 2, 3$ (left to right) at various values of $B_{//}$ and $T = 50$ mK. (b) μ as a function of ν for various values of $B_{//}$ obtained by integrating the measured $d\mu/dn$; μ is referenced to the chemical potential at the CNP, μ_{CNP}. Top inset, μ as a function of $B_{//}$ at selected values of ν (green, red, blue and grey dashed lines in main panel). Bottom inset, the differential magnetization $dM_{//}/dn \equiv -d\mu/dB_{//}$ (extracted from a linear fit to the $B_{//}$ dependence of μ at each ν) as a function of ν measured at $\theta = 1.05°$ (red) and $0.99°$ (blue). However, for $\theta = 0.99°$, $dM_{//}/dn$ remains practically zero throughout, it peaks sharply near ν = 1 for $\theta = 1.05°$, reaching a value of $(4.5 \pm 0.3)\mu_B$, signifying the build-up of spontaneous magnetization that starts around this peak. (c) Temperature dependence: the measured $d\mu/dn$ is shown as a function of ν at various temperatures, T, at $B_{//} = 12$ T.

various $B_{//}$. At every ν, μ depends approximately linearly on $B_{//}$, but with a different slope (Fig. 8-3b, top inset). By Maxwell's relation we know that $dM_{//}/dn \equiv d\mu/dB_{//}$, thus these measurements allow us to determine the differential magnetization, $dM_{//}/dn$, directly. Figure 8-3b, bottom inset, plots $dM_{//}/dn$ as a function of ν for $\theta = 1.05°$ and $0.99°$. At $\theta = 1.05°$, $dM_{//}/dn$ is nearly zero over a finite range around ν = 0, then rises slowly with ν, and near ν = 1 rapidly increases to $dM_{//}/dn \approx (4.5 \pm 0.3)\mu_B$, followed by a sharp drop to near zero (here μ_B is the Bohr magneton). This large $dM_{//}/dn$ indicates a rapid build-up of magnetization near ν = 1. The linear $B_{//}$ dependence of μ, observed to the lowest $B_{//}$ (Fig. 8-3b, top inset), suggests that the system has spontaneous magnetization near and above ν = 1. In contrast, for $\theta = 0.99°$ we see that $dM_{//}/dn \approx 0$ throughout the entire filling factor range, emphasizing that the emergence of flavour symmetry breaking and magnetization near ν = 1 depends sensitively on the proximity of θ to the MA.

8.7 Temperature dependence of the asymmetric sawtooth features

Finally, we show the temperature dependence of $d\mu/dn$ in Fig. 8-3c. The sawtooth features remain strong even at the highest temperature achievable in our scanning setup, $T = 16$ K, and extrapolate to zero at $T \approx 30$ K, seven times higher than the temperatures where insulating behaviour commences in transport measurements [79, 122, 116, 5, 302]. Independently, we estimate the energy scale associated with the Dirac revivals from the measured depth of the kinks in μ (Fig. 8-2d), obtaining $\Delta\mu \approx 4$ mV. This substantially exceeds the activation energies measured in transport [79, 122, 116], which were associated with correlated gaps, but is comparable to the scale over which 'strange metal' behaviour was observed in transport [5, 302]. This suggests that the Dirac revivals underlie the high-energy correlated state of this system.

8.8 Discussion: phase transitions and Dirac revivals model

These robust features of the compressibility call for a theoretical understanding. Many features of our data are captured surprisingly well within a simple model that includes certain key elements but ignores many details of the complex electronic structure of the flat moiré bands. A typical calculated band structure (Fig. 8-4a) shows a strong asymmetry of the conduction and valence flat bands around their centres, evolving from a Dirac-like density of states (DOS) at the CNP to a massive DOS near the band edges. We believe that two features of this band structure are responsible for the observed behaviour: the strong dependence of the DOS on filling, and its inherent asymmetry about the centre of the conduction (or valence) band. We capture these features in a stripped-down model, which replaces the DOS by a linear function that terminates abruptly at the band edges (Fig. 8-4a, right). We assume a contact repulsive interaction, which is independent of the spin/valley flavour index, and solve the model within the Hartree–Fock approximation, allowing for spin/valley symmetry breaking via an unequal population of different flavours (see Supplementary Information sections 10, 15 of reference [111] for details of the theoretical model, not included in this thesis, and a discussion of the applicability and limitations of these approximations).

A typical result for $d\mu/dn$ for an interaction strength comparable to the band width is shown in Fig. 8-4b. The resemblance to the experimental data is apparent, with asymmetric sawtooth-like features appearing at integer values of ν, preceded by sharp drops of $d\mu/dn$ to zero. The corresponding μ (Fig. 8-4c) also captures the main features of the experiments (Fig. 8-2d, c). Figure 8-4d shows the population of the individual flavours versus the total filling factor, revealing a cascade of phase transitions with increasing carrier density. For intermediate interaction strengths, near charge neutrality, all four flavours are populated equally. In this specific example there are first-order transitions near $\nu = 1$ and $\nu = 2$, where one flavour becomes nearly filled, while the other flavours are pushed downwards towards charge neutrality. Closely after these transitions, there are 'Lifshitz' transitions, where the filling of the majority flavour reaches 1. This Lifshitz transition explains the sawtooth

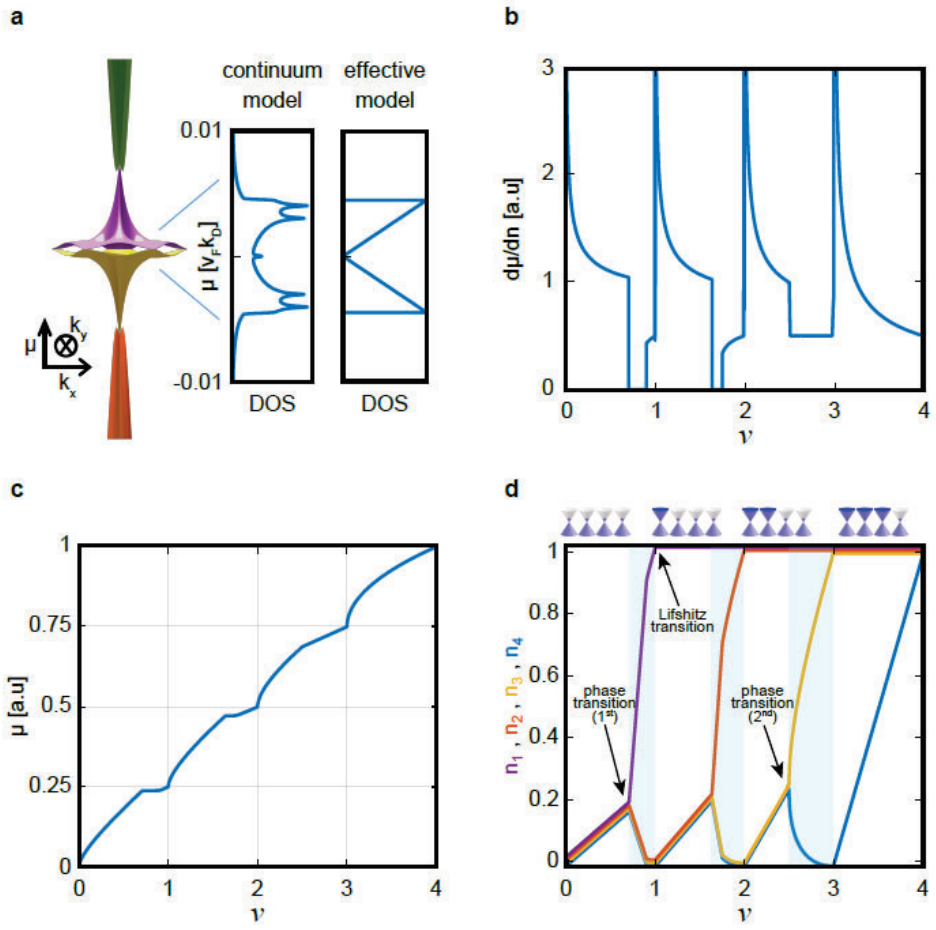

Figure 8-4: Phase transitions and Dirac revivals model. (a) Band dispersion (left) and density of states (DOS; centre) of the valence and conduction flat bands, calculated from a continuum model [81, 95] for a twist angle of $\theta = 1.04°$. Our theory uses a simplified version of this DOS, with a triangular energy dependence (right), capturing the two essential features of the band structure: first, the gradual increase of the DOS from a Dirac-like dispersion at the CNP to a massive dispersion at the top and bottom band edges; and second, the consequential asymmetry of this DOS around the valence and conduction band centres. (b) Calculated $d\mu/dn$ versus ν (obtained using the Hartree–Fock approximation), showing apparent resemblance to the measured data (for example, Fig. 8-2). (c) Calculated chemical potential, μ, versus ν. (d) The partial densities of individual flavours, n_i (i = 1..4) as a function of ν. The flavours start with fourfold degeneracy at charge neutrality, but then, close to an integer ν, experience a phase transition, after which one band takes all carrier from the other three (occurring in the shaded blue region). When the former band becomes full, the other three start refilling again from near the Dirac point. The beginning of this refilling corresponds to the Lifshitz transition (the jump in $d\mu/dn$, in b). This process repeats periodically near all integer filling factors, but each time with one less band, and can start with a first- or a second-order phase transition (arrows). The first-order transitions are followed by phase mixing regions where the partial densities interpolate linearly between those of the two phases. The flavour filling is illustrated on top (blue represents filled states).

features in $d\mu/dn$: before the transition, the density of states at the Fermi level is dominated by the massive majority flavour, whereas after the transition it is strongly decreased owing to the Dirac character of the remaining flavours whose occupations are reset to near the CNP. Depending on model details, the first-order and Lifshitz transitions may coincide and the majority flavour may jump directly to full filling (for a detailed discussion, see the Supplementary Information section 11 of reference [111]). Flavour polarization may also be initiated by a second-order transition (for example, preceding $\nu = 3$ in Fig. 8-4d). In our model, the sharp dips where $d\mu/dn$ approaches zero appear at the first-order phase transitions, and reflect a spatial breakup of the system into domains of the corresponding phases.

For stronger interaction, the spin/valley symmetry may be broken even at charge neutrality, but there is no corresponding evidence for that in our experiments, and thus we focus on intermediate interaction strengths, where in our model the $\nu = 0$ state is valley and spin symmetric. In the Supplementary Information of reference [111], extensions of this minimal model are discussed in more detail, including a more complex DOS with van Hove singularities or long-range Coulomb interactions. While details of the computed $d\mu/dn$ change, the overall features remain similar to those obtained from the simple model.

8.9 Conclusion

Our experiments and corresponding theory predict that the flavour symmetry will be broken with a 4-, 3-, 2-, 1-fold degeneracy following fillings of $\nu = 0$, 1, 2, 3 (for details, see Supplementary Information section 17 of reference [111] and Fig. 2-37). This was indeed observed experimentally [79, 83, 122, 116, 56] (with one possible exception, above $\nu = 1$, possibly due to the rather sparse and inconclusive data). It also predicts that the Landau fans will always point away from the CNP [309], except at $\nu = 4$ where they should point towards the CNP, reproducing experimental observations [79, 83, 122, 116, 56]. Another consequence of Dirac revivals is that correlated gaps will appear at integer filling only if the Dirac spectrum is gapped [309, 320, 313], suggesting a possible connection between a gap at the CNP and the correlated gaps at integer filling factors. From our data we can place an

upper bound of approximately 1 meV on a possible thermodynamic gap hidden within our experimental resolution, consistent with the 0.14-0.9 meV activation gaps measured so far in transport [79, 83, 122, 116].

The observed cascade of sharp asymmetric compressibility features is naturally interpreted in terms of breaking of the spin/valley symmetries at these fillings, which revives the Dirac-like character of the carriers after each transition. These features appear at temperatures far above the onset of the superconducting and correlated insulating states, indicating that the state observed here is the high-energy correlated state from which superconductors and insulators emerge at lower temperatures.

8.10 Entropic evidence for a Pomeranchuk effect in magic-angle graphene

In a follow-up experiment, we observe entropic evidence for a Pomeranchuk effect in magic-angle graphene [314].

Our measurements allow to directly determine the entropy of the system by integrating Maxwell's relation, $(\partial s/\partial \nu)_T = -(\partial \mu/\partial T)_\nu$, to obtain $s(\nu, T)$ (where s is the entropy per moiré unit cell). At temperatures of a few kelvin, we measure unusually large excess entropy, which is rapidly suppressed by a moderate in-plane magnetic field (Fig. 8-5). This suggests that even at such low temperatures, there are strongly fluctuating magnetic moments in the system, a behaviour typically associated with local moments. On the other hand, our measurements find that this state is metallic and has no thermodynamic gap, naturally fitting an itinerant picture. Therefore, surprisingly, the correlated state in MATBG above a filling of one electron per moiré site has a hybrid nature. Some properties resemble those of an itinerant system, and others resemble those of localized electrons.

The presence of fluctuating moments at temperatures much below the electronic bandwidth indicates the existence of a new, anomalously small energy scale associated with the bandwidth of magnetic excitations ($\lesssim 3$ K), which is an order of magnitude smaller than the scale where a jump appears in the compressibility (≈ 30 K), previously described in

this chapter. This jump marks the boundary between the new state at filling factor $\nu > +1$ and the state at lower densities. By tracking the dependence of this boundary on temperature and magnetic field, we find that it exhibits an electronic analogue [321, 322, 323, 324] of the Pomeranchuk effect [325] in ^{3}He, as we explain below.

In the 1950s, Pomeranchuk [325] predicted that, counterintuitively, liquid ^{3}He may solidify on heating. In ^{3}He, the transition from a Fermi liquid to a solid upon increasing the temperature is driven by the high nuclear spin entropy of the atoms in the solid.

Similarly, we find that, in MATBG, the new state above $\nu = +1$ is favoured relative to the metallic state at $\nu < +1$ on raising the temperature (see Fig. 4 and main text of reference [314] for the experimental details), owing to the former's high magnetic entropy. This observation is thus in direct analogy with the Pomeranchuk effect: raising the temperature drives a transition in MATBG from a Fermi liquid phase to a nearly free moments phase with high entropy. The transition near $\nu = +1$ can also be driven by an in-plane magnetic field that polarizes the free moments. Fig. 8-5 shows the measured entropy at $T \approx 10$ K at different in-plane magnetic fields. The strong quenching of entropy by moderate $B_{//}$ strongly suggests a magnetic origin (see inset of Fig. 8-5). The hybrid state observed in this experiment, with itinerant electrons coexisting with strongly fluctuating magnetic moments, calls for a new understanding of electron correlations in MATBG.

In summary, this follow-up experiment reveals a phase diagram consistent with a Pomeranchuk-like temperature- and field-driven transition from a low-entropy electronic liquid to a high-entropy correlated state with nearly free magnetic moments.

We note that a related effect near $\nu = -1$ was proposed recently, on the basis of transport measurements [326], by the group of A. Young; the associated News and Views [327] and Journal Club for Condensed Matter Physics article [328] review and compare both experiments.

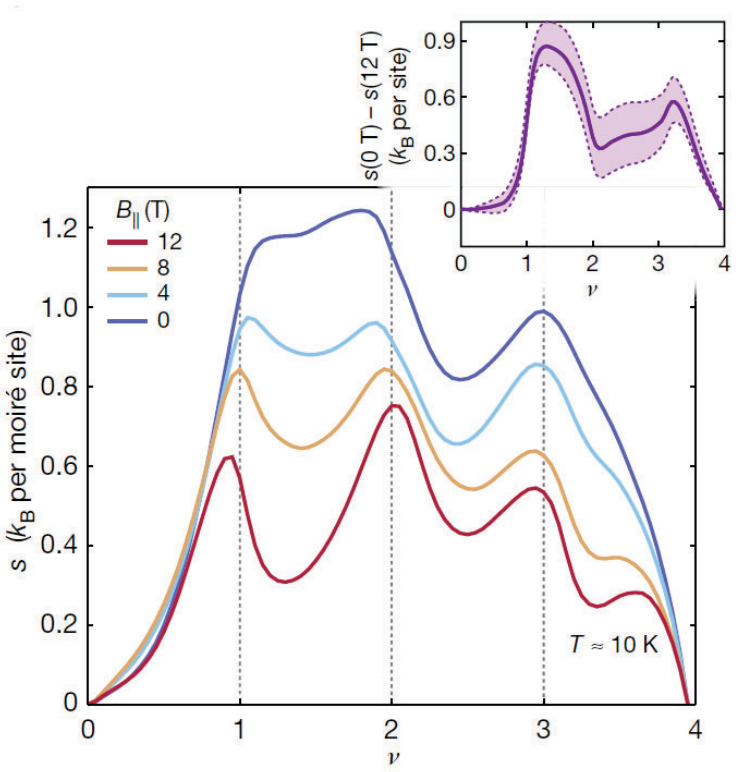

Figure 8-5: Measurement of large magnetic entropy above $\nu = 1$. The electronic entropy s (in units of k_B per moiré unit cell) is plotted as a function of ν at $T \approx 10$ K and at various parallel magnetic fields, $B_{//}$ = 0, 4, 8, 12 T (see key). To obtain the entropy we determine the partial derivative $(\partial\mu/\partial T)_{\nu,B_{//}}$ from a linear fit to the measured ν versus T in the range T = 4.5–15 K. The entropy per moiré cell is then obtained by integrating Maxwell's relation, $(\partial s/\partial\nu)_{T,B_{//}} = -(\partial\mu/\partial T)_{\nu,B_{//}}$, over ν. At $B_{//} = 0$, the entropy climbs rapidly near $\nu = 1$ to a value of about $1.2k_B$ per moiré cell. Inset: difference between the entropies at low and high fields, $s(B_{//} = 0) - s(B_{//} = 12)$. The purple shading shows the estimated standard deviation due to the measurement accuracy. The change in the entropy of the system, $s \approx 0.85k_B$ per moiré unit site, is close to the entropy contribution of freely fluctuating spins. This entropy change can thus be interpreted as caused by an in-plane magnetic field that polarizes the free moments when the Zeeman energy exceeds the temperature.

Chapter 9

Observation of interband collective excitations in twisted bilayer graphene

The single-particle and many-body properties of twisted bilayer graphene (TBG) can be dramatically different from those of a single graphene layer, as discussed in Chapter 2.8. In this chapter, we probe collective excitations of TBG with 20 nanometre spatial resolution, by applying mid-infrared near-field optical microscopy. We find a propagating plasmon mode in charge-neutral TBG with twist angle $\theta = 1.1 - 1.7°$, which is different from the intraband plasmon in single-layer graphene. We interpret it as an interband plasmon associated with the optical transitions between minibands originating from the moiré superlattice. The details of the plasmon dispersion are directly related to the motion of electrons in the moiré superlattice and offer insight into the physical properties of TBG, such as the band nesting between flat band and remote band, local interlayer coupling and losses. We find a strongly reduced interlayer coupling in the regions with AA-stacking, pointing at screening due to electron-electron interactions. Optical nano-imaging of TBG could allow the spatial probing of interaction effects at the nanoscale and potentially elucidate the contribution of collective excitations to many-body ground states.

This chapter follows reference [148], a work performed in collaboration with the groups of Frank Koppens and Marco Poloni.

9.1 Introduction

As explained in Chapter 2.6, when two layers of graphene are superimposed with a small twist angle θ, they form a triangular moiré lattice with a lattice constant d that is related to θ by $\lambda_m = a_0/[2\sin(\theta/2)]$, $a_0 \approx 0.246$ nm being the lattice constant of single-layer graphene [77, 95, 81, 75]. A top view of TBG reveals regions where the two sheets are locally in the AA-stacking configuration surrounded by regions where the stacking configuration is of the more energetically favoured AB- or BA-type (Bernal stacking) [104]. Electrons can tunnel from one layer to the other with an amplitude that depends on the local alignment between the two layers [78, 81]. The interlayer tunnelling amplitude is therefore spatially modulated with the periodicity of the moiré lattice. Effectively, this produces a background scalar potential and non-Abelian gauge field, acting on the graphene Dirac fermions [308]. These two potentials (with an amplitude on the order of 100 meV) localize electronic states close to the charge neutrality point (CNP) in the regions where the alignment between the two layers is AA–like [78, 109, 79, 83]. In a band structure picture, these two contributions yield a pair of narrow bands close to CNP at the magic angle, which, due to their high density of states, are held responsible for the observed correlated phenomena [79, 83, 122, 116, 96, 97, 317, 90, 87, 89, 88] (see Chapter 2.8). Switching off the scalar potential enhances the flatness of the bands making them perfectly flat throughout the superlattice Brillouin zone (BZ) at the magic angle [308, 92].

9.2 Motivation

Several experimental probes have been used to explore the physics of TBG, including electronic transport [79, 83, 122, 116, 96, 97, 106], quantum capacitance [317], scanning tunnelling microscopy [90, 87, 89] and scanning magnetometry [329], also unveiling similar phenomena in twisted double bilayer graphene [330, 331, 332] and trilayer graphene on hexagonal boron nitride (hBN) [333]. However, all these techniques are sensitive only to the static (very low frequency) response of the system. In systems where electron-electron (e-e) interactions play a dominant role, experimental techniques that probe the response to

perturbations carrying a finite in-plane wavevector q and angular frequency ω are expected to be rich sources of information. One of these techniques is scattering-type scanning near-field optical microscopy (s-SNOM) [334, 335, 336, 337, 338], which enables with a spatial resolution of 20 nm the measurement of the dispersion relation of collective electronic excitations, such as Dirac plasmons in doped graphene [334, 335, 339]. The principles of scattering-type scanning near-field optical microscopy technique have been introduced in Chapter 2.11. Here, we apply this technique to study the optical properties of twisted graphene near the magic angle, with a particular focus on the collective excitations related to the moiré minibands.

9.3 Optical properties of TBG

The order of magnitude of the energy separation between the nearly-flat bands and the nearest conduction and valence bands is ≈ 100 meV for θ close to the magic angle. This justifies our interest in the optical properties and collective excitations [340, 341, 342], as probed by s-SNOM (Fig. 9-1a-c), in the MIR region of the electromagnetic spectrum where photons have energies $\hbar\omega$ in the range 80-200 meV, i.e. comparable to the above-mentioned energy scale. These energies are on the other hand much larger than the energy separation between the pair of nearly-flat bands, considered in Ref. [343].

We can qualitatively understand the optical properties of this system in the following way. When light impinges on TBG, its time-periodic electric field shakes electrons around their equilibrium positions (the AA sites, forming a triangular lattice) or—in the more rigorous language of band theory—it induces an interband transition between the ground and excited states at the K point of the Brillouin zone (Fig. 9-1d-e). If the field carries a finite in-plane wavevector q (provided by the sharp AFM tip), the shaking electrons will build up an oscillating charge density with the same wavevector (plus harmonics due to exchange of reciprocal lattice vectors). This oscillating charge density, in turn, creates an oscillating electric field that adds to the external field. If q and ω are correctly matched, this induced field can be strong enough to sustain the oscillation even after the external field has been turned off. This resonant behaviour gives rise to collective modes that are called

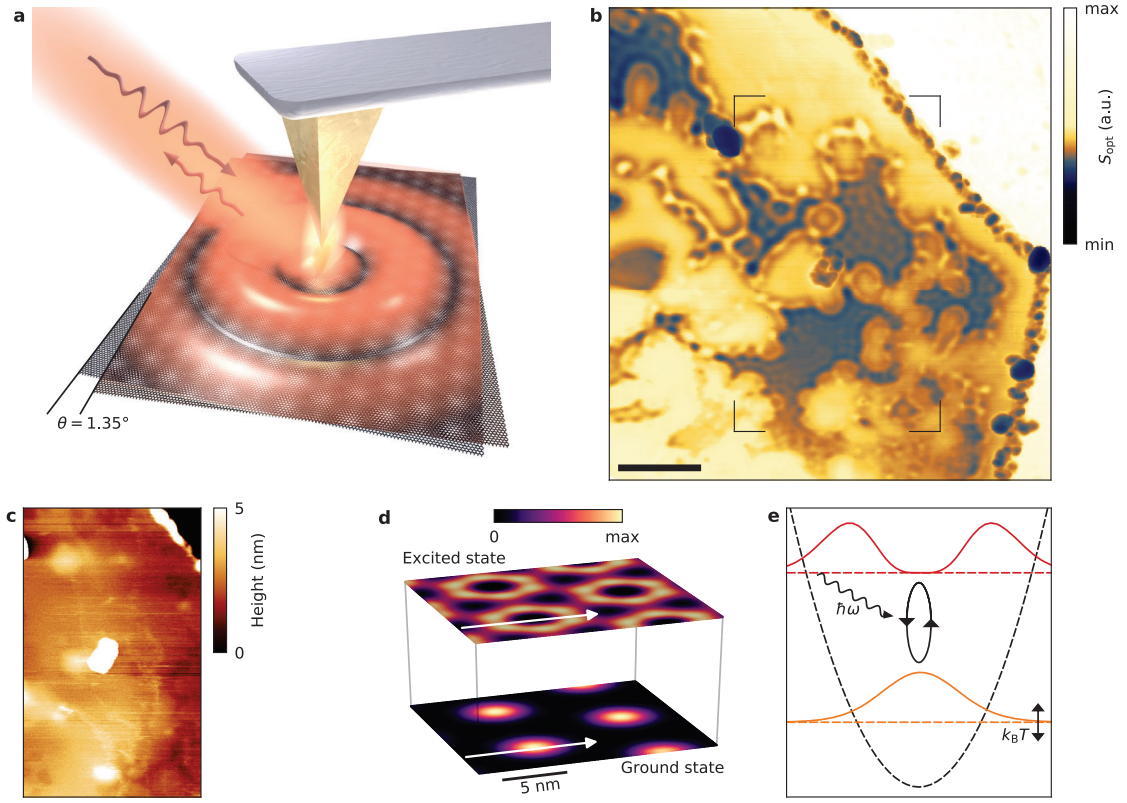

Figure 9-1: Collective excitations in twisted bilayer graphene. (a) Illustration of the scattering-type scanning near-field microscopy experiment: an AFM metallic tip is illuminated by infrared light, which provides sufficient momentum to launch a collective excitation in twisted bilayer graphene. The plasmon can, in turn (e.g. by reflection from an edge or interface), scatter into light at the tip. This scattered light is detected by a photodetector. The curved arrows indicate the light impinging on the tip (coming from the laser) as well as the scattered light (going to the detector). (b) Image of the near-field amplitude obtained by scanning the AFM tip and recording the photodetector signal. Propagating collective excitations are visible in certain areas as periodic interference fringes. The illumination photon energy is $\hbar\omega$=219 meV and the length of the scale bar is 500 nm. (c) AFM image of the marked region in panel b. (d) Square modulus of the wave function $|\langle \mathbf{r}|\mathbf{k}=\mathbf{K},\nu\rangle|^2$, associated with one of the flat bands (bottom) and the first excited band (top), evaluated at the $\mathbf{K}$ point of the moiré superlattice Brillouin zone. These states are mostly localized around the regions with local AA-stacking (which form a triangular lattice) and are involved in the relevant optical transitions. (e) Line cuts of the wave functions along the white arrows in panel c represented in a harmonic confinement potential [308] (black dashed line), with the coloured horizontal dashed lines indicating the energies of the states. An interband transition occurs between the lower-energy state and the excited state. A similar transition is happening, for holes, between the corresponding pair of states, approximately related to the illustrated ones by electron-hole symmetry.

interband plasmons, which have been predicted theoretically to emerge in TBG [344, 85], but were never studied experimentally so far. At $q = 0$, this collective excitation has the same frequency as the bare interband transition. Upon increasing q, as we show in this work, it acquires a finite dispersion. Thus, these excitations do propagate with a finite group velocity, akin to graphene Dirac plasmons [334, 335, 345], albeit with very different dispersion. Here, the dispersion depends on the degree of band nesting, which is the phenomenon of two bands being parallel in energy-wavevector space, and details of the e-e interaction potential, which is heavily influenced by screening from nearby dielectrics. We note that a similar collective mode occurs in topological insulators [346, 347] or between the rigorously flat Landau-level of a two-dimensional (2D) parabolic-band electron gas in a perpendicular magnetic field. In this case, while single electrons oscillate at the cyclotron frequency Ω_c , e-e interactions induce a collective mode, known as a bulk magnetoplasmon, which, at long wavelength, has a linear dispersion [348] $\omega(q) = \Omega_c + sq$ with group velocity $s > 0$ reflecting its propagating character.

9.4 Near-field experiments on TBG

9.4.1 Sample fabrication and pre-characterization

We now turn to a description of our experimental findings. As carefully described in Chapter 2.9, we fabricate TBG samples using the tear-and-stack method [94, 140]. These are encapsulated in hBN, and placed on a metal gate. A detailed list of the different measured devices can be found in the Supplementary Information of reference [148]. The twist angle θ is determined from cryogenic transport measurements (as described in Chapter 2.10.2).

9.4.2 Experimental setup: s-SNOM measurements

We then perform s-SNOM measurements with mid-infrared light (free-space wavelength λ_0 in the range 5-11 μm) in ambient conditions (T=300 K). We generate a nanoscale light hotspot by focussing a laser beam on the apex of a sharp (apex radius ≈25 nm) metallic atomic force microscope (AFM) tip (Fig. 9-1a). This hotspot interacts with the charge

carriers and produces collective excitations that are reflected by interfaces, return to the tip, and are finally converted into a scattered field, which is measured by a photodetector. By scanning the tip position, we acquire, simultaneously, a spatial map of the backscattered light intensity S_{opt} and AFM topography. Noise and far-field contributions to the optical signal are strongly reduced by locking to the third harmonic of the tapping frequency of the tip. The spatial resolution of the obtained images is limited only by the tip radius [349]. We refer to Chapter 2.11 for a more in-depth description of the experimental technique.

9.4.3 Observation of collective excitations

Figure 9-1b shows a typical near-field image of TBG with no gate voltage applied (at zero applied voltage the TBG is close to charge neutrality) and an average twist angle of $\theta = 1.35°$, obtained from transport measurements. Figure 9-1c shows the AFM image recorded at the same time. In the near-field image, for an excitation energy $\hbar\omega = 219$ meV two types or regions can be distinguished. Regions with a rather spatially constant response S_{opt} (yellow) and regions where S_{opt} shows clear spatially varying and periodic features. This contrasts with a near-field map taken at lower energy $\hbar\omega = 146$ meV, in which the periodic features are absent (see Fig. 9-2e). As reported scanning SQUID measurements on similar samples have shown [56], some regions can exhibit magic-angle behaviour while some other regions do not (e.g. due to lattice relaxation into an angle far from magic angle). In this chapter, we focus on the regions with the varying and periodic features of this device. The Supplementary Information of reference [148] provides results from 14 other devices with $\theta = 1.1 - 1.7°$, and a discussion on the correlation of these regions with tiny topographic features.

In the regions of interest, S_{opt} displays an oscillatory spatial behaviour. The latter has a characteristic period ≈ 80 nm in all of the regions of interest (with a ± 10 nm spread), about one order of magnitude larger than d. We attribute this oscillatory behaviour to the excitation of a propagating collective electronic mode. The fact that we observe these interference patterns in ungated TBG is in stark contrast with the intraband collective electronic excitations (Dirac plasmons) of single-layer and bilayer graphene, where high doping lev-

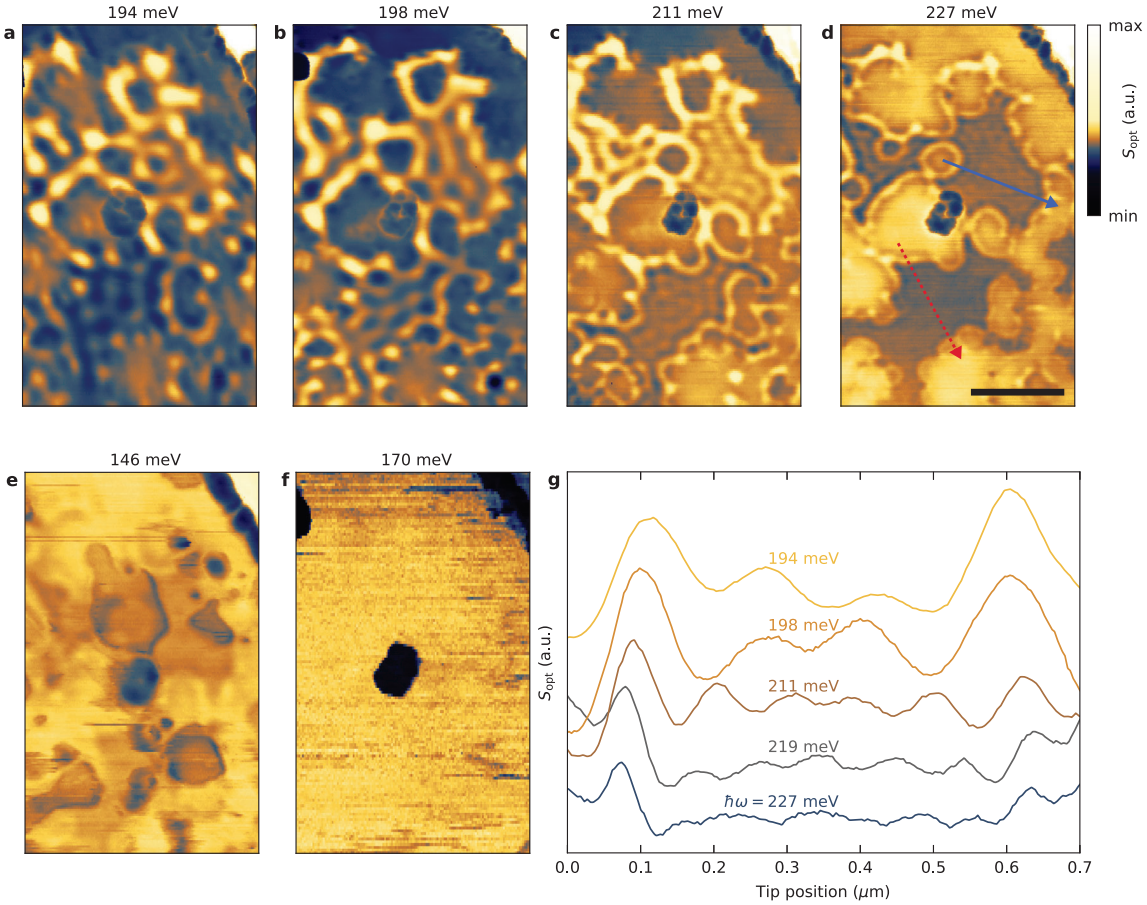

Figure 9-2: Controlling the wavelength of interband plasmons. (a-f) Near-field amplitude images at different excitation energies $\hbar\omega$ of the area marked in Fig. 9-1b. In panels a-d $\hbar\omega > \hbar\Omega_{exp}$, while the data in panels e,f correspond to $\hbar\omega < \hbar\Omega_{exp}$. Solid and dashed arrows in panel d indicate line traces associated to data in panel g and Fig. 9-3a, and the length of the scale bar is 500 nm. (g) Line traces along the solid blue arrow in panel d, visualizing the strong dependence of the plasmon wavelength on the excitation energy. Lines are vertically separated for clarity.

els (above $10^{13} cm^{-2}$) are required to propagate at the frequencies we focus on ($\hbar\omega \sim 200$ meV) [336, 339, 345].

To obtain more insight into the nature of the collective excitations we probe their frequency dependence by repeating the near-field measurements at different excitation energies, changing $\lambda_0 = 2\pi c/\omega$. Figure 9-2a-e shows a dramatic change in the interference pattern for small variations in λ_0, while the boundaries of the areas where the sample is optically active remain at a fixed position. These data show the dispersive character of the propagating collective excitations that move in Fabry-Pérot-like cavities, due to reflecting interfaces [350, 351]. At the same time, the scan in Fig. 9-2f for $\hbar\omega$=170 meV is free of any features. As $\hbar\omega$ coincides with the lower edge of the hBN Reststrahlen band, the near-field signal is dominated by the top hBN layer. Thus, we conclude that the observed features in Fig. 9-2a-e originate from the TBLG itself. If any contamination was present on top of the sample, or if the hBN would exhibit thickness variations, the 170 meV scan would not show such a uniform response as we observe.

9.4.4 Analysis of the propagating collective modes

More quantitatively, we extract one-dimensional (1D) cuts of the measured S_{opt} along two specific lines (see arrows in Fig. 9-2d). The resulting 1D profiles are shown in Fig. 9-2g as lines for a few representative photon energies, while a colour map as a function of tip position and frequency is reported in Fig. 9-3a (other line traces taken in the near-field image are not included in this chapter but can be found in reference [148]). The oscillating signal is well fitted by the following expression, representing a tip-launched, tip-detected wave reflected at an interface: $S_{opt}(x) = Re[Ax^{-1/2}e^{2iqx}] + Bx$. Here, x is the tip position along the line cut, as measured from the interface, $A \equiv A_1 + iA_2$ and $q \equiv q_1 + iq_2$ are complex fit parameters, and B represents a linear background [339]. Note the factor of two in the exponential function that appears because the collective excitation makes a full round trip between the tip and the reflecting interface. Our fitting procedure yields quantitative results for the real part q_1 of the plasmon wavevector q while the imaginary part q_2 is significantly smaller.

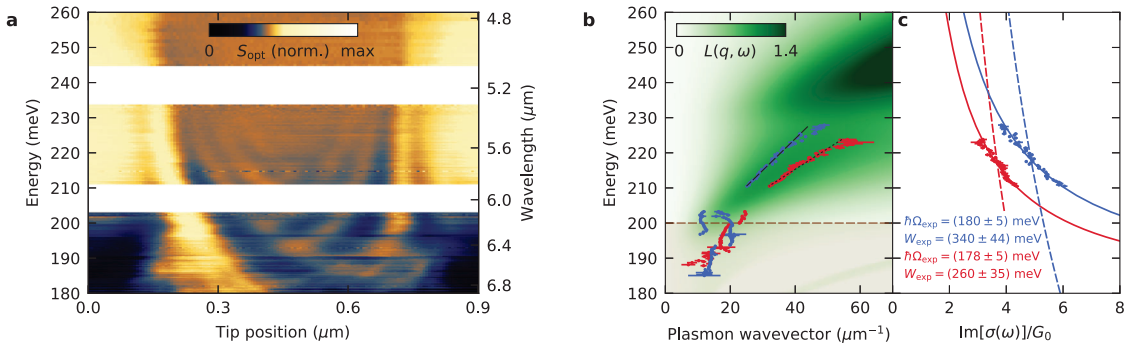

Figure 9-3: Extracting the optical conductivity from the plasmon dispersion. (a) Near-field amplitude along the dashed red arrow in Fig. 2d, for a range of excitation energies. To highlight the plasmonic modes, we normalize each line to the average near-field amplitude within the reflecting interfaces. The white gaps are gaps in the spectrum of the excitation laser. (b) Dispersion relation $q_1(\omega)$ determined from fitting individual line traces in panel a to a sinusoidal function (red points). The blue points are obtained in a similar way but from a slightly different location (solid blue arrow in Fig. 9-2d). We extract the plasmon group velocity (black dashed/dotted lines) from a linear fit on the blue data points. The horizontal dashed line marks the threshold of the hBN Reststrahlen band. The colour plot represents the loss function, calculated from the chirally-symmetric continuum model [92, 99]. (c) Extracted values of the optical conductivity with the same colour coding as in panel b. Dots represent experimental data, dashed lines are Drude fits, while solid lines are fits with resonant profiles.

From the extracted values of $q_1(\omega)$ we can construct a dispersion curve for the collective excitation as shown in Fig. 9-3b. For energies above 200 meV, the dispersion is approximatively linear with a group velocity $s \approx 0.9 - 1.3 \times 10^6$ m/s (dashed and dotted lines in Fig. 9-3b), and crosses the $q_1 = 0$ point for $\hbar\Omega_{exp} \approx 190$ meV. For lower energies, the typical discretization pattern of a finite size cavity appears (i.e. where the distance between the reflecting interfaces is comparable to the plasmon wavelength $2\pi/q_1$). Remarkably, the group velocity is larger than theoretically anticipated. For example, in Ref. [344], flat plasmonic bands were predicted, as discussed below. As we will see, this points to a larger spectral weight in the optical transitions. Clearly, the observed nearly-linear dispersion, initiating from a finite energy $\hbar\Omega_{exp}$ for $q_1 = 0$, is very different from the typical Dirac plasmon dispersion of doped single- and bilayer graphene (more detailed comparisons between TBG and graphene can be found in the supplementary section of reference [148]. Instead, the observed linear dispersion resembles more the one of a bulk magnetoplasmon [348]: $\omega(q) = \Omega_{exp} + sq_1$.

9.4.5 Carrier-density dependence of the collective excitation wavelength

Finally, we measured on one of our devices the carrier-density dependence of the dispersion of the collective excitation by applying a voltage bias between the TBG and the metallic gate (measurement details and experimental results have not been included in this chapter but can be found in ref. [148]). The experimental data show no noticeable change of the collective excitation wavelength inside the range of electronic densities considered. This strengthens the interpretation in terms of collective modes originating from an interband transition, as those are much less affected by the carrier density than intraband plasmons.

9.5 Extraction of the optical conductivity.

To relate our observations to the electronic bands in the moiré superlattice, we extract the value of the optical conductivity $\sigma(\omega)$ for the optically active regions. In the local approximation [352] (i.e., where the optical conductivity is taken to be independent of q and contributions from reciprocal lattice vectors $G \neq 0$ are neglected), the longitudinal dielectric function [353] is given by $\epsilon(q,\omega) = 1 + iq^2 V_{q,\omega}\sigma(\omega)/\omega$, where $V_{q,\omega} = 2\pi F(q,\omega)/[\widetilde{\epsilon}(\omega)q]$ is the 2D Fourier transform of the Coulomb potential [354], the permittivity $\widetilde{\epsilon}(\omega) = \sqrt{\epsilon_{//}(\omega)\epsilon_{\perp}(\omega)}$ takes care of the optical response at frequency ω of the hBN crystal slabs [355] surrounding the TBG sample, and $F(q,\omega)$ is a form factor that takes into account the finite thickness of the hBN slabs (the detailed procedure of the extraction of optical conductivity is available in reference [148]). Finite thickness effects are important close to the upper edge of the hBN Reststrahlen band where the in-plane permittivity $\epsilon_{//}(\omega)$ vanishes and the out-of-plane decay length of the mode diverges. Neglecting the finite thickness of hBN would lead to a wrong dispersion relation, yielding a collective mode that does not enter the upper Reststrahlen band (see Fig. 9-3b). Collective modes can be found by solving [353] $\epsilon(q,\omega) = 0$, or by looking at the peaks of the loss function $L(q,\omega) = -Im[\epsilon(q,\omega)^{-1}]$. From the measured collective excitation dispersion, we can find the imaginary part $\sigma_2(\omega)$ of the local conductivity, using the expression

$\sigma(\omega) = i\omega/(q^2 V_{q,\omega})$ and neglecting the imaginary part of q (the proof that we can safely do this without changing the results is provided in the Supplementary Information of reference [148]). The results are shown in Fig. 9-3c.

The simplest possible fitting function, of the Drude form $\sigma_2(\omega) = G_0 W_0/(\hbar\omega)$ — where $G_0 = 2e^2/h$ is the conductance quantum and W_0 is a fitting parameter with dimensions of energy—yields $W_0 \approx 1100$ meV (that would correspond, for two uncoupled single-layer graphene sheets, to a Fermi energy $\epsilon_F \approx 550$ meV in each layer) and a very poor fit. This confirms that our data are not consistent with a regular intraband graphene Dirac plasmon. A much better fit is obtained by using the following resonant form $\sigma_2(\omega) = G_0 W_{exp}\hbar\omega/(\hbar^2\omega^2 - \hbar^2\Omega_{exp}^2)$, with W_{exp} and Ω_{exp} fitting parameters. We find $\hbar\Omega_{exp} \approx 180$ meV and a spectral weight $W_{exp} \approx 300$ meV for both presented datasets.

9.6 Theory of interband transitions in TBG

We now seek a theoretical justification for the resonant lineshape extracted from the experimental data and for the values we have found for Ω_{exp} and W_{exp}. At the level of the random phase approximation (RPA) for the dynamical dielectric function [353] $\epsilon(q,\omega)$, the unknown quantity $\sigma(\omega)$ is approximated by using its value for the non-interacting 2D electron system in TBG. The latter can be calculated exactly by employing the Kubo formula [353], once the eigenstates $|\mathbf{k},\nu\rangle$ and bands $\epsilon_{\mathbf{k},\nu}$ of the single-particle problem are given. Here $\mathbf{k}$ represents the electronic wavevector. The quantities $|\mathbf{k},\nu\rangle$ and $\epsilon_{\mathbf{k},\nu}$ can be found from a band structure calculation for TBG at a given θ. Here, we have used results obtained from *ab initio* $k \cdot p$ perturbation theory [93], which accurately accounts for the effects of intrinsic atomic relaxation in pristine samples. The resulting bands $\epsilon_{\mathbf{k},\nu}$ are shown in Fig. 9-4a. We clearly see that band nesting occurs near the $\mathbf{K}$ point of the superlattice BZ, where two (relatively flat) bands—say ν and ν', connected by vertical lines with arrows in Fig. 9-4a—are such that $\nabla_{\mathbf{k}}\epsilon_{\mathbf{k},\nu} \simeq \nabla_{\mathbf{k}}\epsilon_{\mathbf{k},\nu'}$ in a range of values of $\mathbf{k}$. In other words, the bands are parallel to each other for a wide range of $\mathbf{k}$. The joint density of states for these pairs of bands is large at the transition frequency and the resultant optical absorption spectrum $\sigma_1(\omega) = Re[\sigma(\omega)]$ has a peak at a near frequency Ω_{th} as shown in Fig. 9-4b. At the CNP, $\theta = 1.35°$, and

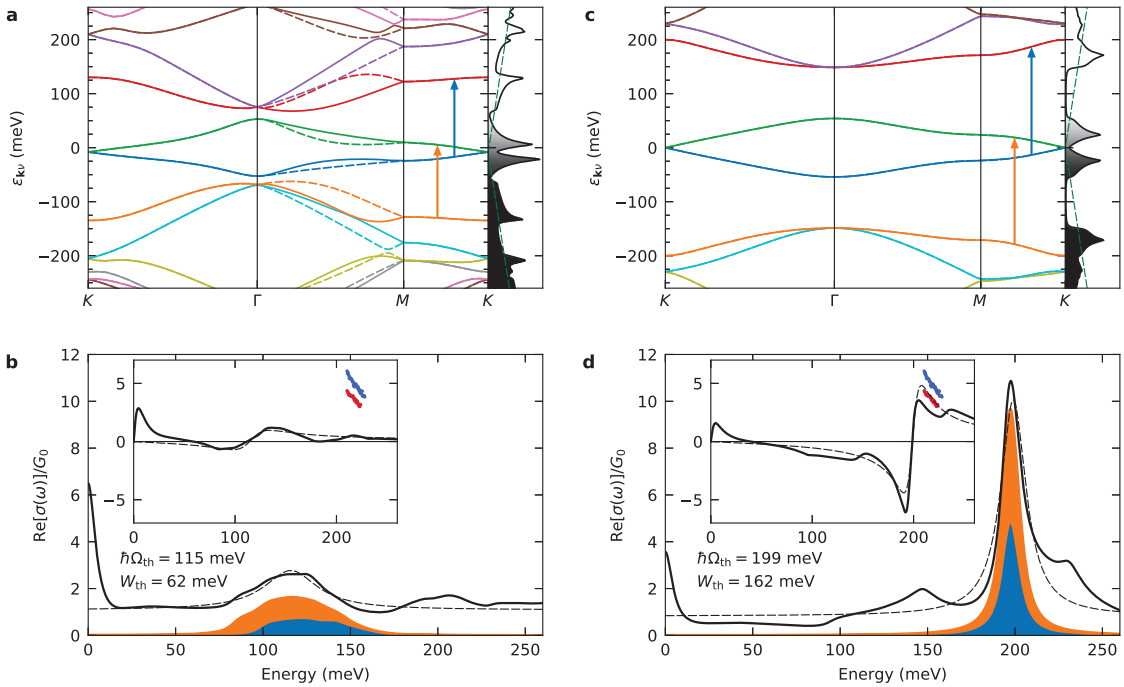

Figure 9-4: Electronic band structure and optical conductivity of twisted bilayer graphene with $\theta = 1.35°$. (a) Electronic band structure $\epsilon_{\mathbf{k}\nu}$ of TBG with $\theta = 1.35°$ along the $K\Gamma MK$ contour of the superlattice Brillouin zone from *ab initio* $k \cdot p$ perturbation theory [93]. The most relevant bands are $\nu = -2$ (orange), $\nu = -1$ (blue), $\nu = 1$ (green), and $\nu = 2$ (red). The corresponding wave functions at the K point for $\nu = -1$ and $\nu = 2$ are shown in Fig. 9-1d. Solid (dashed) lines represent the bands in the valley close to the K (K') point of the original graphene layers. The panel on the right shows the density of states with the colour shading representing band occupation at room temperature. The green dashed line represents the density of states of single layer graphene. Vertical arrows highlight the most relevant interband optical transitions. (b) Calculated real part of the optical conductivity (black thick line) using the Kubo formula and the band structure in panel a. Blue (orange) shading represents the contribution to the total optical conductivity of the pair of bands with $\nu = -2$, $\nu' = 1$ ($\nu = -1$, $\nu' = 2$), corresponding to the transition marked by an orange (blue) arrow in panel a. The dashed line is the Lorentzian fit to the most relevant interband feature and is used to extract the resonance parameters. The inset shows the imaginary part of the optical conductivity (normalized to G_0), together with the experimental data from Fig. 9-3c. (c-d) Same as in panels a-b but with the band structure of the chirally-symmetric continuum model [92, 99].

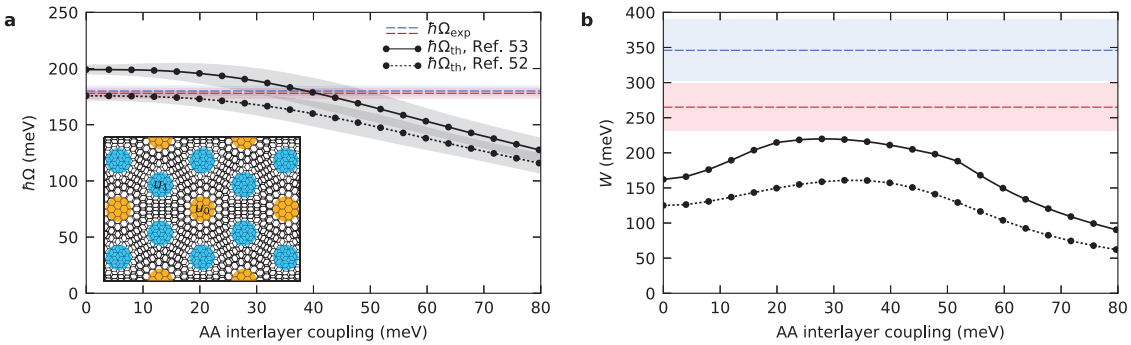

Figure 9-5: Calculated properties of the relevant interband transition as functions of the tunnelling amplitude in the AA regions. (a) Interband energy extracted from a Lorentzian fit of the optical conductivity. The grey shaded areas represent plus/minus the half width at half the maximum of the Lorentzian fit. In both theoretical models used in this work (Ref. [93] = "Ref. 52" in the caption, and [356] = "Ref. 53"), Ω_{th} decreases monotonically upon increasing the AA interlayer coupling u_0. These calculations were performed by setting $\theta = 1.35°$ and $u_1 = 97.5$ meV. The blue and red dashed lines correspond to the experimentally-determined resonant frequencies (Fig. 9-3c), with the corresponding shaded area indicating the uncertainty. The inset illustrates a triangular moiré lattice with the interlayer coupling strengths u_0, u_1 on the AA (yellow) and AB/BA sites (blue), respectively. (b) Same as in a but for the spectral weight W_{th}. The latter displays a maximum for intermediate values of u_0.

T=300 K (used for all calculations in this work), we find $\hbar\Omega_{th} \approx 115$ meV and an associated spectral weight $W_{th} \equiv 2\hbar \int_{peak} d\omega \sigma_1(\omega)/(\pi G_0) \approx 64$ meV. Because of causality, $\sigma_1(\omega)$ and $\sigma_2(\omega)$ are related by a Kramers-Kronig transform [353]. The resonant lineshape introduced above for $\sigma_2(\omega)$ yields $\sigma_1(\omega) = \pi G_0 W_{exp}[\delta(\hbar\omega - \hbar\Omega_{exp}) + \delta(\hbar\omega + \hbar\Omega_{exp})]$. This implies that our simple resonant fitting formula for $\sigma_2(\omega)$ represents the peak seen in the microscopically calculated $\sigma_1(\omega)$ at Ω_{th} (see Fig. 9-4b) with a delta peak at Ω_{exp} with spectral weight W_{exp}.

9.6.1 Chirally-symmetric continuum model

While Ω_{th} is in a reasonable agreement with Ω_{exp}, there is significant disagreement with the spectral weight since $W_{th} \ll W_{exp}$ The sources of this spectral weight mismatch can be multiple. To gain understanding, we resort to a more flexible continuum band-structure model [356]. This contains two parameters, u_0 and u_1, denoting the interlayer coupling in the AA regions and AB and BA regions, respectively. Results based on such continuum

model with the choice [356] $u_0 = 79.7$ meV and $u_1 = 97.5$ meV present only minor quantitative differences with respect to those of *ab initio* $k \cdot p$ perturbation theory shown in Fig. 9-4b. Also, calculations in Ref. [344] give qualitatively similar results. The same continuum model with $u_0 = 0$ and $u_1 \neq 0$, which is endowed with unitary particle-hole symmetry, has been introduced in Ref. [92] as an idealization of reality.

Intriguingly, we find that the conductivity calculated from this chirally-symmetric continuum model (CS-CM)[92, 99]—for $u_0 = 0$ and $u_1 = 97.5$ meV—displays a much better agreement with our experimental data. The bands $\epsilon_{\mathbf{k}\nu}$ of the CS-CM are shown in Fig. 9-4c, while the optical absorption spectrum is reported in Fig. 9-4d. Also here, σ_2 displays a resonant profile, but the resonant energy is $\hbar\Omega_{th} \approx 199$ meV and the spectral weight is $W_{th} \approx 162$ meV, in much better agreement with our experimental results. The loss function, calculated from this CS-CM is shown in Fig. 9-3b and overlaps very well with the superimposed experimental data. This suggests that the optical spectral weight is strongly enhanced in the optically active regions and this enhancement can be explained by an effective suppression of the AA interlayer coupling in the same regions.

9.6.2 Calculated properties of the relevant interband transition as functions of the tunnelling amplitude in the AA regions

Motivated by this finding, we perform a systematic scan of the AA tunnelling amplitude in a range going from $u_0 = 0$ meV —corresponding to the CS-CM—to $u_0 = 79.7$ meV, i.e. the value given in Ref. [356]. For each value of u_0 we calculate the band structure, extract the optical conductivity, and fit it with a resonant profile to extract the parameters $\hbar\Omega_{th}$ and W_{th}. The results are shown in Fig. 9-5. The resonant frequency increases monotonically with decreasing u_0 and crosses the experimentally measured value around $u_0 \approx 40$ meV. The spectral weight has instead a non-monotonic behaviour but gets closest to the experimental data approximately in the range 20 meV $< u_0 <$ 40 meV. We performed the same procedure on the *ab initio* $k \cdot p$ perturbation theory model by scaling the parameters corresponding to the AA tunnelling. The results are qualitatively similar, apart from a rigid shift, as shown in Fig. 9-5. The rigid shift is primarily caused by a small difference between the

models' effective AB coupling u_1. This can also be viewed as a tunable parameter of the theory and controls the location of the magic-angle. An extensive theoretical discussion of collective modes in TBG as a function of the band-structure parameters can be found in Ref. [85].

9.6.3 AA tunneling amplitude reduction: discussion

Our experiments therefore suggest that, in particular regions of the sample, the AA tunnelling amplitude is significantly reduced with respect to the AB tunnelling amplitude but still has a non-vanishing value. This finding is compatible with the results of Refs. [79, 83, 94] that reported on the gap size between the flat bands and the first excited band at the Γ point of the BZ. This quantity provides a direct measure of the difference $u_1 - u_0$ and was found to be in the range 30-60 meV . The apparent suppression of tunnelling in the AA regions compared to the one in the AB and BA regions (i.e. the fact that $u_0 < u_1$) can stem from e-e interactions or extrinsic effects. It is known [308, 92] that u_1 is responsible for a (non-Abelian) gauge field acting on the electron system, while u_0 induces a scalar potential. Electron-electron interactions act between density fluctuations and therefore, because of the continuity equation, between longitudinal current fluctuations. Screening due to e-e interactions will therefore tend to suppress the longitudinal field due to u_0, while having a smaller impact on the transverse gauge field due to u_1.

Extrinsic factors can also alter, locally, the value of u_0. We suspect that these include the way samples are prepared, the AFM-brooming procedure, and, possibly, the hBN encapsulation. It frequently happens that samples prepared in different laboratories display some macroscopic differences in their physical characteristics, such as twist angle [56], electrical transport [79, 83, 116, 122, 97, 106], and spectroscopic features [90, 87, 89, 88].

Before concluding, one may also hypothesize that our samples present a highly inhomogeneous strain distribution with patches where the associated pseudo-magnetic field $\mathbf{B}_s = B_s\hat{\mathbf{z}}$ is finite and nearly uniform [357] and regions where $\mathbf{B}_S = \mathbf{0}$. A resonant conductivity profile, as observed in experiments, would naturally arise in this case at the frequency of the pseudo-cyclotron resonance. This potential explanation of our observations is ana-

lyzed in more detail in the Supplementary Information of ref. [148], and we conclude that it is unlikely since it would require an unreasonably large amount of strain to match the observed resonant frequency.

9.7 Summary and outlook

In summary, we have observed propagating interband collective excitations in TBG in the mid-infrared spectral region, with larger-than-expected group velocity and thus a larger spectral weight of the infrared optical transitions. The usefulness of models with reduced AA tunnel coupling [92, 93, 356] in interpreting our experimental data could point to the enhanced role of e-e interactions. We expect that our work will encourage further theoretical and experimental studies to assess the intrinsic (i.e. e-e) and extrinsic factors that can effectively renormalize the band-structure parameters and the reasons for the observed sample inhomogeneity. Future low-temperature studies can moreover elucidate the role of electronic correlations in the upper bands and the contribution of collective excitations to many-body ground states [358], while terahertz near-field imaging can offer a local probe of the electronic phase transitions [359]. Finally, propagating plasmons with strong wavelength suppression, and without the need for additional doping, are of high use for strong light-matter interactions [360], quantum plasmonics [361] or the creation of metamaterials and nano-photonic devices.

Chapter 10

Tunable correlated states and spin-polarized phases in twisted bilayer–bilayer graphene

The discovery of correlated insulator states and superconductivity in magic-angle twisted bilayer graphene (TBG) [79, 83] (see Chapter 2.8) has paved the way to the experimental investigation of electronic correlations in tunable flat band systems realized in twisted van der Waals heterostructures [95, 81, 78, 82]. This novel twist angle degree of freedom and control should be generalizable to other 2D systems, which may exhibit similar correlated physics behaviour as well as enable new techniques to tune and control the strength of electron-electron interactions. In this chapter, published in reference [331], we report on a novel highly tunable correlated system based on small-angle twisted bilayer-bilayer graphene (TBBG), consisting of two rotated sheets of Bernal-stacked bilayer graphene. We find that TBBG exhibits a rich phase diagram, with tunable correlated insulators states that are highly sensitive to both twist angle and to the application of an electric displacement field, the latter reflecting the inherent polarizability of Bernal-stacked bilayer graphene [362, 21]. The correlated insulator states can be switched on and off by the displacement field at all integer electron fillings of the moiré unit cell. The response of these correlated states to magnetic fields suggests evidence of spin-polarized ground states, in stark contrast to magic-angle TBG. Furthermore, in the regime of lower twist angles, TBBG shows

multiple sets of flat bands near charge neutrality, resulting in numerous correlated states corresponding to half-filling of each of these flat bands, all of which are tunable by the displacement field as well. Our results pave the way to the exploration of novel twist-angle and electric-field controlled correlated phases of matter in novel multi-flat band twisted superlattices.

10.1 Introduction and motivation

Electronic correlations play a fundamental role in condensed matter systems where the bandwidth is comparable to or less than the Coulomb energy between electrons. These correlation effects often manifest themselves as intriguing quantum phases of matter, such as ferromagnetism, superconductivity, Mott insulators, or fractional quantum Hall states. Understanding, predicting, and characterizing these correlated phases is of great interest in modern condensed matter physics research and pose challenges to both experimentalists and theorists. As explained in Chapter 2.8, twisted graphene superlattices provide us with an ideal tunable platform to investigate electronic correlations in two dimensions[79, 83, 96, 116]. Tuning the twist angle of 2D van der Waals heterostructures to realize novel electronic states, an emerging field referred to as 'twistronics', has enabled physicists to explore a variety of novel phenomena [363, 364, 365, 147, 75]. When two layers of graphene are twisted by a specific angle, the phase diagram in the system exhibits correlated insulator states with similarities to Mott insulator systems (Chapter 2.8.4) [79], as well as unconventional superconducting states upon charge doping (sections 2.8.5 and 2.8.8) [83, 122, 116]. These effects are likely to originate from the many-body interactions between the electrons, when the band structure becomes substantially narrow as the twist angle approaches the first magic angle $\theta \approx 1.1°$[95, 81, 78].

Here we extend the twistronics research on graphene superlattices to a novel system with electrical displacement field tunability — twisted bilayer-bilayer graphene (TBBG), which consists of two sheets of untwisted Bernal-stacked bilayer graphene stacked together at an angle θ, as illustrated in Fig. 10-1a. Compared to monolayer graphene, the band structure of bilayer graphene is highly sensitive to the applied perpendicular electric dis-

placement field (Chapter 2.2.2) [362, 40, 39], and therefore provides us with an extra knob to control the relative strength of electronic correlations in the bands[333]. Similar to that of twisted bilayer graphene (TBG) [95, 81, 78], the band structure of TBBG is flattened near $\sim 1.1°$ (see Fig. 10-2e-g) [366]. For devices with twist angle near this value, our experiments show that the correlated insulator behaviour at half-filling $n_s/2$ in TBBG can be sensitively turned on and off by the displacement field, where n_s is the density corresponding to fully filling one spin and valley degenerate superlattice band [94, 367]. For a device with a slightly larger twist angle at 1.23°, we show that it exhibits a rich phase diagram with correlated insulating states at both half ($n_s/2$) and quarter fillings of the superlattice $n_s/4, 3n_s/4$ [83, 122, 333, 368, 116]. From their response to magnetic fields, all of these correlated states are likely to have a spin-polarized nature, with the $n_s/2$ state having a g-factor of 1.5 for parallel fields, close to the bare electron spin g-factor of ~ 2. On the other hand, devices with a smaller twist angle of 0.84° display multiple displacement field tunable correlated states at higher fillings, consistent with the presence of several sets of correlated flat bands in the electronic structure. The combination of twist angle, electric displacement field, and magnetic field provides a rich arena to investigate novel correlated phenomena in the emerging field of twistronics.

10.2 Transport characterization

We fabricated high-mobility dual-gated TBBG devices with the 'tear and stack' method (see Chapter 2.9) [94, 140], using exfoliated Bernal-stacked bilayer graphene instead of monolayer graphene. The devices presumably have an AB-AB stacking configuration where the top and bottom bilayers retain the same AB stacking order, in contrast to the AB-BA structure that was predicted to show topological effects [369]. We measured the transport properties of six small-angle devices, and here we focus on three of the devices with twist angles θ =1.23°, 1.09° and 0.84° respectively (see Fig. 10-5 for other devices). The samples are all of high quality, as evident in the Landau fan diagrams, with Hall mobilities that can exceed 100 000 $cm^2\ V^{-1}\ s^{-1}$, shown in Fig. 10-6 (see also section 10.7). Figures 10-1c-e show the longitudinal resistance R_{xx} and low-field Hall coefficient

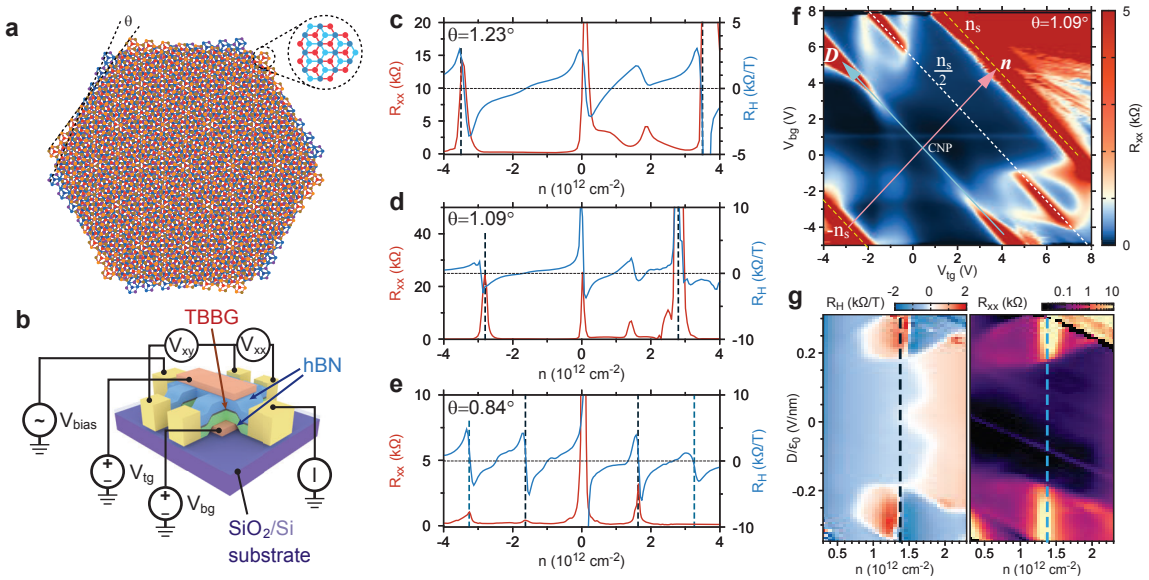

Figure 10-1: Structure and transport characterization of twisted bilayer-bilayer graphene (TBBG). (a) TBBG consists of two sheets of Bernal-stacked bilayer graphene twisted at an angle θ. (b) Schematic of a typical TBBG device with top and bottom gates and a Hall-bar geometry for transport measurements. (c-e) Measured longitudinal resistance $R_{xx} = V_{xx}/I$ and low-field Hall coefficient $R_H = \frac{\mathrm{d}}{\mathrm{d}B}(\frac{V_{xy}}{I})$ as functions of carrier density n in three devices with twist angles θ =1.23°, 1.09° and 0.84° respectively. The vertical dashed lines denote multiples of the superlattice density n_s, where the peaking of R_{xx} and sign changing of R_H indicate the Fermi energy crosses a band edge of the superlattice bands. (f) Resistance of the 1.09° TBBG device versus both top gate and bottom gate voltages V_{tg} and V_{bg}. The charge density n and displacement field D are related to the gate voltages by a linear transformation (see section 10.7). The superlattice densities $\pm n_s$ and the half-filling line at $n_s/2$ are indicated by dashed lines parallel to the D axis. Correlated insulator states are observed at $n_s/2$ filling at finite displacement fields. (g) Map of low-field Hall coefficient R_H (left panel) and resistance R_{xx} (right panel) near the $n_s/2$ correlated states for the 1.09° TBBG device (the vertical dashed lines indicate density $n_s/2$) . We find that accompanying the onset of the correlated insulator states at $D/\varepsilon_0 \approx \pm 0.18\,\mathrm{V\,nm^{-1}}$, a new sign change of the Hall coefficient also emerges.

$R_H = \frac{dR_{xy}}{dB}$ versus charge density for these three devices at $T = 4\,\mathrm{K}$. In a superlattice, the electronic band structure is folded in the mini Brillouin zone (MBZ), defined by the moiré periodicity [81]. Each band in the MBZ can accommodate a total charge density of $n_s = 4/A$, where A is the size of the moiré unit cell and the prefactor accounts for spin and valley degeneracies [81, 94, 366]. The experimental results show a sign change in the Hall coefficient R_H at each multiple of n_s (vertical dashed lines in Fig. 10-1c-e), indicating the switching of hole-like pockets to electron-like pockets, and peaks in R_{xx}, indicating the crossing of new band edges (for $\theta = 0.84°$, the band edges at $-n_s$ and $\pm 2n_s$ may only have small gaps or may even be semi-metallic, and hence do not exhibit prominent peaks in R_{xx}. See Fig. 10-4a-b for band structure calculations). The sharpness of the peaks confirms that the devices exhibit relatively low disorder and have well-defined twist angles.

10.3 Displacement field tunable correlated insulator states

In the $\theta = 1.23°$ and $\theta = 1.09°$ devices, we observe signatures of newly formed gaps also at $n_s/2$ when an electrical displacement field is applied perpendicular to the device. The dual-gate device geometry allows us to independently vary the total charge density $n = (c_{bg}V_{bg} + c_{tg}V_{tg})/e$, where e is elementary charge and c_{tg} and c_{bg} are top and bottom gate capacitances per area respectively, and the electrical displacement field penetrating the sample $D = (c_{bg}V_{bg} - c_{tg}V_{tg})/2$, by applying differential gate voltages. Fig. 10-1f shows the resistance map in the V_{tg}-V_{bg} space for the $\theta = 1.09°$ device. The transformation between gate voltages and (n, D) is given in section 10.7. At $D = 0$, no insulating behaviour other than the full-filling gaps at $\pm n_s$ is observed. However, when a displacement field D is applied in either direction, an insulating state appears at $n_s/2$ for a range of D. This new insulating state induced by the displacement field can be further examined by measuring the Hall coefficient R_H versus n and D, as shown in the left panel of Fig. 10-1g ($\theta = 1.09°$ device), and comparing with R_{xx} shown in the right panel. At the onset of the insulating states at $D/\varepsilon_0 \approx \pm 0.18\,\mathrm{V\,nm^{-1}}$, where ε_0 is the vacuum permittivity, R_H develops addi-

tional sign changes adjacent to the insulating states, suggesting the creation of new gaps by the displacement field. The insulating states disappear when D/ε_0 exceeds ±0.35 V nm^{-1}. In both the $\theta = 1.09°$ device and the $\theta = 1.23°$ devices, we find signatures of the onset of correlated behaviour at $n = -n_s/2, D = 0$, but no well-developed insulating state is observed (see Fig. 10-5 and section 10.7).

In the $\theta = 1.23°$ device, we observe a similar but more intricate hierarchy of tunable insulating states that stem from the interplay of correlations, the superlattice bands, and the magnetic field. Fig. 10-2a shows the n-D resistance map for the $\theta = 1.23°$ TBBG device measured at $T = 0.07$ K. Noticeably, as $|D|$ is increased the insulating state at charge neutrality $n = 0$ strengthens in the same way as in the Bernal-stacked bilayer graphene (see Chapter 2.2.2) [362, 40, 39], while the superlattice gaps at $\pm n_s$ weaken and eventually disappear (for $|D|/\varepsilon_0 > 0.6$ V nm^{-1} for the $+n_s$ insulating state and for $|D|/\varepsilon_0 > 0.35$ V nm^{-1} for the $-n_s$ insulating state). The band structures of TBBG in zero and finite external displacement fields calculated using a continuum approximation are shown in Fig. 10-2e-g (see section 10.7 for details). It should be noted that, although TBBG has twice the number of graphene layers than TBG, the band counting is the same as TBG, *i.e.* each band (spin/valley degenerate) accommodates 4 electrons per moiré unit cell. At zero displacement field, the calculated gap at the charge neutrality ($E = 0$) is negligible while the superlattice gaps above and below the flat bands are nonzero. When the displacement field is increased, the charge neutrality gap quickly widens while the superlattice gaps become smaller and eventually vanish, in agreement with our experimental observations.

At intermediate displacement fields around $D/\varepsilon_0 = -0.38$ V nm^{-1}, we observe the insulating states not only at $n_s/2$ over a wide range of D, but also at $n_s/4$ over a smaller range (Fig. 10-2a). We attribute these states to a Mott-like mechanism similar to those observed in TBG, which results from the Coulomb repulsion of the electrons in the flat bands when each unit cell hosts exactly 1 or 2 electrons, corresponding to $n_s/4$ and $n_s/2$ fillings respectively. The $n_s/4$ state requires a finer tuning of D to reveal, possibly due to the smaller gap size. This is evident from Fig. 10-2b, where we show the resistance versus n and temperature T with displacement field D/ε_0 fixed at –0.38 V nm^{-1}. Both states vanish as the temperature rises. While the $n_s/2$ state persists up to approximately 8 K, the

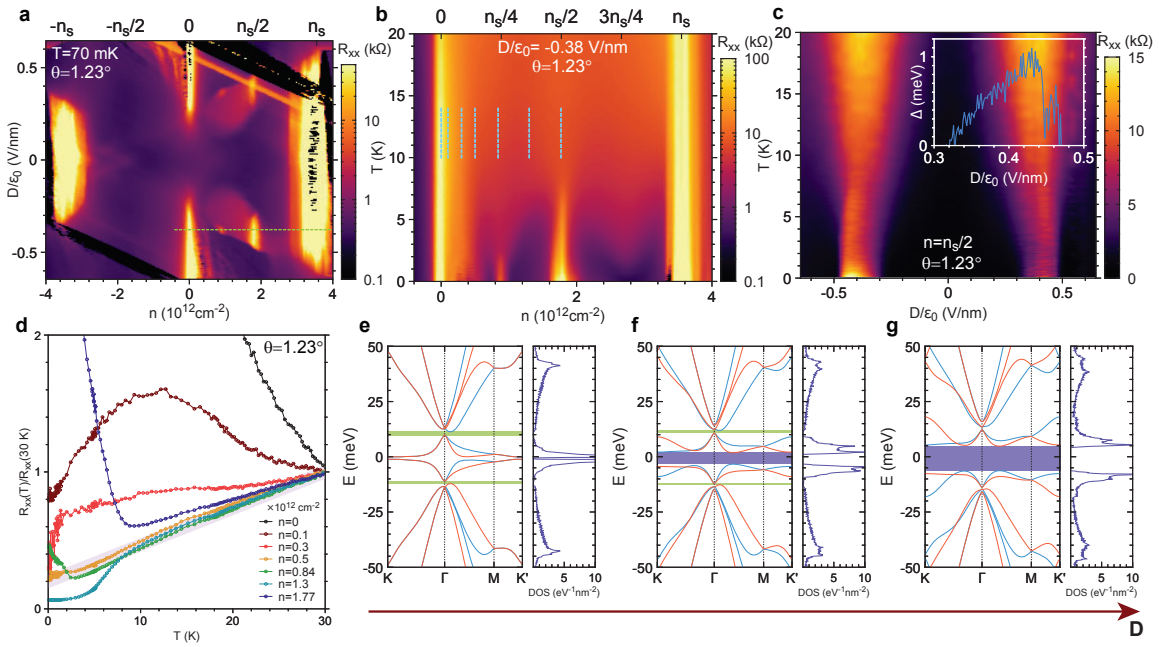

Figure 10-2: Displacement field tunable correlated insulator states in TBBG. (a) Color plot of resistance versus charge density n and displacement field D ($\theta = 1.23°$ device, section 1, see section 10.7). The green dashed line cutting through the $D < 0$ correlated state is the linecut along which (b) is taken (for $\theta = 1.23°$ device, section 2, see section 10.7) (b) Resistance versus n and T at a fixed $D/\varepsilon_0 = -0.38\,\mathrm{V\,nm^{-1}}$. The correlated insulator states at $n_s/4$ and $n_s/2$ are suppressed by raising the temperature. (c) Resistance at density $n_s/2$ versus displacement field and temperature. The resistance shows a maximum at approximately $D/\varepsilon_0 = \pm 0.4\,\mathrm{V\,nm^{-1}}$, the region where the correlated insulator state is present. The inset shows the thermal activation gap extracted from temperature dependence at different values of D across the $n_s/2$ state. (d) Normalized resistance curves versus temperature at different densities between 0 and $n_s/2 \approx 1.77\times10^{12}\,\mathrm{cm^{-2}}$, which are indicated by dashed lines in (b). Away from the charge neutrality point, all resistance curves show approximately linear R-T behaviour above 10 K, with similar slopes (see Fig. 10-7). (e-g) Calculated band structure (left panels) and density of states (right panels) for the $\theta = 1.23°$ TBBG device at (e) $\Delta V = 0$, (f) $\Delta V = 6\,\mathrm{mV}$ and (g) $\Delta V = 12\,\mathrm{mV}$, where ΔV is the potential difference between adjacent graphene layers induced by the external displacement field (assumed to be the same between all layers). Single-particle bandgaps in the dispersion are highlighted by green (below and above the flat bands) and blue (at charge neutrality) bars.

$n_s/4$ disappears at less than 3 K, indicating a smaller energy scale associated with the gap. Fig. 10-2c shows the resistance of the $n_s/2$ state versus the displacement field and temperature. The 'optimal' displacement field for reaching a maximum resistance is approximately ±0.4 V nm^{-1}. As the temperature increases, the peak in R_{xx} not only decreases in value but also broadens in D. As shown in Fig. 10-2d, at temperatures higher than 10 K and away from the charge neutrality point, the transport is dominated by linear R-T behaviour similar to that observed in TBG in Chapter 7 [83, 122, 302]. A more systematic investigation of the T-linear behaviour in TBBG is provided in Fig. 10-7 and in section 10.7.

10.4 Magnetic field response of the displacement-field-tunable correlated insulator states

Figure 10-3 shows the response of the various correlated states to magnetic fields applied in either perpendicular or in-plane direction with respect to the sample plane. Figures 10-3a-c show the n-D maps of the resistance for the $\theta = 1.23°$ device at $B = 0$, $B_\perp = 8$ T and $B_\parallel = 8$ T, respectively. The plots focus on densities from the charge neutrality ($n = 0$) to the first superlattice band edge ($n = n_s$). Fig 3a shows the band insulator states at $n = 0$ and $n = n_s$, as well as the correlated insulating states at $n_s/2$ and $n_s/4$ (encircled by dashed lines). At this zero magnetic field we do not observe an insulating state at 3 electrons per unit cell ($3n_s/4$ filling). Interestingly, at $B_\perp = 8$ T (Fig. 10-3b), the correlated insulating states at $n_s/4$ and $n_s/2$ vanish at their original positions centered around $D/\varepsilon_0 = -0.38$ V nm^{-1}, whereas new insulating states appear at $n = n_s/4$, $D/\varepsilon_0 = -0.2$–-0.35 V nm^{-1} and $n = n_s/2$, $D/\varepsilon_0 = -0.45$–-0.6 V nm^{-1}, above and below their original positions at $B = 0$ respectively. A new correlated insulating state also appears at $3n_s/4$, $D/\varepsilon_0 = -0.4$–-0.5 V nm^{-1}. However, no such strong displacement field shift in the insulating states is observed with in-plane magnetic field (Fig. 10-3c). At $B_\parallel = 8$ T, the correlated insulating states are clearly visible at all integer electron fillings near $D/\varepsilon_0 = -0.38$ V nm^{-1}. Figures 10-3d-e show the evolution of the $n_s/2$ insulating state as a function of $B_\perp$ and $B_\parallel$. An abrupt shift in the range of D for which the insulating

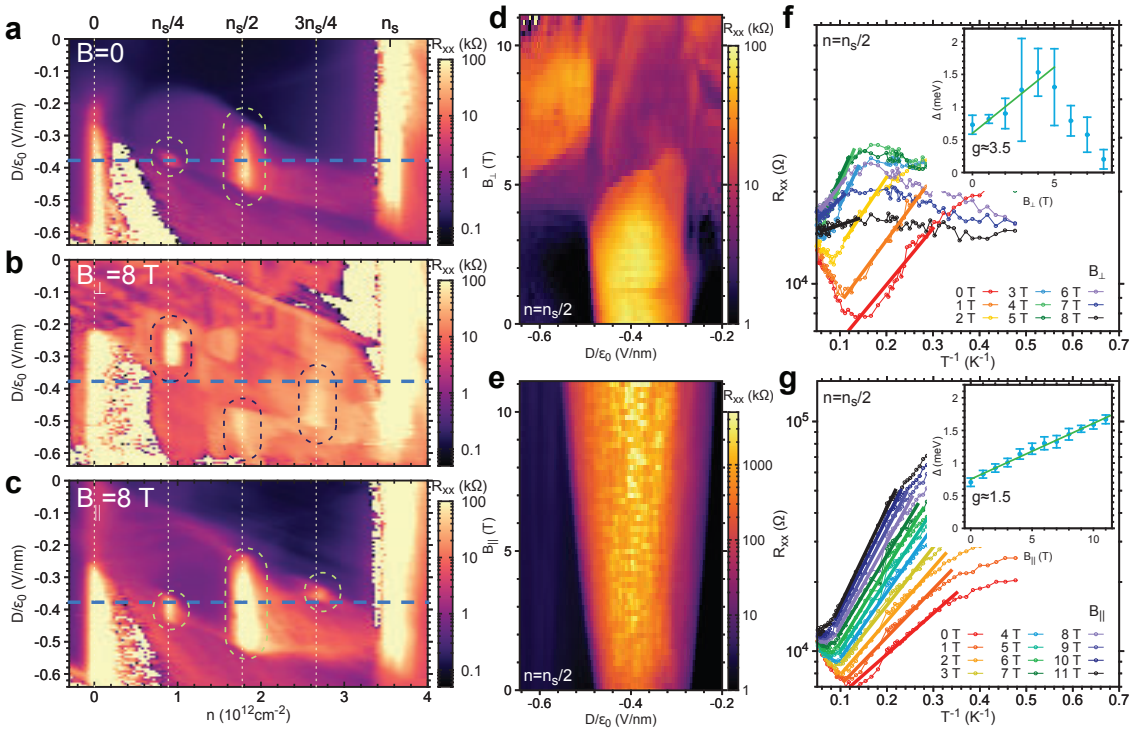

Figure 10-3: Magnetic field response of the displacement-field-tunable correlated insulator states in TBBG. (a-c) Resistance plot for the $\theta = 1.23°$ TBBG device in magnetic fields of $B = 0$, $B_\perp = 8\,\mathrm{T}$ perpendicular to the sample, and $B_\parallel = 8\,\mathrm{T}$ parallel to the sample, respectively. All measurements are taken at sample temperature $T = 0.07\,\mathrm{K}$. Various correlated states at integer electron fillings of the moiré unit cell are indicated by dashed circles. At zero field, only the $n_s/4$ and $n_s/2$ states appear around $|D|/\varepsilon_0 = 0.38\,\mathrm{V\,nm^{-1}}$. In a perpendicular field of $B_\perp = 8\,\mathrm{T}$, the $n_s/4$ state shifts towards lower $|D|$, the $n_s/2$ state shifts towards higher $|D|$, and the $3n_s/4$ state also emerges. In a parallel field of 8 T, on the other hand, the position of the states barely shifts but their resistance increases monotonically. (d-e) Resistance at $n = n_s/2$ versus displacement field and magnetic field applied (d) perpendicular and (e) in-plane with respect to the device. While the correlated insulator state monotonically strengthens in $B_\parallel$, the perpendicular field induces a phase transition at around $B_\perp$ =5 T, where the correlated state abruptly shifts to higher $|D|$. (f-g) Temperature dependence of the resistance at the $n_s/2$ insulators in different magnetic fields, perpendicular in (f) and in-plane in (g). The insets show the thermal activation gaps extracted from the solid Arrenhius fits ($R \sim e^{-\Delta/2kT}$) in the main figures versus the magnitude of the field in the respective direction. Error bars correspond to a confidence level of 0.99. The linear fit of the thermal activation gap gives a g-factor of about 3.5 for perpendicular field (up to 5 T only) and 1.5 for in-plane field (up to 11 T).

state appears occurs at $B_\perp = 5\,\mathrm{T}$, whereas the insulating state strengthens monotonically with in-plane magnetic field.

The key difference between the effects of the perpendicular and in-plane magnetic fields lies in the fact that the lateral dimension of the unit cell in TBBG, $\sim 10\,\mathrm{nm}$, is much larger than the thickness of the system $\sim 1\,\mathrm{nm}$. Therefore, while both fields couple equally to the spins of the correlated electrons, $B_\parallel$ has a much weaker (but nonzero) effect on the orbital movement of the electrons. To theoretically understand the behaviour of the correlated insulating states in a magnetic field, we first have to identify their ground state. Figures 10-3f-g show the evolution of the thermal activation gap of the $n_s/2$ state in both $B_\perp$ and $B_\parallel$. We find a g-factor of ~ 3.5 for the perpendicular direction (up to 5 T before the shift occurs) and a g-factor~ 1.5 for the in-plane direction. $g_\parallel$ is close to (but less than) $g = 2$, which is expected for a spin-polarized ground state with contribution only from the electron spins. The difference between the observed $g_\parallel \sim 1.5$ and $g = 2$ is generally expected because of finite in-plane orbital effects[370]. Therefore, based on these measurements, we may conclude that the correlated insulating states have a spin-polarized nature. Note that these observations establish TBBG as a distinctive system from the previously reported magic-angle TBG system [79, 83, 122], which also exhibits half-filling insulating states, but are shown to be spin unpolarized, as the insulator state is suppressed by an in-plane magnetic field. In $B_\perp$, on the other hand, one would expect orbital effects to play a more substantial role. We may attribute the larger $g_\perp$ of about 3.5 to exchange-induced enhancement effects, similar to what is observed in Landau levels of GaAs quantum wells or for graphene [371, 372]. In Fig. 10-8, we also provide additional magnetic field response data for the $n_s/4$ and the $3n_s/4$ states. Both of these states also exhibit a spin-polarized behaviour, as they become more resistive under the in-plane magnetic field.

In addition to the discussion above, we noticed that all the correlated insulating states in the $\theta = 1.23°$ TBBG device, whether at zero magnetic field or high magnetic fields, lie within the range $D/\varepsilon_0 =$–0.6––0.2 V nm^{-1}. Coincidentally, this is also the range where both the gap at the charge neutrality ($n = 0$) and the gap at the superlattice density ($n = n_s$) are well-developed (*i.e.* the case in Fig. 10-2f). Based on this observation, we suggest that the displacement field tunability of the correlated states is tied to the modulation of

the single-particle band gaps by the displacement field. When either gap at $n = 0$ or $n = n_s$ is absent, the thermally excited or disorder scattered carriers from the upper or lower band would suppress the ordering of the electrons and hence the correlated states. Further theoretical work is needed to reveal the detailed structure of the displacement field dependence of the correlated states.

10.5 Correlated insulator states in small twist angle bilayer-bilayer graphene, a multi-flat-band system

We have also investigated the regime of substantially smaller twist angles. Unlike the case of TBG, further reduction of the twist angle of TBBG to 0.84° results not in one, but rather three pairs of flat bands, separated from other bands by band gaps (Fig. 10-4a). Application of an electrical displacement field further flattens these bands and separates them from each other (Fig. 10-4b). This would imply that all electrons within the density range $-3n_s$ to $+3n_s$ might experience strong Coulomb interactions, and their correlations can get further enhanced by applying a displacement field. These predictions from the band theory are consistent with our experimental observations. In Fig. 10-4c where we show the resistance map of the $\theta = 0.84°$ TBBG device versus n and D, we indeed find that the weak signatures of $-n_s/2$ and $-n_s/4$ correlated insulating states only appear at high displacement fields $|D|/\varepsilon_0 > 0.8\,\mathrm{V\,nm^{-1}}$ (encircled by white dashed lines). The full-filling gaps at $\pm n_s$ and $\pm 2n_s$ are tunable by the displacement field to different extents as well.

As we turn on a perpendicular magnetic field, a series of correlated insulator states appear across the entire density range spanning the multiple flat bands. Figures 10-4d,e show the Landau fan diagrams at $D/\varepsilon_0 = 0.6\,\mathrm{V\,nm^{-1}}$ and $D = 0$ respectively. At zero displacement field, the Landau fan shows a complicated Hofstadter butterfly pattern due to commensurate flux threading into the unit cell [364, 363, 365] (see also section 10.7 and Fig. 10-6), but no correlated state is observed at half-fillings or quarter-fillings. On the other hand, at $D/\varepsilon_0 = 0.6\,\mathrm{V\,nm^{-1}}$, we find clear signatures of correlated states at $n/n_s = \frac{1}{2}$ and $-\frac{1}{2}$ in the center flat bands, and weak evidences at $n/n_s = \frac{3}{2}$ and $\frac{5}{2}$ in the upper

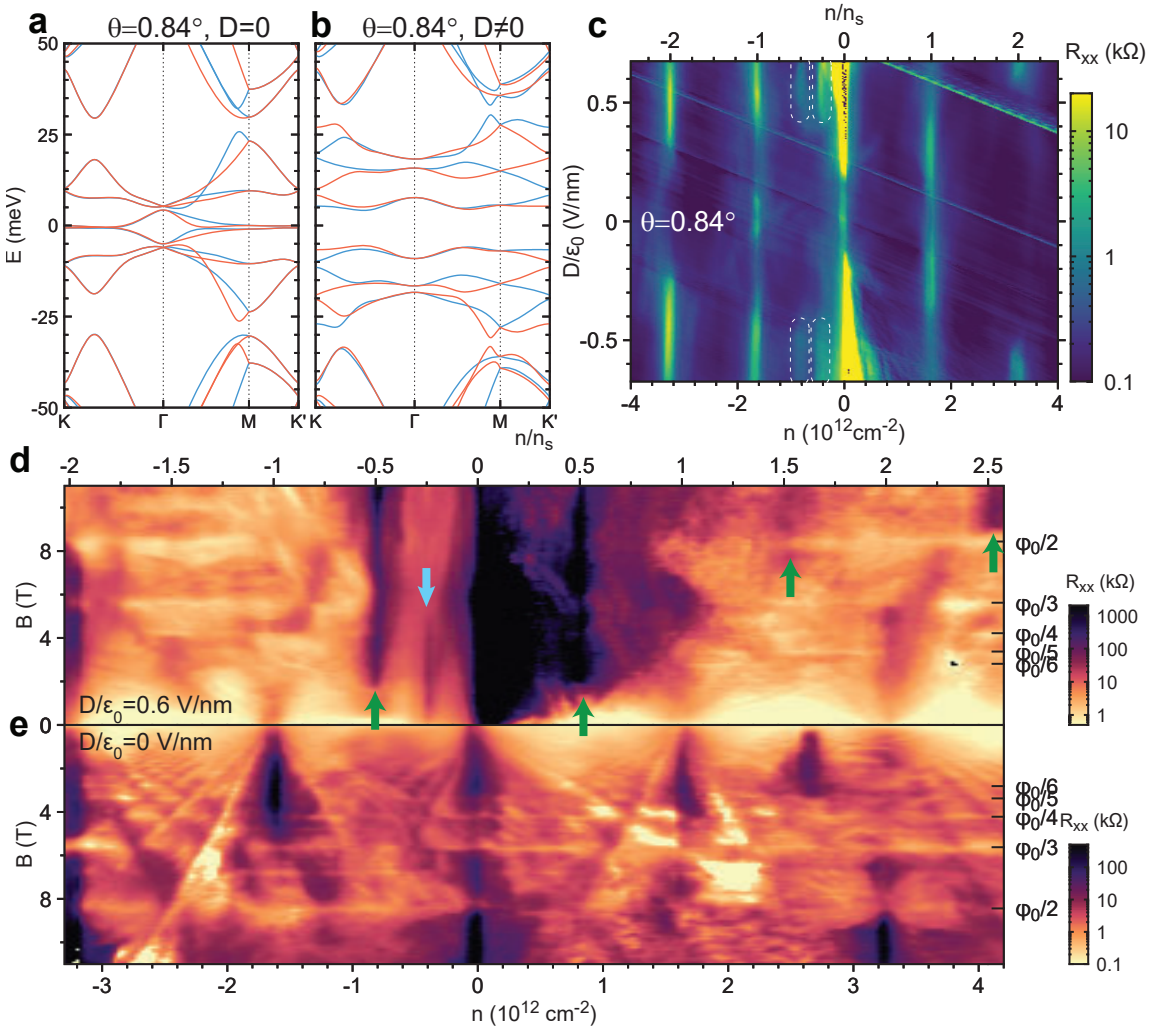

Figure 10-4: Correlated insulator states in a multi flat band system. (a-b) Calculated band structure of $\theta = 0.84°$ TBBG (a) without interlayer potential and (b) with interlayer potential $\Delta V = 18\,\text{mV}$. Near charge neutrality, within a 50 meV window, there are in total six sets of flat bands spanning densities $-3n_s$ to $3n_s$. Upon applying a displacement field, these bands are further flattened and separated from each other, which makes them more prone to giving rise to correlated states at each half-filling. (c) Resistance map of a $\theta = 0.84°$ TBBG device measured at $T = 70\,\text{mK}$. The top axis is the charge density n normalized to the superlattice density n_s. Besides the D-tunable gaps at multiples of n_s, we find signatures of correlated states at $n/n_s = -\frac{1}{2}, -\frac{1}{4}$ for $|D|/\varepsilon_0 > 0.4\,\text{V nm}^{-1}$, which are indicated by dashed circles. (d) Resistance as a function of charge density and perpendicular magnetic field B when a displacement is present, $D/\varepsilon_0 = 0.6\,\text{V nm}^{-1}$. We find clear correlated states at $n/n_s = -\frac{1}{2}$, $-\frac{1}{4}$ and $\frac{1}{2}$, and also evidences at $\frac{3}{2}$ and $\frac{5}{2}$ fillings, as indicated by arrows. (e) For comparison, when no displacement field is present, we do not find signatures of half-filling correlated states. Due to the formation of a superlattice, we also observe Hofstadter butterfly related features when B is such that the magnetic flux in each unit cell is equal to $\varphi_0/2, \varphi_0/3, \varphi_0/4, \ldots$, where $\varphi_0 = h/e$ is the flux quantum.

flat bands as well. All of these half-filling correlated states appear to be enhanced by the application of a perpendicular magnetic field, which we attribute to the same spin/orbital combined enhancement of the correlated gaps as in the $n_s/2$ state of the $\theta = 1.23°$ device (*e.g.* Fig. 10-3f). The correlated states at $n/n_s = \pm\frac{1}{2}$ appear to be significantly stronger than the states at $n/n_s = \frac{3}{2}$ and $\frac{5}{2}$ in high magnetic fields, consistent with the fact that the pair of bands closer to charge neutrality is much flatter than the other two pairs farther away from charge neutrality, as can be seen in Fig. 10-4b. The resistance of the quarter-filling state at $n/n_s = -\frac{1}{4}$, however, does not increase monotonically with perpendicular field, but rather eventually gets suppressed at 5 T. We notice that a resistive region also appears at $n \approx 1.63\,\mathrm{n}_s$ in Fig. 10-4e, which does not coincide with any commensurate filling and might be ascribed to twist angle inhomogeneity in the sample.

10.6 Summary

In this chapter, we show that TBBG exhibits a rich spectrum of correlated phases tunable by twist angle, electric displacement field, and magnetic field, paving the way to further studies of strongly correlated physics and topology in multi-flat band systems [366].

We note that this was a particularly timely experiment, and three related studies appeared simultaneously to ours in the press [330, 332, 373].

10.7 Extended data and supplementary information

10.7.1 Fabrication

The reported devices are fabricated using a similar procedure as the one described in Chapter 2.9. In particular, two sheets of Bernal-stacked bilayer graphene (BLG), instead of two monolayer graphene sheets, are twisted, stacked, and encapsulated by two hBN flakes. We note that BLG is typically harder to tear than monolayer graphene flakes, further reducing the success rate of these devices. The top gate is deposited by thermal evaporation of Cr/Au.

10.7.2 List of measured TBBG devices

Following the definition given in the main text and accounting for offsets in the gate voltages due to impurity doping, n and D are related to the top and bottom gate voltages V_{tg} and V_{bg} by

$$n = [c_{tg}(V_{tg} - V_{tg,0}) + c_{bg}(V_{bg} - V_{bg,0})]/e, \tag{10.1}$$

$$D = [-c_{tg}(V_{tg} - V_{tg,0}) + c_{bg}(V_{bg} - V_{bg,0})]/2. \tag{10.2}$$

Table 10.1 lists the twist angles and parameters c_{tg}, c_{bg}, $V_{tg,0}$, $V_{bg,0}$, and n_s for all devices discussed in this chapter. These parameters are estimated to satisfy that all diagonal features in the V_{tg}-V_{bg} maps are rotated to be vertical in the corresponding n-D maps, and the features should be symmetrical with respect to D after the transformation.

θ(°)	c_{tg} (F m^{-2})	c_{bg} (F m^{-2})	$V_{tg,0}$ (V)	$V_{bg,0}$ (V)	n_s (cm^{-2})
1.09	6.63×10^{-4}	5.02×10^{-4}	0.30	0.58	2.75×10^{12}
1.23	1.06×10^{-3}	7.14×10^{-4}	0.41	-0.04	3.55×10^{12}
1.23	1.06×10^{-3}	7.14×10^{-4}	0.41	-0.04	3.55×10^{12}
0.84	6.87×10^{-4}	6.38×10^{-4}	0.06	0.08	1.65×10^{12}
0.79	1.06×10^{-3}	3.57×10^{-4}	0.18	0.67	1.45×10^{12}
1.09(*)	1.03×10^{-3}	5.12×10^{-4}	0.28	0.45	2.75×10^{12}

Table 10.1: List of TBBG devices discussed in this chapter. The last device is marked with an asterisk to differentiate it from the first device, which happens to have the same twist angle but it is a totally independent device fabricated on a separate chip, and will be hereinafter referred to with the asterisk to avoid confusion.

In Fig. 10-5a-f, we show V_{tg}-V_{bg} resistance maps for all six TBBG devices we measured. Fig. 10-5c-d are measured in the same TBBG sample, but in different sample regions that are approximately 27 μm apart (sections 1 and 2, respectively). Both regions have identical parameters (hence the two identical rows in table 10.1), with the same twist angle $\theta = 1.23°$, and also nearly identical transport characteristics. The two sections are electrically disconnected via etching, but the extracted twist angles from the data have a difference of less than 0.01°, suggesting very uniform twist angles across this entire sample.

In almost all TBBG samples, we noticed a peculiar cross-like pattern around $(n, D) =$

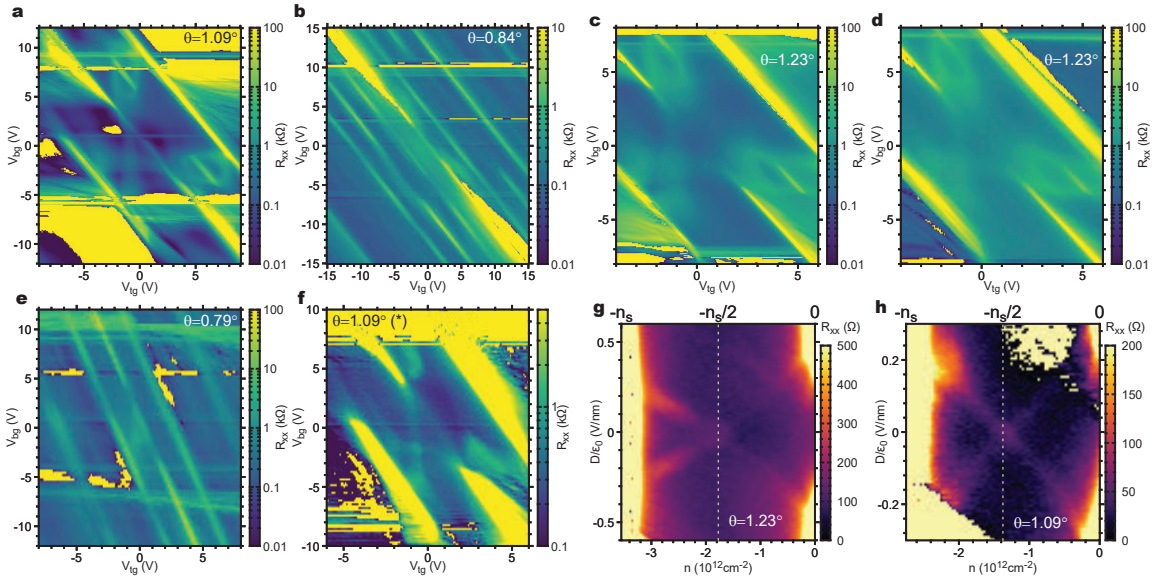

Figure 10-5: V_{tg}-V_{bg} resistance maps of various TBBG devices. (a-f) Resistance versus V_{tg} and V_{bg} for the six TBBG devices measured. (g-h) Cross-like feature near $-n_s/2$ in TBBG samples, which might signal the onset of a correlated state.

$(-n_s/2, 0)$, *i.e.* near p-side half-filling of the superlattice band. This is especially apparent in the 1.09° and 1.23° devices, which are highlighted in Fig. 10-5g-h. The p-side band does not exhibit a strong D-tunable correlated state as elaborated in the main text, possibly due to the larger bandwidth compared to its n-side counterpart.

Note added in proof: These cross-like patterns have later been associated with van Hove singularities in the valence bands [374]. The 'halo'-like features surrounding the insulating states at $n_s/2$ in some of the phase diagrams have also later been linked to the emergence of symmetry-broken correlated states [374]. The phase diagram of AB-AB TBBG has now been extensively studied and reported in many other studies [330, 332, 373, 375].

10.7.3 Sample quality and Landau fans

To demonstrate the high quality of our fabricated TBBG devices, we have measured the Landau fan diagrams and Hall mobilities of all three devices discussed in the main text, as shown in Fig. 10-6. The Hall mobilities are extracted from the ratio between the Hall coefficient R_H and longitudinal resistance at small magnetic fields ($B < 0.5\,\mathrm{T}$). All three samples exhibit high Hall mobilities close to or above $100\,000\,\mathrm{cm^2\,V^{-1}\,s^{-1}}$.

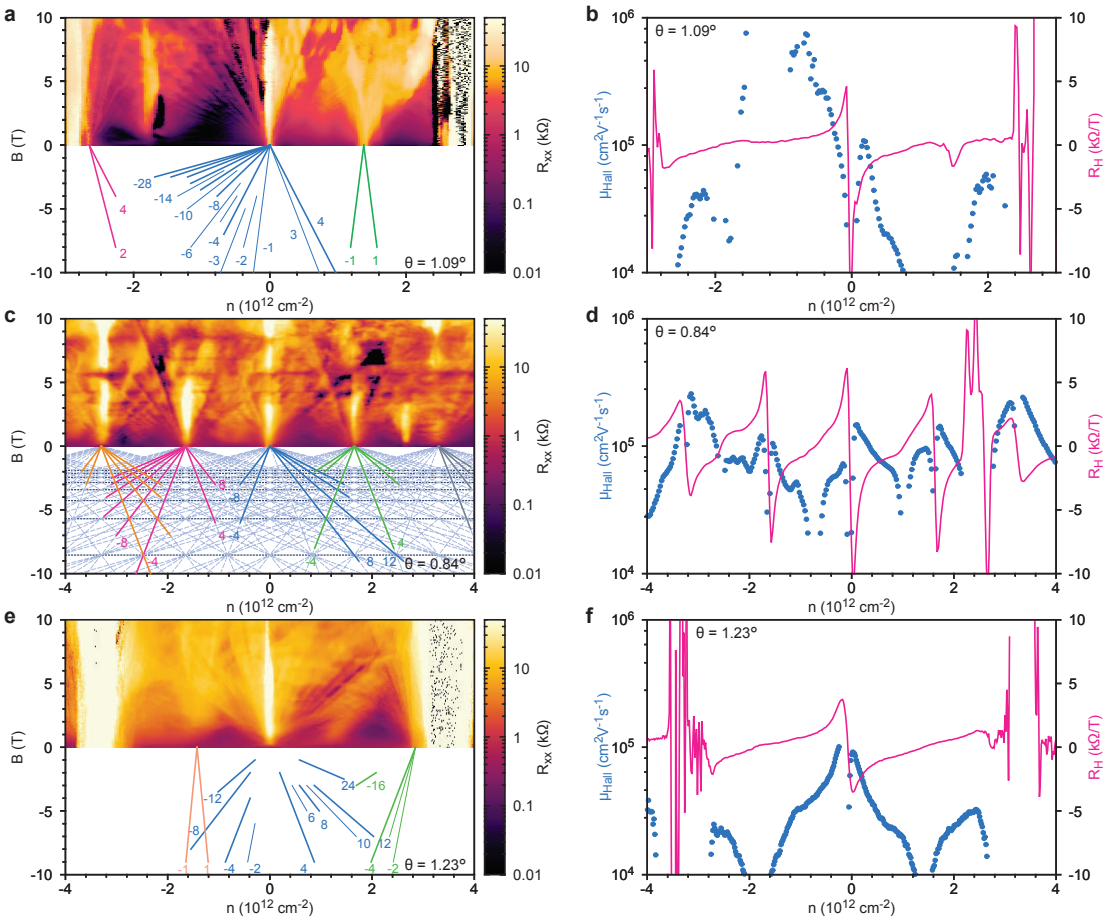

Figure 10-6: Landau fan diagrams and Hall mobilities of the TBBG devices. (a) Resistance of the 1.09° sample versus carrier density and perpendicular magnetic field. (b) Hall mobility μ_{Hall} (left axis) and Hall coefficient R_H (right axis) in the 1.09° sample at different carrier densities. (c-f) Same measurements as in (a-b) but for the 0.84° and 1.23° samples, respectively. All measurements are taken at $T < 100\,\text{mK}$. The data for 1.09° device is taken at $D/\varepsilon_0 = 0.2\,\text{V/nm}$ while data for the other two devices are taken at $D = 0$.

All three devices also show clear Landau fans starting from about 1 T. The filling factor of each level is labeled in the lower panels of each plot. In particular, due to the lower angle of the $\theta = 0.84°$ device, its Landau fan displays a complicated Hofstadter's butterfly pattern starting from 3 T.

10.7.4 Linear R-T behaviour

Fig. 10-7 shows the resistance versus temperature behaviour, at different densities, observed across several small-angle TBBG devices. In the 1.23° device, we find approximately linear R-T behaviour above 10 K for densities ranging from 0.5×10^{12}–2.5×10^{12} cm^{-2}, encompassing the $n_s/2$ correlated state. The resistance slope in this range of densities does not vary very substantially, ranging from 210-350 Ω/K. Since all our devices have length-to-width ratios close to one, these slope values are therefore close to those reported in TBG in Chapter 7 and reference [302]. In stark contrast, the resistance behaviour in the hole-doping side ($n < 0$), as shown in Fig. 10-7b, shows qualitatively different behavior: it does not show linear $R-T$ characteristics, at least up to 30 K, and the resistance value is about an order of magnitude smaller than on the electron-doping side. These data are consistent with the picture that the electron-doping band is flatter than the hole-doping band, therefore exhibiting more pronounced correlated phenomena, examples being the $n_s/2$ insulator state, and the linear resistance-temperature behaviour. Fig. 10-7c shows R-T curves close to the $n_s/2$ state.

The data for the 1.09° device shows a similar trend of linear R-T behaviour starting around 5 to 10 K, as shown in Fig. 10-7d.

In the 0.84° device, we find a very different behaviour. There is a region of sub-linear or approximately linear R-T behaviour at all densities, except at multiples of n_s, but the resistance slope is now strongly dependent on the charge density n. The slope approximately follows a power law $dR_{xx}/dT \propto n^a$ where $a \approx -1.77$ (see inset).

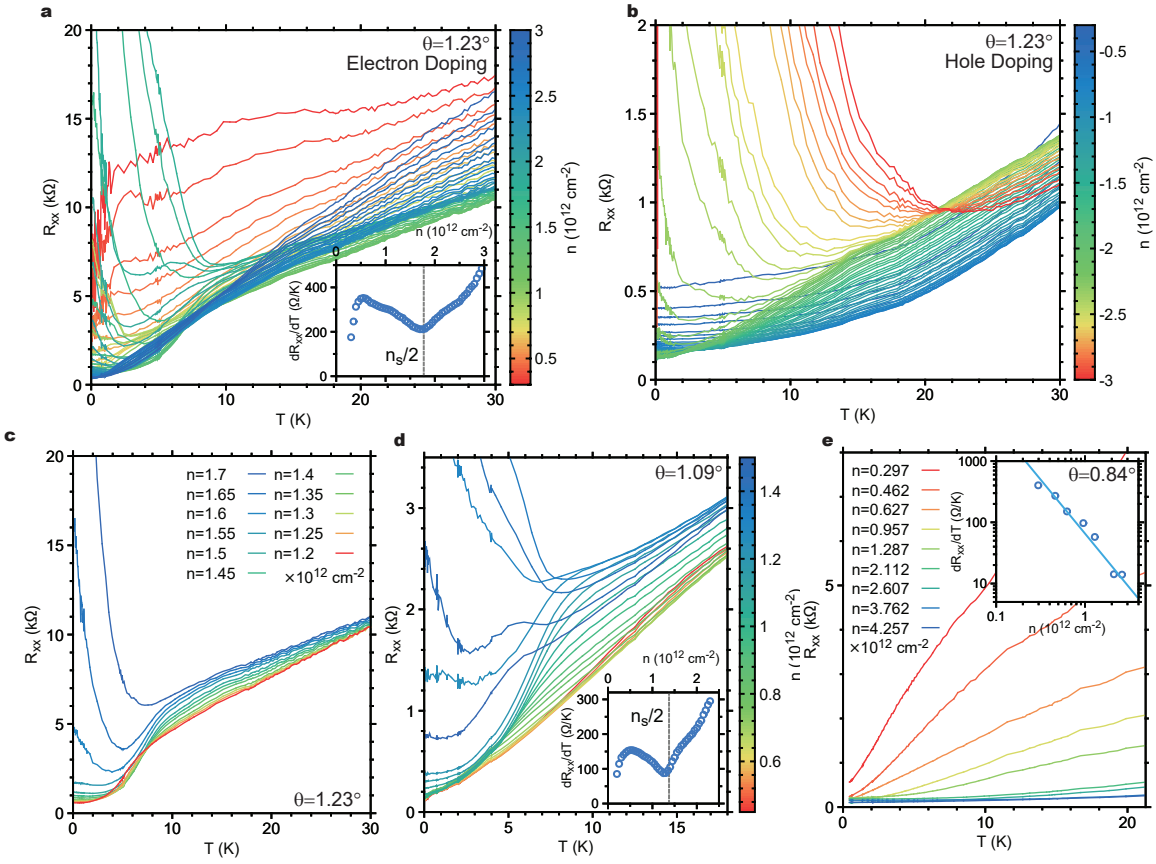

Figure 10-7: Linear resistance vs temperature behaviour in TBBG. (a-b) Resistance versus temperature curves at different charge densities in the 1.23° sample. Inset of (a) shows the slope dR_{xx}/dT of the linear R-T behaviour as a function of n for $T > 10\,\mathrm{K}$. (c) Selected R-T curves near $n_s/2$ from (a). (d) Similar linear R-T behaviour in the 1.09° device. Inset shows the slope dR_{xx}/dT. (e) Density-dependent sublinear/linear R-T behaviour in the 0.84° device. Inset shows the slope dR_{xx}/dT versus n in log-log scale. The slope is proportional to n to the power of -1.77.

10.7.5 Theoretical methods

The band structures shown in the main text are calculated using a continuum model based on the original continuum model for TBG [81, 78], which qualitatively captures most of the important features of the bands in TBBG including displacement field dependence. To lowest order, the continuum model of twisted graphene superlattices is built on the approximation that the interlayer coupling between the A/B sublattice of one layer and the A/B sublattice of the other layer has a sinusoidal variation over the periodicity of the moiré pattern. For the three possible directions of interlayer connections between the wave vectors in the Brillouin zone, there are three connection matrices,

$$H_1 = w \begin{pmatrix} 1 & 1 \\ 1 & 1 \end{pmatrix} \tag{10.3}$$

$$H_2 = w \begin{pmatrix} \omega^2 & 1 \\ \omega & \omega^2 \end{pmatrix} \tag{10.4}$$

$$H_3 = w \begin{pmatrix} \omega & 1 \\ \omega^2 & \omega \end{pmatrix} \tag{10.5}$$

where w is the interlayer hopping energy and $\omega = e^{2\pi i/3}$. $H_{i,\alpha\beta}$, with $\alpha, \beta = A, B$ represents the hopping between sublattice α in the first layer to sublattice β in the second layer, with momentum transfer determined by i (see [81] for definition). Note that in this gauge choice, the origin of rotation is chosen where the B sublattice of the first layer coincides with the A sublattice of the second layer, so that the $H_{i,BA}$ component has zero phase while the other terms acquire phases. A different gauge choice is equivalent to an interlayer translation, which has been shown to have a negligible effect in the case of small twist angles [81, 78].

To extend this formulation to TBBG, we add a simplified bilayer graphene Hamiltonian,

$$H_b = \begin{pmatrix} 0 & 0 \\ w_b & 0 \end{pmatrix} \tag{10.6}$$

between the non-twisted layers. The momentum transfer is zero since the bilayer is not

twisted and the coupling is constant over the moiré unit cell. For simplicity, we only consider the 'dimer' coupling in the bilayer, neglecting second-nearest-neighbor hopping terms and trigonal warping terms. The two bilayers in TBBG (layer 1-2 and layer 3-4) have the same stacking order, *i.e.* for zero twist angle the total stacking would be 'ABAB' instead of 'ABBA'. In the calculations used in the main text, we used parameters $w = 0.1\,\text{eV}$ and $w_b = 0.4\,\text{eV}$, so that when either parameter is turned off we obtain either the two non-interacting bilayer graphene ($w = 0$) or the non-interacting TBG and two monolayer graphene ($w_b = 0$).

10.7.6 Additional magnetic field response data

Fig. 10-7 shows the response of correlated states at $n_s/4$ and $3n_s/4$ in a perpendicular or in-plane magnetic field, similar to Fig. 10-3d-e, for the $\theta = 1.23°$ device. For the $n_s/4$ state, we also find a signature of a phase transition at $D/\varepsilon_0 = -0.36\,\text{V/nm}$, manifesting as a shift of D-location of the correlated insulator as $B_\perp$ exceeds 6 T. The $3n_s/4$ state shows an overall monotonic increase of resistance and exhibits no shift of the position in D. In an in-plane field, on the other hand, as shown in Fig. 10-7b,d, both quarter filling states show a monotonic enhancement as $B_\parallel$ is increased, suggesting that they may have a similar spin-polarized ground state as well.

10.7.7 I-V curves

In Fig. 10-9, we have plotted the I-V curves and differential resistance curves of the $\theta = 1.23°$ device when it is in the correlated insulator states at $n_s/4$ and $n_s/2$. In the insulator states, we find a non-linear region near zero bias $I_b = 0$ where the differential resistance dV_{xx}/dI_b is significantly enhanced. This is in agreement with the existence of a small energy gap, which is overcome at higher bias voltages/currents. Outside of the insulator regions (such as shown in Fig. 10-9b), the I-V curves are mostly linear. For measuring the g-factors at $n_s/2$, we therefore used a much smaller excitation current of $\sim 0.1\,\text{nA}$ in order to truthfully measure the differential resistance at $I_b = 0$.

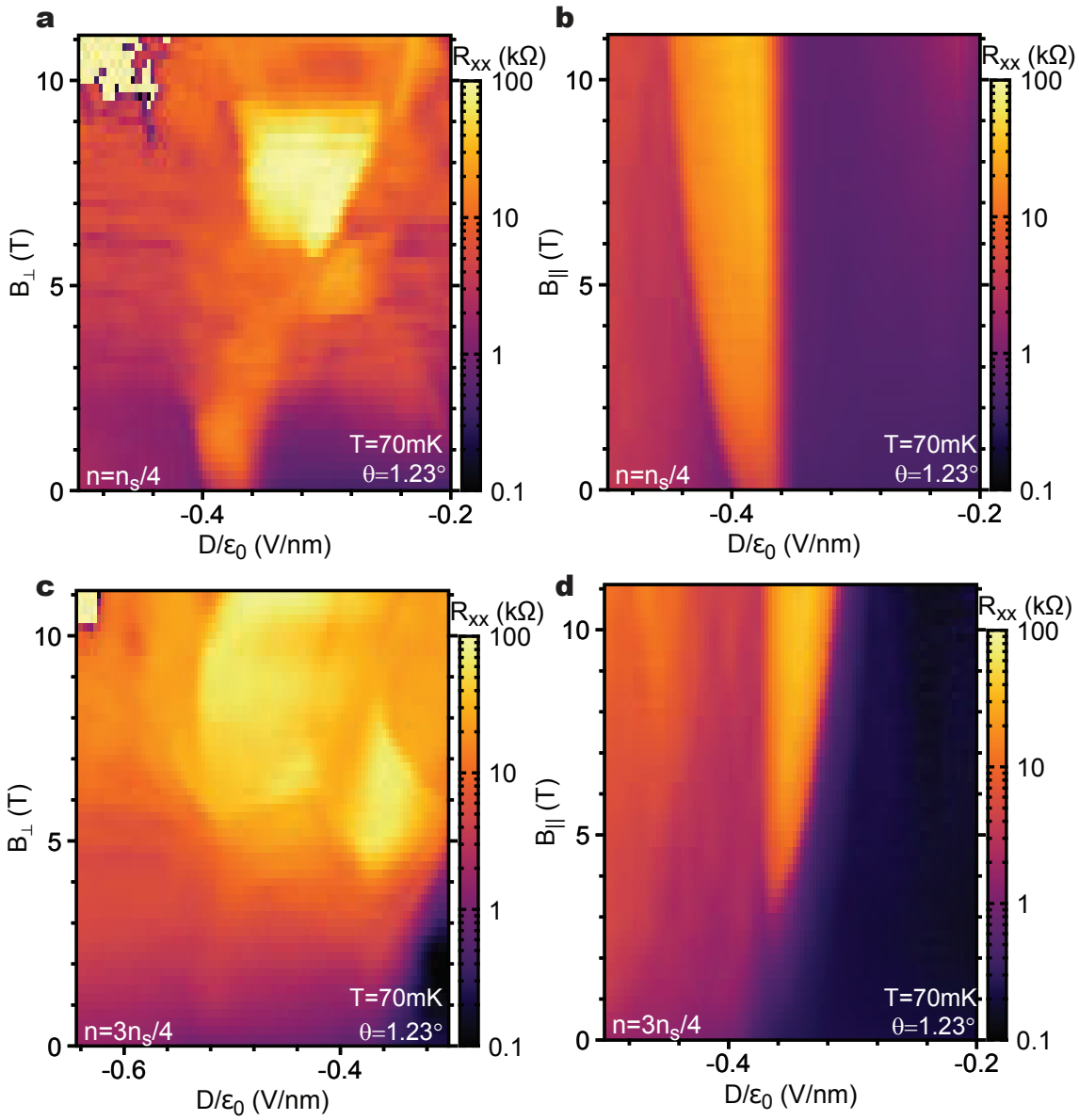

Figure 10-8: Additional magnetic field response of TBBG devices. (a-d) Response of the $n_s/4$ and $3n_s/4$ states in perpendicular magnetic field and in-plane magnetic field.

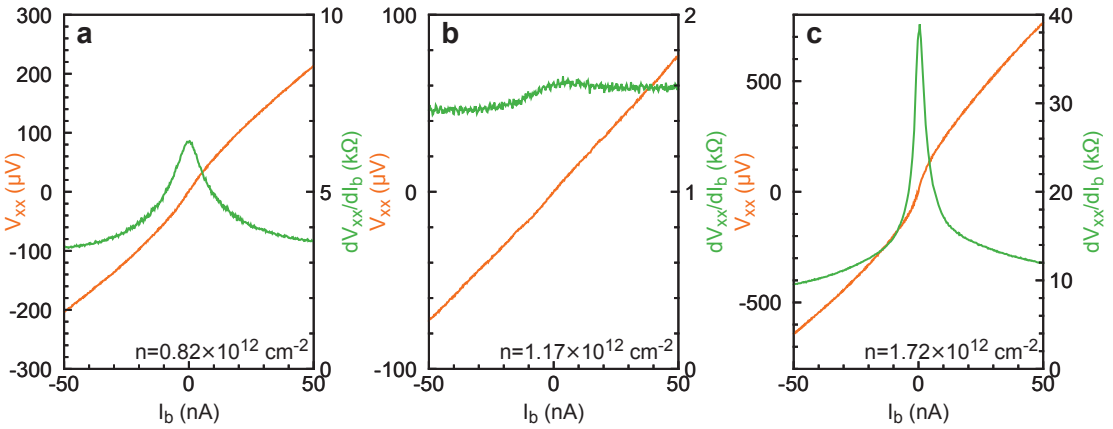

Figure 10-9: I-V curves in $\theta = 1.23°$ TBBG device at different carrier densities. $D/\varepsilon_0 =$ –0.38 V/nm. The densities of (a) and (c) correspond approximately to the $n_s/4$ and $n_s/2$ insulating states, respectively, while (b) lies in between them. Left axis is the longitudinal voltage V_{xx} and right axis is the differential resistance dV_{xx}/dI_b.

Chapter 11

Summary and Outlook

To sum up, in this thesis, I have presented a series of experiments performed with the goal of inducing superconductivity and other strongly correlated phases in graphene-based systems using two different approaches: (1) proximitizing graphene with intrinsic superconductors and (2) creating moiré flat bands with a second graphene layer placed on top of the first and twisted at a small angle. In this final chapter, I summarize the main contributions of this thesis and comment on possible follow-up experiments and future advances that can be achieved in the short-, middle-, and long-term, both from a fundamental point of view and in relation to next-generation technological applications. I offer this summary in five main sections. First, I offer a few general comments on MATBG. Then, I give a more global perspective on moiré flat band engineering beyond MATBG. To follow, I comment on some of the main technical challenges currently facing the field. To close my remarks on MATBG, I briefly discuss its potential for technological applications. I end with some general thoughts on cQED and 2D materials.

11.1 Twisted bilayer graphene: summary, big questions, and follow-up experiments

11.1.1 MATBG

As described in detail in Chapter 2, a moiré pattern emerges when two graphene layers are twisted at a small angle, leading to a long-range modulation of the stacking order. Near what is referred to as the magic-angle, $\theta \approx 1.1^{\circ}$, the low-energy bands become flat due to strong interlayer interactions. Remarkably, for MATBG, the density of the charge carriers can easily be swept throughout the whole range of the flat bands. Multiple phenomena at the frontier of condensed matter physics have been demonstrated in MATBG, including gate-tunable superconductivity, correlated insulating states, magnetism, quantized anomalous Hall, electronic nematicity, cascades of phase transitions, collective excitations (plasmonic modes), linear-in-temperature low-temperature resistivity, and topological order. Several of these exotic phenomena have been directly observed in the experiments presented in this thesis.

In the last few years, MATBG has emerged as a suitable arena for the study of exotic physics phenomena in 2D flat band systems. It enables wide opportunities to discover new phenomenology, opens the door to a range of new lithographically defined device geometries, and offers a promising material for future tunable electronics applications. The appeal of MATBG, therefore, is twofold, given its promise in relation to both basic science and future technological devices.

11.1.2 MATBG: a proxy for understanding strongly correlated systems

As Allan MacDonald, one of the fathers of this field, once said, "The great hope of MATBG research, either boldly declared or modestly unspoken, is that it will teach us something important and general about superconductivity in strongly correlated electron systems" [108]. The present thesis does justice to his insights by identifying two phenomena present both in MATBG and the strongly correlated electronic systems: nematicity and strange metal

behavior.

Chapter 6 focused on evidence of spontaneously broken lattice rotational symmetry in both the superconducting and normal phases. Thus, in MATBG, electrons can break rotational symmetry at certain flat band fillings, even when the underlying crystal does not. This phenomenon, known as nematicity, is present in several other unconventional superconductors. The work presented in chapter 6 also experimentally established the presence of competing orders near filling $\nu = -2$ at the intersection between an anisotropic normal state and the superconducting dome. A similar phenomenology is observed in certain underdoped cuprates as a dip in the superconducting dome at around 1/8 hole doping.

Additionally, Chapter 7 reported on an enhanced T-linear resistivity in MATBG (persisting to very low temperatures), indicating very strong scattering and pointing to a strange-metal phase with Planckian dissipation. This metallic phase, common to several strongly correlated superconductors, including cuprates, pnictides, organic superconductors, and heavy fermions, cannot be described within a conventional Fermi liquid theory and directly conflicts with the well-established Drude model. MATBG has emerged as a privileged arena for studying this phenomenology, both theoretically and experimentally.

11.1.3 MATBG: an attractive material in its own right, a platform for the study of strongly correlated physics

Nematicity and strange metal behavior, and many other discoveries, already made and yet to come, will surely help advance the field of many-particle physics. In addition, MATBG is much more than a *tool* for furthering our understanding of other interesting systems. According to Allan MacDonald [108], "TBG is an interesting quantum material in its own right, since it provides experimental access to a rich variety of strongly correlated electron phenomena"—a claim supported throughout this thesis.

Chapter 8 determined that MATBG displays a cascade of phase transitions and Dirac revivals and entropic evidence for a Pomeranchuk effect. Additionally, Chapter 9 reported on propagating interband plasmon modes in undoped MATBG associated with optical transitions between the moiré minibands.

11.1.4 Big questions

As of the writing of this thesis, several major questions in the field remain unresolved and will surely drive extensive investigation over the next few years. Some of these big questions directly related to the work presented in this thesis are as follows:

- What is the nature of the correlated insulating states observed at integer fillings?
- What is the origin of superconductivity in MATBG?
- What is the underlying microscopic mechanism of superconductivity?
- What is the superconducting order parameter?
- How far can we push the often-stated comparison between MATBG to high-T_c superconductors? Will MATBG truly serve as a *Rosetta stone* for understanding cuprate high-T_c superconductors and other correlated materials?
- Will MATBG ever help us develop a room-temperature superconductor?

11.1.5 Additional open questions and possible follow up experiments to elucidate MATBG's biggest mysteries

Listed below is a selection of follow-up experiments that can be performed based directly on the techniques presented in this thesis. The following ideas are indicative only and non-exhaustive. Some of the experiments are explained in detail, whereas others are referenced with only minimal explanations rendered.

The first experiment proposed builds on the measurements of the pairing symmetry performed in the cuprates in the mid-1990s by Dale Van Harlingen's research group [55] using Josephson interferometry. Crucially, these experiments are sensitive to the anisotropy of the order parameter phase. They made it possible to directly test the sign change in the $d_{x^2-y^2}$ order parameter of the cuprates in different k-space directions. Specifically, Dale Van Harlingen and coworkers [55] investigated two measurement schemes: a SQUID and a corner-junction. In the former, two Josephson tunnel junctions were formed on the orthogonal faces of a cuprate single-crystal and the junctions were joined by a conventional

superconducting loop. In the latter, a junction was fabricated on the corner of a similar crystal. The key point is that the Josephson junctions serve as directional probes of the order parameter phase inside the crystal. In the presence of a magnetic field, the expected SQUID-type pattern or Fraunhofer-like pattern dramatically changes depending on the order parameter of the material under study. Through this experiment, the relative phase between orthogonal directions for a YBCO high-T_c crystal was determined, confirming the predicted $d_{x^2-y^2}$ superconducting order parameter [55]. A similar experiment could be adapted to MATBG. The geometry of the junctions might not be as straightforward as for the Van Harlingen experiment, and intense theoretical work focused on narrowing down the possible superconducting order parameter candidates would be highly beneficial. During my doctoral work, I spent significant time thinking about how to conduct this experiment. In the end, my colleagues and I prioritized other projects, and this idea will pass to future generations of students.

In the short- and middle-term, the experiments presented in Chapters 6-9 raised many new fundamental questions and simultaneously provided a basis for multiple follow-up experiments. The answers to a number of important questions in regard to MATBG remain undetermined such as Why does nematicity arise in MATBG? What is the precise mechanism leading to the C_3 rotational symmetry breaking both in the superconducting state and in the normal state? What determines which of the competing states will win and why is this the case?

Similarly, the interpretation of strange metal behavior in MATBG remains a controversial topic in the condensed matter community [302, 298, 376, 5, 86]. Further theoretical and experimental work is still required if we are to better understand the physics of "strange" metals with Planckian behavior that points to a quantum limit on the scattering rate in this and other systems.

The work performed in collaboration with Shahal Ilani using his state-of-the-art SET scanning technique established the presence of a high-temperature parent state with an asymmetrical populating sequence of bands. Establishing the precise nature of this high-temperature parent state requires further investigation. In addition, the ground state that will dominate at lower temperatures cannot be predicted within a single theoretical framework

at least not at present.

Regarding nano-optics studies of MATBG, the work presented in Chapter 9 lays the foundation for a range of research directions pertaining to this system. As detailed in reference [151], some possible follow-up experiments would involve near-field photocurrent nanoscopy and optical nano-imaging studies at low temperatures (cryogenic s-SNOM) in MATBG-doped samples. These may allow imaging collective excitations with longer lifetimes, and elucidate the contribution of collective excitations to many-body states [358, 148], with a nanometric spatial resolution. Photocurrent experiments and studies involving terahertz excitation frequencies could also offer a local probe for the exploration of novel exotic phases [151, 148].

Many of the questions raised in the previous section point to the need for alternative experimental investigative pathways to elucidate the nature and origin of superconducting states. Possible directions are currently under study by our group and several others around the world.

11.2 Exotic physics in 2D systems with flat bands beyond MATBG

Throughout this thesis, it has been demonstrated that the twist angle plays a unique role in determining the physical properties of vdW heterostructures. The discovery of MATBG has catalyzed the development of a new field of research in condensed matter physics: *twistronics*. In particular, the work presented in the previous chapter paves the way for extending the *twistronics* techniques to other materials beyond two monolayers of graphene.

The family of van der Waals materials beyond graphene is large and continuing to grow. It includes insulators (hBN, ...), metals and semimetals (Si, Ge, Sn, $TiS2_2$, ...), semiconductors (MoS_2, $WS2_2$, InSe, GaS, P, SnS ...), superconductors ($NbSe_2$, TaS_2, high-T_c cuprates, ...), topological insulators (WTe_2, Bi_2Se_3 $MnBi_2Te_4$, ...), and magnets and quantum spin liquids (CrI_3, $Cr_2Ge_2Te_6$, $RuCl_3$, ...). With the techniques described and developed in this thesis, it is now possible to engineer new complex heterostructures with

à la carte electronic band structures beyond graphene, with sub-nanometric control over the thickness of individual 2D atomic crystals and sub-degree control over the twist angle alignment between layers. We can essentially stack any 2D quantum material on top of any 2D crystal at any desired angle and modify existing correlations or introduce correlations when not already present.

Numerous exotic phases are now available to study in relation to moiré van der Waals materials via multiple techniques, including transport, thermodynamic, and scanning probe measurements. Each moiré system presents a unique phenomenology and is an exciting quantum material in its own right. Several of these narrow-band systems have already been explored, although many more are "waiting to be discovered."

In this section, my purpose is not to offer an exhaustive review of this fast-evolving field. Therefore, I do not review these novel systems individually or include citations to studies relevant to them. Instead, in order to offer a brief yet broad perspective of the wide range of possibilities associated with these moiré 2D meta-materials, I present a possible classification based on three main categories [377]:

- Homobilayers: Two layers of the same material stacked with a certain twist angle. This class includes MATBG, semiconducting transition metal dichalcogenides twisted homobilayers, and twisted hexagonal boron nitride structures. Moiré patterns in TMD bilayers with small twist angles are already being explored and are especially attractive for their electronic and optical properties. Certain similarities are shared between those that have already been studied and MATBG, including the presence of a ~ 10-nm superlattice periodicity, resistive states at particular fillings, and in certain cases, emerging zero-resistance states. Some of these materials possess topologically non-trivial, gate-tunable gaps. As they arise from individual constituents with relatively flat bands even in the absence of a moiré potential, these materials display flat bands for a continuous range of angles and displacement fields [91, 378].

- Heterobilayers: Two layers of different materials with a lattice constant mismatch or twisted by an angle. Included in this category of twisted 2D structures are transition metal dichalcogenides (twisted) heterobilayers and rhombohedral trilayer graphene

aligned to hBN.

- Multilayers: Multiple layers of twisted 2D crystals. The most general category in this list, it includes twisted bilayer-bilayer graphene (explored in Chapter 10), twisted N-layer graphene, twisted monolayer-bilayer graphene, twisted double bilayers transition metal dichalcogenides, and twisted multilayers of 2D magnets or 2D superconductors. These heterostructures allow more than one angle to be controlled, further expanding the moiré landscape. Additional interesting heterostructures in this category include double moiré patterns, where two different moiré patterns are placed in close proximity, possibly separated by a thin tunnel barrier.

In summary, new moiré systems with a long wavelength superlattice arising from a lattice mismatch or a rotational misalignment can result in novel flat band systems in the absence of an external magnetic field. Such systems offer new tunable platforms for the exploration of novel electronic, topological, magnetic, and other strongly correlated phenomena.

11.3 Technical challenges

As discussed in Chapter 2, the twist angle allows the ratio between the kinetic energy and the Coulomb interactions to be controlled. In MATBG, with the current state-of-the-art fabrication techniques, the twist angle is set during the fabrication process and cannot be modified a posteriori. It would, therefore, be desirable to be able to control the twist angle locally, as an in situ additional knob (see, for example, ref. [379] pioneering this idea). Extending such a possibility to MATBG makes it possible to study, in a single device, the transition between weak and strong coupling regimes in a continuous way, thereby rendering MATBG an archetypal experimental tool for the study of competing interactions in 2D systems [377, 380]. Studies of this kind can also be expected to facilitate the development of devices with multiple twist angles over controlled regions that could give rise to new platforms for Majorana engineering, shed light on the Cooper-pairing mechanism in MATBG [381], and, more generally, ease the way for a new generation of

2D electronics with an additional tunable degree of freedom. From a fabrication point of view, considerable progress has been made over the last few years. However, several main challenges still remain, including:

1. eliminating twist angle inhomogeneity and control lattice relaxation,

2. developing techniques to make consistently reproducible devices with a controlled average twist angle down to a hundredth of a degree and 100% success yield, and eliminating variability between devices, and

3. developing technical tools to scale this technology beyond the current state-of-the-art where a few MATBG devices take months to fabricate and characterize.

Controlling the twist angle in CVD-grown materials is a promising related direction. The fewer uncontrolled strains and other inhomogeneities a device shows, the cleaner and richer the physics accessible via the device.

In terms of 2D materials research generally, many improvements still need to be made in order to (1) precisely control the twist angle between different 2D materials and (2) improve the interfaces between 2D and 3D materials. Additionally, high-quality growth crystals will undoubtedly remain a key ingredient in developing novel moiré 2D heterostructures.

With fabrication processes fast becoming more complex, these technical advances in sample preparation will soon become critical in advancing this field of research.

11.4 Technological Interest

Magic-angle twisted bilayer graphene has emerged as a highly tunable 2D material platform exhibiting a wide range of phases, such as metal, band insulator, charge neutrality, correlated insulator, and superconductor states.

In Chapter 5, such tunability is exploited to create versatile tunneling junctions defined solely by electrostatic gates. Tunneling devices are ubiquitous in modern electronics, with applications ranging from tunneling diodes to magnetic tunnel junctions and superconducting tunneling junctions.

In particular, one of the elemental superconducting devices omnipresent in superconducting electronics, is Josephson junctions, where two superconductors sandwich a non-superconducting weak link. Josephson junctions find applications in ultrasensitive electromagnetic sensing such as in devices used to monitor brain activity and are among the basic ingredients of any superconducting qubit.

State-of-the-art qubit junctions typically utilize oxide tunnel barriers, although these suffer from disorder and are not electrostatically tunable. Tunability can be achieved by combining several different materials, although these may suffer from non-ideal interfaces and, therefore, present fabrication challenges. Chapter 5 demonstrates a fully tunable 2D Josephson junction made of a single clean material, which enables independent control, in situ, of the electronic state of the weak link and the rest of the junction via multiple electrostatic gates. As all the atoms are carbon, material incompatibilities are automatically suppressed. In the experimental device, the MATBG electrodes can be brought into a superconducting state, either in the hole regime or the electron regime. Further, the narrow junction at the center of the device can be tuned in order to achieve any possible state of the phase diagram of MATBG, which, in turn, allows a tunable critical supercurrent to travel across the junction.

Can this prototype be applied to quantum computing with superconducting circuits to address some of the aforementioned limitations of state-of-the-art qubit junctions? Immediately after we published this work in Arxiv, the journal Science highlighted its capabilities in future voltage-tunable MATBG-based qubits [220]: "That control could simplify quantum computers. Those being developed by Google and IBM rely on Josephson junctions with properties that are fixed during fabrication. To operate the finicky qubits, the junctions must be manipulated jointly in cumbersome ways. With twisted graphene, however, qubits could come from single junctions that are smaller and easier to control."

Another recently proposed [382] possible technological application of MATBG involves using its record-low heat capacity to make an ultrabroad-range single-photon detector for mid-infrared and terahertz frequencies. Such a low-energy detector could then be used in diverse fields, including radio astronomy, quantum sensing, quantum key distribution, and information processing [382].

More generally, the introduction of multiple gates used to subject different material areas to different electric densities may make it possible to implement gate-defined circuits with MATBG in future 2D integrated electronics.

It is hard to say whether these MATBG devices will find applications in industrial electronics at a larger scale beyond mere experimental research, or whether they will truly "power a new generation of superconducting electronics," as claimed in the journal Science [220] featuring our work. Only time will tell. It can take decades for scientific discoveries to find a place in real-life applications. Examples include semiconductors, now serving as the basis of all our electronic devices, and atomic clocks, now enabling precise positioning in GPS setups. Most importantly, none of these applications were even envisioned when the underlying fundamental discovery was initially made. Many scientific breakthroughs were motivated by theoretical interest with applications then taking decades to reach the general public. At only five years old, MATBG is a very new field that needs time to mature. What is certain is that moiré systems have already impacted materials science, condensed matter physics, and (hopefully soon! - see next section) also cQED and quantum computing.

11.5 2D Materials and cQED

Last but not least, the experiments introduced in Chapter 4 can easily be extended to other vdW materials and to more complex heterostructures, the planar geometry of which is highly integrable into cQED architecture. More generally, these studies present a new approach to characterizing the intrinsic properties of van der Waals materials using microwave photons in quantum circuits and to simultaneously drawing on the technological potential of 2D materials to improve the coherence and extensibility of superconducting qubits.

In fact, I see great promise in this interdisciplinary field at the frontier of quantum information, condensed matter physics, and materials science. In particular, the field provides a promising route to constructing next-generation key elements of solid-state quantum computers based on 2D materials. The study presented in Chapter 4 demonstrated the feasibility of realizing coherent quantum devices using atomically thin materials. The proof-of-concept graphene-based superconducting qubit realized in Chapter 4 certainly has room for

improvement in terms of mitigating the sources of decoherence that limit its performance, although it has already demonstrated its potential. The implementation of epitaxial vdW materials in next-generation voltage-tunable superconducting qubits could address several challenges associated with the current technology, including the need to (1) reduce the presence of defects and spurious 2-level systems limiting coherence times, (2) decrease the size of quantum circuits, a key step towards scalability and miniaturization [383, 384], (3) eliminate SQUID loops, which introduce susceptibility to 1/f flux noise and require extensive resources to bias the qubits with DC currents whose infrastructure generates a continual dissipation of power, and (4) mitigate unwanted cross-talk between neighboring qubits, which is critical to realizing high-fidelity multi-qubit operations.

Further, a hybrid superconducting circuit with vdW materials constitutes a fertile arena for studying the light-matter interaction in such materials in a largely unexplored regime using microwave photons and for investigating the materials' electronic degrees of freedom using a non-invasive approach with high precision.

In summary, these two fields perfectly complement each other, and I intend to pursue my scientific career in this direction. I can happily say I will join Will Oliver's group for postdoctoral study next year in order to focus on projects related to these topics.

Bibliography

[1] Joel I-Jan Wang, Landry Bretheau, Daniel Rodan-Legrain, Riccardo Pisoni, Kenji Watanabe, Takashi Taniguchi, and Pablo Jarillo-Herrero. Tunneling spectroscopy of graphene nanodevices coupled to large-gap superconductors. Physical Review B, 98(12):121411, September 2018. Publisher: American Physical Society.

[2] Joel I.-Jan Wang, Daniel Rodan-Legrain, Landry Bretheau, Daniel L. Campbell, Bharath Kannan, David Kim, Morten Kjaergaard, Philip Krantz, Gabriel O. Samach, Fei Yan, Jonilyn L. Yoder, Kenji Watanabe, Takashi Taniguchi, Terry P. Orlando, Simon Gustavsson, Pablo Jarillo-Herrero, and William D. Oliver. Coherent control of a hybrid superconducting circuit made with graphene-based van der Waals heterostructures. Nature Nanotechnology, 14(2):120–125, February 2019. Number: 2 Publisher: Nature Publishing Group.

[3] Daniel Rodan-Legrain, Yuan Cao, Jeong Min Park, Sergio C. de la Barrera, Mallika T. Randeria, Kenji Watanabe, Takashi Taniguchi, and Pablo Jarillo-Herrero. Highly tunable junctions and non-local Josephson effect in magic-angle graphene tunnelling devices. Nature Nanotechnology, 16(7):769–775, July 2021.

[4] Yuan Cao, Daniel Rodan-Legrain, Jeong Min Park, Noah F. Q. Yuan, Kenji Watanabe, Takashi Taniguchi, Rafael M. Fernandes, Liang Fu, and Pablo Jarillo-Herrero. Nematicity and competing orders in superconducting magic-angle graphene. Science, 372(6539):264–271, April 2021. Publisher: American Association for the Advancement of Science.

[5] Yuan Cao, Debanjan Chowdhury, Daniel Rodan-Legrain, Oriol Rubies-Bigorda, Kenji Watanabe, Takashi Taniguchi, T. Senthil, and Pablo Jarillo-Herrero. Strange Metal in Magic-Angle Graphene with near Planckian Dissipation. Physical Review Letters, 124(7):076801, February 2020. Publisher: American Physical Society.

[6] K. S. Novoselov, A. K. Geim, S. V. Morozov, D. Jiang, Y. Zhang, S. V. Dubonos, I. V. Grigorieva, and A. A. Firsov. Electric Field Effect in Atomically Thin Carbon Films. Science, 306(5696):666–669, October 2004. Publisher: American Association for the Advancement of Science.

[7] K. S. Novoselov, A. Mishchenko, A. Carvalho, and A. H. Castro Neto. 2D materials and van der Waals heterostructures. Science, 353(6298), July 2016. Publisher: American Association for the Advancement of Science.

[8] A. K. Geim and I. V. Grigorieva. Van der Waals heterostructures. Nature, 499(7459):419–425, July 2013. Publisher: Nature Publishing Group.

[9] Yu Saito, Tsutomu Nojima, and Yoshihiro Iwasa. Highly crystalline 2D superconductors. Nature Reviews Materials, 2(1):1–18, December 2016.

[10] M. Gibertini, M. Koperski, A. F. Morpurgo, and K. S. Novoselov. Magnetic 2D materials and heterostructures. Nature Nanotechnology, 14(5):408–419, May 2019.

[11] Bevin Huang, Genevieve Clark, Efrén Navarro-Moratalla, Dahlia R. Klein, Ran Cheng, Kyle L. Seyler, Ding Zhong, Emma Schmidgall, Michael A. McGuire, David H. Cobden, Wang Yao, Di Xiao, Pablo Jarillo-Herrero, and Xiaodong Xu. Layer-dependent ferromagnetism in a van der Waals crystal down to the monolayer limit. Nature, 546(7657):270–273, June 2017. Publisher: Nature Publishing Group.

[12] Pulickel Ajayan, Philip Kim, and Kaustav Banerjee. Two-dimensional van der Waals materials. Physics Today, 69(9):38–44, September 2016. Publisher: American Institute of Physics.

[13] Qing Hua Wang, Kourosh Kalantar-Zadeh, Andras Kis, Jonathan N. Coleman, and Michael S. Strano. Electronics and optoelectronics of two-dimensional transition metal dichalcogenides. Nature Nanotechnology, 7(11):699–712, November 2012.

[14] E. Cappelluti, R. Roldán, J. A. Silva-Guillén, P. Ordejón, and F. Guinea. Tight-binding model and direct-gap/indirect-gap transition in single-layer and multilayer MoS 2. Physical Review B, 88(7):075409, August 2013.

[15] Hualing Zeng, Junfeng Dai, Wang Yao, Di Xiao, and Xiaodong Cui. Valley polarization in MoS2 monolayers by optical pumping. Nature Nanotechnology, 7(8):490–493, August 2012.

[16] Kin Fai Mak, Keliang He, Jie Shan, and Tony F. Heinz. Control of valley polarization in monolayer MoS2 by optical helicity. Nature Nanotechnology, 7(8):494–498, August 2012.

[17] S. J. Haigh, A. Gholinia, R. Jalil, S. Romani, L. Britnell, D. C. Elias, K. S. Novoselov, L. A. Ponomarenko, A. K. Geim, and R. Gorbachev. Cross-sectional imaging of individual layers and buried interfaces of graphene-based heterostructures and superlattices. Nature Materials, 11(9):764–767, September 2012.

[18] Mingsheng Xu, Tao Liang, Minmin Shi, and Hongzheng Chen. Graphene-Like Two-Dimensional Materials. Chemical Reviews, 113(5):3766–3798, May 2013.

[19] Xiangming Xu, Tianchao Guo, Hyunho Kim, Mrinal K. Hota, Rajeh S. Alsaadi, Mario Lanza, Xixiang Zhang, and Husam N. Alshareef. Growth of 2D Materials at the Wafer Scale. Advanced Materials, page 2108258, 2022.

[20] Liusi Yang, Wenjun Chen, Qiangmin Yu, and Bilu Liu. Mass production of two-dimensional materials beyond graphene and their applications. Nano Research, 14(6):1583–1597, June 2021.

[21] A. H. Castro Neto, F. Guinea, N. M. R. Peres, K. S. Novoselov, and A. K. Geim. The electronic properties of graphene. Reviews of Modern Physics, 81(1):109–162, January 2009. Publisher: American Physical Society.

[22] P. R. Wallace. The Band Theory of Graphite. Physical Review, 71(9):622–634, May 1947. Publisher: American Physical Society.

[23] S. Das Sarma, Shaffique Adam, E. H. Hwang, and Enrico Rossi. Electronic transport in two-dimensional graphene. Reviews of Modern Physics, 83(2):407–470, May 2011. Publisher: American Physical Society.

[24] M. O. Goerbig. Electronic properties of graphene in a strong magnetic field. Reviews of Modern Physics, 83(4):1193–1243, November 2011. Publisher: American Physical Society.

[25] Eva Y. Andrei and Allan H. MacDonald. Graphene bilayers with a twist. Nature Materials, 19(12):1265–1275, December 2020. Number: 12 Publisher: Nature Publishing Group.

[26] Hubert B. Heersche, Pablo Jarillo-Herrero, Jeroen B. Oostinga, Lieven M. K. Vandersypen, and Alberto F. Morpurgo. Bipolar supercurrent in graphene. Nature, 446(7131):56–59, March 2007. Publisher: Nature Publishing Group.

[27] Landry Bretheau, Joel I.-Jan Wang, Riccardo Pisoni, Kenji Watanabe, Takashi Taniguchi, and Pablo Jarillo-Herrero. Tunnelling spectroscopy of Andreev states in graphene. Nature Physics, 13(8):756–760, August 2017.

[28] I O Kulik. Macroscopic quantization and the proximity effect in S-N-S junctions. Sov. Phys. JETP, 30(5):944–950, 1970.

[29] Akira Furusaki and Masaru Tsukada. Dc Josephson effect and Andreev reflection. Solid State Commun., 78(4):299–302, 1991.

[30] C W J Beenakker and H van Houten. Josephson current through a superconducting quantum point contact shorter than the coherence length. Phys. Rev. Lett., 66(23):3056–3059, 1991.

[31] P. F. Bagwell. Suppression of the Josephson current through a narrow, mesoscopic, semiconductor channel by a single impurity. Phys. Rev. B, 46(19):12573–12586, 1992.

[32] K. S. Novoselov. Nobel Lecture: Graphene: Materials in the Flatland. Reviews of Modern Physics, 83(3):837–849, August 2011. Publisher: American Physical Society.

[33] Antonio H. Castro Neto. Selected Topics in Graphene physics. arXiv:1004.3682 [cond-mat], April 2010. arXiv: 1004.3682.

[34] N. M. R. Peres. Colloquium: The transport properties of graphene: An introduction. Reviews of Modern Physics, 82(3):2673–2700, September 2010. Publisher: American Physical Society.

[35] A. K. Geim and K. S. Novoselov. The rise of graphene. Nature Materials, 6(3):183–191, March 2007. Publisher: Nature Publishing Group.

[36] N. M. R. Peres, J. N. B. Rodrigues, T. Stauber, and J. M. B. Lopes dos Santos. Dirac electrons in graphene-based quantum wires and quantum dots. Journal of Physics: Condensed Matter, 21(34):344202, July 2009. Publisher: IOP Publishing.

[37] Fengnian Xia, Damon B. Farmer, Yu-Ming Lin, and Phaedon Avouris. Graphene field-effect transistors with high on/off current ratio and large transport band gap at room temperature. Nano Letters, 10(2):715–718, February 2010.

[38] Kin Fai Mak, Chun Hung Lui, Jie Shan, and Tony F. Heinz. Observation of an Electric-Field-Induced Band Gap in Bilayer Graphene by Infrared Spectroscopy. Physical Review Letters, 102(25):256405, June 2009. Publisher: American Physical Society.

[39] Yuanbo Zhang, Tsung-Ta Tang, Caglar Girit, Zhao Hao, Michael C. Martin, Alex Zettl, Michael F. Crommie, Y. Ron Shen, and Feng Wang. Direct observation of a widely tunable bandgap in bilayer graphene. Nature, 459(7248):820–823, June 2009. Number: 7248 Publisher: Nature Publishing Group.

[40] Jeroen B. Oostinga, Hubert B. Heersche, Xinglan Liu, Alberto F. Morpurgo, and Lieven M. K. Vandersypen. Gate-induced insulating state in bilayer graphene devices. Nature Materials, 7(2):151–157, February 2008. Publisher: Nature Publishing Group.

[41] Eduardo V. Castro, K. S. Novoselov, S. V. Morozov, N. M. R. Peres, J. M. B. Lopes dos Santos, Johan Nilsson, F. Guinea, A. K. Geim, and A. H. Castro Neto. Biased Bilayer Graphene: Semiconductor with a Gap Tunable by the Electric Field Effect. Physical Review Letters, 99(21):216802, November 2007. Publisher: American Physical Society.

[42] Hongki Min, Bhagawan Sahu, Sanjay K. Banerjee, and A. H. MacDonald. Ab initio theory of gate induced gaps in graphene bilayers. Physical Review B, 75(15):155115, April 2007. Publisher: American Physical Society.

[43] Edward McCann. Asymmetry gap in the electronic band structure of bilayer graphene. Physical Review B, 74(16):161403, October 2006. Publisher: American Physical Society.

[44] Thiti Taychatanapat and Pablo Jarillo-Herrero. Electronic Transport in Dual-Gated Bilayer Graphene at Large Displacement Fields. Physical Review Letters, 105(16):166601, October 2010. Publisher: American Physical Society.

[45] Tinkham Michael. Introduction to Superconductivity. Dover Publications, Mineola, N.Y., 2nd ed. edition, 2004.

[46] Rudolf Gross, Achim Marx, and Frank Deppe. Applied Superconductivity: Josephson Effect and Superconducting Electronics. Walter De Gruyter Incorporated, 2016. Google-Books-ID: 4SIzrgEACAAJ.

[47] J. Bardeen, L. N. Cooper, and J. R. Schrieffer. Microscopic Theory of Superconductivity. Physical Review, 106(1):162–164, April 1957. Publisher: American Physical Society.

[48] J. Bardeen, L. N. Cooper, and J. R. Schrieffer. Theory of Superconductivity. Physical Review, 108(5):1175–1204, December 1957. Publisher: American Physical Society.

[49] C. C. Tsuei and J. R. Kirtley. Pairing symmetry in cuprate superconductors. Rev. Mod. Phys, 72:969, 2000.

[50] Xingjiang Zhou, Wei-Sheng Lee, Masatoshi Imada, Nandini Trivedi, Philip Phillips, Hae-Young Kee, Päivi Törmä, and Mikhail Eremets. High-temperature superconductivity. Nature Reviews Physics, 3(7):462–465, July 2021. Number: 7 Publisher: Nature Publishing Group.

[51] B. D. Josephson. Possible new effects in superconductive tunnelling. Physics Letters, 1(7):251–253, July 1962.

[52] The Feynman Lectures on Physics Vol. III Ch. 21: The Schrödinger Equation in a Classical Context: A Seminar on Superconductivity.

[53] J. Q. You and Franco Nori. Atomic physics and quantum optics using superconducting circuits. Nature, 474(7353):589–597, June 2011. Number: 7353 Publisher: Nature Publishing Group.

[54] Raymond W. Simmonds. Quantum interference heats up. Nature, 492(7429):358–359, December 2012. Number: 7429 Publisher: Nature Publishing Group.

[55] D. J. Van Harlingen. Phase-sensitive tests of the symmetry of the pairing state in the high-temperature superconductors—Evidence for ${d}_{{x}^{2}\ensuremath{-}{y}^{2}}$ symmetry. Reviews of Modern Physics, 67(2):515–535, 1995. Publisher: American Physical Society.

[56] A. Uri, S. Grover, Y. Cao, J. A. Crosse, K. Bagani, D. Rodan-Legrain, Y. Myasoedov, K. Watanabe, T. Taniguchi, P. Moon, M. Koshino, P. Jarillo-Herrero, and E. Zeldov. Mapping the twist-angle disorder and Landau levels in magic-angle graphene. Nature, 581(7806):47–52, May 2020. Publisher: Nature Publishing Group.

[57] A. Wallraff, D. I. Schuster, A. Blais, L. Frunzio, R.-S. Huang, J. Majer, S. Kumar, S. M. Girvin, and R. J. Schoelkopf. Strong coupling of a single photon to a superconducting qubit using circuit quantum electrodynamics. Nature, 431:162–167, 2004.

[58] A. Blais, S. M. Girvin, and W. D. Oliver. Quantum information processing and quantum optics with circuit quantum electrodynamics. Nature Physics, 16:247–256, 2020.

[59] A. Blais, R-S. Huang, A. Wallraff, S. M. Girvin, and R. J. Schoelkopf. Cavity quantum electrodynamics for superconducting electrical circuits: An architecture for quantum computation. Phys. Rev. A, 69:062320, 2004.

[60] J. M. Martinis, M. H. Devoret, and J. Clarke. Quantum josephson junction circuits and the dawn of artificial atoms. Nature Physics, 16:234–237, 2020.

[61] P. Krantz, M. Kjaergaard, F. Yan, T. P. Orlando, S. Gustavsson, and W. D. Oliver). A quantum engineer's guide to superconducting qubits. Applied Physics Reviews, 6:021318, 2019.

[62] S. Haroche, M. Brune, and J. M. Raimond. From cavity to circuit quantum electrodynamics. Nature Physics, 16:243–246, 2020.

[63] J. M. Fink, M. Göppl, M. Baur, R. Bianchetti, P. J. Leek, A. Blais, and A. Wallraff. Climbing the Jaynes–Cummings ladder and observing its nonlinearity in a cavity qed system. Nature, 454:315–318, 2008.

[64] M. H. Devoret and R. J. Schoelkopf. Superconducting Circuits for Quantum Information: An Outlook. Science, 339(6124):1169–1174, March 2013. Publisher: American Association for the Advancement of Science.

[65] S.M. Girvin. Circuit QED: Superconducting Qubits Coupled to Microwave Photons. Oxford University Press, 2014.

[66] I. Schuster. Circuit Quantum Electrodynamics. PhD dissertation, Yale University.

[67] Jens Koch, Terri M. Yu, Jay Gambetta, A. A. Houck, D. I. Schuster, J. Majer, Alexandre Blais, M. H. Devoret, S. M. Girvin, and R. J. Schoelkopf. Charge-insensitive qubit design derived from the Cooper pair box. Physical Review A, 76(4):042319, October 2007. Publisher: American Physical Society.

[68] Irfan Siddiqi. Engineering high-coherence superconducting qubits. Nature Reviews Materials, September 2021.

[69] William D. Oliver and Paul B. Welander. Materials in superconducting quantum bits. MRS Bulletin, 38(10):816–825, October 2013. Publisher: Cambridge University Press.

[70] Morten Kjaergaard, Mollie E. Schwartz, Jochen Braumüller, Philip Krantz, Joel I.-J. Wang, Simon Gustavsson, and William D. Oliver. Superconducting Qubits: Current State of Play. Annual Review of Condensed Matter Physics, 11(1):369–395, 2020.

[71] P. Krantz, M. Kjaergaard, F. Yan, T. P. Orlando, S. Gustavsson, and W. D. Oliver. A quantum engineer's guide to superconducting qubits. Applied Physics Reviews, 6(2):021318, June 2019.

[72] F. Arute et al. Quantum supremacy using a programmable superconducting processor. Nature, 574:505–510, 2019.

[73] Alexandre Blais, Steven M. Girvin, and William D. Oliver. Quantum information processing and quantum optics with circuit quantum electrodynamics. Nature Physics, 16(3):247–256, March 2020. Number: 3 Publisher: Nature Publishing Group.

[74] Isaac Amidror. The Theory of the Moiré Phenomenon. Computational Imaging and Vision. Springer Netherlands, Dordrecht, 2000.

[75] Guohong Li, A. Luican, J. M. B. Lopes dos Santos, A. H. Castro Neto, A. Reina, J. Kong, and E. Y. Andrei. Observation of Van Hove singularities in twisted graphene layers. Nature Physics, 6(2):109–113, February 2010. Publisher: Nature Publishing Group.

[76] Wikipedia contributors. Moiré pattern — Wikipedia, the free encyclopedia, 2022. [Online; accessed 1-April-2022].

[77] J. M. B. Lopes dos Santos, N. M. R. Peres, and A. H. Castro Neto. Graphene Bilayer with a Twist: Electronic Structure. Physical Review Letters, 99(25):256802, December 2007. Publisher: American Physical Society.

[78] J. M. B. Lopes dos Santos, N. M. R. Peres, and A. H. Castro Neto. Continuum model of the twisted graphene bilayer. Physical Review B, 86(15):155449, October 2012. Publisher: American Physical Society.

[79] Yuan Cao, Valla Fatemi, Ahmet Demir, Shiang Fang, Spencer L. Tomarken, Jason Y. Luo, Javier D. Sanchez-Yamagishi, Kenji Watanabe, Takashi Taniguchi, Efthimios Kaxiras, Ray C. Ashoori, and Pablo Jarillo-Herrero. Correlated insulator behaviour at half-filling in magic-angle graphene superlattices. Nature, 556(7699):80–84, April 2018. Publisher: Nature Publishing Group.

[80] Pilkyung Moon and Mikito Koshino. Energy spectrum and quantum Hall effect in twisted bilayer graphene. Physical Review B, 85(19):195458, May 2012.

[81] Rafi Bistritzer and Allan H. MacDonald. Moiré bands in twisted double-layer graphene. Proceedings of the National Academy of Sciences, 108(30):12233–12237, July 2011.

[82] Stephen Carr, Daniel Massatt, Shiang Fang, Paul Cazeaux, Mitchell Luskin, and Efthimios Kaxiras. Twistronics: Manipulating the electronic properties of two-dimensional layered structures through their twist angle. Physical Review B, 95(7):075420, February 2017.

[83] Yuan Cao, Valla Fatemi, Shiang Fang, Kenji Watanabe, Takashi Taniguchi, Efthimios Kaxiras, and Pablo Jarillo-Herrero. Unconventional superconductivity in magic-angle graphene superlattices. Nature, 556(7699):43–50, April 2018. Publisher: Nature Publishing Group.

[84] Leon Balents. General continuum model for twisted bilayer graphene and arbitrary smooth deformations. SciPost Physics, 7(4):048, October 2019.

[85] Pietro Novelli, Iacopo Torre, Frank H. L. Koppens, Fabio Taddei, and Marco Polini. Optical and plasmonic properties of twisted bilayer graphene: Impact of interlayer tunneling asymmetry and ground-state charge inhomogeneity. Physical Review B, 102(12):125403, September 2020. Publisher: American Physical Society.

[86] Yuan Cao. Study of electronic correlation and superconductivity in twisted graphene superlattices. Thesis, Massachusetts Institute of Technology, 2020. Accepted: 2021-01-06.

[87] Alexander Kerelsky, Leo J. McGilly, Dante M. Kennes, Lede Xian, Matthew Yankowitz, Shaowen Chen, K. Watanabe, T. Taniguchi, James Hone, Cory Dean, Angel Rubio, and Abhay N. Pasupathy. Maximized electron interactions at the magic angle in twisted bilayer graphene. Nature, 572(7767):95–100, August 2019. Publisher: Nature Publishing Group.

[88] Yuhang Jiang, Xinyuan Lai, Kenji Watanabe, Takashi Taniguchi, Kristjan Haule, Jinhai Mao, and Eva Y. Andrei. Charge order and broken rotational symmetry in magic-angle twisted bilayer graphene. Nature, 573(7772):91–95, September 2019. Number: 7772 Publisher: Nature Publishing Group.

[89] Yonglong Xie, Biao Lian, Berthold Jäck, Xiaomeng Liu, Cheng-Li Chiu, Kenji Watanabe, Takashi Taniguchi, B. Andrei Bernevig, and Ali Yazdani. Spectroscopic signatures of many-body correlations in magic-angle twisted bilayer graphene. Nature, 572(7767):101–105, August 2019. Publisher: Nature Publishing Group.

[90] Youngjoon Choi, Jeannette Kemmer, Yang Peng, Alex Thomson, Harpreet Arora, Robert Polski, Yiran Zhang, Hechen Ren, Jason Alicea, Gil Refael, Felix von Oppen, Kenji Watanabe, Takashi Taniguchi, and Stevan Nadj-Perge. Electronic correlations in twisted bilayer graphene near the magic angle. Nature Physics, 15(11):1174–1180, November 2019. Publisher: Nature Publishing Group.

[91] Leon Balents, Cory R. Dean, Dmitri K. Efetov, and Andrea F. Young. Superconductivity and strong correlations in moiré flat bands. Nature Physics, 16(7):725–733, July 2020. Number: 7 Publisher: Nature Publishing Group.

[92] Grigory Tarnopolsky, Alex Jura Kruchkov, and Ashvin Vishwanath. Origin of Magic Angles in Twisted Bilayer Graphene. Physical Review Letters, 122(10):106405, March 2019.

[93] Stephen Carr, Shiang Fang, Ziyan Zhu, and Efthimios Kaxiras. Exact continuum model for low-energy electronic states of twisted bilayer graphene. Physical Review Research, 1(1):013001, August 2019. Publisher: American Physical Society.

[94] Y. Cao, J.Y. Luo, V. Fatemi, S. Fang, J.D. Sanchez-Yamagishi, K. Watanabe, T. Taniguchi, E. Kaxiras, and P. Jarillo-Herrero. Superlattice-Induced Insulating States and Valley-Protected Orbits in Twisted Bilayer Graphene. Physical Review Letters, 117(11):116804, September 2016. Publisher: American Physical Society.

[95] E. Suárez Morell, J. D. Correa, P. Vargas, M. Pacheco, and Z. Barticevic. Flat bands in slightly twisted bilayer graphene: Tight-binding calculations. Physical Review B, 82(12):121407, September 2010. Publisher: American Physical Society.

[96] Aaron L. Sharpe, Eli J. Fox, Arthur W. Barnard, Joe Finney, Kenji Watanabe, Takashi Taniguchi, M. A. Kastner, and David Goldhaber-Gordon. Emergent ferromagnetism near three-quarters filling in twisted bilayer graphene. Science, 365(6453):605–608, August 2019. Publisher: American Association for the Advancement of Science.

[97] M. Serlin, C. L. Tschirhart, H. Polshyn, Y. Zhang, J. Zhu, K. Watanabe, T. Taniguchi, L. Balents, and A. F. Young. Intrinsic quantized anomalous Hall effect in a moiré heterostructure. Science, 367(6480):900–903, February 2020.

[98] E. J. Mele. Band symmetries and singularities in twisted multilayer graphene. Physical Review B, 84(23):235439, December 2011.

[99] Patrick J. Ledwith, Eslam Khalaf, and Ashvin Vishwanath. Strong coupling theory of magic-angle graphene: A pedagogical introduction. Annals of Physics, 435:168646, December 2021.

[100] Shiang Fang and Efthimios Kaxiras. Electronic structure theory of weakly interacting bilayers. Physical Review B, 93(23):235153, June 2016. Publisher: American Physical Society.

[101] Stephen Carr, Daniel Massatt, Steven B. Torrisi, Paul Cazeaux, Mitchell Luskin, and Efthimios Kaxiras. Relaxation and domain formation in incommensurate two-dimensional heterostructures. Physical Review B, 98(22):224102, 2018. Publisher: American Physical Society.

[102] Shiang Fang, Stephen Carr, Ziyan Zhu, Daniel Massatt, and Efthimios Kaxiras. Angle-Dependent {\it Ab initio} Low-Energy Hamiltonians for a Relaxed Twisted Bilayer Graphene Heterostructure. arXiv:1908.00058 [cond-mat], July 2019. arXiv: 1908.00058.

[103] Shiang Fang. Multi-scale Theoretical Modeling of Twisted van der Waals Bilayers. PhD dissertation, Harvard University, Graduate School of Arts and Sciences, 2019.

[104] Nguyen N. T. Nam and Mikito Koshino. Lattice relaxation and energy band modulation in twisted bilayer graphene. Physical Review B, 96(7):075311, August 2017. Publisher: American Physical Society.

[105] Kazuyuki Uchida, Shinnosuke Furuya, Jun-Ichi Iwata, and Atsushi Oshiyama. Atomic corrugation and electron localization due to Moir\'e patterns in twisted bilayer graphenes. Physical Review B, 90(15):155451, October 2014. Publisher: American Physical Society.

[106] Hyobin Yoo, Rebecca Engelke, Stephen Carr, Shiang Fang, Kuan Zhang, Paul Cazeaux, Suk Hyun Sung, Robert Hovden, Adam W. Tsen, Takashi Taniguchi, Kenji Watanabe, Gyu-Chul Yi, Miyoung Kim, Mitchell Luskin, Ellad B. Tadmor, Efthimios Kaxiras, and Philip Kim. Atomic and electronic reconstruction at the van der Waals interface in twisted bilayer graphene. Nature Materials, 18(5):448–453, May 2019. Publisher: Nature Publishing Group.

[107] Teemu J. Peltonen, Risto Ojajärvi, and Tero T. Heikkilä. Mean-field theory for superconductivity in twisted bilayer graphene. Physical Review B, 98(22):220504, 2018. Publisher: American Physical Society.

[108] Allan H. MacDonald. Bilayer Graphene's Wicked, Twisted Road. Physics, 12:12, May 2019. Publisher: American Physical Society.

[109] Francisco Guinea and Niels R. Walet. Electrostatic effects, band distortions, and superconductivity in twisted graphene bilayers. Proceedings of the National Academy of Sciences, 115(52):13174–13179, December 2018. Publisher: National Academy of Sciences.

[110] Patrick A. Lee, Naoto Nagaosa, and Xiao-Gang Wen. Doping a Mott insulator: Physics of high-temperature superconductivity. Reviews of Modern Physics, 78(1):17–85, 2006. Publisher: American Physical Society.

[111] U. Zondiner, A. Rozen, D. Rodan-Legrain, Y. Cao, R. Queiroz, T. Taniguchi, K. Watanabe, Y. Oreg, F. von Oppen, Ady Stern, E. Berg, P. Jarillo-Herrero, and S. Ilani. Cascade of phase transitions and Dirac revivals in magic-angle graphene. Nature, 582(7811):203–208, June 2020. Number: 7811 Publisher: Nature Publishing Group.

[112] Jianpeng Liu and Xi Dai. Orbital magnetic states in moiré graphene systems. Nature Reviews Physics, 3(5):367–382, May 2021. Number: 5 Publisher: Nature Publishing Group.

[113] M. Serlin, C. L. Tschirhart, H. Polshyn, Y. Zhang, J. Zhu, K. Watanabe, T. Taniguchi, L. Balents, and A. F. Young. Intrinsic quantized anomalous Hall effect in a moir\'e heterostructure. arXiv:1907.00261 [cond-mat], June 2019. arXiv: 1907.00261.

[114] Jianpeng Liu, Junwei Liu, and Xi Dai. Pseudo Landau level representation of twisted bilayer graphene: Band topology and implications on the correlated insulating phase. Physical Review B, 99(15):155415, 2019. Publisher: American Physical Society.

[115] Zhida Song, Zhijun Wang, Wujun Shi, Gang Li, Chen Fang, and B. Andrei Bernevig. All Magic Angles in Twisted Bilayer Graphene are Topological. Physical Review Letters, 123(3):036401, July 2019.

[116] Xiaobo Lu, Petr Stepanov, Wei Yang, Ming Xie, Mohammed Ali Aamir, Ipsita Das, Carles Urgell, Kenji Watanabe, Takashi Taniguchi, Guangyu Zhang, Adrian Bachtold, Allan H. MacDonald, and Dmitri K. Efetov. Superconductors, orbital magnets and correlated states in magic-angle bilayer graphene. Nature, 574(7780):653–657, October 2019. Publisher: Nature Publishing Group.

[117] Shuang Wu, Zhenyuan Zhang, K. Watanabe, T. Taniguchi, and Eva Y. Andrei. Chern insulators, van Hove singularities and topological flat bands in magic-angle twisted bilayer graphene. Nature Materials, 20(4):488–494, April 2021. Number: 4 Publisher: Nature Publishing Group.

[118] Ipsita Das, Xiaobo Lu, Jonah Herzog-Arbeitman, Zhi-Da Song, Kenji Watanabe, Takashi Taniguchi, B. Andrei Bernevig, and Dmitri K. Efetov. Symmetry-broken Chern insulators and Rashba-like Landau-level crossings in magic-angle bilayer graphene. Nature Physics, 17(6):710–714, June 2021. Number: 6 Publisher: Nature Publishing Group.

[119] Kevin P. Nuckolls, Myungchul Oh, Dillon Wong, Biao Lian, Kenji Watanabe, Takashi Taniguchi, B. Andrei Bernevig, and Ali Yazdani. Strongly correlated Chern insulators in magic-angle twisted bilayer graphene. Nature, 588(7839):610–615, December 2020. Number: 7839 Publisher: Nature Publishing Group.

[120] Yu Saito, Jingyuan Ge, Louk Rademaker, Kenji Watanabe, Takashi Taniguchi, Dmitry A. Abanin, and Andrea F. Young. Hofstadter subband ferromagnetism and symmetry-broken Chern insulators in twisted bilayer graphene. Nature Physics, 17(4):478–481, April 2021. Number: 4 Publisher: Nature Publishing Group.

[121] Jeong Min Park, Yuan Cao, Kenji Watanabe, Takashi Taniguchi, and Pablo Jarillo-Herrero. Flavour Hund's coupling, Chern gaps and charge diffusivity in moiré graphene. Nature, 592(7852):43–48, April 2021. Number: 7852 Publisher: Nature Publishing Group.

[122] Matthew Yankowitz, Shaowen Chen, Hryhoriy Polshyn, Yuxuan Zhang, K. Watanabe, T. Taniguchi, David Graf, Andrea F. Young, and Cory R. Dean. Tuning superconductivity in twisted bilayer graphene. Science, 363(6431):1059–1064, March 2019.

[123] Kyounghwan Kim, Ashley DaSilva, Shengqiang Huang, Babak Fallahazad, Stefano Larentis, Takashi Taniguchi, Kenji Watanabe, Brian J. LeRoy, Allan H. MacDonald, and Emanuel Tutuc. Tunable moiré bands and strong correlations in small-

twist-angle bilayer graphene. Proceedings of the National Academy of Sciences, 114(13):3364–3369, March 2017.

[124] G. Cassabois, P. Valvin, and B. Gil. Hexagonal boron nitride is an indirect bandgap semiconductor. Nature Photonics, 10(4):262–266, April 2016.

[125] Jiamin Xue, Javier Sanchez-Yamagishi, Danny Bulmash, Philippe Jacquod, Aparna Deshpande, K. Watanabe, T. Taniguchi, Pablo Jarillo-Herrero, and Brian J. LeRoy. Scanning tunnelling microscopy and spectroscopy of ultra-flat graphene on hexagonal boron nitride. Nature Materials, 10(4):282–285, April 2011.

[126] R. Thomas Weitz and Amir Yacoby. Graphene rests easy. Nature Nanotechnology, 5(10):699–700, October 2010.

[127] C. R. Dean, A. F. Young, I. Meric, C. Lee, L. Wang, S. Sorgenfrei, K. Watanabe, T. Taniguchi, P. Kim, K. L. Shepard, and J. Hone. Boron nitride substrates for high-quality graphene electronics. Nature Nanotechnology, 5(10):722–726, October 2010.

[128] T. Taniguchi and K. Watanabe. Synthesis of high-purity boron nitride single crystals under high pressure by using Ba–BN solvent. Journal of Crystal Growth, 303(2):525–529, May 2007.

[129] Mark Zastrow. Meet the crystal growers who sparked a revolution in graphene electronics. Nature, 572(7770):429–432, August 2019. Publisher: Nature Publishing Group.

[130] Plasma cleaning, December 2021. Wikipedia, Page Version ID: 1058913013.

[131] I.-Jan Wang. Superconducting Proximity Effect in Graphene Nanodevices: A Transport and Tunneling Study. PhD thesis, Harvard University, January 2016. Accepted: 2016-04-21.

[132] Yuan Huang, Eli Sutter, Norman N. Shi, Jiabao Zheng, Tianzhong Yang, Dirk Englund, Hong-Jun Gao, and Peter Sutter. Reliable Exfoliation of Large-Area High-Quality Flakes of Graphene and Other Two-Dimensional Materials. ACS Nano, 9(11):10612–10620, November 2015. Publisher: American Chemical Society.

[133] Jonathan N Coleman. Liquid Exfoliation of Defect-Free Graphene. Accounts of Chemical Research, 46(1):14–22, January 2013. Publisher: American Chemical Society.

[134] Jinseon Kim, Sanghyuk Kwon, Dae-Hyun Cho, Byunggil Kang, Hyukjoon Kwon, Youngchan Kim, Sung O. Park, Gwan Yeong Jung, Eunhye Shin, Wan-Gu Kim, Hyungdong Lee, Gyeong Hee Ryu, Minseok Choi, Tae Hyeong Kim, Junghoon Oh, Sungjin Park, Sang Kyu Kwak, Suk Wang Yoon, Doyoung Byun, Zonghoon Lee, and Changgu Lee. Direct exfoliation and dispersion of two-dimensional materials in pure water via temperature control. Nature Communications, 6(1):8294, September 2015.

[135] Roman V. Gorbachev, Ibtsam Riaz , Rahul R. Nair, Rashid Jalil, Liam Britnell, Branson D. Belle , Ernie W. Hill, Kostya S. Novoselov, Kenji Watanabe, Takashi Taniguchi, Andre K. Geim, Peter Blake. Hunting for Monolayer Boron Nitride: Optical and Raman Signatures. Small, 7(4):465–468, 2011.

[136] Daniel Rodan Legrain. Ionic liquid gating in encapsulated hBN/MoS2/hBN devices, May 2016. Accepted: 2016-06-17.

[137] P. J. Zomer, M. H. D. Guimarães, J. C. Brant, N. Tombros, and B. J. van Wees. Fast pick up technique for high quality heterostructures of bilayer graphene and hexagonal boron nitride. Applied Physics Letters, 105(1):013101, July 2014. Publisher: American Institute of Physics.

[138] Filippo Pizzocchero, Lene Gammelgaard, Bjarke S. Jessen, José M. Caridad, Lei Wang, James Hone, Peter Bøggild, and Timothy J. Booth. The hot pick-up technique for batch assembly of van der Waals heterostructures. Nature Communications, 7(1):11894, June 2016.

[139] D. G. Purdie, N. M. Pugno, T. Taniguchi, K. Watanabe, A. C. Ferrari, and A. Lombardo. Cleaning interfaces in layered materials heterostructures. Nature Communications, 9(1):5387, December 2018.

[140] Kyounghwan Kim, Matthew Yankowitz, Babak Fallahazad, Sangwoo Kang, Hema C. P. Movva, Shengqiang Huang, Stefano Larentis, Chris M. Corbet, Takashi Taniguchi, Kenji Watanabe, Sanjay K. Banerjee, Brian J. LeRoy, and Emanuel Tutuc. van der Waals Heterostructures with High Accuracy Rotational Alignment. Nano Letters, 16(3):1989–1995, March 2016. Publisher: American Chemical Society.

[141] Jeong Min Park, Yuan Cao, Kenji Watanabe, Takashi Taniguchi, and Pablo Jarillo-Herrero. Tunable strongly coupled superconductivity in magic-angle twisted trilayer graphene. Nature, 590(7845):249–255, February 2021. Number: 7845 Publisher: Nature Publishing Group.

[142] Zeyu Hao, A. M. Zimmerman, Patrick Ledwith, Eslam Khalaf, Danial Haie Najafabadi, Kenji Watanabe, Takashi Taniguchi, Ashvin Vishwanath, and Philip Kim. Electric field–tunable superconductivity in alternating-twist magic-angle trilayer graphene. Science, 371(6534):1133–1138, March 2021. Publisher: American Association for the Advancement of Science.

[143] L. Wang, I. Meric, P. Y. Huang, Q. Gao, Y. Gao, H. Tran, T. Taniguchi, K. Watanabe, L. M. Campos, D. A. Muller, J. Guo, P. Kim, J. Hone, K. L. Shepard, and C. R. Dean. One-Dimensional Electrical Contact to a Two-Dimensional Material. Science, 342(6158):614–617, November 2013.

[144] A. M. Goossens, V. E. Calado, A. Barreiro, K. Watanabe, T. Taniguchi, and L. M. K. Vandersypen. Mechanical cleaning of graphene. Applied Physics Letters, 100(7):073110, February 2012.

[145] Matthew R. Rosenberger, Hsun-Jen Chuang, Kathleen M. McCreary, Aubrey T. Hanbicki, Saujan V. Sivaram, and Berend T. Jonker. Nano-"Squeegee" for the Creation of Clean 2D Material Interfaces. ACS Applied Materials & Interfaces, 10(12):10379–10387, March 2018.

[146] H. Zu, W. Dai, and A. T. A. M. de Waele. Development of dilution refrigerators—A review. Cryogenics, 121:103390, 2022.

[147] R. Krishna Kumar, X. Chen, G. H. Auton, A. Mishchenko, D. A. Bandurin, S. V. Morozov, Y. Cao, E. Khestanova, M. Ben Shalom, A. V. Kretinin, K. S. Novoselov, L. Eaves, I. V. Grigorieva, L. A. Ponomarenko, V. I. Fal'ko, and A. K. Geim. High-temperature quantum oscillations caused by recurring Bloch states in graphene superlattices. Science, July 2017. Publisher: American Association for the Advancement of Science.

[148] Niels C. H. Hesp, Iacopo Torre, Daniel Rodan-Legrain, Pietro Novelli, Yuan Cao, Stephen Carr, Shiang Fang, Petr Stepanov, David Barcons-Ruiz, Hanan Herzig Sheinfux, Kenji Watanabe, Takashi Taniguchi, Dmitri K. Efetov, Efthimios Kaxiras, Pablo Jarillo-Herrero, Marco Polini, and Frank H. L. Koppens. Observation of interband collective excitations in twisted bilayer graphene. Nature Physics, 17(10):1162–1168, October 2021. Publisher: Nature Publishing Group.

[149] M. Honig, J. A. Sulpizio, J. Drori, A. Joshua, E. Zeldov, and S. Ilani. Local electrostatic imaging of striped domain order in LaAlO3/SrTiO3. Nature Materials, 12(12):1112–1118, December 2013. Publisher: Nature Publishing Group.

[150] M. J. Yoo, T. A. Fulton, H. F. Hess, R. L. Willett, L. N. Dunkleberger, R. J. Chichester, L. N. Pfeiffer, and K. W. West. Scanning Single-Electron Transistor Microscopy: Imaging Individual Charges. Science, April 1997. Publisher: American Association for the Advancement of Science.

[151] Niels Hesp. Exploring twisted bilayer graphene with nano-optics. PhD dissertation, ICFO – Institut de Ciències Fotòniques, 2021.

[152] Çağlar Girit, V. Bouchiat, O. Naaman, Y. Zhang, M. F. Crommie, a. Zettl, and I. Siddiqi. Tunable graphene dc superconducting quantum interference device. Nano Lett., 9(1):198–199, 2009.

[153] C. Ojeda-Aristizabal, M. Ferrier, S. Guéron, and H. Bouchiat. Tuning the proximity effect in a superconductor-graphene-superconductor junction. Phys. Rev. B, 79(16):1–5, 2009.

[154] Katsuyoshi Komatsu, Chuan Li, S. Autier-Laurent, H. Bouchiat, and S. Guéron. Superconducting proximity effect in long superconductor/graphene/ superconductor junctions: From specular Andreev reflection at zero field to the quantum Hall regime. Phys. Rev. B, 86(11):115412, 2012.

[155] M. Ben Shalom, M. J. Zhu, V. I. Fal'ko, A. Mishchenko, A. V. Kretinin, K. S. Novoselov, C. R. Woods, K. Watanabe, T. Taniguchi, A. K. Geim, and J. R. Prance. Quantum oscillations of the critical current and high-field superconducting proximity in ballistic graphene. Nature Physics, 12(4):318–322, April 2016. Publisher: Nature Publishing Group.

[156] V. E. Calado, S. Goswami, G. Nanda, M. Diez, A. R. Akhmerov, K. Watanabe, T. Taniguchi, T. M. Klapwijk, and L. M. K. Vandersypen. Ballistic Josephson junctions in edge-contacted graphene. Nature Nanotechnology, 10(9):761–764, September 2015. Publisher: Nature Publishing Group.

[157] M. T. Allen, O. Shtanko, I. C. Fulga, A. R. Akhmerov, K. Watanabe, T. Taniguchi, P. Jarillo-Herrero, L. S. Levitov, and A. Yacoby. Spatially resolved edge currents and guided-wave electronic states in graphene. Nature Physics, 12(2):128–133, February 2016. Publisher: Nature Publishing Group.

[158] F. Amet, C. T. Ke, I. V. Borzenets, J. Wang, K. Watanabe, T. Taniguchi, R. S. Deacon, M. Yamamoto, Y. Bomze, S. Tarucha, and G. Finkelstein. Supercurrent in the quantum Hall regime. Science, 352(6288):966–969, May 2016. Publisher: American Association for the Advancement of Science.

[159] C. Tonnoir, A. Kimouche, J. Coraux, L. Magaud, B. Delsol, B. Gilles, and C. Chapelier. Induced superconductivity in graphene grown on rhenium. Phys. Rev. Lett., 111(24):246805, 2013.

[160] Fabian D Natterer, Jeonghoon Ha, Hongwoo Baek, Duming Zhang, William G Cullen, Nikolai B Zhitenev, Young Kuk, and Joseph A Stroscio. Scanning tunneling spectroscopy of proximity superconductivity in epitaxial multilayer graphene. Phys. Rev. B, 93:045406, 2016.

[161] Adrien Allain, Zheng Han, and Vincent Bouchiat. Electrical control of the superconducting-to-insulating transition in graphene–metal hybrids. Nat. Mater., 11(7):590–594, 2012.

[162] Zheng Han, Adrien Allain, Hadi Arjmandi-Tash, Konstantin Tikhonov, Mikhail Feigel'man, Benjamin Sacépé, Vincent Bouchiat, Mikhail Feigel'man, Benjamin Sacépé, and Vincent Bouchiat. Collapse of superconductivity in a hybrid tin–graphene Josephson junction array. Nat. Phys., 10(5):380–386, 2014.

[163] Netanel H. Lindner, Erez Berg, Gil Refael, and Ady Stern. Fractionalizing majorana fermions: Non-abelian statistics on the edges of abelian quantum hall states. Phys. Rev. X, 2(4):041002, 2012.

[164] David J Clarke, Jason Alicea, and Kirill Shtengel. Exotic non-abelian anyons from conventional fractional quantum Hall states. Nat. Commun., 4:1348, 2013.

[165] Roger S K Mong, David J. Clarke, Jason Alicea, Netanel H. Lindner, Paul Fendley, Chetan Nayak, Yuval Oreg, Ady Stern, Erez Berg, Kirill Shtengel, and Matthew P A

Fisher. Universal topological quantum computation from a superconductor-abelian quantum hall heterostructure. Phys. Rev. X, 4(1):011036, 2014.

[166] Pablo San-Jose, Ramón Aguado, Francisco Guinea, J Fernandez-Rossier, and Jose Lado. Majorana Zero Modes in Graphene. Phys. Rev. X, 5:041042, 2015.

[167] H. Le Sueur, P. Joyez, H. Pothier, C. Urbina, and D. Esteve. Phase controlled superconducting proximity effect probed by tunneling spectroscopy. Phys. Rev. Lett., 100(19):197002, 2008.

[168] J-D Pillet, C H L Quay, P Morfin, C Bena, A Levy Yeyati, and P Joyez. Andreev bound states in supercurrent-carrying carbon nanotubes revealed. Nat. Phys., 6(12):965–969, 2010.

[169] W. Chang, V. E. Manucharyan, T. S. Jespersen, J. Nygård, and C. M. Marcus. Tunneling spectroscopy of quasiparticle bound states in a spinful josephson junction. Phys. Rev. Lett., 110(21):217005, 2013.

[170] J.-D. Pillet, P. Joyez, Rok Žitko, and M. F. Goffman. Tunneling spectroscopy of a single quantum dot coupled to a superconductor: From Kondo ridge to Andreev bound states. Phys. Rev. B, 88(4):045101, jul 2013.

[171] L Bretheau, Ç Ö Girit, H Pothier, D Esteve, and C Urbina. Exciting Andreev pairs in a superconducting atomic contact. Nature, 499(7458):312–315, jul 2013.

[172] L Bretheau, Ç Ö Girit, C Urbina, D Esteve, and H Pothier. Supercurrent Spectroscopy of Andreev States. Phys. Rev. X, 3(4):041034, 2013.

[173] F. Amet, J. R. Williams, A. G. F. Garcia, M. Yankowitz, K. Watanabe, T. Taniguchi, and D. Goldhaber-Gordon. Tunneling spectroscopy of graphene-boron-nitride heterostructures. Phys. Rev. B, 85(7):073405, feb 2012.

[174] Dorri Halbertal, Moshe Ben Shalom, Aviram Uri, Kousik Bagani, Alexander Y. Meltzer, Ido Marcus, Yuri Myasoedov, John Birkbeck, Leonid S. Levitov, Andre K. Geim, and Eli Zeldov. Imaging resonant dissipation from individual atomic defects in graphene. arXiv:1710.01486, 2017.

[175] D. C. Ralph, C. T. Black, and M. Tinkham. Spectroscopic measurements of discrete electronic states in single metal particles. Phys. Rev. Lett., 74(16):3241–3244, 1995.

[176] C. T. Black, D. C. Ralph, and M. Tinkham. Spectroscopy of the Superconducting Gap in Individual Nanometer-Scale Aluminum Particles. Phys. Rev. Lett., 76(4):688–691, 1996.

[177] A. Eichler, M. Weiss, S. Oberholzer, C. Schönenberger, A. Levy Yeyati, J. C. Cuevas, and A. Martín-Rodero. Even-odd effect in andreev transport through a carbon nanotube quantum dot. Phys. Rev. Lett., 99(12):5–8, 2007.

[178] Yong J. Doh, Silvano De Franceschi, E. P A M Bakkers, and Leo P. Kouwenhoven. Andreev reflection versus Coulomb blockade in hybrid Semiconductor nanowire devices. Nano Lett., 8(12):4098–4102, 2008.

[179] Clemens B. Winkelmann, Nicolas Roch, Wolfgang Wernsdorfer, Vincent Bouchiat, and Franck Balestro. Superconductivity in a single-C60 transistor. Nat. Phys., 5(12):876–879, 2009.

[180] Y. Nakamura, Yu A. Pashkin, and J. S. Tsai. Coherent control of macroscopic quantum states in a single-Cooper-pair box. Nature, 398(6730):786–788, April 1999. Publisher: Nature Publishing Group.

[181] T.W. Larsen, K.D. Petersson, F. Kuemmeth, T.S. Jespersen, P. Krogstrup, J. Nygård, and C.M. Marcus. Semiconductor-Nanowire-Based Superconducting Qubit. Physical Review Letters, 115(12):127001, September 2015. Publisher: American Physical Society.

[182] F. Luthi, T. Stavenga, O.W. Enzing, A. Bruno, C. Dickel, N.K. Langford, M.A. Rol, T.S. Jespersen, J. Nygård, P. Krogstrup, and L. DiCarlo. Evolution of Nanowire Transmon Qubits and Their Coherence in a Magnetic Field. Physical Review Letters, 120(10):100502, March 2018. Publisher: American Physical Society.

[183] Lucas Casparis, Malcolm R. Connolly, Morten Kjaergaard, Natalie J. Pearson, Anders Kringhøj, Thorvald W. Larsen, Ferdinand Kuemmeth, Tiantian Wang, Candice Thomas, Sergei Gronin, Geoffrey C. Gardner, Michael J. Manfra, Charles M. Marcus, and Karl D. Petersson. Superconducting gatemon qubit based on a proximitized two-dimensional electron gas. Nature Nanotechnology, 13(10):915–919, October 2018. Publisher: Nature Publishing Group.

[184] J. Kelly, R. Barends, A. G. Fowler, A. Megrant, E. Jeffrey, T. C. White, D. Sank, J. Y. Mutus, B. Campbell, Yu Chen, Z. Chen, B. Chiaro, A. Dunsworth, I.-C. Hoi, C. Neill, P. J. J. O'Malley, C. Quintana, P. Roushan, A. Vainsencher, J. Wenner, A. N. Cleland, and John M. Martinis. State preservation by repetitive error detection in a superconducting quantum circuit. Nature, 519(7541):66–69, March 2015. Publisher: Nature Publishing Group.

[185] Fei Yan, Simon Gustavsson, Archana Kamal, Jeffrey Birenbaum, Adam P. Sears, David Hover, Ted J. Gudmundsen, Danna Rosenberg, Gabriel Samach, S. Weber, Jonilyn L. Yoder, Terry P. Orlando, John Clarke, Andrew J. Kerman, and William D. Oliver. The flux qubit revisited to enhance coherence and reproducibility. Nature Communications, 7(1):12964, November 2016. Publisher: Nature Publishing Group.

[186] Gershon Kurizki, Patrice Bertet, Yuimaru Kubo, Klaus Mølmer, David Petrosyan, Peter Rabl, and Jörg Schmiedmayer. Quantum technologies with hybrid systems. Proceedings of the National Academy of Sciences, 112(13):3866–3873, March 2015. Publisher: National Academy of Sciences.

[187] Audrey Cottet, Matthieu C. Dartiailh, Matthieu M. Desjardins, Tino Cubaynes, Lauriane C. Contamin, Matthieu Delbecq, Jérémie J. Viennot, Laure E. Bruhat, Benoit Douçot, and Takis Kontos. Cavity QED with hybrid nanocircuits: from atomic-like physics to condensed matter phenomena. Journal of Physics: Condensed Matter, 29(43):433002, September 2017. Publisher: IOP Publishing.

[188] Andor Kormányos, Viktor Zólyomi, Neil D. Drummond, and Guido Burkard. Spin-Orbit Coupling, Quantum Dots, and Qubits in Monolayer Transition Metal Dichalcogenides. Physical Review X, 4(1):011034, March 2014. Publisher: American Physical Society.

[189] Nils M. Freitag, Larisa A. Chizhova, Peter Nemes-Incze, Colin R. Woods, Roman V. Gorbachev, Yang Cao, Andre K. Geim, Kostya S. Novoselov, Joachim Burgdörfer, Florian Libisch, and Markus Morgenstern. Electrostatically Confined Monolayer Graphene Quantum Dots with Orbital and Valley Splittings. Nano Letters, 16(9):5798–5805, September 2016. Publisher: American Chemical Society.

[190] Sina Khorasani and Akshay Koottandavida. Nonlinear graphene quantum capacitors for electro-optics. npj 2D Materials and Applications, 1(1):1–7, May 2017. Publisher: Nature Publishing Group.

[191] Felix E. Schmidt, Mark D. Jenkins, Kenji Watanabe, Takashi Taniguchi, and Gary A. Steele. A ballistic graphene superconducting microwave circuit. Nature Communications, 9(1):4069, October 2018. Publisher: Nature Publishing Group.

[192] J. G. Kroll, W. Uilhoorn, K. L. van der Enden, D. de Jong, K. Watanabe, T. Taniguchi, S. Goswami, M. C. Cassidy, and L. P. Kouwenhoven. Magnetic field compatible circuit quantum electrodynamics with graphene Josephson junctions. Nature Communications, 9(1):4615, November 2018. Publisher: Nature Publishing Group.

[193] K. S. Novoselov, A. K. Geim, S. V. Morozov, D. Jiang, M. I. Katsnelson, I. V. Grigorieva, S. V. Dubonos, and A. A. Firsov. Two-dimensional gas of massless Dirac fermions in graphene. Nature, 438(7065):197–200, November 2005. Publisher: Nature Publishing Group.

[194] G. Nanda, J. L. Aguilera-Servin, P. Rakyta, A. Kormányos, R. Kleiner, D. Koelle, K. Watanabe, T. Taniguchi, L. M. K. Vandersypen, and S. Goswami. Current-Phase Relation of Ballistic Graphene Josephson Junctions. Nano Letters, 17(6):3396–3401, June 2017. Publisher: American Chemical Society.

[195] F. Hassler, A. R. Akhmerov, and C. W. J. Beenakker. The top-transmon: a hybrid superconducting qubit for parity-protected quantum computation. New Journal of Physics, 13(9):095004, September 2011. Publisher: IOP Publishing.

[196] A. Kringhøj, L. Casparis, M. Hell, T. W. Larsen, F. Kuemmeth, M. Leijnse, K. Flensberg, P. Krogstrup, J. Nygård, K. D. Petersson, and C. M. Marcus. Anharmonicity

of a superconducting qubit with a few-mode Josephson junction. Physical Review B, 97(6):060508, February 2018. Publisher: American Physical Society.

[197] G. Giovannetti, P. A. Khomyakov, G. Brocks, V. M. Karpan, J. van den Brink, and P. J. Kelly. Doping Graphene with Metal Contacts. Physical Review Letters, 101(2):026803, July 2008. Publisher: American Physical Society.

[198] C. W. J. Beenakker. Universal limit of critical-current fluctuations in mesoscopic Josephson junctions. Physical Review Letters, 67(27):3836–3839, December 1991. Publisher: American Physical Society.

[199] Monica T. Allen, Oles Shtanko, Ion C. Fulga, Joel I.-J. Wang, Daniyar Nurgaliev, Kenji Watanabe, Takashi Taniguchi, Anton R. Akhmerov, Pablo Jarillo-Herrero, Leonid S. Levitov, and Amir Yacoby. Observation of Electron Coherence and Fabry–Perot Standing Waves at a Graphene Edge. Nano Letters, 17(12):7380–7386, December 2017. Publisher: American Chemical Society.

[200] M. J. Zhu, A. V. Kretinin, M. D. Thompson, D. A. Bandurin, S. Hu, G. L. Yu, J. Birkbeck, A. Mishchenko, I. J. Vera-Marun, K. Watanabe, T. Taniguchi, M. Polini, J. R. Prance, K. S. Novoselov, A. K. Geim, and M. Ben Shalom. Edge currents shunt the insulating bulk in gapped graphene. Nature Communications, 8(1):14552, February 2017. Publisher: Nature Publishing Group.

[201] X. Mi, J. V. Cady, D. M. Zajac, J. Stehlik, L. F. Edge, and J. R. Petta. Circuit quantum electrodynamics architecture for gate-defined quantum dots in silicon. Applied Physics Letters, 110(4):043502, January 2017. Publisher: American Institute of Physics.

[202] Valla Fatemi, Sanfeng Wu, Yuan Cao, Landry Bretheau, Quinn D. Gibson, Kenji Watanabe, Takashi Taniguchi, Robert J. Cava, and Pablo Jarillo-Herrero. Electrically tunable low-density superconductivity in a monolayer topological insulator. Science, 362(6417):926–929, November 2018. Publisher: American Association for the Advancement of Science.

[203] K. K. Likharev. Superconducting weak links. Reviews of Modern Physics, 51(1):101–159, January 1979. Publisher: American Physical Society.

[204] J. Pearl. Current distribution in superconducting films carrying quantized fluxoids. Applied Physics Letters, 5(4):65–66, August 1964.

[205] Maayan Moshe, V. G. Kogan, and R. G. Mints. Edge-type Josephson junctions in narrow thin-film strips. Physical Review B, 78(2):020510, July 2008.

[206] Yu. M. Ivanchenko and T. K. Soboleva. Nonlocal interaction in Josephson junctions. Physics Letters A, 147(1):65–69, June 1990.

[207] A. A. Boris, A. Rydh, T. Golod, H. Motzkau, A. M. Klushin, and V. M. Krasnov. Evidence for Nonlocal Electrodynamics in Planar Josephson Junctions. Physical Review Letters, 111(11):117002, September 2013.

[208] A. A. Abdumalikov, G. L. Alfimov, and A. S. Malishevskii. Nonlocal electrodynamics of Josephson vortices in superconducting circuits. Superconductor Science and Technology, 22(2):023001, January 2009.

[209] John R. Clem. Josephson junctions in thin and narrow rectangular superconducting strips. Physical Review B, 81(14):144515, April 2010.

[210] V. G. Kogan, V. V. Dobrovitski, J. R. Clem, Yasunori Mawatari, and R. G. Mints. Josephson junction in a thin film. Physical Review B, 63(14):144501, March 2001.

[211] Peter A. Rosenthal, M. R. Beasley, K. Char, M. S. Colclough, and G. Zaharchuk. Flux focusing effects in planar thin-film grain-boundary Josephson junctions. Applied Physics Letters, 59(26):3482–3484, December 1991.

[212] Shoichi Nagata, H. C. Yang, and D. K. Finnemore. Oscillations in the temperature dependence of Josephson supercurrents in SNS junctions. Physical Review B, 25(9):6012–6014, May 1982.

[213] A. L. Efros and B. I. Shklovskii. Coulomb gap and low temperature conductivity of disordered systems. Journal of Physics C: Solid State Physics, 8(4):L49–L51, February 1975.

[214] Mark Lee, J. G. Massey, V. L. Nguyen, and B. I. Shklovskii. Coulomb gap in a doped semiconductor near the metal-insulator transition: Tunneling experiment and scaling ansatz. Physical Review B, 60(3):1582–1591, July 1999.

[215] B.L. Altshuler and A.G. Aronov. Zero bias anomaly in tunnel resistance and electron—electron interaction. Solid State Communications, 88(11-12):1033–1035, 1993.

[216] M E Gershenzon, V N Gubankov, and M I Falei. Tunnel spectroscopy of the electron-electron interaction in disordered aluminum films. Sov. Phys. JETP, 63:8, 1986.

[217] I. N. Kotel'nikov, S. E. Dizhur, E. N. Morozova, E. V. Devyatov, and V. T. Dolgopolov. Zero-bias tunneling anomaly in a two-dimensional electron system with disorder. JETP Letters, 96(9):577–581, January 2013.

[218] T. Ihn, J. Güttinger, F. Molitor, S. Schnez, E. Schurtenberger, A. Jacobsen, S. Hellmüller, T. Frey, S. Dröscher, C. Stampfer, and K. Ensslin. Graphene single-electron transistors. Materials Today, 13(3):44–50, March 2010.

[219] Folkert K. de Vries, Elías Portolés, Giulia Zheng, Takashi Taniguchi, Kenji Watanabe, Thomas Ihn, Klaus Ensslin, and Peter Rickhaus. Gate-defined Josephson junctions in magic-angle twisted bilayer graphene. Nature Nanotechnology, pages 1–4, May 2021. Publisher: Nature Publishing Group.

[220] Twisted graphene could power a new generation of superconducting electronics - Science - AAAS.

[221] Jonathan R. Prance and Moshe Ben Shalom. Building devices in magic-angle graphene. Nature Nanotechnology, pages 1–2, May 2021. Publisher: Nature Publishing Group.

[222] M. Octavio, M. Tinkham, G. E. Blonder, and T. M. Klapwijk. Subharmonic energy-gap structure in superconducting constrictions. Physical Review B, 27(11):6739–6746, June 1983. Publisher: American Physical Society.

[223] B. I. Halperin and David R. Nelson. Resistive transition in superconducting films. Journal of Low Temperature Physics, 36(5):599–616, September 1979.

[224] Michael R. Sinko, Sergio C. de la Barrera, Olivia Lanes, Kenji Watanabe, Takashi Taniguchi, David Pekker, Michael Hatridge, and Benjamin M. Hunt. Superconducting Edge Contact and Quantum Interference Between Two-Dimensional van der Waals and Three-Dimensional Conventional Superconductors. arXiv:1911.09711 [cond-mat], November 2019. arXiv: 1911.09711.

[225] P. Heij. Single-charge transport in coupled nanostructures. PhD thesis, 2001. Publisher: Delft University Press.

[226] W. G. van der Wiel, S. De Franceschi, J. M. Elzerman, T. Fujisawa, S. Tarucha, and L. P. Kouwenhoven. Electron transport through double quantum dots. Reviews of Modern Physics, 75(1):1–22, December 2002.

[227] John R. Clem. Effect of nearby Pearl vortices upon the I c versus B characteristics of planar Josephson junctions in thin and narrow superconducting strips. Physical Review B, 84(13):134502, October 2011.

[228] John David Jackson. Classical electrodynamics. 2nd ed. edition, 1975.

[229] Hyekyung Won and Kazumi Maki. d-wave superconductor as a model of high-t_c superconductors. Physical Review B, 49:1397–1402, Jan 1994.

[230] G. E. Blonder, M. Tinkham, and T. M. Klapwijk. Transition from metallic to tunneling regimes in superconducting microconstrictions: Excess current, charge imbalance, and supercurrent conversion. Physical Review B, 25(7):4515–4532, April 1982. Publisher: American Physical Society.

[231] F. Gross, B. S. Chandrasekhar, D. Einzel, K. Andres, P. J. Hirschfeld, H. R. Ott, J. Beuers, Z. Fisk, and J. L. Smith. Anomalous temperature dependence of the magnetic field penetration depth in superconducting UBe13. Zeitschrift für Physik B Condensed Matter, 64(2):175–188, June 1986.

[232] P. W. Anderson. More Is Different. Science, 177(4047):393–396, August 1972.

[233] Subir Sachdev. Colloquium: Order and quantum phase transitions in the cuprate superconductors. Reviews of Modern Physics, 75(3):913–932, July 2003. Publisher: American Physical Society.

[234] B. Keimer, S. A. Kivelson, M. R. Norman, S. Uchida, and J. Zaanen. From quantum matter to high-temperature superconductivity in copper oxides. Nature, 518(7538):179–186, February 2015. Number: 7538 Publisher: Nature Publishing Group.

[235] Eduardo Fradkin, Steven A. Kivelson, Michael J. Lawler, James P. Eisenstein, and Andrew P. Mackenzie. Nematic Fermi Fluids in Condensed Matter Physics. Annual Review of Condensed Matter Physics, 1(1):153–178, 2010.

[236] R. M. Fernandes, A. V. Chubukov, and J. Schmalian. What drives nematic order in iron-based superconductors? Nature Physics, 10(2):97–104, February 2014. Number: 2 Publisher: Nature Publishing Group.

[237] V. Hinkov, D. Haug, B. Fauqué, P. Bourges, Y. Sidis, A. Ivanov, C. Bernhard, C. T. Lin, and B. Keimer. Electronic Liquid Crystal State in the High-Temperature Superconductor YBa2Cu3O6.45. Science, 319(5863):597–600, February 2008. Publisher: American Association for the Advancement of Science.

[238] Jiun-Haw Chu, Hsueh-Hui Kuo, James G. Analytis, and Ian R. Fisher. Divergent Nematic Susceptibility in an Iron Arsenide Superconductor. Science, 337(6095):710–712, August 2012. Publisher: American Association for the Advancement of Science.

[239] T.-M. Chuang, M. P. Allan, Jinho Lee, Yang Xie, Ni Ni, S. L. Bud'ko, G. S. Boebinger, P. C. Canfield, and J. C. Davis. Nematic Electronic Structure in the "Parent" State of the Iron-Based Superconductor Ca(Fe1–xCox)2As2. Science, 327(5962):181–184, January 2010. Publisher: American Association for the Advancement of Science.

[240] E. P. Rosenthal, E. F. Andrade, C. J. Arguello, R. M. Fernandes, L. Y. Xing, X. C. Wang, C. Q. Jin, A. J. Millis, and A. N. Pasupathy. Visualization of electron nematicity and unidirectional antiferroic fluctuations at high temperatures in NaFeAs. Nature Physics, 10(3):225–232, March 2014. Number: 3 Publisher: Nature Publishing Group.

[241] Benjamin E. Feldman, Mallika T. Randeria, András Gyenis, Fengcheng Wu, Huiwen Ji, R. J. Cava, Allan H. MacDonald, and Ali Yazdani. Observation of a nematic quantum Hall liquid on the surface of bismuth. Science, 354(6310):316–321, October 2016. Publisher: American Association for the Advancement of Science.

[242] Y. Sato, S. Kasahara, H. Murayama, Y. Kasahara, E.-G. Moon, T. Nishizaki, T. Loew, J. Porras, B. Keimer, T. Shibauchi, and Y. Matsuda. Thermodynamic evidence for a nematic phase transition at the onset of the pseudogap in YBa 2 Cu 3 O y. Nature Physics, 13(11):1074–1078, November 2017. Number: 11 Publisher: Nature Publishing Group.

[243] Laimei Nie, Gilles Tarjus, and Steven Allan Kivelson. Quenched disorder and vestigial nematicity in the pseudogap regime of the cuprates. Proceedings of the National Academy of Sciences, 111(22):7980–7985, June 2014.

[244] E. Fradkin, S. A. Kivelson, and J. M. Tranquada. Theory of intertwined orders in high temperature superconductors. Rev. Mod. Phys, 87:457, 2015.

[245] Rafael M. Fernandes, Peter P. Orth, and Jörg Schmalian. Intertwined Vestigial Order in Quantum Materials: Nematicity and Beyond. Annual Review of Condensed Matter Physics, 10(1):133–154, March 2019. Publisher: Annual Reviews.

[246] Cyril Proust and Louis Taillefer. The Remarkable Underlying Ground States of Cuprate Superconductors. Annual Review of Condensed Matter Physics, 10(1):409–429, 2019.

[247] J. Chang, E. Blackburn, A. T. Holmes, N. B. Christensen, J. Larsen, J. Mesot, Ruixing Liang, D. A. Bonn, W. N. Hardy, A. Watenphul, M. v Zimmermann, E. M. Forgan, and S. M. Hayden. Direct observation of competition between superconductivity and charge density wave order in YBa 2 Cu 3 O 6.67. Nature Physics, 8(12):871–876, December 2012. Number: 12 Publisher: Nature Publishing Group.

[248] S. D. Edkins, A. Kostin, K. Fujita, A. P. Mackenzie, H. Eisaki, S. Uchida, Subir Sachdev, Michael J. Lawler, E.-A. Kim, J. C. Séamus Davis, and M. H. Hamidian. Magnetic field–induced pair density wave state in the cuprate vortex halo. Science, 364(6444):976–980, June 2019. Publisher: American Association for the Advancement of Science.

[249] Jun Li, Paulo J. Pereira, Jie Yuan, Yang-Yang Lv, Mei-Ping Jiang, Dachuan Lu, Zi-Quan Lin, Yong-Jie Liu, Jun-Feng Wang, Liang Li, Xiaoxing Ke, Gustaaf Van Tendeloo, Meng-Yue Li, Hai-Luke Feng, Takeshi Hatano, Hua-Bing Wang, Pei-Heng Wu, Kazunari Yamaura, Eiji Takayama-Muromachi, Johan Vanacken, Liviu F. Chibotaru, and Victor V. Moshchalkov. Nematic superconducting state in iron pnictide superconductors. Nature Communications, 8(1):1880, December 2017. Number: 1 Publisher: Nature Publishing Group.

[250] Junying Shen, Wen-Yu He, Noah Fan Qi Yuan, Zengle Huang, Chang-woo Cho, Seng Huat Lee, Yew San Hor, Kam Tuen Law, and Rolf Lortz. Nematic topological superconducting phase in Nb-doped Bi 2 Se 3. npj Quantum Materials, 2(1):1–7, October 2017. Number: 1 Publisher: Nature Publishing Group.

[251] A. Yu Kuntsevich, M. A. Bryzgalov, V. A. Prudkoglyad, V. P. Martovitskii, Yu G. Selivanov, and E. G. Chizhevskii. Structural distortion behind the nematic superconductivity in Sr x Bi2Se3. New Journal of Physics, 20(10):103022, October 2018. Publisher: IOP Publishing.

[252] K. Matano, M. Kriener, K. Segawa, Y. Ando, and Guo-qing Zheng. Spin-rotation symmetry breaking in the superconducting state of Cu x Bi 2 Se 3. Nature Physics, 12(9):852–854, September 2016. Number: 9 Publisher: Nature Publishing Group.

[253] Tomoya Asaba, B.J. Lawson, Colin Tinsman, Lu Chen, Paul Corbae, Gang Li, Y. Qiu, Y.S. Hor, Liang Fu, and Lu Li. Rotational Symmetry Breaking in a Trigonal Superconductor Nb-doped Bi2Se3. Physical Review X, 7(1):011009, January 2017. Publisher: American Physical Society.

[254] Y. Pan, A. M. Nikitin, G. K. Araizi, Y. K. Huang, Y. Matsushita, T. Naka, and A. de Visser. Rotational symmetry breaking in the topological superconductor Sr x Bi 2 Se 3 probed by upper-critical field experiments. Scientific Reports, 6(1):28632, June 2016. Number: 1 Publisher: Nature Publishing Group.

[255] M. P. Smylie, K. Willa, H. Claus, A. E. Koshelev, K. W. Song, W.-K. Kwok, Z. Islam, G. D. Gu, J. A. Schneeloch, R. D. Zhong, and U. Welp. Superconducting and normal-state anisotropy of the doped topological insulator Sr 0.1 Bi 2 Se 3. Scientific Reports, 8(1):7666, May 2018. Number: 1 Publisher: Nature Publishing Group.

[256] X. Lu, P. Stepanov, W. Yang, M. Xie, M. A. Aamir, I. Das, C. Urgell, K. Watanabe, T. Taniguchi, G. Zhang, A. Bachtold, A. H. MacDonald, D. K. Efetov, Orbital Magnets Superconductors, and Correlated States. in magic angle bilayer graphene. Nature, 574:653–657, 2019.

[257] B. J. Ramshaw, S. E. Sebastian, R. D. McDonald, James Day, B. S. Tan, Z. Zhu, J. B. Betts, Ruixing Liang, D. A. Bonn, W. N. Hardy, and N. Harrison. Quasiparticle mass enhancement approaching optimal doping in a high-Tc superconductor. Science, 348(6232):317–320, April 2015. Publisher: American Association for the Advancement of Science.

[258] P. Walmsley and I. R. Fisher. Determination of the resistivity anisotropy of orthorhombic materials via transverse resistivity measurements. Rev. Sci. Instruments, 88:043901, 2017.

[259] J. Wu, A. T. Bollinger, X. He, and I. Božović. Spontaneous breaking of rotational symmetry in copper oxide superconductors. Nature, 547(7664):432–435, July 2017. Number: 7664 Publisher: Nature Publishing Group.

[260] P. Walmsley and I. R. Fisher. Determination of the resistivity anisotropy of orthorhombic materials via transverse resistivity measurements. Review of Scientific Instruments, 88(4):043901, April 2017. Publisher: American Institute of Physics.

[261] J. W. F. Verderbos, V. Kozii, and L. Fu. Identification of nematic superconductivity from the upper critical field. Phys. Rev. B, 94:094522, 2016.

[262] Vladyslav Kozii, Hiroki Isobe, Jörn W. F. Venderbos, and Liang Fu. Nematic superconductivity stabilized by density wave fluctuations: Possible application to twisted bilayer graphene. Physical Review B, 99(14):144507, April 2019. Publisher: American Physical Society.

[263] Hiroki Isobe, Noah F.Q. Yuan, and Liang Fu. Unconventional Superconductivity and Density Waves in Twisted Bilayer Graphene. Physical Review X, 8(4):041041, December 2018. Publisher: American Physical Society.

[264] Rafael M. Fernandes and Jörn W. F. Venderbos. Nematicity with a twist: Rotational symmetry breaking in a moiré superlattice. Science Advances, 6(32):eaba8834, August 2020. Publisher: American Association for the Advancement of Science.

[265] Matthias Hecker and Jörg Schmalian. Vestigial nematic order and superconductivity in the doped topological insulator Cu x Bi 2 Se 3. npj Quantum Materials, 3(1):1–6, May 2018. Number: 1 Publisher: Nature Publishing Group.

[266] A. Luican, G. Li, A. Reina, J. Kong, R. R. Nair, K. S. Novoselov, A. K. Geim, and E. Y. Andrei. Phys. Rev. Lett., 106:126802, 2011.

[267] Si-Yu Li, Ke-Qin Liu, Long-Jing Yin, Wen-Xiao Wang, Wei Yan, Xu-Qin Yang, Jun-Kai Yang, Haiwen Liu, Hua Jiang, and Lin He. Splitting of Van Hove singularities in slightly twisted bilayer graphene. Physical Review B, 96(15):155416, October 2017. Publisher: American Physical Society.

[268] Jian Kang and Oskar Vafek. Strong Coupling Phases of Partially Filled Twisted Bilayer Graphene Narrow Bands. Physical Review Letters, 122(24):246401, June 2019. Publisher: American Physical Society.

[269] J. F. Dodaro, S. A. Kivelson, Y. Schattner, X. Q. Sun, and C. Wang. Phases of a phenomenological model of twisted bilayer graphene. Physical Review B, 98(7):075154, August 2018. Publisher: American Physical Society.

[270] Dmitry V. Chichinadze, Laura Classen, and Andrey V. Chubukov. Valley magnetism, nematicity, and density wave orders in twisted bilayer graphene. Physical Review B, 102(12):125120, September 2020. Publisher: American Physical Society.

[271] Daniel Blankschtein, Yonathan Shapir, and Amnon Aharony. Potts models in random fields. Physical Review B, 29(3):1263–1267, February 1984. Publisher: American Physical Society.

[272] Shang Liu, Eslam Khalaf, Jong Yeon Lee, and Ashvin Vishwanath. Nematic topological semimetal and insulator in magic-angle bilayer graphene at charge neutrality. Physical Review Research, 3(1):013033, January 2021. Publisher: American Physical Society.

[273] Yu Saito, Jingyuan Ge, Kenji Watanabe, Takashi Taniguchi, and Andrea F. Young. Independent superconductors and correlated insulators in twisted bilayer graphene. Nature Physics, 16(9):926–930, September 2020. Number: 9 Publisher: Nature Publishing Group.

[274] Manfred Sigrist and Kazuo Ueda. Phenomenological theory of unconventional superconductivity. Reviews of Modern Physics, 63(2):239–311, April 1991. Publisher: American Physical Society.

[275] Rafael M. Fernandes and Andrew J. Millis. Nematicity as a Probe of Superconducting Pairing in Iron-Based Superconductors. Physical Review Letters, 111(12):127001, September 2013. Publisher: American Physical Society.

[276] N. E. Hussey, A. P. Mackenzie, J. R. Cooper, Y. Maeno, S. Nishizaki, and T. Fujita. Normal-state magnetoresistance of $\mathrm{sr_2ruo_4}$. Phys. Rev. B, 57:5505–5511, Mar 1998.

[277] L. Klein, J. S. Dodge, C. H. Ahn, G. J. Snyder, T. H. Geballe, M. R. Beasley, and A. Kapitulnik. Anomalous spin scattering effects in the badly metallic itinerant ferromagnet $\mathrm{srruo_3}$. Phys. Rev. Lett., 77:2774–2777, Sep 1996.

[278] S. Y. Li, Louis Taillefer, D. G. Hawthorn, M. A. Tanatar, Johnpierre Paglione, M. Sutherland, R. W. Hill, C. H. Wang, and X. H. Chen. Giant electron-electron scattering in the fermi-liquid state of $Na_{0.7}CoO_2$. Phys. Rev. Lett., 93:056401, Jul 2004.

[279] Yayu Wang, Nyrissa S. Rogado, R. J. Cava, and N. P. Ong. Spin entropy as the likely source of enhanced thermopower in $\mathrm{na}_x\mathrm{co}_2\mathrm{o}_4$. Nature, 423:425–, May 2003.

[280] T. Shibauchi, A. Carrington, and Y. Matsuda. A quantum critical point lying beneath the superconducting dome in iron pnictides. Annual Review of Condensed Matter Physics, 5(1):113–135, 2014.

[281] H. Takagi, B. Batlogg, H. L. Kao, J. Kwo, R. J. Cava, J. J. Krajewski, and W. F. Peck. Systematic evolution of temperature-dependent resistivity in $\mathrm{la}_{2-x}\mathrm{sr}_x\mathrm{cuo}_4$. Phys. Rev. Lett., 69:2975–2978, Nov 1992.

[282] P. Giraldo-Gallo, J. A. Galvis, Z. Stegen, K. A. Modic, F. F. Balakirev, J. B. Betts, X. Lian, C. Moir, S. C. Riggs, J. Wu, A. T. Bollinger, X. He, I. Božović, B. J. Ramshaw, R. D. McDonald, G. S. Boebinger, and A. Shekhter. Scale-invariant magnetoresistance in a cuprate superconductor. Science, 361(6401):479–481, 2018.

[283] Hilbert v. Löhneysen, Achim Rosch, Matthias Vojta, and Peter Wölfle. Fermi-liquid instabilities at magnetic quantum phase transitions. Rev. Mod. Phys., 79:1015–1075, Aug 2007.

[284] Andrea Damascelli, Zahid Hussain, and Zhi-Xun Shen. Angle-resolved photoemission studies of the cuprate superconductors. Rev. Mod. Phys., 75:473–541, Apr 2003.

[285] D. van der Marel, H. J. A. Molegraaf, J. Zaanen, Z. Nussinov, F. Carbone, A. Damascelli, H. Eisaki, M. Greven, P. H. Kes, and M. Li. Quantum critical behaviour in a high-tc superconductor. Nature, 425:271, Sep 2003.

[286] S.-C. Wang, H.-B. Yang, A. K. P. Sekharan, H. Ding, J. R. Engelbrecht, X. Dai, Z. Wang, A. Kaminski, T. Valla, T. Kidd, A. V. Fedorov, and P. D. Johnson. Quasiparticle line shape of $\mathrm{sr_2ruo_4}$ and its relation to anisotropic transport. Phys. Rev. Lett., 92:137002, Apr 2004.

[287] Jan Zaanen. Superconductivity: Why the temperature is high. Nature, 430(6999):512–513, Jul 2004.

[288] Debanjan Chowdhury, Yochai Werman, Erez Berg, and T. Senthil. Translationally invariant non-fermi-liquid metals with critical fermi surfaces: Solvable models. Phys. Rev. X, 8:031024, Jul 2018.

[289] Mike Blake. Universal charge diffusion and the butterfly effect in holographic theories. Phys. Rev. Lett., 117:091601, Aug 2016.

[290] Thomas Hartman, Sean A. Hartnoll, and Raghu Mahajan. Upper bound on diffusivity. Phys. Rev. Lett., 119:141601, Oct 2017.

[291] J. A. N. Bruin, H. Sakai, R. S. Perry, and A. P. Mackenzie. Similarity of scattering rates in metals showing t-linear resistivity. Science, 339(6121):804–807, 2013.

[292] A. Legros, S. Benhabib, W. Tabis, F. Laliberté, M. Dion, M. Lizaire, B. Vignolle, D. Vignolles, H. Raffy, Z. Z. Li, P. Auban-Senzier, N. Doiron-Leyraud, P. Fournier, D. Colson, L. Taillefer, and C. Proust. Universal t-linear resistivity and planckian dissipation in overdoped cuprates. Nature Physics, 14, 2018.

[293] Interestingly for both devices at fillings near $\nu = -2 - \delta$ (MA1) and $\nu = 2 + \delta$ (MA4), we observe a broad shoulder around 5 K where the resistivity drops by a substantial fraction. The suppression in the resistivity, before the eventual onset of SC, could be a signature of strong local pairing fluctuations. We will elaborate on this elsewhere.

[294] The term “strange metal" is typically used to denote a wide variety of unusual metallic behavior, seemingly at odds with the expectations in a weakly interacting Fermi liquid. All strange metals do not necessarily have identical reasons for the strangeness. Our usage of the term is in keeping with this practice.

[295] Jian-Hao Chen, Chaun Jang, Shudong Xiao, Masa Ishigami, and Michael S. Fuhrer. Intrinsic and extrinsic performance limits of graphene devices on sio2. Nature Nanotechnology, 3:206 –, Mar 2008.

[296] C. R. Dean, A. F. Young, I. Meric, C. Lee, L. Wang, S. Sorgenfrei, K. Watanabe, T. Taniguchi, P. Kim, K. L. Shepard, and J. Hone. Boron nitride substrates for high-quality graphene electronics. Nature Nanotechnology, 5:722, Aug 2010.

[297] S. Das Sarma, Shaffique Adam, E. H. Hwang, and Enrico Rossi. Electronic transport in two-dimensional graphene. Rev. Mod. Phys., 83:407–470, May 2011.

[298] Fengcheng Wu, Euyheon Hwang, and Sankar Das Sarma. Phonon-induced giant linear-in-T resistivity in magic angle twisted bilayer graphene: Ordinary strangeness and exotic superconductivity. Physical Review B, 99(16):165112, April 2019.

[299] Indra Yudhistira, Nilotpal Chakraborty, Girish Sharma, Derek Y. H. Ho, Evan Laksono, Oleg P. Sushkov, Giovanni Vignale, and Shaffique Adam. Gauge-phonon dominated resistivity in twisted bilayer graphene near magic angle. Phys. Rev. B, 99:140302, Apr 2019.

[300] Héctor Ochoa. Moir\'e-pattern fluctuations and electron-phason coupling in twisted bilayer graphene. arXiv e-prints, page arXiv:1905.10850, May 2019.

[301] Ting-Fung Chung, Yang Xu, and Yong P. Chen. Transport measurements in twisted bilayer graphene: Electron-phonon coupling and landau level crossing. Phys. Rev. B, 98:035425, Jul 2018.

[302] Hryhoriy Polshyn, Matthew Yankowitz, Shaowen Chen, Yuxuan Zhang, K. Watanabe, T. Taniguchi, Cory R. Dean, and Andrea F. Young. Large linear-in-temperature resistivity in twisted bilayer graphene. Nature Physics, 15(10):1011–1016, October 2019.

[303] Peter T. Brown, Debayan Mitra, Elmer Guardado-Sanchez, Reza Nourafkan, Alexis Reymbaut, Charles-David Hébert, Simon Bergeron, A. M. S. Tremblay, Jure Kokalj, David A. Huse, Peter Schauss, and Waseem S. Bakr. Bad metallic transport in a cold atom Fermi-Hubbard system. arXiv e-prints, page arXiv:1802.09456, February 2018.

[304] Connie H. Mousatov, Ilya Esterlis, and Sean A. Hartnoll. Bad metallic transport in a modified Hubbard model. arXiv e-prints, page arXiv:1803.08054, March 2018.

[305] Joseph Orenstein, G. A. Thomas, A. J. Millis, S. L. Cooper, D. H. Rapkine, T. Timusk, L. F. Schneemeyer, and J. V. Waszczak. Frequency- and temperature-dependent conductivity in $\mathrm{yba_2cu_3o_{6+x}}$ crystals. Phys. Rev. B, 42:6342–6362, Oct 1990.

[306] C. C. Homes, S. V. Dordevic, M. Strongin, D. A. Bonn, Ruixing Liang, W. N. Hardy, Seiki Komiya, Yoichi Ando, G. Yu, N. Kaneko, X. Zhao, M. Greven, D. N. Basov, and T. Timusk. A universal scaling relation in high-temperature superconductors. Nature, 430:539, Jul 2004.

[307] Tamaghna Hazra, Nishchhal Verma, and Mohit Randeria. Upper bounds on the superfluid stiffness and superconducting T_c: Applications to twisted-bilayer graphene and ultra-cold Fermi gases. arXiv e-prints, page arXiv:1811.12428, November 2018.

[308] P. San-Jose, J. González, and F. Guinea. Non-Abelian Gauge Potentials in Graphene Bilayers. Physical Review Letters, 108(21):216802, May 2012. Publisher: American Physical Society.

[309] Hoi Chun Po, Liujun Zou, Ashvin Vishwanath, and T. Senthil. Origin of Mott Insulating Behavior and Superconductivity in Twisted Bilayer Graphene. Physical Review X, 8(3):031089, September 2018.

[310] Ya-Hui Zhang, Hoi Chun Po, and T. Senthil. Landau level degeneracy in twisted bilayer graphene: Role of symmetry breaking. Physical Review B, 100(12):125104, September 2019.

[311] Hoi Chun Po, Liujun Zou, T. Senthil, and Ashvin Vishwanath. Faithful tight-binding models and fragile topology of magic-angle bilayer graphene. Physical Review B, 99(19):195455, May 2019.

[312] Ming Xie and Allan H. MacDonald. On the nature of the correlated insulator states in twisted bilayer graphene. arXiv:1812.04213 [cond-mat], December 2018. arXiv: 1812.04213.

[313] Masayuki Ochi, Mikito Koshino, and Kazuhiko Kuroki. Possible correlated insulating states in magic-angle twisted bilayer graphene under strongly competing interactions. Physical Review B, 98(8):081102, August 2018.

[314] Asaf Rozen, Jeong Min Park, Uri Zondiner, Yuan Cao, Daniel Rodan-Legrain, Takashi Taniguchi, Kenji Watanabe, Yuval Oreg, Ady Stern, Erez Berg, Pablo Jarillo-Herrero, and Shahal Ilani. Entropic evidence for a Pomeranchuk effect in magic-angle graphene. Nature, 592(7853):214–219, April 2021. Number: 7853 Publisher: Nature Publishing Group.

[315] I. Brihuega, P. Mallet, H. González-Herrero, G. Trambly de Laissardière, M. M. Ugeda, L. Magaud, J. M. Gómez-Rodríguez, F. Ynduráin, and J.-Y. Veuillen. Unraveling the Intrinsic and Robust Nature of van Hove Singularities in Twisted Bilayer Graphene by Scanning Tunneling Microscopy and Theoretical Analysis. Physical Review Letters, 109(19):196802, November 2012. Publisher: American Physical Society.

[316] Dillon Wong, Yang Wang, Jeil Jung, Sergio Pezzini, Ashley M. DaSilva, Hsin-Zon Tsai, Han Sae Jung, Ramin Khajeh, Youngkyou Kim, Juwon Lee, Salman Kahn, Sajjad Tollabimazraehno, Haider Rasool, Kenji Watanabe, Takashi Taniguchi, Alex Zettl, Shaffique Adam, Allan H. MacDonald, and Michael F. Crommie. Local spectroscopy of moiré-induced electronic structure in gate-tunable twisted bilayer graphene. Physical Review B, 92(15):155409, October 2015.

[317] S.L. Tomarken, Y. Cao, A. Demir, K. Watanabe, T. Taniguchi, P. Jarillo-Herrero, and R.C. Ashoori. Electronic Compressibility of Magic-Angle Graphene Superlattices. Physical Review Letters, 123(4):046601, July 2019. Publisher: American Physical Society.

[318] J. Waissman, M. Honig, S. Pecker, A. Benyamini, A. Hamo, and S. Ilani. Realization of pristine and locally tunable one-dimensional electron systems in carbon nanotubes. Nature Nanotechnology, 8(8):569–574, August 2013. Number: 8 Publisher: Nature Publishing Group ls.

[319] J. P. Eisenstein, L. N. Pfeiffer, and K. W. West. Negative compressibility of interacting two-dimensional electron and quasiparticle gases. Physical Review Letters, 68(5):674–677, February 1992. Publisher: American Physical Society.

[320] Ming Xie and A.H. MacDonald. Nature of the Correlated Insulator States in Twisted Bilayer Graphene. Physical Review Letters, 124(9):097601, March 2020. Publisher: American Physical Society.

[321] D. B. McWhan, J. P. Remeika, T. M. Rice, W. F. Brinkman, J. P. Maita, and A. Menth. Electronic Specific Heat of Metallic Ti-Doped V2O3. Physical Review Letters, 27(14):941–943, October 1971. Publisher: American Physical Society.

[322] Boris Spivak and Steven A. Kivelson. Phases intermediate between a two-dimensional electron liquid and Wigner crystal. Physical Review B, 70(15):155114, October 2004. Publisher: American Physical Society.

[323] M. A. Continentino, A. S. Ferreira, P. G. Pagliuso, C. Rettori, and J. L. Sarrao. Solid state Pomeranchuk effect. Physica B: Condensed Matter, 359-361:744–746, April 2005.

[324] A. Pustogow, M. Bories, A. Löhle, R. Rösslhuber, E. Zhukova, B. Gorshunov, S. Tomić, J. A. Schlueter, R. Hübner, T. Hiramatsu, Y. Yoshida, G. Saito, R. Kato, T.-H. Lee, V. Dobrosavljević, S. Fratini, and M. Dressel. Quantum spin liquids unveil the genuine Mott state. Nature Materials, 17(9):773–777, September 2018. Number: 9 Publisher: Nature Publishing Group.

[325] Pomeranchuk. On the theory of He3. Zhurnal Eksperimental'noi i Teoreticheskoi Fiziki, (20):919–24, 1950.

[326] Yu Saito, Fangyuan Yang, Jingyuan Ge, Xiaoxue Liu, Kenji Watanabe, Takashi Taniguchi, J. I. A. Li, Erez Berg, and Andrea F. Young. Isospin Pomeranchuk effect and the entropy of collective excitations in twisted bilayer graphene. Nature, 592(7853):220–224, April 2021. arXiv: 2008.10830.

[327] Biao Lian. Heating freezes electrons in twisted bilayer graphene. Nature, 592(7853):191–193, April 2021. Bandiera_abtest: a Cg_type: News And Views Number: 7853 Publisher: Nature Publishing Group Subject_term: Condensed-matter physics, Physics.

[328] Francisco Guinea. Pomeranchuk effect in twisted bilayer graphene, November 2020.

[329] Aviram Uri, Sameer Grover, Yuan Cao, J. A. Crosse, Kousik Bagani, Daniel Rodan-Legrain, Yuri Myasoedov, Kenji Watanabe, Takashi Taniguchi, Pilkyung Moon, Mikito Koshino, Pablo Jarillo-Herrero, and Eli Zeldov. Mapping the twist angle and unconventional Landau levels in magic angle graphene. arXiv:1908.04595 [cond-mat], August 2019. arXiv: 1908.04595.

[330] Xiaomeng Liu, Zeyu Hao, Eslam Khalaf, Jong Yeon Lee, Yuval Ronen, Hyobin Yoo, Danial Haei Najafabadi, Kenji Watanabe, Takashi Taniguchi, Ashvin Vishwanath, and Philip Kim. Tunable spin-polarized correlated states in twisted double bilayer graphene. Nature, 583(7815):221–225, July 2020. Number: 7815 Publisher: Nature Publishing Group.

[331] Yuan Cao, Daniel Rodan-Legrain, Oriol Rubies-Bigorda, Jeong Min Park, Kenji Watanabe, Takashi Taniguchi, and Pablo Jarillo-Herrero. Tunable correlated states and spin-polarized phases in twisted bilayer–bilayer graphene. Nature, 583(7815):215–220, July 2020. Number: 7815 Publisher: Nature Publishing Group.

[332] Cheng Shen, Yanbang Chu, QuanSheng Wu, Na Li, Shuopei Wang, Yanchong Zhao, Jian Tang, Jieying Liu, Jinpeng Tian, Kenji Watanabe, Takashi Taniguchi, Rong Yang, Zi Yang Meng, Dongxia Shi, Oleg V. Yazyev, and Guangyu Zhang. Correlated states in twisted double bilayer graphene. Nature Physics, 16(5):520–525, May 2020. Number: 5 Publisher: Nature Publishing Group.

[333] Guorui Chen, Lili Jiang, Shuang Wu, Bosai Lyu, Hongyuan Li, Bheema Lingam Chittari, Kenji Watanabe, Takashi Taniguchi, Zhiwen Shi, Jeil Jung, Yuanbo Zhang, and Feng Wang. Evidence of a gate-tunable Mott insulator in a trilayer graphene moiré superlattice. Nature Physics, 15(3):237–241, March 2019. Number: 3 Publisher: Nature Publishing Group.

[334] D. N. Basov, M. M. Fogler, and F. J. García de Abajo. Polaritons in van der Waals materials. Science, 354(6309), October 2016. Publisher: American Association for the Advancement of Science.

[335] Tony Low, Andrey Chaves, Joshua D. Caldwell, Anshuman Kumar, Nicholas X. Fang, Phaedon Avouris, Tony F. Heinz, Francisco Guinea, Luis Martin-Moreno, and Frank Koppens. Polaritons in layered two-dimensional materials. Nature Materials, 16(2):182–194, February 2017. Number: 2 Publisher: Nature Publishing Group.

[336] S. S. Sunku, G. X. Ni, B. Y. Jiang, H. Yoo, A. Sternbach, A. S. McLeod, T. Stauber, L. Xiong, T. Taniguchi, K. Watanabe, P. Kim, M. M. Fogler, and D. N. Basov. Photonic crystals for nano-light in moiré graphene superlattices. Science, 362(6419):1153–1156, December 2018. Publisher: American Association for the Advancement of Science.

[337] G. X. Ni, H. Wang, J. S. Wu, Z. Fei, M. D. Goldflam, F. Keilmann, B. Özyilmaz, A. H. Castro Neto, X. M. Xie, M. M. Fogler, and D. N. Basov. Plasmons in graphene moiré superlattices. Nature Materials, 14(12):1217–1222, December 2015. Number: 12 Publisher: Nature Publishing Group.

[338] F. Hu, Suprem R. Das, Y. Luan, T.-F. Chung, Y.P. Chen, and Z. Fei. Real-Space Imaging of the Tailored Plasmons in Twisted Bilayer Graphene. Physical Review Letters, 119(24):247402, December 2017. Publisher: American Physical Society.

[339] Achim Woessner, Mark B. Lundeberg, Yuanda Gao, Alessandro Principi, Pablo Alonso-González, Matteo Carrega, Kenji Watanabe, Takashi Taniguchi, Giovanni Vignale, Marco Polini, James Hone, Rainer Hillenbrand, and Frank H. L. Koppens. Highly confined low-loss plasmons in graphene–boron nitride heterostructures. Nature Materials, 14(4):421–425, April 2015. Number: 4 Publisher: Nature Publishing Group.

[340] Pilkyung Moon and Mikito Koshino. Optical absorption in twisted bilayer graphene. Physical Review B, 87(20):205404, May 2013. Publisher: American Physical Society.

[341] Tobias Stauber, Pablo San-Jose, and Luis Brey. Optical conductivity, Drude weight and plasmons in twisted graphene bilayers. New Journal of Physics, 15(11):113050, November 2013. Publisher: IOP Publishing.

[342] C. J. Tabert and E. J. Nicol. Optical conductivity of twisted bilayer graphene. Physical Review B, 87(12):121402, March 2013. Publisher: American Physical Society.

[343] Cyprian Lewandowski and Leonid Levitov. Intrinsically undamped plasmon modes in narrow electron bands. Proceedings of the National Academy of Sciences, 116(42):20869–20874, October 2019.

[344] Tobias Stauber and Heinerich Kohler. Quasi-Flat Plasmonic Bands in Twisted Bilayer Graphene. Nano Letters, 16(11):6844–6849, November 2016. Publisher: American Chemical Society.

[345] S. Das Sarma and Qiuzi Li. Intrinsic plasmons in two-dimensional Dirac materials. Physical Review B, 87(23):235418, June 2013. Publisher: American Physical Society.

[346] Jun-Yu Ou, Jin-Kyu So, Giorgio Adamo, Azat Sulaev, Lan Wang, and Nikolay I. Zheludev. Ultraviolet and visible range plasmonics in the topological insulator Bi 1.5 Sb 0.5 Te 1.8 Se 1.2. Nature Communications, 5(1):5139, October 2014. Number: 1 Publisher: Nature Publishing Group.

[347] Alexander M. Dubrovkin, Giorgio Adamo, Jun Yin, Lan Wang, Cesare Soci, Qi Jie Wang, and Nikolay I. Zheludev. Visible Range Plasmonic Modes on Topological Insulator Nanostructures. Advanced Optical Materials, 5(3):1600768, 2017.

[348] Alexander L. Fetter. Edge magnetoplasmons in a two-dimensional electron fluid confined to a half-plane. Physical Review B, 33(6):3717–3723, March 1986. Publisher: American Physical Society.

[349] Fritz Keilmann and Rainer Hillenbrand. Near-field microscopy by elastic light scattering from a tip. Philosophical Transactions. Series A, Mathematical, Physical, and Engineering Sciences, 362(1817):787–805, April 2004.

[350] Bor-Yuan Jiang, Guang-Xin Ni, Zachariah Addison, Jing K. Shi, Xiaomeng Liu, Shu Yang Frank Zhao, Philip Kim, Eugene J. Mele, Dimitri N. Basov, and Michael M. Fogler. Plasmon Reflections by Topological Electronic Boundaries in Bilayer Graphene. Nano Letters, 17(11):7080–7085, November 2017. Publisher: American Chemical Society.

[351] Jianing Chen, Maxim L. Nesterov, Alexey Yu. Nikitin, Sukosin Thongrattanasiri, Pablo Alonso-González, Tetiana M. Slipchenko, Florian Speck, Markus Ostler, Thomas Seyller, Iris Crassee, Frank H. L. Koppens, Luis Martin-Moreno, F. Javier García de Abajo, Alexey B. Kuzmenko, and Rainer Hillenbrand. Strong Plasmon Reflection at Nanometer-Size Gaps in Monolayer Graphene on SiC. Nano Letters, 13(12):6210–6215, December 2013. Publisher: American Chemical Society.

[352] Phaedon Avouris, Tony F. Heinz, and Tony Low. 2D materials: Properties and devices. Cambridge University Press, January 2017.

[353] Gabriele Giuliani and Giovanni Vignale. Quantum Theory of the Electron Liquid. Cambridge University Press, Cambridge, 2005.

[354] Pablo Alonso-González, Alexey Y. Nikitin, Yuanda Gao, Achim Woessner, Mark B. Lundeberg, Alessandro Principi, Nicolò Forcellini, Wenjing Yan, Saül Vélez, Andreas J. Huber, Kenji Watanabe, Takashi Taniguchi, Félix Casanova, Luis E. Hueso, Marco Polini, James Hone, Frank H. L. Koppens, and Rainer Hillenbrand. Acoustic terahertz graphene plasmons revealed by photocurrent nanoscopy. Nature Nanotechnology, 12(1):31–35, January 2017. Number: 1 Publisher: Nature Publishing Group.

[355] Yongqing Cai, Litong Zhang, Qingfeng Zeng, Laifei Cheng, and Yongdong Xu. Infrared reflectance spectrum of BN calculated from first principles. Solid State Communications, 141(5):262–266, February 2007.

[356] Mikito Koshino, Noah F.Q. Yuan, Takashi Koretsune, Masayuki Ochi, Kazuhiko Kuroki, and Liang Fu. Maximally Localized Wannier Orbitals and the Extended Hubbard Model for Twisted Bilayer Graphene. Physical Review X, 8(3):031087, September 2018. Publisher: American Physical Society.

[357] F. Guinea, M. I. Katsnelson, and A. K. Geim. Energy gaps and a zero-field quantum Hall effect in graphene by strain engineering. Nature Physics, 6(1):30–33, January 2010. Bandiera_abtest: a Cg_type: Nature Research Journals Number: 1 Primary_atype: Research Publisher: Nature Publishing Group.

[358] Girish Sharma, Maxim Trushin, Oleg P. Sushkov, Giovanni Vignale, and Shaffique Adam. Superconductivity from collective excitations in magic-angle twisted bilayer graphene. Physical Review Research, 2(2):022040, May 2020. Publisher: American Physical Society.

[359] María J. Calderón and Elena Bascones. Correlated states in magic angle twisted bilayer graphene under the optical conductivity scrutiny. npj Quantum Materials, 5(1):1–6, August 2020. Number: 1 Publisher: Nature Publishing Group.

[360] Nicholas Rivera and Ido Kaminer. Light–matter interactions with photonic quasiparticles. Nature Reviews Physics, 2(10):538–561, October 2020. Number: 10 Publisher: Nature Publishing Group.

[361] Jamie M. Fitzgerald, Prineha Narang, Richard V. Craster, Stefan A. Maier, and Vincenzo Giannini. Quantum Plasmonics. Proceedings of the IEEE, 104(12):2307–2322, December 2016.

[362] Edward McCann and Mikito Koshino. The electronic properties of bilayer graphene. Reports on Progress in Physics, 76(5):056503, April 2013.

[363] B. Hunt, J. D. Sanchez-Yamagishi, A. F. Young, M. Yankowitz, B. J. LeRoy, K. Watanabe, T. Taniguchi, P. Moon, M. Koshino, P. Jarillo-Herrero, and R. C. Ashoori. Massive Dirac Fermions and Hofstadter Butterfly in a van der Waals Heterostructure. Science, 340(6139):1427–1430, June 2013.

[364] L. A. Ponomarenko, R. V. Gorbachev, G. L. Yu, D. C. Elias, R. Jalil, A. A. Patel, A. Mishchenko, A. S. Mayorov, C. R. Woods, J. R. Wallbank, M. Mucha-Kruczynski, B. A. Piot, M. Potemski, I. V. Grigorieva, K. S. Novoselov, F. Guinea, V. I. Fal'ko, and A. K. Geim. Cloning of Dirac fermions in graphene superlattices. Nature, 497(7451):594–597, May 2013.

[365] C. R. Dean, L. Wang, P. Maher, C. Forsythe, F. Ghahari, Y. Gao, J. Katoch, M. Ishigami, P. Moon, M. Koshino, T. Taniguchi, K. Watanabe, K. L. Shepard, J. Hone, and P. Kim. Hofstadter's butterfly and the fractal quantum Hall effect in moiré superlattices. Nature, 497(7451):598–602, May 2013.

[366] Ya-Hui Zhang, Dan Mao, Yuan Cao, Pablo Jarillo-Herrero, and T. Senthil. Nearly flat Chern bands in moir\'e superlattices. Physical Review B, 99(7):075127, February 2019.

[367] Youngwook Kim, Patrick Herlinger, Pilkyung Moon, Mikito Koshino, Takashi Taniguchi, Kenji Watanabe, and Jurgen H. Smet. Charge Inversion and Topological Phase Transition at a Twist Angle Induced van Hove Singularity of Bilayer Graphene. Nano Letters, 16(8):5053–5059, August 2016.

[368] Guorui Chen, Aaron L. Sharpe, Patrick Gallagher, Ilan T. Rosen, Eli J. Fox, Lili Jiang, Bosai Lyu, Hongyuan Li, Kenji Watanabe, Takashi Taniguchi, Jeil Jung, Zhiwen Shi, David Goldhaber-Gordon, Yuanbo Zhang, and Feng Wang. Signatures of tunable superconductivity in a trilayer graphene moiré superlattice. Nature, 572(7768):215–219, August 2019.

[369] Mikito Koshino. Band structure and topological property of twisted double bilayer graphenes. Physical Review B, 99(23):235406, June 2019.

[370] Jong Yeon Lee, Eslam Khalaf, Shang Liu, Xiaomeng Liu, Zeyu Hao, Philip Kim, and Ashvin Vishwanath. Theory of correlated insulating behaviour and spin-triplet superconductivity in twisted double bilayer graphene. Nature Communications, 10:5333, 2019. arXiv: 1903.08685.

[371] A. Raymond, J. L. Robert, C. Bousquet, W. Zawadzki, F. Alexandre, and I. M. Masson. Gigantic exchange enhancement of spin g-factor for two-dimensional electron gas in GaAs. Solid State Communications, 55(4):271–274, July 1985.

[372] A. F. Young, C. R. Dean, L. Wang, H. Ren, P. Cadden-Zimansky, K. Watanabe, T. Taniguchi, J. Hone, K. L. Shepard, and P. Kim. Spin and valley quantum Hall ferromagnetism in graphene. Nature Physics, 8(7):550–556, July 2012.

[373] G. William Burg, Jihang Zhu, Takashi Taniguchi, Kenji Watanabe, Allan H. MacDonald, and Emanuel Tutuc. Correlated Insulating States in Twisted Double Bilayer Graphene. Physical Review Letters, 123(19):197702, November 2019. Publisher: American Physical Society.

[374] Minhao He, Jiaqi Cai, Ya-Hui Zhang, Yang Liu, Yuhao Li, Takashi Taniguchi, Kenji Watanabe, David H. Cobden, Matthew Yankowitz, and Xiaodong Xu. Chirality-dependent topological states in twisted double bilayer graphene. arXiv:2109.08255 [cond-mat], September 2021. arXiv: 2109.08255.

[375] Minhao He, Yuhao Li, Jiaqi Cai, Yang Liu, K. Watanabe, T. Taniguchi, Xiaodong Xu, and Matthew Yankowitz. Symmetry breaking in twisted double bilayer graphene. Nature Physics, 17(1):26–30, January 2021. Number: 1 Publisher: Nature Publishing Group.

[376] Alexandre Jaoui, Ipsita Das, Giorgio Di Battista, Jaime Díez-Mérida, Xiaobo Lu, Kenji Watanabe, Takashi Taniguchi, Hiroaki Ishizuka, Leonid Levitov, and Dmitri K. Efetov. Quantum-critical continuum in magic-angle twisted bilayer graphene. arXiv:2108.07753 [cond-mat], August 2021. arXiv: 2108.07753.

[377] Eva Y. Andrei, Dmitri K. Efetov, Pablo Jarillo-Herrero, Allan H. MacDonald, Kin Fai Mak, T. Senthil, Emanuel Tutuc, Ali Yazdani, and Andrea F. Young. The marvels of moiré materials. Nature Reviews Materials, 6(3):201–206, March 2021. Number: 3 Publisher: Nature Publishing Group.

[378] Trithep Devakul, Valentin Crépel, Yang Zhang, and Liang Fu. Magic in twisted transition metal dichalcogenide bilayers. Nature Communications, 12(1):6730, November 2021. Number: 1 Publisher: Nature Publishing Group.

[379] Rebeca Ribeiro-Palau, Changjian Zhang, Kenji Watanabe, Takashi Taniguchi, James Hone, and Cory R. Dean. Twistable electronics with dynamically rotatable heterostructures. Science, 361(6403):690–693, August 2018. Publisher: American Association for the Advancement of Science.

[380] Feliciano Giustino, Jin Hong Lee, Felix Trier, Manuel Bibes, Stephen M. Winter, Roser Valentí, Young-Woo Son, Louis Taillefer, Christoph Heil, Adriana I. Figueroa, Bernard Plaçais, QuanSheng Wu, Oleg V. Yazyev, Erik P. A. M. Bakkers, Jesper Nygård, Pol Forn-Díaz, Silvano De Franceschi, J. W. McIver, L. E. F. Foa Torres, Tony Low, Anshuman Kumar, Regina Galceran, Sergio O. Valenzuela, Marius V. Costache, Aurélien Manchon, Eun-Ah Kim, Gabriel R. Schleder, Adalberto Fazzio, and Stephan Roche. The 2021 quantum materials roadmap. Journal of Physics: Materials, 3(4):042006, October 2020. Publisher: IOP Publishing.

[381] Alex Thomson, Ina Sorensen, Stevan Nadj-Perge, and Jason Alicea. Gate-defined wires in twisted bilayer graphene: from electrical detection of inter-valley coherence to internally engineered Majorana modes. arXiv:2105.02891 [cond-mat], June 2021. arXiv: 2105.02891.

[382] Paul Seifert, Xiaobo Lu, Petr Stepanov, José Ramón Durán Retamal, John N. Moore, Kin-Chung Fong, Alessandro Principi, and Dmitri K. Efetov. Magic-Angle Bilayer Graphene Nanocalorimeters: Toward Broadband, Energy-Resolving Single Photon Detection. Nano Letters, 20(5):3459–3464, May 2020. Publisher: American Chemical Society.

[383] Joel I-J. Wang, Megan A. Yamoah, Qing Li, Amir H. Karamlou, Thao Dinh, Bharath Kannan, Jochen Braumüller, David Kim, Alexander J. Melville, Sarah E. Muschinske, Bethany M. Niedzielski, Kyle Serniak, Youngkyu Sung, Roni Winik, Jonilyn L. Yoder, Mollie E. Schwartz, Kenji Watanabe, Takashi Taniguchi, Terry P. Orlando, Simon Gustavsson, Pablo Jarillo-Herrero, and William D. Oliver. Hexagonal boron nitride as a low-loss dielectric for superconducting quantum circuits and qubits. Nature Materials, January 2022.

[384] Abhinandan Antony, Martin V. Gustafsson, Guilhem J. Ribeill, Matthew Ware, Anjaly Rajendran, Luke C. G. Govia, Thomas A. Ohki, Takashi Taniguchi, Kenji Watanabe, James Hone, and Kin Chung Fong. Miniaturizing Transmon Qubits Using van der Waals Materials. Nano Letters, 21(23):10122–10126, December 2021. Publisher: American Chemical Society.